# INTERNATIONAL SYMPOSIUM ON APPLIED SCIENCES AND ENGINEERING

**26-28 November 2018**
Ataturk University, **Erzurum / Turkey**

# ISASE2018

ATATÜRK ÜNİVERSİTESİ | ERZURUM TEKNİK ÜNİVERSİTESİ | UPM UNIVERSITI PUTRA MALAYSIA

2018

# ISASE2018

## INTERNATIONAL SYMPOSIUM ON APPLIED SCIENCES AND ENGINEERING

## BOOK OF FULL TEXT

### 26-28 November 2018 / Erzurum, Turkey

**Organized by**

**Sponsored by**

**15 December 2018**

# Book of Full Text of the International Syposium on Applied Sciences and Engineering (ISESA2018)

It is a pleasure for me to offer you Full Text Book for the International Symposium on Applied Sciences and Engineering (ISASE2018). Our goal was to create a scientific platform between our universities that introduces the newest results on internationally recognized experts to local students and colleagues and simultaneously displays relevant Turkish achievements to the world. The positive feedback of the community encouraged us to proceed and transform a single event into a conference series. Now, ISASE2018 is honored by the presence of over 150 colleagues from 6 different countries. We accepted contributions from all fields of science and applied engineering to promote multidisciplinary discussions. The focal points of the conference emerged spontaneously from the submitted full- texts: civil, metalurrgy, material, food sciences, bioengineering, electrical engineering, energy applications, advanced materials, electronics engineering, optoelectronic devices, nanodiveces, foresty and others. UPM has participated this conference with 25 faculty members and 5 students. There are also participations from Jordan, Iran, Spain, Morocco and also regional universities. In this conference, 13 invited, 71 oral and 24 poster presentations presented in 16 session in 2 parallel rooms. Our warmest thanks go to all invited speakers, authors, and contributors of ISASE2018 for attending to the conference. We look forward to meeting you again in one of the forthcoming ISASE2018 events in Malaysia.

Prof. Dr. Mehmet ERTUGRUL

Editor

# Copyright

Original material in this book may be reproduced with the permission of the publisher, provided that (1) the material is not reproduced for sale or profitable gain, (2) the author is informed, and (3) the material is prominently identified as coming from the International Symposium of Appliend Sciences and Engineering: The authors are responsible for the contents of their abstracts and full pappers. The views expressed in the abstracts and fulltex in this publication are those of the individual authors and are not necessarily shared by the editor or the reviewers.

# Committees

## Honorary Committee

Prof. Dr. Ömer Çomaklı (Rector, Ataturk University)

Prof. Datin Paduka Dato' Dr. Aini Ideris (Rector, Universiti Putra Malaysia)

Prof. Dr. Muammer Yaylalı (Rector, Erzurum Technical University)

## Organizing Committee

Prof. Dr. Bülent Çakmak

Prof. Dr. Ayhan Çelik

Prof. Dr. Medine Güllüce

Prof. Dr. Sezai Ercişli

Prof. Dr. Hikmet Altun

Prof. Dr. Cavit Kazaz

Prof. Dr. Taşkın Öztaş

Prof. Dr. İrfan Kaymaz

Assoc. Prof. Dr. Mohd Nizar Hamidon

Prof. Dr. Mehmet Ertuğrul

Assoc. Prof. Dr. Birol Soysal

Assoc. Prof. İ. Yücel Özbek

Assoc. Prof. Dr. Bülent Çavuşoğlu

Assist. Prof. Dr. Serdar Aydın

Assist. Prof. Dr. Emin A. Oral

Assist. Prof. Dr. Ömer Faruk Karataş

# Scientific Committee

Prof. Dr. Mehmet Ertuğrul, Ataturk University, Turkey

Prof. Dr. Karim Abbasian, Tabriz University, Iran

Prof. Dr. Xerman De la Fuente Leis, University of Zaragoza, Spain

Prof. Dr. Bülent Çakmak, Erzurum Tecnical University, Turkey

Prof. Dr. Dia İbrahim Abu-Al-Nadi, University of Jordan, Jordan

Prof. Dr. İrfan Kaymaz, Erzurum Technical University, Turkey

Prof. Dr. Mohd Basyaruddin Abdul Rahman, University of Putra Malaysia, Malaysia

Prof. Dr. Hasan Efeoğlu, Ataturk University, Turkey

Prof. Dr. Tevhit Karacalı, Ataturk University, Turkey

Prof. Dr. Taşkın Öztaş, Ataturk University, Turkey

Prof. Dr. Cavit Kazaz, Ataturk University, Turkey

Prof. Dr. Taner Tekin, Ataturk University, Turkey

Prof. Dr. Ergün Yıldız, Ataturk University, Turkey

Prof. Dr. Yaşar Totik, Ataturk University, Turkey

Prof. Dr. Ahmet Tortum, Ataturk University, Turkey

Prof. Dr. Burak Dikici, Ataturk University, Turkey

Prof. Dr. Nihat Akbulut, Ataturk University, Turkey

Prof. Dr. A. Samet Haşıloğlu, Ataturk University, Turkey

Prof. Dr. Yakup Kurucu, Ataturk University, Turkey

Prof. Dr. Esabi Başaran Kurbanoğlu, Ataturk University, Turkey

Prof. Dr. Abdullah Kopuzlu, Ataturk University, Turkey

Prof. Dr. Ahmet Adıgüzel, Ataturk University, Turkey

Prof. Dr. Cahit Yeşilyaprak, Ataturk University, Turkey

Prof. Dr. Köksal Erentürk, Ataturk University, Turkey

Assoc. Prof. Dr. Birol Soysal, Ataturk University, Turkey

Assoc. Prof. Dr. Nizar Bin Hamidon, University of Putra Malaysia, Malaysia

Assoc. Prof. Dr. Abdul Halim Abdullah, University of Putra Malaysia, Malaysia

Assoc. Prof. Dr. Suraya Abdul Rashid, University of Putra Malaysia, Malaysia

Assoc. Prof. Dr. Mohd Nizar Hamidon, University of Putra Malaysia, Malaysia

Assoc. Prof. Dr. Khamirul Amin Matori, University of Putra Malaysia, Malaysia

Assoc. Prof. Dr. Rosnita A Talib, University of Putra Malaysia, Malaysia

Assoc. Prof. Dr. Zulkiflle Leman, University of Putra Malaysia, Malaysia

Assoc. Prof. Dr B.T. Hang Tuah Bin Baharudin, University of Putra Malaysia, Malaysia

Assoc. Prof. Dr. Jasronita Jasni, University of Putra Malaysia, Malaysia

Assoc. Prof. Dr. Bülent Çavuşoğlu, Ataturk University, Turkey

Assoc. Prof. Dr. İ. Yücel Özbek, Ataturk University, Turkey

Assist. Prof. Dr. Emin A. Oral, Ataturk University, Turkey

Assit. Prof. Abdullah Basci, Turkey

Assist Prof. Muhammed Fatih Çorapsız, Turkey

Assist. Prof. Dr. Gökay Akkaya, Ataturk University, Turkey

Assist. Prof. Dr. Ömer Faruk Karakaş, Ataturk University, Turkey

## Local Conference Venue Committee

Atakan Abuşoğlu, Atatürk University, Turkey

Meltem Gör Bölen, Erzurum Technical University, Turkey

Merve Acar, Ataturk University, Turkey

Hilal Koç, Erzurum Technical University, Turkey

Işıl Karabey, Erzurum Technical University, Turkey

Ayşe Bağıran, Ataturk University, Turkey

Kaan Can, Ataturk University, Turkey

Mehmet Yılmaz, Ataturk University, Turkey

Aslınur Ömeroğlu, Ataturk University, Turkey

Bahadır Özkılbaç, Ataturk University, Turkey

# CONTENTS

## INVITED PAPERS

## ORAL PRESENTATIONS

# Welcome to ISASE2018

As it is known, our relations between Atatürk University and Universiti Putra Malaysia (UPM) have evolved into a strategic partnership in the last few years. Within the scope of this strategic partnership developed between our university and UPM, the "International Symposium on Applied Sciences and Engineering" will be carried out by the other partner in every other year. The reason we are here is to start the first of this conference with the strong support of the Erzurum Technical University. In this conference, scientific studies by faculty members and their students will be presented as oral and poster presentation. This meeting will be a platform to develop a long-term cooperation both during the conference and after the conference with department and laboratory visits. In addition, students and co-advisors from both sides for dual and joint degree programs will be tried to find and thesis topics and projects will be tried to be develop.

UPM has participated this conference with 25 faculty members and 5 students. There are also participations from Jordan, Iran, Spain, Morocco and also regional universities. In this conference, 13 invited, 71 oral and 24 poster presentations presented in 16 session in 2 parallel rooms.

I would like to express my gratitude to Prof. Dr. Ömer Çomaklı, the rector of the Atatürk University, and Prof. Datin Paduka Dr. Aini Ideris, the rector of the UPM to start to strong collaboration between us. I also have to give a special thanks to our rector who provided all kinds of material and spiritual support in our meeting. I would also like to thank Prof. Dr. Muammer Yaylalı, the Rector of Erzurum Technical University, who gave strong support to the conference. In addition, I would like to thank Asso. Prof. Dr. Bülent Çavuşoğlu, Prof Dr Mohd Nizar Hamidon, Dr. İsmayadi İsmail, the organizing and scientific committee members who contributed to the organization of the conference.

Best regards,


Chairman of the Conference

**Prof. Dr. Mehmet ERTUĞRUL**

# Ataturk University Rector's Welcome

**Dear Esteemed Members of Scientific World,**

I would like to express my happiness in being here with you in the "International Symposioum on Appplied Science and Engineering 2018 (ISASE 2018)", which has contributed to the renewal of our relations in the context of our mutual friendship and scientific relations of our universities that have been becoming stronger for several years.

Turkey and Malaysia, the two brother countries connected with deep scientific and cultural relations, have always been in a good relationship. It is a pleasure for us to see that this old friendship and bilateral relations between our countries increasingly continue today. In this context, one of our strong relationships is the academic cooperation between our universities.

Ataturk University, opened its doors to the world at the center of an extraordinary historical and cultural richness on the historical Silk Road linking Asia to Europe, has an experience of 61 academic years with 23 faculties, 2 schools, 12 vocational schools, 8 institutes, 2400 academic staff, up to 350,000 students and takes firm steps to the future to be a world university with cultural democracy.

One of the most important goals of the restructuring YÖK, the goal of internationalization, has urgently brought our universities to the point of carrying out studies related to this subject. It is now important that universities find an international place with what they do for internationalization, not how old or new, how big or small they are. As Atatürk University administration, the most sensitive issue that we focus on is always to go one step ahead on internationalization with the opportunities that we have.

As you know, higher education takes a central role in not only bringing individuals' professional formation, but also raising individuals that contribute to the enrichment of universal fund of knowledge.

The way to accomplish this is through internationalization. We give great importance to internationalization which we see as an important roadmap for becoming a world university within the theoretical and practical framework of the construction of our university according to the necessities of time. We plan academic and student mobility, taking into account current global trends in exchange programs and this type of jointly structured international symposiums. Taking into consideration the information society and economy, we initiate the transformation movements of the "new generation Entrepreneur University" model.

To increase the international visibility and credibility of our university, to strengthen our international collaborations, to develop new international opportunities for our academicians, students and administrative staff, to transform our university into an international brand, to provide superior education at universal level, to make the most possible comprehensive scientific, technical and educational cooperation possible are among our important goals that we have set.

I believe this symposium is a very good initiative to strengthen the relations between UPM and Atatürk University. I also believe that more solid scientific relationships can be constructed between Malaysia and Turkey by the means of the scientific and cultural bridge we have been establishing.

As the last word I would like to express that I believe that the conference we are hosting now is not just a scientific conference but also it is a big connecting bridge between our countries towards having very strong relations between two countries. I hope to meet with you all again in the second of these conference series at UPM in 2019.

**Prof. Dr. Ömer ÇOMAKLI**
**Rector of Ataturk University**

# Universiti Putra Malaysia Rector's Welcome

**In the Name of Allah, the most Beneficent, the most Merciful.**

**Assalamualaikum Warahmatullahi Wabarakatuh**

I am truly happy to see that Malaysian and Turkish Scientific Committees have come together through the International Symposium on Applied Sciences and Engineering 2018 (ISASE 2018) organized by both countries. As two strong members of Islamic community, we need to take the pioneering role to increase the scientific collaborations among Islamic nations especially.

Universiti Putra Malaysia (UPM), as a premier institution of higher learning and research will always support efforts towards achieving excellence through various programs which are in line with our mission to make meaningful contributions towards wealth creation, nation building and universal human advancement through the exploration and dissemination of knowledge. Known as one of the top Research Universities in Malaysia, UPM strives to continue to provide new meaning to the progress, growth and development of the nation and the world every year.

UPM has boosted its ranking to the 202nd position in the Quacquarelli Symonds (QS) World University Rankings 2018/19 and jumped 27 notches from the 229th position last year, its fifth consecutive rise since 2013. The entire university community should maintain momentum to sustain international excellence as higher education is a very competitive industry.

I would like to thank all presenters for their valuable contributions. UPM, Ataturk University and Erzurum Technical University had put forth great efforts to make this conference possible. Our delegates had an opportunity to see the facilities in Turkey, and scientists from both countries had a chance to discuss further collaborations. I sincerely hope that these conference series open the path for successful and fruitful international collaborations. We are honored and would like to welcome all of you for the second series of this conference which is going to be held in UPM, Malaysia in 2019.

Thank you.

**"With Knowledge We Serve"**

**PROF. DATIN PADUKA DATO' DR. AINI IDERIS,** *FASc.*

# Erzurum Technical University Rector's Welcome

**Dear Valuable Guests,**

It is my pleasure to see this scientific community in Erzurum. As Erzurum Technical University, our goal is to make every effort possible to create international collaborations. We believe that internationally organized scientific committees, projects and studies tend to evolve more quickly and efficiently. We are honored to see our brothers from Malaysia here. Especially, we have great hope that Erzurum Technical University, Ataturk University and UPM will be able to take necessary actions to make this scientific collaborations possible. All three universities have strong background in the area of science and Applied Engineering. I see here many scientists who are really good at their area of studies. I am hoping that next year when we come together again we would be talking about solid and exciting projects of which the first milestones will have already been established. I would like to thank you all for your valuable contributions.

**Prof. Dr. Muammer YAYLALI**

**Rector of Erzurum Technical University**

# Ataturk University OIA Director's Welcome

**Dear Distinguished Scientists and Participants,**

Firstly, I would like to express my deepest thanks to the Scientific Committee and all the participants from Ataturk University and the University of Putra Malaysia who put extraordinary efforts to make this symposium successful.

Atatürk University has been successfully continuing its education and research activities for more than 60 years. Our University is one of the most peaceful university with the highest life standards among the universities in Turkey. With its nearly 400 000 students, more than 2 500 academic staff, modern research facilitates and a fully constructed campus, Atatürk University is open for collaborations with the well-known universities around the World. It has more than 3 000 international students from 87 different countries and international collaborations with more than 60 countries.
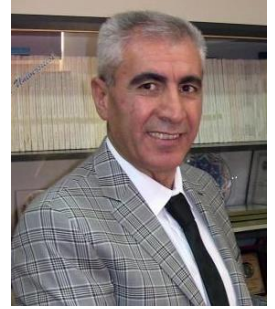
Atatürk University aims to maximize the interactions among education, research and social contribution with the "New Generation University Design and Transformation Project" initiated recently. In this context, Atatürk University aims at more internationalization and rapidly develops its scientific cooperation with reputable universities on a universal scale. Therefore, Atatürk University is strongly willing to increase and promoting international activities in the fields of scientific research programs and projects, and exchange of students and academic staff.

The International Symposium on Applied Sciences and Engineering 2018 is a concrete outcome of the joint efforts initiated by Atatürk University and the University of Putra Malaysia under academic cooperation. This symposium is also an important starting point for academic and student mobility programs between two Universities.

I believe that this symposium experience not only help to broaden our academician's horizons in both Universities and to encourage them for developing new joint research projects, but also help to strengthen the relations between Atatürk University and the University of Putra Malaysia.

I hope to meet with you all again in another meeting under this scope.

**Prof. Dr. Taşkın Öztaş**

**General Coordinator**
**The Office of Foreign Affairs, Atatürk University**

# INVITED PAPERS

# Fuel Cell Materials

Ayşe Bayrakçeken Yurtcan
*Engineering Faculty, Department of*
*Chemical Engineering*
*Atatürk University*
Erzurum, Turkey
abayrakceken@atauni.edu.tr

*Abstract*—**Fuel cells are the electrochemical devices that directly convert the chemical energy into electrical energy. Proton exchange membrane (PEM) fuel cells are the most promising fuel cell types for mobile and portable applications due to their high power densities and low operating conditions. The heart of a PEM fuel cell, comprised of the electrodes and the membrane, is the key component for improved performance. This component is called as membrane electrode assembly (MEA). In this study, a brief summary of the studies conducted in Atatürk University related with the components of MEA will be given.**

*Keywords—fuel cell, catalyst, carbon, hydrophobicity*

## I. INTRODUCTION

Electricity generation is of great importance in our century due to the technological developments. Fuel cells are important electricity generation devices that can be used either for stationary or mobile and portable applications. Depending on the types of the fuel cells the application areas are changed. Fuel cells are the electrochemical devices that directly convert the chemical energy into electrical energy. Proton exchange membrane (PEM) fuel cells seem to be the most suitable ones for mobile and portable applications due to their high power density and low operating conditions. PEM fuel cell components strongly affect the performance. The most important component in a PEM fuel cell is the membrane electrode assembly (MEA) in which the half cell reactions and proton conduction occur.

A single PEM fuel cell is comprised of a polymer electrolyte membrane sandwiched in between two thin electrodes (Figure 1). Hydrogen, is fed to the anode, in which hydrogen oxidation reaction occurs, where Pt catalyst separates hydrogen's negatively charged electrons from positively charged ions (protons). At the cathode, oxygen/air is combined with electrons and protons and produce water. The protons pass through anode to cathode with the help of a proton conducting membrane (which allows only $H^+$ ions, not electrons), and electrons pass through the cathode via an external circuit and electricity produced.
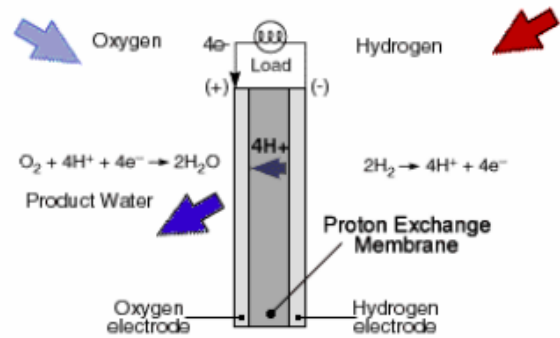


Fig. 1. Schematic representation of PEM fuel cell
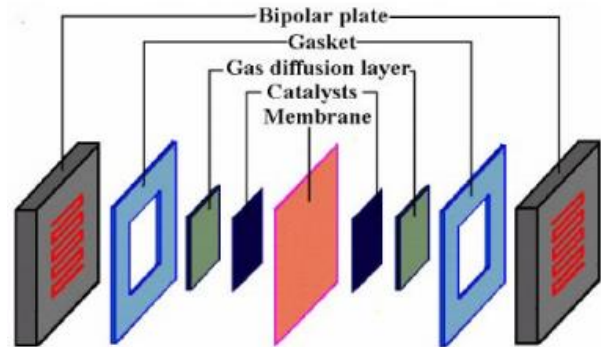


Fig. 2. PEM fuel cell components

A PEM fuel cell consists of the parts given in Figure 2 in which each component is very critical for high performance fuel cells.

Electrolyte is in the form of a proton conducting membrane, and its thickness varies typically between 50 and 175 microns. The properties of the membrane are; conductance of protons, separation of hydrogen and air, and electronic isolation.

A PEMFC contains two electrodes, an anode and a cathode electrode. At the anode, hydrogen is oxidized to protons, while at the cathode oxygen (from air) is reduced to water. The state-of-the-art electrodes contain carbon supported platinum catalysts. The platinum loading is generally 0.2-0.4 mg platinum per $cm^2$ electrode area. Current state of the art of catalyst layers for gas diffusion electrodes utilizes carbon supported Pt as the catalyst for oxygen reduction at the cathode. The primary role of the carbon support is to provide electrical conduction between the Pt catalyst particles and the porous current collector (carbon cloth or paper) [1]. Platinum is the basic metal that is used for anode and cathode electrodes of PEMFCs because

of its high catalytic activity for both oxidation and reduction reactions [2]. However, platinum is an expensive metal which causes the price of MEAs to be prohibitively high for commercialization and widespread usage of fuel cells [3]. For both anode and cathode sides, carbon supported Pt is used as the electrodes. In order to facilitate transport of protons into the catalyst layer, a proton conducting polymer (e.g.Nafion) is mixed with the catalyst. Nafion impregnation is extending the three-dimensional reaction zone.

The electrode backing (gas diffusion layer) serves as current collector, gas distributor and improves water management in the fuel cell. Both carbon cloths and carbon papers are used. The carbon cloths generally contain one or two gas diffusion layers, having a thin (20-30 microns) microporous hydrophobic layer. The gas diffusion layer in a PEMFC consists of a thin layer of carbon black mixed with hydrophobic material that is coated onto a sheet of 12 macroporous carbon backing [4]. These layers are porous enough to allow the distribution of the gases to unexposed areas of the flow channel whereby this distribution permits the complete utilization of the electrode area. The electrical conductivity of these layers may affect the transport of electrons to the current collector from the electrode. The hydrophobicity of these layers may compete with the hydrophilicity of water available for hydration at the membrane. The performance variations may also be due to changes in the porosity, the electrical contact resistance, and the excluded water at the membrane [5].

## II. STUDIES IN ATATÜRK UNIVERSITY

### A. Catalyst Preparation Methods

In our fuel cell research laboratory, mainly two catalyst preparation methods are used; microwave irradiation and supercritical carbon dioxide deposition methods in order to synthesize either single or binary supported catalysts.

Microwave irradiation has a wide variety of applications in chemistry. Many chemical reactions can be accelerated by the utilization of the microwave field which depends on the material having high dielectric constant. For the supported catalysts the dispersion and the uniform distribution is very important for the particle size which will affect the catalyst activity. Microwave irradiation also can be used for the preparation of the fuel cell catalysts which require high quality catalyst properties. In microwave heating there are a lot of parameters which will affect the properties of the material in the microwave oven. Microwave irradiation duration is one of these parameters which affects the temperature.

Pt based carboneous supported catalysts were prepared by using microwave heating of ethylene glycol solutions of the metal precursors. At first, 0.05 M aqueous solutions of metal precursors were prepared. A required volume of these solutions which corresponds to the desired Pt loading was mixed with 50 ml ethylene glycol (EG) in a 100 ml beaker. Then, 0.1 g carboneous support material was added to the solution. After ultrasonication for half an hour, the mixture was put in the center of the microwave oven and heated for 60 s by means of a 800 W microwave power. The resulting suspension was cooled immediately, and then filtered and the residue was washed with acetone. The solid product was dried at 373 K overnight in a vacuum oven (Figure 3).
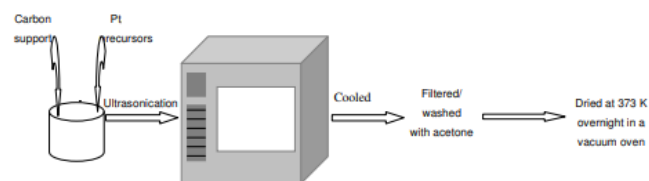

Fig. 3. Microwave irradiation catalyst synthesis method
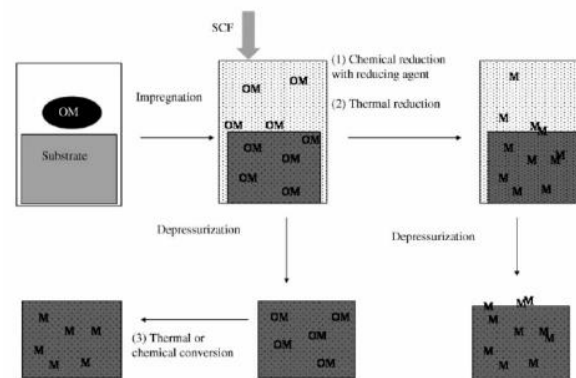

Fig. 4. Schematic of supercritical carbon dioxide deposition method

Metal nanoparticles dispersed on high surface area substrates are used widely as catalysts for a variety of reactions. Carbon supported precious metals are very important in fuel cells. There are several ways of deposition of the metal on carbon support. Among other catalyst preparation techniques, $scCO_2$ deposition method is also attracting increasing attention. There are a lot of parameters that affect the catalytic activity of the catalysts which arise from the catalyst preparation techniques. The impurities left from the solvent or precursor may influence the catalytic activity in a bad manner. The particle size of the metal deposited onto the carbon support also depends on the conditions of the reaction medium and so the preparation technique. Supercritical deposition involves the dissolution of an organometallic precursor in a supercritical fluid and the impregnation of the substrate by exposure to this solution. Subsequent treatment of the impregnated substrate results in metal/substrate nanocomposites [6] (Figure 4).

The deposition apparatus consists of a 54 ml custom-manufactured stainless steel vessel equipped with two sapphire windows, 25 mm in diameter, and sealed with poly ether ether ketone O-rings. A T-type thermocouple assembly, a vent line and a rupture disk assembly are also attached to the vessel (Figure 5).
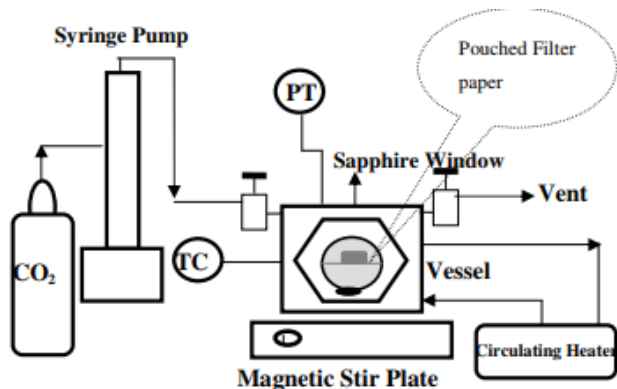
Fig. 5. Supercritical carbon dioxide deposition set up

Impregnation of the organometallic precursors depends on the dissolution of the precursor in scCO$_2$ and then exposure of this solution to the carbon support. Firstly, the heat-treated carbon support was placed into a pouch made of filter paper and placed into the vessel together with a certain amount of either PtMe$_2$COD or other precursors, and a stirring bar. For the desired metal loading, the amounts of the corresponding precursors were determined by using the adsorption isotherm of the precursor onto the carbon support [7]. A stainless steel screen was used to separate the stirring bar from the filter paper pouch. The vessel was sealed and heated to 343 K using a circulating heater/cooler apparatus  and then charged slowly with carbon dioxide to a pressure of 24.2 MPa using a syringe pump. These conditions were maintained for a period of 6 h which was enough for the system to reach equilibrium and then the vessel was depressurized. After allowing the vessel to cool, the pouch was removed and the impregnated carbon support was weighed to determine the amount of precursor adsorbed using an analytical balance accurate to ±0.1 mg. Subsequently, the carbon support was placed in an alumina process tube in a tube furnace, and the Pt and Ru precursors were reduced thermally under flowing N$_2$ (100 cm$^3$ min$^{-1}$) for 4 h at 473 K and 673 K.

Supercritical carbon dioxide deposition method was used to synthesize carboneous materials supported Pt, PtCu, PtNi and PtFe catalysts. Graphene or graphene-carbon hybrid carbon supports were used.

### B. Hydrophobic Surfaces for PEM Fuel Cells

In order to conduct the protons formed at the anode electrode, the electrolyte required to be humidified. This is achieved by the humidification of the fed gases. Also, at the cathode electrode water is formed. In this respect, it is essential to manage the total amount of water either fed to the fuel cell or produced at the cathode side. Excess water resulted in flooding and caused the fuel cell performance to be decreased. In order to eliminate the water related issues, thin microporous layers which includes the hydrophobic materials are used. In our fuel cell research laboratory, PTFE, FEP and PDMS materials were used as hydrophobic materials. The importance of the utilization of different kinds of hydrophobic materials at different ratios were observed.

### C. Carbon Based Materials for PEM Fuel Cells

Carbon based support materials are crucial in PEM fuel cell electrocatalysts which provide either high surface area or high electrical conductivity. In our research laboratory, commercially available carbon black and graphene materials were used. Also, carbon aerogel, reduced graphene oxide and graphene aerogel materials were synthesized. In order to change the properties of the carbon based materials heteroatom such as nitrogen was doped to these materials. In situ and ex-situ nitrogen doping were conducted for this purpose.
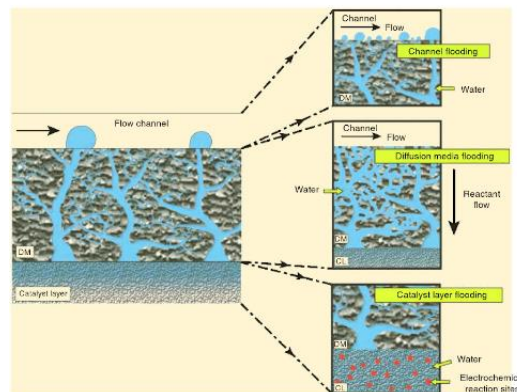


Fig. 6. Hydrophobic channels in PEM fuel cell

### D. Catalysts for Liquid Feed Fuel Cells

Single or binary metal nanoparticles supported on various support materials for formic acid and methanol oxidation reactions are also synthesized in our research laboratory.

### III. CONCLUSIONS

Our studies conducted in our research laboratory in Atatürk University are mostly concentrated on the fuel cell materials and especially on the supported nanoparticles either for PEM fuel cell or liquid feed fuel cells. We use both synthesized and commercial support materials. We also concentrated on the improvement of fuel cell performances by changing the properties of the materials.

### REFERENCES

[1] Z. Qi, M.C. Lefebvre, P.G. Pickup, Electron and proton transport in gas diffusion electrodes containing electronically conductive proton-exchange polymers",  Journal of Electroanalytical Chemistry, vol. 459, pp. 9-14, 1998.

[2] P. Costamagna, S. Srinivasan, "Quantum jumps in the PEMFC science and technology from the 1960s to the year 2000: Part I. Fundamental scientific aspects", Journal of Power Sources, vol. 102, pp. 242, 2001.

[3] L., Xiong L., A. Manthiram, "High performance membrane-electrode assemblies with ultra-low Pt loading for proton exchange membrane fuel cells", Electrochimica Acta, vol. 50, pp. 3200-3204, 2005.

[4] H.K. Lee, J.H. Park, D.Y. Kim, T.H. Lee, "A study on the characteristics of the diffusion layer thickness and porosity of the PEMFC", Journal of Power Sources, vol. 131, pp. 200-206, 2004.

[5] W.K. Lee, C.H. Ho, J.W.V. Zee, M. Murthy, "The effects of compression and gas diffusion layers on the performance of a PEM fuel cell", Journal of Power Sources, vol. 84, pp. 45-51, 1999.

[6] C. D. Saquing, D. Kang, M. Aindow, C. Erkey, "Investigation of the supercritical deposition of platinum nanoparticles into carbon aerogels", Microporous and Mesoporous Materials, vol. 80, pp. 11-23, 2005.

[7] Y. Zhang, C. Erkey, "Preparation of Platinum-Nafion-Carbon black nanocomposites via a supercritical fluid route as electrocatalysts for Proton Exchange Membrane Fuel Cells", Ind. Eng. Chem. Res., vol. 44, pp. 5312-5317, 2005.

# Growth Rate Enhancement of TiO2 by R-HiPIMS and Application to Memristor Fabrication

Banafsheh Alizadeh Arashloo
*Department of Nanoscience and Nanoengineering*
*Ataturk University,*
*Erzurum/Turkey*
alizadeh_banafsheh@yahoo.com

Hasan Efeoglu
*Department of Electrical & Electronics Engineering*
*Department of Nanoscience and Nanoengineering*
*Ataturk University,*
*Erzurum/Turkey*
hefeoglu@atauni.edu.tr

Tevhit Karacali
*Department of Electrical & Electronics Engineering*
*Department of Nanoscience and Nanoengineering*
*Ataturk University,*
*Erzurum/Turkey*
tevhit@atauni.edu.tr

*Abstract*—**High power impulse magnetron sputtering (HiPIMS) with its unique properties is becoming a main technique for deposing or coating of the thin films. HiPIMS technique use high power and low duty cycle unipolar pulses to the magnetron target by low repetition frequency or up to a few hundred kHz, which a high ionization part of the sputtered atoms is produced by high discharge power. To deposit of the metal oxide thin films, metal targets are sputtered in addition of oxygen to argon within the growth chamber. That is called as Reactive-HiPIMS technique. The experimental results show that transparent metal oxides (TiO$_2$) films grown by R-HiPIMS are denser and have flatter surface and high degree of crystallinity than the other sputter methods. Due to oxygen deficiency, the resistance of TiO$_2$ has dependence to concentration of oxygen which affects the conductivity of TiO$_2$. If an ion or an atom has a mobility under the current flow, conductivity of host material continuously changes during the current flow. This behavior is called as memristive property. Experimental realization of memristive property requires to fabricate metal/metal-oxide/metal structures. Where metal-oxide thickness is limited to a few nm range for observable memristive behavior. Unfortunately, the poisoning problem for DC or RF based sputter is one of the limiting problem. In this study comparison of the target poisoning for RF and HiPIMS is given. Memristive property of TiO$_2$ thin film grown by R-HiPIMS is characterized using, optical and electrical measurements.**

*Keywords—HiPIMS,R-HiPIMS,TiO2,Memristor*

## I. INTRODUCTION

Thin film growth dates by sputter process back to the mid-nineteenth century. Although magnetron based sputtering for effective sputter, was available for researchers in the 1970s. The primary ions for sputtering in the plasma is enabled by low pressure when the plasma electrons are effectively used. In the other words, the necessary electrons in the plasma to be achieved easily by magnetron at low pressure, thus a sputtering device with effective electron trapping and enhance glow discharge are considered. One of the primary advantage of magnetron is to use it for the metal oxide thin film coating just by introducing reactive gas into the plasma chamber. Although efficiency of the magnetron sputter is considered to be high for some of the metal oxide growth rates are effectively goes down. Alternatively, DC pulse and high

power impulse magnetron sputter (HiPIMS) techniques are developed for sputter coating. However, the physical mechanism of sputter processes suggesting that the thin film growth rate reduction expected when the mode of operation is switched from DC to HiPIMS [1]. But in this comparison, the time averaged power used for HiPIMS was used for normalization. On the other hand, higher rates are possible under special circumstances [2], such as very high target temperature [3] and its great importance is the high film quality even better than the usual DC and RF sputter. The presence of reactive gas in a region of high energy and freshly exposed metal surfaces, which is the sputtering of the magnetron, leads to the rapid reaction. If the surface reacts faster than its sputters, a surface compound film is formed, in that case the sputtering has much lower rate than the metal, and the target poisoning occurs. Transition between metal sputtering and poisoning has dependence to the power applied to magnetron and partial pressure of the reactive gas.

Hysteresis being seen between the sputtering parameters and the flow rate of reactive gas. There is a region of reactive gas flow where the sputtering process is unstable. Selected parameters define the rapid deposition of a partially reacted metal or the slow down deposition from a poisoned target of a fully reacted film. This problem can be solved by controlling the partial pressure of the reactive gas, following the light emitted by the sputtering metal or other gases in the discharge, or adjusting the voltage/power/current applied to the sputtering cathode. These techniques need a fast feedback for controlling the film growth rate. Competition between the target erosion and compound layer formation which causing the target poisoning within pulse durations in a reactive HiPIMS can be controlled simply by altering duty cycle without changing the reactive gas mixture [4]. High power pulses generate high-density plasma in which 40%–80% of the sputtered target material is ionized. In addition, the substrate bias can be used for controlling the kinetic energy of the depositing ion flux which provide control over microstructure of the films. TiO$_2$ is one of the metal oxide widely used for memristor fabrication. Due to the nature of memristor [5], thickness of the metal oxide must be at the level of a few ten nano-meter scale [6]. Even a few nano-meter thick of oxide growth may take several hours [7]

because of poisoning problem when we used DC or RF sputter. Low frequency HiPIMS used to $TiO_2$ thin film growth in this study due to the high growth rate capability, the stability and crystallization as mentioned above.

## II. EXPERIMENTAL SETUP AND MEASUREMENTS

Memristor structures processed on a silicon wafer. Initially organic and inorganic cleaning process called as RCA1 and RCA2 applied to silicon wafers. Then a thermal $SiO_2$ grown silicon at 1000°C for 10 min. Al deposition and annealing process carried out at 580°C for 2min for getting back ohmic contact. A lithography used for opening window through oxide layer. Lift-Off used for $TiO_2$ growth and for top metallization. Device size was $100x100um^2$. Output of homemade pulsed DC source was set to 580V, with pulse duration 20msec and repetition rate 20Hz. Ar and $O_2$ flow rates were set to 30sccm and 0.4sccm respectively. During the process, base pressure was $5.1x10^{-3}$Torr. During the film growth, plasma emission was recorded using fiber optic coupled Ocean HR4000 spectrometer. Same spectrometer also used for absorption measurements. Time depended (I-V-t) measurements were carried out computer controlled Keithley 2400 and 6514 at room temperature.

## III. RESULTS AND DISCUSSION

### E. Hysteresis for reactive RF and HiPIMS

In general, oxide growth rate is limited process under the certain conditions when reactive DC or RF sputter techniques used. In this study a comparison between the reactive RF and HiPIMS sputters were given for $TiO_2$ thin film growth. In-situ thin film thickness measured by calibrated thickness monitor. Emission spectrum of Ti and Ar in the plasma are given in Fig. 1.

$TiO_2$ growth is effectively controlled by oxygen flow rate. This growth is slow down due to the target poisoning as oxygen flow rate increased with respect to constant Ar flow rate. As the oxygen rate increased Ti emission in the plasma steadily decreased and reached to steady state value above 0.45sccm oxygen flow, Fig. 2. When oxygen flow decreased as shown in Fig. 2, Ti emission sharply increased to the initial value at around of 0.37sccm oxygen flow. This observation shows that Ti sputtering from the target is affected by oxygen amount in the chamber. This slow down is due to early poising of Ti target. Same experiment is carried out using HiPIMS power source and the total Ti



Fig. 2. Ti plasma emission dependence to $O_2$ flow rate for reactive RF sputter.
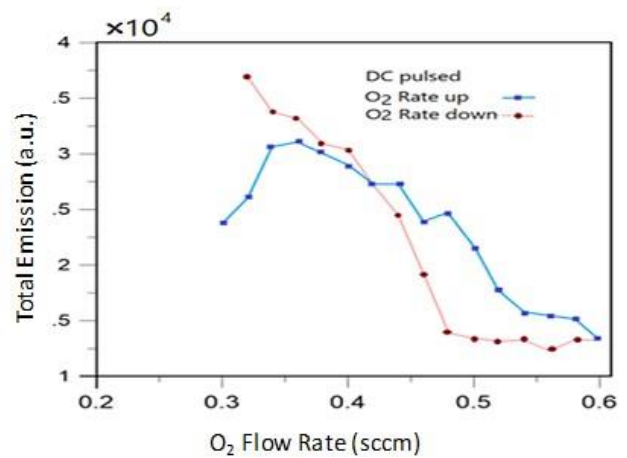


Fig. 3. Ti plasma emission dependence to $O_2$ flow rate for reactive HiPIMS sputter.

emission intensity in the plasma is given in the Fig. 3. During the oxygen flow rate up, the total emission steadily goes down up to 0.6sccm oxygen flow. This transition is quite smooth when compared with RF excitation. By decreasing of the oxygen flow rate in Fig. 3 Ti emission steadily increased below 0.5sccm. In Fig. 2 and 3 a hysteresis is appearing. RF sputter hysteresis appear between 0.37-0.45sccm with the sharp change. On the other hand, hysteresis is appearing above 0.45sccm with smooth change.

Oxygen flow dependence of the plasma emission intensity of Ar is given in Fig. 4. As RF bias applied, the plasma intensity goose down above 0.4sccm oxygen flow. Same measurement for HiPIMS case shows that the plasma emission intensity remains constant up to 0.6sccm oxygen flow. In each case there is no apparent hysteresis, as seen in Fig. 4.



Fig. 1. The Optical spectrum of plasma while Ti powered HiPIMS power supply.
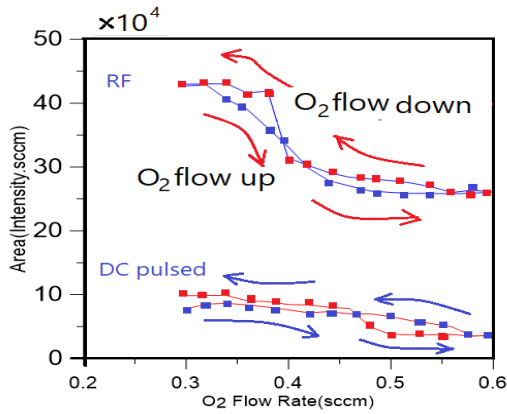
Fig. 4. Ar plasma emission dependence to the oxygen flow rate for each of the RF and HiPIMS excitation sources.

## F. I-V-t measurement and Memristiv property

Time depended current–voltage measurements (I-V-t) were carried out on the fabricated devices. As seen in Fig. 5 hysteresis is appearing. While the positive voltage sweeps up, the current steadily increases and levelling at complimentary current limited by 2400. In the same measurement and under the negative voltage sweep the current decreases, Fig. 6. Pinched loop appearence is one of the evidence for memristor character and the resistance increase under the negative bias also supports memrsitor formation.
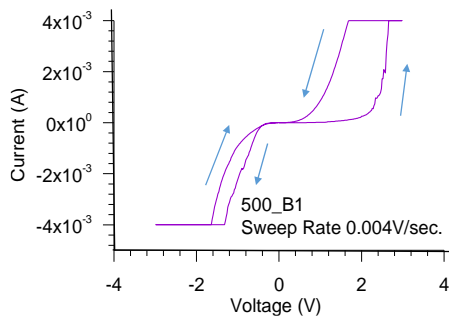


Fig. 5. Hysteresis of the single loop I-V-t behavior of TiO$_2$ based memristor
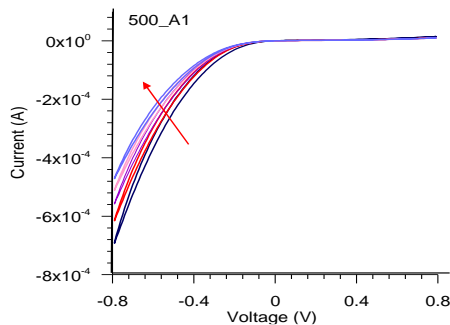


Fig. 6. Repeated I-V-t character of the memristor under the full negative bias. As loop repeated, the resistance of the device is increasing

## IV. CONCLUSION

In the present study the advantage of the reactive HiPIMS technique over RF sputter is shown experimentally. Industrial applications require high deposition rates in terms of cost. The average power applied to magnetron do not exceed its capacity because of the heat dissipation limits. With this limitation power level can be increase up to kW/cm$^2$ range for a short time period with low repetition rate which allow enough time for the heat dissipation. In Fig. 3 Ti emission reduction is getting smaller above 0.45sccm oxygen flow. A reduction of ionized Ti in the plasma is indicating that the sputter yield of Ti at target is reduced as compound is formed. The emission intensity reduction in RF sputter is faster than HiPIMS sputter while increasing oxygen flow, which that shows why HiPIMS has advantage at high oxygen flow which growth rate is considerably higher than RF plasma coating. Finally, the optical emission spectroscopy as a useful tool for checking the plasma conditions is realized.

## REFERENCES

[1] A. Anders "Deposition rates of high power impulse magnetron sputtering: Physics and economics" J. Vac. Sci. Technol. A 28(4), 2010, pp783-790

[2] S. M. Rossnagel, and J. Hopwood "Magnetron sputter deposition with high levels of metal ionization" Appl. Phys. Lett. 63, 1993, pp3285-3287

[3] K. Macak, V. Kouznetsov, J. Schneider, U. Helmersson, and I. Petrov "Ionized sputter deposition using an extremely high plasma density pulsed magnetron discharge" Journal of Vacuum Science& Technology A 18, 2000, pp1533-1537

[4] C. Nouvellon, M. Michiels, J.P. Dauchot, C. Archambeau, F. Laffineur, E. Silberberg, S. Delvaux, R. Cloots, S. Konstantinidis, R. Snyders "Deposition of titanium oxide films by reactive HiPIMS Influence of the peak current value on the transition from metallic to poisoned regimes" Surface&Coatings Technology 206 (2012), pp3542–3549

[5] L.O. Chua "Memristor: the missing circuit element" IEEE Trans. Circuit Theory 18 (5) (1971).

[6] D.B. Strukov, G.S. Snider, D.R. Steward, S. Williams "The missing memristor found" Nature 458 (1) (2008).

[7] H. Efeoglu, S. Gullulu, T. Karacali, "Resistive switching of reactive sputtered TiO2 based memristor in crossbar geometry" Applied Surface Science, 350, 2015, pp10-13

# Mechanistic Studies on the Epoxidation and Aziridination Reactions

Hamdullah Kılıç

East Anatolia High Technology Application
and Research Center, Atatürk University,
Erzurum, Turkey

Phone: +90 442 231 7001

hkilic@atauni.edu.tr

**Abstract-Epoxides and aziridines are valuable intermediates which can be converted into many useful compounds. In addition, these heterocycles are part of some natural products. Therefore, much effort has been made for the development of chemo and diastereoselective synthesis of epoxides and aziridines.**
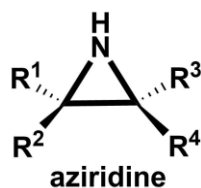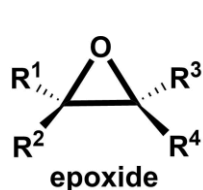
epoxide          aziridine

**In the first part of talk, manganese catalyzed epoxidation of chiral allylic alcohols will be discussed** from mechanistic viewpoints.[1–4] **In the second part of talk, I will discuss stereochemical insights on the aziridination of chiral allylic alcohols by** *in situ* **generated aziridination reagent.**

*Keywords: epoxidation, allylic alcohol, epoxy alcohol, aziridination, aziridine.*

## REFERENCES

[1] Kilic, H.; Adam, W.; Alsters, P. L. *J. Org. Chem.* **2009**, *74*, 1135–1140.

[2] Cakici, M.; Ulukanli, S.; Ekinci, D.; Kilic, H. *Tetrahedron*, **2018**, 74, 49-57.

[3] Cakici, M.; Karabuga, S.; Kilic, H.; Ulukanli, S.; Sahin, E.; Sevin F. *J. Org. Chem.* **2009,** *74*, 9452–9459.

[4] Celik, S.; Cakici, M.; Kilic H.; Sahin, E. *Tetrahedron: Asymmetry*, **2015**, 26, 152–157.

# Stent Manufacturing using Medical Grade ASTM F75 Cobalt Chromium (CoCrMo) by Selective Laser Melting (SLM) Technology

M. Asnawi Omar
Fakulti Kejuruteraan, Universiti Putra Malaysia, Serdang, Selangor, Malaysia
asnawi@kktmkuantan.edu.my

B.T.H.T. Baharudin
Fakulti Kejuruteraan, Universiti Putra Malaysia, Serdang, Selangor, Malaysia
hangtuah@upm.edu.my

S. Sulaiman
Fakulti Kejuruteraan, Universiti Putra Malaysia, Serdang, Selangor, Malaysia
shamsuddin@upm.edu.my

M.I.S. Ismail
Fakulti Kejuruteraan, Universiti Putra Malaysia, Serdang, Selangor, Malaysia
ms_idris@upm.edu.my

M. Afian Omar
SIRIM Bhd, Lot 34, Kulim Hi-Tech Park, Kulim Kedah, Malaysia
afian@sirim.my

*Abstract*-This paper explains and demonstrates the capabilities of Metal Additive Manufacturing (MAM) technology in producing intricate stent structure with a customize design by using ASTM F75 Cobalt Chromium (CoCrMo) powder. The design, process parameter, powder characterization, part density and microstructure are being investigate and thus exploring the potential area of MAM process for future proof stent manufacturing. By alternatively switching to MAM, the step of production can be minimized and thus customization of stent can be carried out according to the patient need. The suggested stent model was taken from the third-party vendor and fabrication process was carried out using EOSINT M280 metal printer with the aid of Materialise Magics 19.0 software for support generation.

*Keywords*-Metal Additive Manufacturing, Cobalt Chromium, Stent, Selective Laser Melting, microCLIP.

# Laser Surface Modification Of Materials

German F. de la Fuente

*Instituto de Ciencia de Materiales de Aragón
(ICMA), CSIC-Universidad de Zaragoza,
C/ María de Luna 3, E-50018 Zaragoza,
Spain*
german.delafuente.leis@csic.es

Lasers are widely used in Industry to perform many types of transformations on most types of materials, although the most commonly known uses of lasers include metal cutting, welding and surface processing. A wide variety of phenomena may be induced with different types of lasers available at the industrial level, however, which surpass the expectations generated by the success of cutting and welding advances [1]. The unique properties of Lasers allow choosing emission parameters such as intensity, pulsed or cw operation, pulse length and wavelength. The use of lasers fitted with beam and line scanning optical systems [2] provides ideal conditions to induce a plethora of transformations inaccessible to conventional methods, where induced processes are essentially based on intense thermal transfer or on vacuum and chemical deposition methods, particularly on surfaces [3, 4]. Amongst recently developed processes in our laboratory, it is worth emphasizing those based on an intense photothermal interaction, on the one hand [5-7], and those based on mixed type photothermal, photophysical and, sometimes photochemical interactions, on the other. Examples will be given of decontamination, melting and ablation processes, applied to controled surface finish in metals. In addition, decoration processes via surface melting within a furnace will be described for ceramics and glass products.
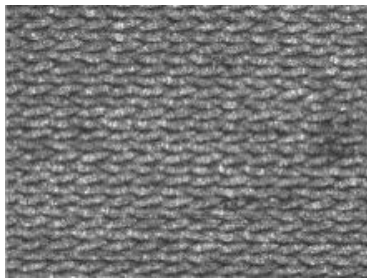


Figure 1. Examples of products obtained by laser surface treatment of an alloy (left), and Laser Furnace decorated ceramic (centre) and glass (right).

## REFERENCES

[1] [1] W. Steen and J. Mazumder, Laser Material Processing, 4th ed. Springer, 2010.

[2] [2] V. V. Lennikov, B Özkurt, L A Angurel, A, Sotelo, B Özçelik, G. F. de la Fuente, *J. Supercond. Novel Magn.*, **2013**, *26,* 947-952.

[3] [3] Rubahn, Laser Applications in Surface Science and Technology, Wiley, 1999.

[4] [4] D. Fischer, G. F. de la Fuente, M. Jansen, A new pulsed laser deposition technique: Scanning multi-component pulsed laser deposition method, Rev. Sci. Instr. **2012**, 83, 043901.

[5] [5] R. Lahoz, J. P. Espinós, G. F. de la Fuente, A. R. González-Elipe, *Surf. Coat. Technol.*, **2008**, *202*, 1486-1492.

[6] [6] R. Lahoz, J. P. Espinós, F. Yubero, A. R. González-Elipe, G. F. de la Fuente, J. Mater. Res. **2015**, 30, 2967-2976.

[7] [7] F. Rey-García, F. Gutiérrez-Mora, C. J. Borrell, L. C. Estepa, L. A. Angurel, G. F. de la Fuente, *Ceram. Int..*, **2018**, *44*, 6997-7005.

# Functional Depositions and Applications for Defense Industry

İhsan Efeoğlu
Atatürk University
iefeoglu@atauni.edu.tr

Being an active player in the new world order shaped by globalization is only possible with the development of original products and technologies. One of the most fundamental areas that feed technological developments in the way of increasing the international competitiveness of our country is the aviation and aerospace industry. Air and space industry; It is a field that uses state-of-the-art technologies, always needs new approaches, and develops a dynamic research and development with different disciplines. The most important problem encountered in the design of air and space vehicles; cryogenic-high temperature in service conditions, chemical-mechanical-tribological formation because of the structural elements can not be obtained from the performance. Many countries around the world set up their own aerospace agencies and invest in large R&D in this field.

Today, the ideal functional coatings combine the hardness of diamond, the toughness of high speed steel, the chemical inertness of alumina and excellent adhesion to the substrate with the lowest coefficient of friction (CoF) and the highest wear resistance. A main problem with hard/ultra hard coatings has the high residual stress that develops during the deposition. With technological developments, there is great interest in ceramic-composite based coating for many applications. Deposition of functionally gradient composite coatings is deposited on different engineering materials by a variety of deposition techniques till now. The ability to use machine elements under dynamic effects is only possible by the development of mechanical and chemical wear-resistant functional composite coatings with deposition single and multi-layer nano structures using different surface treatments.

In industrial and technological applications, PVD-magnetron sputtering systems are used from day today. In these magnetron systems, one of the new magnetron system by Teer can offer all the requirements necessary for a modern production for functional coating system. This system is based on a Closed-Field Unbalanced Magnetron System (CFUBMS) and was used to coat many kind of ceramic-composite based metallurgical coatings for many industrial-technological-strategic applications. Putting out the advantages of functional properties (dense plasma, high-velocity ions, no target poisining); dense microstructure and will preferably be able to control growth. In Surface Technology R&D Laboratory that the technique used in the CFUBMS PLASMAG-550 System; two weak, two strong magnets course was intensive-control can be configured with the formation of a plasma can be achieved.

Composite structured soft, hard, ultra hard films were deposited onto different tool steels by co-sputtering from $MoS_2$, C, Ti, Nb, Ta, CrY, B4C and TiB2 targets using closed-field unbalanced magnetron sputtering process (CFUBMS) using different power sources such as dc-bias, pulsed-dc and HiPIMS. It is observed very clearly, all different types of the powers applied to the targets or substrates have been obtained different microstructure orientation, hence the coatings consisting of composite-multilayers to meet the requirements in demanding applications can be a possible solution.

# Model Order Reduction of LTI Systems Using Particle Swarm Optimization

D.I. Abu-Al-Nadi
Department of Electrical Engineering
The University of Jordan

dnadi@ju.edu.jo

O.M. ALsmadi
Department of Electrical Engineering
The University of Jordan

Othman_mk@ju.edu.jo

Z.S. Abo-Hammour
Department of Mechatronics
Engineering
The University of Jordan
zaer@ju.edu.jo

*Abstract*-Physical systems are translated into mathematical model via higher order differential equations. It is usually recommended to reduce the order of this model while keeping the dominant behavior of the original system. This will help to better understanding of the physical system, reduce computational complexity, reduce hardware complexity and simplify the controller design.

Different techniques for order reduction of linear Time Invariant (LTI) systems in time domain as well as in frequency domain are available in the literature. For model order reduction, there are different scenarios that can be performed. One scenario obtains reduced models that are completely new and not related to the original models in terms of their critical frequencies of either single-input-single-output (SISO) or multi-input-multi-output (MIMO) systems. On the other hand, another scenario obtains reduced models that preserve the original system important properties, such as dominant frequencies of either SISO or MIMO systems. It is to be noted that the later scenario is more preferable, if possible, due to its meaningful physical interpretation in obtaining similar models and due to minimum changes in the original systems

In this work, a model order reduction (MOR) technique for a linear multivariable system is proposed using the combined advantage of retaining the dominant poles and the error minimization using the particle swarm optimization. The state space matrices of the reduced order system are chosen such that the dominant eigenvalues of the full order system are unchanged. The other system parameters are chosen using the Particle Swarm Optimization (PSO) with objective function to minimize the mean squared errors between the outputs of the full order system and the outputs of the reduced order model when the inputs are unit step. The proposed algorithm has been applied successfully , a $10^{th}$ order MIMO linear model for a practical power system was reduced to a $4^{th}$ order and an $8^{th}$ order SISO system was reduced to a $2^{nd}$ order.

# Growth of 2D WS$_2$ by RF Sputtering and Applications

Yusuf Koçak
Atatürk University, DAYTAM,
25240, Erzurum, Turkey

Emre Gür
Atatürk University,
Faculty of Science, Dept. of Physics,
25240, Erzurum, Turkey

*Abstract*-Recently, 2D layered semiconductors have been rapidly emerging as a new class of functional materials for various applications such as nanoelectronics, transistors, solar cells, photodetectors and energy storage [1]. Transition-metal dichalcogenides (TMDC) of TX$_2$ type (T = Mo, W, Nb, etc., X = S, Se, etc.) are the member of these classes [2]. The bonding between the sheets is relatively weak due to the weak wan der waal. Best known 2D semiconductors materials are MoS$_2$, WS$_2$, MoSe$_2$, WSe$_2$. These materials show very important properties such as indirect-to-direct band-gap transition from monolayer to bulk regime, coupled spin and valley physics, and band structure tunability with strain. Furthermore, the combination of WS$_2$ thin layers with other 2D materials has given rise to a large category of 2D hetero-structures.

In the present study, WS$_2$ was grown by RF magnetron sputter method by changing the growth parameters such as growth pressure, RF power and growth time to find out free from defects, stoichiometric, single crystal WS$_2$. Grown thin films were followed through the X-ray Diffraction, X-ray Photoelectron Spectroscopy, Raman Spectroscopy, Scanning Electron Microscopy and Atomic Force Microscopy measurements. In the talk, the route to obtain a stoichiometric, high quality 2D WS$_2$ will be given by the RF Sputtering method.

## I. INTRODUCTION

The Unique optical and electrical properties of 2D materials permit many important device applications. One of the most well-known 2D material, graphene attracts attention for semiconductor device applications due to its strong interaction with photons in a broad wavelength range and its high carrier mobility [1-3]. However, field effect transistors produced from graphene cannot be effectively switched off and have low on/off switch ratios due to lack of bandgap [4]. This brings up the importance of other 2D materials at least for the transistors applications. These 2D semiconductors are Transition Metal Dicalcogenides (TMDCs) given by the MX2, M;transition metal (Mo, W, i.e) and X; chalcogenide (S, Se, i.e) [4]. Best known 2D semiconductors materials are MoS2, WS2, MoSe2, WSe2. These materials show very important properties such as indirect-to-direct band-gap transition from monolayer to bulk regime, coupled spin and valley physics, and band structure tunability with strain. Furthermore, the combination of WS2 thin layers with other 2D materials has given rise to a large category of 2D hetero-structures. Changing its properties mainly from a single layer to thick layers makes these materials very suitable for in-situ structural analysis.

In this study, thin films of WS$_2$ were grown by radio frequency magnetron sputtering (RFMS) down to a few layer to 700 nm on different type of substrates in different growth conditions. Effects of growth conditions, such as RF power, temperature of the substrate, thickness, different type of substrates, on the grown thin films were investigated by X-ray diffraction (XRD), X-ray Photoelectron Spectroscopy (XPS), Raman Spectroscopy (RS), Atomic Force Microscopy (AFM), Photoluminescence (PL), and optical absorption measurements.

## II. EXPERIMENTAL

WS$_2$ thin films were deposited by RFMS, using % 99.99 WS$_2$ target. Substrates were chemically cleaned prior to the insertion in the vacuum chamber. In all growth, Si, c-plane sapphire, quartz and glass substrate was included into the chamber to follow up the effect on the different substrates. Base pressure of $2 \times 10^{-7}$ Torr was reached in the sputtering chamber before the growth process by the help of liquid nitrogen cold finger. The substrate temperature was kept constant at 350 $^0$C during deposition. First set of the samples were grown under different Ar growth pressures of 5, 10, 15, 20, 25 mTorr. The thicknesses of the samples were 10-100 nm confirmed by the stylus profilometer KLA tencor P7 that has sub Å resolution. Second set of samples was grown time dependent, which are 5s, 10s, 15s, 20s, 25s, under 20mTorr pressure at 350 $^0$C substrate temperature in order to show the thickness dependence of the characteristics of the samples.

Structure of the thin films was studied by grazing incident angle XRD with Empyrean, PANalytical with Cu K$\alpha$ radiation. The measurement angle was kept constant at 0.5 degree. Raman spectroscopy measurements were performed by Witec confocal micro-Raman Alfa 300R system. In order to show the large area uniformity, Raman surface mapping also performed. Further evidence for composition of the grown thin films was obtained by the Specs Flex-Mod high-performance XPS system. X-rays monochromatized through single quartz crystal with an Al anode K-α with an energy of 1486.6 eV was used. The measurements were performed with pass energy of 50 eV and 20 eV for survey spectra and high-resolution elemental spectra, respectively. The photoelectrons were collected by the 150 mm radius hemispherical analyzer, which is attached to 2D CCD detector.

## III. RESULTS AND DISCUSSION

A comparison of the XRD profiles of WS$_2$ thin films with the thickness is shown in Fig. 1. In the figure, all the peaks observed belongs to the WS$_2$ thin films and no other phases has been observed. Poly crystalline structure of the thin films are confirmed. It is observed that thinner WS$_2$ samples (25-50-100nm) don't show (002) plane peaks. On the contrary, 290nm and 700nm thickness have shown peaks coming from (002) plane. This proves that basal planes for thinner samples of sputtered WS$_2$ exists primarily with c-axis oriented parallel to the substrate surface [7].
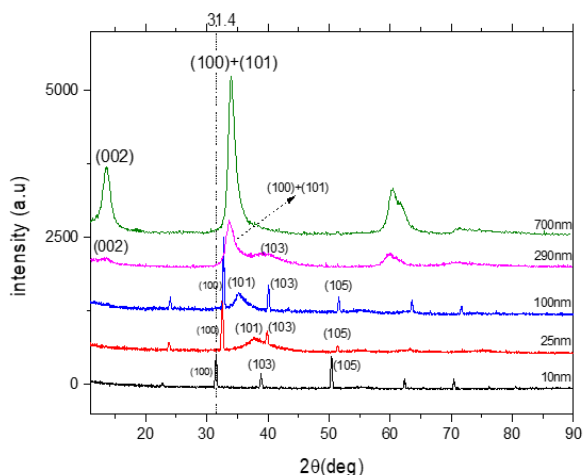
Figure 1. XRD-patterns in different thickness of WS2 films on p-Si(100) substrate.



Figure 2. Room-temperature Raman spectra of some WS$_2$ thin films.

Raman Spectroscopy was used to characterize the samples' structural quality and vibrational properties. Since it is non-devastating technique and it is widely used to characterize the structural and electronic properties of monolayer materials such as graphene, WS$_2$ and MoS$_2$ [4-7]. To reason out this observation we fitted the Raman peaks using a Voigh function and positions and modes depending on the type of the substrate. The clear observation of the raman modes indicates good quality of the material. The Raman spectra for the various substrate (p-Si(100), n-Si(111) and fused silica) in 310nm WS$_2$ thin films are shown in Fig. 2. It is confirmed that the WS$_2$ exhibit first order modes at wavenumber of 348 cm$^{-1}$ and 418 cm$^{-1}$ separated by about 64 cm-1, corresponding to the modes from in plane and out-of plane vibrations, respectively.

To identify the chemical composition of WS$_2$ thin films grown by RFMS, XPS was used to track the binding energies of the W, S, C and O. As shown Fig. 3, as a representative of WS$_2$ thin films, only C, O, W and S XPS survey analysis of the films observed in XPS survey spectrum of WS$_2$. The binding energy profile for W4f$_{7/2}$ and W4f$_{5/2}$ is represented by the peaks at 31.5eV and 33.8eV [8-10]. Depth profile of the peaks of WS$_2$ thin films were investigated as shown in the figure 4.
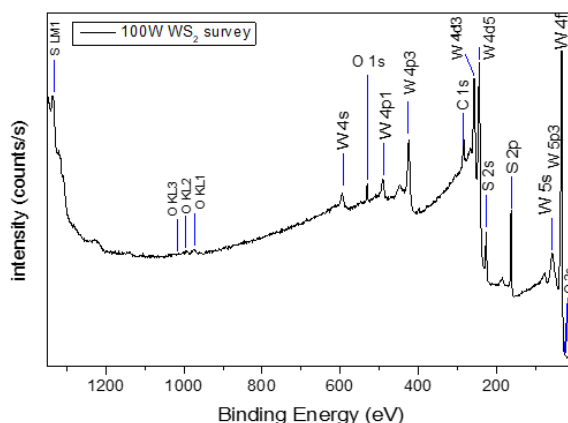


Figure 3. A representation of XPS survey spectrum of WS$_2$ thin film after 100s etched which shows only W, S, O and C elements are present in the samples.
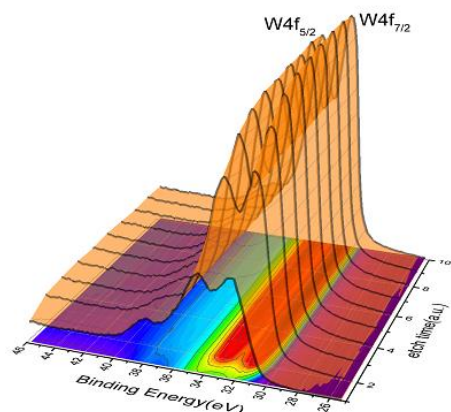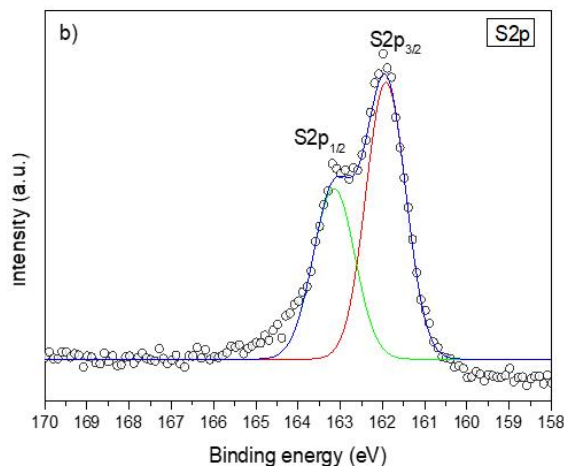


Figure 4. Depth profile XPS analysis of WS2 thin film; depth profile of W4f7/2-5/2 and binding energy shifts with the depth (inset) which shows the clear preferential sputtering. b) Sulfur 2p peaks and the devconvolution.

13

Depth resolved XPS measurements were used to understand the elemental profile of W and S. Ar gun was used to achive etching process. XPS data was acquired 120s of sputter between every measurement. The characteristic W4f and S2p XPS spectrum of $WS_2$ thin film is shown in figure 4. The binding energy profile for $W4f_{7/2}$ and $W4f_{5/2}$ is represented by two peak at 31.5eV and 33.8eV, respectively, corresponding to W in $WS_2$, after the film is etched for the first 120s. the W 4f spectrum has consisted of 4 peaks for the last three XPS measuments (see fig. 4). The appeared peaks show a shift to higher binding energy values i.e. 35.7eV and 37.6 which might be corresponding to tungsten in $WO_3$ (W6+) While $W4f_{7/2}$ peak intensity of $WS_2$ decreases with the depth profile, possible observed peaks belong to the WO3 starts to increase, as shown in Fig. 4. a. As shown in figure 4.d, the S2p spectrum is deconvoluted to a dublet consisting of S2p3/2 and S2p1/2 peaks centered at binding energy values of 161.88eV and 163.18eV which correspond to S2- in WS2. In order to find the peak energy position of the W 4f belonging to $WS_2$, Lorentz function were used to fit observed data (see fig.4.c). Binding energy shifts has observed in 4f features as shown in the inset of figure 4c.

## IV. CONCLUSIONS

The deposition of $WS_2$ thin films by reactive magnetron sputtering in Ar atmosphere from a $WS_2$ target has been studied. The diffraction analysis reveals that $WS_2$ thin films grown under the conditions of high RF power and thick show strong (002). It is also observed strain effects due to shift observed in the peak positions. From the Raman peaks, the sharp peaks of the vibration modes show that quality of the grown thin films. It is confirmed that the WS2 nanosheets exhibit first order modes at approximately 352 $cm^{-1}$ and 418 $cm^{-1}$, corresponding to the $E_{2g1}$ and $A_{1g}$ modes from in plane and out-of plane vibrations, respectively. From the XPS analysis, depth profile of $WS_2$ thin films indicated the shift in binding energies with depth. Stable films were obtained at higher RF powers.

## REFERENCES

[1]  Berkdemir, A. et al., *Scientific reports*. 3, 2013.
[2]  Wang, QH. et al. *Nature nanotechnology*. 7(11):699-712 2012.
[3]  Kuc, A. et al. *Physical Review B*. 83(24):245213 2011.
[4]  Shi, Y. et al. *Nano Lett.* 12(6):2784-91 2012.
[5]  Browning, R. Nanoscale. 2016.
[6]  Adelifard, M. et al. Journal of Materials Science: Materials in Electronics.1-8.
[7]  Scharf, T. et al. Acta Mater. 54(18):4731-43, 2006.
[8]  Deepthi, B. et al. Surf Coat Technol. 205(2):565-74, 2010.
[9]  Sundberg, J. et al. Appl Surf Sci. ;305:203-13, 2014.
[10]  Yin, G. et al. Tribology Letters. ;22(1):37-43, 2006.

# LED, Solar-Cell and Gas Sensor Applications of Micro and Nano-Structures in Oxide and Perovskite Materials

Ali Baltakesmez
*Ardahan Vocational School of Technical Sciences*
*Ardahan University*
Ardahan, Turkey
alibaltakesmez@ardahan.edu.tr

Ömer Çoban
*İspir Hamza Polat Vocational High School*
*Atatürk University*
Erzurum, Turkey
omercoban@atauni.edu.tr

Sebahattin Tüzemen
*Department of Physics,*
*Atatürk University*
Erzurum, Turkey
stuzemen@atauni.edu.tr

*Abstract—* **Electroluminescent Light Emitting Diode (LED) applications has been performed on p-n junctions constructed by ZnO thin films grown by electrochemical deposition on commercially available bulk Si substrates. Electroluminescence measurements of obtained homo-junctions exhibited three main broad electroluminescence bands, giving rise to white light emission consolidated by Fabry-Perot oscillations between the interface layers. As the solar applications, we present high quality perovskite thin films prepared by spin coating at various deposition temperatures. The perovskite solar cells prepared by a unique approach with hot deposition have resulted in better values for all the performance parameters culminating high efficiencies at around 15% and overcoming serious problems of the field such as stability and hysteresis. Finally, various oxides were fabricated on glass substrates by RF Magnetron Sputtering technique. To investigate the optical responses of these semiconductors to oxygen and hydrogen gases, an optical gas sensor test system was set up and programmed during the studies, using charged coupled device (CCD) signal processing. A nano-layer metal sensitizing have also been observed in the range of 450 nm-850 nm wave lengths, covering the VIS-IR range.**

*Keywords—LED, Solar-Cell, Perovskite Materials, Micro and Nano-Structures, Gas sensor*

## I. INTRODUCTION

Among wide-band-gap II–VI compound semiconductor oxides, ZnO is one of the most promising material used in potential optoelectronics applications: as light-emitting diodes (LEDs), gas sensors, transparent conductive oxide layer in solar cells [1-3]. The reasons for these wide area of applicability of ZnO are its direct wide bandgap (3.37 eV) and large exciton binding energy of around 60 meV at room temperature which is nearly 3 times greater than the room temperature thermal energy of 25 meV.

On the other hand, organometallic perovskite light harvesters have been recently invoked as a promising photovoltaic material due to their unique properties such as direct band gap (1.55 eV) [4], large absorption coefficient ($105$ cm$^{-1}$ ) [5], low exciton binding energy (25 meV) [6], high carrier mobility (12 cm$^2$/V.s) [7], and long carrier diffusion length (from 100 nm to 1 micron) [8]. With these optoelectronic properties, these semi-organic perovskite materials (AMX$_3$), having a component A being an organic cation (CH$_3$NH$_3$) or CH(NH$_2$)$_2$ surrounded by a metal halide MX$_3$ (M:Pb or Sn, X:I, Br, or Cl) in an octahedral structure, are extraordinarily promising as optoelectronic materials because of their controllable bandgap ranging from 1.5 to 3.2 eV [9,10].

In this paper, we present three of the successful applications of oxide and perovskite materials on respectively LEDs, Solar Cells and Gas Sensors.

## II. EXPERIMENTAL

In order to produce electroluminescent p-n junctions, the p-type ZnO films were deposited on the commercial p-Si:B substrates grown by PLD, having thicknesses of 500–550 microns and resistivity of around $10^3$ ohm-cm. Before electrodeposition of p-ZnO, a chemical cleaning process was applied onto the pSi:B substrates in order to remove the unintentionally formed oxide layer. In this work, we used NaN3, MgCl2, SbCl3, and TiO2 as p-type dopants' sources. N-type ZnO was grown on p-type without any doping. Electrochemical depositions were performed in a conventional three-electrode cell.

For the solar device applications, the ITO substrates were cleaned subsequently in an ultrasonic bath of acetone and isopropyl alcohol (IPA) for 15 min and then dried out under nitrogen gas flow. After substrate cleaning, the PEDOT:PSS as a hole transport layer (HTL) was coated onto the cleaned ITO substrates at 4000 rpm for 60 s, and all the PEDOT:PSS covered substrates were annealed at 120 $^O$C for 25 min in ambient air. In this coating process, spin coating was used. Following the annealing process, all the substrates were transferred to a glove box with controlled Ar atmosphere. All the preparation of perovskite and PCBM precursor solutions, cell fabrication, and measurement of cell performance were performed in the glove box.

Finally all the oxides for gas sensing applications are grown on glass substrates by the RF magnetron sputtering technique. An homemade system for these gas sensor applications is described elsewhere [11].

15

## III. RESULTS AND CONCLUSIONS

As can be seen in Fig.1, ZnO p-n homo-junctions on Si substrates exhibited appropriate I-V characteristics, resulting in an electroluminescent device as shown in Figs.2(a) and (b). The luminescence can be seen with the naked eye having high color temperature that can be a good indication of obtaining LED devices. On the top of the electroluminescence spectra, we observe noisy oscillations, most probably coming from the oscillations due to the mirror like surfaces of the p-n interfaces called the Febri-Perot oscillations [12].
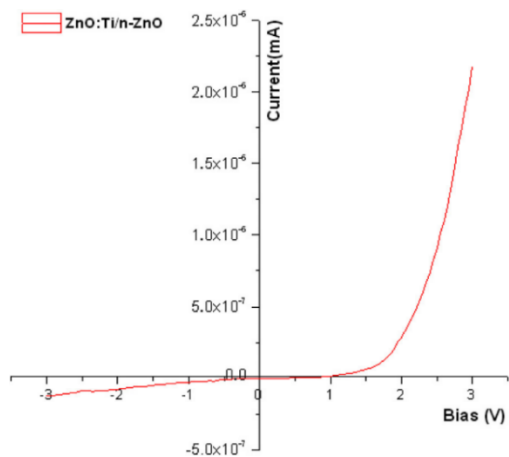


Figure 1. ZnO p-n homo-junctions on Si substrates, exhibiting appropriate I-V characterisitcs
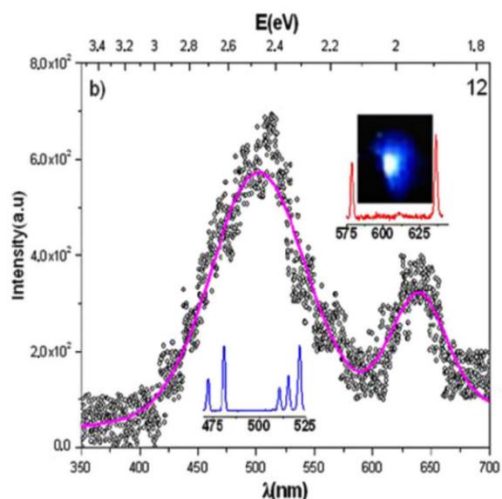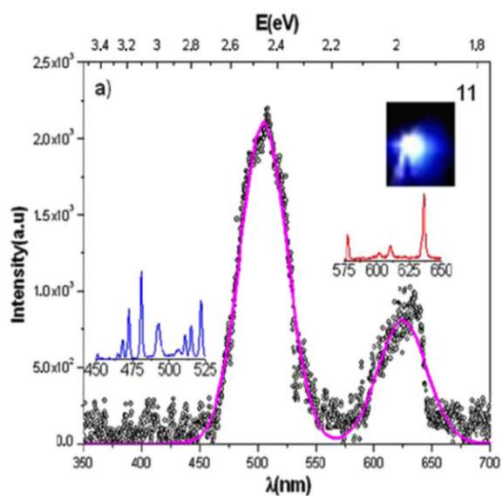




Figure 2. Electroluminescence spectra of ZnO p-n homo-junctions on Si substrates.

In Figure 3 (a) and (b), it has been shown an application of solar cell on perovskite materials. With the important process modifications and device design, we have overcome the two important problem of stability and hysteresis [13].



| | Jsc | Voc | FF | PCE |
|---|---|---|---|---|
| SC-FB | 22.03 | 0.908 | 0.734 | 14.68 |
| FB-SC | 22.39 | 0.911 | 0.751 | 15.32 |
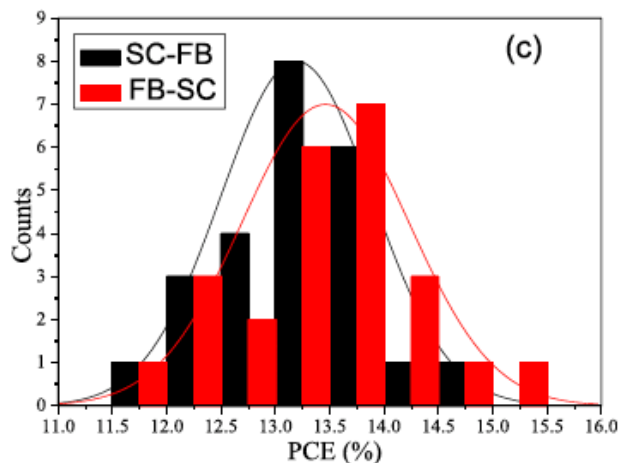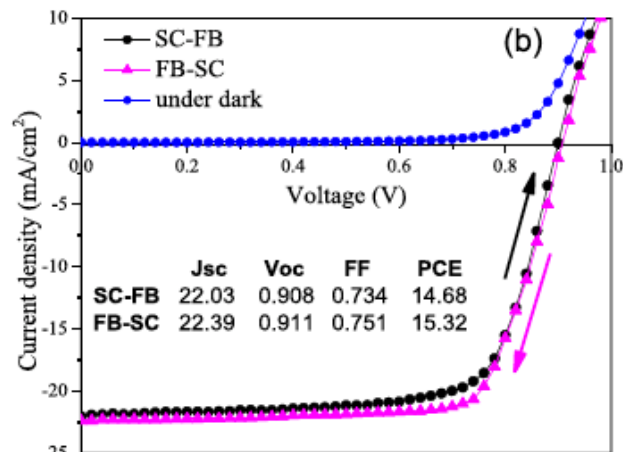


Figure 3. (a) Solar cell characteristic of a typical device with a perovskite active layer, (b) Diagram showing the power conversion efficiencies of all grown samples with dual hot spin coating process.

Finally, we present the hydrogen gas sensing properties of oxide materials with their absorbance verifications. As seen in Figure 4 and Figure 5 absorbance change give rather extraordinary behavior, exhibiting an increase in n-type and a decrease in p-type material. This has been explained in terms of the differences of surface energy in the n and p-type oxide materials [14].

P-TYPE
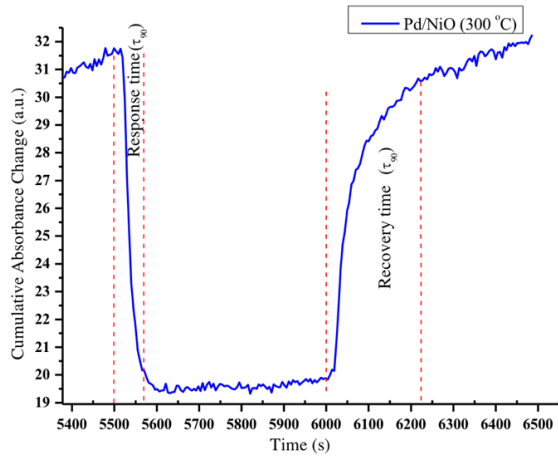


Figure 4. Absorbance change decrease in p-type material under $H_2$ gas ambient.

N-TYPE
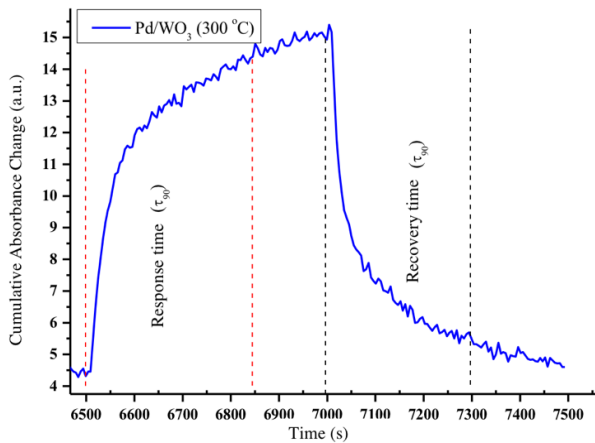


Figure 5. Absorbance change increase in n-type material under $H_2$ gas ambient.

REFERENCES

[1] J. Y. Lee, J. H. Lee, H. S. Kim, C. H. Lee, H. S. Ahn, H. K. Cho, Y. Y. Kim, B. H. Kong, and H. S. Lee, Thin Solid Films 517, 5157 (2009)

[2] K. Liu, M. Sakurai, M. Liao, and M. Aono, J. Phys. Chem. C 114, 19835 (2010).

[3] L. F. Dong, Z. L. Cui, Z. K. Zhang, Nanostruct. Mater. 8, 815 (1997).

[4] M. M. Lee, J. Teuscher, T. Miyasaka, T. N. Murakami, and H. J. Snaith, Science 338, 643 (2012).

[5] Y. Wang, Y. Zhang, P. Zhang, and W. Zhang, Phys. Chem. Chem. Phys. 17, 11516 (2015).

[6] K. Galkowski, A. Mitioglu, A. Miyata, P. Plochocka, O. Portugall, G. E. Eperon, J. T.-W. Wang, T. Stergiopoulos, S. D. Stranks, H. J. Snaith, and R. J. Nicholas, Energy Environ. Sci. 9, 962 (2016).

[7] C. Motta, F. El-Mellouhi, and S. Sanvito, Sci. Rep. 5, 12746 (2015).

[8] S. D. Stranks, G. E. Eperon, G. Grancini, C. Menelaou, M. J. P. Alcocer, T. Leijtens, L. M. Herz, A. Petrozza, and H. J. Snaith, Science 342, 341 (2013).

[9] S. M. H. Qaid, M. S. Al Sobaie, M. A. Majeed Khan, I. M. Bedja, F. H. Alharbi, M. K. Nazeeruddin, and A. S. Aldwayyan, Mater. Lett. 164, 498 (2016).

[10] A. Sadhanala, S. Ahmad, B. Zhao, N. Giesbrecht, P. M. Pearce, F. Deschler, R. L. Hoye, K. C. Godel, T. Bein, P. Docampo, S. E. Dutton, M. F. De Volder, and R. H. Friend, Nano Lett. 15, 6095 (2015).

[11] E. Turgut, Ö. Çoban, S. Sarıtaş̧ S. Tüzemen, M. Yıldırım, E. Gür, Oxygen partial pressure effects on the RF sputtered p-type NiO hydrogen gas sensors, Applied Surface Science 435 (2018) 880–885.

[12] A. Baltakesmez, S. Tekmen, and S. Tüzemen ZnO homojunction white light-emitting diodes Journal of Applied Physics 110, 054502 (2011)

[13] A. Baltakesmez, M. Biber, and S. Tüzemen Improved perovskite film quality and solar cell performances using dual single solution coating, Journal of Applied Physics 122, 085502 (2017)

[14] Ö. Çoban, S. Tüzemen, Gasochromic Properties of Thin Film Oxides in terms of Surface Physics, Materials Today: Proceedings (2019)

# Oral Presentation Tumor Suppressive Role of ING5 in Prostate Cancer

Omer Faruk Karatas[1,*]

[1]Molecular Biology and Genetics Department, Erzurum Technical University, Erzurum, Turkey

*Correspondence:

Omer Faruk Karatas, Ph.D. Department of Molecular Biology and Genetics, Erzurum Technical University, Omer Nasuhi Bilmen Mah. Havaalani Yolu Cad. No:53, Yakutiye, Erzurum, Turkey

Tel: +90 444 5 388 - 2390

Fax: +90 442 230 00 39

e-mail: faruk.karatas@erzurum.edu.tr

Prostate cancer (PCa) is one of the most common types of cancer in men. In several recent studies, chromosomal deletions in the q arm of 2. chromosome, where *ING5* gene resides within, have been identified in various cancer types including PCa. In this study, we aimed at investigation of the function of ING5 as a tumor suppressor in PCa.

We examined the expression level of ING5 in tissue samples and cell lines using quantitative real-time PCR (qRT-PCR) and Western blot analysis. We tested the *in vitro* tumor suppressor potential of PC3 and LNCaP cells stably transfected with ING using cell viability, colony formation, migration, invasion, and apoptosis assays. We then investigated the effects of ING5 on the Akt and p53 signaling pathways using Western blot analysis.

We showed that ING5 is significantly downregulated in PCa tumor tissue samples and cell lines compared to the corresponding controls. *In vitro* assays demonstrated that ING5 effectively suppress proliferative, clonogenic, migratory, and invasive potential and induce apoptosis in PCa cells. ING5 might potentially exert its anti-tumor potential through inhibiting AKT and inducing p53 signaling pathways.

Our findings demonstrated that ING5 possesses tumor suppressor roles *in vitro*, pointing its importance during the prostatic carcinogenesis processes.

# Fabrication of Piezoresistive Nanocomposite Using Functionalized Carbon Nanotubes (fCNT) and Polydimethylsiloxane (PDMS) Towards Pressure Sensing Applications

Mohd Nizar Hamidon

Faculty of Engineering, University Putra Malaysia, 43400 UPM Serdang, Selangor, Malaysia

Institute of Advanced Technology, University Putra Malaysia, 43400 UPM Serdang, Selangor, Malaysia

*Abstract-*In recent years, conductive and piezoresistive pastes fabricated via nanomaterials are attracting a lot of attention. Polydimethylsiloxane (PDMS) is the most common silicone based organic polymer. Mechanical and electrical properties of PDMS make it ideal polymeric material for nano fluidic, wearable and flexible sensory applications. One of the most common issues that are not fully resolved is CNTs tendency to aggregate while being mixed in polymeric matrix. Our goal for this work is to fabricate a homogenous CNTs/PDMS nanocomposite with piezoresistive properties for applications in flexible electronics and sensory devices, which later can be implemented for the haptic sensory system. In this work, various methods to prepare CNTs/PDMS nanocomposite are compared. Moreover, the electrical properties of samples and the effect of mixing techniques and curing time on aggregation of CNTs are studied. Different purification processes and advantages of functional CNTs are studied and functional CNTs are utilized to fabricate a homogenously dispersed CNTs/PDMS nanocomposite. Purification of CNTs increases the crystallinity and functionalization enhances the dispersion rate of CNTs in PDMS. There is a direct relation between mixing method and curing time with aggregation rate of CNTs in PDMS; CNTs/PDMS nanocomposite exhibits measurable conductance at above 10 wt%. Piezoresistive measurements indicate this material could be a suitable replacement for piezoreisitive materials used for sensory devices due to their high sensitivity, accuracy and flexibility in addition to their adjustable size.

# Current Trend and Status of Bioceramics for Dental Applications in UPM, Malaysia

Khamirul Amin Matori
Department of Physics, Faculty of Science, Universiti Putra Malaysia, 43400 UPM Serdang, Selangor, Malaysia

Mohd Hafiz Mohd Zaid
Department of Physics, Faculty of Science, Universiti Putra Malaysia, 43400 UPM Serdang, Selangor, Malaysia

Norhazlin Zainuddin
Department of Chemistry, Faculty of Science, Universiti Putra Malaysia, 43400 UPM Serdang, Selangor, Malaysia

Sidek Hj. Abdul Aziz
Department of Physics, Faculty of Science, Universiti Putra Malaysia, 43400 UPM Serdang, Selangor, Malaysia

Mohammad Zulhasif Ahmad Khiri
Material Synthesis and Characterization Laboratory, Institute of Advanced Technology, Universiti Putra Malaysia, 43400 UPM Serdang, Selangor, Malaysia

Nadia Asyikin Abdul Rahman
Department of Physics, Faculty of Science, Universiti Putra Malaysia, 43400 UPM Serdang, Selangor, Malaysia

*Abstract*—The many facets of research in the area of solid state materials chemistry have been presented and discussed. The article focuses on the present status in load bearing applications especially in dental and orthopedics since they have ability to make a bond with the tissue in physical environment. While many of the materials properties such as aesthetic look, mechanical strength, biological compatibility, functionality and so on have been explored mainly in bioceramics contribute towards many properties in the areas of Glass ionomer cements (GIC). Possible directions for future research along with identifying and highlighting the strengths of the expertise available in this country are also mentioned. The GIC are produced through acid base reaction between calcium-fluoro-alumino-silicate (CFAS) bioglass powder and polyacrylic acid (PAA). The preparation of CFAS bioglass is composed of Clam Shells (CS), Soda Lime Silicate (SLS), $CaF_2$, $P_2O_5$, and $Al_2O_3$ with the empirical formula $[xCS(45-x)SLS15CaF_220P_2O_520Al_2O_3]$ where x = 20, 15, 10 and 5 (wt.%). The waste materials that were used to produce CFAS bioglass are CS and SLS. The elemental analysis of the raw materials and samples had been determined by using are X-ray fluorescence (XRF), Thermogravimetric Analysis (TGA), Differential Scanning Calorimetry (DSC), Field Emission Scanning Electron Microscopy (FESEM), density and molar volume, X-ray diffraction (XRD), Fourier Transform Infrared Spectroscopy (FTIR) and Compressive Strength. The XRF result for raw SLS glass and CS sample shown that largest percentage of element in SLS glass is silica ($SiO_2$) and lime (CaO) which is 56% and 37% while CS has 99.5% of CaO after calcination. From TGA it shown that percentage of weight loss from glass sample is not more than 0.3% while DSC shown glass transition temperature, $T_g$ in the range of 520-580 °C and crystallization temperature, $T_c$ is about 850-950 °C. The FESEM shows that the glass sample in irregular shape with a sharp particle edge of glass. Synthesized glasses were then used to produce GIC, in which the properties were characterized using Fourier transform infrared spectroscopy (FT-IR) and compressive test (from 1 to 28 days). The density had shown that as the ageing time increase the density of GIC increase. But for molar volume, as the ageing time increase the molar volume of GIC decrease. From, XRD analysis, GIC sample in glassy structure and amorphous phase. Next, FTIR shown a presence of various band and stretching vibration due to the water molecule elimination process, polymerization of Si□OH to Si□O□Si and hardening process of GIC had been proven within the samples throughout the ageing time from 7 to 28 days. The compressive Strength shows that as the ageing time increase, the compressive strength increase due to the hardening process of GIC.

*Keywords—Bioceramics, GIC, Crystallization, Polymerization*

# ORAL PRESENTATIONS

# Indices and Computer Models Used to Calculate and Estimate Outdoor Human Thermal Comfort

Süleyman Toy
*City and Regional Planning Dept.*
*Architecture and Design Faculty*
*Atatürk University*
Erzurum, Turkey
suleyman.toy@atauni.edu.tr

*Abstract*—Humans feel the features of atmosphere all together at one time i.e. combined effect of ambient air conditions. This effect is felt as temperature. Effect of atmospheric features on humans is called thermal effect. People are satisfied or dissatisfied with the conditions of the atmosphere. When they are satisfied with them so they are in comfort and vice versa. Although the definition of thermal comfort is very diverse and changeable depending on the fields, it can often be defined as the condition of ambient air where 80% of the people present there feels no discomfort with it. Thermal comfort is effective on human health, workforce performance, emergence and dissemination of critical illnesses, energy consumption, ecological destruction, water consumption etc. Therefore, due to its various aspects this concept is worth studying scientifically. Since the beginning of 20th century scientists have been interested in under what air conditions people are comfortable. To date more than 200 indices and models have been developed to calculate, estimate, determine, categorise, compare and even distribute thermal comfort values and also use this information to design spaces and buildings. This study is related to the indices and models used to calculate / estimate human thermal comfort and even design spaces considering the bioclimatic information they produce. In the scope of the study, brief information is given about the concept of human thermal comfort and the simple and complex indices (e.g. RayMan) calculating it and some detailed information is also given about the computer models (e.g. ENVIMET) used to design spaces considering several human thermal comfort factors.

*Keywords—human thermal comfort, simple indices, complex indices, ENVIMET, Rayman, bioclimatic comfort*

## I. INTRODUCTION

Atmosphere, a gaseous envelope surrounding the earth, is accepted to be the first environment to touch human body at its birth. Atmosphere provides all the opportunities for humans to live on the earth where they are surrounded by its effective factors given in Fig. 1 [1]. Therefore, atmosphere involves the most effective factors on humans including all their activities from clothing to eating.
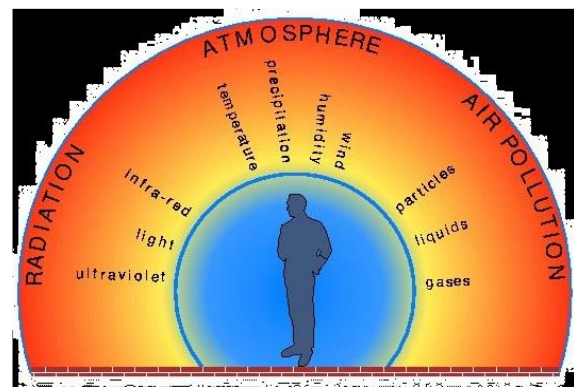


Fig 1. Atmospheric environment and human

Atmospheric features such as temperature, humidity, wind and solar radiation have combined effect on human body, i.e. human body does not sense any atmospheric elements (features) individually. Combined effect of atmospheric elements is represented by thermal sensation of human of thermal component of atmosphere. Human thermal sensation of the atmospheric elements may sometimes be more severe than others i.e. the effect of temperature may be negatively or positively larger when it is accompanied by higher or lower relative humidity or wind speed (causing strong/weak cold/heat stress).

Humans feel the features of atmosphere all together at one time i.e. combined effect of ambient air conditions. This effect is felt as temperature. Effect of atmospheric features on humans is called thermal effect. People are satisfied or dissatisfied with the conditions of the atmosphere. When they are satisfied with them so they are in comfort and vice versa. Although the definition of thermal comfort is very diverse and changeable depending on the fields, it can often be defined as the condition of ambient air where 80% of the people present

there feels no discomfort with it. Thermal comfort is effective on human health, workforce performance, emergence and dissemination of critical illnesses, energy consumption, ecological destruction, water consumption etc. Therefore, due to its various aspects this concept is worth studying scientifically.

This study is related to the indices and models used to calculate / estimate human thermal comfort and even design spaces considering the bioclimatic information they produce. In the scope of the study, brief information is given about the concept of human thermal comfort and the simple and complex indices (e.g. RayMan) calculating it and some detailed information is also given about the computer models (e.g. ENVIMET) used to design spaces considering several human thermal comfort factors.

II. HUMAN SENSATION OF THERMAL COMPONENTS

The thermal component of the atmospheric environment includes air temperature (Ta), air humidity (VP or RH), wind velocity (v), mean radiant temperature (Tmrt short- and long-wave radiation.

Humans sense the atmospheric features as temperature which means sensible temperature which may combine all the atmospheric thermal factors mentioned above (ambient temperature etc.) and those depending on human body like working, sitting or standing, effects of the insulation of clothes, body weight etc.

For the determination of the combined effect of these variables on human body, several calculations, models and indices have been developed for longer than an age since the work of Haldane [2]. There are several approaches to the calculation or estimation of thermal effect including Psychologic, Thermophysiological and human body energy balance [3]. The factors effective on thermal balance of human body are given in Fig 2. [4].

These conditions can be evaluated by using various thermal comfort (or stress) indices based either on simple empirical approaches or on more complex and reliable human-biometeorological approaches.

Earlier indices combined only a couple of meteorological parameters either in the forms of simple equations (such as Dıscomfort Index; [5]) or on different thermal comfort charts (e.g. [6]). They combined generally air temperature with wind velocity in cold climate regions while air temperature with humidity in the case of warm climates. With the advancement of computer technology several complex calculation and formulation models began to be used to determine thermal comfort thus using simulation models.

*G. Indices and Models*

One of the most popular indices used to calculate thermal conditions of human is the Physiological Equivalent Temperature – PET index. This index is in the category of complex indices used for the assessment of both hot and cold conditions and all year and day round [7,8].
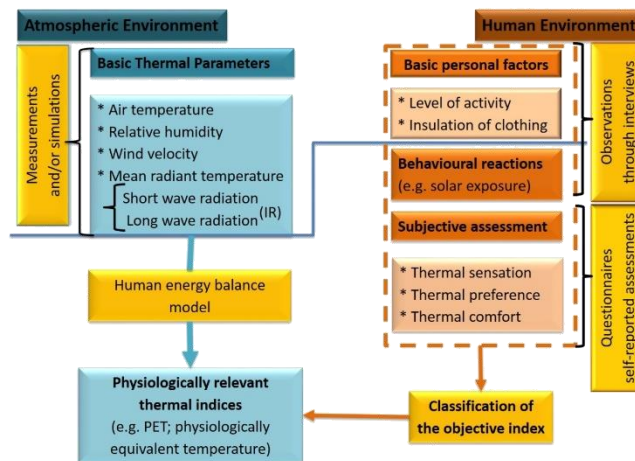


Fig. 2. Effective factors on human thermal conditions

Human – bioclimatological conditions are analysed resulting in PET values (˚C) which are generally categorised into previously defined "thermal comfort-ranges" (Table 1; [9]) in order to demonstrate the spatial and/or temporal characteristics of human thermal comfort conditions.

RANGES OF THERMAL COMFORT

| PET (°C) | Thermal Sensation | Thermal stress |
|---|---|---|
| < 4 | Very cold | Extreme cold stress |
| 4,1 – 8,0 | Cold | Strong cold stress |
| 8,1 – 13,0 | Cool | Moderate cold stress |
| 13,1 – 18,0 | Slightly cool | Slight cold stress |
| 18,1 – 23,0 | Neutral (comfortable) | No thermal stress |
| 23,1 – 29,0 | Slightly warm | Slight heat stress |
| 29,1 – 35,0 | Warm | Moderate heat stress |
| 35,1 – 41,0 | Hot | Strong heat stress |
| > 41,0 | Very hot | Extreme heat stress |

The widely-known RayMan software [10, 11, 12] is a calculation model of human thermal comfort model which can model radiation parameter (i.e. Tmrt) depending on the sky view factor from the cloudiness/shadowiness data. The model can calculate instant thermal comfort values for three indices Predicted Mean Vote (PMV; [13]), PET and Standard Effective Temperature (SET; [14]). As can be seen from Fig 3, the model can be input all effective meteorological parameters as well as body features and clothing, activity and position.
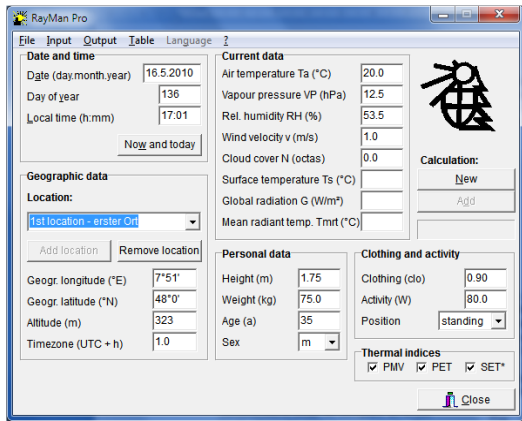
Fig 3. Interface of rayman model

The model can also use long term climatic data by inputting them in a text file in the model as can be seen in Fig. 4.
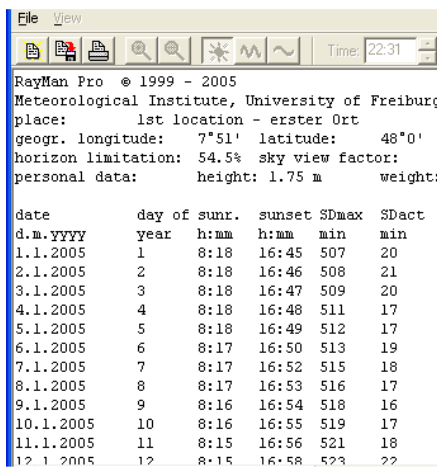


Fig 4. Longterm data input

The model can also consider sky – view to calculate solar radiation impact as can be seen in Fig. 5.
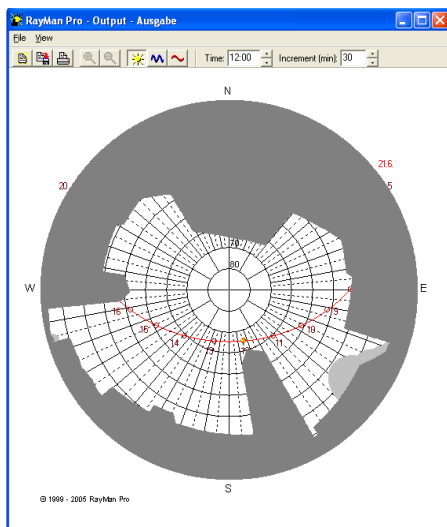


Fig. 5. SKY – View Factor

ENVI_MET V4 is a holistic three-dimensional non-hydrostatic model for the simulation of surface-plant-air interactions not only limited to, but very often used to simulate urban environments and to asses the effects of green architecture visions. It is designed for microscale with a typical horizontal resolution from 0.5 to 5 metres and a typical time frame of 24 to 48 hours with a time step of 1 to 5 seconds. This resolution allows to analyze small-scale interactions between individual buildings, surfaces and plants.

Buildings are not independent systems, because the indoor climate and the physics of the building interact continuously with the outside microclimate. Moreover, especially in urban areas, the buildings interact with each other through the modification of wind flows, solar access and temperature effects.

It has four basic elements which are cities and health, wind and sun, buildings and climate and trees and vegetation. Cities and health ingredient is related to the simulation of air pollution and thermal comfort matters. Wind and sun includes solar access and wind flow. Buildings and climate is related to building physics and climate, trees and vegetation includes sustainable landscape architecture matters by giving simulation opportunities.

## III. CONCLUSION

The terms climate, bio-climate and bioclimatic (thermal) comfort are among the vital elements in spatial planning and design. People have long been challenging to develop several indices and models to estimate thermal comfort conditions for their numerous social, psychological, economic and health benefits to humans.

These terms and their use in planning and design for every type of space are new in especially developing countries including Turkey by taking places in only small scale designs and modellings. In order to make settlements more livable, bioclimatic comfort conditions must be considered in designs and constructions in order to be successful in struggling with climate change. In the developing process of computer technologies new approaches are very useful to model all the situations in urban areas.

## REFERENCES

[1] WMO. Climate and human health. World climate News 1999, 14: 3-5

[2] J.S. Haldane, 1905. The influence of high air temperature J Hyg 5, 494–513.

[3] A. K. Shakir. Thermal Comfort Modelling of an Open Space (Sport Stadium) A thesis submitted for the degree MSc Energy Systems & the Environment Faculty of Engineering Department of Mechanical Engineering Energy Systems Research Unit University of Strathclyde Glasgow U.K. , 2006. 105pp.

[4] S. Toy, Kántor, N. Evaluation of human thermal comfort ranges in the respect of urban climate of winter cities on the example of Erzurum city. In: Proceedings of International Winter Cities Symposium, 2016.

[5] E.C. Thom. The discomfort index. Weatherwise 1959, 12, 57–60.

[6] V. Olgay, Design with the climate: Bioclimatic approach to architectural regionalism. Princeton University Press. New Jersey 1963.

[7] H. Mayer and P. Höppe, Thermal comfort of man in different urban environments. Theor. Appl. Climatol. 1987, 38, 43-49.

[8] P. Höppe, The physiological equivalent temperature-a universal index for the biometeorological assessment of the thermal environment. Int. J. Biometeorol. 1999, 43:71-75.

[9] A. Matzarakis, H. Mayer, Another kind of environmental stress: thermal stress. WHO Newsletters, 1996, 18: 7-10.

[10] Matzarakis, Rutz, F.; Mayer, H., Estimation and calculation of the mean radiant temperature within urban structures. In: Biometeorology and Urban Climatology at the Turn of the Millenium (ed. by R.J. de Dear, J.D. Kalma, T.R. Oke and A. Auliciems): Selected Papers from the Conference ICB-ICUC'99, Sydney, WCASP-50, WMO/TD No. 1026, 2000 273-278.

[11] Matzarakis, Rutz, F., Mayer, H., Modelling Radiation fluxes in simple and complex environments – Application of the RayMan model. International Journal of Biometeorology 2007, 51, 323-334.

[12] Matzarakis, Rutz, F., Application of RayMan for tourism and climate investigations. Annalen der Meteorologie 2005, 41 (2), 631-636.

[13] P.O. Fanger, Thermal Comfort. Copenhagen, Danish Technical Press, 1970, 244 pp.

[14] A.P., Gagge, Fobelets A.P, Berglund L.G., A Standard predictive index of human response to the thermal environment. ASHRAE Trans 1986, 92, 709–31.

[15] https://www.envi-met.com/intro/

# Hepatoprotective Role of Boric Acid Supplementation on Liver Injury Induced by Renal Ischemia-Reperfusion

Nihal Simsek Ozek
Department of Biology, Faculty of Science
Ataturk University
Erzurum, Turkey

Berna Kavakcioglu Yardımcı
Department of Chemistry, Faculty of Science
Dokuz Eylul University
Izmir, Turkey

Serkan Yildirim
Department of Pathology, Faculty of Veterinary
Ataturk University
Erzurum, Turkey
syildirim@atauni.edu.tr

East Anatolian High Technology Research and Application Center (DAYTAM), Ataturk University, Erzurum, TURKEY
nihal.ozek@atauni.edu.tr

Department of Biology, Faculty of Science
Ataturk University
Erzurum, Turkey
berna.kavakcioglu@deu.edu.tr

*Abstract*—**Renal Ischemia-Reperfusion (RIR) has been known to cause different remote organ dysfunction including liver. This injury may be arisen from the alterations in the microcirculation and increased hepatic oxidative stress. To prevent these stress-oriented liver injuries, the antioxidant agents such as boric acid can be used as a protective purpose. Therefore, the current study was conducted to determine hepatoprotective role of boric acid on I-R induced liver injuries. Rats were divided into 4 different groups, Sham-operated, RIR (50 min/3 h), BA (14 mg/kg), and BA + RIR (14 mg/kg, 50 min/3 h). BA was given to mentioned groups through intragastric administration 1 h before RIR procedure. Hepatic damages were determined by the examination of H&E-stained liver sections. The oxidative stress was evaluated by immunohistochemical staining of 8-hydroxy-2'-deoxyguanosine (8-OHdG). Moreover, the alterations of biomolecular makeup of liver tissues were revealed using Fourier Transform Infrared (FTIR) Spectroscopy and unsupervised chemometric analysis approaches. Histopathological analysis indicated a congestion, hemorrhage, mild degeneration of hepatocyte, perivascular cellular infiltration and sinusoidal dilatation in the RIR group. Moreover, an increased level of 8-OHdG was found in this group. However, the decreased the RIR-induced the histological injuries and the level of 8-OHdG were acquired with BA pretreatment. Spectroscopic results also indicated the differences in the macromolecular compositions of the RIR and the BA + RIR groups. Chemometric analysis revealed a clear discrimination of RIR from other groups. The findings of the current study clarified that boric acid has an efficient hepatoprotective agent against RIR-induced liver injuries.**

*Keywords—renal ıschemia/reperfusion, liver, oxidative stress, FTIR spectroscopy, unsupervised chemometric analysis.*

## I. INTRODUCTION

Ischemia-reperfusion (I/R) is characterized by restriction of blood supply to the particular organ followed by restoration of blood flow and re-oxygenation, which may occur especially after infarction, sepsis and organ transplantation [1]. In the case of kidney, I/R causes to pathological condition known as acute renal injury that is accepted as a clinical syndrome with high morbidity and, ultimately high mortality rates [2-3].

Although the pathophysiology of RIRinjury is quite complicated, it is well known that activation of neutrophils, release of reactive oxygen species (ROS) and other various inflammatory mediators are involved this phenomenon [4]. Moreover, there is a link between RIRinjury and remote liver damage that seems to be in part the result of the oxidative burst and the inflammatory response according to the clinical trials [5, 6]. In other words, renal ischemia can induce hepatic oxidative stress, as evidenced by the studies showing the alterations in oxidant-antioxidant status of liver tissue [4, 7, 8].

Some papers have demonstrated the beneficial effects of certain agents and components including phenolic diterpene carnosol, organic isothiocyanate sulforaphane, 3-aminobenzamide, flavone baicalein, plant natural polyphenol mangiferin and Pistacia lentiscus oil remote liver injury based on oxidative stress induced by I/R [9-14]. Besides these limited number of molecules, antioxidative boron and/or its compounds could be an alternative for the protection of liver from I/R mediated injury. Boron, essential element for plants and probably for human and animal healths, have been reviewed from the point of view of vitamin D metabolism, steroid hormone biosynthesis, calcium homeostasis, healthy bone development, and maintenance of cell membranes [15, 16]. Additionally, the simplest boron compound boric acid (BA) has been found as protective against oxidative stress in numerous models [17-19]. However, there is no information on this boron compound for oxidative stress related hepatic injury. Thus, this study aimed to investigate the protective effects of BA on the liver from RIRinjury in rat model based on histopathological examinations, immunohistochemical staining of 8-OHdG and total biomolecular compositions using Fourier Transform Infrared (FTIR) Spectroscopy.

## II. MATERIAL AND METHODS

### A. Animals

Sprague-Dawley rats (ATADEM of Atatürk University, Erzurum, Turkey) about 250–300 g were used for the study. We maintained the animals in air conditional room with 12 h light/dark cycle, fed them with regular chows, and allowed them free access to tap water. All experimental procedures in this study were approved by the Atatürk University Local Ethics Committee for Animal Experiments (No. 66, 22.03.2018).

### B. Boric acid preparation and experimental design

BA, supplied from Sigma-Aldrich Chemical Company (St. Louis, MO, USA), was dissolved in 100 ml distilled water. Then, the solution was diluted at 14 mg/kg concentration. The dose of BA was selected according to the literature data [20]. The solutions were given to rats as 1 cc by gavage 1 h before ischemia onset.

Twenty animals were randomly separated into four equal groups (n=7 per group) in the experiments;

Group 1 (Control): These animals were sham group (the abdominal wall was only opened and closed).

Groups 2 (Experimental group): These animals were exposed to ischemia produced for 50 min and followed by reperfusion of 3 h.

Groups 3: These animals were treated with BA via gavage at 14 mg per kg body weight.

Groups 4: These animals were treated with BA via gavage at 14 mg per kg body weight, 1 hours before ischemia.

I/R injuries were created as described previously [21]. Briefly, each rat was anesthetized via intraperitoneal injection of a combination of ketamine (75 mg/kg, i.p) and xylazine (10 mg/kg, i.p.). An abdominal incision was created, and unilateral ischaemia was induced by clamping the left renal artery. After 50 min of ischemia, the clamp was removed to allow reperfusion. Body temperature was maintained at 36 °C using heating pads throughout the experiment. At 3h of reperfusion, rats were killed and liver tissues were collected. Liver samples were stored at -20 °C for a period before they were used in later analysis; liver slices were also processed for histopathological studies.

### C. Histopathological examination and assessments

Liver tissue samples were fixed in 10% formalin solution for 72 h, embedded in paraffin, sectioned (5 μm), and placed on slides. The samples were stained with hematoxylin and eosin (H&E) for identification of architectural changes. The high-resolution pictures of samples (200×) were taken under bright field using an Olympus BX60 microscope (Olympus, Hamburg, Germany).

### D. Immunohistochemical examination of 8-OH-dG level

Immunohistochemical staining for 8-OHdG was performed by an automated method on the VENTANA BenchMark GX System (Ventana Medical Systems) with an Ultra View Universal DAB Detection Kit, on 4-μ-thick sections from a representative block in each rat. After deparaffinization, the antigenic determinant site for 8-OHdG

was unmasked in citrate buffer with steam for 60 min. The primary antibody 8-OHdG (Santa Cruz sc-393871) was used at a dilution of 1:300 for 32 min at 37°C. The slides were then incubated with the diluted antibody, followed by pplication of the Ultraview Universal DAB detection kit (Ventana Medical Systems). DAB was used as a chromogen and hematoxylin as a counterstain. The specificity of staining was confirmed by the inclusion of negative control slides processed in the absence of primary antibody on tissue from the same animal.

### E. Fourier Transform Infrared (FTIR) spectroscopy and unsupervised chemometric analysis

#### 1) FTIR spectral data collection and analysis

For FTIR spectroscopy measurements, frozen liver tissues were ground and homogenized in a mortar and pestle under liquid nitrogen. The spectra of homogenized liver samples were collected using Bruker Vertex 70 FTIR spectrometer in attenuated total reflectance (ATR) mode (Ettlingen, Germany) at East Anatolian High Technology Research and Application Center (DAYTAM) of Ataturk University. The powdered tissue samples were directly put on the ATR crystal and compressed a constant pressure to obtain good surface contact. The 7 spectra/group were collected at 4000-400 cm$^{-1}$ spectral region, 4 cm$^{-1}$ resolution and 25 scans. Data collection and manipulation were performed using OPUS 5.5 software (Bruker Optics, GmbH).

To obtain differences in the biochemical makeup of studied groups, the spectra of sample were firstly baseline corrected and normalized using same software.

#### 2) Principal component analysis (PCA) and hierarchical cluster analysis (HCA)

To explore whether there is clear discrimination between studied groups or not, principal component analysis (PCA) and hierarchical cluster analysis (HCA) were performed to base-line corrected absorbance spectra of studied groups in the whole IR region (4000-400 cm$^{-1}$) using Unscrambler X 10.3 (CAMO Software AS., Oslo, Norway) multivariate analysis (MVA) software. PCA were demonstrated as score plot while HCA was shown ns as dendrogram, which was obtained from Ward's algorithm.

## III. RESULTS

### H. Effect of boric acid on histopathological changes

Histopathological examination by H&E staining of tissue sections revealed normal histology of liver in control group (Figure-1A). The RIRcaused severe Congestion (C), heomarrage (black thick arrows), perivascular cell infiltration (white arrows), hydropic degeneration (thin arrows) (Figure-1B) and sinusoidal dilatation (Figure-1C) in liver tissue. On the contrary, when boric acid was applied before I/R, the reduction in the number of histopathological change was observed (Figure-1D).

### İ. Effect of boric acid on 8-OH-dG level

The image representing the levels of 8-OHdG in rat liver is depicted in Figure-2. RIRmarkedly stimulated the formation of 8-OHdG in rat liver cells in comparison with control (Figures-2A and -B). Pretreatment with boric acid led to a

slightly decrease in the 8-OHdG formation in liver (Figure-2D).
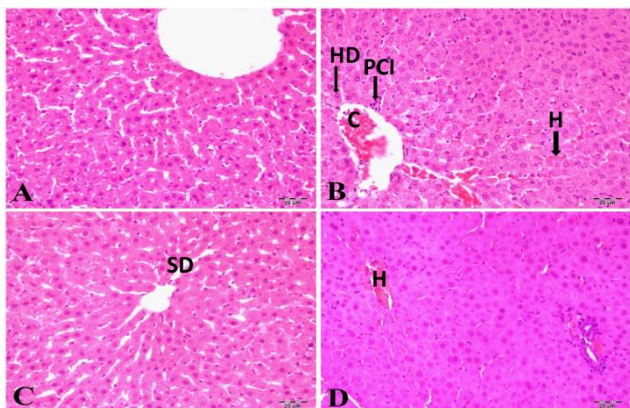


**Figure 1**. Representative photographs from the liver showing the effect of boric acid on hepatic injury with RIRin rats. A – Control, B – RIR; Congestion (C), hemorrhage (H), perivascular cell infiltration (PCI), hydropic degeneration (HD) C –RIR; sinusoidal dilatation SD) D – RIR+ Boric acid; mild hemorrhage (H) Bar: 20 µm.
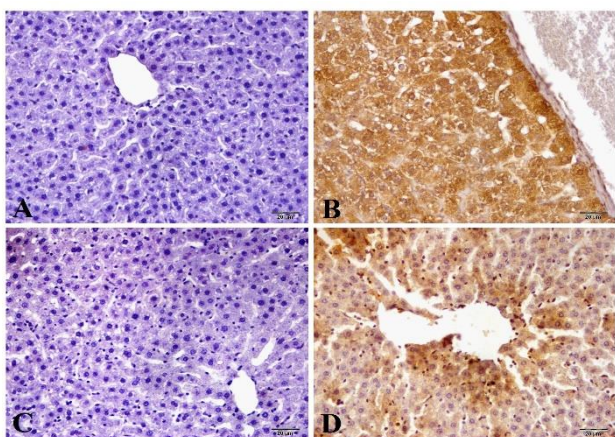


**Figure 2**. 8-OHdG immunohistochemical staining in rat liver sections. The immunohistochemical localization of 8-OHdG appears as brown staining **A** – Control. **B** – RIR; the 8-OHdG-positive area **C** – Boric acid, same to control **D** – RIR+ Boric acid; slightly decreased 8-OHdG-positive area. Bar: 20 µm.

### J. Effect of boric acid on biomolecular composition and their spectral discrimination

#### 1) Qualitative spectral analysis

To identify the differences in the biomolecular composition of the studied groups, qualitative spectral analysis was performed. Firstly, average spectra/group were obtained, then baseline corrected and normalized. This analysis was performed in two different spectral regions. The first region located at 3025-2800 cm$^{-1}$, called C-H stretching region while the second region located at 1760-900 cm$^{-1}$, called fingerprint region. The former includes unsaturated and saturated lipid associated spectral bands while the second includes triglyceride, cholesterol ester, protein and nucleic acid related spectral bands [22].Figures 3A and 4B indicated the normalized spectra of the studied groups in the C-H stretching and fingerprint regions. As can be seen from these figures, RIRled to alterations in the signal intensities of the various biomolecules such as lipid, protein and nucleic acid associated spectral bands, implying the changes in the concentrations of liver molecules due to renal ischemia.

However, the BA pretreatment prevented the formation of these changes.
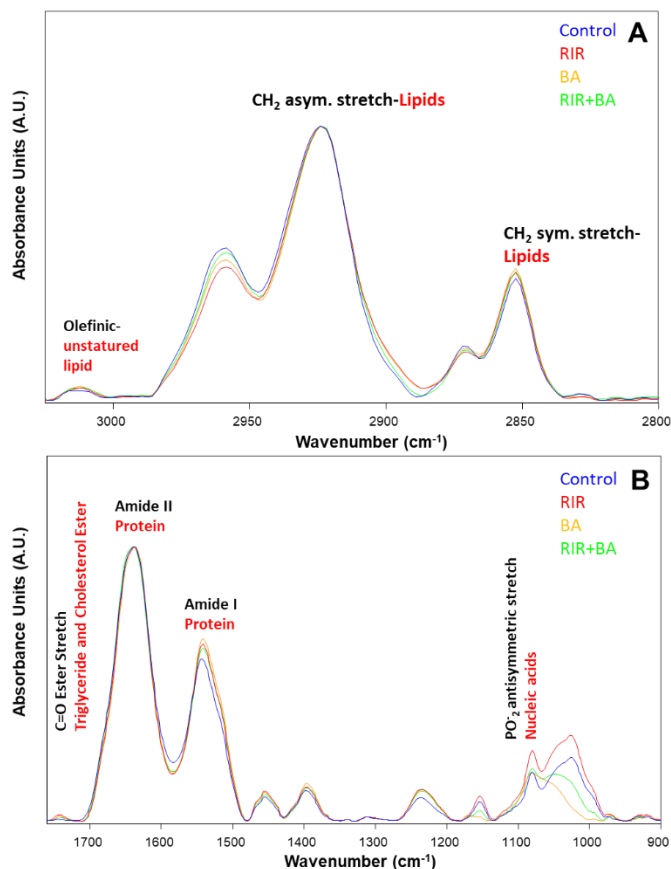


**Figure 3**. Average IR spectra of control, RIR, BA and RIR+BA groups in the 3028-2800 cm$^{-1}$ (**A**) and 1760-900 cm$^{-1}$ (**B**) spectral regions.

#### 2) Principal component analysis (PCA) and hierarchical cluster analysis (HCA)

Figure 4 demonstrated the PCA score plots of control, RIR, BA and RIR+BA groups in 4000-400 cm-$^1$ spectral region. As can be clearly depicted from the figure, RIR group were discriminated from other groups. The samples in the BA and RIR+BA groups were located close to control samples, implying the degree of similarity between them. To prove this differentiation, HCA was performed. The HCA dendrogram was given in Figure 5, indicating that RIR group segregated different from the other studied groups with a higher heterogeneity values.
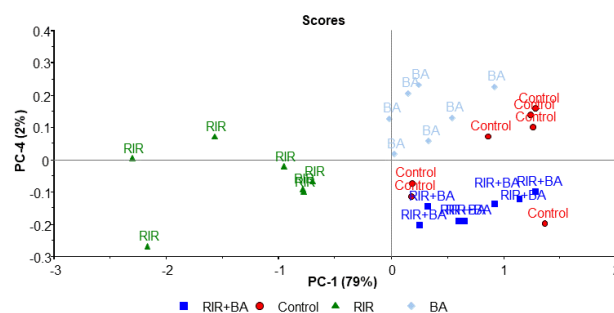


**Figure 4.** PCA score plots of control, RIR, BA and RIR+BA groups in 4000-400 cm$^{-1}$ spectral region.
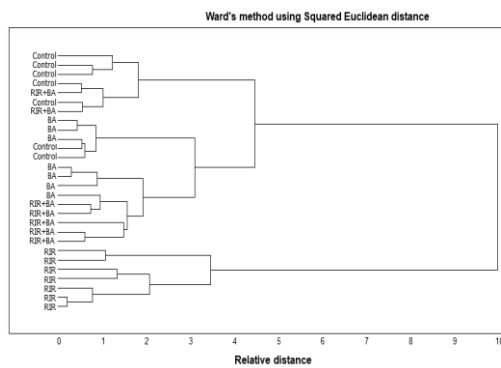
**Figure 5**. HCA dendrogram of control, RIR, BA and RIR+BA groups in the 4000-400 cm$^{-1}$ spectral region.

## IV. DISCUSSION

Its well known that damaged tissue during I/R injury produces excessive amount of free radicals, which trigger oxidative stress. As a consequnce of I/R-induced oxidative stress, changes in mitochondrial oxidative phosphorylation, ATP depletion, increase in intracellular calcium, activation of membrane phospholipids proteases, damages in biological macromolecules, and ultimately cell death could be seen. Moreover, I/R injury mediated oxidative stress in a particular organ seems to influence the function of many remote organs and may lead to the multiple organ dysfunction syndrome. For instance, RIRis associated with acute kidney injury and it is important to note that despite widespread availability of renal replacement therapy, the patients faces a mortality risk as high as 40–60% due to the distant organ effects of this syndrome [8]. In order to fight with these global consequences of I/R injury, the researchers have focused to benefit from healthful effects of free radical scavengers and antioxidants [14, 23-28]. In this study, we firstly aimed to use boric acid, a weakly acidic hydrate of boric oxide with mild antiseptic, antifungal, and antiviral properties, as an antioxidant to protect liver from RIRinjury. According to our findings, although there was still mild heomarrage, 14 mg/kg boric acid pretreatment 1 h before RIRinjury supressed histopathological changes as congestion, perivascular cell infiltration, hydropic degeneration and sinusoidal dilatation in liver, which was clearly detected in I/R injury. Another parameter investigated was the 8-OHdG that is one of the main markers of DNA damage as a result of oxidative stress. Unsurprisingly, while RIRmarkedly stimulated the formation of 8-OHdG in rat liver cells, the slight decreases were observed with the pretreatment of boric acid. In addition, boric acids pretreatment prevented ischemia–induced alterations in liver tissue biomolecules Supportingly, the protective effect of boric acid against liver damage induced by carbon tetrachloride ($CCl_4$) was found in mice [29]. In addition, boric acid decreased inflammation, oxidative stress and apoptosis caused by cisplatin toxicity and increased ER stress in kidney [19]. Sogut et al. indicated antioxidant and anti-apoptotic effects of boric acid on hepatoxicity in chronic alcohol-fed rats [17]. In an another research, the protective effect of boric acid against cyclophosphamide-induced oxidative stress and renal damage in rats was shown [30].

Collectively, this is a preliminary study revealed that RIRis capable of triggering oxidative stress and cell damage in the rat liver and boric acid exerts protective effect against distant liver damage with renal I/R. This benefical effect is most probably originated from radical scavenging activity of boric acid. On the other hand, further studies should be conducted in order to highlight the underlying mechanism of boric acid protection and to develop more efficient strategies for the remediation of I/R induced tissue damages.

## ACKNOWLEDGMENT

## REFERENCES

[1] M. Malek, M. Nematbakhsh, "Renal ischemia/reperfusion injury; from pathophysiology to treatment," Journal of renal injury prevention, 4(2), pp. 20, 2015.

[2] K. J. Kelly, "Distant effects of experimental renal ischemia/reperfusion injury," Journal of the American Society of Nephrology, 14(6), pp. 1549-1558, 2003.

[3] S. M. Bagshaw, K. B. Laupland, C. J. Doig, G. Mortis, G. H. Fick, M. Mucenski,... & T. Rosenal, "Prognosis for long-term survival and renal recovery in critically ill patients with severe acute renal failure: a population-based study," Critical Care, 9(6), pp. 700, 2005.

[4] F. Golab, M. Kadkhodaee, M. Zahmatkesh, M. Hedayati, H. Arab, R. Schuster,... & M. Soleimani, "Ischemic and non-ischemic acute kidney injury cause hepatic damage," Kidney international, 75(8), pp. 783-792, 2009.

[5] Y. Shang, Y. L. Siow, C. K. Isaak, "Downregulation of glutathione biosynthesis contributes to oxidative stress and liver dysfunction in acute kidney injury," Oxidative Medicine and Cellular Longevity, 2016.

[6] H. Zhao, H. Huang, A. Alam, Q. Chen, K. C. Suen, J. Cui, ... & D. Ma, "VEGF mitigates histone-induced pyroptosis in the remote liver injury associated with renal allograft ischemia–reperfusion injury in rats," American Journal of Transplantation, 2018.

[7] M. Serteser, T. Koken, A. Kahraman, K. Yilmaz, G. Akbulut, & O. N. Dilek, "Changes in hepatic TNF-α levels, antioxidant status, and oxidation products after renal ischemia/reperfusion injury in mice," Journal of Surgical Research, 107(2), pp. 234-240, 2002

[8] M. E. Grams, H. Rabb, "The distant organ effects of acute kidney injury," Kidney international, 81(10), pp. 942-948, 2012.

[9] J. H. Yao, X. S. Zhang, S. S. Zheng, Y. H. Li, L. M. Wang, Z. Z. Wang, ... & X. F. Tian, "Prophylaxis with carnosol attenuates liver injury induced by intestinal ischemia/reperfusion," World Journal of Gastroenterology: WJG, 15(26), pp. 3240, 2009.

[10] H. D. Zhao, F. Zhang, G. Shen, Y. B. Li, Y. H. Li, H. R. Jing, ... & X. F. Tian, "Sulforaphane protects liver injury induced by intestinal ischemia reperfusion through Nrf2-ARE pathway," World journal of gastroenterology: WJG, 16(24), pp. 3002, 2010.

[11] A. T. Hekimoglu, G. Toprak, H. Akkoc, O. Evliyaoglu, T. Tas, I. Kelle, & L. Colpan, "Protective effect of 3-aminobenzamide, an inhibitor of poly (ADP-ribose) polymerase in distant liver injury induced by renal ischemia-reperfusion in rats,". Eur Rev Med Pharmacol Sci, 18(1), pp. 34-38, 2014.

[12] C. C. Lai, P. H. Huang, A. H. Yang, S. C. Chiang, C. Y. Tang, K. W. Tseng, & C. H. Huang, "Baicalein reduces liver injury induced by myocardial ischemia and reperfusion," The American journal of Chinese medicine, 44(03), pp. 531-550, 2016.

[13] S. M. El-Sayyad, A. A. Soubh, A. S. Awad, & H. S. El-Abhar, "Mangiferin protects against intestinal ischemia/reperfusion-induced liver injury: Involvement of PPAR- γ, GSK-3β and Wnt/β-catenin pathway," European journal of pharmacology, 809, pp. 80-86, 2017.

[14] S. A. Saidi, M. Ncir, R. Chaaben, K. Jamoussi, J. van Pelt, & A. Elfeki, "Liver injury following small intestinal ischemia reperfusion in rats is attenuated by Pistacia lentiscus oil: antioxidant and anti-inflammatory effects," Archives of physiology and biochemistry, 123(4), pp. 199-205. 2017.

[15] C.D. Hunt, "One possible role of dietary boron in higher animals and humans," Biol. Trace Elem. Res., 66 pp. pp. 205-225, 1998.

[16] Y. C. Bai, Y. C. Hsia, Y. T. Lin, K. H. Chen, F. I. Chou, C. M. Yang, Y. J. Chuang, "Effect of Tumor Microenvironment on Selective Uptake of Boric Acid in HepG2 Human Hepatoma Cells," Anticancer Res, 37(11), pp. 6347-6353, 2017.

[17] I. Sogut, A. Oglakci, K. Kartkaya, K. K. Ol, M. S. Sogut, G. Kanbak, & M. E. Inal, "Effect of boric acid on oxidative stress in rats with fetal alcohol syndrome. Experimental and therapeutic medicine," 9(3), pp. 1023-1027, 2015.

[18] B. E. Tepedelen, E. Soya, & M. Korkmaz, "Boric acid reduces the formation of DNA double strand breaks and accelerates wound healing process," Biological trace element research, 174(2), pp. 309-318, 2016.

[19] Ö. Hazman, M. F. Bozkurt, A. F. Fidan, F. E. Uysal, & S. Çelik, "The Effect of Boric Acid and Borax on Oxidative Stress, Inflammation, ER Stress and Apoptosis in Cisplatin Toxication and Nephrotoxicity Developing as a Result of Toxication," Inflammation, 41(3), pp. 1032-1048, 2018.

[20] H. Bahadoran, M. R. Naghii, M. Mofid, M. H. Asadi, K. Ahmadi, & A. Sarveazad, "Protective effects of boron and vitamin E on ethylene glycol-induced renal crystal calcium deposition in rat," Endocrine regulations, 50(4), pp. 194-206, 2016.

[21] D. E. Choi, J. Y. Jeong, B. J. Lim, S. Chung, Y. K. Chang, S. J. Lee, ... & K. W. Lee, "Pretreatment of sildenafil attenuates ischemia-reperfusion renal injury in rats," American Journal of Physiology-Renal Physiology, 297(2), pp. 362-370, 2009.

[22] F. Severcan, P. I. Haris, (Eds.). Vibrational spectroscopy in diagnosis and screening (Vol. 6). IOS Press. 2012.

[23] S. Cuzzocrea, D. P. Riley, A. P. Caputi, & D. Salvemini, "Antioxidant therapy: a new pharmacological approach in shock, inflammation, and ischemia/reperfusion injury," Pharmacological reviews, 53(1), pp. 135-159, 2001.

[24] Y. Yang, Y. Sun, W. Yi, Y. Li, C. Fan, Z. Xin, ... & D. Yi, "A review of melatonin as a suitable antioxidant against myocardial ischemia–reperfusion injury and clinical heart diseases," Journal of pineal research, 57(4), pp. 357-366, 2014.

[25] Z. Fan, J. Yao, Y. Li, X. Hu, H. Shao, & X. Tian, "Anti-inflammatory and antioxidant effects of curcumin on acute lung injury in a rodent model of intestinal ischemia reperfusion by inhibiting the pathway of NF-Kb," International journal of clinical and experimental pathology, 8(4), pp. 3451, 2015.

[26] D. Impellizzeri, M. Cordaro, M. Campolo, E. Gugliandolo, E. Esposito, F. Benedetto, ... & M. Navarra, "Anti-inflammatory and antioxidant effects of flavonoid-rich fraction of bergamot juice (BJe) in a mouse model of intestinal ischemia/reperfusion injury," Frontiers in pharmacology, 7, pp. 203, 2016.

[27] A. Kezic, I. Spasojevic, V. Lezaic, & M. Bajcetic, "Mitochondria-targeted antioxidants: future perspectives in kidney ischemia reperfusion injury," Oxidative medicine and cellular longevity, 2016.

[28] R. Di Paola, R. Fusco, E. Gugliandolo, R. D'Amico, M. Campolo, S. Latteri, ... & S. Cuzzocrea, "The Antioxidant Activity of Pistachios Reduces Cardiac Tissue Injury of Acute Ischemia/Reperfusion (I/R) in Diabetic Streptozotocin (STZ)-Induced Hyperglycaemic Rats," Frontiers in pharmacology, 9, pp. 51, 2018.

[29] S. Ince, H. Keles, M. Erdogan, O. Hazman, & I. Kucukkurt, "Protective effect of boric acid against carbon tetrachloride–induced hepatotoxicity in mice," Drug and chemical toxicology, 35(3), pp. 285-292, 2012.

[30] M. Cengiz, "Boric acid protects against cyclophosphamide-induced oxidative stress and renal damage in rats," Cellular and molecular biology (Noisy-le-Grand, France), 64(12), pp. 11-14, 2018.

# Evaluation of the Protective Effect of Boric Acid against Renal Ischemia-Reperfusion Injury

Kubra Koc
Department of Biology,
Faculty of Science, Ataturk
University, Erzurum,
TURKEY

Ferhunde Aysin
Department of Biology,
Faculty of Science, Ataturk
University, Erzurum,
TURKEY
East Anatolian High
Technology Research and
Application Center
(DAYTAM), Ataturk
University, Erzurum,
TURKEY

Huseyin Serkan Erol
Department of
Biochemistry, Faculty of
Veterinary, Ataturk
University, Erzurum,
TURKEY

Fatime Geyikoglu
Department of Biology,
Faculty of Science, Ataturk
University, Erzurum,
TURKEY

**Corresponding author:** Ferhunde Aysin (email: ferhunde.aysin@atauni.edu.tr)

*Abstract*-Ischemia/reperfusion (I/R) related acute kidney injury is a critical condition, associated with the development of chronic kidney disease. Boron has been reported to play an essential role in various organ development and metabolism. However, there is not any knowledge whether boron is also able to modulate the renal I/R injury. The present study aimed to investigate the putative protective effects of boron as boric acid (BA) against renal I/R injury. In a renal I/R model, rats were subjected to 50 minutes of renal ischemia followed by 3 h of reperfusion. The study included 28 Sprague-Dawley rats which were categorized into control group; I/R group; BA 14 mg/kg + I/R groups, and BA 14 mg/kg therapy group. Kidneys were examined histopathologically and their homogenates were used in determining the intracellular levels of oxidative stress and inflammation markers. The present results demonstrated that pretreatment with BA significantly reduced the kidney injury and potentiated the recovery of renal function in I/R rats. Oxidative stress and inflammation markers were revealed to be significantly downregulated by the following pretreatment with BA in I/R rats. Our findings indicated that BA may ameliorate the renal I/R injury and promote tubular cell survival mainly through the modulation of antioxidant capacity in rats. In this aspect, BA designated as a sustainable alternative to bark for the prevention of ischemic kidney tissue damage.

*Keywords-Boric acid; ischemia-reperfusion; kidney; inflammation; oxidative stress.*

## I. INTRODUCTION

Acute Ischemia/reperfusion (I/R) injury of the kidney lead to local and systemic changes which can hinder renal function and be life threatening (Rowart et al. 2015). A wealth of clinical evidence has demonstrated that the severity of I/R injury positively associated with the frequency of acute rejection episodes. Hence, acute kidney injury affects millions of patients worldwide with high mortality, morbidity and cost. New agents under pharmacological development that manipulate I/R injury may provide new and exciting possibilities for the treatment of acute kidney disease as well as in multiple other disease states involving cardiopulmonary resuscitation (Mehaffey et al. 2018).

Boron is thought to be an essential micronutrient for humans and animals (Sun et al. 2018). It has multiple effects on bone and mineral metabolism (Naghii et al. 2012), production of vitamin D (Bustamante-Rangel et al. 2006), hormone (Lauro et al. 2015), enzyme (Ugwu et al. 2017), energy metabolism (Reipa et al. 2018), and ROS formation (Zhou et al. 2017). However, the mechanism of the biochemical effects of boron compounds, most notably boric acid, is not yet completely known. Based on the good antioxidant potential of BA *in vitro*, it was under interest to evaluate the protective effects *in vivo*. Therefore, its clinical applications need further evaluation, the current study was intended to contribute further studies in this area. Accordingly, rats were subjected to arterial-vein clamping to induce renal I/R injury and the effects of BA on antioxidant profile, inflammatory markers, and LPO were investigated, respectively. Additionally, histological changes of kidney tissues were assessed.

## II. MATERIAL AND METHODS

### A. Animals

Adult Sprague-Dawley rats (n = 28), weighing 250-300 g, were purchased from Atatürk University Experimental Research Center (Erzurum/Turkey). The rats were kept under standard laboratory conditions, maintained in temperature- and humidity- controlled rooms on a 12-hour/12-hour light/dark cycle, and had free access to food and water. Experiments were performed according to the Guide for the Care and Use of Laboratory Animals published by the US National Institutes of Health (NIH publication No. 85-23, revised 1996). All experimental procedures in this study were approved by the Atatürk University Local Ethics Committee for Animal Experiments (No. 66, 22.03.2018).

### B. BA preparation and experimental design

Boric acid, supplied from Sigma-Aldrich Chemical Company (St. Louis, MO, USA), was dissolved in 100 ml distilled water. Then, the solution was diluted at 14 mg/kg concentrations. The dose of BA was selected according to the literature (Bahadoran et al. 2016) and our preliminary studies. The solutions were given to rats as 1 cc by gavage 1 h before ischemia onset. The rats were randomly divided into 4 groups (n = 7 per group): I) Control group (sham-

operation), II) Ischaemia/Reperfusion group (I/R group), III) I/R group protected by previous administrations of BA, and IV) BA alone treatment groups (14 mg/kg).

I/R injuries were created as described previously (Choi et al. 2009). Briefly, each rat was anesthetized via intraperitoneal injection of a combination of ketamine (75 mg/kg, i.p) and xylazine (10 mg/kg, i.p.). An abdominal incision was created and unilateral ischaemia was induced by clamping the left renal artery. After 50 min of ischemia, the clamp was removed to allow reperfusion. Body temperature was maintained at 36 °C using heating pads throughout the experiment. At 3h of reperfusion, rats were killed and kidney tissues were collected. Kidney samples were stored at −20 °C for a period before they were used in later analysis; kidney slices were also processed for histological studies.

### C. Measurement of biochemical parameters

The kidney samples were homogenized, and the supernatants were used to determine the antioxidant enzyme profile, oxidative status and cytokine levels. The levels of superoxide dismutase (SOD), catalase (CAT), glutathione (GSH), lipid peroxidation (LPO), and tumour necrosis factor (TNF-α) in the rat renal tissue were measured with the Clinical Automatic Biochemistry Analyzer 7600 (Hitachi, Japan) employing ELISA kits (R&D Systems, Minneapolis, MN) according to the manufacturer's instructions. All experiments were performed with triplicate samples and repeated three times.

### D. Histological examinations

Kidney tissues were fixed in 10% neutral buffered formalin overnight, dehydrated, embedded in paraffin and sectioned at 4 μm. For histological analysis, sections were stained with hematoxylin&eosin (H&E) and Congo red.

### E. Statistical analysis

All data are expressed as the mean ± SEM and the differences in variance were analysed statistically using a one-way analysis of variance (ANOVA) test by Graphpad prism 5.0 statistics software (GraphPad, La Jolla, CA, USA). Tukey's test was used as a post hoc. $p < 0.05$ was considered as statistically significant. The superscripts of a and b were used to compare the control and IR groups with other studied groups.

### III. RESULTS

Histopathological examination by H&E staining of tissue sections revealed normal histology of kidney in control group (Figure 1A). The renal I/R caused severe congestion, haemorrhage, hydropic degeneration and necrosis of tubules (Figure 1B). In BA + I/R group, necrosis in tubules and very few degenerations in tubular epithelium with nearly normal histological structures were determined (Figure 1C). In the group receiving BA alone, normal histological structures were observed (Figure 1D).
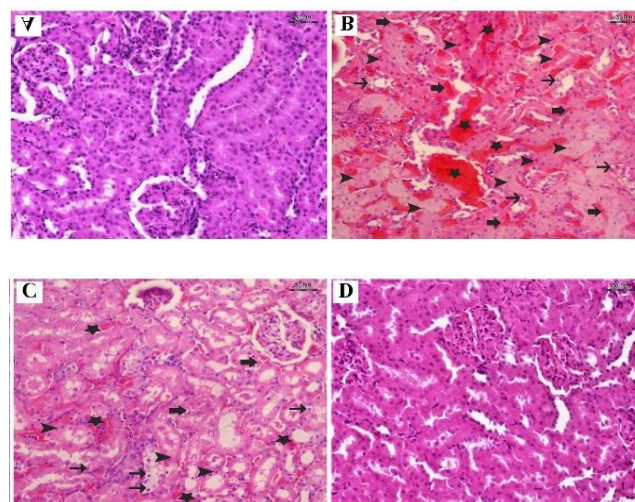


Fig 1. Rat kidney (H&E). (A): The control group with normal kidney histology, (B): The kidney histology in I/R group; Arrow heads: Necrosis, Thin arrows: Hydropic degeneration Asterisk: Congestion, Thick arrows: Hemorrhage, (C): I/R group protected by previous administrations of BA, (D): BA alone treatment group, Bar: 20 μm. Abbreviations used: I/R: Ischaemia/Reperfusion, BA: Boric acid.

Furthermore, Congo red staining was negative for amyloid deposition in kidney of control group (Figure 2A), whereas positive in I/R group (Figure 2B). On the other hand, I/R + BA group had less Congo red staining.
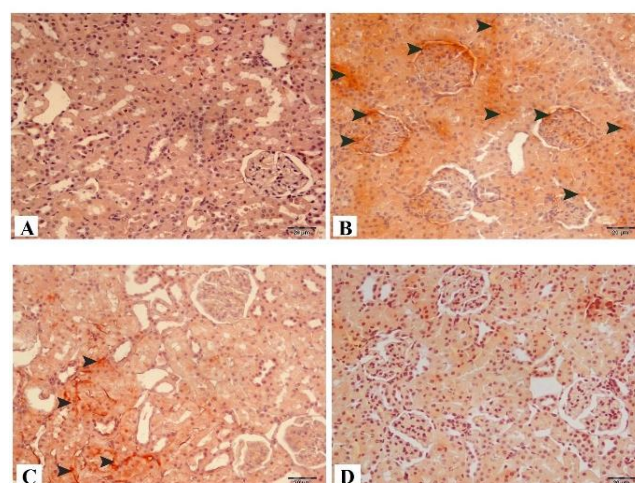


Fig 2. Rat kidney (Congo Red). (A): Kidney without amyloid in control group, (B): Amyloidosis in I/R group; Arrow head: Congo Red+ (C): I/R group protected by previous administrations of BA; Arrow head: Congo Red+ (D): BA alone treatment group, Bar: 20 μm. For abbreviations see legend Figure 1.

As shown in Figure 3, comparing with the sham-operated rats, the renal I/R ones showed significantly higher levels of the LPO ($p < 0.0001$) but significant lower levels of SOD and CAT (respectively, $p < 0.05$ and $p < 0.0001$). At the time of examination, there was no difference for the releasing of GSH between the two groups. The pretreatment of BA resulted in alternated releasing of LPO, SOD and CAT levels similar to sham-operated group. Interestingly, BA caused a decrease in GSH ($p < 0.01$).
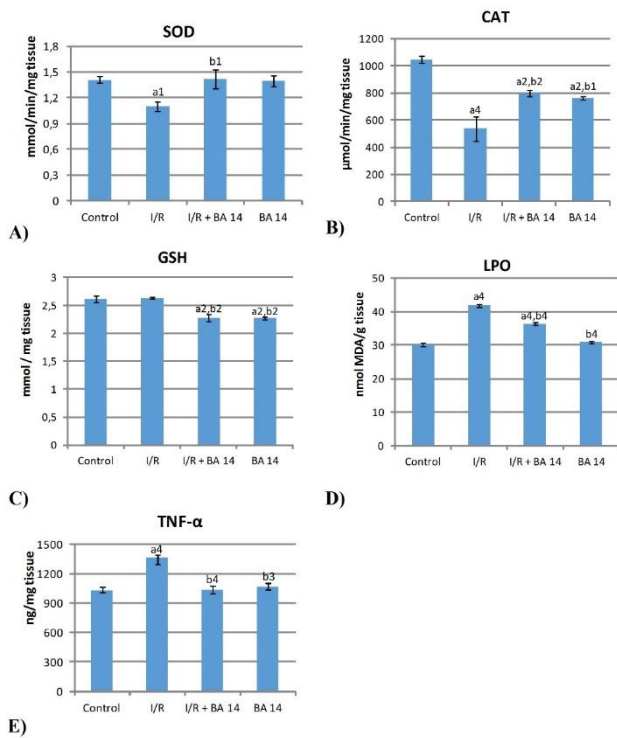
Fig 3. The effects of BA on kidney SOD, CAT, GSH, LPO and TNF-α levels after I/R. Data are presented as mean ± SEM (n=7). a denotes significant differences between other studied groups and control (a1: $p<0.05$, a2: $p<0.01$, a3: $p<0.001$, a4: $p<0.0001$), b denotes significant differences between other studied groups and I/R group (b1: $p<0.05$, b2: $p<0.01$, b3: $p<.0.001$, b4: $p<0.0001$) by Tukey's multiple range tests. For abbreviations see legend Figure 1.

## IV. DISCUSSION

Among many boron compounds, boric acid (also known as orthoboric acid with amolecular formula of $H_3BO_3$) has received particular attention due to its technological and medical importance (Adriztina et al. 2018). In spite of the increasing attention to this compound, currently there is not any information about the prevention of I/R injury. In this study, a renal I/R injury model in rats was used to assess whether BA inhibited the development of renal I/R injury. The possible mechanism may be related with the ROS that could interact with many biological macromolecules, such as lipids, proteins and DNA, causing structural changes, functional abnormalities, and nephrotic syndromes (Suzuki et al. 2016). Clinically, the complications were associated with organ damage, mainly focused on liver, kidney, pancreas and heart (van Williigenburg et al. 2018). Therefore, antioxidants may play an important role for preventing I/R injury and its complications by directly interfering with the generation of ROS (Xie et al. 2018). In our study, the activities of the antioxidant enzymes (SOD and CAT), lipid content (LPO), and intracellular levels of GSH were determined to investigate the protective effects of BA on kidney damage against oxidative stress. In the present research, all the results indicated that BA exhibited potentially superior protective effects on kidney damage. The biological functions, including antioxidant properties of BA, were mainly associated with its composition. Based on the previous reports, BA contains electron-withdrawing groups, indicating that BA may play an essential role in

maintaining protective effects against tissue damage (Pérez-Rodríguez et al. 2017; Ugwu et al. 2017). Furthermore, the antioxidant analysis of BA consistent with the preliminary test results. According to Preetha et al. (2018), increased SOD activity could be considered direct evidence of enhanced ROS production. In our experiments, the increased SOD activity of kidney supported the hypothesis that SOD is tightly controlled in response to I/R injury. It also indicated that I/R caused oxidative damage to kidney. Similar to our results, boron supplementation was shown to induce SOD activity in hepatotoxicity (Ince et al. 2011) and enterocolitis (Yazıcı et al. 2014). Meanwhile, similar results observed for CAT activity indicated that $H_2O_2$ was stimulated under different I/R conditions (Fahmy et al. 2007). The decrease in the SOD activity could lead to an excess amount of superoxide anion and hydrogen peroxide (which in turn generated hydroxyl radicals) in biological systems, resulting in the initiation and propagation of lipid peroxidation. In the free radical hypothesis, the reactive radicals could react with polyunsaturated fatty acids in cell membranes, leading to lipid peroxidation and dysfunction of membranes and subsequently resulting in the tissue injury (Tanko et al. 2017). Wang et al. (2016) indicated that the *in vivo* organ damage caused by I/R was probably due to free radicals produced by lipid peroxidation.

In our study, the generation of LPO is significantly increased in cells after I/R injury. It is reported that the blood flow during reperfusion phase of I/R can produce oxygen free radicals which lead to the LPO formation to destroy the antioxidant defence system (Mahalakshmi and Kurian 2018; Cakir et al. 2017). Based on *in vivo* findings, the anti-oxidant activity of BA significantly decreased the LPO level in kidney cells when compared with I/R group. The level of reduced glutathione (GSH), the most important intracellular antioxidant molecule, is a sensitive index of the efficiency of cellular antioxidant defences and its decrease during focal cerebral ischemia in rats leads to the development of severe complications (Luo et al. 2017). Boron can cause changes in the structure and function of proteins by interacting with them (Cao et al. 2008). In the present study, as a result of the increasing free radical formation caused by I/R, the renal cells did not allow GSH synthesis in order to protect from the effects of free radicals. In our experimental model, BA is believed to help the release free radicals by working together with GSH, thereby leading a decrease in the level of GSH used.

Our results provide strong evidence that I/R can not only induce oxidative stress in kidney cells, but also interfere with the inflammatory processes that are essential for regulating cell functions. TNF-α is a pro-inflammatory cytokine involved in systemic inflammation, stimulating the acute phase reaction (Dumaine and Ashley 2018). In the present study, I/R led to the production of this cytokine and the measured values were higher than those measured for controls. BA alone did not elicit any effect to cells also at 14 mg/kg concentration. The results showed that TNF-α production is significantly decreased in comparison to I/R group at BA 14 mg/kg concentration. A possible mechanism involves TNF-α release, that can stimulate cytokine production associated with the inflammatory

reaction, such as IL-6 and oxidative stress (Rauch et al. 2013). Thus, I/R injury may contribute to the increase in the cross-talk between oxidative stress and inflammation in kidney. Hence, we concluded that BA was the main influencing factor on inflammation and oxidative stress after renal I/R injury in rats. In a study conducted by Durick et al. (2005), it was found that boron prevented the activation of pro-inflammatory cytokines through NF-κB signalling pathway, and therefore, it blocked the inflammation process. In addition, boron supplementation reduced inflammatory response against phyto-hemagglutinin (PHA-P) in gilts (Armstrong et al. 2001), enhanced immunity by increasing serum levels of TNF-α and interferon-gamma (IFN-γ) in pigs (Armstrong et al. 2003), and increased serum levels of TNF-α in steers inoculated with bovine herpes virus type-1 (Fry et al. 2011).

Reperfusion of previously ischemic renal tissue initiates death of renal cells due to a combination of apoptosis and necrosis. At this point, the prevention of necrosis represents a major unmet clinical need (Schumer et al. 1992). In our study, BA could be considered as a potential therapeutic target to ameliorate renal necrosis in I/R. The changes observed with 14 mg/kg BA are remarkable in comparison to those observed in I/R group. A previous study showed that BA reduced apoptotic damage in kidney tissue, but the decrease was statistically significant only in 14 mg/kg boric acid-administered group. Further studies on the effects of BA at diverse doses on apoptosis may clarify this issue. Thus, possible side effects or if there are new usage areas of borone compounds which have many usage areas in clinics can be detected (Hazman et al. 2018).

These results demonstrated that BA can suppress necrosis and haemorrhage from I/R injury through attenuating oxidative stress and inflammation. It is thought that it can be a promising agent for renal I/R treatment.

## REFERENCES

[1] Adriztina, I., Adenin, L. I., & Lubis, Y. M. (2018). Efficacy of Boric Acid as a Treatment of Choice for Chronic Suppurative Otitis Media and Its Ototoxicity. *Korean journal of family medicine*, *39*(1), 2-9.

[2] Armstrong, T. A., Spears, J. W., & Lloyd, K. E. (2001). Inflammatory response, growth, and thyroid hormone concentrations are affected by long-term boron supplementation in gilts. *Journal of animal science*, *79*(6), 1549-1556.

[3] Armstrong, T. A., & Spears, J. W. (2003). Effect of boron supplementation of pig diets on the production of tumor necrosis factor-α and interferon-γ. *Journal of animal science*, *81*(10), 2552-2561.

[4] Bahadoran, H., Naghii, M. R., Mofid, M., Asadi, M. H., Ahmadi, K., & Sarveazad, A. (2016). Protective effects of boron and vitamin E on ethylene glycol-induced renal crystal calcium deposition in rat. *Endocrine regulations*, *50*(4), 194-206.

[5] Bustamante-Rangel, M., Delgado-Zamarreño, M.M., Sánchez-Pérez, A., Carabias-Martínez, R. (2006). Microemulsion electrokinetic chromatography for the separation of retinol, cholecalciferol, delta-tocopherol and alpha-tocopherol. Chromatogr A. 1, 1125(2), 270-3.

[6] Cakir, S., Eren, M., Senturk, M., & Sarica, Z. S. (2018). The effect of boron on some biochemical parameters in experimental diabetic rats. *Biological trace element research*, *184*(1), 165-172.

[7] Cao, J., Jiang, L., Zhang, X., Yao, X., Geng, C., Xue, X., & Zhong, L. (2008). Boric acid inhibits LPS-induced TNF-α formation through a thiol-dependent mechanism in THP-1 cells. *Journal of Trace Elements in Medicine and Biology*, *22*(3), 189-195.

[8] Choi, D. E., Jeong, J. Y., Lim, B. J., Chung, S., Chang, Y. K., Lee, S. J., ... & Lee, K. W. (2009). Pretreatment of sildenafil attenuates ischemia-reperfusion renal injury in rats. *American Journal of Physiology-Renal Physiology*, *297*(2), F362-F370.

[9] Dumaine, J. E., & Ashley, N. T. (2018). Acute sleep fragmentation does not alter pro-inflammatory cytokine gene expression in brain or peripheral tissues of leptin-deficient mice. *PeerJ*, *6*, e4423.

[10] Durick, K., Tomita, M., Santoro, T., Hunt, C., & Bradley, D. (2005). Evidence that boron down-regulates inflammation through the Nf-(Kappa) b pathway. *J Federation Am Soc Exp Biol*, *19*(5), A1705.

[11] Fahmy, S. R., Soliman, A. M., El Ansary, M., Elhamid, S. A., & Mohsen, H. (2017). Therapeutic efficacy of human umbilical cord mesenchymal stem cells transplantation against renal ischemia/reperfusion injury in rats. *Tissue and Cell*, *49*(3), 369-375.

[12] Fry, R. S., Brown Jr, T. T., Lloyd, K. E., Hansen, S. L., Legleiter, L. R., Robarge, W. P., & Spears, J. W. (2011). Effect of dietary boron on physiological responses in growing steers inoculated with bovine herpesvirus type-1. *Research in veterinary science*, *90*(1), 78-83.

[13] Hazman, Ö., Bozkurt, M. F., Fidan, A. F., Uysal, F. E., & Çelik, S. (2018). The Effect of Boric Acid and Borax on Oxidative Stress, Inflammation, ER Stress and Apoptosis in Cisplatin Toxication and Nephrotoxicity Developing as a Result of Toxication. *Inflammation*, *41*(3), 1032-1048.

[14] Ince, S., Keles, H., Erdogan, M., Hazman, O., & Kucukkurt, I. (2012). Protective effect of boric acid against carbon tetrachloride–induced hepatotoxicity in mice. *Drug and chemical toxicology*, *35*(3), 285-292.

[15] Lauro, F. V., Francisco, D. C., Elodia, G. C., Eduardo, P. G., Maria, L. R., Marcela, R. N., ... & Bety, S. A. (2015). Synthesis and antibacterial activity evaluation of two androgen derivatives. *Steroids*, *93*, 8-15.

[16] Luo, Y. P., Zhang, H., Hu, H. F., Cao, Z. Y., Zhang, X. Z., Cao, L., ... & Xiao, W. (2017). Protective effects of Ginkgo Terpene Lactones Meglumine Injection on focal cerebral ischemia in rats. *Zhongguo Zhong yao za zhi= Zhongguo zhongyao zazhi= China journal of Chinese materia medica*, *42*(24), 4733-4737.

[17] Mahalakshmi, A., & Kurian, G. A. (2018). Evaluating the impact of diabetes and diabetic cardiomyopathy rat heart on the outcome of ischemia-reperfusion associated oxidative stress. *Free Radical Biology and Medicine*, *118*, 35-43.

[18] Mehaffey, J. H., Money, D., Charles, E. J., Schubert, S., Piñeros, A. F., Wu, D., ... & Mas, V. R. (2018). Adenosine 2A Receptor Activation Attenuates Ischemia Reperfusion Injury During Extracorporeal Cardiopulmonary Resuscitation. *Annals of surgery*.

[19] Naghii, M. R., Ebrahimpour, Y., Darvishi, P., Ghanizadeh, G., Mofid, M., Torkaman, G., ... & Hedayati, M. (2012). Effect of consumption of fatty acids, calcium, vitamin D and boron with regular physical activity on bone mechanical properties and corresponding metabolic hormones in rats.

[20] Pérez-Rodríguez, M., García-Mendoza, E., Farfán-García, E. D., Das, B. C., Ciprés-Flores, F. J., Trujillo-Ferrara, J. G., ... & Soriano-Ursúa, M. A. (2017). Not all boronic acids with a five-membered cycle induce tremor, neuronal damage and decreased dopamine. *Neurotoxicology*, *62*, 92-99.

[21] Rani, M. P., Anupama, N., Sreelekshmi, M., & Raghu, K. G. (2018). Chlorogenic acid attenuates glucotoxicity in H9c2 cells via inhibition of glycation and PKC α upregulation and safeguarding innate antioxidant status. *Biomedicine & Pharmacotherapy*, *100*, 467-477.

[22] Rauch, J., Kolch, W., Laurent, S., & Mahmoudi, M. (2013). Big signals from small particles: regulation of cell signaling pathways by nanoparticles. *Chemical reviews*, *113*(5), 3391-3406.

[23] Reipa, V., Atha, D. H., Coskun, S. H., Sims, C. M., & Nelson, B. C. (2018). Controlled potential electro-oxidation of genomic DNA. *PloS one*, *13*(1), e0190907.

[24] Rowart, P., Erpicum, P., Detry, O., Weekers, L., Grégoire, C., Lechanteur, C., ... & Jouret, F. (2015). Mesenchymal stromal cell therapy in ischemia/reperfusion injury. *Journal of immunology research*, *2015*.

[25] Schumer, M., Colombel, M. C., Sawczuk, I. S., Gobe, G., Connor, J., O'toole, K. M., ... & Buttyan, R. (1992). Morphologic, biochemical, and molecular evidence of apoptosis during the reperfusion phase after brief periods of renal ischemia. *The American journal of pathology*, *140*(4), 831.

[26] Sun, A., Xu, Q., Wei, G., Zhu, H., & Chen, X. (2018). Differentiation analysis of boron isotopic fractionation in different forms within plant organ samples. *Phytochemistry*, *147*, 9-13.

[27] Suzuki, T., Yamaguchi, H., Kikusato, M., Hashizume, O., Nagatoishi, S., Matsuo, A., ... & Ohba, Y. (2015). Mitochonic acid 5 binds mitochondria and ameliorates renal tubular and cardiac myocyte damage. *Journal of the American Society of Nephrology*, ASN-2015060623.

[28] Tanko, Y., Kabiru, A., Abdulrazak, A., Mohammed, K. A., Salisu, A. I., Jimoh, A., ... & Sada, N. M. (2017). Effects of Fermented Ginger Rhizome (Zingiber officinale) and Fenu Greek (Trigonella foenum-graceum) Supplements on Oxidative stress and Lipid Peroxidation Biomarkers in Poloxamer-407 Induced-Hyperlipidemic Wistar Rats. *Nigerian Journal of Physiological Sciences*, *32*(2), 137-143.

[29] Ugwu, D. I., Okoro, U. C., & Ahmad, H. (2017). New carboxamide derivatives bearing benzenesulphonamide as a selective COX-II inhibitor: Design, synthesis and structure-activity relationship. *PloS one*, *12*(9), e0183807.

[30] Ugwu, D. I., Okoro, U. C., Ukoha, P. O., Okafor, S., Ibezim, A., & Kumar, N. M. (2017). Synthesis, characterization, molecular docking and in vitro antimalarial properties of new carboxamides

[31] van Willigenburg, H., de Keizer, P. L., & de Bruin, R. W. (2018). Cellular senescence as a therapeutic target to improve renal transplantation outcome. *Pharmacological research*.

[32] Wang, S. X., Wang, J., Shao, J. B., Tang, W. N., & Zhong, J. Q. (2016). Plumbagin mediates cardioprotection against myocardial ischemia/reperfusion injury through Nrf-2 signaling. *Medical science monitor: international medical journal of experimental and clinical research*, *22*, 1250.

[33] Xie, C. J., Gu, A. P., Cai, J., Wu, Y., & Chen, R. C. (2018). Curcumin protects neural cells against ischemic injury in N2a cells and mouse brain with ischemic stroke. *Brain and behavior*, *8*(2), e00921.

[34] Yazc, S., Aksit, H., Korkut, O., Sunay, B., & Çelik, T. (2014). Effects of boric acid and 2-aminoethoxydiphenyl borate on necrotizing enterocolitis. *Journal of pediatric gastroenterology and nutrition*, *58*(1), 61-67.

[35] Yilmaz, M. T. (2012). Minimum inhibitory and minimum bactericidal concentrations of boron compounds against several bacterial strains. *Turkish Journal of Medical Sciences*, *42*(Sup. 2), 1423-1429.

[36] Zhou, L., Peng, Y., Wang, Q., & Lin, Q. (2017). An ESIPT-based two-photon fluorescent probe detection of hydrogen peroxide in live cells and tissues. *Journal of Photochemistry and Photobiology B: Biology*, *167*, 264-268.

# Trapped Magnetic Field Properties of Multi-Seeded Bulk YBCO Superconductors Fabricated by Top-Seeded Melt Growth Process

Sait Barış Güner
Department of Physics, Faculty of
Arts and Sciences, RecepTayyip
Erdogan University, Rize, Turkey

Burcu Savaşkan
Energy Systems Engineering,
Faculty of Technology,
Karadeniz Technical University,
61830, Of, Trabzon, Turkey

*Abstract*— **Multi-seeded bulk YBCO superconductors (32 mm in diameter, 7.5 mm in height) were fabricated by top-seeded melt growth (TSMG) using two seeds with (100) / (100) type junctions. In this study, the effects of the distance ($d$) between two seeds on the trapped magnetic field were investigated. These distances are $d$ = 1, 2, 10 and 18 mm and they are called as MS-1, MS-2, MS-10 and MS-18 samples. All field-cooling magnetization (FCM) experiments were conducted with a 5 T low-temperature superconducting solenoid magnet system (Tokyo University, Department of Applied Physics (TUAT)) with a room-temperature core of 60 mm in diameter. The trapped field on the top surface of each sample measured using Lakeshore two Hall sensors (H1 and H2) were placed at the centre of each top surface at positions 0 and 6 mm from the centre of the sample. At the first step of the experiments, the two multi-seeded samples were evaluated by the FCM in a field of 1 T at 77 K (LN2). The maximum trapped field of MS-1 sample is 0.78 T, which is the best values observed and that of the other samples decreases from MS-2, MS-10 and MS-18 samples with values 0.55 T, 0.72 T and 0.62 T as d increases from 2 to 18 mm.**

*Keywords*— S*uperconductors, Crystal Growth, Trapped Field, Hall Probe*

## I. INTRODUCTION

Conventional permanent magnets (PM) such asNd-Fe-B or Sm-Co are very essential materials for many applications especially required high magnetic field. However, their magnetic fields are limited generally to less than 2 Teven when it's most powerful. A bulk superconductor can act effectively as a quasi-permanent magnet when magnetised by an applied magnetic field below its superconducting transition temperature, $T_C$ [1].When a bulk superconductor magnetized, concentric supercurrents induced throughout the sample persist even when the external field is reduced to zero. The magnetic field associated with these supercurrents decline extremely slowly causing a relatively stable magnetic field, so it called "Trapped Field" [2].Trapped field is generally most important superconducting property for practical applications. The magnitude of the trapped field is proportional to the critical current density, $J_c$, and the volume of the superconductor. Bulk Y-Ba-Cu-O with the highest $J_c$ performance takes the form of a large single grain, as the presence of misoriented grain boundaries significantly impedes current flow and therefore causes a poor macroscopic $J_c$. Such a bulk can be produced by top-seeded melt growth (TSMG). TSMG has appeared over the past 30 years as a practical route for fabricating large, single grains

of cuprate high temperature bulk superconductors (HTS), such as $(RE)Ba_2Cu_3O_7$, more simply (RE)BCO[where RE is a rare earth element, most commonly Y or Gd]. These materials are able to generate magnetic fields that are considerable higher than those produced by iron-based permanent magnets. Notably, Tomita and Murakami reported a trapped field of 17. 24 T at 29 K in an arrangement of two YBCO samples, which was reinforced with an epoxy resin [3]. The present authors have very recently demonstrated a world record trapped field of 17.6 T at 29 K in the centre of a stack of two 25 mm in diameter GdBCO-Ag bulks fabricated by TSMG [4]. Although larger single grains are required in applications, they have very low growth rates observed for single crystals, which represent a limitation to the sample size.

Multi-seeding using two or more separate seeds was developed initially by Kim et al in 2000 to fabricate larger samples [5]. They showed the potentiality of the process as a time saving process. In addition, the multi-seeding process provides an opportunity to study the grain boundaries in the bulk material [6].

In this work, we studied trapped field of multi-seeded YBCO bulk superconductors for the practical application bulks in large-scale HTS magnetic devices.

## II. EXPERIMENTAL

Four melt processed samples grown using two seeds and seeds distance for YBCO samples were investigated as part of this study. The compositions of the precursor powder for these samples were (75 wt %Y-123 + 25 wt % Y- 211) +0.5 wt % $CeO_2$,.$CeO_2$ powder was added to prevent the grain growth of Y-211 phase. The mix precursor powders were pressed uniaxial into pellets 26 mm in diameter and 8 mm in height. $Nd_{1.8}Ba_{2.4}Cu_{3.4}O_7$ single crystal seeds was placed on the top surface of pressed pellet, before being loaded into a furnace for melt processing in air using a conventional TSMG heating profile. Two seeds are arranged to form a style of (100) // (100) grain boundary (GB), i.e., the growth fronts two adjacent grains encountered at the a-axis direction of the bulk and formed a GB at that position. In this study, we changed the distance ($d$) between the two seeds. These distances are

$d$ = 1, 2, 10 and 18 mm and they are called as MS-1, MS-2, MS-10 and MS-18 samples, respectively. Two Y123 grains were grown at the two seeds and covered the entire top surfaces. As a result of the two Y123 grain growth, the (100)

// (100) type grain junctions were formed at the centre region of the top surfaces.

The field-cooled (FC) method was used to magnetize the single-seeded and multi-seeded bulk YBCO samples prior to trapped magnetic field. All field-cooling magnetization (FCM) experiments were conducted with a 5 T low-temperature superconducting solenoid magnet system with a room-temperature core of 60 mm in diameter at Technology Faculty, Tokyo University. The trapped field was measured by using two cryogenic Hall sensors (Lakeshore, HGT-2101-10) mounted on the centre and 6 mm away from the centre of the bulk surface using varnish.

### III. RESULTS AND DISCUSSION

The top surfaces of four samples were polished flat for trapped field measurements. At the first step of the experiments, liquid nitrogen (LN2) was used as coolant to cool the bulk. The LN2 temperature was approximately taken as 77 K. Each sample was field cooled to 77 K using nitrogen in 1 T applied perpendicular to its top surface.

The field-cooling magnetization procedures were as follows: 1) The sample was placed at centre of the bore.

2) The applied field was set to 1 T, in which the bulk was progressively cooled down into a superconductivity state. The field-sweep rate was 0.02 A/s during the field adding and removing processes.

3) After a sufficient cooling time of 25 min, the applied field was removed.

The trapped field on the top surface of each sample measured using Lakeshore two Hall sensors (HGT-2101-10). The two Hall sensors (H1 and H2) were placed at the centre of each top surface at positions 0 and 6 mm from the centre of the sample.

Figure 1 shows the trapped field of all multi-seeded bulk YBCO samples with (100) / (100) grain junctions and various distances ($d$ = 1, 2, 10 and 18 mm) between two seeds measured at 77 K. The maximum trapped field of MS-1 sample is 0.78 T, which is the best values observed for MS series. The maximum values of trapped field in figure 1 of the other samples decreases from MS-2, MS-10 and MS-18 samples with values 0.55 T, 0.72 T and 0.62 T as the distance between the two seeds increases from 2 mm to 18 mm. It can be deduced for MS-1 and MS-18 samples that the depth of the grain boundaries increases with increasing distance between seeds, as evidenced by the lower trapped field values at positions where the distance between adjacent seeds is larger. The trapped fields of multi-seeded samples decrease when the distance between the seeds increases, which is good agreement with a previous observation in the literature [7]. The effect of grain boundaries in multi-seeded samples can be reduced by decreasing the distance of seeds.
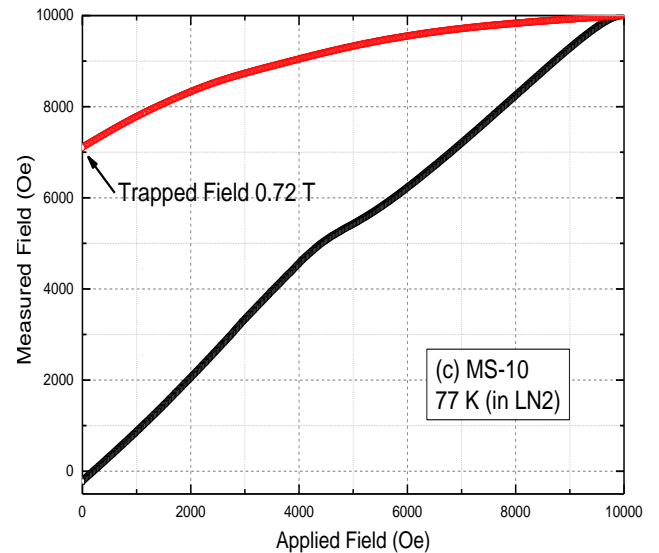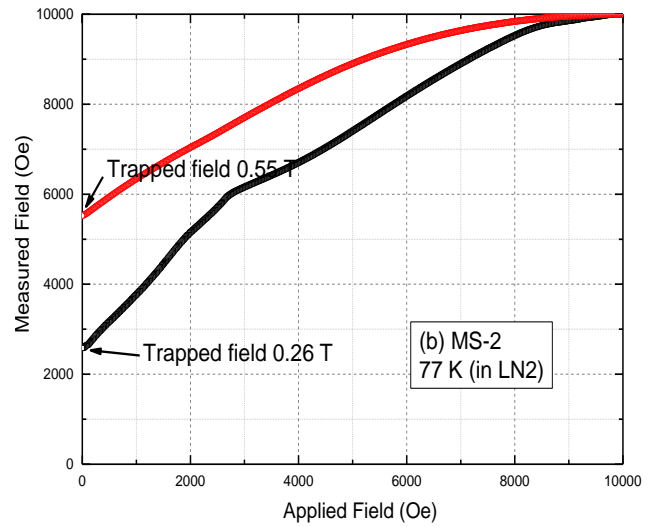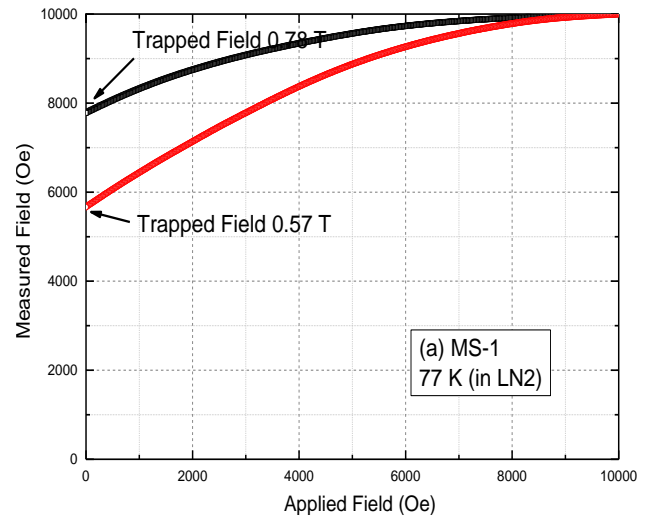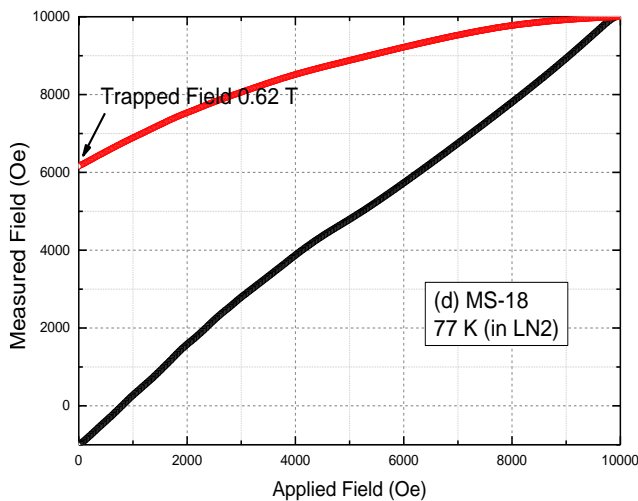
Fig 1. The field measured at the top surface of multi-seeded YBCO (a) MS-1 (b) MS-2 (c) MS-10 and (d) MS-18 samples by two Hall probes were placed at the centre of the sample at positions 0; 6 mm.

## ACKNOWLEDGMENT

## REFERENCES

[1] A. Yamamoto, A. Ishihara, M. Tomita, K. Kishio, "Permanent magnet with MgB$_2$ bulk superconductor", Appl. Phys. Lett. 105, 032601, 2014.

[2] A. G. Bhagurkar, A. Yamamoto, L. Wang, M. Xia, A. R. Dennis, J. H. Durell, T. A. Alijohani, N. H. Babu, D. A. Cardwell, "High Trapped Fields in C-doped MgB$_2$ Bulk Superconductors Fabricated by Infiltration and growth process", *Nature*, DOI: 10. 1038/s41598-018-31416-3, August 2018.

[3] M. Tomita, M. Murakami, "High- temperature superconductor bulk magnets that can trap magnetic fields of over 17 Tesla at 29 K.", *Nature*, 421, 2003.

[4] J. H. Durrell, A. R. Dennis, J. Jaroszynski, M. D. Ainslie, K. G. B. Palmer, Y. H. Shi, and D. A. Cardwell, "A trapped field of 17.6 T in melt-processed, bulk Gd-Ba-Cu-O reinforced with shrink-fit steel", *Supercond. Sci. Technol.* 27, 082001, 2014.

[5] C-J Kim, H-J Kim, Y. A. Jee, G-W Hong, J-H Joo, S-C Han and S-J Kim, *Physica C*, 338 205-12, 2000.

[6] [6] Y-H Shi, J. H. Durell, A. R. Dennis and D. A. Cardwell, "Bulk YBCO seeded with 45°-45° bridge-seeds of different lengths", *Supercond. Sci. Technol.* 26, 015012, 2013.

[7] Y-H Shi, J. H. Durell, A. R. Dennis, Z. Zhang, W. Zhai, N. Hari Babu, and D. A. Cardwell, "A Comparison of 0°–0° and 45°–45° bridge-Seeded, YBCO single grains" *Am. Ceram. Soc.*, 96, 1757-1762, 2013.

# Synthesis of Ag₃PO₄/ Nb₂O₅ as light photocatalyst for degradation of dye

Nur Syazwani Osman
*Department of Chemistry, Faculty of Science, Universiti Putra Malaysia, 43400 UPM Serdang, Selangor, Malaysia*

Siti Norhasimah Sulaiman
*Department of Chemistry, Faculty of Science, Universiti Putra Malaysia, 43400 UPM Serdang, Selangor, Malaysia*

Abdul Halim Abdullah
*Department of Chemistry, Faculty of Science, Universiti Putra Malaysia, 43400 UPM Serdang, Selangor, Malaysia*
Email: halim@upm.edu.my

***Keywords- $Ag_3PO_4/Nb_2O_5$, Methyl orange, Photocatalyst, Photocatalysis, Visible light.***

## I. INTRODUCTION

The use of semiconductor photocatalyst has become an increasing trend for the purification and disinfection of contaminated water. This technology has been extensively researched especially for the development of active and sustainable materials and its function in degrading wide variety of pollutants. In particular, the energy conversion from the light source (UV, visible and sunlight) is a necessary to activate the catalytic activity and to completely annihilate the pollutant presence in the water. Of particular interest are the materials with visible-light-driven active so that the sunlight conversion efficiency can be fully utilized even at low intensity. Previous literatures have suggested that coupling the AgX (X=Cl, Br, I), $TiO_2$, $SnO_2$, $Fe_3O_4$ and carbon quantum dots on the surface of $Ag_3PO_4$ improved its catalytic activity and stability. Carbon based materials also proven to enhance the stability and photocatalytic stability of $Ag_3PO_4$ such as graphene graphene oxide, reduced graphene oxide, carbon nanotube, and multiwall carbon nanotube by acting as electron acceptor to suppress the recombination and prevent photocorrosion of $Ag_3PO_4$. Herein, we present a simple chemical route for the successful synthesis of composite materials of $Ag_3PO_4/Nb_2O_5$ photocatalyst via deposition precipitation method.The photocatalytic activity of the catalyst was investigated by photodegradation of methyl orange (MO) under visible light irradiation(Fluorescence, 23 W).

## II. EXPERIMENT

The $Ag_3PO_4/Nb_2O_5$ photocatalyst was prepared via facile deposition-precipitation method. $AgNO_3$ powder and disodium hydrogen phosphate, $Na_2HPO_4$ were dissolved completely in separately beaker contained 150 mL of distilled water. A certain amount of Nb2O5 was added into the AgNO3 solution. The phosphate solution was then added dropwisely into the solution mixture until yellow precipitate is formed under continuous stirring. The yellow precipitate was collected by filtration and washed several times with distilled water and ethanol before dried in oven overnight at 80 ºC. Finally, the obtained product was ground to produce fine powder and characterized by using X-Ray Diffraction , Photoluminisce , UV-vis DR, BET, and FESEM. The photocatalytic activities of the photocatalyst were evaluated by degradation of methyl orange (MO) under the irradiation

23W fluorescence lamp (Philips) The degradation process was monitored sing UV-vis Perkin Lambda 30 spectrophotometer at $\lambda_{max}$ = 464.4 nm.

## III. RESULT AND DISCUSSION

The XRD pattern of $Ag_3PO_4/Nb_2O_5$ (Figure 1) clearly shows peaks, be attributed to cubic structure of $Ag_3PO_4$ ( JCPDS No. 010840510) and orthorhombic structure of $Nb_2O_5$ (JCPDS No.000271003), confirmed the formation of $Ag_3PO_4/Nb_2O_5$ composite.
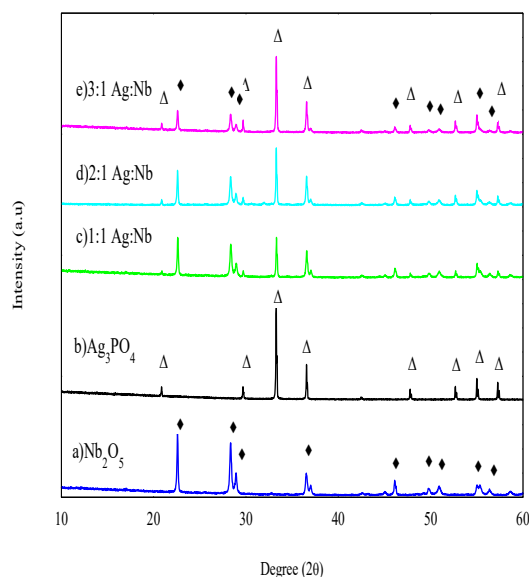


Figure 1. XRD patterns of the Nb₂O₅, Ag₃PO₄, and Ag3PO4/Nb2O5 photocatalysts
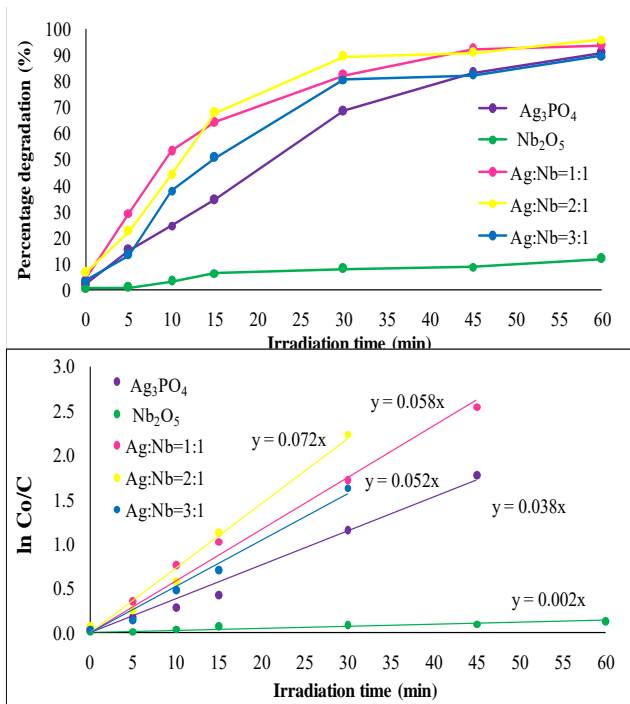
Figure 2. The degradation of MO as a function of irradiation time for $Nb_2O_5$, $Ag_3PO_4$, and $Ag_3PO_4/Nb_2O_5$ photocatalysts

**Figure 2** shows the photocatalytic degradation of methyl orange with different photocatalysts under visible light irradiation. Due to its large band gap energy (3.2 eV), lowest MO degradation was observed when $Nb_2O_5$ was used. The $Ag_3PO_4$ photocatalyst, however, showed a good performance with about 90.6% percentage degradation within 60 min. A slight enhancement of MO degradation (95.8%) was observed for $Ag_3PO_4/Nb_2O_5$ photocatalyst (Ag:Nb=2:1 molar ratio). To correlate the percentage of degradation and the efficiency of photocatalyst, the graph of $\ln C_0/C$ versus time is plotted in order to determine the order of reaction, the rate constant and the rate of reaction. The rate constant for pure $Ag_3PO_4$ and pure $Nb_2O_5$ are 0.038 $min^{-1}$ and 0.002 $min^{-1}$, respectively. However, the combination of $Ag_3PO_4$ and $Nb_2O_5$ increase the rate of reaction. As the mole ratio of $Ag_3PO_4$ to $Nb_2O_5$ is increased, the potocatalytic activity also increased. However, further increment molar ratio of $Ag_3PO_4$ to $Nb_2O_5$ cause decrease in photocatalyst performance as similar reported by Shao et al., (2015) [3]. It was observed that the highest rate constant is 0.072 $min^{-1}$ when Ag:Nb=2:1 photocatalyst was used. Moradi et al., (2016) stated that when the molar ratio is increased, the light penetration will be decreased due to photocatalyst suspension, hence, reduces the degradation rate [15]. Thus, it can be concluded that the photocatalytic degradation efficiency of MO follows the order of Ag:Nb=2:1 >Ag:Nb=3:1 > Ag:Nb=1:1 > $Ag_3PO_4$> $Nb_2O_5$.

# Characterization of Latex-Graphene Composite for Flexible Electronic Applications

Nadia Amalyna, Ramly
Faculty of Engineering, University
Putra Malaysia, 43400 UPM Serdang,
Selangor, Malaysia

Nur Haziqah, Abd Aziz
Faculty of Engineering, University
Putra Malaysia, 43400 UPM Serdang,
Selangor, Malaysia

Suhaidi, Shafie
Faculty of Engineering, University
Putra Malaysia, 43400 UPM Serdang,
Selangor, Malaysia
Institute of Advanced Technology,
University Putra Malaysia, 43400 UPM
Serdang, Selangor, Malaysia

Mohd Nizar, Hamidon
Faculty of Engineering, University
Putra Malaysia, 43400 UPM Serdang,
Selangor, Malaysia
Institute of Advanced Technology,
University Putra Malaysia, 43400 UPM
Serdang, Selangor, Malaysia

Mohd Amrallah, Mustaffa
Faculty of Engineering, University
Putra Malaysia, 43400 UPM Serdang,
Selangor, Malaysia
Institute of Advanced Technology,
University Putra Malaysia, 43400 UPM
Serdang, Selangor, Malaysia

Haslina, Jaafar
Faculty of Engineering, University
Putra Malaysia, 43400 UPM Serdang,
Selangor, Malaysia
Institute of Advanced Technology,
University Putra Malaysia, 43400 UPM
Serdang, Selangor, Malaysia
*Email: jhaslina@upm.edu.my

*Abstract-Flexible electronics is one of the growing technologies and will become more important in the future. Graphene is recognized as the best carbon material and widely used for electronic applications other than carbon nanotube (CNT). In this study, the characterization of latex composites through two different preparation methods such as dip and casting methods were studied. Some characterization tests were carried out on latex composites such as electrical and mechanical properties. Physical characterization using FESEM, EDX and Raman Spectroscopy tools was carried out to study the structure of the layers and compositions of elements in composites for both methods of preparation. Result shows the graphene dispersion into the latex for cast film is better than the dipped film. Thus, the cast film samples with graphene is conductive while dipped film sample is not conductive. Results also show the higher percentage of graphene (4phr) in the composite has high conductivity than the 3phr samples. In this project, sample-five (S5) shows the best performance than other samples. The conductivity of this sample is the highest compared to other samples which is 1.1051m (Ωm)$^{-1}$. This composite has almost 90% of strechability. Thus, this latex-graphene material is a good sensing material for flexible and wearable electronic application for human motion detection, personal health monitoring, sports performance monitoring and other applications.*

# Weight Value Modification in Transformer Health Index Assessment Model

A. Azmi, J. Jasni

Centre for Electromagnetic and Lightning Protection Research (CELP)

Faculty of Engineering

Serdang, Selangor, MALAYSIA

akmalina.azmi@gmail.com, jas@upm.edu.my

*Abstract*— Power transformer is one of the most important component in a power system. Fault that occurs in transformer may result in power supply interruption which will also cause environmental damage, revenue losses and disruption in end users activities. Utility companies have adopting transformer asset management (TAM) with the aid of transformer health index (THI) to examine the health condition of transformers. Over the years, the weight value for components and parameters in THI assessment model were determined by subjective judgment of transformers' expert. Presently, general research on mathematical weight value identification is still very much in its infancy. Therefore, a substantial study on weight value identification by proper mathematical approach is essential in order to justify the use of THI assessment model for assessing health condition of transformers. Two existing THI assessment models, named THI Assessment Models 1 and 2 are used as reference to compare with the two proposed THI assessment models, named as THI Assessment Models A and B. It is demonstrated that THI determination in the proposed THI Assessment Models A and B are easier to be implemented compared to THI Assessment Models 1 and 2. This is due to the reason that direct mathematical steps are employed in the proposed THI Assessment Models A and B, whereas THI Assessment Models 1 and 2 are solely based on experts' judgment and prediction. Therefore, the proposed models are more reliable and does not deal with arguments from different experts. The results revealed that THI values and transformer condition in THI Assessment Models A and B are in good agreement with THI Assessment Model 2 and contradict with the THI Assessment Model 1. The results of this study clearly support that the new proposed THI assessment models are more reliable to be used in order to obtain THI value.

*Keywords—transformer asset management, transformer health index, score, weight, entropy weight method*

# Catechin for Cancer Immunotherapy

Kübra Solak
Dept. of Nanoscience and
Nanoengineering,
*Ataturk University*
*Erzurum, Turkey*
kubra.solak@ogr.atauni.edu.tr

Ahmet Mavi
Dept. of Nanoscience and
Nanoengineering,
*Ataturk University*
*Erzurum, Turkey*
amavi@atauni.edu.tr

*Abstract*— **Interferon beta (IFNβ) is used in the treatment of the cancer for years. Recently, it is revealed that a sensor protein called STING (Stimulator of Interferon Genes), causes IFNβ production in the present of double strand DNA. The studies show that some flavonoids stimulate IFNβ production via STING activation in mice. Besides, the flavonoids have an apoptotic effect on cancer. The aim of this study is to investigate the role of catechin for IFNβ production on lung cancer (A549) cell line. Quantitative polymerase chain reaction (qPCR) and Enzyme-Linked ImmunoSorbent Assay (ELISA) assays used for determination of relation between catechin and STING activation. Our results show that catechin can induce gene expression of IFNβ and STING, so, it could be a candidate for cancer immunotherapy.**

*Keywords— STING, IFNβ, catechin, cancer*

## I. INTRODUCTION

Organisms have a defense system called immunity to protect themselves from infections and some diseases like cancer [1]. Receptors on the cell surface or sensor proteins in the cytoplasm have a capability to recognize the un-known proteins, polysaccharides or bacteria and virus [2]. For example, sensor proteins such as DAI, DDX41, IFI16 etc. are activated when double strand DNA (dsDNA) is in cytoplasm [2]. In addition, it is expected that immune system recognizes cancer cells, but, according to tumor micro environment studies, cancer cells produce mediators such as IDO (indoleamine-2,3-dioxygenase) enzyme, TGF-β and IL-10 to hide from host defense [3], [4]. Therefore, reactivation of suppressed immunity might be useful for killing cancer cells.

Typically, infected cells secrete chemokines and cytokines which are responsible to regulate the activation of immune cells (T, B or Natural Killer cells) and to induce the programmable cell death (apoptosis) [5]–[7]. Interferons (IFNs) are the large class of cytokines and have anti-viral, anti-cancer, immune modulator and anti-proliferative activity [8]–[10]. Especially interferon β (IFNβ) have been used for cancer immunotherapy for many years [11], [12]. The researchers discovered a DNA sensor protein, which can secrete IFNβ in the presence of dsDNA in cytoplasm. This sensor protein has been called as STING (Stimulator of Interferon Genes) [9]. STING is a transmembran protein and induce IFNβ secretion through the phosphorylation reaction of a series of proteins such as TBK-1 and NF-κB [13].

Kim et al. observed that FAA (flavone acetic acid) and DMXAA (5,6-Dimethylxanthenone-4-acetic acid, Vadimezan), are a member of flavonoids, induce IFN β production through STING activation in mice [14]. In addition, flavonoids prevent vascular formation, induce apoptosis, and suppress cell proliferation in cancer [15].

Therefore, flavonoids may have a great potential for human STING activation. Furthermore, flavonoids are natural drug and used against cancer and infectious diseases. Catechin is a kind of flavonoids and polyphenolic antioxidant. A study showed that catechin activate NF-κB which is a protein complex that controls transcription of DNA, cytokine production and cell survival [16]. In this study, therefore, we aimed to investigate relationship between STING activation and catechin.

## II. METHOD

### K. In vitro Studies

A549 lung cancer cell line was growth with Dulbecco's modified Eagle's medium (DMEM, Gibco) supplemented with 10% fetal bovine serum (FBS, Gibco) and 1% penicillin-streptomycin antibiotic (Gibco). The cells were growth under condition of 37 ºC, 90% humidify and 5% $CO_2$.

Before the tests catechin (Fluka) was dissolved in DMSO (Merck) and DMSO was kept below 0.1% in cell culture media. All results were compared with commercially cGAMP (cyclic [G(3',5')pA(3',5')p], Invivogen) which is a STING activator. To increase cellular uptake of cGAMP, Lipofectamine transfection was used.

### L. Cell Viability Assay

To measurement of cell viability and proliferation, MTT test was applied according to manufacturer's protocols (TOX1, Sigma). A549 cells were seeded 96-well plates by density of 5000 cells/well. After 24 hours, cells were exposed to catechin. After incubation of cells for 8 and 12 hours, the absorbance was read at 570 nm by BioTek-EPOCH plate reader.

### M. ELISA Assay

After cells were seeded and treated with catechin and cGAMP, mediums were collected to measure amount of secreted interferon β (IFN-β) by enzyme-linked immunosorbent assay (ELISA) according to manufacturer's protocols (Bioassay Technology Laboratory, Cat. No: E0154Hu).

### N. Gene Expression

Total RNA isolation was performed on catechin and cGAMP treated cells by RNeasy assay kit (QIAGEN). Transcriptor First Strand cDNA Synthesis kit was used to produce cDNA from total RNA. For specific amplification of cDNAs, IFNβ, STING, P53, Bax and β-actin primers were used to observe gene expression by using Rotor gene 5 Real-Time PCR device. RT2 Profiler PCR Array Data Analysis v3.5 was used for data analysis after PCR application.

## III. RESULTS

### O. Cell Viability Assay

50, 100 and 250 μM catechin was applied A549 cells and the cells were incubated for 8 and 12 hours. The cell viability test indicates that only 250 μM catechin treatment shows significant toxicity for 12 hours (Fig. 1). When cGAMP was applied with LyoVec, the cell viability decreased after 8 hours consistent with the previously reports because free cGAMP is not permeable from cell membrane. Fig. 1 also shows that catechin is not toxic to the cells.
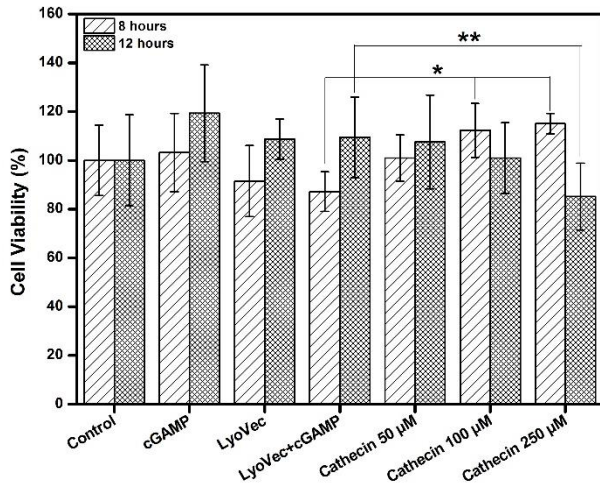


Fig. 1 Cell viability of A549 cells. * indicates that p<0.05 (OneWay ANOVA,Tukey)

### P. Amount of Interferon β

Cell mediums were harvested 8, 12, 24 and 48 hours after the applied cells and the amount of IFNβ was measured using the ELISA test kit produced for IFNβ. The highest IFNβ amount was measured at the end of 12 hours Fig. 2.
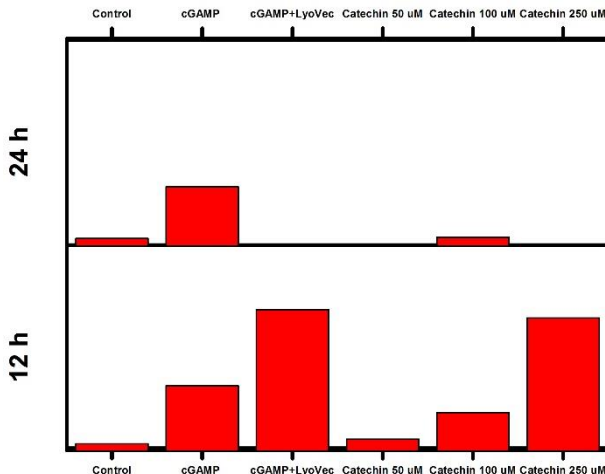


Fig. 2 ELISA results, the amount of IFNβ

According to ELISA results, cGAMP treatment increased IFNβ secretion as expected in the literature. While the best amount of IFNβ was observed at 24 hours in cGAMP treated groups, the best amount of IFNβ was observed in 12 hours in the cells where cGAMP was applied with LyoVec. In the Catechin-treated cell groups, IFNβ production was observed to initiate the immune response in 12 hours without the need

for a carrier agent such as LyoVec. There is also a dose-dependent increase of IFNβ production in catechin groups. However, 8-hour incubation of the cells after catechin treatment is insufficient to increase IFNβ generation.

### Q. Gene Expression

In real-time PCR studies, increased expression of apoptotic genes was observed in catechin treated groups. IFNβ expression was increased at the end of 24 hours, but no expression after 30 hours. These results are consistent with ELISA results. Apoptotic gene p53 expression increased dose-dependent in groups treated with catechin. As a result, it is thought that catechin increases the expression of IFNβ by STING.
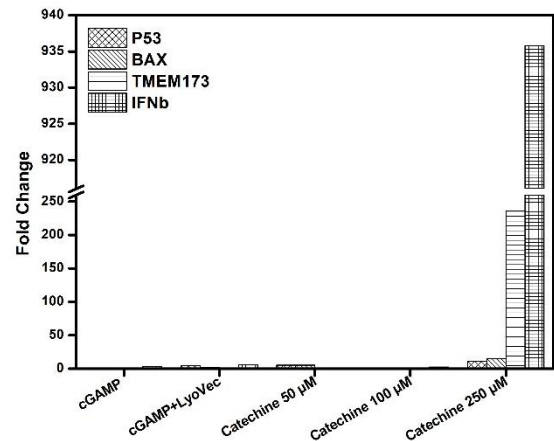


Fig. 3 Results of real time PCR for 24 hours

## REFERENCES

[1] S. M. Candeias and U. S. Gaipl, "The Immune System in Cancer Prevention, Development and Therapy.," *Anticancer. Agents Med. Chem.*, vol. 16, no. 1, pp. 101–7, 2015.

[2] L. Unterholzner, "The interferon response to intracellular DNA: Why so many receptors?," *Immunobiology*, vol. 218, no. 11, pp. 1312–1321, 2013.

[3] J. N. Blattman and P. D. Greenberg, "Cancer immunotherapy: a treatment for the masses.," *Science*, vol. 305, no. 5681, pp. 200–205, 2004.

[4] S. Woo, L. Corrales, and T. F. Gajewski, "The STING pathway and the T cell- inflamed tumor microenvironment," *Trends Immunol.*, vol. 36, no. 4, pp. 250–256, 2015.

[5] G. Trinchieri, "Type I interferon: friend or foe?," *J. Exp. Med.*, vol. 207, no. 10, pp. 2053–63, 2010.

[6] M. B. Fuertes, S. R. Woo, B. Burnett, Y. X. Fu, and T. F. Gajewski, "Type I interferon response and innate immune sensing of cancer," *Trends Immunol.*, vol. 34, no. 2, pp. 67–73, 2013.

[7] J. Yen and D. Ganea, "Interferon B induces mature dendritic cell apoptosis through caspase-11/caspase-3 activation," *Immunobiology*, vol. 114, no. 7, pp. 1344–1354, 2009.

[8] L. Corrales and T. F. Gajewski, "Endogenous and pharmacologic targeting of the STING pathway in cancer immunotherapy," *Cytokine*, pp. 1016–1018, 2015.

[9] G. N. Barber, "STING-dependent cytosolic DNA sensing pathways," *Trends in Immunology*, vol. 35, no. 2. Elsevier Ltd, pp. 88–93, 2014.

[10] G. N. Barber, "STING: infection, inflammation and cancer," *Nat. Publ. Gr.*, vol. 15, no. 12, pp. 760–770, 2015.

[11] J. Bekisz, S. Baron, C. Balinsky, A. Morrow, and K. C. Zoon, "Antiproliferative Properties of Type I and Type II Interferon," pp.

994–1015, 2010.

[12] J. Yoshida, M. Mizuno, and T. Wakabayashi, "Interferon-β gene therapy for cancer : Basic research to clinical application," *Cancer Sci*, vol. 95, no. 11, pp. 858–865, 2004.

[13] S. Paludan and A. Bowie, "Immune Sensing of DNA," *Immunity*, vol. 38, no. 5. pp. 870–880, 2013.

[14] S. Kim, L. Li, Z. Maliga, Q. Yin, H. Wu, and T. J. Mitchison, "Anticancer flavonoids are mouse-selective sting agonists," *ACS Chem. Biol.*, vol. 8, no. 7, pp. 1396–1401, 2013.

[15] N. Sharma, M. Dobhal, Y. Joshi, and M. Chahar, "Flavonoids: A versatile source of anticancer drugs," *Pharmacognosy Reviews*, vol. 5, no. 9. p. 1, 2011.

[16] H. Sipahi, J. M. Gostner, K. Becker, M. Charehsaz, H. Kirmizibekmez, H. Schennach, A. Aydin, and D. Fuchs, "Bioactivites of two common polyphenolic compounds: Verbascoside and catechin," *Pharm. Biol.*, vol. 54, no. 4, pp. 712–719, 2016.

# Microstructure Comparison of Superconducting Joints Fabricating by Using Different Techniques

Canan Aksoy
Elect&Communication Eng., Faculty of Technology, Karadeniz Technical University, 61830, Of, Trabzon, Turkey

B.Savaşkan
Energy Systems Eng., Faculty of Technology, Karadeniz Technical University, 61830, Of, Trabzon, Turkey

*Abstract*—**Magnets working with persistent mode are highly dependent on the existence of high-quality superconducting joints between superconducting wires used on technological applications. There are some techniques are quite effective for continues current such as spot welded, cold pressed and soldered joints. In this study, we produced joints with these techniques and compared them in terms of advantage and disadvantages by investigating their microstructural properties. Among those techniques soldering showed the best properties if considered reproducibility.**

*Keywords— Joint, Superconductor, Magnet*

## I. INTRODUCTION

Jointing of the play a crucial role in the production of electrical and mechanical devices using for technological applications, particularly high magnetic field required such as magnets for magnetic resonance measurements, superconducting magnetic energy storage systems and the Large Hadron Collider [1]. These application needs high magnetic field by using the persistent current joints which are integral component between the superconducting wires because since their terminals must be short-circuited in order to confine the supercurrent to the circuit [2].

NbTi and Nb3Sn wires are best wires, having good superconducting properties, for currently used MRI magnets and superconducting applications. However, there is need to be a joint for combine large magnets together. For this, researchers have been working to create novel jointing techniques to obtain a persistent current between the superconducting magnets. There are some ways to make persistent joints between the superconductors such as cold press, spot welding and soldering. Although, they all have good advantages in a one way but between them soldering is much promising than the others. In this study, fabricated joints were discussed with the advantages and disadvantages in terms of superconducting and microstructural properties.

### R. Jointing Techniques

#### a) Cold-Pressed Joints

To make cold press joints, firstly the the Cu layer is removed from the NbTi wires by using mechanical process and using HF or $HNO_3$. HF is not promising acid for using due to the safety problems. Then the two wires twisted or breading together and putting into the Nb tubes and they pressed at around 600 MPa.
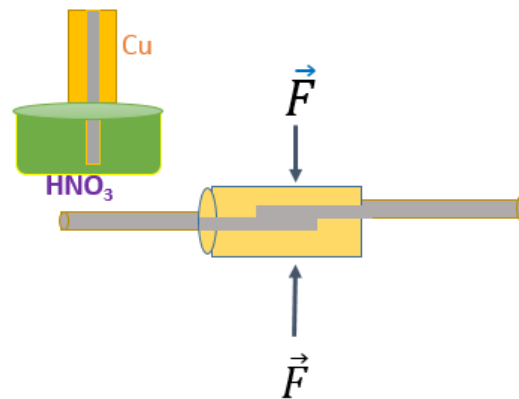


Fig.2 Schematic of typical NbTi cold-pressed joint

#### b) Spot Welded Joints

Spot welding is a kind of resistive welding, a technique commonly used to make joint for joint sheet metal. Spot-welded joints were manufactured by removing the Cu-matrix from the filaments by etching in $HNO_3$, and then braiding the filaments from the two wires and spot- welding between Cu plates as shown in Fig.2 [1]
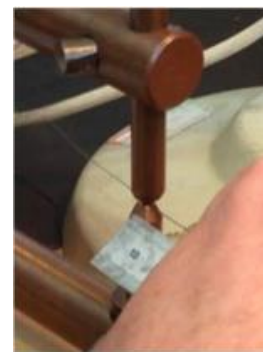


Fig. 2. Photograph of Spot-welded joints [2]

#### c) Soldered Joints

Soldering is one of the promising technique to use a joint between the superconductor wires. First step is removing protect layer from the filaments by using grinding paper and as other techniques it can be used etching by $HNO_3:H_2O$ acid solution to remove the Cu matrix from the wires. However, to protect the wires from the oxidation, soldering is a good way by using Sn which has a good metal-metal interaction

with the wetting properties. After tinning the wires at least 10 minutes, to be jointed two wires are twisted and braiding together and they immerse in to the molten eutectic binary or ternary solder which generally have low temperature melting point around 80°C-400°C. Currently most used solder for technological application is PbBi solder.
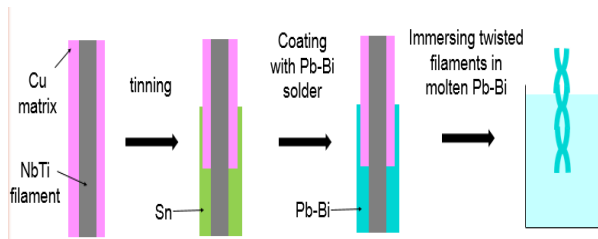


Fig.3 It shows that Schematic of soldering process

*S. Characterisation of the joints*

Brittles et al. discussed the method of the characterization of the superconducting properties in detail [3] by used a magnetic properties measurement system (MPMS) that the jointed coil is mounted in a standard 5 mm straw and the loop is centered in the MPMS. The coil is then zero field cooled below to the desired measurement temperature decided the critical temperature (Tc) of the superconducting wire. Currents (I) can then be induced to flow around the coil (through the joint) by changes in applied magnetic field (H) [4].

For microstructural characterization scanning microscopy (SEM) in a JEOL 5510 or Zeiss Merlin microscope were used and chemical analysis by energy dispersive X-ray (EDX) analysis using an Oxford Instruments OISDD X Max 150 mm detector and Aztec software were carried out.

## II. RESULTS AND DISCUSSION

The joints by using cold pressed, spot-welded and soldering technique for superconducting low temperature NbTi wires were fabricated.

The cold pressed joint is easily fabricated with a direct bonding technique and easy reproducible [5]. However, removing the Cu matrix totally from the filaments is a problem unless used a strong acid as HF due to the fact that Cu it blocks the bonds between the superconducting wires. Besides, NbTi is easily oxidised material which is not desired for jointing process. As you seen in the EDX map of the cold pressed joints in Fig. 4 [2]
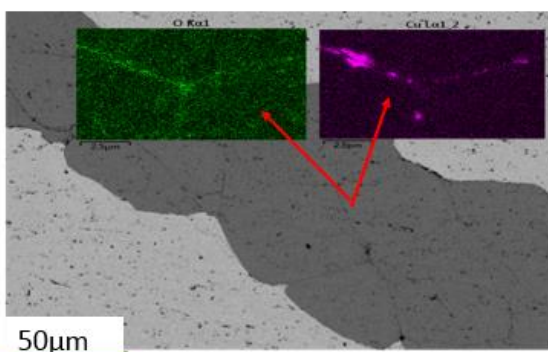


Fig.4 The EDX maps of the Cold-pressed Joints

The same issue is a problem in the spot-welded technique, as well. The cleansing is quite important for joint quality. However, the microstructure of the fused filaments are melted by the welding process which induced the Nb rich and Ti rich phases as a dendritic microstructure, showed in Fig.5.These phases are expected to have poor superconducting properties and degrade joint performance [4].
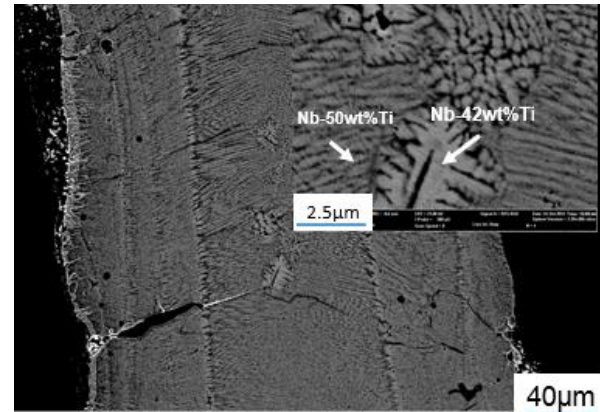


Fig.5 The dendritic microstructure with Nb rich and Ti rich phases after spot welded [4]

Soldered joints are much more effective for obtaining full bonding between the NbTi wires as seen in the cross section of the joints and EDX maps in Fig. 6. However, the tinning process need to be operated very well otherwise Sn residues can be presents on the interphase which are also effected the superconducting properties as Sn induced to the resistance.
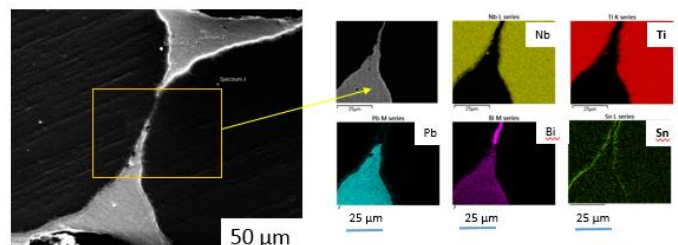


Fig.6 The cross section of the joints and EDX maps of the soldered joints.

Because of the health concerns, the novel solder material have been used instead of Pb based solders such as one of the promising solder is SnInBi [6-7] if compared to the currently used solders for technology [8].

REFERENCES

[1] Rossi L 2010 Superconductivity: its role, its successes and its setbacks in the Large Hadron Collider of CERN Supercond. Sci. Technol. 23 034001

[2] G D Brittles, T Mousavi, C R M Grovenor, C Aksoy and S C Speller. Persistent current joints between technological superconductors. Supercond. Sci. Technol. 28 (2015) 093001

[3] G. D. Brittles, P. Noonan, S. A. Keys, C. R. M. Grovenor, and S. Speller, "Rapid characterisation of persistent current joints by SQUID magnetometry," Supercond. Sci. Technol., vol. 27, no. 12, Nov. 2014, Art. no. 122002.

[4] G. D. Brittles, C. Aksoy, C. R. M. Grovenor, T. Bradshaw, S. Milward, and S. C. Speller 2016 "Microstructural Properties and Magnetic Testing of Spot-Welded Joints Between Nb–Ti Filaments" IEEE Transactions On Applied Superconductivity, Vol. 26

[5] Nuding J M 1969 Method of making a superconductive joint US Patent 3422529

[6] Mousavi, C. Aksoy, C. R. M. Grovenor, and S. C. Speller, "Microstructure and superconducting properties of Sn-In, Sn-In-Bi alloys as Pbfree superconducting solders," Supercond. Sci. Technol, vol. 29, no. 1, Dec. 2015, Art. no. 015012.

[7] T. Mousavi, C. Aksoy, C. Grovenor, and S. Speller, "Phase evolution of superconducting Sn-In-Bi solder alloys," IEEE Trans. Appl. Supercond., to be published, doi: 10.1109/TASC.2016.2514843.

[8] C. Aksoy, T. Mousavi, G. Brittles, C. R. M. Grovenor, and S. C. Speller, 2016, Lead-free solders for superconducting applications.IEEE Trans. Appl. Supercond., vol. 26 (2016), p.3.

# Novel Approaches in Synthesis of Chiral Nanostructures

Mehmet Yilmaz

*East Anatolia High Technology Application and
Research Center (DAYTAM)
Department of Chemical Engineering
Ataturk University*
Erzurum, Turkey

*Abstract*— **Despite of the recent progress in both bottom-up and top-down fabrication techniques to create chiral plasmonic nanostructures, some major limitations still remain. In this respect, it is clear that we need novel, simple, inexpensive and sensitive methods to fabricate chiral plasmonics in large scale. In the context of this study, to eliminate the drawbacks of present techniques, core/shell nanostructures of metallic nanostructures through bio-inspired polydopamine (PDOP) was proposed. For this, firstly, CdTe helices were fabricated and then gold nanoparticles were deposited over the helices. Both plasmonic behavior and chiroptical activity could be manipulated by tuning PDOP and gold deposition time.**

*Keywords*—**chiral plasmonic nanostructures, circular dichroism, CdTe helices, polydopamine.**

## I. INTRODUCTION

The interaction of light with chiral plasmonic nanostructures leads to strong chiroptical effects [1]. These type of nanostructures can be used to enhance the chiroptical response of chiral molecules and could also significantly increase the enantiomeric excess of direct asymmetric synthesis and catalysis [2-5]. Basically, for the fabrication of chiral plasmonic nanostructures two different approaches may be employed: top-down and bottom-up. In the top-down approach the techniques such as ion lithography, electron beam lithography and direct laser writing can be used [6]. With these techniques, well controlled nanostructrctures with high resolution can be fabricated. However, this approach has some drawbacks such as expensive and complicated devices, time-consuming procedure and limited size of fabricated substrate. In the second approach, bottom-up, colloid nanostructures can be synthesized through the self-assembly mechanism. Self-assembly provides some advantages such as being fast, inexpensive and large scale production. In this approach, the main limitation is the fabrication of nanoparticles in well-controlled size distribution.

In the context of this study, to eliminate the limitations of present chiral plasmonic nanostructures, surface of these as-prepared CdTe helices were decorated with plasmonic gold nanoparticles via bio-inspired polydopamine (PDOP) layer. PDOP having abundant amine, imine and catechol functional groups can reduce the gold ions and create plasmonic nanoparticle decorated system. This study indicated that both plasmonic and circular dichroism (CD) characteristics of CdTe@PDOP@Au helices can be controlled easily by tuning experimental parameters such as PDOP and gold deposition time. Remarkable enhancement in CD signal intensity was detected after gold deposition. I strongly believe that the as-prepared plasmonic helices can be used in different applications including catalysis and sensing.

## II. MATERIALS AND METHODS

### T. Synthesis of Cysteine Modified CdTe Nanoparticles (Cys-CdTe NPs)

The synthesis of nanoparticles was conducted according to previous reports [7, 8]. Briefly, $Cd(ClO_4)_2 \cdot 6H_2O$ (0.985 g) and L-cysteine hydrochloride monohydrate (0.985 g) were dissolved in 125 ml of deionized (DI) water. Then, the pH was adjusted to 11.2 by using 1 M NaOH. This solution was transferred to a three-neck, round-bottom flask and purged with $N_2$ for 30 min. $H_2Te$ gas which was produced by reaction of 0.10 g of $Al_2Te_3$ with 10 ml of 0.5 M $H_2SO_4$ was slowly passed through the solution. The solution was refluxed under $N_2$ at 100°C for 60 min to obtain the Cys-CdTe NPs. Finally, NP solution was throughly purged with $N_2$ for at least 30 min and then kept in the dark at 4°C.

### U. Preparation of CdTe Helices

Before preparation of Cys-CdTe helical assemblies the as-synthesized NP dispersion was allowed to age under dark conditions at 4°C for 1 day or more. During aging procedure, it seems that residual oxygen is likely to react with NPs. Black precipitates could be observed at the bottom of the container as aging proceeded. The aging process resulted in a blueshift of the first excitonic absorption peak indicating a decrease in NP size [8]. After sufficient aging of NPs, a solvent exchange step was performed to transfer the NPs from water to methanol to create assembled helices. For this, the NP aqueous dispersion and methanol were mixed at a volume ratio of 1:1.5 to precipitate the NPs. This solution was then centrifuged at 1500 rpm for 3 min, the supernatant was discarded, and the precipitate was redispersed in methanol. This step provides the elimination of excess Cys ligand and activate NPs for assembly. The assembly process proceed overnight. Finally, the as-assembled helices in methanol were transferred to DI water via centrifuge at 1500 rpm for 3 min.

### V. Preparation of CdTe@PDOP helices

For the deposition of PDOP layer, firstly, the Cys-CdTe helices dispersion was centrifuged at 6000 rpm for 3 min and then dispersed in dopamine solution (2 mg mL$^{-1}$ in 10 mM Tris buffer, pH 8.5) at room temperature for different deposition times (1-3h). After PDOP deposition, CdTe@PDOP helices were collected via centrifuge (6000 rpm for 3 min) and re-dispersed in DI water.

## W. Preparation of CdTe@PDOP@Au helices

For the deposition of gold nanoparticles, firstly, the CdTe@PDOP helices dispersion was centrifuged at 6000 rpm for 3 min and then dispersed in chloroauric acid solution (0.5 mg /mL) at room temperature for different deposition times (1-6h). After gold deposition, CdTe@PDOP@Au helices were collected via centrifuge (6000 rpm for 3 min) and re-dispersed in DI water.

## X. Characterization

JASCO J-815, equipped with two photomultiplier (PMT) detectors with 200 to 900 and 700 to 1100 nm ranges, CD spectrophotometer was used for the CD studies. Absorption spectra were also obtained from the same CD device. Typical scanning parameters were as follows: scanning speed, 200 nm/min; data pitch, 1 nm; bandwidth, 1 nm, digital integration time, 1 s; and one accumulation.

FEI Nova 200 Nanolab Dualbeam SEM was used for SEM imaging and EDX elemental analysis.

## III. RESULTS AND DISCUSSION

For Cys-CdTe NPs, earlier reports depicted the nanoparticles with the size of ~4 nm [7, 8]. Accordingly, an excitonic absorption peak at 521 nm was detected through absorption spectra (Figure 1). In CD measurements, I could observe a weak CD band at 550 nm (Figure 2). This clearly shows that Cys-CdTe NPs are weakly CD active. The low intensity of CD signal can be attributed to absence of the defects on the surface of the nanoparticles. To obtain high CD signal via chiral molecule modified nanostructures, the formation of defects at or around their bandage is required11. When Cys-Cd TE NPs were examined via SEM, aggregation of tiny nanoparticles were observed clearly (Figure 3).
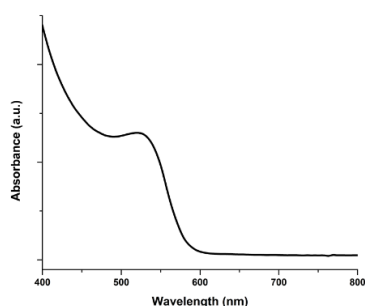


Figure 1. Absorption spectra of Cys-CdTe NPs.
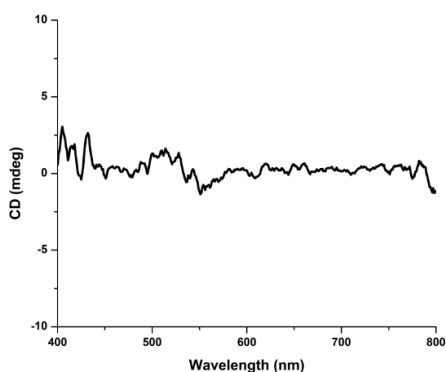


Figure 2. CD spectra of Cys-CdTe NPs.
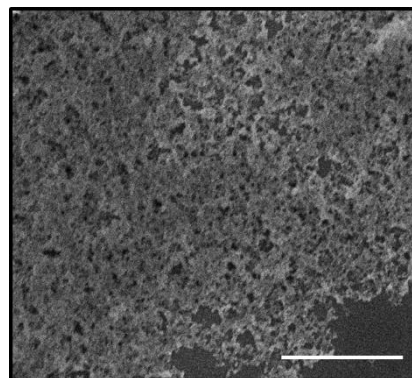


Figure 3. SEM image of Cys-CdTe NPs.

The report by Feng et al.[8] depicted that the change of medium from water to methanol resulted in higher attractive forces between polar Cys-CdTe NPs become than repulsive electrostatic ones due to reduced ionization of the carboxyl and amino groups. This change provided the self-assembly with chiral asymmetry influenced by short-range interactions. Although most of the NPs in the dispersion produce aggregates, only a small portion of NPs (~0.1%) create well-defined helices. SEM images (Figure 4a, b) shows the helices having nanoscale, mesoscale, and microscale features with the thickness below 100 nm, diameter ~300 nm, and their length ~2 µm. The shape of the assembled structure is a helicoid instead of a spiral, with no intrahelical racemization.

Individual Cys-CdTe NPs generally have weak chiroptical activity. However, after assembling into CdTe helices, the high CD activity was measured at 495 nm with 19 mdeg CD value (Figure 6) which is more than two orders of magnitude higher than that of the NPs and significantly improved than previously reports on chiral CdTe nanostructures [9, 10]. Besides, this value is comparable to those reported for chiral nanoscale assemblies based on metallic components such as Au/Ag pyramids [11] and Au helices [12], as well as helical organic polymers including protein secondary structures [13]. Also, in the Uv-Vis spectra, there has been a red-shift after fabrication of CdTe helices compared with CdTe NPs (from 521 to 531 nm).

To decorate gold nanoparticles onto the as-prepared CdTe helices, PDOP was employed to reduce gold ions and stabilise nanoparticles. After PDOP deposition, no morphological change was observed via SEM images (Figure 4c,d) due to the low thickness (less than 5 nm) of PDOP. However, PDOP layer led to a dramatic change in the Uv-Vis spectra (Figure 5). Absorption at 531 was almost disappeared and two shoulder type bands were detected. This issue may be attributed to change in dielectric constants as a result of emergence of PDOP layer. Similarly, the PDOP layer also resulted in somewhat lower CD signal with a small red-shift in the band (Figure 6) compared with uncoated CdTe helices.
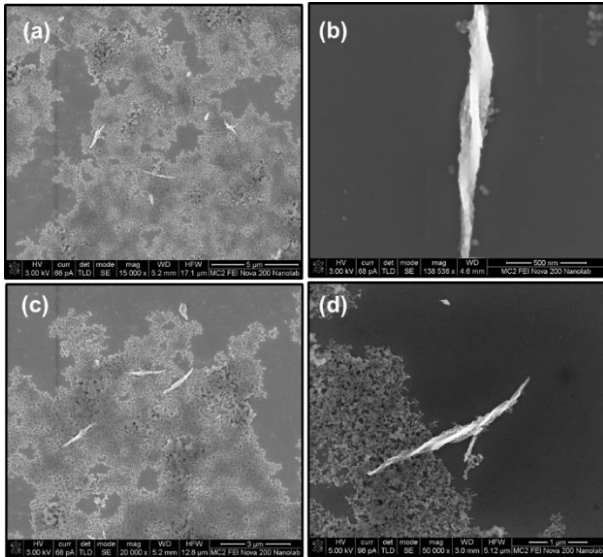
Figure 4. SEM images of CdTe (a and b) and CdTe@PDOP helices (c and d) at different magnifications. PDOP deposition time is 1 h.
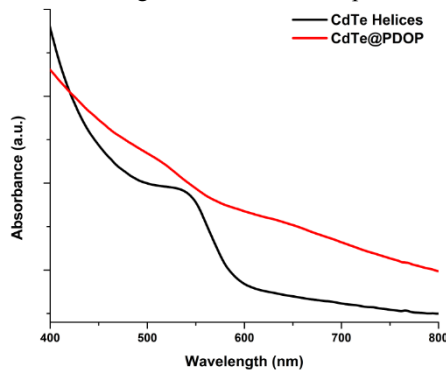


Figure 5. Absorption spectra of CdTe and CdTe@PDOP helices.
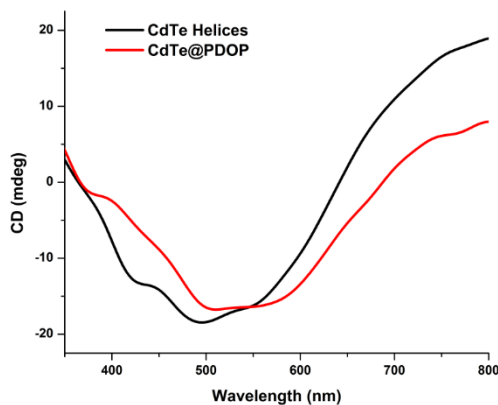


Figure 6. CD spectra of CdTe and CdTe@PDOP helices.

After PDOP deposition, CdTe@PDOP helices were decorated with gold nanoparticles by using chloroauric acid solution. PDOP layer having abundant amine, imine and catechol functional group can both reduce gold ions and stabilize gold nanoparticles. Firstly, to determine the effect of thickness of PDOP layer on CD activity and final morphology of CdTe@PDOP@Au helices, CdTe helices were kept in PDOP solution for different times. The study by Messersmith group indicated that the thickness of the PDOP layer can be manipulated by tuning deposition time [14]. After PDOP deposition helices were decorated with gold nanoparticles by immersing into gold ions solution for 6 h. Figure 8 summarizes the relevant CD spectra of

CdTe@PDOP@Au helices for different PDOP deposition times. From this data, it seems that for all cases a significant decrease in CD signal with remarkable red-shift (>100 nm) was observed compared with CdTe bare and CdTe@PDOP helices (see Figure 6). Firstly, the red-shift in CdTe@PDOP@Au helices can be attributed to the emergence of gold nanoparticles. The presence of plasmonic gold nanoparticles was also confirmed via absorption spectra of helices (Figure 8). Uv-Vis spectra depicted that absorption peak positions are ranged from 620 to 650 nm and this data is well-correlated with PDOP thickness. Also, broadness of absorption band compared with bare helices is a good indicator of gold size distribution. As the PDOP deposition time (i.e. PDOP thickness) increases, both gold nanoparticles' size and size distribution increase, as well. To further analyze the PDOP thickness effect, SEM is employed to obtain morphology of CdTe@PDOP@Au helices (Figure 9). It is clear that for all cases helices were coated with gold nanoparticles. Gold nanoparticle analysis performed via free ImageJ software indicated that for all PDOP thickness case nanoparticle size is ranged from 10 to 40 nm. This data is well-correlated with both CD and Uv-vis absorption spectra data. These images also enlighten the mechanism behind the decrease in CD signal compared with CdTe@PDOP helices. It seems that after gold deposition, helices lost their helical structure due to deposition of excess amount of gold. From this section, we can conclude that for each PDOP thickness we can deposit gold nanoparticles onto helices and instead of PDOP thickness, the experimental parameters that determine final morphology of gold nanoparticles must be considered to obtain CD signals with higher intensity.
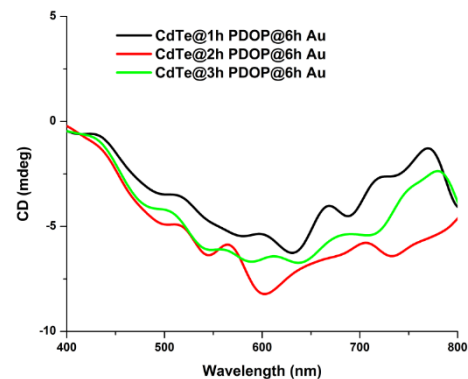


Figure 7. Effect of PDOP deposition time on CD spectra of CdTe@PDOP@Au helices.
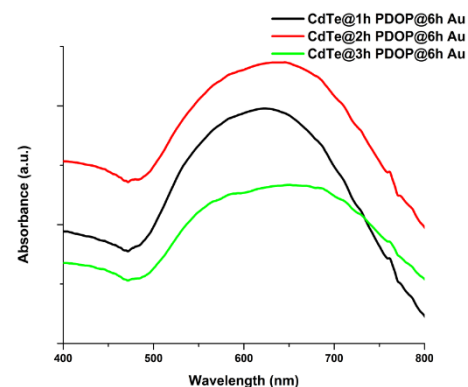


Figure 8. Effect of PDOP deposition time on absorption spectra of CdTe@PDOP@Au helices.
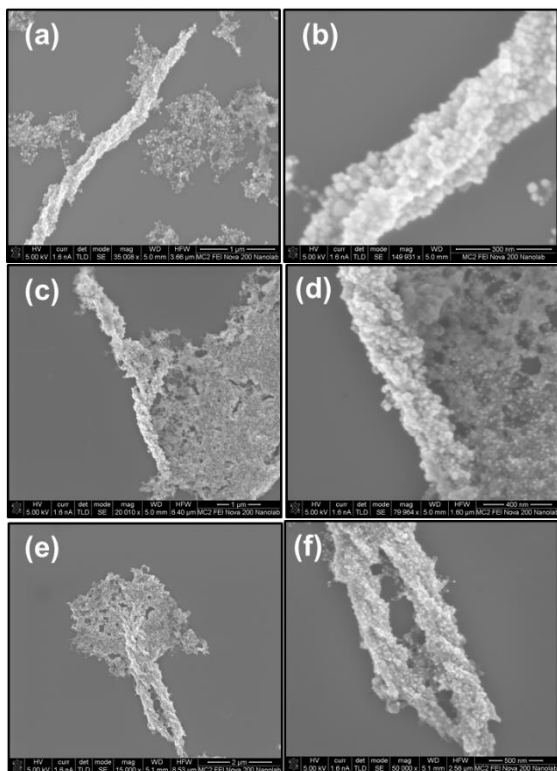
Figure 9. Effect of PDOP deposition time on final morphology of CdTe@PDOP@Au helices at different magnifications. PDOP deposition times: a,b; 1 h, c,d: 2 h and e,f:3 h. Gold deposition time is 6 h.

In this part, to eliminate the disappearance of helical structure, the deposition time (1-3 h) of gold ions was reduced for the constant PDOP deposition time (1 h). Uv-Vis spectra of CdTe@PDOP helices (Figure 10) at different gold deposition times clearly depicts the emergence gold nanoparticles. For each case, although we can not observe the distinct absorption maxima, the presence of the nanoparticles was confirmed via arisen broad shoulder. To emphasize this point, this data was normalized to make it more apparent (Figure 11). The emergence of the shoulder instead of distinct peaks may be attributed to small size and low surface coverage of gold nanoparticles onto the helices. However, CD spectra of CdTe@PDOP@Au helices resulted in higher chiral optical activity compared with bare CdTe and CdTe@PDOP helices (Figure 12). This is due to strong chiroptical responses from multipole plasmon resonances of Au nanoparticles onto the helices [15-17]. Also, the emergence of gold nanoparticles led to a remarkable red-shift in CD spectra helices. To further analyze effect of the gold deposition time, SEM is employed to obtain morphology of CdTe@PDOP@Au helices (Figure 13). It is clear that for all cases helices were coated with gold nanoparticles. Nanoparticle size analysis via ImageJ indicated that the size of gold nanoparticles is ranged from 5 to 30 nm. Gold nanoparticles were decorated all over the surface of the helices and their size and surface coverage can be controlled simply by tuning deposition time. As the deposition time increases, both nanoparticle size and number density of nanoparticles increase, as well. This data is well-correlated with both CD and Uv-vis absorption spectra data. It seems that 2 h of gold deposition time optimum value to obtain the highest CD signal intensity for the proposed system. Further

increase of deposition time led to disappearance of helical structure and low CD signal. To confirm the emergence of gold nanoparticles onto the helices, we performed elemental mapping of some helices. A representative mapping of a CdTe@PDOP@Au helice was summarized in Figure 14. These images clearly indicate that gold nanoparticles were created not only onto the helices but also in the dispersion due to the residue of PDOP. From this section, we can conclude that for each gold deposition time, we can deposit gold nanoparticles onto helices and the size, surface coverage and resultant CD signal of helices can be controlled by tuning deposition time of gold ions.
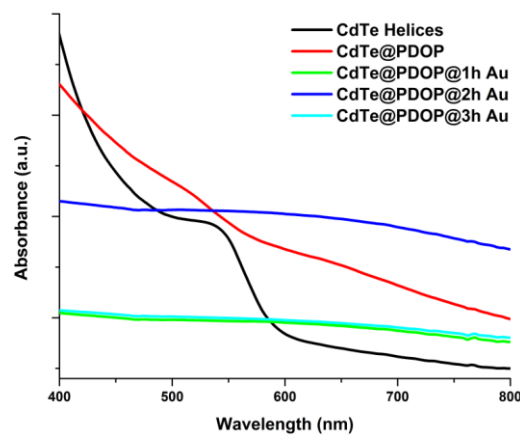


Figure 10. Effect of gold deposition time on absorption spectra of CdTe@PDOP@Au helices.
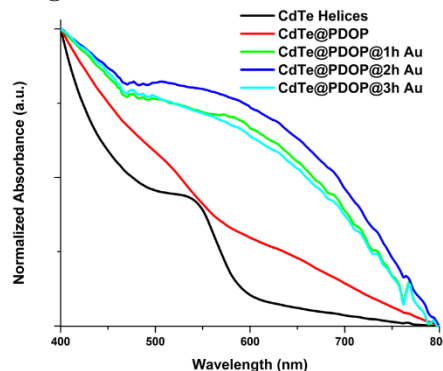


Figure 11. Effect of gold deposition time on normalized absorption spectra of CdTe@PDOP@Au helices.
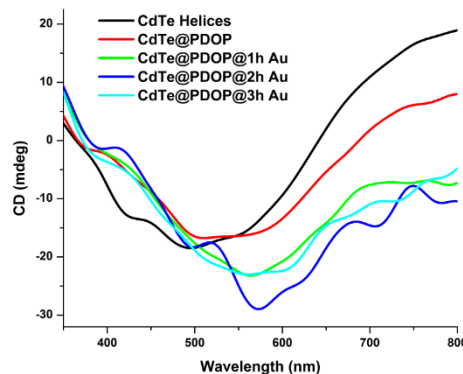


Figure 12. Effect of gold deposition time on CD spectra of CdTe@PDOP@Au helices.
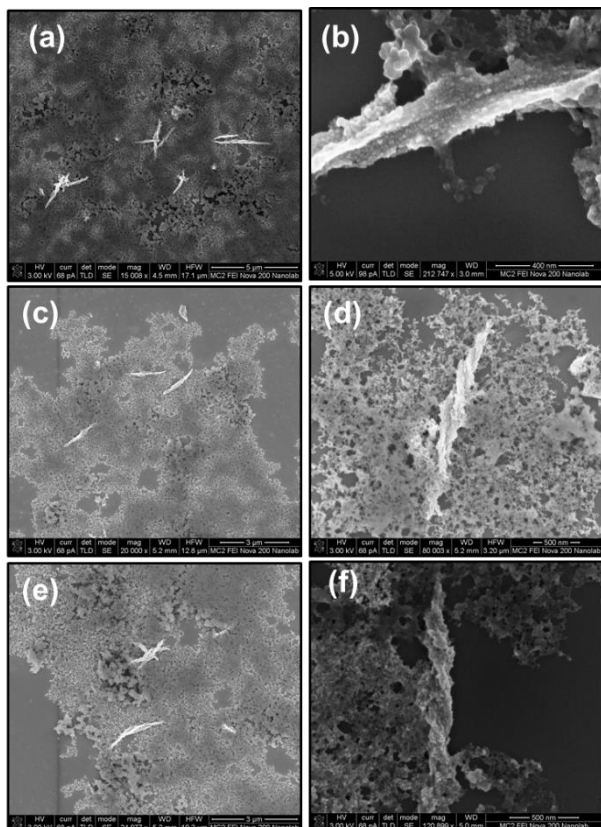
Figure 13. Effect of gold deposition time on final morphology of CdTe@PDOP@Au helices at different magnifications. Gold deposition times: a,b; 1 h, c,d: 2 h and e,f:3 h. PDOP deposition time is 1 h.
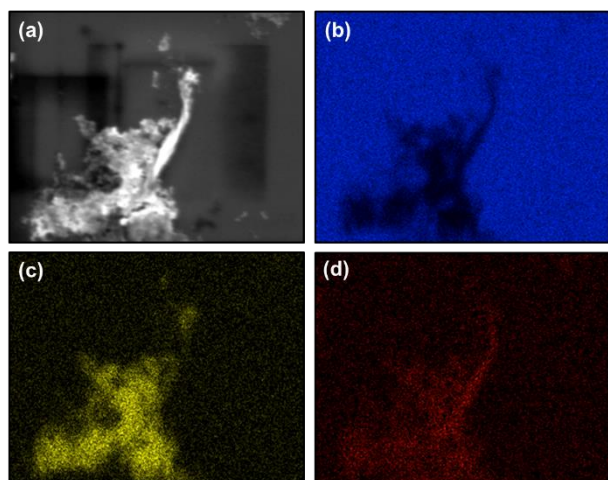


Figure 14. Elemental mapping of CdTe@PDOP@Au helices. a; SEM image, b; Si, c; Au and d: C. PDOP and gold deposition times are 1 and 2 h, respectively.

## IV. CONCLUSION

In the context of this study, chiral plasmonic nanostructures were fabricated by employing CdTe helices. For this, surface of these helices were decorated with plasmonic gold nannoparticles via bio-inspired PDOP layer. PDOP having abundant amine, imine and catechol functional groups reduced the gold ions. This study indicated that both plasmonic and CD characteristics of CdTe@PDOP@Au helices can be controlled easily by tuning experimental parameters such as PDOP and gold deposition time. I strongly believe that the as-prepared plasmonic helices can be used in different applications including catalysis and sensing.

## REFERENCES

[1] V. K. Valev, J. J. Baumberg, C. Sibilia, and T. Verbiest, "Chirality and chiroptical effects in plasmonic nanostructures: fundamentals, recent progress, and outlook," *Advanced Materials,* vol. 25, no. 18, pp. 2517-2534, 2013.
[2] K.-H. Dostert, M. Álvarez, K. Koynov, A. n. del Campo, H.-J. r. Butt, and M. Kreiter, "Near field guided chemical nanopatterning," *Langmuir,* vol. 28, no. 8, pp. 3699-3703, 2012.
[3] T. Chen *et al.*, "Hotspot-induced transformation of surface-enhanced Raman scattering fingerprints," *Acs Nano,* vol. 4, no. 6, pp. 3087-3094, 2010.
[4] A. Nitzan and L. Brus, "Theoretical model for enhanced photochemistry on rough surfaces," *The Journal of Chemical Physics,* vol. 75, no. 5, pp. 2205-2214, 1981.
[5] C. Chen and R. Osgood, "Direct observation of the local-field-enhanced surface photochemical reactions," *Physical Review Letters,* vol. 50, no. 21, p. 1705, 1983.
[6] A. Radke, T. Gissibl, T. Klotzbücher, P. V. Braun, and H. Giessen, "Three-dimensional bichiral plasmonic crystals fabricated by direct laser writing and electroless silver plating," *Advanced Materials,* vol. 23, no. 27, pp. 3018-3021, 2011.
[7] N. Gaponik *et al.*, "Thiol-capping of CdTe nanocrystals: an alternative to organometallic synthetic routes," *The Journal of Physical Chemistry B,* vol. 106, no. 29, pp. 7177-7185, 2002.
[8] W. Feng *et al.*, "Assembly of mesoscale helices with near-unity enantiomeric excess and light-matter interactions for chiral semiconductors," *Science advances,* vol. 3, no. 3, p. e1601159, 2017.
[9] J. Yeom *et al.*, "Chiral templating of self-assembling nanostructures by circularly polarized light," *Nature materials,* vol. 14, no. 1, p. 66, 2015.
[10] Y. Zhou *et al.*, "Biomimetic hierarchical assembly of helical supraparticles from chiral nanoparticles," *ACS nano,* vol. 10, no. 3, pp. 3248-3256, 2016.
[11] W. Yan *et al.*, "Self-assembly of chiral nanoparticle pyramids with strong R/S optical activity," *Journal of the American Chemical Society,* vol. 134, no. 36, pp. 15114-15121, 2012.
[12] A. Kuzyk *et al.*, "DNA-based self-assembly of chiral plasmonic nanostructures with tailored optical response," *Nature,* vol. 483, no. 7389, p. 311, 2012.
[13] P. McPhie, "Circular dichroism studies on proteins in films and in solution: estimation of secondary structure by g-factor analysis," *Analytical biochemistry,* vol. 293, no. 1, pp. 109-119, 2001.
[14] H. Lee, S. M. Dellatore, W. M. Miller, and P. B. Messersmith, "Mussel-inspired surface chemistry for multifunctional coatings," *science,* vol. 318, no. 5849, pp. 426-430, 2007.
[15] B. N. Khlebtsov and N. G. Khlebtsov, "Multipole plasmons in metal nanorods: scaling properties and dependence on particle size, shape, orientation, and dielectric environment," *The Journal of Physical Chemistry C,* vol. 111, no. 31, pp. 11516-11527, 2007.
[16] C. Noguez, "Surface plasmons on metal nanoparticles: the influence of shape and physical environment," *The Journal of Physical Chemistry C,* vol. 111, no. 10, pp. 3806-3819, 2007.
[17] E. K. Payne, K. L. Shuford, S. Park, G. C. Schatz, and C. A. Mirkin, "Multipole plasmon resonances in gold nanorods," *The Journal of Physical Chemistry B,* vol. 110, no. 5, pp. 2150-2154, 2006.

# Silver Nanowire Based Transparent Electrodes and Heaters

Sahin Coskun
Department of Physics, Erzincan
Binali Yıldırım University,
Erzincan 24100, Turkey

Doga Doganay
Department of Metallurgical and
Materials Engineering, METU,
Ankara 06800, Turkey

Husnu Emrah Unalan
Department of Metallurgical and
Materials Engineering, METU,
Ankara 06800, Turkey

Transparent electrodes are widely used in optoelectronics, organic photovoltaics (OPVs) touchscreens, smartphones and organic light emitting diodes (OLEDs). High transparency and conductivity and are required properties for those applications. The most widely used transparent conductor is indium tin oxide

(ITO). However, increasing indium price, low flexibility and low chemical stability are seem main disadvantages of ITO. Hence, investigation of alternative transparent conducting materials is a very popular subject. Among offered alternatives, silver nanowire networks seem to be one of the most promising candidates. Transparency and sheet resistance values of Ag NW networks are very close to that of ITO's. Silver nanowires were synthesized through a simple solution based polyol process. Then these nanowires were purified through multiple centrifuge process. Following purification process, nanowires were suspended in ethanol and spray coated onto glass substrates. A post annealing process was applied in order to decrease nanowire-nanowire junction resistance and remove residual capping agent. The electrical and optical properties of the silver nanowire networks are then investigated. The networks are found to be highly transparent (88% at 550 nm) and conducting (11 ohms/square) with values comparable to indium tin oxide.

Furthermore, in order to decrease surface roughness of Ag NW networks, a parametric study on spin coating of PEDOT: PSS was investigated. Finally, Ag NW networks were used as anode in polymer light emitting diodes (PLEDs). On the other hand, silver nanowires can be used as heating element for heaters. Silver nanowire based thin film heaters can be made transparent and can be easily integrated to textiles. For transparent heaters (TH), Ag NWs were deposited onto quartz substrates via simple spray coating. The effect of nanowire density, contact geometry, applied bias, flexing and incremental bias application on TH performance of Ag NW networks were investigated. Ag NW network based THs with a sheet resistance, percent transmittance of 4.3 $\Omega$/sq and 83.3% with a nanowire density of 1.6 NW/$\mu$m2 reached to a maximum temperature of 275°C under incremental bias application (5V maximum). On the other hand, silver nanowire decorated cotton fabrics can be heated to 50°C under an applied power density of as low as 0.05 W/cm$^2$. Time dependent thermal response of the fabrics under different applied voltages was investigated.

*sahin.coskun@erzincan.edu.tr, sahincoskun@gmail.com

# Pulsed Laser Deposited CeO₂/LaAlO₃ Thin Film Orientations at Different Temperatures

Mustafa Tolga Yurtcan
Department of Nanoscience and Nanoengineering
Atatürk University
Erzurum, Turkey
yurtcan@atauni.edu.tr

*Abstract* — **$CeO_2$ thin films deposited at different temperatures with 200 Celsius steps to 800 Celsius onto $LaAlO_3$ substrates with Pulsed Laser Deposition technique. The effect of deposition temperatures was investigated for comparison. Crystallinity and orientations of thin films investigated by Grazing Incidence X-Ray Diffraction (GIXRD) method. The best result from XRD pattern was obtained for the deposition temperature of 200 Celsius. Surface morphology of the thin films was compared by scanning electron microscope (SEM) and the only cracked surface was observed at 800 Celsius.**

*Keywords—$CeO_2$, $LaAlO_3$, temperature, PLD, thin film*

## I. INTRODUCTION

Cerium(IV)Oxide ($CeO_2$) is a good insulator and chemically stable material. It is used as catalyst, solid oxide fuel cell electrolyte, metal oxide semiconductor interface material and Silicon-On-Insulator interface material. It also has potential to replace $SiO_2$ in Dynamic Random Access Memories (DRAMs) [1]. $CeO_2$ is a good buffer layer for high temperature superconductors with a cubic structure and 5.411 Å lattice parameter [2].

$LaAlO_3$ (LAO) is a suitable substrate for high temperature superconductors, magnetic and ferro-electric thin films [3]. It is a cheap alternative to $SrTiO_3$ substrates and can be cleaned easily. Physical properties of the LAO used as substrate can be seen in Table I [3].

Table 1. Physical Properties Of LAO [3]

| Crystal Structure | Rhombohedral @ 25 °C: a=3.79 Å c= 13.11 Å Cubic @ > 435 °C : a=3.821 Å |
|---|---|
| Growth Method | Czochralski |
| Density | 6.52 g/cm³ |
| Melt Point | 2080 °C |
| Thermal Expansion | 10 (x10⁻⁶ / °C) |
| Dielectric Constant | ~ 25 |
| Loss Tangent @ 10 GHz | ~ 3x10⁻⁴ @ 300K, ~ 0.6x10⁻⁴ @ 77K |
| Color and Appearance | Tan to Brown based on annealing condition Visible twins on polished substrate |
| Chemical Stability | Insoluble in mineral acids @ 25 °C Soluble in $H_3PO_3$ @ > 150 °C |

Pulsed Laser Deposition (PLD) is a physical vapor deposition technique used for thin and thick film growth. Pulsed Laser Deposition system consists of a laser source, optics, computer and chamber. Growth environment is isolated in a vacuum chamber cleaned by a turbo molecular pump. After the pulsed laser beam lefts the laser source, beam redirected to the chamber and focused on the target material by a lens. When focused beam pulse hits the target,

huge energy transferred to the target. This energy results a plasma plume with the help of a background gas, which deposits the substrate. Target materials stoichiometry can be preserved during the depositions. Annealing can be made in-situ without contaminating the samples. Pulsed Laser Deposition technique has lots of variables like; spot size, laser density, deposition temperature, temperature change rates, base pressure, deposition pressure, deposition gas type, pulse number, pulse frequency, rotation speeds, target-substrate distance, etc. [4]. Spot size and laser energy is used to calculate laser fluence on the target and base pressure ensures the absence of contaminating atoms in the thin film.

In this study, Pulse Laser Deposition technique is used in order to prepare $CeO_2$ thin films deposited onto $LaAlO_3$ substrates at different temperatures from room temperature to 800°C. Surface morphology and the crystallinity of the prepared thin films were determined by using Grazing Incidence X-Ray Diffraction (GIXRD) and Scanning Electron Microscope (SEM) techniques.

## II. EXPERIMENTAL DETAILS

High purity $CeO_2$ powder used for pellet preparation. $CeO_2$ powder pressed into a die set and then sintered at 1150 °C for 2 hours in air [5] in order to use it as a target material.

LAO(100) substrates bought as 3" wafer and sliced as substrates by a diamond saw. All the sliced $LaAlO_3$ substrates cleaned with acetone and methanol in an ultrasonic cleaner prior to the deposition. Silver paste used to paste $LaAlO_3$ substrates to the substrate holder and a halogen lamp used for drying.

Pulsed Laser Deposition variables except for temperature were fixed for all depositions. Chamber was evacuated to 9x10⁻⁶ Torr before heating procedure. Target to substrate distance was set to 5 cm by changing the rod sizes. Deposition pressure was chosen as 150 mTorr. High purity $O_2$ gas used for depositions. Target rotated at constant velocity to avoid shooting the same spot. All the samples heated to their set point by 20 °C/min and cooled down to room temperature by 10 °C/min ramp rate until natural cooling took over. Total number of pulses was 10000 and laser fluence calculated as ~ 3 J/cm².

Deposition temperature was the only variable for all depositions. Samples deposited from room temperature to 800 °C by 200 °C steps and all the samples annealed after the depositions.

## III. RESULTS

Thin film thicknesses are very small compared to the substrate thickness. In order to eliminate peaks coming from

substrate, Grazing Incidence X-Ray Diffraction (GIXRD) method was used to analyze peaks of the deposited thin films. Samples prepared at room temperature, 400 °C and 800 °C were oxygen deficient. Sample prepared at 600 °C had some corresponding $CeO_2$ peaks with a significantly high oxygen deficient peak. The best result was obtained for the sample prepared at 200 °C with all orientations of $CeO_2$.

Surface morphology checked with Scanning Electron Microscope (SEM) for cracks. Fig. 1 shows the sample which only had the cracks prepared at 800 °C. Cracks were parallel and very large. These cracks believed to be formed by thermal expansion coefficient differences of the LAO substrate and $CeO_2$ coating during the high temperature deposition.
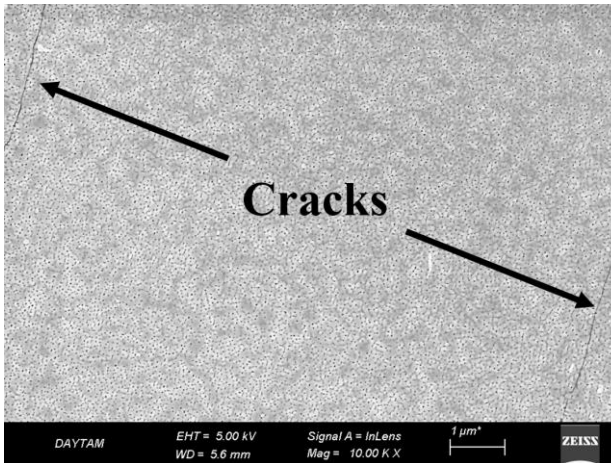


Fig 1.Surface of the cracked 800 °C sample.

These results show that ceria thin films can be deposited on $LaAlO_3$ substrates at various temperatures. Oxygen deficiency in ceria films is the main problem to overcome. Deposition at high temperature results cracking of the thin film. In order to avoid cracking at high temperatures, cooling rate must be lowered than 10 °C/min.

## REFERENCES

[1] I. Iordanova *et al.*, "X-ray investigation of annealed CeO2 films prepared by sputtering on Si substrates," *Thin Solid Films,* vol. 515, no. 20, pp. 8078-8081, 2007/07/31/ 2007.

[2] X. D. Wu *et al.*, "Epitaxial CeO2 films as buffer layers for high-temperature superconducting thin films," *Applied Physics Letters,* vol. 58, no. 19, pp. 2165-2167, 1991/05/13 1991.

[3] MTI. (2002, 15.05.2011). *LaAlO₃ Single Crystal*. Available: http://www.mtixtl.com/xtlflyers/LaAlO3.doc

[4] D. B. Chrisey and G. K. Hubler, G. H. DB Chrisey, Ed. *Pulsed Laser Deposition of Thin Films*. New York: Wiley-Interscience, 1994, p. 613.

[5] S. Nakane, T. Tachi, M. Yoshinaka, K. Hirota, and O. Yamaguchi, "Characterization and sintering of reactive cerium(IV) oxide powders prepared by the hydrazine method," (in English), *Journal of the American Ceramic Society,* vol. 80, no. 12, pp. 3221-3224, Dec 1997.

# PID Type Sliding Mode Controller Design for an Autonomous Electric Wheelchair

Ahmet Dumlu
Department of Electrical & Electronics
Engineering
Erzurum Technical University
Erzurum, Turkey
ahmetdumlu@erzurum.edu.tr

Kağan Koray Ayten
Department of Electrical & Electronics
Engineering
Erzurum Technical University
Erzurum, Turkey
kagan.koray@erzurum.edu.tr

*Abstract*— In this study, all mathematical modelling of an autonomous electric wheelchair (AEWC) has been made and then the real time trajectory tracking control of the AEWC has been performed by using the PID type sliding mode control method. For the mathematical modelling, the kinematic and dynamic analysis of the designed AEWC has been made by using the Cartesian space approach and Lagrangian method considering all its kinematic constraints, respectively. After the mathematical modelling required for the controller design, the AEWC's trajectory tracking control has been performed using the PID type sliding mode control method, which takes into account the system dynamic model. According to the results obtained from the experiments, the mathematical modelling made for the system proved to be correct and especially the trajectory tracking control of the system has become more robust by using the PID type sliding mode control method.

*Keywords*— *Autonomous guided vehicle, PID control, Sliding mode control, Trajectory control*

## I. INTRODUCTION

Autonomous electric wheelchairs (AEWC) are tools which are developed for people with disabilities who cannot use the manual wheelchair. There are usually two direct current motors used to drive the rear right and left wheels in AEWC. These DC motors are connected to the wheels by means of a gear system or belt pulley mechanism. Depending on the commands of people with disabilities, the orientation of the vehicle is carried out by the angular velocity variations of the direct current motors operating independently of each other. The speed and direction information requested by the disabled driver is sent to the vehicle control unit by means of a joystick, and then the voltage or current of the motors are adjusted according to the desired speed and direction by the motor drives. For example, when it is desired to move the chair in a certain direction, it is ensured that the two drives rotate at the same speed by applying the same voltage to the two driven motors. When it is desired to carry out any guidance for the vehicle, it is necessary to increase the rotation speed of a motor, depending on the other, in relation to the other. In the literature, many researchers have developed different types of closed-loop control algorithms for the trajectory tracking control of AEWC. Fuzzy control algorithm and neural network based diagonal decoupling control have been used for electric power-assisted wheelchair in [1]-[2]. In these studies, they have been shown that the designed speed controllers make the wheelchair suitable for use in various road conditions. Saadatzi *et al.* used the genetic algorithm method for trajectory control of the electric wheelchair, Chai *et al.* benefited from the optimized PID control method with artificial neural networks [3]-[4].

However, none of these studies have considered system dynamics and there has been a considerable delay in system responses due to the high processing load of control algorithms. For the adaptive control technique, model reference adaptive control and adaptable optimal controller have been performed to their designed robotic wheelchair [5]-[6]. In addition to these, different types of robust sliding mode multivariable control strategies have been used for controlling to wheelchair [7-10].

In this study, the design, analysis and real-time trajectory tracking control of an AEWC have been performed. First, all the kinematic equations of the system have been obtained for the position analysis of the designed system. Thus, the angular velocity variables of the vehicle wheels can be determined, so that the system can perform this target trajectory when a specific target trajectory for giving the designed AEWC. Secondly, the fully dynamic model of the system has been made by using the Lagrangian technique. In order to increase the trajectory tracking performance of the designed AEWC, PID type model-based sliding control method is used by taking into account the full dynamic model of the system. The PID type model-based sliding control technique is used to control the complex systems in particular and this proposed technique minimizes the position and speed errors for certain predefined trajectories. According to the results obtained from the experiments, the mathematical modelling made for the system proved to be correct and especially the trajectory tracking control of the system has become more robust by using the PID type sliding mode control method over the classical PID control.

## II. MATERIALS AND METHODS

In Fig. 1, the details of designed AEWC are shown. The system consists of two rear driving wheels and two freely moving wheels on the front. The driving wheels on the rear are connected to the DC motors using a gear system. The rear output shaft of each DC motor has an optical position sensor. For the power requirement of the system, two 24 Volt batteries are used. There is also a control card and a computer that can work with MATLAB program for real-time control of the designed system.

Fig.1. Electric power-assisted wheelchair.

*Y. Kinematic analysis of electric wheelchair*

For the designed AEWC system, inverse kinematic analysis refers to the use of the mathematical equations of the system to determine the angular velocity of the right and the left wheels that provided the desired trajectory of the AEWC system. In Fig.2, schematic top view of the designed AEWC system is shown. The orientation and motion of the system are actualized by independent by two DC motors. As shown in Fig. 2, global coordinate system $\{X_I, Y_I\}$ and local coordinate system $\{X_r, Y_r\}$ are defined for the robotic system. The origins of the global and local coordinate systems are represented by points $O$ and $P_o$, the distance between the two wheels and diameter of the wheels is equal to $2L$ and $2R$ and also the angular velocities of the left and right wheel are given by $\dot{\theta}_l$ and $\dot{\theta}_r$, respectively.

Using the orthogonal rotation matrix, the position of any point in the platform can be defined as follows;

$$X^I = R(\phi)X^r \tag{1}$$

$$R(\phi) = \begin{bmatrix} cos(\phi) & -sin(\phi) & 0 \\ sin(\phi) & cos(\phi) & 0 \\ 0 & 0 & 1 \end{bmatrix} \tag{2}$$
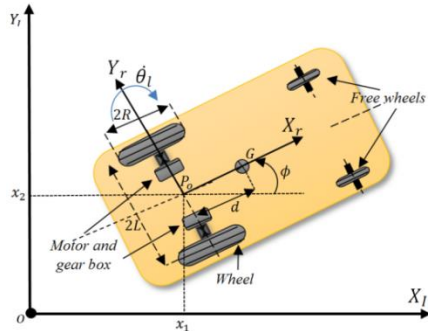


Fig.2. Schematic top view of the designed AEWC system.

On the conditions of no lateral slip motion, using the linear velocities of the right and left wheels, the body and the angular velocities of the mobile robot are expressed by Eq. 3 and Eq. 4.

$$v = \frac{v_r + v_l}{2} = R\frac{(\dot{\theta}_r + \dot{\theta}_l)}{2} \tag{3}$$

$$\dot{\phi} = \frac{v_r - v_l}{2L} = R\frac{(\dot{\theta}_r - \dot{\theta}_l)}{2} \tag{4}$$

Hence, electric wheelchair robot velocities can be defined as follows;

$$\begin{bmatrix} \dot{x}_1 \\ \dot{x}_2 \\ \dot{\phi} \end{bmatrix} = \begin{bmatrix} \frac{R}{2}cos(\phi) & \frac{R}{2}cos(\phi) \\ \frac{R}{2}sin(\phi) & \frac{R}{2}sin(\phi) \\ \frac{R}{2L} & -\frac{R}{2L} \end{bmatrix} \begin{bmatrix} \dot{\theta}_r \\ \dot{\theta}_l \end{bmatrix} \tag{5}$$

*Z. Constraint Equations of Mobile Robot*

The mobile robot is classified as non-holonomic systems. Therefore, it has two main constraint equations. First one is that, mobile robot cannot move in a lateral direction. The mathematical description of this constraint is expressed in Eq. 6.

$$\dot{x}_2 cos(\phi) - \dot{x}_1 sin(\phi) = 0 \tag{6}$$

where, $x_1$ and $x_2$ are defined as two redundant coordinates. The second one is that, two driving wheels pure rolling constraint. This means that each wheel maintains a one contact point $P$ with the ground as shown in Fig. 3. The mathematical description of this constraint is expressed in Eq. 7 and Eq. 8.

$$\dot{x}_1 cos(\phi) + \dot{x}_2 sin(\phi) + L\dot{\phi} = R\dot{\theta}_r \tag{7}$$

$$\dot{x}_1 cos(\phi) + \dot{x}_2 sin(\phi) - L\dot{\phi} = R\dot{\theta}_l \tag{8}$$

On the other hand, the mobile robot has a one holonomic constraint equation and to obtain it, first of all we subtract Equation (7) from Equation (8) and then integrating with choosing the initial condition;

$$2L\dot{\phi} = R(\dot{\theta}_r - \dot{\theta}_l) \tag{9}$$

$$\phi = c(\theta_r - \theta_l) \tag{10}$$

where $c$ is equal to $R/2L$. For the obtain second non-holonomic constraint equations now we add the Equation (7) and Equation (8);

$$\dot{x}_1 cos(\phi) + \dot{x}_2 sin(\phi) = cL(\dot{\theta}_r + \dot{\theta}_l) \tag{11}$$

Hence we may write two non-holonomic constraint equations in matrix form;

$$A(q)\dot{q} = 0 \tag{12}$$

where;

$$q = \begin{bmatrix} q_1 \\ q_2 \\ q_3 \\ q_4 \end{bmatrix} = \begin{bmatrix} x_1 \\ x_2 \\ \theta_r \\ \theta_l \end{bmatrix}, A(q)$$

$$= \begin{bmatrix} a_{11} & a_{12} & a_{13} & a_{14} \\ a_{21} & a_{22} & a_{23} & a_{24} \end{bmatrix}$$

$$= \begin{bmatrix} -sin(\phi) & cos(\phi) & 0 & 0 \\ -cos(\phi) & -sin(\phi) & cL & cL \end{bmatrix} \tag{13}$$
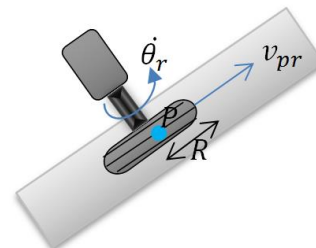
Fig 3. Pure rolling motion constraint.

*AA. Dynamic Modelling of the Mobile robot*

The dynamic model of the system has been derived using Lagrangian approach. The Lagrange's equations have been employed by using the generalized coordinates as $q = [x_1, x_2, \theta_r, \theta_l]^T$. For the robotic system, the Lagrangian equations can be written as given in Eq. 14.

$$\frac{d}{dt}\left(\frac{\partial L}{\partial \dot{q}_i}\right) - \frac{\partial L}{\partial q_i} = Q_i - a_{1i}\lambda_1 - a_{2i}\lambda_2 \quad for \ i = 1 \ to \ 4 \tag{14}$$

where $Q_i$ represents the external force, $\lambda_1$ and $\lambda_2$ are the multipliers and $L$ is the Lagrangian function.

The kinetic energy of the platform can be denoted as follows;

$$\begin{aligned} K = &\frac{1}{2}(m_c + 2m_w)\left(\dot{x}_1^2 + \dot{x}_2^2\right) \\ &+ m_c cL(\dot{\theta}_r - \dot{\theta}_l)(\dot{x}_2 \cos(\phi) \\ &- \dot{x}_1 \sin(\phi)) \\ &+ \frac{1}{2}I_w\left(\dot{\theta}_r^2 + \dot{\theta}_l^2\right) + \frac{1}{2}(I_c \\ &+ 2m_w L^2 \\ &+ 2I_m)c^2(\dot{\theta}_r - \dot{\theta}_l)^2 \end{aligned} \tag{15}$$

where, $m_c$ is the mass of the mobile robot without the driving wheels and actuators (DC motors), $m_w$ is the mass of each driving wheel (with actuator), $I_c$ is the moment of inertia of the mobile robot about the vertical axis through the centre of mass, $I_w$ is the moment of inertia of each driving wheel with a motor about the wheel axis, and $I_m$ is the moment of inertia of each driving wheel with a motor about the wheel diameter. Using equation 15 along with the Lagrangian function, L = K the equations of motion of the mobile robot are given by;

$$(m_c + 2m_w)\ddot{x}_1 - m_c d\left(\ddot{\phi}\sin\phi + \dot{\phi}^2\cos\phi\right) = \lambda_1 \sin\phi + \lambda_2 \cos\phi \tag{16}$$

$$(m_c + 2m_w)\ddot{x}_2 + m_c d\left(\ddot{\phi}\cos\phi - \dot{\phi}^2\sin\phi\right) = -\lambda_1 \cos\phi + \lambda_2 \sin\phi \tag{17}$$

$$\begin{aligned} m_c cd(\ddot{x}_2\cos\phi &- \ddot{x}_1\sin\phi) \\ &+ \left((I_c + 2m_w L^2 + 2I_m)c^2 \\ &+ I_w\right)\ddot{\theta}_r \\ &- (I_c + 2m_w L^2 + 2I_m)c^2\ddot{\theta}_l \\ &= \tau_1 - cL\lambda_2 \end{aligned} \tag{18}$$

$$\begin{aligned} -m_c cd(\ddot{x}_2\cos\phi &- \ddot{x}_1\sin\phi) \\ &- (I_c + 2m_w L^2 + 2I_m)c^2\ddot{\theta}_r \\ &- (I_c + 2m_w L^2 + 2I_m)c^2\ddot{\theta}_l \\ &= \tau_2 - cL\lambda_2 \end{aligned} \tag{19}$$

Hence the actuator torques acting on the two wheels of mobile robot can be determined in the standard form as;

$$M(q)\ddot{q} + C(q,\dot{q})q = E(q)\tau - A^T(q)\lambda \tag{20}$$

Equation (20) can be rewritten as in the standard form;

$$\tau = M(q)\ddot{q} + N(q,\dot{q}) + \tau_d \tag{21}$$

where, $M(q)$ is the mass matrix, $N(q,\dot{q})$ is the sum of the centrifugal, Coriolis and gravity terms, $\tau_d$ is disturbance and friction component of directly related to mobile robot system using a complete dynamic model of systems, respectively. On the other hand equation (21) shows that the mobile robot dynamics are expressed as a function of the right and left wheel angular velocities $\dot{\theta} = [\dot{\theta}_r \quad \dot{\theta}_l]$, and the driving motor torques $\tau = [\tau_r \quad \tau_l]^T$. As it is seen from equation 21, the desired tracking control of the mobile robot can be achieved by changing or controlling the supply voltage of the DC motors.

If the both sides of Eq. 24 is multiplied by $M(q)^{-1}$, $\ddot{q}$ can be defined as follows;

$$\begin{aligned} \ddot{q}_{2x1} = f(q)_{2x1} &+ g(q)_{2x1}u(t)_{2x1} \\ &+ \zeta(t,u(t))_{2x1} \end{aligned} \tag{22}$$

where, $f(q)_{2x1} = -M(q)^{-1}H(q,\dot{q})$, $g(q)_{2x1} = M(q)^{-1}$, $u(t)_{2x1} = \tau$ and $\zeta(t,u(t))_{2x1}$ stands the bounded uncertainties of the system. The aim of the proposed control technique in this study is to control the system variables, $q_{2x1}$, accurately for the given reference trajectory, $q_{d_{2x1}}$. In order to meet the accurate trajectory tracking, the tracking error $e(t)_{2x1} = q_{d_{2x1}} - q_{2x1}$ should be minimized as much as possible.

## III. PID TYPE SLIDING MODE CONTROL

In this study, the PID-type sliding surface is performed to increase the performance and robustness of the mobile robot. The PID-type sliding surface function is selected as follows.

$$\dot{s}(t)_{2x1} + \beta_{2x1}s(t) = k_{p_{2x2}}e(t)_{2x1} + k_{i_{2x2}}\int e(\tau)_{2x1}d\tau + k_{d_{2x2}}\dot{e}(t)_{2x1} \tag{23}$$

where, $k_{p_{2x2}}$, $k_{d_{2x2}}$ and $k_{i_{2x2}}$ are control gain matrix and $\beta_{2x1}$ is constant matrix. Differentiating Eq. (23), the following equation can be obtained.

$$\ddot{s}(t)_{2x1} + \beta_{2x1}\dot{s}(t)_{2x1} = k_{p_{2x2}}\dot{e}(t)_{2x1} + k_{i_{2x2}}e(t)_{2x1} + k_{d_{2x2}}\ddot{e}(t)_{2x1} \tag{24}$$

Using the derivative of the error function, Eq. (24) can be re-written as follows;

$$\begin{aligned} \ddot{s}(t)_{2x1} + \beta_{2x1}\dot{s}(t)_{2x1} = k_{p_{2x2}}\dot{e}(t)_{2x1} &+ k_{i_{2x2}}e(t)_{2x1} + \\ k_{d_{2x2}}\{\ddot{x}_d(t)_{2x1} &- \ddot{x}(t)_{2x1}\} \end{aligned} \tag{25}$$

Substituting $\ddot{x}(t)_{2x1}$ from Eq. (22) into Eq. (25) yields;

$$\begin{aligned} \ddot{s}(t)_{2x1} + \beta_{2x1}\dot{s}(t)_{2x1} = k_{p_{2x2}}\dot{e}(t)_{2x1} &+ k_{i_{2x2}}e(t)_{2x1} + \\ k_{d_{2x2}}\{\ddot{x}_d(t) - f(x)_{2x1} &- g(x)_{2x1}u(t)_{2x1} - \zeta(t,u(t))_{2x1}\} \end{aligned} \tag{26}$$

In the PID type second order sliding surface condition, if $s(t)_{2x1}$, $\dot{s}(t)_{2x1}$ and $\ddot{s}(t)_{2x1}$ are equal to null then the tracking error $e(t)_{2x1}$ reaches to zero. Hence, the reaching

phase control law, $u_{rp_{2x1}}$, can be obtained by using the $\ddot{s}(t)_{2x1} = 0$ as follows;

$$u_{rp_{2x1}} = [k_{d_{2x2}}g(x)_{2x1}]^{-1}\{k_{p_{2x2}}\dot{e}(t)_{2x1} + k_{i_{2x2}}e(t)_{2x1} + k_{d_{2x2}}(\ddot{x}_d(t) - f(x)_{2x1} - \zeta(t,u(t))_{2x1}) - \beta_{2x1}\dot{s}(t)_{2x1}\} \quad (27)$$

In addition to this, a switching control law, $u_{sc_{2x1}}$, in Equation (28), should be added to the phase control law to ensure the robustness of the system against the external or system disturbances.

$$u_{sc_{2x1}} = g(x)_{2x1}^{-1}\{\lambda_{2x2}s(t)_{2x1} + \mu_{2x2}sign(\dot{s}(t)_{2x1})\} \quad (28)$$

where, $\lambda_{2x2}$ and $\mu_{2x2}$, are the switching gains. Thus, the total feed-back control law, ($u_{fd_{2x1}}$), for the system without uncertainties is written as follows;

$$u_{fd_{2x1}} = [k_{d_{2x2}}g(x)_{2x1}]^{-1}\{k_{p_{2x2}}\dot{e}(t)_{2x1} + k_{i_{2x2}}e(t)_{2x1} + k_{d_{2x2}}(\ddot{x}_d(t) - f(x)_{2x1} - \zeta(t,u(t))_{2x1}) - \beta_{2x1}\dot{s}(t)_{2x1}\} + g(x)_{2x1}^{-1}\{\lambda_{2x2}s(t)_{2x1} + \mu_{2x2}sign(\dot{s}(t)_{2x1})\} \quad (32)$$

## IV. EXPERIMENTAL RESULTS

In order to demonstrate the efficiency of the proposed PID type sliding mode control over a conventional PID controller, an eight shaped trajectory for the designed AEWC has been used in this study. Using the kinematic equations of the AEWC obtained in Section II, the angular velocity variations of AEWC's right and left wheels required to perform defined eight shaped trajectory, and also performance of the controllers have been shown in Figs. 4 and 5. Angular velocity error values of the right and left wheels that occur during AEWC trajectory tracking have been shown in Figs 6 and 7.
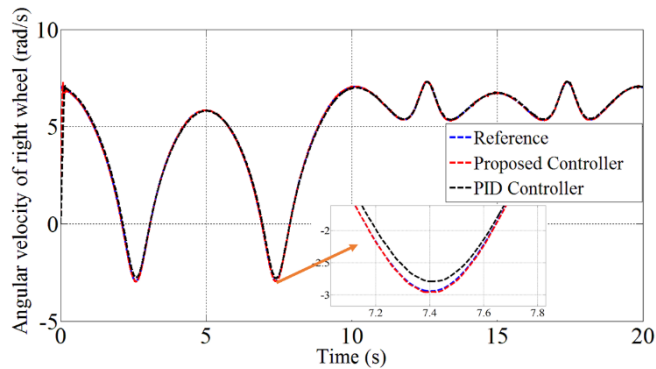


Fig. 7. Angular velocity of the right wheel for defined trajectory.
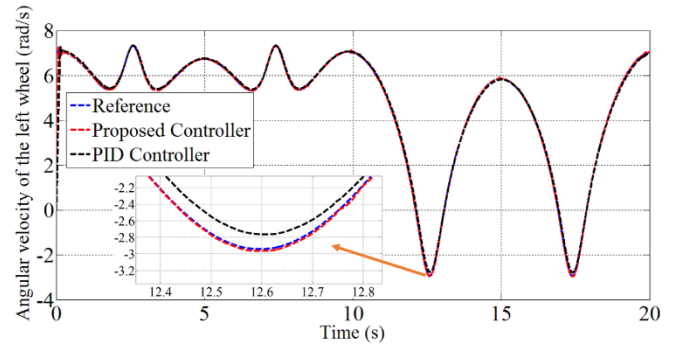


Fig 4. Angular velocity of the left wheel for defined trajectory.
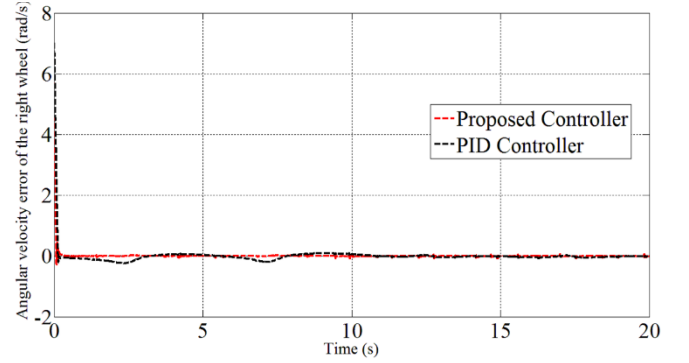


Fig 5.The angular velocity error of the right wheel for defined tranjectory.
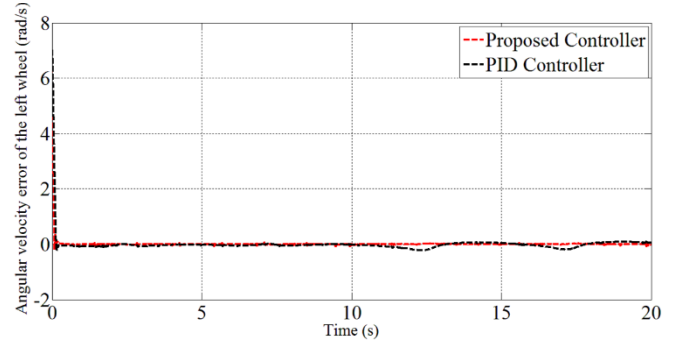


Fig 6. Angular velocity error of the left wheel for defined tranjectory.

When the graphical results are compared, it is seen that the proposed PID type sliding mode controller performs much better than the PID controller. It is seen that, an AEWC can follow the defined trajectory with high deviation errors if used with well-tuned PID controller for trajectory control. Although the gain parameters of the PID controller are chosen to be the most appropriate value, angular velocity errors occurring on the right and left wheels cause the AEWC to deviate from the defined trajectory.

It is seen that if the PID type sliding mode control is used instead of the conventional PID control method for trajectory control, the trajectory control performance of the system is increased. The main reason why the proposed method performs better than PID control is that it uses the system's fully dynamic model and takes into account the non-linear expressions that exist in the system.

## V. CONCLUSION

In this study, all mathematical analysis of an AEWC with 3 (three) degrees of freedom has been made and its trajectory tracking control has been performed using

proposed PID type sliding mode controller. Firstly, the electromechanical structure of the designed AEWC has been introduced and then the kinematic and dynamic modelling of the system has been obtained. According to the results obtained from the real-time trajectory tracking control experiments, the PID type sliding mode controller based on the system model had provided better trajectory tracking performance than the conventional PID controller. However, it is seen that a complete and accurate dynamic model of the system is used and especially if this model is used in PID type sliding mode control method, the system improves the trajectory control performance.

Acknowledgment

REFERENCES

[1] H. Seki and N. Tanohata, "Fuzzy Control for Electric Power-Assisted Wheelchair Driving on Disturbance Roads," in *IEEE Transactions on Systems, Man, and Cybernetics, Part C (Applications and Reviews)*, vol. 42, no. 6, pp. 1624-1632, Nov. 2012.

[2] T. N. Nguyen, S. Su and H. T. Nguyen, "Neural Network Based Diagonal Decoupling Control of Powered Wheelchair Systems," in *IEEE Transactions on Neural Systems and Rehabilitation Engineering*, vol. 22, no. 2, pp. 371-378, March 2014.

[3] M. N. Saadatzi, J. Poshtan and M. H. Saadatzi, "Optimal multivariable two-degree-of-freedom control of electric wheelchair using non-dominated sorting genetic algorithm-II," *2011 IEEE International Conference on Control Applications (CCA)*, Denver, CO, 2011, pp. 376-381.

[4] R. Chai, S. H. Ling, G. P. Hunter, Y. Tran and H. T. Nguyen, "Brain–Computer Interface Classifier for Wheelchair Commands Using Neural Network With Fuzzy Particle Swarm Optimization," in *IEEE Journal of Biomedical and Health Informatics*, vol. 18, no. 5, pp. 1614-1624, Sept. 2014.

[5] R. A. Cooper, T. L. Fletcher-Shaw and R. N. Robertson, "Model reference adaptive control of heart rate during wheelchair ergometry," in *IEEE Transactions on Control Systems Technology*, vol. 6, no. 4, pp. 507-514, July 1998.

[6] K. E. Brown, R. M. Inigo and B. W. Johnson, "Design, implementation, and testing of an adaptable optimal controller for an electric wheelchair," in *IEEE Transactions on Industry Applications*, vol. 26, no. 6, pp. 1144-1157, Nov.-Dec. 1990.

[7] T. N. Nguyen, S. W. Su and H. T. Nguyen, "Robust Neuro-Sliding Mode Multivariable Control Strategy for Powered Wheelchairs," in *IEEE Transactions on Neural Systems and Rehabilitation Engineering*, vol. 19, no. 1, pp. 105-111, Feb. 2011.

[8] A. Filipescu, R. Solea, A. Filipescu, G. Stamatescu and G. Ciubucciu, "Trajectory-Tracking Sliding-Mode Control of the Autonomous Wheelchair Modeled as a Nonholonomic WMR," *2018 IEEE 14th International Conference on Control and Automation (ICCA)*, Anchorage, AK, 2018, pp. 1168-1173.

[9] S. Amagai and T. Murakami, "An approach to robust velocity control of two-wheel wheelchair," *IECON 2016 - 42nd Annual Conference of the IEEE Industrial Electronics Society*, Florence, 2016, pp. 494-499.

[10] B. Yang and L. Xi, "Development of an Omni-Directional Wheelchair Robot," *2018 International Conference on Engineering Simulation and Intelligent Control (ESAIC)*, Hunan, China, 2018, pp. 126-130.

# The Effect of Spray Characteristics on Drop Diameters and SMD Correlations

Faruk Yeşildal
Ağrı İbrahim Çeçen University Patnos
Sultan Alparslan Natural Sciences and
Engineering Faculty Mechanical
Engineering
Ağrı, TURKEY
fayesildal@agri.edu.tr

Kenan Yakut
Ataturk University Engineering Faculty
Mechanical Engineering
Erzurum, TURKEY
kyakut@atauni.edu.tr

Altuğ Karabey
Van Yüzüncüyıl University
Engineering Faculty Mechanical
Engineering
Van, TURKEY
akarabey@yyu.edu.tr

Ahmet Numan Özakin
Ataturk University Engineering Faculty
Mechanical Engineering
Erzurum, TURKEY
ahmet.ozakin@atauni.edu.tr

***Abstract***: *Spray cooling depends on many parameters in different geometry and operating conditions. The material of the cooled sample and the heat sink design are the important factors. In addition, the type of nozzle and the method of atomization are the determining factors of the cooling. However, the spray structure and homogeneity better defines the cooling facility. Therefore, it is necessary to know the spray average drop diameters. Studies to determine spray flow characteristics are quite complex. For this reason, it is necessary to perform laser measurement which allows a detailed analysis of the spray flow structure. In some situations, an adequate solution to calculate SMD, which best characterizes heat and mass transfer on spray cooling, with correlations in the literature is not possible. It is useful to find the average drop diameter or SMD rather than finding the entire drop diameter distribution. The drop size is important in understanding the cooling effectiveness. In this study, SMD correlations were compiled in accordance with the different operational conditions.*

***Keywords:*** *Spray cooling, Characteristic diameters, SMD correlations*

## I. INTRODUCTION

In most applications, the function of the atomizer is not only the separation of liquid into small drops, but also the symmetrical or uniform distribution to the environment. The droplet diameter distribution depends on the cone angle, average drop diameter and physical properties. For example, droplets are more uniform in twin-fluid atomizers. Spray geometry depends on the properties of both fluids.

The modeling of the spray system is related to the find out of the droplet diameter distribution after splitting the liquid jet. The parameters such as nozzle diameter, droplet velocity, drop temperature, working fluid used in spray cooling, droplet diameter, heat flux and their interaction should be examined in detail.

### BB. Spray Spesifications

First of all, the spray characteristics are affected by liquid properties and atomizer conditions. In addition, the following spray properties must be known for a detailed examination.

a. Spray Distribution:

The advantage of a good spray dispersion is its homogeneity, as well as its evaporation rate and whether the spray is suitable for its location.

b. Penetration:

Penetration defines the maximum distance that the spray can reach. This depends on the aerodynamic air resistance and the kinetic energy of the jet. For example, the narrower (acute) and dense spray has a higher penetration. The wide-angle and fine spray is exposed to more air resistance and has less penetration. Penetration is especially important in diesel sprays. Many researchers have investigated on the penetration of diesel engines. They obtained correlations related to penetration according to whether the injection time is less or more than jet breakup. The correlation of Sitkei for diesel jet is as follows [1]:

$$S = 0.2d_0 \left(\frac{U_L t}{d_0}\right)^{0.48} \left(\frac{U_L d_0}{\nu_L}\right)^{0.3} \left(\frac{\rho_L}{\rho_A}\right)^{0.35} \quad (1)$$

In addition, many spray properties such as cone angle, patternation, radial fluid distribution, equivalent spray angle, ambient fluid distribution and evaporation should be examined.

### CC. Types of atomizers and droplet diameter correlations

a. Plain Orifice Atomizers:
Breakup of the jet in the plain orifice nozzles is achieved by an increase in the flow rate. This increases both the turbulence in the jet and the aerodynamic drag force exerted by the ambient air. A rough correlation is given below widely used for flat orifice nozzles [2].

$$SMD = \frac{500 d_0^{1.2} \nu_L^{0.2}}{U_L} \quad (2)$$

Many researchers have applied plain orifice atomizers on diesel engines. Some studies conducted in the early years yielded favorable correlations. Panasenkov [3], examined the effect of turbulence in jet breakup. It correlated the mean drop diameter (MMD) in the range of 1000 <Re <12000.

$$MMD = 6d_0 Re_L^{-0.15} \quad (3)$$

Harmon [4] also obtained another correlation with the ambient air effects.

$$SMD = 3330 d_0^{0.3} \mu_L^{0.07} \rho_L^{-0.648} \sigma^{-0.15} U_L^{-0.55} \mu_G^{0.78} \rho_G^{-0.052} \quad (4)$$

An unusual feature of this equation is that an increase in surface tension is expected to yield finer atomization. The

important correlations developed for plain orifice nozzles are given below.

Table 1. Droplet diameter correlations in plain orifice atomizers

| Correlation | Author |
|---|---|
| $SMD = \dfrac{500 d_0^{1.2} \nu_L^{0.2}}{U_L}$ | [2] |
| $MMD = 6 d_0 Re_L^{-0.15}$ | [3] |
| $SMD = 3330 d_0^{0.3} \mu_L^{0.07} \rho_L^{-0.648} \sigma^{-0.15} U_L^{-0.55} \mu_G^{0.78} \rho_G^{-0.052}$ | [4] |
| $SMD = 47 d_0 U_L^{-1} (\dfrac{\sigma}{\rho G})^{0.25} [1 + 331 \dfrac{\mu_L}{(\rho_L \sigma d_0)^{0.5}}]$ | [5] |
| $SMD = 2330 \rho_A^{0.121} Q^{0.131} \Delta P^{-0.135}$ | [6] |
| $SMD = 3.08 \nu_L^{0.385} (\sigma \rho L)^{0.737} \rho_A^{0.06} \Delta P_L^{-0.54}$ | [7] |

It is also an advantageous type of atomizer in cross flow. When a plain orifice is exposed to the atomizer air flow, larger drops enter the air stream. This disadvantageous behavior of the spray is advantageous, for example, by positioning the igniter in the region of small drops in a turbojet combustion chamber.

b. Pressure-Swirl Atomizers:

Due to its wide application, pressure-swirl atomizers are widely used. Besides, the physics of the event is not still well understood. The researchers obtained correlations with a low validity to understand the relationship between fluid properties, nozzle diameter and mean drop diameter. There are many factors affecting the mean drop diameter. These; fluid properties, surface tension, viscosity, flow rate, flow coefficient, Nozzle pressure difference, air characteristics, nozzle dimensions and swirl chamber length / diameter ratio (L / D). Table 2 presents the SMD correlations for pressure-swirl atomizers.

Table 2. Droplet Diameter Correlations in Pressure-Swirl Atomizers

| Correlation | Author | Description |
|---|---|---|
| $SMD = 7.3 \sigma^{0.6} \nu_L^{0.2} \dot{m}_L^{0.25} \Delta P_L^{-0.4}$ | [8] | Nozzle dimensions and air characteristics have no effect. |
| $SMD = 4.4 \sigma^{0.6} \nu_L^{0.16} \dot{m}_L^{0.22} \Delta P_L^{-0.43}$ | [9] | Nozzle dimensions and air characteristics have no effect. |
| $SMD = 133 \dfrac{FN^{0.64291}}{\Delta P_L^{0.22565} \rho_L^{0.3215}}$ | [10] | $\Delta P_L < 2.8\ MPa$ |
| $SMD = 607 \dfrac{FN^{0.75344}}{\Delta P_L^{0.19936} \rho_L^{0.3767}}$ | [10] | $\Delta P_L > 2.8\ MPa$ |
| $SMD = 2.25 \sigma^{2.25} \mu_L^{0.25} \dot{m}_L^{0.25} \Delta P_L^{-0.5} \rho_A^{-0.25}$ | [11] | |

The flow number can be calculated as follows

$$FN = \frac{\dot{m}_L}{(\Delta P_L \rho_L)^{0.5}} \quad (5)$$

Furthermore, the SMD correlation obtained in a wide flow number range using 6 different nozzles in 25 different fuels in internal combustion engines is below [13].

$$SMD = 10^{-3} \sigma_L (6.11 + 0.32 x 10^5 FN \sqrt{\rho_L} - 6.973 x 10^{-3} \sqrt{\Delta P_L} + 1.89 x 10^{-6} \Delta P_L) \quad (6)$$

In this correlation the droplet diameter is strongly dependent on the surface tension. However, the effect of viscosity is not observed.

c. Rotary Atomizers:

In these atomizers, the mean drop diameter is expected to decrease as the rotation speed increases and to increase with liquid flow and viscosity. Matsumoto et al. [14] showed that the dimensionless drop diameter strongly depends on the number of We in the correlation obtained. This correlation for direct drop formation is given as follows.

$$\frac{SMD}{d} = 1.6 We^{-0.523} \quad (7)$$

Here, We number is calculated as $= \frac{\rho_L d^3 \omega^2}{8\sigma}$ ;

They [12] developed the following correlation for the case where atomization occurred with the formation of ligaments around the outer periphery of the rotating disk.

They developed this correlation when atomization occurred with the formation of ligaments around the outer periphery of the rotating disk:

$$SMD = \frac{0.177 Q^{0.2}}{N d^{0.3}} \quad (8)$$

In another correlation, a relationship was given between the ligament diameter and the mean drop diameter. [13].

$$\frac{SMD}{d_l} = (1.5\pi)^{\frac{1}{3}} (1 + 3 \frac{We}{Re^2})^{1/6} \quad (9)$$

In another study, the researchers developed the following correlation with a wide range of use, including disc diameter, rotational speed, flow and fluid characteristics for mean drop diameter correlation [14].

$$SMD = 0.119 \frac{Q^{0.1} \sigma^{0.5}}{N d^{0.5} \rho_L^{0.4} \mu_L^{0.1}} \quad (10)$$

An interesting feature of this equation is that it shows that drop sizes will increase slightly with a decrease in liquid viscosity. As is known, the reduction in fluid viscosity results in a finer drop size.

A more consistent correlation with a wide range of uses has been developed as follows [15].

$$SMD = 0.26 N^{-0.79} Q^{0.32} d^{-0.69} \rho_L^{-0.29} \sigma^{0.26} (1 + 1.027 \mu_L^{0.65}) \quad (11)$$

If the atomization takes place in the form of layer breakdown, the following correlation will be appropriate [14].

$$SMD = 15.6 \frac{Q^{0.5}}{N} (\frac{\sigma}{d^2 \rho_L})^{0.4} \quad (12)$$

d. Air-assisted Atomizers:

These atomizers should be divided into two as internal and external mixtures. It is common to using internal mixing. It is often difficult to decide whether these atomizers are air assisted or air blasted. Air-assisted nozzles require less air than the other. Therefore, they are especially used in combustion chambers.

Wigg [16] explained that the dominant factor in the average drop diameter was the energy difference between the emerging spray and the inlet air. Then, in his studies, he gave the dimensionless mean drop diameter correlation as follows:

$$MMD = 20v_L^{0.5}\dot{m}_L^{0.1}(1+\frac{\dot{m}_L}{\dot{m}_A})^{0.5}h^{0.1}\sigma^{0.2}\rho_A^{-0.3}U_R^{-1}$$

$$(13)$$

In another study consistent with this correlation, they developed the following correlation [17]:

$$MMD = 1 + 5(\frac{\dot{m}_L}{\dot{m}_A})^{0.6}\dot{m}_L^{0.1} \qquad (14)$$

In another study using water as a liquid and air as a gas, they developed the following empirical formula for SMD [18].

$$SMD = 14x10^{-6}d_0^{0.75}(\frac{\dot{m}_L}{\dot{m}_A})^{0.75} \qquad (15)$$

e. Air-blast Atomizers:

The importance of air-blast nozzles has emerged with the potential to produce high-pressure gas turbine engines and to achieve significant reductions in exhaust fumes. According to the design of these atomizers have some varieties. These classified as flat, jet, and mixed.

$$SMD = \frac{0.585}{U_R}(\frac{\sigma}{\rho_L})^{0.5} + 53\left(\frac{\mu_L^2}{\sigma\rho_L}\right)^{0.225}(\frac{Q_L}{Q_A})^{1.5} \qquad (16)$$

In this correlation, which is valid for flat jet air blast atomizers, the effect of relative velocity and surface tension is seen in the first term on the right, while in the second term, the effect of viscosity with surface tension is seen. To illustrate this, the dimensionless drop diameter in a low viscosity fluid is proportional to the relative velocity.

Prefilming air blast atomizers are more suitable for combustion applications because they intensify fuel droplets in a small area compared to flat jets. Bryan et al. [19] Bryan developed the following correlation in prefilming nozzles:

$$SMD = 10^{-3}(1+\frac{1}{ALR})^{0.5}[\frac{(\sigma\rho_L)^{0.5}}{\rho_A U_A} + 0.06\left(\frac{\mu_L^2}{\sigma\rho_A}\right)^{0.425}] \quad (17)$$

This correlation has less dependence on ALR (air-liquid mass ratio) than many similar correlations.

Spray Measurement Techniques

High-speed photographing is often used to capture instantaneous images of spray droplets. It allows stochastic analysis of droplets. But it does not give a time-dependent droplet size distribution. The reason for this is that the deceleration rate of the drops is higher for small droplets. Photographs taken in this region require more control over small droplets. It is possible to calculate the average droplet velocity into a real time-dependent distribution.

In recent years, laser measurement techniques have been used to determine particle size and velocity with significant advances. These are high-speed pulsed micro-photography, cinematography and holography. It provides information on the droplet size distribution and spray structure. The Laser-Doppler Anemometer allows instantaneous droplet diameter, velocity, and regional drag coefficients to be detected by signal processing and high-speed data acquisition.

Table 3. Spray Measurement Methods

| Spray Mesurement Methods | |
|---|---|
| *Mechanical* | *Optical* |
| Collecting droplets in cells | High speed photography |
| Molten wax technique | Holography |
| Drop freezing technique | Single particul calculation with laser |
| Water sensitive paper method | Malvern particul size analyzer |
| | Density ratio method |

III. Empirical droplet diameter distribution functions

*DD. Nukiyama-Tanasawa*

The Nukiyama - Tanasawa equation uses four parameters to simulate differential distribution frequencies for particle size diameters, so it is not easy to apply the distribution function to match experimental data [20]. It should be normalized by particle size distribution to be more useful. Some researchers suggested p = 2 [15].

$$\frac{dN}{dD} = aD^p exp - (bD)^q \qquad (18)$$

*EE. Rosin-Rammler*

The Rosin-Rammler function represents the distribution of drop sizes in a spray as a function of the two parameters.

$$1 - Q = exp - (\frac{D}{X})^q \qquad (19)$$

Here Q is the volumetric ratio of the total drop volume of those smaller than D. X and q are constants. q allows the measurement of the dispersion of the drop diameter. More uniform spray is obtained at higher q values. For example, if q is assumed to be infinite, all spray droplets will be of the same size. However, this value generally ranges between 1.5-4. Rotary atomizers are up to 7.

*FF. Upper-Limit Function*

The volume distribution equation is as follows:

$$\frac{dQ}{dy} = \delta e^{\frac{-\delta^2 y^2}{\sqrt{\pi}}} \qquad (20)$$

Here y; it is calculated in the following way, although it varies from -∞ to +∞.

$$y = \ln\frac{aD}{D_m - D} \qquad (21)$$

Accordingly, the SMD is expressed as follows:

$$SMD = \frac{D_m}{1 + a\exp(\frac{1}{4\delta^2})} \qquad (22)$$

Reduction of δ in the SMD function indicates that we get more uniform spray.

The upper limit distribution function accepts a realistic spray for finite minimum and maximum drop sizes.

As a result, it is seen that the drop diameter distribution should be given with the best empirical representation that can be obtained in each case.

In order to relate the atomization mechanisms to one or more distribution functions, a function must generally represent the drop size distribution. There is no theoretical justification for a belief (or expectations) about the superiority of any function. Probably the best reason to choose a particular distribution function would be its mathematical simplicity, ease of calculation, and consistency with the physics of the event.

## II. CHARACTERISTIC DROP DIAMETERS

For most engineering applications, the distribution of drop sizes in a spray can be briefly represented as a function of the two parameters; one is a representative diameter and the other is a measure of the drop size range.

Figure 1 shows the location of the various representative diameters over the distribution.
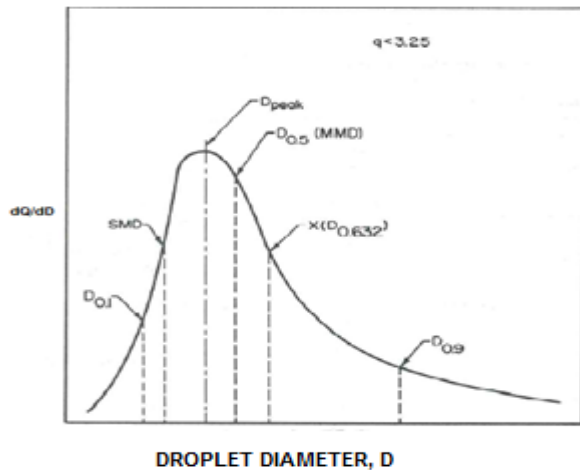


Figure 1. The location of some representative drop diameters in distribution

The general formulation of characteristic drop diameters is as follows.

$$D_{pq} = \left[\frac{\sum N_i D_i^p}{\sum N_i D_i^q}\right]^{1/(p-q)} \qquad (23)$$

Table 4 presents important characteristic drop diameters and application areas.

Table 4. Avarage droplet diameters

| p | q | p+q | Symbol | Name | Application |
|---|---|-----|--------|------|-------------|
| 1 | 0 | 1 | $D_{10}$ | Length | Comparison |
| 2 | 0 | 2 | $D_{20}$ | Surface area | Surface area control |
| 3 | 0 | 3 | $D_{30}$ | Volume | Volume control |
| 2 | 1 | 3 | $D_{21}$ | Surface area and Length | Absorption |
| 3 | 1 | 4 | $D_{31}$ | Volume and length | Evaporation, molecular diffusion |
| 3 | 2 | 5 | $D_{32}$ | SMD | Heat and mass transfer, reaction |
| 4 | 3 | 7 | $D_{43}$ | Herdan | Combustion |

It is important to make clear the difference between the representative diameter and the SMD, which is an indicator of the quality of atomization. For example, representative diameters such as MMD play an important role in determining droplet diameter distribution. However, only the SMD can accurately show the sensitivity of the spray in terms of cooling and combustion applications.

As a result, no single parameter can fully define the drop diameter distribution. The following figure shows the drop diameter spectrum. Here, the usage intervals according to the diameter are given briefly.
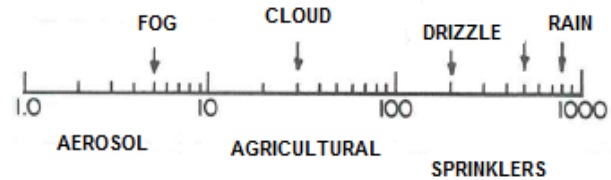


Figure 2. Droplet diameter spectrum (D, µm)

Droplet diameter distributions are as important as the mean drop diameter. Some spray applications such as painting and aerosol need narrow size distribution, and combustion applications such as gas turbine engines need wide-range distribution. It is also an issue that should be examined in a very wide range, such as agricultural and food sprays where low number of small droplets is desired, as well as internal combustion engines where low number of very large droplets is desired.

Droplet diameter distributions are defined by 4 methods. These are the empirical method, MEF (maximum entropy formalization), DPF (Discrete probability function) and stochastic method.

MEF assumes that spray formation is a random process that can be defined using the entropy maximization principle [21] [22]. Most probable droplet diameter distribution conforms to entropy maximization under physical constraints [18]. The DPF method assumes spray formation as a combination of random and non-random processes. The stochastic (estimated) breakup model assumes that the possibility of forming small drops by the separation of spray pieces is independent of the main drop size. Which of the empirical methods is more appropriate is controversial. For example, Déchelette et al. [23] reported that Nukiyama-Tanasawa was most suitable in the droplet diameter distribution study. They showed that Rosin-Rammler gave a weak result and that the Log-normal distribution was stable. Although he gave the best results, they mentioned some of the problems of Nukiyama-Tanasawa.

In addition, a disadvantage of the empirical method is to make extrapolation in the calculations outside the experimental range. As a result, the empirical method is flexible if these methods are compared. It can be used in any non-pathological model. MEF provides good results in many cases. It is useful for the physics of breakup and drop diameter distribution. It gives better results in secondary atomization regimes. The DPF method tries to re-solve the difficulties encountered in the mathematical definition in the MEF method. If the PDF is obtained experimentally, the

predictive power of DPF is reduced. The stochastic method is suitable for both primary and secondary atomization. However, it can only be used in high We numbers.

## III. HEAT TRANSFER DURING SPRAY

The heat transfer in the spray can be analyzed depending on the conservation rate of the energy equation for the open thermodynamic system shown in Figure 3.
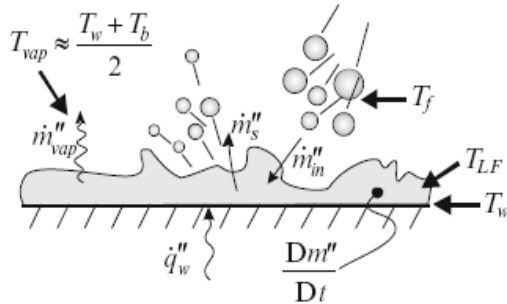


Figure 3. Heat transfer mechanism on spray cooling

Liquid evaporation takes place with the heat flux on the surface. The mass flow of the impinging droplets accumulates on the surface and is collected on the surface as a liquid film. This occurs away from the surface in the form of secondary droplets or evaporates into the environment. Initial surface temperature is a key parameter in the analysis. According to classical boiling theory, the liquid is evaporated from the surface by heat. In film evaporation and boiling regimes, the liquid film on the surface is considered a wet regime. Due to the bubbling of the surface due to boiling, the secondary atomization mechanism is forced [24] [25].

Heat transfer should be analyzed locally and generally on all surfaces. Depending on the surface temperature, geometry, roughness and heat source, the heat flux can be increased or limited locally and generally due to the contact of liquid to the surface. The result of this definition locally is an empirical correlation for Nu number.

SMD is helpful in combustion or droplet evaporation studies, but the energy released by chemical reaction or fuel volatilization is dependent on the surface area of the spray. That's why it may not necessarily be the most appropriate for use in spray cooling heat transfer since the droplets impact the surface and form a thin film that evaporates. An estimate of $d_{32}$ can be obtained from a correlation suggested by [26]

$$\frac{d_{32}}{d_0} = 3.07(\frac{\rho_v^{0.5}\Delta P d_0^{1.5}}{\sigma^{0.5}\mu_l})^{-0.259} \qquad (24)$$

## IV. CONCLUSIONS

In this study, the results of the researches on spray characteristic diameter correlations in published documents and the approaches followed in the studies are given. The following issues can be highlighted in the light of current articles:

- For different working conditions and spray characteristic diameters in a single frame and double phase flow have been focused. In particular, droplet diameter distribution correlations that give us detailed information about the spray have been compiled.

- The collecting computable correlations were compiled for SMD, which is commonly used for spray cooling, combustion and engine applications.

- Some of the correlations is generally limited information about the diameter of the spray while others are selected according to the working conditions gives us detailed information about the process.

- The appropriately selected correlation for the process is quite useful for estimating roughly. The particle diameter obtained from the correlation used in accordance with the selected nozzle is important to control operational conditions and availability.

-The advantages and disadvantages of empirical corelations for drop distribution in different diameter were discussed in detail.

In addition, many spray properties such as cone angle, patternation, radial particle distribution, equivalent spray angle, environment flow distribution and evaporation should be examined.

## REFERENCES

[1] G. Sitkei, Kraftstoffaufbereitung und Verbrennung bei Dieselmotoren: Springer-Verlag, 2013.

[2] A. Merrington, and E. Richardson, "The break-up of liquid jets," Proceedings of the Physical Society, vol. 59, no. 1, pp. 1, 1947.

[3] N. Panasenkov, "O Vliyanii Turbulentnosti Zhidkoi Strui Na Ee Raspylenie," Zhurnal Tekhnicheskoi Fiziki, vol. 21, no. 2, pp. 160-166, 1951.

[4] D. B. Harmon Jr, "Drop sizes from low speed jets," Journal of the Franklin Institute, vol. 259, no. 6, pp. 519-522, 1955.

[5] Y. Tanasawa, "On the atomization of liquid jet issuing from a cylindrical nozzle," Technol. Rep. Tohoku Univ., vol. 19, pp. 135, 1955.

[6] H. Hiroyasu, and T. Kadota, Fuel droplet size distribution in diesel combustion chamber, 0148-7191, SAE Technical Paper, 1974.

[7] M. Elkotb, "Fuel atomization for spray modelling," Progress in Energy and Combustion Science, vol. 8, no. 1, pp. 61-91, 1982.

[8] A. Radcliffe, "Fuel Injection, High Speed Aerodynamics and Jet Propulsion," XID, Princeton University Press, New Jersey, Princeton, 1960.

[9] A. Jasuja, "Atomization of crude and residual fuel oils," Journal of Engineering for Power, vol. 101, no. 2, pp. 250-258, 1979.

[10] K. R. Babu, "Prediction of mean drop size of fuel sprays from swirl spray atomizers." pp. 99-106.

[11] A. H. Lefebvre, Gas turbine combustion: alternative fuels and emissions: CRC press, 2010.

[12] Y. Oyama, "On the Centrifugal disk Atomization and Studies on the Atomization of Water Drops," Kagaku Kogaku, vol. 19, pp. 269-275, 1953

[13] S. Matsumoto, K. Saito, And Y. Takashima, "The Thickness of Aviscous Liquid Film On A Rotating Disk," Journal of Chemical Engineering of Japan, vol. 6, no. 6, pp. 503-507, 1974.

[14] Y. Tanasawa, "Effect of shape of rotating disks and cups on liquid atomization." pp. 165-172.

[15] A. Lefebvre, Atomization and sprays: CRC press, 1988

[16] L. Wigg, "The Effect of Scale on Fine Sprays Produced by Large Airblast Atomizers," NGTE Report No. 236, 1959.

[17] P. Mullinger, "The design and performance of internal mixing multijet twin-fluid atomizers," Journal of the Insititute of Fuel, vol. 47, pp. 251-261, 1974.

[18] N. Ashgriz, Handbook of atomization and sprays: theory and applications: Springer Science & Business Media, 2011.

[19] R. Bryan, P. Godbole, and E. Norster, "Characteristics of airblast atomizers." pp. 343-359.

[20] P. González-Tello, F. Camacho, J. Vicaria, and P. González, "A modified Nukiyama–Tanasawa distribution function and a Rosin–Rammler model for the particle-size-distribution analysis," Powder Technology, vol. 186, no. 3, pp. 278-281, 2008.

[21] R. Sellens, and T. Brzustowski, "A prediction of the drop size distribution in a spray from first principles," Atomisation Spray Technology, vol. 1, pp. 89-102, 1985.

[22] L. Xianguo, and R. S. Tankin, "Droplet size distribution: A derivation of a Nukiyama-Tanasawa type distribution function," Combustion Science and Technology, vol. 56, no. 1-3, pp. 65-76, 1987.

[23] A. Déchelette, E. Babinsky, and P. Sojka, "Drop size distributions," Handbook of Atomization and Sprays, pp. 479-495: Springer, 2011.

[24] G. Cossali, M. Marengo, and M. Santini, "Thermally induced secondary drop atomisation by single drop impact onto heated surfaces," International Journal of Heat and Fluid Flow, vol. 29, no. 1, pp. 167-177, 2008.

[25] A. L. Moreira, J. Carvalho, and M. R. Panao, "An experimental methodology to quantify the spray cooling event at intermittent spray impact," International Journal of Heat and Fluid Flow, vol. 28, no. 2, pp. 191-202, 2007.

[26] Estes, K.A., Mudawar, I., 1995. Correlation of Sauter mean diameter and critical heat flux for spray cooling of small surfaces. International Journal of Heat and Mass Transfer 38 (16), 2985–2996.

# Sub-Optimal Consensus-Based Formation Control of Fixed-Wing MUAV's

H. M. Guzey
Erzurum Technical University
Electrical-Electronics Engineering Department
mehmet.guzey@erzurum.edu.tr

*Abstract—* **Sub-optimal consensus based formation control is designed in this paper for a team of fixed-wing Unmanned Aerial Vehicles (UAV's). The group of UAV's moving at fixed altitudes are controlled through a formation controller to drive them to a pre-defined formation shape. Feedback linearization method is utilized to cancel the nonlinear dynamics of the UAVs and the linearized dynamics are controlled through the optimal consensus based formation controller.**

*Keywords- multiple UAVs; consensus; formation control; optimal control; feedback linearization;*

## [2]  INTRODUCTION

Formation control of multiple aerial vehicles (MUAVs) are payed attention by researchers in the last decades [1]-[9] due to potential civilian and military applications of MUAVs. Using MUAVs together in larger environments, provides much more advantageous when compare to a single UAV. For instance, searching and rescuing operation in a large field [1]; load transformation task when the load can't be carried and stabilized by a single UAV [2]; tracking a moving target [3]; observing larger fields in public safety applications [4] or area surveillance [5] or so on.

Several different formation control approaches [6]-[9] are proposed for MUAV's such as leader-follower approach [8], virtual structure approach [9], and consensus based approach [6][7]. In this paper, consensus-based formation control approach is considered due to scalability and robustness properties. The UAVs share their position errors from their desired locations. The shared information is then synthesized into a control law which seeks to achieve the same position error for all UAVs until each UAV has reached its goal position. By reaching and maintaining consensus on the position errors, the desired formation shape is achieved and maintained. The main tasks in consensus-based controllers are described as: i) given an initial state, achieve a pre-defined formation, and ii) maintain the formation while the MUAVs reach their desired locations.

In this work, the Argebraic Riccati Equetion based linear optimal controller is utilized for a networked fixed-winged UAV formation. The nonlinear dynamics of the UAV formation is linearized by using feedback linearization similar to [10]. Then the linearized dynamics are stabilized optimally

The paper is organized as follows. The backgrounds on leader follower based formation control design, regulation control and consensus based formation controller design developed in [10] for fixed-wing UAVs are given respectively in Section II. Secondly, in Section III, the sub-optimal consensus-based formation control approach for fixed-wing UAVs is discussed. Section V finally provides some concluding remarks.

## [3]  BACKGROUND AND PRELIMINARIES

In this section, background on leader-follower formation controller, regulation control and consensus-based formation control of UAV's is given.

### A.  Leader-Follower Based Formation Control of UAVs

The simplified model of the $i^{th}$ fixed-wing UAV given in Fig. 3 is given as [8]

$$\begin{bmatrix} \dot{x}_i \\ \dot{y}_i \\ \dot{\varphi}_i \end{bmatrix} = \begin{bmatrix} \cos(\varphi_i) & 0 \\ \sin(\varphi_i) & 0 \\ 0 & 1 \end{bmatrix} \begin{bmatrix} v_i \\ w_i \end{bmatrix} \qquad (1)$$

$$\dot{v}_i = -\frac{1}{k_v} v_i + \frac{1}{k_v} v_{ic} \quad , \qquad \dot{w}_i = -\frac{1}{k_w} w_i + \frac{1}{k_w} w_{ic} \quad ,$$

$$\ddot{h}_i = -\frac{1}{k_{ha}} \dot{h}_i - \frac{1}{k_{hb}} h_i + \frac{1}{k_{hb}} h_{ic} , \qquad (2)$$

where $x_i$ and $y_i$ are the Cartesian positions, $\varphi_i$ is the heading angle, $v_i$ is the linear velocity, and $h_i$ is altitude of the $i^{th}$ UAV. In addition, $h_{ic}, w_{ic},$ and $v_{ic}$ are the *altitude hold, heading-turn-rate hold*, and the comments to the *March hold* channels of the autopilot, respectively. $k_v, k_w, k_{ha},$ and $k_{hb}$ are known positive design constants those depend on the autopilot.

In Fig. 3, there are two fixed-wing UAV's, one of them is the wing (follower) and the other one is the leader UAV. The leader tracks a desired trajectory and the follower maintains a desired relative bearing angle and a relative distance to the leader UAV. Now, assume that the $k^{th}$ UAV is the leader and the $j^{th}$ UAV is the follower, then the desired relative separation and bearing is given in [8] as $F_{ij}^d = \begin{bmatrix} l_{jk}^d & \eta_{jk}^d \end{bmatrix}^T$ with $l_{jk}^d$ being the desired distance and $\eta_{jk}^d \in \begin{bmatrix} \dfrac{\pi}{2} & \dfrac{3\pi}{2} \end{bmatrix}$ is the desired relative bearing angle between the follower and the leader UAV's as shown in Fig. 3.
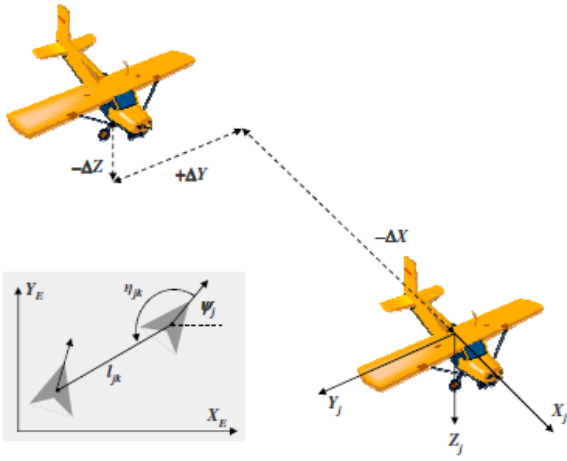
Fig. 3 Wing-leader Configuration [8]

The actual formation of the $k^{th}$ UAV is given as

$$F_{jk} = \begin{bmatrix} l_{jk} & \eta_{jk} \end{bmatrix}^T \in \mathbf{R} \times \begin{bmatrix} \dfrac{\pi}{2} & \dfrac{3\pi}{2} \end{bmatrix} , \qquad (3)$$

in which the relative bearing and the relative distance are defined, respectively as

$$\eta_{jk} = \pi + \tan^{-1}\left( y_j - y_k / x_j - x_k \right) - \varphi_j ,$$
$$l_{jk} = \sqrt{\left(x_j - x_k\right)^2 + \left(y_j - y_k\right)^2}$$

. Then, the formation errors and filtered formation errors are defined respectively for the $k^{th}$ UAV as $\xi_{kj} = F_{jk}^d - F_{jk}$ and

$$r_k = \dot{\xi}_k + K\xi_k , \qquad (4)$$

with $K$ being a designed positive definite matrix.

The dynamics of filtered formation errors (4) are given after some steps followed in [8] as

$$\dot{r}_k = \ddot{F}_{jk}^d - \left( \frac{\partial g_1(\bullet)}{\partial \chi_{jk}} + \frac{\partial g_1(\bullet)}{\partial l_{jk}} \right) v_k$$
$$+ g(\bullet) u_k + f_1(\bullet) \bar{v}_j + f_2(\bullet) \dot{\bar{v}}_j + K\dot{\xi}_k \qquad (5)$$

where $g_1(\bullet), g(\bullet), f_1(\bullet),$ and $f_2(\bullet)$ are the dynamics matrices defined similar to [8], $\bar{v}_j = \begin{bmatrix} v_j & w_j \end{bmatrix}^T$, $u_k = \begin{bmatrix} \dot{v}_k & w_k \end{bmatrix}$.

Formation controller which solves the filtered formation error dynamics (5) is developed in [8] as

$$u_k = g^{-1}(\bullet) \left| \begin{array}{c} -\ddot{F}_{jk}^d + \left( \dfrac{\partial g_1(\bullet)}{\partial \chi_{jk}} + \dfrac{\partial g_1(\bullet)}{\partial l_{jk}} \right) v_k \\ -f_1(\bullet)\bar{v}_j - f_2(\bullet)\dot{\bar{v}}_j - K\dot{\xi}_k - \psi(r_k) \end{array} \right| \qquad (6)$$

with $\psi(r_k) \in \mathbf{R}^2$ being a sliding vector function so that the sliding condition is guaranteed.

***Lemma 2 [8]:*** The control law (6) ensures stable sliding surface dynamics of the system in (4) and that all system signals are bounded under closed loop operation and the tracking error is asymptotically stable: $\lim_{t\to\infty} \xi_k(t), \dot{\xi}_k(t) = 0$.

Next, a regulation controller is designed for the $k^{th}$ UAV to drive it to its desired location.

## B. Regulation Control of UAVs

The desired formation is defined for the $k^{th}$ UAV as $F_{ij}^d = \begin{bmatrix} l_{jk}^d & \eta_{jk}^d \end{bmatrix}^T$ in the previous section. To bring the UAV to a desired location, define the regulation errors for the $k^{th}$ UAV as $e_k = \begin{bmatrix} l_k & \eta_k \end{bmatrix}^T$ where $l_k = \sqrt{\left(x_k - x_k^d\right)^2 + \left(y_k - y_k^d\right)^2}$ is the distance from the desired location and $\eta_k = \pi + \tan^{-1}\left( y_k^d - y_k / x_k^d - x_k \right) - \varphi_k^d$ is the bearing angle error with $x_k^d, y_k^d,$ and $\varphi_k^d$ are the desired Cartesian positions and the bearing angle, respectively. The filtered regulation errors can be given as

$$\mu_k = \dot{e}_k + Ke_k . \qquad (7)$$

Then, the dynamics of the filtered regulation errors (7) can be given as

$$\dot{\mu}_k = -\left( \frac{\partial g_1(\bullet)}{\partial \chi_{jk}} + \frac{\partial g_1(\bullet)}{\partial l_{jk}} \right) v_k + g(\bullet) u_k + K\dot{e}_k \qquad (8)$$

The regulation controller to stabilize the error dynamics (8) is given as

$$u_k = g^{-1}(\bullet) \left[ \left( \frac{\partial g_1(\bullet)}{\partial \chi_{jk}} + \frac{\partial g_1(\bullet)}{\partial l_{jk}} \right) v_k - K\dot{e}_k - \psi(\mu_k) \right]. \qquad (9)$$

with $\psi(r_k) \in \mathbf{R}^2$ being any sliding vector function so that the sliding condition is guaranteed.

***Lemma 1[14]:*** The control law (9) ensures stable sliding surface dynamics of the system in (7) and that all system signals are bounded under closed loop operation and the tracking error is asymptotically stable in the sense that $\lim_{t\to\infty} e_k(t), \dot{e}_k(t) = 0$.

Next, the consensus-based formation controller is given.

## C. Consensus Based Formation Control of UAVs

In this section, consensus-based formation controller developed in the previous work [10] for MUAV's shown in Fig. 3 is given. The goal of the consensus control is bringing all regulation errors to a same consensus-value,

$$e_k(t_f) \to \sum_{k=1}^{N} e_k(t_0) \text{ where } t_f, t_0 \text{ are the final and the initial time.}$$

***Assumption 1:*** The connectivity network forms a spanning tree [11].

Recall the regulation errors for each UAV in the network, $e_k = \begin{bmatrix} l_k & \eta_k \end{bmatrix}^T$ in terms of their positions and orientations.

The consensus errors are defined for each UAV as a function of the regulation error of the UAV and its neighbors as

$$\delta_{lk} = \frac{1}{\varsigma_k} \sum_{i \in N_k} (l_k - l_i) = l_k - \frac{1}{\varsigma_k} \sum_{i \in N_k} l_i ,$$
$$\delta_{\eta k} = \frac{1}{\varsigma_k} \sum_{i \in N_k} (\eta_k - \eta_i) = \eta_k - \frac{1}{\varsigma_k} \sum_{i \in N_k} \eta_i , \qquad (10)$$

with $N_k, \varsigma_k$ being the set of UAVs and number of UAVs in the neighborhood of the $k^{th}$ UAV.

Now, define the states for the virtual UAV as

$$l_j = \frac{1}{\varsigma_k} \sum_{i \in N_k} l_i, \, , \eta_j = \frac{1}{\varsigma_k} \sum_{i \in N_k} \eta_i$$

Then, the formation errors (10) can be rewritten as $\delta_{lk} = l_k - l_j$ $\delta_{\eta k} = \eta_k - \eta_j$. Define the formation error ,

$\delta_{kj} = \begin{bmatrix} \delta_{lk} & \delta_{\eta k} \end{bmatrix}^T$, and the filtered formation error as

$$\sigma_k = \dot{\delta}_{kj} + K\delta_{kj} . \tag{11}$$

Then, the filtered formation error dynamics becomes

$$\dot{\sigma}_k = -\left( \frac{\partial g_1(\bullet)}{\partial \chi_{jk}} + \frac{\partial g_1(\bullet)}{\partial l_{jk}} \right) v_k \tag{12}$$
$$+ g(\bullet) u_k + f_1(\bullet) \bar{v}_j + f_2(\bullet) \dot{\bar{v}}_j + K\dot{\delta}_k$$

The consensus-based formation controller can be proposed as

$$u_k = g^{-1}(\bullet) \left[ \begin{array}{l} \left( \frac{\partial g_1(\bullet)}{\partial \chi_{jk}} + \frac{\partial g_1(\bullet)}{\partial l_{jk}} \right) v_k - f_1(\bullet) \bar{v}_j \\ -f_2(\bullet) \dot{\bar{v}}_j - K\dot{\delta}_k - \psi(r_k) \end{array} \right] \tag{13}$$

with $\psi(r_k) \in \mathbf{R}^2$ can be choosen by using linear control tecniques.

**Lemma 2 [2]:** The control law (13) ensures stable sliding surface dynamics of the system in (11) and that all system signals are bounded under closed loop operation and the formation error is asymptotically stable: $\lim_{t \to \infty} \delta_k(t), \dot{\delta}_k(t) = 0$.

Next, the optimal consensus-based formation controller design is presented for UAV's.

### [4]  Optimal Consensus-Based Formation Control of UAV's

In this section, the sub-optimal consensus-based formation controller is developed for a group of fixed-wing UAV's described by (1) and (2).

In the controller formula (15), define

$$\psi(r_k) = Ar_k + Bu_k^* \tag{16}$$

where $A \in \mathbf{R}^{2x2}, B \in \mathbf{R}^2$ are the state matrix and control vector defined by the user, $u_k^* \in \mathbf{R}^2$ is the optimal control input. Then, the closed loop error dynamics become linear. Now, the goal is to find the optimal controller gain $u_k^*$.

For the optimal consensus-based formation controller of linear systems, solution of the Ricatti equation can be used. Define the finite horizon cost function as

$$C(r_k, u_k^*) = \int_0^T \left( r_k^T(s) Qr_k(s) + u_k^{*T}(s) Ru_k^* \right) ds + r_k^T(T) S r_k(T) \tag{17}$$

with $Q \in \mathbf{R}^{2x2}, R \in \mathbf{R}^{2x2}$ are positive definite matrices, $S \in \mathbf{R}^{2x2}$ is positive semi definite matrix, then, the following controleer is proposed

$$u_k^* = -B^T \Pr_k \tag{18}$$

with P being the solution of the following algebraic Riccati Equetion

$$-\dot{P} = -PBB^T P + PA + A^T P + Q$$
$$P(T) = S. \tag{19}$$

Next, some concluding remarks are provided.

### [5]  Conclusions and future work

In this paper, the consensus based formation controller design was extended to the sub-optimal consensus-based formation controller for the fixed wing UAVs. Future work will investigate extending the approach in the presence of unknown UAV dynamics. Nonlinear adaptive optimal consensus based formation control for fixed-winged UAVs also can be considered a potential future work.

### References

[1] M. A. Goodrich, L. Lin and B. S. Morse, Using camera-equipped mini-UAVS to support collaborative wilderness search and rescue teams, *International Conference on Collaboration Technologies and Systems (CTS),* Denver, CO, 2012, pp. 638-638.

[2] A. S. Aghdam, M. B. Menhaj, F. Barazandeh and F. Abdollahi, Cooperative load transport with movable load center of mass using multiple quadrotor UAVs, *2016 4th International Conference on Control, Instrumentation, and Automation (ICCIA),* Qazvin, 2016, pp. 23-27.

[3] H. Oh, D. Turchi, S. Kim, A. Tsourdos, L. Pollini and B. White, Coordinated Standoff Tracking Using Path Shaping for Multiple UAVs, in *IEEE Transactions on Aerospace and Electronic Systems,* vol. 50, no. 1, pp. 348-363, January 2014.

[4] Maza I. , Caballero F. , Capit´an J. , de Dios J. M. , and Ollero A. , Experimental results in multi-uav coordination for disaster management and civil security applications, Journal of Intelligent and Robotic Systems, vol. 64, no. 1-4, pp. 563–585, December 2010.

[5] Zheng-Jei W. and Wei L. , A solution to cooperative area coverage surveillance for a swarm of muavs, Internation Journal of Advanced Robotic Systems, vol. 10, no. 398, pp. 1–8, 2013.

[6] Kuriki Y. and Namerikawa T. , Consensus-based cooperative formation control with collision avoidance for a multi-UAV system, American Control Conference (ACC), 2014 , vol., no., pp.2077,2082, 4-6 June 2014

[7] Chen X. and Zhang C. , The Method of Multi Unmanned Aerial Vehicle Cooperative Tracking in Formation Based on the Theory of Consensus, Intelligent Human-Machine Systems and Cybernetics (IHMSC), 2013 5th International Conference on , vol.2, no., pp.148,151, 26-27 Aug. 2013.

[8] Xie F. , Zhang X. , Fierro R. and Motter M. , Autopilot-based Nonlinear UAV Formation Controller with Extremum-Seeking, 44th IEEE Conference on Decision and Control, 2005 and 2005 European Control Conference. CDC-ECC '05., vol., no., pp.4933,4938, 12-15 Dec. 2005.

[9] Low C. B. and San Ng Q., A flexible virtual structure formation keeping control for fixed-wing UAVs, Control and Automation (ICCA), 2011 9th IEEE International Conference on , vol., no., pp.621,626, 19-21 Dec. 2011.

[10] H. M. Guzey 'Hybrid Consensus-Based Formation Control of Fixed-Wing MUAVs,' *Cybernetics and Systems,* vol.48, pp 71-83, February 2017, doi:10.1080/01969722.2016.1263513.

[11] Ren W. and Atkins E. , Distributed multi-vehicle coordinated control via local information exchange, International Journal of Robust and Nonlinear Control, vol. 17, no. 10-11, pp. 1002–1033, 2007.

# Sliding Mode Controller Design for PMDC Motor

Kağan Koray Ayten
Department of Electrical & Electronics Engineering
Erzurum Technical University
Erzurum, Turkey
kagan.koray@erzurum.edu.tr

*Abstract*—**This study presents an accurate control for the PMDC motor by using a sliding mode control (SMC) technique to increase the trajectory tracking of the speed during the motion. Two different control techniques are taken into account for the experimental study. The first control technique is the SMC method which is utilised to improve the system's performance of the speed trajectory tracking, while the second method is the proportional-integral-derivative (PID) controller. As a result of this study, the experimental outcomes demonstrates that the SMC method provides a quite good trajectory tracking response and smaller magnitude overshot compared with the classical PID controller.**

*Keywords—PMDC motor, PID control, Sliding mode control, trajectory control*

## I. INTRODUCTION

As we know that the electrical energy is converted to mechanical energy by electric motors. Due to direct current motor's high torque, high efficiency, easy controllability and continuous control characteristic, many fields of daily life, such as paper machines, electric cars, robotic field, home applications prefer to use DC motors [1-3]. Due to the easy design of the DC motors, such motors are usually controlled by the PID controller and the parameters of this controller are adjusted either experimentally or by defining the best mathematical model of the system. Therefore, when DC motors operate at high speeds, non-linear conditions occur. Generally, these non-linear states are not taken into account because they do not affect the system much during the operation of DC motors. Also, if the system to be controlled is in a non-linear complex structure and the model is not precisely defined, conventional controllers such as PID are insufficient in the precise control of the system [4-5]. In addition, the parameters of the electric motor vary over time depending on the motor load, operating speed and temperature.

In the cases mentioned above, the PID controller loses its effectiveness and is negatively affected during the motion and may likely fail to provide the desired output in desired time. Therefore, it is necessary to control the system with a more reliable and effective controller to eliminate the stated situations.

In some studies in the literature, the SMC method has been performed to overcome the unwanted effects mentioned above during the motion [6]. In [6], to show the performance of the SMC method, the experimental application was also executed with the PID type controller. The experimental system was first operated without the disturbance effect and then operated with variable load conditions. It was observed that the SMC controller had a good settling time, fast response to disturbing effects and a good trajectory tracking response during the motion.

In other studies [7-9], the speed of the DC motor was controlled by the SMC method and the results were compared with the PID method. SMC has been shown to be a powerful controller against sudden disturbing effects.

In this study, due to the advantages of the above-mentioned SMC method, the SM speed control of a permanent magnet synchronous motor under load was carried out experimentally. All the dynamic model of the permanent magnet synchronous motor has been made for the experimental study. The proposed SMC technique minimizes the speed errors for certain predefined trajectories. According to the experimental results, it was observed that mathematical modelling for PMDC motor was correct and SMC method increased the trajectory tracking performance, according to the classical PID method during the motion and SMC is a more robust controller against the uncertainties in the system.

## II. DYNAMIC MODEL OF PMDC MOTOR

Electrical and mechanical model for PMDC motor is given as in figure 1. First, electrical circuit equations will be obtained for the PMDC motor. According to these electrical equations, the equations of motion related to the load angular speed will be obtained in terms of the voltage applied to the input of the PMDC motor. After this step, mechanical structure equations of PMDC motor will be defined as shown Fig.1 and the equations of the mechanical part of PMDC will be combined with the equations of the electrical part.

### A. Electrical Equation of the PMDC Motor

The relation between the back-emf voltage $e_b(t)$ with the back-emf constant, $k_m$, and the motor shaft speed, $\omega_m$, presented in (1).

$$e_b(t) = k_m \omega_m(t) \tag{1}$$

The electric circuit part in Fig. 1 is given as follows;

$$V_m(t) - R_m I_m(t) - L_m \frac{dI_m(t)}{dt} - k_m \omega_m(t) = 0 \tag{2}$$

As noted in Table 1, $L_m$ is much smaller than $R_m$ in Eq. 2. Therefore, $L_m$ was neglected, in this case, if we rearrange Eq. 2, the following electrical equation is given as follows;

$$V_m(t) - R_m I_m(t) - k_m \omega_m(t) = 0 \tag{3}$$

Considering the Eq. (3), the motor current $I_m(t)$ is given as;

$$I_m(t) = \frac{V_m - k_m \omega_m(t)}{R_m} \tag{4}$$

### B. Mechanical Equation of the PMDC Motor

The load equation of the movement of the PMDC motor based on Newton's second law is given by;

$$J_l \frac{d\omega_l(t)}{dt} + B_l \omega_l(t) = \tau_l(t) \tag{5}$$

The total torque applied to the load is indicated by $\tau_l$ in Eq. (5).
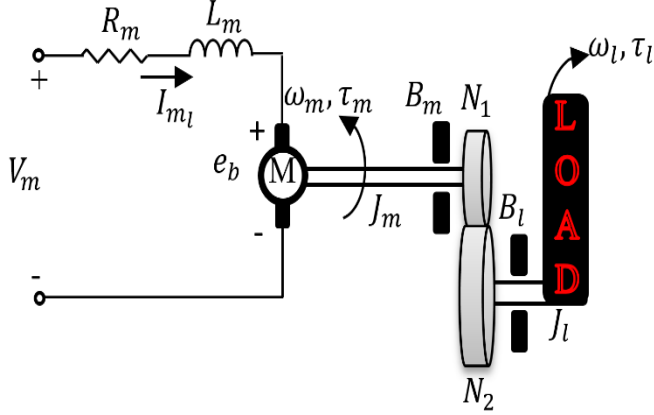


Fig. 1.   Schematic of the PMDC motor

In addition, the following equation defines the motor shaft.

$$J_m \frac{d\omega_m(t)}{dt} + B_m \omega_m(t) + \tau_{ml}(t) = \tau_m(t) \tag{6}$$

The load torque caused by the load at the motor shaft is defined by $\tau_{ml}$. Eq. (7) defines the load shaft torque as follows;

$$\tau_l(t) = \eta_g K_g \tau_{ml}(t) \tag{7}$$

Hence, the motor shaft torque including the gear is defined as follows;

$$\tau_{ml}(t) = \frac{\tau_l(t)}{\eta_g K_g} \tag{8}$$

The relation of the motor shaft and the load shaft is given as follow;.

$$\theta_m(t) = K_g \theta_l(t) \tag{9}$$

The equation between the angular velocities is obtained by taking the time derivatives of the above equation as follows;

$$\omega_m(t) = K_g \omega_l(t) \tag{10}$$

If we put the above equations (5), (8) and (10) into the equation (6), the differential equation of motion according to the applied motor torque is as follows;

$$J_m K_g \frac{dw_l(t)}{dt} + B_m K_g \omega_l(t) + \frac{J_l\left(\frac{dw_l(t)}{dt}\right) + B_l w_l(t)}{\eta_g K_g} = \tau_m(t) \tag{11}$$

The sum of the coefficients of the load shaft velocity and acceleration gives the following equation;

$$\left(\eta_g K_g^2 J_m + J_l\right)\frac{dw_l(t)}{dt} + \left(\eta_g K_g^2 B_m + B_l\right)\omega_l(t) = \eta_g K_g \tau_m(t) \tag{12}$$

Obtained the following equations;

$$J_{eq} = \eta_g K_g^2 J_m + J_l \tag{13}$$

$$B_{eq} = \eta_g K_g^2 B_m + B_l \tag{14}$$

and simplify the equation as;

$$J_{eq} \frac{d\omega_l(t)}{dt} + B_{eq} \omega_l(t) = \eta_g K_g \tau_m(t) \tag{15}$$

Combines electric and mechanic equations to define the load shaft speed according to the voltage applied to the PMDC motor.
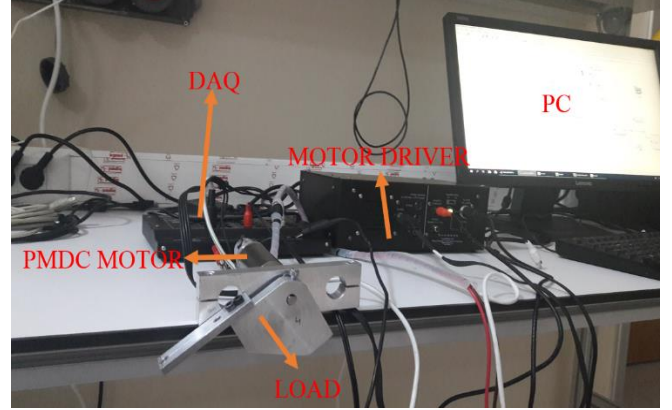


Fig. 2.   Experimental platform

As seen from the equation given below, there is proportionality between voltage and motor torque and is described as follows;

$$\tau_m(t) = \eta_m k_t I_m(t) \tag{16}$$

In Eq. (16), the motor efficiency, the current torque constant and the armature current are shown by $\eta_m$, $k_t$ and $I_m$, respectively. If $I_m$ in Eq. (4) is substituted into the Eq. (16), the following equation is observed;

$$\tau_m(t) = \frac{\eta_m k_t (V_m(t) - k_m \omega_m(t))}{R_m} \tag{17}$$

In Eq. (17), if $\omega_m(t)$ is replaced with Eq. (10), $\tau_m(t)$ is as follow;

$$\tau_m(t) = \frac{\eta_m k_t (V_m(t) - k_m K_g \omega_l(t))}{R_m} \tag{18}$$

If we substitute (18) into (16), we get:

$$J_{eq} \left(\frac{d}{dt}\omega_l(t)\right) + B_{eq} \omega_l(t) = \frac{\eta_g K_g \eta_m k_t (V_m(t) - k_m K_g \omega_l(t))}{R_m} \tag{19}$$

If we edit the equation above, the (19) can be shown as follows;

$$\left(\frac{d}{dt}\omega_l(t)\right)J_{eq} + \left(\frac{k_m \eta_g K_g^2 \eta_m k_t}{R_m} + B_{eq}\right)\omega_l(t) = \frac{\eta_g K_g \eta_m k_t V_m(t)}{R_m} \tag{20}$$

The Eq. (20) can be given as;

$$\left(\frac{d}{dt}\omega_l(t)\right)J_{eq} + B_{eq,v}\omega_l(t) = A_m V_m(t) \tag{21}$$

$B_{eq,v}$ is the equivalent damping term and this equation is defined by;

$$B_{eq,v} = \frac{\eta_g K_g^2 \eta_m k_t k_m + B_{eq} R_m}{R_m} \tag{22}$$

and the actuator gain

$$A_m = \frac{\eta_g K_g \eta_m k_t}{R_m} \qquad (23)$$

## III. SLIDING MODE CONTROL

In this section, Sliding Mode Control technique is designed considering the uncertainty and external disturbances for a PMDC motor that works under load. The control signal used in the sliding-mode control method consists of two components. The first is the equivalent control component used to minimize the error values. The second component is the switching control component, which can sensitize the system to the disturbing effects caused by unknown uncertainties. As is known, the purpose of all control methods is to minimize the tracking error function ($e$) between the input ($q_d$) and the system output ($q$) as shown in Eq. (24).

$$e = [q_d - q] \qquad (24)$$

In order to minimize this error function in the sliding-mode control method, a s-slip surface function, first indicated by Eq. (25), must be defined.

$$s = \lambda e + \dot{e} \qquad (25)$$

In Eq. (25), the defined value $\lambda$ is a positive matrix with constant coefficient. If, in one way, the error function is dependent on the first derivative and $\lambda$ values of this function, the equivalent control function, which is the first stage of the sliding-mode control method, can be correctly defined if the slip surface function and its $n$ th degree derivatives are close to zero. For this purpose, the first derivative of the sliding surface function is obtained as in Eq. (26) by taking the derivative of Eq. (25) according to the time.

$$\dot{s} = \lambda \dot{e} + \ddot{e} \qquad (26)$$

If the second derivative of the error function defined in Eq. (24) is taken and put into the Eq. (26), the first derivative of the sliding surface function can be defined by Eq. (27) with a different representation as follows;

$$\dot{s} = \lambda \dot{e} + (\ddot{q}_d - \ddot{q}) \qquad (27)$$

Standard output of the motor is expressed as follows;

$$\ddot{q} = f(q, \dot{q}, t) + g(q, t)u(t) + \xi(t, u(t)) \qquad (28)$$

If the $\ddot{q}$ function defined in Eq. (28) is put into the Eq. (27), the first derivative of the sliding surface function can be redefined by Eq. (29) as follows;

$$\dot{s} = \lambda \dot{e} + \ddot{q}_d - f(q) - g(q)u \qquad (29)$$

If we equalize this equation to zero, the equivalent control function can be found as follows;

$$u_{eq} = \frac{-f(q)}{g(q)} + \frac{\lambda \dot{e}}{g(q)} + \frac{\ddot{q}_d}{g(q)} \qquad (30)$$

In order to minimize unwanted disturbance effects, in addition to the defined equivalent control function, a switched control function, ($u_{sc}$), expressed in Eq. (31), must be added to the control signal.

$$u_{sc} = k_x sgn(s) \qquad (31)$$

The $k_x$ value defined in Eq. (31) is referred to as the switched-over gain matrix. The mathematical expression of the $sgn(s)$ function in the equation is as follows;

$$sgn(s) = \begin{cases} 1 \rightarrow s > 0 \\ 0 \rightarrow s = 0 \\ -1 \rightarrow s < 0 \end{cases} \qquad (32)$$

Thus, the total feedback sliding mode control function ($u$) for the PMDC motor can be written as follows;

$$u = u_{eq} + u_{sc} = \frac{-f(q)}{g(q)} + \frac{\lambda \dot{e}}{g(q)} + \frac{\ddot{q}_d}{g(q)} + k_x sgn(s) \qquad (33)$$

In practice, the control signal given in Eq. (33) may cause oscillations due to high frequency switching, and these oscillations are called the chattering effect. In order to overcome this unwanted effect during the application, the *sat* function is used instead of the *sgn* function.

## IV. EXPERIMENT

In this study, a PMDC motor was run in real time to show the superiority of the proposed SMC controller over the conventional PID controller. The square speed reference is given for the predetermined reference trajectory. Using the dynamic model of the PMDC mentioned in the second section, the angular speed change required by the PMDC motor to follow the reference trajectory is given in Fig. 3 and the performance of the controller is also given in Fig. 5. In addition, the angular speed error that occurs when the PMDC motor is tracking the reference trajectory is given in Fig. 4.

Given the results of the graphs shown, it is seen that the recommended controller provides trajectory tracking with much less errors than the classical PID. Although the gain parameters of the PID are chosen to optimally follow the reference trajectory, the classical PID controller is not able to respond robustly to the sudden changes in the given square reference during the motion. This causes angular velocity errors in the trajectory tracking of the PMDC motor. Hence, using the SMC instead of PID, it was seen that the system's trajectory tracking control performance increased. The reason for this is that the SMC uses the full dynamic model of the PMDC motor and takes into account the non-linear expressions that exist in the system. Thus, it is seen that the proposed controller gives a more robust trajectory monitoring performance under load.

Table 1. PMDC Motor Parameters

| Sym | Description | Value |
|---|---|---|
| $R_m$ | Motor armature resistance | $2.6\Omega$ |
| $L_m$ | Motor armature inductance | $0.18$ mH |
| $k_m$ | Motor back-emf constant | $7.68 \times 10^{-3}$ V/rad/s |
| $k_t$ | Motor current-torque constant | $7.68 \times 10^{-3}$ Nm/A |
| $K_g$ | Ration of the gear | 14 |
| $\eta_m$ | Efficiency of the PMDC motor | 0.69 |
| $\eta_g$ | Efficiency of the Gearbox | 0.90 |
| $J_m$ | Moment of inertia of the Motor shaft | $3.90 \times 10^{-7}$ kgm$^2$ |
| $J_l$ | Moment of inertia of the Load | $1.03 \times 10^{-4}$ kgm$^2$ |
| $B_m$ | The motor shaft's viscous friction | $1.07 \times 10^{-9}$ Nm/rad/s |
| $B_l$ | The load shaft's viscous friction | $4.41 \times 10^{-6}$ Nm/rad/s |
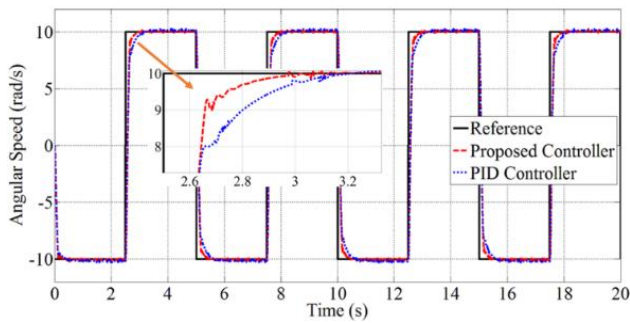
Fig. 3.   Angular speed graph
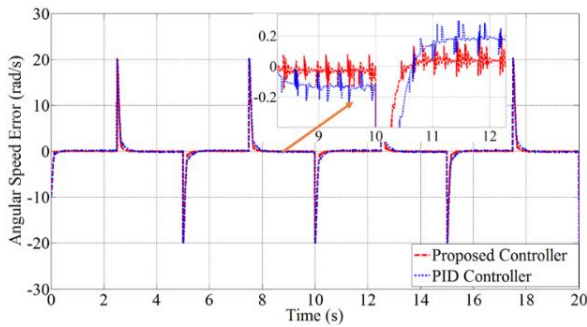


Fig. 4.   Angular speed error
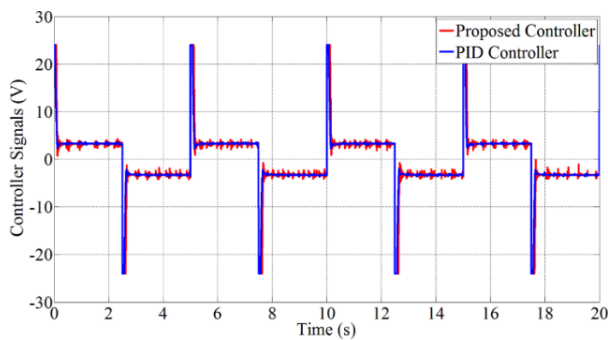


Fig. 5.   Control signal during the motion

## V. CONCLUSION

In this study, firstly a mathematical model of a PMDC motor was extracted and a dynamic model was obtained. In order for this dynamic model to follow the given reference trajectory with the least error, SMC technique, which is a strong and robust controller against the unknown disturbing effects in the system, has been designed. Considering the real-time control of the PMDC motor, it is seen that the recommended controller follows the reference trajectory better than the PID controller. The reason for this is that the proposed controller uses the full dynamic model of the system and takes into account the uncertainties in the system.

REFERENCES

[1] Dong Yulin, "The analysis and implement of PLC- based PI control for the permanent magnet DC motor," *2010 Second International Conference on Communication Systems, Networks and Applications*, Hong Kong, 2010, pp. 448-451.

[2] S. Heidarpoor, M. Tabatabaei and H. Khodadadi, "Speed control of a DC motor using a fractional order sliding mode controller," *2017 IEEE International Conference on Environment and Electrical Engineering and 2017 IEEE Industrial and Commercial Power Systems Europe (EEEIC / I&CPS Europe)*, Milan, 2017, pp. 1-4.

[3] Dil Kumar T R and Mija S.J, "Design and performance evaluation of robust SMC schemes for speed control of DC motor," *2014 IEEE International Conference on Advanced Communications, Control and Computing Technologies*, Ramanathapuram, 2014, pp. 88-92.

[4] K. Nouri, R. Dhaouadi and N. B. Braiek, "Nonlinear speed control of a dc motor drive system with online trained recurrent neural network," *9th IEEE International Workshop on Advanced Motion Control*, 2006., Istanbul, 2006, pp. 704-708.

[5] Guoshing Huang and Shuocheng Lee, "PC-based PID speed control in DC motor," *2008 International Conference on Audio, Language and Image Processing*, Shanghai, 2008, pp. 400-407.K. Elissa, "Title of paper if known," unpublished.

[6] A. M. A. Mohamed, "Sliding mode control design and application to permanent magnet dc motor speed control," *2006 Eleventh International Middle East Power Systems Conference*, El-Minia, 2006, pp. 25-29.

[7] V. Singh and V. Sharma, "Sliding mode controller design for DC motor with non-linearities," *2015 International Conference on Computation of Power, Energy, Information and Communication (ICCPEIC)*, Chennai, 2015, pp. 0558-0563.

[8] C. U. Maheswararao, Y. S. K. Babu and K. Amaresh, "Sliding Mode Speed Control of a DC Motor," *2011 International Conference on Communication Systems and Network Technologies*, Katra, Jammu, 2011, pp. 387-391.

[9] V. M. Panchade, L. M. Waghmare, B. M. Patre and P. P. Bhogle, "Sliding Mode Control of DC Drives," *2007 International Conference on Mechatronics and Automation*, Harbin, 2007, pp. 1576-1580.

# Synthesis of core-shell SiO2/ZnO Nanoparticles and Determination of their Photocatalytic Activity

Taner Tekin
*Department of Chemical Engineering*
*Atatürk University*
Erzurum/TURKEY
ttekin@atauni.edu.tr

Derya Tekin
*Department of Metallurgical and*
*Materials Engineering*
*Atatürk University*
Erzurum/TURKEY
deryatekin@atauni.edu.tr

Hakan Kızıltaş
*Department of Chemical Engineering*
*Atatürk University*
Erzurum/TURKEY
h.kiziltas@atauni.edu.tr

*Abstract*— SiO2 and SiO2@ZnO nanoparticles were synthesized by Stöber and sol-gel method, respectively. The characterization of synthesized nanoparticles was determined by SEM-EDS and XRD analyzes. The photocatalytic activity tests were tested on Acid Red 27 dye and the photocatalytic activity of SiO2 @ZnO photocatalysts was found to have higher photocatalytic activity compared to commercial ZnO.

*Keywords*— *photocatalyst, core-shell, photocatalytic decomposition, SiO2@ZnO.*

## I. INTRODUCTION

Photo-catalytic degradation of organic pollutants by semiconductor photocatalysts is a promising approach for environmental treatment [1]. Among these photocatalysts, TiO2 and ZnO are the two semiconductors most frequently studied because of their lower cost, biocompatibility and high thermal and chemical properties [2, 3]. Compared to TiO2, ZnO has a direct band gap of 10-100 times higher electron mobility and consequently a lower electrical resistance and improved electron transfer efficiency. Therefore, ZnO is considered as a suitable alternative to TiO2 [4]. However, the photocatalytic performance of ZnO is not high enough to meet the practical requirements due to the broadband gap (3.37 eV) and rapid recombination of electron-gap pairs [5]. It has been found that photo-induced carriers can be effectively separated in composite materials to prepare a highly efficient ZnO for practical application [6].

SiO2 is a promising material because it is chemically stable except for a strong acid or base. In addition, silica has a low refractive index that can contribute to effective stimulation with ultraviolet light [7]. SiO2 is combined with some semiconductor photocatalysts to improve the photocatalytic process. SiO2 has high thermal stability, excellent mechanical strength and can create new catalytic active regions due to the interaction between semiconductor photocatalysts and SiO2. In addition, SiO2 can act as carriers of semiconductor photocatalysts and can help to obtain a suitable porous structure as well as a large surface area [8].

The photocatalytic property of the semiconductor oxide depends on its physical and chemical properties. Several studies have been conducted to improve the photocatalytic performance of ZnO by improving the synthesis methods [9]. Among the solution-based methods, the sol-gel method is well suited for preparing both simple and complex metal oxides.

The aim of this study was to investigate the change in the photocatalytic activity of the synthesized SiO2 @ ZnO photocatalysts against ZnO nanoparticles. In addition, SEM-EDS and XRD analyzes were performed to investigate the morphological and crystal structure of the synthesized nanocomposite SiO2 @ ZnO photocatalyst. Acid red 27 dye was used for photocatalytic studies.

## II. EXPERIMENTAL

### A. Materials

Ethanol (Sigma Aldrich, 99.8%), tetraethyl orthosilicate (Sigma Aldrich, 99%), ammonium hydroxide (Sigma Aldrich, 25%) and distilled water were used for the synthesis of SiO2 nanoparticles.

Ethanol (Sigma Aldrich, 99.8%), zinc acetate dehydrate (Sigma Aldrich, 99%), sodium hydroxide (Sigma Aldrich, 99%) and distilled water were used to add ZnO on the produced SiO2 nanoparticles.

### B. Synthesis of SiO2 Nanoparticles

5 ml of 25% (w / w) NH4OH was added the solution consisting of 80 ml of ethanol + 20 ml of deionized water and continue to be stirred for 5 minutes. 1 ml of TEOS was added the solution medium under ultrasonic stirring. the solution was ultrasonically stirred for 3 h under 45% amplitude. SiO2 nanoparticles are removed from the solution medium at 5000 rpm by centrifugation. After washing with ethanol, it is allowed to dry at 110 ° C for 2 hours.

### C. Synthesis of SiO2 @ ZnO Nanoparticles

0.2 g of SiO2 nanoparticles, previously synthesized and dried, are added to a solution of 100 ml of ethanol + 1 g of Zn (Ac) 2.2H2O to provide a homogeneous solution by ultrasonication at 60 °C for 15 minutes. Then, 20 ml of 0.25 M NaOH solution is added dropwise to the solution and stirred at 60 °C for 45 hours under a 45% amplitude. After completion of the time, the solution is cooled to room temperature and the nanoparticles is removed by centrifugation. The nanoparticles were washed 5 times with distilled water and ethanol, and dry at 60°C for 3 hours. Lastly, the nanoparticles were calcined for 2 hours at 200 °C.

*D. Photocatalytic Activity Tests*

Photocatalytic experiments were carried out in a jacketed reactor.The reaction temperature was kept constant at 25°C with a programmable constant temperature water circulator.Aa 44 W/m2 (257 nm) UV lamp was immersed the dye solution as a source of light. O2 is provided the reaction medium by pumping air at constant flow rate.

## III. RESULT AND DISCUSSION

The results of SEM and EDS analysis was used for the characterization of SiO2 nanocomposites, are given in Figure 1.
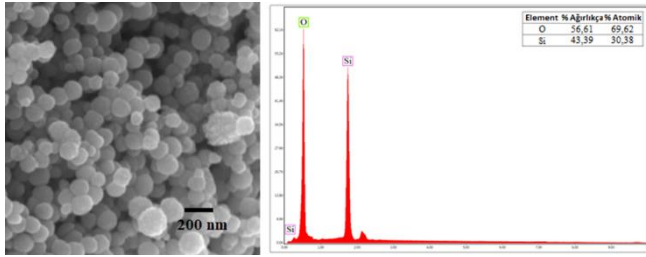


Figure 1. SEM and EDS analysis of SiO2 nanoparticles

As shown in Figure 1, the SiO2 nanoparticles show good monodispersion and have completed their spherical formation. SiO2 nanoparticles have diameters in the range of 160 to 260 nm, with an average diameter of approximately 220 nm. Silicon and oxygen have been proven by EDS analysis of SiO2 nanoparticles.

The results of SEM and EDS analysis for the characterization of SiO2@ZnO nanoparticles synthesized by solvothermal method are given in Figure 2.
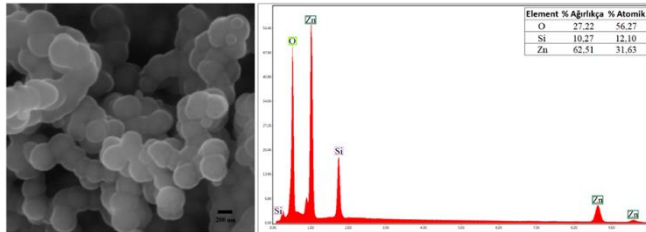


Figure 2. SEM and EDS analysis of SiO2@ZnO nanoparticles

As shown in Figure 2, the synthesized SiO2® ZnO nanocomposite does not show a homogeneous distribution such as SiO2, but has a smoother surface than SiO2. The ZnO coating produced agglomeration in the FSiO2 nanocomposites and caused the particles to form due to deformations. The SiO2® ZnO nanocomposite has diameters ranging from 175 to 385 nm, with an average diameter of approximately 230 nm and greater than SiO2 nanocomposites. With the EDS analysis of SiO2® ZnO nanocomposite, the presence of silicon, zinc and oxygen in nanocomposite has been proven.

Figure 3 shows the XRD analysis of the SiO2 synthesized by the Stöber method and the SiO2 @ ZnO nanocomposites synthesized by the sol-gel method.
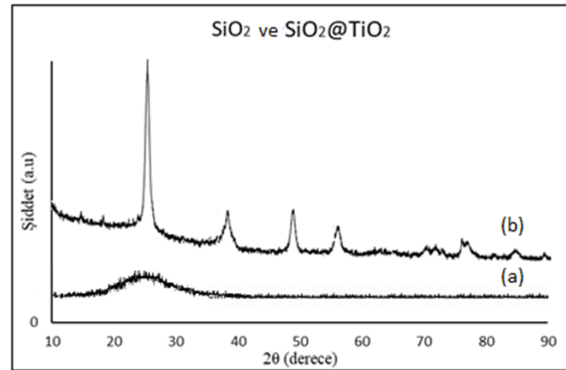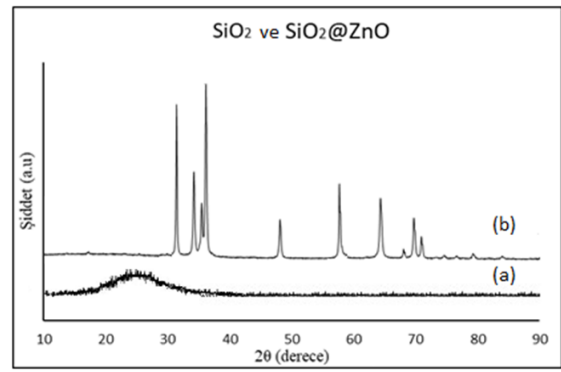


Figure 3. XRD results of SiO2 and SiO2 @ ZnO nanoparticles

As shown in Figure 3, no sharp peak corresponding to SiO2 was observed due to the fact that the synthesized SiO2 nanoparticle had amorphous structure, but a wide peak at a low diffraction angle of 20 ° to 30 ° was observed. The diffraction peaks at 32,48, 35,00, 36,43, 47,92, 56,87, 63,04, 67,08, 68,12 and 69,06 were determined (100), (002), (101), (102), (110), (103), (200), (112) and (201) of the hexagonal wurtzit structure for ZnO, respectively. The results overlap with the JCPDS: 36-1451 card.

The photocatalytic degradation graph of Acid Red 27 dye are given in Figure 4 for SiO2 nanoparticles synthesized by Stöber method, SiO2 @ ZnO nanoparticles synthesized by sol-gel method and ZnO nanoparticles.
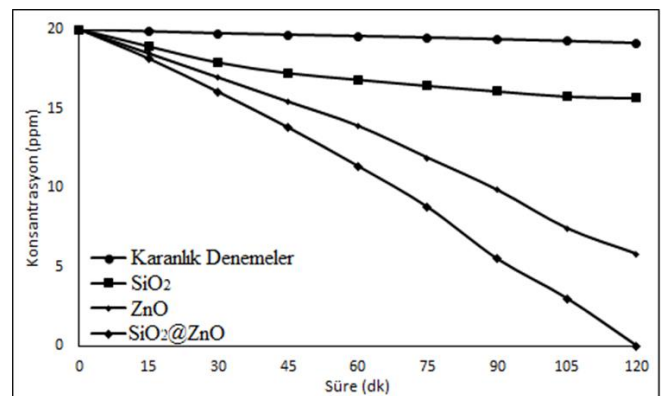


Figure 4. Graph for photocatalytic decomposition of Acid Red 27 solution

The photocatalytic activity of the nanoparticles was performed on Acid Red 27 dye in a batch reactor. Figure 4 shows a graph of dye decomposition on the nanoparticles in the batch reactor. During the 120-minute period, the nanoparticles adsorbed the average 4.4% of dye in the dark

medium. After 120 minutes, SiO2 nanoparticles was decomposed 11.5% of the dye. ZnO nanoparticles was 70.8%, while the SiO2@ZnO nanoparticles showed 100% removal over 120-minute period.

## IV. CONCLUTION

SiO2 synthesized by and SiO2@ZnO synthesized by nanoparticles were synthesized by Stöber and sol-gel method. The characterization of synthesized nanoparticles was determined by SEM-EDS and XRD analyzes. The photocatalytic activity tests were tested on Acid Red 27 dye and the photocatalytic activity of SiO2@ZnO photocatalysts was found to have higher photocatalytic activity compared to commercial ZnO.

## REFERENCES

[1] Gaya, U.I. and A.H. Abdullah, Heterogeneous photocatalytic degradation of organic contaminants over titanium dioxide: A review of fundamentals, progress and problems. Journal of Photochemistry and Photobiology C: Photochemistry Reviews, 2008. 9(1): p. 1-12.

[2] Zhou, J., N.S. Xu, and Z.L. Wang, Dissolving Behavior and Stability of ZnO Wires in Biofluids: A Study on Biodegradability and Biocompatibility of ZnO Nanostructures. Advanced Materials, 2006. 18(18): p. 2432-2435.

[3] Linsebigler, A.L., G. Lu, and J.T. Yates, Photocatalysis on TiO2 Surfaces: Principles, Mechanisms, and Selected Results. Chemical Reviews, 1995. 95(3): p. 735-758.

[4] ZnO Hierarchical Micro/Nanoarchitectures: Solvothermal Synthesis and Structurally Enhanced Photocatalytic Performance. Advanced Functional Materials, 2008. 18(7): p. 1047-1056.

[5] Zheng, M. and J. Wu, One-step synthesis of nitrogen-doped ZnO nanocrystallites and their properties. Applied Surface Science, 2009. 255(11): p. 5656-5661.

[6] Balachandran, S. and M. Swaminathan, Facile Fabrication of Heterostructured Bi2O3–ZnO Photocatalyst and Its Enhanced Photocatalytic Activity. The Journal of Physical Chemistry C, 2012. 116(50): p. 26306-26312.

[7] Hagura, N., et al., Enhanced photoluminescence of ZnO–SiO2 nanocomposite particles and the analyses of structure and composition. Journal of Luminescence, 2011. 131(1): p. 138-146.

[8] Comedi, D., et al., Randomly oriented ZnO nanowires grown on amorphous SiO2 by metal-catalyzed vapour deposition. Journal of Alloys and Compounds, 2010. 495(2): p. 439-442.

[9] Yao, K.X., R. Sinclair, and H.C. Zeng, Symmetric Linear Assembly of Hourglass-like ZnO Nanostructures. The Journal of Physical Chemistry C, 2007. 111(5): p. 2032-2039.

# Antifungal potential of *Serratia plymuthica* chitinase against phytopathogens

Sumeyra Gurkok
Department of Biology
Ataturk University
Erzurum, Turkey
sumeyrag@gmail.com

Arzu Gormez
Department of Molecular Biology and Genetics
Erzurum Technical University
Erzurum, Turkey
arzugormez@erzurum.edu.tr

Ebru Oztas Gulmus
Department of Molecular Biology and Genetics
Erzurum Technical University
Erzurum, Turkey
ebru.oztas@erzurum.edu.tr

*Abstract*— **Chitinases are the hydrolytic enzymes that break down *β*-(1-4) glycosidic bonds in chitin. Chitin, a linear polymer of *β*-1,4-N-acetylglucosamine, is one of the most abundant polysaccharides in nature and it is the main structural component of cell walls of fungi, exoskeletons of insects and other arthropods and shells of crustaceans. The use of chitinolytic microorganisms and their derived chitinases for the biological control of fungal plant pathogens are gaining great interest in agriculture. In the present study, a total of 20 soil and water samples were collected from 5 different locations in Erzurum Province. More than 200 isolates were screened for chitinolytic activity on colloidal chitin incorporated media. Based on the chitin hydrolysis zones, 15 chitinolytic bacterial isolates were chosen for further study. The best chitinase producer isolate was identified as *Serratia plymuthica* by 16s ribosomal RNA sequencing and tested for their antifungal potential against the phytopathogens. The crude extract was ineffective in preventing spore germination in 24 hours and was slightly effective on the inhibition of the growth of *Verticillium dahliae* and *Fusarium sp.***

*Keywords—chitinase, Serratia plymuthica, antifungal activity, biocontrol, phytopathogen, Verticillium dahliae, Fusarium sp.*

## I. INTRODUCTION

Chitin is the polymer of *β*-1,4 linked N-acetyl D-glucosamine (GlcNAc) and is the second most abundant natural polymer after cellulose [1]. Chitin is widely distributed as a structural component of crustaceans, insects and other arthropods, as well as a component of the cell walls of most fungi and some algae [2]. Chitinases (EC 3.2.11.14) are the enzymes responsible for hydrolyzing the *β*-(1-4) glycosidic bonds of chitin into oligomeric, dimeric (chitobiose) and monomeric (N-acetyl D-glucosamine, GlcNAc) compounds [3]. The chitinase are widely distributed among bacteria, fungi, insects, plants and animals [4, 5]. Some of the best known chitinolytic bacterial genera include *Aeromonas* [6], *Serratia* [7], *Streptomyces* [8] and *Bacillus* [9]. Among the wide range of applications, chitinases recently have gained great interest in the use of biocontrol of phytopathogens. As plants have no immune system, they are vulnerable to pathogen infections. Fungi are one of the most important pathogens in plants leading to remarkable yield loss. The existing practices in agriculture industry is the use of chemical fungicides to control phytopathogens. However, the major concerns about the chemical fungicides are the environmental contamination and human health risk associated with fungicide toxicity and resistance of phytopathogens against most of the synthetic chemicals [10]. Recent advances in biocontrol using microorganisms or their derived enzymes like chitinase to prevent plant diseases offer an attractive alternative to synthetic chemicals. Chitinases provide a defense mechanism to the plant against chitin-containing pathogens, such as insects, nematodes and fungi [11]. The chitinase from *Trichoderma* showed antifungal potential against fungal pathogens like *Aspergillus*, *Rhizopus*, *Mucor* [12]. The chitinases from *Bacillus* was used against *Colletotrichum* [13] and *Fusarium* [14]. Despite their antifungal potential, chitinases are still not used extensively in commercial practices due to low yield and activity and high production cost. The search for better microbial chitinase sources with high antifungal properties is needed for environmentally friendly, effective and inexpensive alternative to synthetic fungicides. Therefore, the present study aimed to isolate and identify new chitinolytic bacterial sources and apply them in the biocontrol of phytopathogens, *V. dahliae* and *Fusarium sp.*.

## II. MATERIALS AND METHODS

### A. Sample Collection and Isolation of Chitinolytic Bacteria

A total of 20 soil and water samples were collected from five different locations (Karasu, Akdağ, Dumlu, Ilıca, Pasinler) in Erzurum Province. Samples were diluted in phosphate buffer solution and sample dilutions were spread on nutrient agar and trypticase soy agar and were incubated at 27 °C for 2–7 days. Morphologically different colonies were picked and streaked onto new agar plates for purification. Pure cultures were cryopreserved in LB (Luria-Bertani Broth) with 15% glycerol at -86 °C.

### B. Preparation of Colloidal Chitin

Colloidal chitin (CC) was prepared from chitin powder (Sigma, Germany) by the method of Monreal and Reese [15] with minor modifications. Chitin powder (30 gr) was slowly added to 300 mL of concentrated HCl and kept overnight at 4 °C. The suspension was mixed with 1200 mL of cold ethanol (96%) with vigorous stirring and kept overnight at 4 °C. The precipitate was collected by centrifugation at 9000 rpm for 10 minutes, washed several times with distilled water until the colloidal chitin became neutral (pH 7.0). Final precipitate was dried to a constant weight at 50 °C and stored at room temperature until further use [16].

### C. Screening of Chitinase Producing Bacteria

Chitinase producing bacterial isolates were screened on colloidal chitin containing agar media (0.3 g/L $MgSO_4 7H_2O$, 3 g/L $NH_4SO_4$, 2 g/L $KH_2PO_4$, 1 g/L citric acid monohydrate, 15 g/L agar, 200 μL tween 80, 4.5 g/L colloidal chitin). Purified isolates were streaked on colloidal chitin agar (CCA) and incubated 3–5 days at 27 °C. Potent chitinase-producing

bacterial colonies were selected on basis of clear zone formation.

## D. Chitinase Activity Assay

Bacterial isolates were incubated in chitinase production broth media (3 g/L $(NH_4)_2SO_4$, 0.3 g/L $NaH_2PO_4$, 2 g/L $KH_2PO_4$, 0.3 g/L $MgSO_4.7H_2O$, 0.02 g/L $FeSO_4.7H_2O$, 0.016 g/L $MnSO_4$, 0.014 g/L $ZnSO_4$, 0.02 g/L $CaCl_2.2H_2O$, 200 μL tween 80, 10 g/L colloidal chitin) for 3 days at 27 °C. The chitinase activity was assayed by measuring reducing sugar released from colloidal chitin. The reaction mixture contained 0.5 mL of properly diluted crude enzyme solution and 2% colloidal chitin in 0.5 mL 0.1 M phosphate buffer (pH 7). The mixture was vortexed and incubated at 50 °C for 30 minutes. Reaction was terminated by the addition of 1 mL of 3,5-dinitrosalicylic acid solution (10 g/L NaOH, 10 g/L DNS, 2 g/L phenol and 0.2 g/L Rochelle salt) and the mixture was boiled for 10 minutes. After cooling to room temperature, the mixture was centrifuged at 5000 rpm for 5 min and absorbance was measured at 540 nm using UV spectrophotometer along with substrate and blanks. For determination of enzyme unit, serial dilutions of N-acetyl D-glucosamine were prepared as standard. One unit (U) of the chitinase activity was defined as amount of enzyme required to release 1 μmol of N-acetyl D-glucosamine from chitin per min.

## E. Genomic DNA Isolation

The DNA of the bacteria was extracted by using Wizard® Genomic DNA purification Kit (Promega). Briefly, 24 h old cultures were used to isolate genomic DNA. Purity was evaluated by spectrophotometer (per wavelength) NanoDrop® 2000 (Thermo Scientific). The samples were preserved at -86 °C until they were used.

## F. 16S rRNA Sequencing

The 16S ribosomal RNA gene was amplified using the following primers: 27 forward primer (5' AGA GTT TGA TCG TGG CTC AG 3') and 1492 reverse primer (3' GGT TAC CTT GTT ACG ACT T 5'). The reactions were performed with 3 μL 10X PCR buffer, 0.6 μL dNTP mix, 3 μL primers each, 1.2 μL DMSO, 1.8 μL $MgCl_2$, 12.1 μL $sdH_2O$, 0.3 μl 5 unit/μL Taq DNA polymerase and 5 μL DNA mixture under following cycling conditions; 5 min at 95 °C, 1 min at 94 °C, 1 min at 48 °C, 1.5 min at 72 °C and 8 min at 72 °C [17]. The amplified 16S rRNA gene regions were cloned into pGEM®-T Easy vector system and the recombinant vectors were transferred into *Escherichia coli* JM101 by $CaCl_2$ method was made competent with, by using. Eventually, plasmid isolations were performed by using plasmid DNA extraction kit (Vivantis GF-1). Base sequence analyses of plasmids that include 16S rRNA gene regions were sequenced, and the sequences obtained were made meaningful after the results were interpreted using BioEdit software. 16S rRNA sequences were compared to available bacterial sequences registered in the NCBI database (http://blast.ncbi.nlm.nih.gov/blast.cgi) [18]

## G. Antifungal activity

Antifungal activity of the chitinase from *S. plymuthica* was tested using the crude enzyme on spore germination and fungal growth. The phytopathogens, *V. dahliae* and *Fusarium sp.*, were used as test fungi.

To observe the effect of *S. plymuthica* on the germination of test fungi, one ml of fungus spore solution ($10^5$ spore/ml) was inoculated into 250 ml erlen containing 50 ml malt extract broth and incubated at 27 ºC, 150 rpm for 24 hours. After incubation, 5 ml of bacterial fermentation fluid was added. The mixture was incubated at 27 ºC, 150 rpm for 0, 4, 8, 12 and 24 hours. As negative control group sterile distilled water was used. At the end of incubation periods, liquid cultures were filtered through Whatman No1 filter papers and dried to constant weight at 100 °C and then the increase in biomass were determined by dry mycelium weight measurement.

On the other way, to observe the effect of bacterial crude enzyme on fungal growth both fungi were grown on potato dextrose agar plates at 27 °C for 3 days. Crude enzyme was applied on the fungal plates by spraying and incubated for 3 more days at 27 °C.

## III. RESULTS AND DISCUSSION

A total of 200 morphologically different bacteria were isolated from 20 soil and water samples collected from 5 different locations of Erzurum, Turkey. On the basis of clear hydrolysis zone formation on colloidal chitin containing media, 15 colonies were selected for secondary screening in broth media and tested for enzyme activity.

Based on the chitinolytic activity, the most potent 5 chitinase producer *Serratia* species were chosen and identified by 16s ribosomal RNA sequencing. The results of the NCBI nucleotide BLAST were given in Table 1. Among these strains, *S. plymuthica* with the AS55 code showed maximum chitinase production and antifungal activity was tested using this strain.

The extracellular extracts from *S. plymuthica* were obtained by centrifuging the bacterial culture at 10000 rpm for 10 min. Firstly, the crude extract was tested on fungal spore germination of *V. dahliae* and *Fusarium sp*. The crude extract was found to be ineffective in preventing germination of the test fungi in the first 24 hours. The antifungal activity of the extracellular extract was also tested on growth inhibition of *V. dahliae* and *Fusarium sp*. Crude enzyme was directly by sprayed on the plates where the fungi were grown for 3 days and incubated for 3 more days in the presence of bacterial crude enzyme. The results are given in Fig. 1 and Fig. 2 for *V. dahliae* and *Fusarium sp.*, respectively.

Table 1. Strain identification by 16S rRNA sequencing

| Code | Strain name | Ident. | Accession No |
|------|-------------|--------|--------------|
| AS 54 | *Serratia plymuthica* strain UBCF_13 16S ribosomal RNA gene, partial sequence | 95% | KX394779.1 |
| **AS 55** | ***Serratia plymuthica* strain BSW-12 16S ribosomal RNA gene, partial sequence** | **97%** | **KX901796.1** |
| AS 67 | *Serratia plymuthica* strain UBCF_13 16S ribosomal RNA gene, partial sequence | 96% | KX394779.1 |
| AS 75 | *Serratia marcescens* strain N80 16S ribosomal RNA gene, partial sequence | 96% | GQ351502.1 |
| AS 117 | *Serratia marcescens* strain 100 16S ribosomal RNA gene, partial sequence | 100% | KX821734.1 |
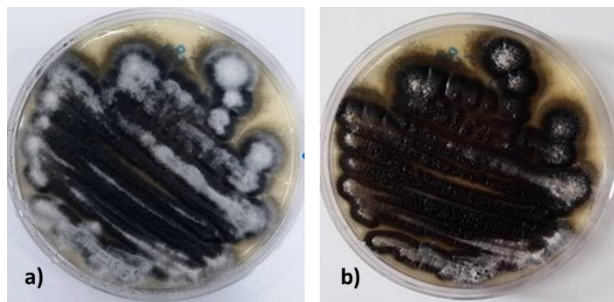
Fig. 1. The petri dishes showing the antifungal activity of *S. plymuthica* against *V. dahliae*. a) untreated b) treated
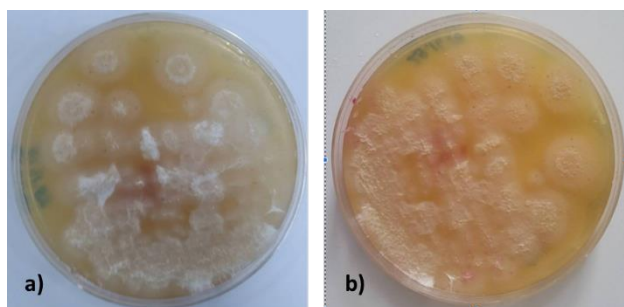


Fig. 2. The petri dishes showing the antifungal activity of *S. plymuthica* against *Fusarium sp.* a) untreated b) treated

Protection of plants from diseases caused by phytopathogenic fungi is one of the most important problems in agriculture industry. Most of these problems is a result of fungal infections [19]. Therefore, developing biological solutions that could be used for biocontrol of fungi is quite important. Recent studies demonstrated that chitinase from plants [19,20] and microorganisms [21,22] are able to inhibit the fungal growth.

In the present study, *Serratia* species were focused on due to its antifungal and antimicrobial properties. The genus of *Serratia* have been used as biological control agent against several fungal pathogens in agriculture [21,23,24]. Serralysin and related proteases play an important role in the protection of plants against pathogen infection [25]. Serralysin family members have a wide range of substrates such as host immunoglobulins, complement proteins, cell matrix and cytoskeletal proteins, antimicrobial peptides [26]. In case of antibiosis, production of siderophores and the fungal cell wall degrading enzymes like chitinases and $\beta$-1,3 glucanases is responsible for antifungal activity and they are very valuable for control of phytopathogen fungi [27]. Especially, the non-diffusible red pigment prodigiosin is known to be an antifungal antibiotic and toxic to protozoa [28]. So, all of them are important virulence factors in pathogenic bacteria.

We examined the antifungal activity of crude extract of *S. plymuthica* against *V. dahliae* and *Fusarium sp.* using different methods as described in materials and methods section. The results showed that the crude extract was ineffective in preventing spore germination in 24 hours. On the other hand, the crude extract stopped the growth of both pathogenic fungi; however, the inhibitory effect was very low on both fungi. The reason behind this may be the use of crude extract instead of purified chitinase enzyme. In literature, the purified chitinase from *Serratia sp.* was found to be very effective in biocontrol of phytopathogens [24,25]. The antifungal activity of the purified chitinase from *S. marcescens* against *Rhizoctonia solani* and *Fusarium oxysporum* using the agar-disk diffusion method was very effective in the growth inhibition of both pathogenic fungi; however, the inhibitory activity was slightly higher against *Fusarium oxysporum* than *Rhizoctonia solani* [25].

Therefore, the next aim of this study is the purification of the chitinase enzyme and its application on various phytopathogen fungi and harmful insects. In addition, the red pigment of *Serratia plymuthica*, prodigiosin has been also extracted and will be applied to phytopathogenic fungi.

## ACKNOWLEDGMENT

## REFERENCES

[1] K. P. Dutta, J. Dutta, and V. S. Tripathi, "Chitin and chitosan:Chemistry, properties and applications," J. Sci. Ind. Res., vol. 63, no. 1, pp. 20–31, 2004.

[2] S. Nicol, "Life after death for empty shells." New Sci., vol. 129, pp. 46–48, 1991

[3] R. Yan, J. Hou, D. Ding, W. Guan, C. Wang, Z. Wu, M. Li, "In vitro antifungal activity and mechanism of action of chitinase against four plant pathogenic fungi", J. Basic Microbiol., vol. 48, pp. 293–301, 2008.

[4] S. Adrangi, M. A. Faramarzi, "From bacteria to human: a journey into the world of Chitinases", Biotechnol. Adv., vol. 31, no. 8, pp. 1786–1795, 2013.

[5] R. Salvador, M. L. Ferrelli, A. Sciocco-Cap, V. Romanowski, "Analysis of a chitinase from EpapGV, a fast killing betabaculovirus". Virus Genes vol. 48 (2), pp. 406–409, 2014.

[6] S. Halder, C. Maity, A. Jana, A. Das, T. Paul, P. Mohapatra, B. Pati, K. Mondal, "Proficient biodegradation of shrimp shell waste by *Aeromonas hydrophila* SBK1 for the concomitant production of antifungal chitinase and antioxidant chitosaccharides", Int. Biodeterior. Biodegrad. vol. 79, pp. 88–97, 2013.

[7] S. Okay, M. Özdal, E. Kurbanoğlu, "Characterization, antifungal activity, and cell immobilization of a chitinase from *Serratia marcescens* MO-1", Turkish J. Biol., vol. 37, no.6 pp. 639–644, 2014.

[8] N. Karthik, P. Binod, A. Pandey, "Purification and characterisation of an acidic and antifungal chitinase produced by a *Streptomyces sp.*", Bioresour. Technol., vol. 188, pp. 195–201, 2015.

[9] K. S. Rishad, S. Rebello, P. S. Shabanamol, M. S. Jisha, "Biocontrol potential of halotolerant bacterial chitinase from high yielding novel *Bacillus pumilus* MCB-7 autochthonous to mangrove ecosystem", Pest. Biochem. Physiol., vol. 137, pp. 36–41, 2017.

[10] P. Kashyap, X. Xiang, P. Heiden, "Chitosan nanoparticle based delivery systems for sustainable agriculture". Int. J. Biol. Macromol., vol. 77, pp. 36–51, 2015.

[11] M. Kriaa, I. Hammami, M. Sahnoun, M. C. Azebou, M. A. Triki, R. Kammoun, "Biocontrol of tomato plant diseases caused by *Fusarium solani* using a new isolated *Aspergillus tubingensis* CTM 507 glucose oxidase", C. R. Biol., vol. 338, pp. 666–677, 2015.

[12] K. M. Nampoothiri, T. V. Baiju, C. Sandhya, A. Sabu, G. Szakacs, A. Pandey, "Process optimization for antifungal chitinase production by *Trichoderma harzianum*", Process Biochem., vol. 39, pp. 1583–1590, 2004.

[13] N. Ashwini and S. Srividya, "Potentiality of Bacillus subtilis as biocontrol agent for management of anthracnose disease of chilli caused by *Colletotrichum gloeosporioides* OGC1", 3 Biotech., vol. 4, pp. 127–136, 2014.

[14] S. Bhattacharya, A. Das, S. Samadder, S. Rajan, "Biosynthesis and characterization of a thermostable, alkali-tolerant chitinase from *Bacillus pumilus* JUBCH08 displaying antagonism against phytopathogenic *Fusarium oxysporum*", 3 Biotech. vol. 6, p. 87, 2016.

[15] J. Monreal and E. Reese, "The chitinase of *Serratia marcescens*." Can. J. Microbiol. vol. 15, pp. 689–696, 1969.

[16] S. Gurkok and A. Gormez, "Isolation and characterization of novel chitinolytic bacteria" AIP Conf. Proc., vol. 1726, pp. 020017, 2016.

[17] Görmez, (2011) Erzurum İli'nde kayısı ağaçlarından izole edilen *pseudomonas* türlerinin tanısı, karakterizasyonu ve çeşit reaksiyonları. PhD Thesis, Institue of Natural and Applied Sciences, Ataturk University, Erzurum.

[18] A. Adiguzel, H. Nadaroglu, G. Adiguzel, "Purification and characterization of β-mannanase from *Bacillus pumilus* (M27) and its applications in some fruit juices". J. Food Sci. Technol. vol. 52, no. 8, pp. 5292–5298, 2015.

[19] A. Singh, S. Isuas Kirubakavan, N. Sakthivel, "Heterologous expression of new antifungal chitinase from wheat", Protein Expr Purif. vol. 56, pp. 100–109, 2007

[20] X. Ye, T. B. Ng, "A chitinase with antifungal activity from the Mung bean", Protein Expr. Purif. vol. 40, pp. 230–236, 2005.

[21] M. Kamensky, M. Ovadis, I. Chet, L. Chernin, "Soil-borne strain IC14 of *Serratia plymuthica* with multiple mechanisms of antifungal activity provides biocontrol of *Botrytis cinerea* and *Sclerotinia sclerotiorum diseases*", Soil Biol. Biochem., vol. 35, no. 2, pp. 323–331, 2003.

[22] M. Zarei, S. Aminzadeh, H. Zolgharnein, A. Safahieh, M. Daliri, K.A. Noghabi, A. Ghoroghi and A. Motallebi, "Characterization of a chitinase with antifungal activity from a native *Serratia marcescens* B4A", Braz. J. Microbiol., vol. 42, no. 3, pp. 1017–1029, 2011.

[23] G. Berg, "Diversity of antifungal and plant-associated *Serratia plymuthica* strains", J. Appl. Microbiol. vol. 88, no.6, pp. 952–960. 2000.

[24] J. Frankowski, M. Lorito, F. Scala, R. Schmid, G. Berg, H. Bahl, "Purification and properties of two chitinolytic enzyme of *Serratia plymuthica* HRO_C48", Arch. Microbiol. vol. 176, pp. 421–426, 2001.

[25] T. T. Do, T. T. Nguyen, T. L. S. Nguyen, H. T. Le, "Optimization, purification, and characterization of an extracellular antifungal protein from *Serratia marcescens* DT3 isolated from soil in Vietnam", Turk J Biol vol. 41, pp. 448–457, 2017.

[26] A. Marchler-Bauer, M. K. Derbyshire, N. R. Gonzales, S. Lu, F, Chitsaz, L. Y. Geer, R. C. Geer, J, M. He Gwadz, D. I. Hurwitz et al,. "CDD: NCBI's conserved domain database". Nucleic Acids Res. vol. 43, pp. 222–226, 2015.

[27] C. Kalbe, P. Marten, G. Berg, Members of the genus *Serratia* as beneficial rhizobacteria of oilseed rape. Microbiological Research, vol. 151, pp. 4400–4433, 1996.

[28] J. A. Groscop and M. M. Brent, The effects of selected strains of pigmented microorganisms on small free-living amoeba. Can. J. Microbiol. vol. 10, pp. 579–584, 1964.

# Graphene Aerogel Synthesis Methods for Energy Conversion and Storage Applications

Meryem Samancı
Chemical Engineering
Atatürk University
Erzurum, Turkey
meryemsamanci@gmail.com

Ayşe Bayrakçeken Yurtcan
Chemical Engineering
Atatürk University
Erzurum, Turkey
ayse.bayrakceken@gmail.com

*Abstract*— **Graphene aerogel has attracted extensive research interest due to its strictly 3-dimensional (3D) structure, which results in its unique electronic, thermal, mechanical, and chemical properties and potential technical applications. This study reviews the methods of preparing graphene aerogel. Regarding graphene aerogel synthesis, four most commonlu used methods were identified, namely, hydrothermal reduction, sol–gel, template-directed reduction and chemical reduction**.

*Keywords—graphene aerogel, graphene oxide, hydrothermal reduction, sol–gel, template-directed reduction, chemical reduction*

## I. INTRODUCTION

In recent years, global energy use has increased considerably due to the rising demand for energy in developed countries and the rapidly increasing demand in developing economies. In order to meet the increasing energy demand, high performance, low cost and environmentally friendly benign energy systems need to be developed. Therefore, large-scale research efforts are underway in various locations around the world to develop fuel cells for the direct production of electricity from chemical energy and to develop supercapacitors and advanced batteries for electrical storage [1].

Nowadays, various carbon materials (fig. 1) has been widely used as electrode materials for energy storage and conversion devices due to their several advantages: (1) good conductivity for rapid electron transfer; (2) superior chemical stability for resistance of acid and alkaline corrosion; (3) super large active surface area for ion adsorption; (4) various forms like zero-dimensional (0D) fullerene, carbon spheres, one-dimensional (1D) carbon nanotubes (CNTs), carbon fibers (CFs), two-dimensional (2D) graphene, carbon films, three-dimensional (3D) carbon sponges, carbon foam, carbon cloth, aerogels [2].
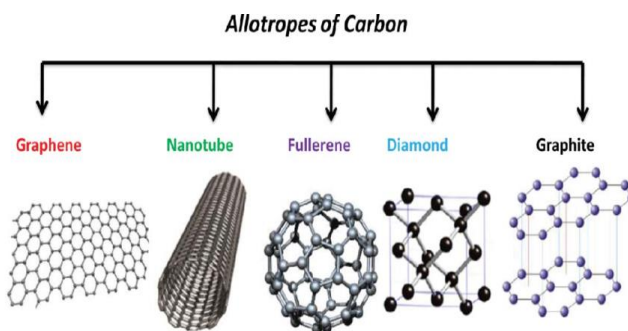


Fig. 1. Various carbon materials

This research describes the most widely used methods of graphene aerogels used in energy conversion and storage applications.

Generally, graphene oxide (modified graphene) is used as a starting material for the synthesis. Graphene oxide (GO) is prepared by several methods. The most commonly used method is the Hummer method [3]. Chemically derived GO-based aerogels are the most common 3D graphene structures in the literature because of their facile synthesis route, and the control of pore morphology that they provide (Fig. 2) [4,5].
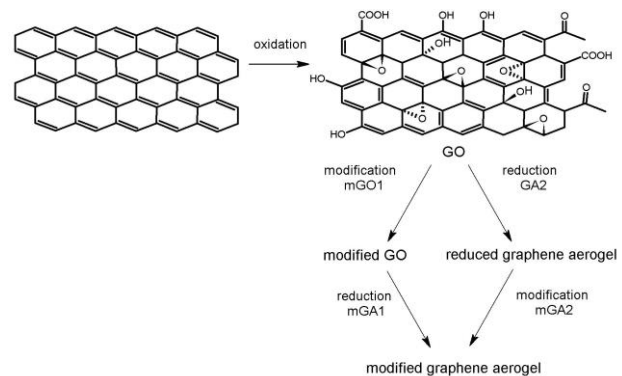


Fig. 2. Scheme of modified graphene aerogels preparation [6].

## II. PRODUCTION METHODS OF GRAPHENE AEROGELS

### A. *Hydrothermal Reduction Method*

Hydrothermal reduction method (Fig. 3) is one of the most widely used graphene aerogel production techniques.
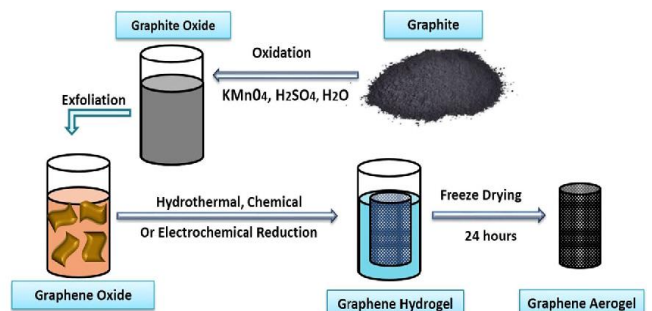
Fig. 3. Representation of hydrothermal reduction method [7].

In this method, firstly, a suspension of graphene oxide is prepared using the Hummers method, where the graphite powder is oxidized with the use of $NaNO_3$, $H_2SO_4$ and $KMnO_4$.

In this method, the graphene oxide solution is first subjected to high temperature and high pressure to produce graphene hydrogel. Then, supercritical or freeze-drying methods are used to prepare graphene aerogel structures.

Xu et al. reported a method in which reduction of graphene oxide could be obtained under lower temperatures than it was described above. They carried out one-step hydrothermal process by heating the graphene oxide aqueous dispersion in a Teflon-line autoclave at 180 °C for 12 h. They managed to produce GA with high specific capacitance (175 F/g) that could be used as a supercapacitor electrode material [4]. Another research conducted by Nguyen et al. showed that it was possible to perform GA synthesis at 95 °C without the use of any binders [8]. They took graphene oxide water dispersion and reduced it using L-ascorbic acid. The electrical conductivity of such structure was 0.04 S/m and its surface area was 394 $m^2$/g. The density was 0.042 g/cm$^3$ [8].

## B. Sol-gel Method

The graphene aerogels were prepared using traditional organic sol-gel chemistry (Fig. 4). One of the synthesis route is resorcinol-formaldehyde (RF) sol-gel synthesis. RF acts as a binder that helps to cross-link individual graphene oxide sheets with sodium carbonate as a catalyst.

The sol-gel mixture was then transferred to glass molds, sealed and cured in an oven at 85 $^0$C for 12-72 h. The resulting gels were then removed from the molds and washed with acetone for 72 h to remove all the water from the pores of the gel network. The wet gels were subsequently dried with supercritical $CO_2$ to yield the GO and GO/RF aerogels. These aerogels were reduced via pyrolysis at 1050 $^0$C under $N_2$ atmosphere for 3 h. The graphene aerogel materials were isolated as black cylindrical monoliths. Worsley and colleagues synthesized high electrical conductivity (87 S/m) and surface area (584 $m^2$/g) materials. The density was 0.025 g/cm$^3$ [9].
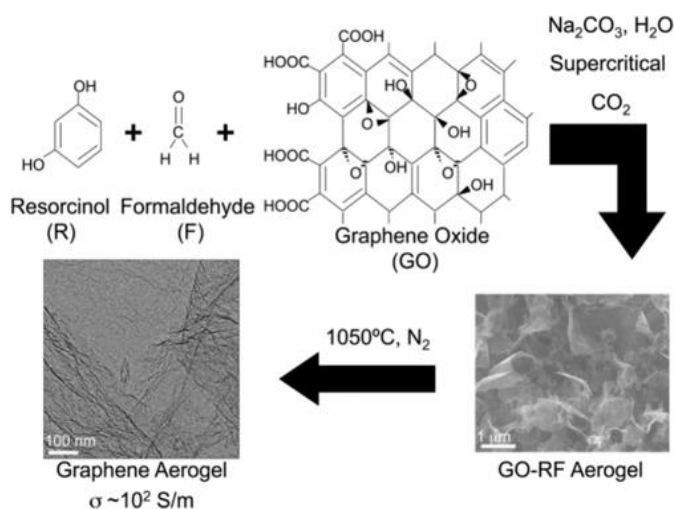


Fig. 4. Representation of sol-gel method [10]

## C. Template-Directed Reduction Method

Template-directed reduction (Fig. 5) is a very useful method for obtaining porous graphene aerogels because it prevents random interconnection structures while it favours controllable and uniform macropores and tailorable microstructure as well. The template-directing method uses ice crystals, water droplets, or colloidal particles as the templates for the pore formation, and generally requires precise control over the amount of graphene used and subsequent template removal.

Chen et al. have reported the synthesis of a macroporous 'bubble' graphene film through a template-directed reduction method. Some latex spheres of monodisperse polymethyl methacrylate (PMMA) acted as the hard templates in this material. GO hydrosol and a PMMA spheres suspension were mixed, and after filtration, a composite film was extracted and calcinated at 800 °C leading to the PMMA template and to thermally reduced GO into graphene at the same time. From the thermogravimetric results, it was found that the oxygen-containing functional groups of GO are removed at 230 °C, while the PMMA spheres are pyrolyzed and removed at 400 °C. Graphene was finally derived with the PMMA spheres acting as the interlayer spacer. The synthesized material exhibited high electrochemical capacitance [11].
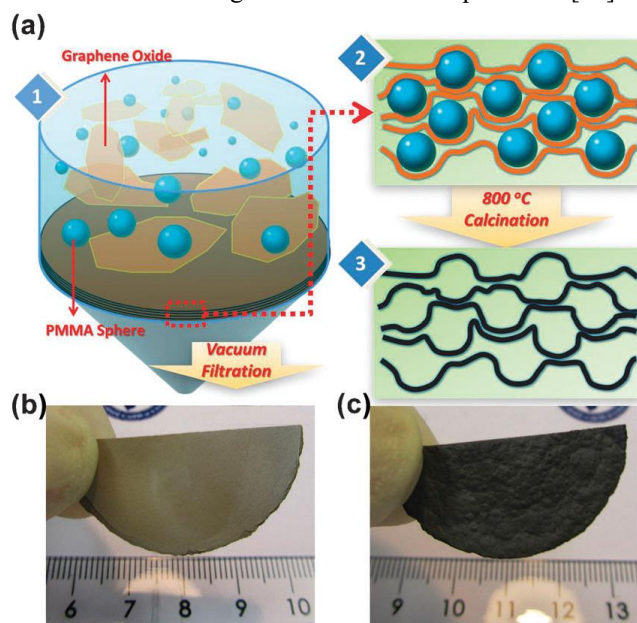


Fig. 5. a) . Representation of Template-Directed Reduction Method
 (b) GO/PMMA composite film and (c) as-prepared GA [12]

## D. Chemical Reduction Method

Chemical reduction (Fig. 6) is an easy method consisting of a single stage. Graphene hydrogel is obtained by adding reducing agents to the graphene oxide solution. Then, graphene aerogels are obtained using supercritical drying or freeze drying methods.

Zhang et al. have used oxalic acid (OA) and sodium iodine (NaI), which are low cost and eco-friendly, instead of toxic HI widely used as reducing agent in their study. The surface area of the graphene aerogel is 151 $m^2$/g and electrical conductivity is 24.8 S/m [12].
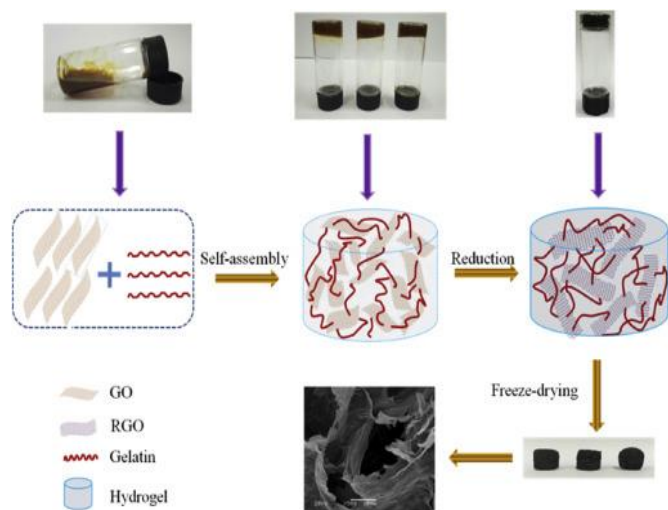
Fig. 6. Representation of Chemical Reduction Method [13]

## III. CONCLUSIONS

In this review, a summary of recent progress on the synthesis methods of GAs was presented. Regarding synthesis, four most commonly used methods were identified, namely, hydrothermal reduction, sol–gel, template-directed reduction and chemical reduction.

The unique of excellent properties of graphene aerogels including good electrical conductivity, great chemical stability, and the possibility to obtain free-standing structures allow such graphene-based structures to be used in electrochemical energy storage and conversion devices such as: fuel and biofuel cells, lithium ion batteries, supercapacitors. Graphene-based aerogels with high porosity and an interconnected network have been developed to improve material performance. Studies on this subject will continue to be developed.

## REFERENCES

[1] Junbo Hou, Yuyan Shao, Michael W. Ellis, Robert B. Moored and Baolian Yie, "Graphene-based electrochemical energy conversion and storage: fuel cells, supercapacitors and lithium ion batteries", DOI: 10.1039/c1cp21915d, Phys. Chem. Chem. Phys., 2011, **13**, 15384–15402

[2] Qiurong Shi, Younghwan Cha, Yang Song, Jung-In Lee, Chengzhou Zhu, Xiaoyu Li, Min-Kyu Song, Dan Du, and Yuehe Lina, "3D Graphene Based Hybrid Materials: Synthesis and Applications in Energy Storage and Conversion", Nanoscale, 2016, DOI: 10.1039/C6NR04770J.

[3] William S. Hummers Jr., and Richard E. Offeman, "Preparation of Graphitic Oxide", J. Am. Chem. Soc., 1958, 80 (6), pp-1339–1339 DOI: 10.1021/ja01539a017

[4] Xu Y., Sheng K., Li C., Shi G., "Self-assembled graphene hydrogel via a one step hydrothermal process", ACS Nano., 2010, 4-4324–30

[5] George Gorgolis and Costas Galiotis, "Graphene aerogels: a review" 2D Mater. 4 (2017) 032001, doi.org/10.1088/032001, 2053-1583/aa7883

[6] Izabela Kondratowicz, Kamila Z. Elechowska, Dominika Majdecka, Renata Bilewicz, "Synthesis and modification of reduced graphene oxide aerogels for biofuel cell applications", Materials Science-Poland, 33(2), 2015, pp. 292-300, DOI: 10.1515/msp-2015-0042

[7] Muhammad Adil Riaz, Gordon McKay and Junaid Saleem, "3D graphene-based nanostructured materials as sorbents for cleaning oil spills and for the removal of dyes and miscellaneous pollutants present in water", Environ. Sci. Pollut. Res. https://doi.org/10.1007/s11356-017-0606-x

[8] Nguyen S.T., Nguyen H.T., Rinaldi A., Nguyen N.P.V., Fan Z., Duong H.M., Colloid. Surface. A, 414 (2012), 352.

[9] Marcus A. Worsley, Tammy Y. Olson, Jonathan R. I. Lee, Trevor M. Willey, Michael H. Nielsen, Sarah K. Roberts, Peter J. Pauzauskie, Juergen Biener, Joe H. Satcher, Jr., and Theodore F. Baumann, "High Surface Area, sp2 -Cross-Linked Three-Dimensional Graphene Monoliths", dx.doi.org/10.1021/jz200223x, J. Phys. Chem. Lett. 2011, 2, 921–925

[10] Marcus Worsley et al, "Synthesis of Graphene Aerogel with high electrical conductivity", J. Am. Chem. Soc., 2010, 132 (40), pp 14067–14069)

[11] Cheng-Meng Chen, Qiang Zhang, Chun-Hsien Huang, Xiao-Chen Zhao, Bing-Sen Zhang, Qing-Qiang Kong, Mao-Zhang Wang, Yong-Gang Yang, Rong Caia and Dang Sheng Su, "Macroporous 'bubble' graphene film via template-directed ordered-assembly for high rate supercapacitors", Chem. Commun., 2012, 48, 7149–7151 7149

[12] Lianbin Zhang, Guoying Chen, Mohamed Nejib Hedhili, Hongnan Zhanga and Peng Wang, "Three-dimensional assemblies of graphene prepared by a novel chemical reduction-induced self-assembly method", DOI: 10.1039/c2nr32157b, Nanoscale, 2012, 4, 7038–7045

[13] C. Liu, H. Liu, A. Xu, K. Tang, Y. Huang, C. Lu, "In situ reduced and assembled three-dimensional graphene aerogel for efficient dye removal", Journal of Alloys and Compounds (2017), doi: 10.1016/j.jallcom.2017.04.245.-

# A Comparison of Proton transfer properties of PS and Nafion

Meltem Gör Bölen
Electrical and Electronics Engineering Department
Erzurum Teknik University
Erzurum, Turkey
meltem.gor@erzurum.edu.tr

Tevhit Karacali
Electrical and Electronics Engineering Department
Atatürk University
Erzurum, Turkey
tevhit@atauni.edu.tr

*Abstract—* **There are many parameters affecting performance of the fuel cell. One of these parameters is fuel crossover. In this work, first, porous silicon membrane that attracting attention due to its superior properties was produced using easier and less costly methods than the literature. Then, the fuel crossover performance of the produced membrane and Nafion membrane which is mostly preferred as the proton exchange membrane were tested and compared.**

**The fuel crossover performance of produced membrane was compared with the**

*Keywords-component; porous silicon membrane, fuel cell, crossover, formic acid*

## I. INTRODUCTION

Nanoporous silicon provides proton transmission through the nano-sized pores. In addition, the pores form diffusion barriers within large fuel molecules. Because of these properties, it is used as proton exchange membrane at proton exchange membrane fuel cells [1].

In our work, we have produced a porous silicon membrane for proton exchange membrane fuel cells and compared the fuel crossover test with Nafion 212, which is the most preferred proton exchange membrane. Nafion, which is often preferred as the proton exchange membrane, is not stable at high temperatures [1]. But porous silicon is resistant to high temperatures that affect fuel cell performance. For this reason, porous silicon membrane was used as an alternative of Nafion.

In this study, the wafer used was a boron doped (100) oriented p-type wafer with a resistivity of 0.001-0.005 $\Omega$cm and thickness of 200 $\mu$m. Anodization was preferred for controlled pore formation in hydrofluoric acid. The etching solution consists of ethane and hydrofluoric acid (1: 2 (v / v) HF (40%) / EtOH (99%)) [2,3]. In the literature, KOH, which is one of the anisotropic wet etchant, is usually used for etching. However, the etching rate of KOH is very low and depends on the temperature [4]. It has been proposed to increase the KOH temperature for reducing the etching time [5]. In this case, it is difficult to apply because all of the silicon surface needs to be contacted with KOH at the same temperature throughout the wafer. Therefore, a different solution was used to thining the silicon wafer. The solution known by the trade name "AFN 549" (HF: $HNO_3$: $CH_3COOH$: $H_2O$ = 10.2%: 39.5%: 23.2%: 27.1%) [6] which is one of the isotropic wet etchant for the convenience of application and time saving is preferred for thinning the silicon wafer.

## II. EXPERIMENTAL

When producing porous silicon, first, back surface of the silicon wafer with an area of 4.41 $cm^2$ was etched for 10 minutes. The wafer was thinned to 180 $\mu$m with the AFN 549 by placing in the Teflon® double tank cell. The cell was designed by us. Etching process was detailed in our study given in reference [7]. Second, the silicon wafer was cleaned with the RCA method. Third, due to the formation of pores through the silicon wafer, the grid structure was transferred onto the silicon wafer by photolithography to prevent the silicon wafer from scattering.

When determining of porous layer thickness as a function of current density and time, it has been observed that the linear relationship between porous layer thickness and time. But after some period of time, the relationship seems to be nonlinear rather than linear. For this reason, to form of porous layer with a thickness of 180 $\mu$m and with an active area of 3.61 $cm^2$, the anodization was carried out in a double tank cell by applying current densities of 5 and 10 mA/$cm^2$ for 80 and 40 minutes repeating 9 cycles respectively. The constant current density is applied between the two Pt electrodes with Keithley 2400 DC SourceMeter during anodization [8].

Table I. The effect of current density change on porous layer thickness

| Current Densitiy (mA/cm²) | Duration (min.) | Layer Tickness (µm) | Active Surface Area (cm²) |
|---|---|---|---|
| 5 | 80 | 10 | 3.61 |
| 10 | 40 | 10 | 3.61 |

Finally, instead of the preferred reactive ion etching (RIE) in the literature, the back surface of the sample was applied - 10 V for 1 hour to ensure that the pore tips were opened. In this way, pores opened through the sample and porous silicon membrane produced at lower cost, less time and simplicity [9]. The steps of our work are seen Fig. 1.
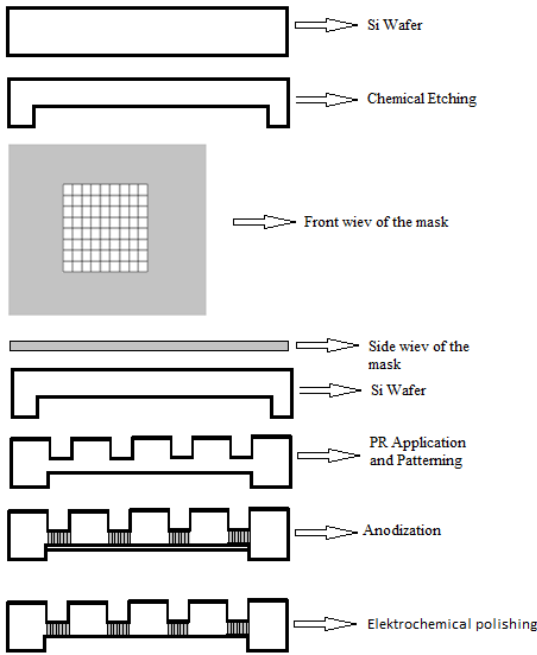
Figure 1. Thinning and PS formation steps

After membrane production was complete, the current values were measured without applying an electric field to the electrodes in order to study the crossover of the fuel through the membrane. The measurements were performed at room temperature. For fuel crossover test, formic acid was preferred due to its slowness and ease of water management [10].

III. RESULTS

The top view of the porous silicon produced with a layered structure by using current densities of 5 and 10 mA / cm$^2$ is seen Fig. 2. We obtained pores diameter of about 20 nm and porosity of 50%.
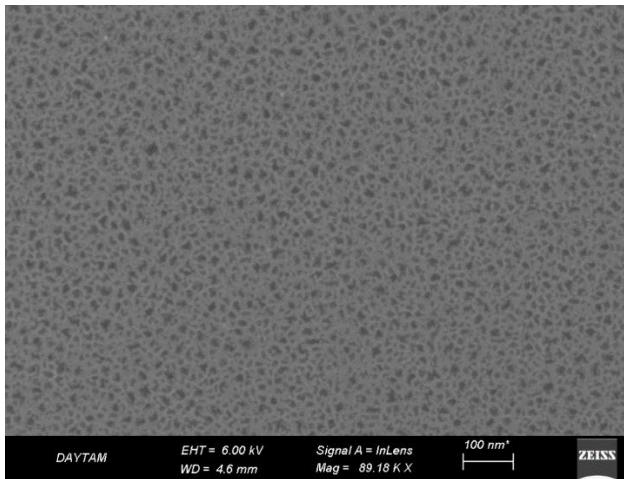


Figure 2. Top view of the porous silicon layer produced by a current density of 5 mA/cm$^2$ for 80 minutes and by 10 mA/cm$^2$ for 40 minutes

Produced porous silicon and Nafion 212 fuel crossover test were performed. Deionized water was placed on the cathode side and three formic acid solutions of 2,3 and 4M was placed on the anode side of the double tank cell. The current, between the two Pt electrodes, was measured as a function of time. Measurements were taken at room temperature and without any electric field applied. The

changes of the current values as a function of time were measured with Keithley 6514 for porous silicon membrane and Nafion 212 membrane. These results were recorded with the LABVIEW software developed by us. They are shown these values at Fig. 3 and Fig. 4 obtained with MATLAB.
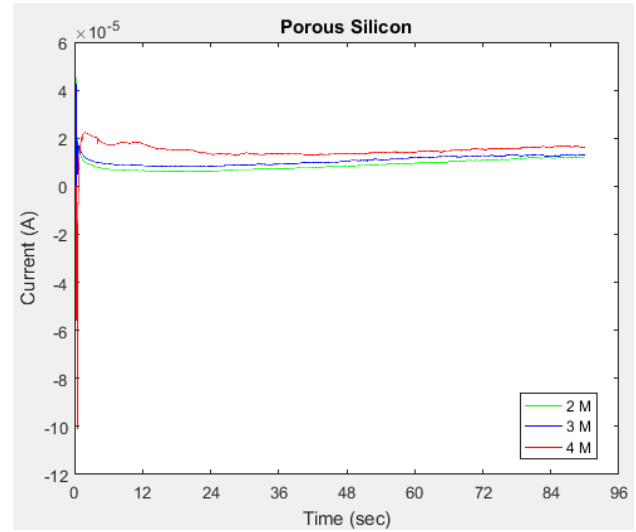


Figure 3. The current change for porous silicon membrane containing the formic acid solution during the experiments
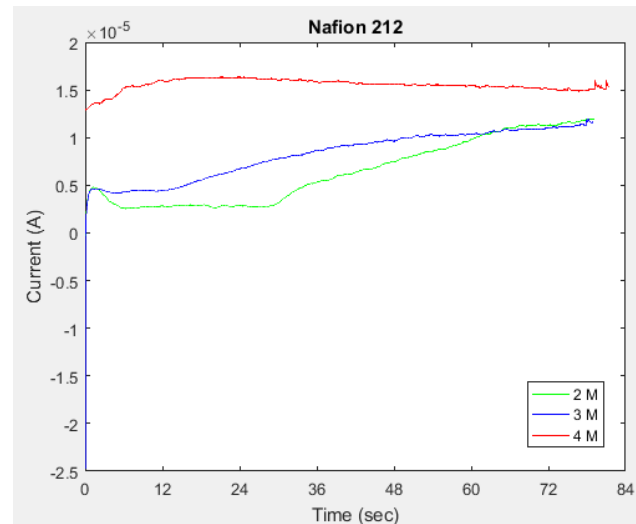


Figure 4. The current change for Nafion 212 membrane containing the formic acid solution during the experiments

As can be seen from the Figures, the currents started to vary from a certain value, but after some period of time, it started to take fixed values. It is understood that while the ion transfer occurs during the change of current, the concentrations were equalized from the steady state [9]. Nafion 212 reached the steady state later when the steady-state time to porous silicon was shorter. In addition, the current values were measured during ion passage were higher at porous silicon than Nafion 212. This indicates that the ratio of porosity in the porous silicon is high and the active surface area is wide, so that the ions are in the same time more and faster ion transition.

## ACKNOWLEDGEMENT

## REFERENCES

[1] Gold, S., Chu, K., Lu, C., Shannon, M.A., Masel, R.I. 2004. Acid loaded porous silicon as a proton exchange membrane for micro-fuel cells. Journal of Power Sources 135, 198–203. USA.

[2] T. Karacali, Darbeli anodizasyon tekniği ile gözenekli ve Si tabanlı fabry-perot yapılarının üretimi: Yapısal ve optik özelliklerinin incelenmesi. Doktora Tezi, Atatürk Üniversitesi.Fen Bilimleri Enstitüsü, Erzurum, 2014.

[3] M. Gör, ve T. Karacalı, The Production of a Silicon- Based Prooton-Excjange Membrane with Different Porosity Layers. Journal of Science and Technology,58-65, (2018).

[4] Nayak, A. P., Islam, M. S., & Logeeswaran, V. J. (2012). Wet Etching. Encyclopedia of Nanotechnology, 2829-2830. [5] Z. Xiang, C. Liu, C. Lai, Int. J. Electrıchem Sci., 3935-3948, (2014).

[5] Xiang Z., Liu C., Lai C., (2014). Corrosion of Fresh Porous Silicon in Potassium Hydroxide Solution Int. J. Electrıchem Sci., 3935-3948.

[6] www.microchemicals.eu/technical_information,

"Wet-Chemical Etching of Silicon" 2011-01-17.

A.   [7] M. Gör, ve T. Karacalı, Porous Silicon Based Membrane Fabrication for Proton Transportation. 13. Nanobilim & Nanoteknoloji konferansı, 2017.

[8] P. Granitzer, & K. Rumpf, Porous silicon—a versatile host material. Materials, 3(2), 943-998, 2010.

[9] M. Gör, ve T. Karacalı, Crossover of Ion Through Porous Silicon Based Membrane. 5th International Conferance on Electrical and Electronics (2018).

[10] Y. W. Rhee, S. Y. Ha, R. I. Masel, Crossover of formic acid through Nafion® membranes. Journal of Power Sources, 117(1-2), 35-38, 2003.

# Investigation of the effect of particulate size and stirring rate on copper removal from aqueous solutions with thermal drying-incineration waste

Sinan Kul
Emergency Aid and Disaster
Management *Bayburt University*
Bayburt, Turkey
sinankul@bayburt.edu.tr

Atila Taşdemir
Environmental Engineering
*Atatürk University* Erzurum,
Turkey atila.tasdemir@atauni.edu.tr

İbrahim Cengiz
Emergency Aid and Disaster
Management *Bayburt University*
Bayburt, Turkey
ibrahimcengiz@bayburt.edu.tr

*Abstract*—**In this study, biological wastewater treatment plant sludge is used as adsorbent for removal of Cu$^{2+}$ from aqueous solutions after thermal drying and incineration processes. Effect of different particle sizes of *(0,045-0,2 mm)* and stirring rates of *(100-400 rpm)* on adsorption capacity were investigated in batch studies. Removal efficiencies of Cu$^{2+}$ after one hour for particle sizes of <0,045mn, 0,045-0,18mm and 0,18-0,2mm were found as %51.2, %46.8 and %42.6. For stirring rates of 100, 200, 300, 400 rpm, removal efficiencies are calculated as %48.1, %49.7, %57.7 and %51.2.**

*Keywords—Adsorption; Cu$^{2+}$ removal*

## I. INTRODUCTION

Heavy metals formed as a result of industrial agricultural activities etc. are among the pollutants that need to be removed due to their toxic and carcinogenic effects to humans and aquatic life [1].

Wastewaters containing heavy metal ions are discharged to natural water bodies after a series of treatment processes [1]. Recent studies focus on the most appropriate alternative strategies that are cheaper but effective for treatment of heavy metal containing wastewaters [2].

Nowadays different methods are being used for treatment of heavy metal wastewaters. Most common methods used among these methods are coagulation, filtration, reverse osmosis, ion exchange and adsorption processes [3].

Eventhough use of low-cost and natural absorbents has become widespread, various modification processes are being applied to increase the adsorption capacity of natural adsorbents [2].

Sedimentable or floatable solid waste that is produced as a result of water and wastewater treatment can be defined as sludge. Sludge coming out from wastewater treatment effluent must be treated because of its harmful composition and without proper treatment it will cause damage to environment [4]. Treatment sludge contain high organic matter, nutrients, pathogenic microorganisms, and 70-80% water. Additionally, it includes 50-70% C, 6.5-7.3H, 21-24% O, 15-18% N, 1-1.5% P and 0-2.4 S before stabilization processes [4]. Such sludges are large in volume and their processing and disposal are faced with complexities to overcome in wastewater treatment area. It can be seen from Fig. 1 and Table 1 that especially some sludges like biological wastewater treatment plant's have high organic load create odor and degradation problems [5].



Fig. 1. Figures below are from different sludge dewatering methods. a) Sludge drying bed, b) Vakum filtration, c) Sludge belt press

Table 1. Typical solid concentrations of different sludge dewatering methods

| Sludge Type | Solid Concentration, %S | |
|---|---|---|
| | **Range** | **Typical** |
| **Primary Sedimentation** | 4,0 - 10,0 | 5,0 |
| **Activated Sludge** | 0,8 - 2,5 | 1,3 |
| **Trickling Filter Humus** | 1,0 – 3,0 | 1,5 |
| **Primary Sedimentation+ Activated Sludge** | 0,5 – 1,5 | 0,8 |
| **Anaerobic Digester Sludge** | 5,0 – 10,0 | 8,0 |

The thermal value of the sludge depends on the type of the sludge and the volatile solids content of the sludge. Thermal value of sludge is equivalent to the thermal value of some low quality coals (7700 cal/g dry matter). Average thermal value of raw primary sedimentation sludge is 6100 cal/g, activated sludge 5000 cal/g and anaerobic digester sludge is 2750-3000 cal/g. If thermal processes are to be used for final disposal of sludge, sludge must be dewatered enough to increase its thermal value [5].

Firstly, treatment sludge containing 73% water  is dewatered to 60% with thermal drying unit. After that sludge is taken into incineration unit where its water content is decreased to 1% by evaporating all water. At last, sludge is combusted at 650°C [5].

In this study, inorganic content of sludge obtained after thermal and combustion procedure of biological treatment sludge, is salvaged as adsorbent. With absorbent copper is removed from aqueous solutions by adsorption process and effect of particulate size and stirring rate is investigated [5].

## II. MATERIAL and METHOD

### A. Material

All chemicals used in the study were provided from Merck and Sigma brands.

In this study inorganic content of sludge obtained after thermal and combustion procedure of biological treatment sludge, is salvaged as adsorbent. Adsorbent used for

adsorption is washed with distilled water+$H_2SO_4$ to balance pH value and to increase its adsorption capacity. At last it's dried in 105°C oven. The adsorption capacity was increased by modifying the adsorbent without any additional cost.

### B. Method

The effects of particle size and stirring rate on the adsorption of copper ($Cu^{2+}$) from aqueous solutions were investigated by using waste activated treatment sludge in the wastewater treatment plant of Gaziantep Central Wastewater Treatment Plant. In studies in which particle size changes were examined, the adsorbents prepared in sizes of <0.0450, 0.045-0.18 and 0.18-0.2 mm were added to 250 mL erlenmayer in concentration of 0.2 g / 100 mL. The initial pH value was adjusted to 3.5 in aqueous solution containing 20 mg/L $Cu^{2+}$ at 20°C and a stirring rate of 200 rpm. In the study for changes in the stirring rate, the stirring rate was set to 100, 200, 300 and 400 rpm. In aqueous solution containing initial concentration of 20 mg/L $Cu^{2+}$ and particle size of 0.045-0.18 mm, pH value of 5 and adsorbent dosage of to 0.2 g / 100 mL were selected. The removal efficiencies of adsorption experiments were calculated by using Equation (1).

$$\% \, Removal = \frac{C_0 - C_t}{C_0} \times 100 \qquad (1)$$

In equation (1), $C_o$: Initial $Cu^{2+}$ concentration (mg/L), $C_t$: $Cu^{2+}$ concentration in time (mg/L).

### III. RESULTS and DISCUSSION

### C. Effect of Particle Size

Adsorbent obtained from the thermal drying-incineration of sludge used for adsorption of $Cu^{2+}$ from aqueous solution and effect of changing particle sizes of 0.045, 0.045-0.18 and 0.18-0.2 mm at 200 rpm, 20°C temperature, 3.5 pH and adsorbent dosage of 0.2g/100ml were investigated for 60 min. Results obtained are shown in Figure 2.
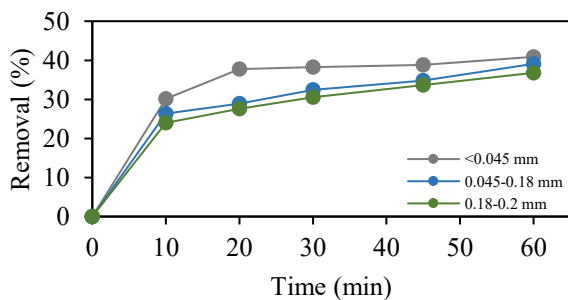


**Fig. 2.** Effect of particle size on adsorbtion (pH: 3.5 (natural), stirring speed: 200 rpm, initial concentration: 20 mg/L, adsorbent dosage: 0.2 gr/100 mL and temperature: 20°C±1)

Figure 2 shows that the removal effciency increases with decreasing particul size. Removal efficiencies of $Cu^{2+}$ for one hour calculated as %51.2, 46.8, 42.6 with particle size of <0,045 mm, 0,045-0,18 mm and 0,18-0,2 mm, respectively. Similar results are available in the literature [6].

### D. Effect of Stirring Rate

With adsorbent obtained from treatment sludge used to remove $Cu^{2+}$ from aqueous solutions. Effect of different stirring rate varied from 100 to 400 rpm was investigated at adsorbent dose of 0,2 g/100 mL, pH of 5 and temperature of 20°C for 60 mins. The results are shown in Fig. 3.
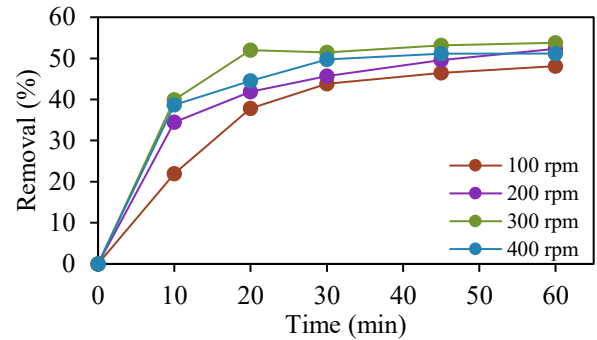


Fig. 3. Effect of stirring rate on adsorbtion of $Cu^{2+}$ (particle size: 0.045-0.18 mm, pH: 5, initial concentration: 20 mg/L, adsorbent dosage: 0.2 gr/100 ml, temperature: 20°C±1)

The $Cu^{2+}$ removal was determined as 48.1, 49.7, 57.7, and 51.2% at 100, 200, 300, and 400 rpm stirring speed respectively. A maximum removal of 57.7% was observed at stirring rate of 300 rpm. Moreover, when stirring rate increased from 300 to 400 rpm, the adsorption capacity decreased to 51.2% in 60 min. Increasing stirring rates increased the removal efficiencies to some extent, but after a point increasing stirring rate decreased the removal efficiency. Increasing stirring rates cause negative effects on the adsorption process after a point. Similar studies are available in the literatüre [7].

### IV. CONCLUSIONS

In this study, inorganic content of sludge obtained after thermal and incineration procedure of biological treatment sludge, is salvaged as adsorbent. With the absorbent copper is removed from aqueous solutions by adsorption process and effect of particulate size and stirring rate are investigated and results are listed below:

- Adsorbent used for removal of Copper from aqueous solutions is found to be useful.

- If results are examined, study shows that adsorbent used can be amplified for removal of copper.

### ACKNOWLEDGMENT

### REFERENCES

[1] B. Göze, "Sulu ortamdan ağır metal iyonlarının ve boyar maddelerin mikropolimerik malzemeler, kitin ve kitosan kullanılarak adsorpsiyon yöntemiyle giderilmesi," in Fen Bilimleri Enstitüsü, Hacettepe Üniversitesi, Ankara, 2013.

[2] O. Gök, Ö.Ç. Mesutoğlu, Ağır metallerin giderimi için düşük maliyetli adsorban olarak pirina kullanımı, Gazi Üniversitesi Mühendislik-Mimarlık Fakültesi Dergisi, 32 (2017).

[3] R. Hamutoğlu, A.B. Dinçsoy, D. Cansaran-Duman, S. Aras, Biyosorpsiyon, adsorpsiyon ve fitoremediasyon yöntemleri ve uygulamaları, Türkiye Hijyen ve Deneysel Biyoloji Dergisi, 69 (2012) 69.

[4] Ş. İrdemez, A.E. Yılmaz, E. Anlatıcı, Evsel atıksu arıtma çamurlarının termal kurutma-yakma prosesi ile uzaklaştırılmasında arıtma verimi–enerji ilişkisinin incelenmesi, Iğdır Üniversitesi Fen Bilimleri Enstitüsü Dergisi, 6 (2016) 65-73.

[5] E. Anlatıcı, Evsel atıksu arıtma çamurlarının termal kurutma-yakma prosesi ile bertaraf edilmesinde arıtma verimi–enerji verimliliği ilişkisinin incelenmesi, in: Fen Bilimleri Enstitüsü, Atatürk Üniversitesi, Erzurum, 2014.

[6] Z.E. Kul, Y. Nuhoğlu, S. Kul, Ç. Nuhoğlu, F.E. Torun, Mechanism of heavy metal uptake by electron paramagnetic resonance and FTIR: Enhanced manganese (II) removal onto waste acorn of Quercus ithaburensis, Separation Science and Technology, 51 (2016) 115-125.

[7] O. Sözüdoğru, B.A. Fil, R. Boncukcuoğlu, E. Aladağ, S. Kul, Adsorptive removal of cationic (BY2) dye from aqueous solutions onto Turkish clay: Isotherm, kinetic, and thermodynamic analysis, Particulate Science and Technology, 34 (2016) 103-111.

# Drawbacks in Carbon Supported Electrocatalysts of PEM Fuel Cells

Ayşe Bayrakçeken Yurtcan
Engineering Faculty, Department of
Chemical Engineering
Atatürk University
Erzurum, Turkey
abayrakceken@atauni.edu.tr

*Abstract*— **Proton exchange membrane fuel cells (PEMFCs) seem to be a good candidate for mobile and portable applications. The heart of a PEMFC is comprised of the electrode that half cell reactions occur and also a proton conducting membrane used as the electrolyte. Mostly carbon supported Pt based electrocatalysts are used as electrodes in PEMFCs. Carbon serves as a supporting material for Pt based nanoparticles by providing high surface area and high electrical conductivity. Material based issues affect the commercialization of PEMFCs. Supported nanoparticles used as electrode materials in PEMFCs have some problems during the long term operations of PEMFCs. Nanoparticles supported on carbon material tend to agglomerate in order to decrease its surface energy. Carbon material used can be corroded during the fuel cell operations. In this study, the drawbacks related with the carbon supported electrocatalysts of PEMFCs will be given.**

*Keywords—fuel cell, catalyst, carbon corrosion, Pt dissolution*

## I. INTRODUCTION

Proton exchange membrane (PEM) fuel cells are thought to be one of the most promising energy conversion system alternatives of the present century. They are compact, have light-weight and high power density. Besides, they do not need higher temperatures to operate. Considering all these good features, in recent years, concentration has been given to PEM fuel cells for making them commercial products. The most important component of a PEM fuel cell is the membrane electrode assembly where the half cell reactions and proton conduction occur. Hydrogen is fed at the anode side and it is oxidized to its protons and electrons. Protons pass through the proton conducting membrane and electrons are collected via an external circuit. These protons and electrons are reacted with the oxygen fed at the cathode side and water is formed (Fig. 1).
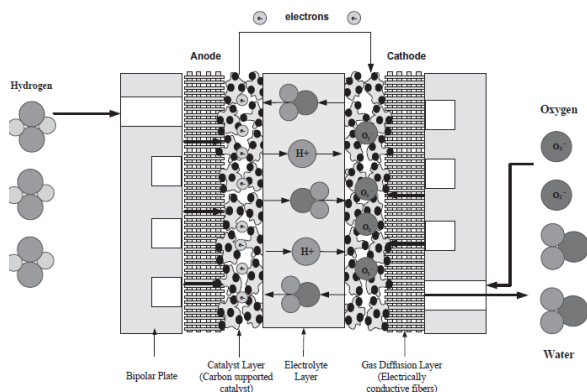


Fig. 1. Operating principle of a PEM fuel cell

Mostly carbon supported electrocatalysts are used in PEM fuel cells. It is targeted to increase the metal nanoparticle surface area by using a support material having high surface area and high electrical conductivity. In this respect, carbon based materials seem to be the most promising materials as supports. In PEM fuel cells, reactions are mentioned as half reactions because separate reactions occur at anode and cathode electrodes and their overall reaction gives the water production reaction.

Anode half cell reaction:

$$2H_2 \longrightarrow 4H^+ + 4e^- \quad E = 0.00V$$

Cathode half cell reaction:

$$O_2 + 4H^+ + 4e^- \longrightarrow 2H_2O \quad E = 1.23V$$

Overall reaction:

$$2H_2 + O_2 \longrightarrow 2H_2O \quad E = 1.23V$$
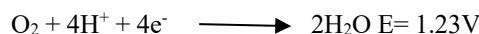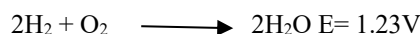
## II. DRAWBACKS IN CARBON SUPPORTED ELECTROCATALYSTS

Carbon supported Pt or Pt based catalysts are mostly used in PEM fuel cells [1]. Catalyst degradation is one of the major reasons for gradual performance losses and these losses can be mainly related to a loss in accessible surface area of the active catalysts. PEM fuel cells operate under harsh conditions. Anode side catalyst layer undergoes the effects of reducing $H_2$ atmosphere and on the other hand cathode side is exposed to high oxidized situations under high potentials [2]. Catalyst degradation in the long-term operation of PEM fuel cells is given as follows [3] (Fig. 2):

a) Pt dissolution

b) Migration and concomitant coalescence of Pt nanoparticles on the support

c) Detachment of Pt nanoparticles from the support
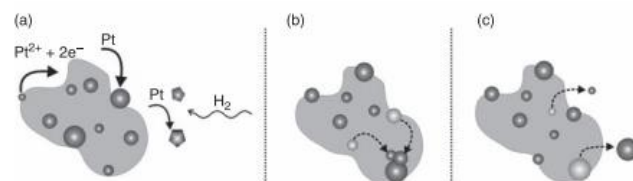


Fig. 2. Different degradation mechanisms (a) Pt dissolution leading either to re-deposition on larger Pt particle (electrochemical Ostwald ripening) or to the formation of Pt crystallites via the reduction with $H_2$ from the anode side

(b) Particle migration and coalescence (c) Particle detachment from the carbon support [3]

Pt dissolution is followed by two mechanisms; a) Pt re-deposition onto larger particles (electrochemical Ostwald ripening) b) precipitation of Pt crystallites close to the membrane electrolyte due to reduction via hydrogen diffusing through the membrane (Fig. 3). Both effects involve the transport of soluble platinum species through the electrolyte. In Ostwald Ripening mechanism, small particles have the lower stability which depend on the higher surface energy of the chemical potential of the phases [4]. Small particles migrate into through the electrolyte to the surface of larger particles where they are reduced again, while electrons are reaching the site via the carbon support. Ostwald ripening is potential dependent and happens above potentials of 0.8 V. Platinum dissolution leads to change in the morphology of the catalysts which causes decrease in the electrochemical surface area of the electrode [5].
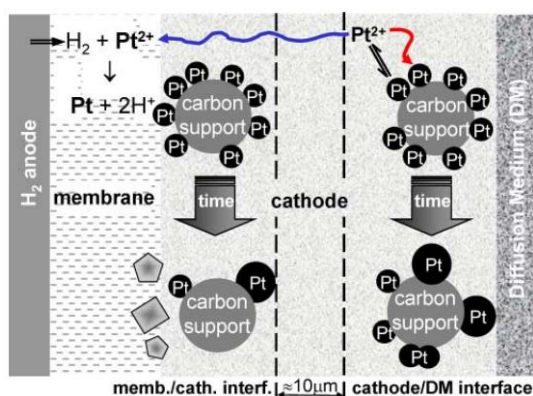


Fig. 3. Pt dissolution mechanisms [5]

Pt particles migration-coalescence can occur in PEM fuel cells without the need of Pt dissolution and re-deposition. The migration-coalescence degradation mechanism involves the migration of intact Pt nanoparticles on the carbon support and their coalescence upon impact with other Pt particles (Fig. 4). In general this process is readily observed in gas-phase sintering studies of Pt/C catalysts. Its identification at the solid–liquid interface is more difficult and based on comparison with models. The basis of these comparisons is that in contrast to the electrochemical Ostwald ripening process, a migration-coalescence mechanism should result in a tailing towards larger particle sizes in log-normal plots of the particle size distribution of aged catalysts. Crystallite migration of Pt on the carbon and coalescence cause a particle size growth and reduces the electrochemically active surface area. In contrast to Pt dissolution, migration and coalescence occur at operation potentials below 0.8 V which is predicted to be driven by Brownian motion and here Pt dissolution does not occur [4].
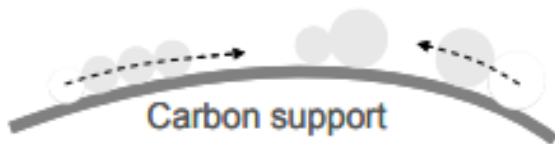


Fig. 4. Migration and concomitant coalescence of Pt nanoparticles on the support [4]

In addition to these mechanisms concerning Pt, the complete oxidation of the carbon support to carbon dioxide can occur under certain conditions, which results in the loss of electrical contact in between the Pt nanoparticles which is called carbon corrosion. The detachment of Pt nanoparticles from the carbon support and agglomeration of Pt nanoparticles, generally caused by carbon corrosion. In this mechanism, the loss of the mechanical/electrical contact of the Pt nanoparticles to the support is seen. The loss of electrochemical activity of fuel cell electrodes via carbon corrosion is dependent on the cell voltage, the nature of interactions between Pt nanoparticles and the carbon support, the degree of graphitization of carbon support, and potentially other factors, such as the RH value [4].
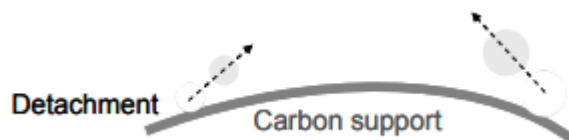


Fig. 5. Detachment of Pt nanoparticles on the support and/or agglomeration due to carbon corrosion [4]

Carbon corrosion of the commonly used carbon supports such as Vulcan is considered negligible at cell potentials lower than 0.8 V in low-temperature fuel cells, carbon corrosion and weight loss get significant at voltages higher than 1.1 V vs. RHE. The drawback related with carbon corrosion get significant at holding fuel cell for long operation periods, or at start and stop procedures or local fuel starvation where the local potential is increased. Besides the potential, the carbon corrosion kinetics depends on temperature, potential excursion duration, and catalysts and reactant concentration.

## III. CONCLUSIONS

Durability of PEM fuel cells strongly dependent on the materials used. Especially, for mobile and stationary applications, the durability targets of Department of Energy (DOE) for 2015 and the Japanese New Energy and Industrial Technology Development Organization (NEDO) to promote massive commercialization are 5,000 hours of operation for automotive application and 40,000 hours for stationary fuel cells over 10 years [6].

## REFERENCES

[1] P. Costamagna, S. Srinivasan, "Quantum jumps in the PEMFC science and technology from the 1960s to the year 2000: Part I. Fundamental scientific aspects", Journal of Power Sources, vol. 102, pp. 242, 2001.

[2] Y. Shao, G. Yin, Y. Gao, "Understanding and approaches for the durability issues of Pt-based catalysts for PEM fuel cell", Journal of Power Sources, vol. 171, pp. 558-566, 2007.

[3] C. Hartnig, C. Roth, "Polymer electrolyte membrane and direct methanol fuel cell technology". vol. 1, 2012.

[4] Y. Shao-Horn, W. C. Sheng, S. Chen, P. J. Ferreira, E. F. Holby, D. Morgan, "Instability of supported platinum nanoparticles in low-temperature fuel cells", Topic in Catalysis, vol. 46, pp. 285-305, 2007.

[5] W. Schmittinger, A. Vahidi, "A review of main parameters influencing long-term performance and durability of PEM fuel cells", Journal of Power Sources, vol. 180, pp. 1-14, 2008.

C. A. Rice, P. Urchaga, A. O. Pistono, B. W. McFerrin, B. T. McComb, J. Hu, "Platinum dissolution in fuel cell electrodes: Enhanced degradation from surface area assessment in automotive accelerated stress tests", Journal of The Electrochemical Society, vol. 162 (10), pp. F1175-F1180, 2015.

# The formation of transparent Glass-Ceramic thin film with changeable optical absorption

Mojtaba Farhangmehr

Nanoscience and Nanoengineering department of Tesla Tajhiz Nano company, Tabriz, Iran mfarhangm@gmail.com

Mehmet Ertugrul

Ataturk University, Engineering Faculty

25240 Erzurum

*Abstract*-In the research, nano crystalline of SrF2-Ge was deposited for optic applications. In this glass-ceramic systems, RF sputtering magnetron systems has been used for creating SrF2-Ge crystallization. The targets with the mole % combination 12.3SrO/3.7Al2O3/8.0Na2O/5.3K2O/10.4SrF2/60.3SiO2 and Ge (3%, 5% and 10%). nano crystalline SrF2-Ge samples is formed in 6h, 8h, 10h, 12h, 14h and 16h. After heat treatment, samples were obtain for different thickness using magnetron RF Sputtering system than heat treatment was made for the samples for selected temperatures from 570 to 610°C for 3 hours. The XRD analyses show good crystallization structure for 16h sample with ~500 nm thickness. Absorption and Transmittance analyses showed increasing light scattering with increasing time of coating and changing amount of absorption wavelength with adding germanium percentage.

*Keywords*- SrF2-Ge, XRD, Absorption & Transmittance analyses

## I. INTRODUCTION

In recent, there is an increasing interest in Glass-ceramics crystals. Their unique properties indicate a great potential for multiple photonic uses. Glass-ceramics including metal fluoride crystals, such as alkaline earth fluorides, with crystallite sizes in the limitation from 5 to 100 nm has numerous another uses too. [1–4]

So far, partially crystalline materials are not extensively used in photonic technology. The cause is the general problem of materials compound by more than one phase. In these materials generally light dispersion happens which can only be eluded, if either the refractile indices of the happening phases are the same at all related physical properties (like temperature, wavelength or size) of the crystals are little than moiety of incoming light 'wavelength. [5-6]

In principle, some different methods may lead to nano crystalline glass-ceramics. In one of these two methods, the first step is the growth of a liquid/liquid phase separated microstructure. The one of other ways is the deposition methods. in this research, used from thin film layers method for growing SrF2-Ge crystals by used of RF sputtering Magnetron Coating device from targets in composition of K2O/Na2O/ SrF2/SiO2/Al2O3/SrO/Ge.

## II. METHODS & MATERIALS

Target preparation is the first stage for the RF sputtering methods. We have used some materials with different percent of molarity for make a target of materials system. This target made from composition of 10.4SrF2, 12.3SrO, 3.7Al2O3, 5.3K2O, 8.0Na2O, 60.3SiO2 and Ge with three different percent (3%, 5% and 10%). Two of these materials i.e. K2O and Na2O were earn from reagent grade raw materials K2CO3 and Na2CO3 by using calcination method in 650°C. The 15 grams of this composition was cast in porcelain mortar and mixed for 3 hours then pour in 2 inch die-set and pressed under about 12 ton pressure then come to tablet form. So bring out the tablet from inside of die-set very slowly. put the tablet inside of furnace and heated to 700°C for 5 hour. then turned off the furnace and letting the target been cooling slowly.. For earning of better conductivity, must be stick a cooper disk (2inch × 2mm) with metal adhesive to the target for using in RF magnetron devices.

Because of low melting point of glass, we used quartz (10×10×1 mm) for substrate. All substrates were ultrasonically cleaned in heated acetone then ethanol. The target was placed in gun and substrates were fasten there places and distance between of them was 6 cm. after putting cover of device, vacuum process starting with mechanics pomp till pressure come $3.2 \times 10^{-3}$ torr, then starting turbo pomp and pressure come $5.6 \times 10^{-6}$ torr. For making plasma, we using argon and oxygen gases with high purity. Strontium fluoride-germanium films in vertical directions were deposited on quartz substrates by RF magnetron sputtering at 400°C temperatures of substrate and $2.3 \times 10^{-6}$ torr pressure.

At first, deposition process doing in 2 hour but XRD analyzes don't show any peaks and we examed this process for 6h, 8h, 10h, 12h, 14h and 16 hours too and the peaks of XRD analyzes was going to better result in create of glass-ceramic crystals. The best result was earned in 16h deposited samples. These samples thermally annealed in the range from 570°C up 610°C for 3h and crystals structure analyses earned by XRD results. XRD patterns were recorded by utilizing X-ray diffraction (D 5000 Siemens) with CuKα radiation. The absorption and transmittance spectrum of the heated instances were designated by using of UV Scanning Spectrophotometer.

## III. RESULTS & DISCUSSION

The no annealed samples showed increasing light scattering with increasing time of coating as shown in Fig.1. To obtain better crystal structure, we added Ge ( 3%, 5% and 10% ) powder to get the SrF2-Ge targets. We formed thin samples on quartz substrate for 16h using sputtering system. XRD analyses of samples don't show peaks for 3% samples and it means is amorphous but the first crystalline fraction of strontium can be observed in intensity peaks (2Θ = 29.06°) appear in 5% samples and in 10% coated samples, the peaks of germanium and strontium appears in 26°, 27°, 29° and 37°.

For the transmittance analyzes, transmittance was fallen near of 215 nm wavelength in 3% sample, it means that there is absorption in 215 nm (Fig.2.a). In second sample, the

absorption occur in 220 nm wavelength (Fig.2.b) and in third sample, the absorption occur in 225nm (Fig.2.c). So we can see that when the percentage of germanium changed, the amount of absorption is change too.

Figure 2b. Transmittance of %5Ge added sample



Figure 1. Absorption sprectrum of pure sample
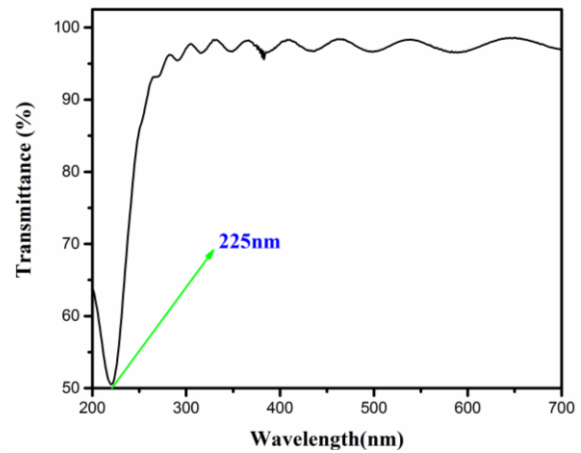


Figure 2.c. Transmittance of %10Ge added sample



Figure 2a. Transmittance of %3Ge added sample



Figure 2. Transmittance of %3Ge added sample

REFERENCES

[1]   Dejneka MJ. The luminescence and structure of novel transparent oxyfluoride glass-ceramics. J Non-Cryst Solids 1998;239:149–55.
[2]   Beall GH. Glass-ceramics for photonic applications. Glass Sci Technol 2000;73:3–11.
[3]   Mortier M, Monteville A, Patriarche G, Maze G, Auzel F. New progresses in transparent rare-earth doped glass-ceramics. Opt Mater 2001;16:255–67.
[4]   Kenyon AJ. Recent developments in rare-earth doped materials for optoelectronics. Prog. Quantum Electron 2002;26:225–84.
[5]   Qiao X, Fan X, Wang M, Zhang X. Spectroscopic properties of Er3+ and Yb3+ co-doped glass ceramics containing SrF2 nanocrystals. J Phys D: Appl Phys 2009;42:055103.
[6]   Qiao XS, Fan XP, Xue Z, Xu XH, Luo Q. Upconversion luminescence of Yb3+/Tb3+/Er3+-doped fluorosilicate glass ceramics containing SrF2 nanocrystals. J Alloys Compd 2011;509:4714–21.

# Antibiofilm Effect of Levofloxacin-Loaded Polymeric Nanoparticles against *Staphylococcus aureus*

Ayşe Üstün
Department of Molecular Biology and Genetics
Erzurum Technical University
Erzurum / Turkey
ayseustun2@gmail.com

Alpgiray Turgut
Department of Molecular Biology and Genetics
Erzurum Technical University
Erzurum / Turkey
agiraytrgt@gmail.com

Büşra Albayrak
Department of Molecular Biology and Genetics
Erzurum Technical University
Erzurum / Turkey
busra.albayrak.b@gmail.com

Abdul Saltuk Buğra Daş
Department of Molecular Biology and Genetics
Erzurum Technical University
Erzurum / Turkey
bugra.das@gmail.com

Ayşenur Yazıcı
Department of Molecular Biology and Genetics
Erzurum Technical University
Erzurum / Turkey
aysenur.ozdemir@erzurum.edu.tr

*Abstract*— Biofilm is a group of microorganisms living in a polymeric structure that is sticked to biotic and abiotic surfaces. The strategies developed for the prevention of bacterial biofilms that cause many infections are great importance. In this study, the effect of levofloxacin loaded poly-lactic-co-glycolic acid (PLGA) drug delivery system against *Staphylococcus aureus* (ATCC 25923) biofilm was evaluated. Firstly, levofloxacin-loaded nanoparticles were prepared by emulsification solvent evaporation (ESE). The prepared drug delivery system was applied to *S. aureus*. Crystal violet (CV) assay was used to evaluate the antibiofilm effect of the drug delivery system. For the purpose of the control, only the drug (levofloxacin) and the empty polymer which were only drug free, were examined for the presence of antibiofilm effect. As a result, PLGA nanoparticles loaded with levocloxacin were found to be more effective on biofilm cells compared to the drug alone.

*Keywords— Biofilm, Drug delivery system, Levofloxacin, Staphylococcus aureus*

# Synthesis of core-shell SiO2 / TiO2 Nanoparticles and Determination of their Photocatalytic Activity

Taner Tekin
Department of Chemical Engineering
Atatürk University
Erzurum/TURKEY
ttekin@atauni.edu.tr

Derya Tekin
Department of Metallurgical and
Materials Engineering
Atatürk University
Erzurum/TURKEY
deryatekin@atauni.edu.tr

Hakan Kızıltaş
Department of Chemical Engineering
Atatürk University
Erzurum/TURKEY
h.kiziltas@atauni.edu.tr

*Abstract*— SiO2 and SiO2@TiO2 nanoparticles were synthesized by Stöber and solvothermal method, respectively. The characterization of synthesized nanoparticles was determined by SEM-EDS and XRD analyzes. The photocatalytic activity tests were tested on Acid Red 27 dye and the photocatalytic activity of SiO2 @ TiO2 photocatalysts was found to have higher photocatalytic activity compared to commercial TiO2 (Degussa 25).

*Keywords*— *photocatalyst, core-shell, photocatalytic decomposition, SiO2/TiO2*

## I. INTRODUCTION

Due to its electronic, optical properties and good chemical stability, TiO2 is still the most widely used photocatalyst based on cost-benefit ratio. TiO2 is frequently used in photocatalysis, self-cleaning coatings, dye-sensitive solar cells, nanoparticul face masks, medical devices in antibacterial coatings and optoelectronic energy storage devices [1-3]. However, photocatalysis with TiO2 is very closely related to physical properties such as surface area of titanium, crystallinity, morphology, particle size and crystalline phase, and anatase is the most active form of photocatalyst of TiO2. Despite the excellent properties of TiO2, there are some problems with nanometric TiO2, which makes practical applications difficult and costly. Such problems include agglomeration of the nanoparticles, phase transformation, reduction in surface areas after heat treatment, recombination of the photorealized electron-hole pair, lack of visible photoactivity due to the broadband range, and difficulty in recovering the nanoparticles from the aqueous suspension [4, 5].

In order to overcome these problems, titanium and other functional metals / metal oxide nanoparticles are coated in the form of a layer on the surface of thermally stable, low cost and high surface area core materials such as SiO2, ZrO2, MoO3 and Fe2O3. The ability to synthesize silicon, rich and well-known surface chemistry and adsorption capacity as easy and controllable by the Stöber method is one of the best core materials to prepare catalysts due to optical transparency [2, 6, 7]. Another advantage of using SiO2 as the core material is that, for example, with improved properties, the shell material can be easily separated from the core @ shell structure with an alkali solution to obtain porous hollow spheres [8].

In order to increase the photocatalytic activity of TiO2, TiO2 nanoparticles were synthesized as a shell by the solvothermal method. SEM-EDS and XRD analyzes were performed to characterize the synthesized SiO2 @ TiO2 core-shell photocatalysts. The photocatalytic effect of the photocatalysts produced is based on Acid Red 27 dye.

## II. EXPERIMENTAL

### A. Materials

Ethanol (Sigma Aldrich, 99.8%), tetraethyl orthosilicate (Sigma Aldrich, 99%), ammonium hydroxide (Sigma Aldrich, 25%) and distilled water were used for the synthesis of SiO2 nanoparticles.

Ethanol (Sigma Aldrich, 99.8%), zinc acetate dehydrate (Sigma Aldrich, 99%), sodium hydroxide (Sigma Aldrich, 99%) and distilled water were used to add ZnO on the produced SiO2 nanoparticles.

### B. Synthesis of SiO2 Nanoparticles

5 ml of 25% (w / w) NH4OH was added the solution consisting of 80 ml of ethanol + 20 ml of deionized water and continue to be stirred for 5 minutes. 1 ml of TEOS was added the solution medium under ultrasonic stirring. the solution was ultrasonically stirred for 3 h under 45% amplitude. SiO2 nanoparticles are removed from the solution medium at 5000 rpm by centrifugation. After washing with ethanol, it is allowed to dry at 110 ° C for 2 hours.

### C. Synthesis of SiO2 @ TiO2 Nanoparticles

1 g of SiO2 nanoparticles, which have been previously synthesized and subjected to drying, are added to a solution of 56 ml of ethanol + 3.5 ml of titanium butoxide (TBT) and mixed under ultrasound for 15 minutes. Then 200 ml of Teflon autoclave is placed in the reactor. 14 ml of distilled water is placed in the reactor in a way not to touch the solution and kept in the oven at 150°C for 12 hours. The autoclave reactor was cooled to room temperature and the nanoparticles were removed from the solution medium at 5000 rpm by centrifugation. The nanoparticles were washed 5 times with distilled water and ethanol, and dried at 60 ° C for 3 hours. The calcination process was performed at 500°C for 3 hours.

### D. Photocatalytic Activity Tests

Photocatalytic experiments were carried out in a jacketed reactor. The reaction temperature was kept constant at 25°C with a programmable constant temperature water circulator. A 44 W/m2 (257 nm) UV lamp was immersed the dye solution as a source of light. O2 is provided the reaction medium by pumping air at constant flow rate.

## III. RESULT AND DISCUSSION

The results of SEM and EDS analysis for SiO2 nanocomposites are given in Figure 1.
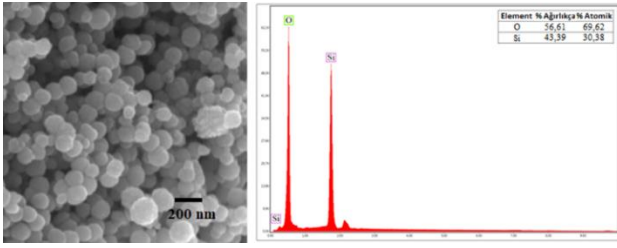


**Figure 1.** SEM and EDS analysis of SiO2 nanoparticles

As shown in Figure 1, the SiO2 nanoparticles show good monodispersion and have completed their spherical formation. SiO2 nanoparticles have diameters in the range of 160 to 260 nm, with an average diameter of approximately 220 nm. Silicon and oxygen have been proven by EDS analysis of SiO2 nanoparticles.

The results of SEM and EDS analysis for the characterization of SiO2@TiO2 nanoparticles synthesized by solvothermal method are given in Figure 2.
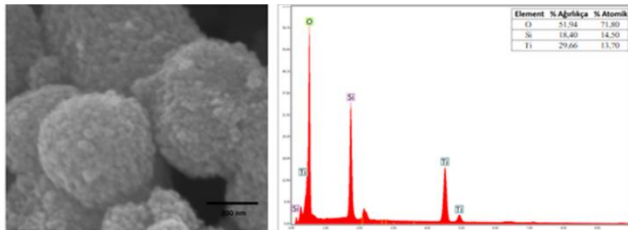


Figure 2. SEM and EDS analysis of SiO2@TiO2 nanoparticles

As shown in Figure 2, the synthesized SiO2@TiO2 nanoparticles show a homogeneous distribution. TiO2 nanoparticles coated on the surface of SiO2 appear to be scattered on the surface in the form of granules. This porous structure increases the contact surface area and increases the efficiency of photocatalytic decomposition. The SiO2@TiO2 nanoparticles have diameters in the range of 185 to 285 nm, with an average diameter of approximately 240 nm and are larger than SiO2 nanoparticles. The presence of silicon, titanium and oxygen has been proven by the EDS analysis of SiO2 @ TiO2 nanoparticle.

Figure 3 shows the XRD analysis of SiO2 and SiO2 @ TiO2 nanoparticles.
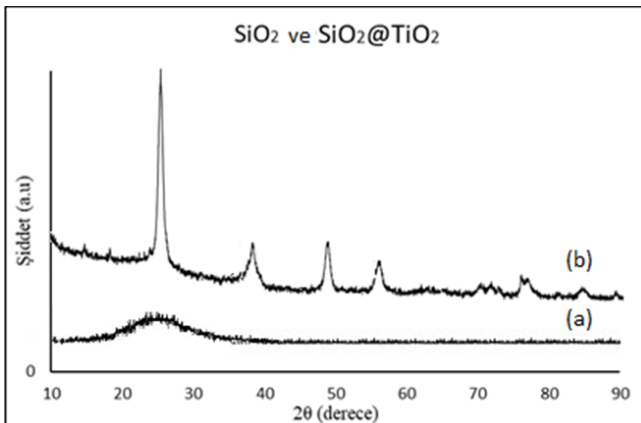


Figure 3. XRD pattern of SiO2 and SiO2 @ TiO2 nanoparticles

As shown in Figure 3, no sharp peak corresponding to SiO2 was observed due to the fact that the synthesized SiO2 nanoparticle had amorphous structure, but a wide peak at a low diffraction angle of 20 ° to 30 ° was observed. The diffraction peaks of the synthesized SiO2@TiO2 nanoparticles at 25,27, 37,48, 48,87 and 58,262 show the planes of the (101), (004), (200) and (211) tetragonal anatase of the TiO2, respectively. Due to the amorphous shell SiO2 nanoparticles, a wide peak at a low diffraction angle of 20 ° to 30 ° is observed.

The photocatalytic degradation graph of Acid Red 27 dye is given in Figure 4 for SiO2, SiO2@TiO2 and TiO2 nanoparticles (Degussa-25).
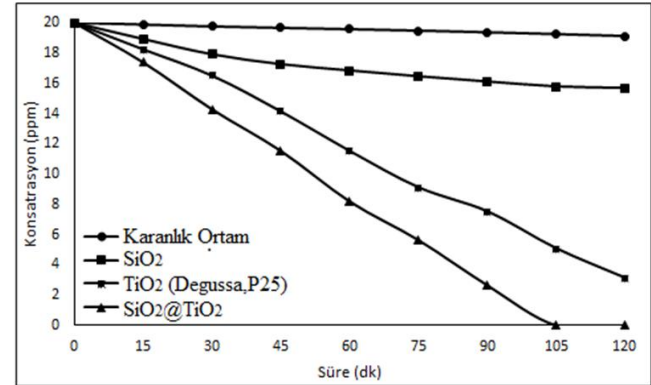


Figure 4. Graph for photocatalytic decomposition of Acid Red 27 solution

The photocatalytic activity of the nanoparticles was performed on Acid Red 27 dye in a batch reactor. Figure 4 shows a graph of dye decomposition on the nanoparticles in the batch reactor. During the 120-minute period, the nanoparticles adsorbed the average 4.4% of dye in the dark medium. After 120 minutes, SiO2 nanoparticles removed 11.5% of the dye. While the 120-minutes removal of TiO2 (Degussa, P25) nanoparticles was 84.36%, SiO2 @ TiO2 nanoparticles showed 100% removal within a period of 90-105 minutes.

## IV. CONCLUTION

SiO2 and SiO2@TiO2 nanoparticles were synthesized by Stöber and sol-gel method, respectively. The characterization of synthesized nanoparticles was determined by SEM-EDS and XRD analyzes. The photocatalytic activity tests were tested on Acid Red 27 dye and the photocatalytic activity of SiO2@TiO2 photocatalysts was found to have higher photocatalytic activity compared to commercial TiO2.

## REFERENCES

[1] Linsebigler, A.L., G. Lu, and J.T. Yates, Photocatalysis on TiO2 Surfaces: Principles, Mechanisms, and Selected Results. Chemical Reviews, 1995. 95(3): p. 735-758.

[2] Ullah, S., et al., Enhanced photocatalytic properties of core@shell SiO2@TiO2 nanoparticles. Applied Catalysis B: Environmental, 2015. 179: p. 333-343.

[3] Evans, P. and D.W. Sheel, Photoactive and antibacterial TiO2 thin films on stainless steel. Surface and Coatings Technology, 2007. 201(22): p. 9319-9324.

[4] Mandzy, N., E. Grulke, and T. Druffel, Breakage of TiO2 agglomerates in electrostatically stabilized aqueous dispersions. Powder Technology, 2005. 160(2): p. 121-126.

[5] Herrmann, J.M., Heterogeneous photocatalysis: Fundamentals and applications to the removal of various types of aqueous pollutants. Catalysis Today, 1999. 53(1): p. 115-129.

[6]   Li, W. and D. Zhao, Extension of the stöber method to construct mesoporous SiO2 and TiO2 shells for uniform multifunctional core-shell structures. Advanced Materials, 2013. 25(1): p. 142-149.

[7]   Fink, D.J., Strategic Warfare. Science and Technology, 1968: p. 62.

[8]   Joo, S.H., Biomol. Ther., 2012. 20: p. 2.

# Investigation of multiple enzyme activity of thermophilic *Bacıllus* specıes

Damla Ruzgar
Department of Molecular Biology and Genetics
Erzurum Technical University
Erzurum, Turkey
damlaaruzgar@gmail.com

Arzu Gormez
Department of Molecular Biology and Genetics
Erzurum Technical University
Erzurum, Turkey
arzugormez@erzurum.edu.tr

Ebru Oztas Gulmus
Department of Molecular Biology and Genetics
Erzurum Technical University
Erzurum, Turkey
ebru.oztas@erzurum.edu.tr

Derya Efe
Department of Medicinal and Aromatic Plants
Espiye Vocational School
Giresun University
Giresun, Turkey
deryayanmis@yahoo.com

*Abstract*— The most commonly used group to produce biotechnological enzymes is thermophilic microorganisms. Their enzymes can catalyze biochemical reactions at very high temperatures. Thermophilic enzymes are more stabile and active against pH changes and high temperatures, exhibit optimum activity at higher temperatures than the optimum growth temperatures of microorganisms and do not allow microorganism contamination in the environment at high temperatures, they significantly increase the diffusion rates and solubilities of the materials involved in the reaction, thus allowing more product formation. In this study, it is aimed to isolate thermophilic *Bacillus* species with industrial enzyme activities from hot water sources in Erzurum province. The isolates were identified by amplification and analyses of 16 S rRNA gene region. As a result of identification of 16 bacterial isolates, four different *Bacillus* strain (*B. firmus*, *B. siralis*, *B. pumilus* and *B. circulans*) were determined. Besides, the bacteria were evaluated for protease, amylase and lipase activities.

*Keywords*— *Bacillus spp., Protease, amylase, lipase, 16s rRNA sequence*

## I. INTRODUCTION

Temperature is an important factor for microbial growth. Microorganisms can be classified under three main groups as psychophiles, mesophiles and thermophiles based on their temperature for growth. Psychrophiles are microorganisms that can grow in temperatures less than 15 °C, mesophiles in temperature 15-45 °C, and thermophiles above 45 °C [1,2]. The extremophiles can live from volcanoes with very high temperature values, to poles with very low temperatures, from high pH values (pH 10-12) to low pH values (pH 0-3) due to their cell membranes, enzymes, nucleic acids, proteins and a number of cell structures. They have an enzyme called as reverse DNA gyrase making positive supersarmal in DNA. This enzyme increases the melting point of DNA and makes more resistant to a denaturation which occur with heat effect [6,7,8]. They have also saturated fatty acids in the cell membranes that give a hydrophobic structure to the cell and hydrophobic interactions and electrostatic disulfide bridges that give stability to biological structures. Additionally, structures based on the interaction of two opposing charged ions, called salt bridges or ion pairs, are another adaptation mechanism seen in thermophiles [9,10].

Thermophilic microorganisms have been widely used for biotechnological applications due to the ability of their enzymes catalyzing biochemical reactions at very harsh conditions. The enzymes originating from the microorganisms preferred in the industry. Because, they have higher catalytic activity and stability compared to the enzymes of plants and animals. In addition, they can be more economically obtained in large quantities as well as high purity. They do not even create by-products. Also, microorganisms grow rapidly and can utilize from cheap sources. Many industrial wastes can be considered as substrates for the enzymes of microorganisms [5, 19,20,21,22,23].

Recently, the demand for thermophilic enzymes have been increasing due to their benefits in industrial applications [24,25]. In terms of biotechnological processes, if temperature increases, solubility, diffusion rates of organic compounds and reaction speed will increased and unwanted viscosity of the environment will be reduced [23,25]. At the same time, the use of thermophilic enzymes in biotechnological applications will prevent contamination of other microorganisms. The biotechnologically important thermophilic enzymes have marketshare 59% for proteases, 28% enzymes of carbohydrates and 3% for lipases. Proteinase is used for milk precipitation, meat smoothing, cakes, bread, biscuits, crackers, silage production, fabric bleaching, detergent industry, leather, lipase for oil based detergent industry, interesterification of oils, milk and food industry, galactosidase for milk and cheese industry, amylase for starch hydrolysis, baking, silage production, alcohol fermentation, detergent industry, cheese making, textile, food industry, cellulose for animal feed industry, food industry, testill and paper industry, chitinase for pharmaceutical industry, for xylinase for starch gluten separation, bread volume expansion, paper industry and pectinase for food and textile industry [17,27,28]. The isolations of thermophile bacteria have been carried out generally from various hot water sources and hydro-wells [3,4,5].

In this study, it is aimed to isolate thermophilic *Bacillus* species with industrial enzyme activities from hot

water sources in Erzurum province. Then, the bacteria were searched to have protease, amylase and lipase activities.

## II. MATERYAL-METOD

### A. Isolation and Purification of Thermophilic Bacteria

In the research, water samples were taken from the thermal water sources in winter (December-January) and spring periods (April) under aseptic conditions. The samples were grown in NA, TSA, PCA and LBA solid and NB, TSB and LB broth media. Cultures were incubated at 45 °C, 55 °C and 65 °C. Developing bacterial colonies were examined and morphologically different ones were selected and pure cultures of these colonies were prepared and incubated for 24 hours. At the end of the incubation, stored at -80 °C in 30% glycerol and Luria Bertani Broth (LB) for further studies.

### B. Identification of Bacterial Isolates

The isolation of DNA from bacterial isolates was performed according to the method described by Kohoodoo and Jaufeerally-Fakim (2004). Sequencing of 16S rRNA of the isolates and amplifications of the target gene were done using the universal bacterial primer 1492R (5′- TAC GGY TAC CTT GTT ACG ACT T-3′) and the domain bacteria-specific primer 27F (5′- AGA GTT TGA TCM TGG CTC AG-3′). Amplification of DNA was carried out under the following conditions: denaturation at 94°C for 5 min followed by 34 cycles of 94°C for 1 min, binding 34 cycles of 48°C for 30 s, 72°C for 1.5 min, and final extension at 72°C for 8 min. Amplified PCR products of bacterial isolates were analyzed by electrophoresis with 1% agarose gel.

Amplified PCR products were cloned into pGEM-T Easy vector. 50 μl of plasmid samples were taken. Samples was sent to the Medsantek Company for sequence analysis (Turkey). Sequence results were interpreted using the BioEdit program. 16S rDNA sequences were compared to the bacterial sequences registered with the GenBank (http://blast.ncbi.nlm.nih.gov/blast.cgi) (BLAST analysis). In this way, bacterial isolates were identified at species level [29].

### C. Determination of Enzyme Properties of Bacterial Isolates

#### Amylase Test

This test is carried out to determine whether bacterial isolates break down starch through the enzyme amylase. Bacterial isolates were incubated for 3 days by striking in NA medium containing 1% starch. At the end of the incubation period, petri dish was treated with leucol solution.The ones giving blue color were negatif, the ones forming open zone around the lines were considered positive [22].

#### Protease Test

This test is carried out to determine the hydrolysis casein protein of bacteria isolate with presence of protease enzyme. For this purpose, medium containing 10% skim milk was incubated for 3 days by streaking. The zones around the colonies were evaluated as positive [22].

#### Lipase Test

This test is performed in order to analyze the presence of lipase enzyme that hydrolyzes oils in bacterial isolates. The used medium was prepared with 1.25 g pepton, 0.75 g meat extract, 2.5 g butter and 3.79 g agar in 250 ml. Bacterial isolates were incubated for 3 days by streaking.The zone formation seen after incubation was evaluated as positive [18].

## III. RESULTS AND DISCUSSION

The identification of the isolates was assessed by the 16S rRNA sequencing. Sequence analysis showed high similarity with those of the reference strains available in the GenBank databases. (Table I).

Bacterial isolates collected from hot water sources were evaluated for amylase, protease, lipase activities (Table II). Fourteen isolates have both amylase and protease and lipase activity. Multiple enzyme activity is very important in detergent industry. It has a high rate of preference because of the high activity of the product.

There are many literatures reported that *Bacillus* species have remarkable protease, amylase and lipase activities among thermophilic bacteria. Our results supported by the literature. Microorganisms have generally special adaptions their living environment. Therefore, the same species of the same genus can show different characteristics if they grow in different conditions. In the light of this information, the enzymes of the isolated bacteria can be more suitable than the enzymes searced before. In the future, it is planned to study biochemical characterization and purification of the enzymes.

Table 1. the results of 16s rrna sequencing

| Strain Code | Strain Name |
|:-----------:|:------------|
| IK2 | *Bacillus circulans* |
| IK3 | *Bacillus firmus* |
| IK5 | *Bacillus firmus* |
| IK7 | *Bacillus circulans* |
| IK8 | *Bacillus firmus* |
| IK10 | *Bacillus circulans* |
| IK12 | *Bacillus circulans* |
| IK15 | *Bacillus siralis* |
| NK14 | *Bacillus pumilus* |
| HY3 | *Bacillus siralis* |
| HY9 | *Bacillus firmus* |
| IY3 | *Bacillus firmus* |
| IY8 | *Bacillus firmus* |
| IY10 | *Bacillus firmus* |
| IY11 | *Bacillus circulans* |
| HK7 | *Bacillus circulans* |

Table 2. The results of Enzyme activities

| Isolates Code | Enzymes | | |
|---|---|---|---|
| | Amylase | Protease | Lipase |
| HK7, IK2, IK7, IK10, IK12, IY11, IK3, IK5, , IK8, , HY9, IY3, IY8, HY3, IY10 | + | + | + |
| IK15 NK14 | - | + | + |

## REFERENCES

[1] Baker, G.C., Gaffar, S., Cowan, D.A. and Suharto, A.R., 2001. Bacterial community analysis of Indonesian hot springs. FEMS Microbiology Letters, 200(1), pp.103-109.

[2] Madigan, M.T. and Martinco, J.M. and Parker, J., 2008. Procaryotic Diversity The Archaea. Brock Biology of Microorganisms, 546-571.

[3] López-García, P. 1999. DNA Supercoiling and Temperature Adaptation: A Clue to Early Diversification of Life? Journal of Molecular Evolution, 49(4), 439-452. doi:10.1007/PL00006567

[4] Kumar, S. and Nussinov, R. 2001. How Do Thermophilic Proteins Deal With Heat? Cell Mol Life Sci, 58(9): 1216-1233.

[5] Haki G. D., Rakshit S. K., 2003. Developments in Industrially Important Thermostable Enzymes a Review. Bioresource Technology., vol. 89, p. 17-34.

[6] Fujiwara S (2002) Extremophiles: Developments of their special functions and potential resources. Journal of Bioscience and Bioengineering 94, 518-525

[7] Hakamada, Y., Hatada, Y., Ozawa, T., Ozaki, K., Kobayashi, T., & Ito, S. (2001). Identification of thermostabilizing residues in a Bacillus alkaline cellulase by construction of chimeras from mesophilic and thermostable enzymes and site-directed mutagenesis. FEMS microbiology letters, 195(1), 67-72.

[8] Castro, G.R., 1999. Enzymatic Activities of Proteases Dissolved in Organic Solvent. Enzyme and Microbial Technology, Vol.25, p. 689-694.

[9] lame, S, Pembeci, C., Borcakl, M., Batumi, M. Rice, Ö., 2000. Investigation of Turkey's agricultural microflora of Industrial Importance Some Enzymatic Activity II: Amylase, Protease, Lipase. Turk J Biol. vol., 24, p. 79-93

[10] Özdemir S., 2004. Production of α-amylase by Bacillus sp. Master Thesis, D.Ü. Graduate School of Natural and Applied Sciences

[11] Matpan, F., 2007. Diyadin (Ağrı) Isolation of Bacteria from Hot Water Resources and Studies on Some Enzymes. Dicle University, Institute of Science and Technology, Department of Biology

[12] Malle, D., Pıcarıma, J., Huwae, L.C., Rahmawatı, I. and Purbowasıto, W., 2012. Isolation and Identification of a Thermostable Amylase-Producing Bacterium from Hatuasa Hotspring. Microbiology Indonesia, 6(2), p.5.

[13] İnce, E., 2006. Isolations of extreme thermophilic anaerobic bacteria produce xylanase and determination of their enzymes properties.

[14] Malle, D., Pıcarıma, J., Huwae, L.C., Rahmawatı, I. and Purbowasıto, W., 2012. Isolation and Identification of a Thermostable Amylase-Producing Bacterium from Hatuasa Hotspring. Microbiology Indonesia, 6(2), p.5.

[15] Castro, H., Abreu, P., Geraldo, R., Martins, R., Santos, R., Loureiro, N., Cabral, L. and Rodrigues, C. 2010. Looking at the Proteases from a Simple Perspective. Journal of Molecular Recognition, 24, 165-181

[16] Adiguzel, A., Agar, G., Baris, O., Gulluce, M., Sahin ,F., Sengul, M., 2006. RAPD and FAME analysis of Astragalus species growing in eastern Anatolia region of Turkey. Biochemical Systematics and Ecology, 34(5): 424-432.

[17] Beldüz, A. O., Dülger, S., Demirbağ, Z., 2003. Anoxybacillus gonensis sp. nov., a Moderately Thermophilic, Xylose-Utilizing, Endosporeforming Bacterium. Int J Syst Evol Micr, 53: 1315-1320.

[18] Adiguzel A., I. K., Sahin F., Ozbek T., Gulluce M., Belduz A.O., Baris O., 2011. Molecular Diversity of Thermophilic Bacteria Isolated From Erzurum City Pasinler Hot Spring (Erzurum/Turkey). Turkish Journal of Biyology, 35(3): 267-274.

[19] Pirinççioğlu, H., 2010. Isolation and Identification of Thermophilic Bacteria from Dargeçit and Güçlükonak Hot Water Resources. Master Thesis, Dicle University, Institute of Science, Department of Biology

# Isolation and Identification of Pigment Producing Bacteria and Evaluation of Their Usage Potentials as Biocolorants in Biotechnology

Merve Simsek
Department of Molecular Biology and Genetics
Erzurum Technical University
Erzurum, Turkey
merve.simsek49@erzurum.edu.tr

Arzu Gormez
Department of Molecular Biology and Genetics
Erzurum Technical University
Erzurum, Turkey
arzugormez@erzurum.edu.tr

Fatma Necmiye Kaci
Department of Molecular Biology and Genetics
Erzurum Technical University
Erzurum, Turkey
necmiyekaci@gmail.com

Derya Efe
Department of Medicinal and Aromatic Plants
Espiye Vocational School
Giresun University
Giresun, Turkey
deryayanmis@yahoo.com

*Abstract*—**Colourants are widely used as additive in many foods to make them more appealing and remarkable for consumers. To date, synthetic dyes have been mostly preferred due to their low cost, easy availability and efficacy. However, it was determined that synthetic dyes cause serious environmental problems. They are highly mutagenic, toxic and carcinogenic to every living organisms. Therefore, there is a big necessity to find natural dyes which are unharmful for environmental health. For this purpose, various soil samples from different areas of Erzurum city were used to isolate colourful and pigment-producing bacteria. Nutrient broth and Nutrient agar were used for enrichment and isolation of pigmented bacteria. Among many bacterial isolates, red coloured bacterial isolate was selected and gram staining property and morphological characters such size, shape and colour were determined. Then, 16 S rRNA analysis was carried out for taxonomic classification. According to the results of this study, the isolate was identified as *Serratia plymuthica*. Besides, the pigments of the bacteria was extracted by methanol extraction. The antimicrobial activity of the obtained pigments was evaluated. After this test, the isolated pigments were applied to epithelial cells to evaluate toxic.**

**Keywords— Pigment producing, *Serratia plymuthica*, Biocolorant, Natural dyes**

## I. INTRODUCTION

Synthetic dyes are extensively used in many industrial areas such as textile, paper, photography, food, cosmetic, and leather [1, 2]. Nowadays, over $10^5$ different dyes have been produced worldwide and their annual production is over $7 \times 10^5$ metric tons [3]. Due to largescale production and extensive application, synthetic dyes can cause considerable environmental pollution and are serious health-risk factors because of their extreme production and extensive usage [4]. The usage of synthetic dyes brings out huge amount of coloured wastewater causing very serious environmental problems such as damages of aesthetic nature, transmission of sunlight into natural water sources photosynthetic action of autotrophic aquatic bioata [5]. Besides, synthetic dyes contamination decreases food intake, growth and fertility rates, damages liver, spleen, kidney, heart, eye, lungs, etc. of organisms because of being highly mutagenic and toxic and carcinogenic to mammalian cells [6]. As the usage of synthetic dyes have many disadvantages, the usage of natural dyes has been increasing day by day. The plants, the animals, the fungi and the bacteria are the sources to obtain different pigments which supply different colours. Especially, bacteria are preferred to biotechnological production and application of dyes because of their easy and rapid reproduction and easy manipulation. Microbial sources, especially bacteria and some fungi can produce pigments that give the bacteria colourful being. There are many researches about bacteria producing different colour pigments. *Staphylococcus aureus*, *Micrococcus luteus* and *Malleomyces mallei* produce yellow pigments and besides various *Mycobacteria* strains, *Prevotella melaninogenicus*, *Serratia marcescens*, *Chromobacterium violaceum* and *Planococcus citreus* produce orange, black, red, purple and lemon-yellow pigments, respectively. *Pseudomonas aeruginosa* is an another bacteria known as green, blue and fluorescence pigments producing [7]. Bacterial pigment production is now one of the emerging fields of research to demonstrate its potential for various industrial applications. Some pigments are produced by bacteria as extracellular or intracellular. Intracellular pigments do not change the colour of the medium as they do not dissolve in water. Therefore the colour is limited to the bacterial colony. However, extracellular produced pigments can easily dissolve in water, they give their colours on media [8, 9, 10, 11]. They can be obtained different processes such as, extraction, isolation or synthesis. In the light of these information, the pigment producing bacteria was isolated from the soil sample and identified by classical and molecular methods. Then, the pigments of the

bacteria were obtained by methanol extraction to evaluate the antimicrobial and toxic activities.

## II. MATERIALS AND METHODS

### A. Sample Collection and Isolation of Bacteria

Various soil samples from different areas of Erzurum Province were used for the isolation of pigment-producing bacteria. The media used for enrichment and isolation of pigmented bacteria were Nutrient agar and Nutrient broth. From the collected soil samples, soil suspensions were prepared using sterile distilled water. Loopful of soil suspension was streaked on sterile nutrient agar plates and the plates were incubated at 27 °C for 24-72 hours. Only the pigmented bacterial colonies were selected and sub-cultured on the nutrient agar plates for further studies. During the incubation time, representative colonies were selected and purified by repeated re-streaking on NA, and were then stored at –80°C in 30% glycerol and Luria Bertani Broth (LB) for further studies.

### B. Identification of Bacteria

At first, the properties of cell and colony morphology, gram reactions were determined using the methods described by Harley and Prescott (2002) [12]. To identify the bacteria, determination and analyses of gene region called as '16S rRNA' were performed. DNA isolation, 16S rDNA amplification with 27F and 1492R universal bacterial primers by PCR, cloning the PCR product into pGEMT vector and sequence analyses were performed by the methods described by Gulluce et.al (2014) [13].

### C. Pigment Extraction

The pigments were isolated using with methanol extraction method. The pigment producing bacterial colony was inoculated in Nutrient broth of 300 ml and was incubated at room temperature for four to five days. Four to five days old cultured broth was centrifuged at 10,000 rpm for 10 minutes; pellet was suspended in 95% methanol and centrifuged again at 10,000 rpm for 10 minutes. Supernatant was collected which red in colour, is filtered using 0.2μm Whatmann paper. Filtrate was concentrated by rotary evaporator. Extract was added with 5 ml of 95% methanol and transferred to a petridish, dried in oven [14].

### D. Antimicrobial Tests

To check if the extracted pigments have any antibacterial property, The method described by Gormez et. al. (2016) [15].

### E. Hemolytic Activity

Hemolytic activity assay was performed with red blood cells to evaluate the effect of isolated pigments on erythrocyte cells. A commercially available whole blood sample was used during the experiment. 3 replicates were run for each sample. Measurements were taken at 577 nm, where hemoglobin was maximized. 200 μl of diluted red blood cell + 800 μl $dH_2O$ as positive control, 200 μl of diluted red blood cell + 800 μl D-PBS were used as negative control [16].

## III. RESULTS AND DISCUSSION

The isolated bacterium was Gram-negative, facultatively anaerobic and rod-shaped bacterium of the Enterobacteriaceae family. The isolate was identified by 16 S rDNA PCR as *Serratia plymuthica*. Isolated pigments evaluated about antimicrobial potential. However, antimicrobial activity was not observed.

According to the results of hemolytic activity, the pigments showed cytotoxic effects. Initial concentration was 7.32 mg/ml. Then, $10^2$, $10^{-1}$, $10^{-2}$ and $10^{-4}$ fold decreasing pigment concentrations were applied blood cells and our results showed that applied in all doses showed hemolytic activity (Figure 1).

This research is a prestudy to find new sources for red colour from natural sources. *Serratia* spp. are bacteria commonly found in soil, natural water sources, floras of plants and animals. The usage of these bacteria can be dangerous for health. However, it is planned to determine and clone the gene region that is responsible for the pigment production in to expression vector in the next step of ourstudy. The pigments obtained from bacteria showed toxic effect on blood cells at concentration $10^2$, $10^{-1}$, $10^{-2}$ and $10^{-4}$. These results can show because of the osmotic shock caused by high pigment concentrations. Therefore, additional studies should be performed to find the concentration level that is not toxic. If it is determined that all the concentrations are toxic, the colour pigment can be evaluated to use intextile industry.
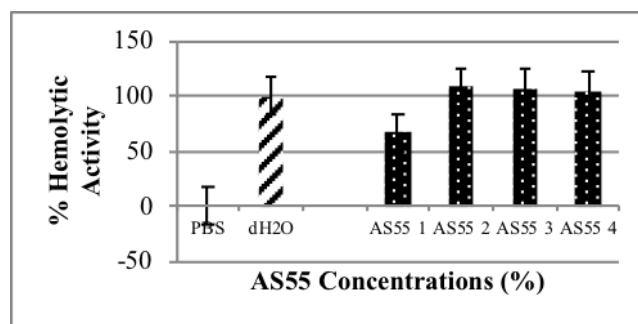


Fig. 3.   Hemolytic activity of pigments



Fig. 4.   *Growth of Serratia plymuthica on NA.*

## REFERENCES

[1]   R.C. Kuhad, N. Sood, K.K. Tripathi, A. Singh, & O. P. Ward, Developments inmicrobial methods for the treatment of dye effluents, Advances in Applied Microbiology., vol 56, pp 185–213, 2004.

[2]   S.R. Couto, Dye removal by immobilized fungi, Biotechnology Advances, vol 27, pp 227–235, 2009.

[3]   K.C. Chen, J.Y. Wu, D.J. Liou, S.C.J. Huang, Decolorization of the textile dyes by newly isolated bacterial strains, Journal of Biotechnology.,vol 101, pp 57–68, 2003.

[4]     E. Forgacs, T. Cserhati, & G. Oros, Removal of synthetic dyes from wastewaters: a review, Environment International., vol 30, pp 953-971, 2004.

[5]     E. Sudova, J. Machova, Z. Svobodova, T. Vesely, Negative effects of malachite green and possibilities of its replacement in the treatment of fish eggs and fish: a review, Vet. Med. Vol 12 pp. 527-539, 2007.

[6]     T. Robinson, G. McMullan, R. Marchant, P. Nigam, Remediation of dyes in textile effluent: a critical review on current treatment technologies with a proposed alternative. Bioresource Techn., vol 77, no 3, pp 247-255, May 2001.

[7]     H. Budzikiewicz, "Secondary metabolites from fluorescens pseudomands", FEMS Microbiol. Rev., vol 104, pp 209-228, 1993.

[8]     M. Aydın, "Endodontik Mikrobiyoloji", Editör Alacam Tayfun, Endodonti. Barış Yayınları, pp. 313-385, 2000.

[9]     V.K. Joshi, D. Attri, A. Bala, S. Bhushan, "Microbial pigments", Ind J Biotechnol, vol 2, pp 362–9, 2003.

[10]    C.K. Venil, P. Lakshmanaperumalsamy, "An insightful overview on microbialpigment: prodigiosin", Ele J Biol, vol. 5, no 3, pp 49–61. 2009.

[11]    A.S. Ahmad, W.Y.W. Ahmad, Z.K. Zakaria, N.Z. Yosof, "Applications of bacterial pigments as colorant: the Malaysian perspective", New York: Springer Briefs in Molecular Science, 2012.

[12]    J.P. Harley, L.M. Prescott, Laboratory Exercises in Microbiology, 5th edition. NewYork: McGraw−Hill, p 466, 2002.

[13]    M. Gulluce, T. Bal, H. Ozkan, A. Adiguzel, F. Sahin, D. Yanmis, Conventional and Molecular Identification of Bacteria with Magnesite Enrichment Potential from Local Quarries in Erzurum, Geomicrobiol. J 2014.

[14]    A.A. Shetti, Antibacterial Potentials of Red Pigment Extracted from Soil Isolate *Serratia* sp., IOSR-JBB,vol 3, pp 49-52, 2002.

[15]    A. Gormez, S. Bozari, D. Yanmis, M. Gulluce, G Agar, and F. Sahin, Chemical composition and antibacterial activity of essential oils of two species of Lamiaceae, Polish Journal of Microbiology, vol 64(2), pp 121-127, 2002.

[16]    T. Yu, A. Malugin, H. Ghandehari, Impact of Silica Nanoparticle Design on Cellular Toxicity and Hemolytic Activity. ACS Nano, vol *5*, no 7, pp 5717–5728, 2011.

# Fabrication of YBCO Metametarials by Screen Printing Method

Aykut Coskun
Department of Electrical and Electronics Engineering
Ataturk University
Erzurum, Turkey
https://orcid.org/0000-0002-7240-6865

Ahmet Ozmen
Department of Electrical and Electronics Engineering
Ataturk University
Erzurum, Turkey
https://orcid.org/0000-0002-3631-4883

Muhammet Ali Aksoy
Department of Electrical and Electronics Engineering
Ataturk University
Erzurum, Turkey
maliaksoy@hotmail.com

Mehmet Ertugrul
Department of Electrical and Electronics Engineering
Ataturk University
Erzurum, Turkey
ertugrul@atauni.edu.tr

*Abstract*— **Screen printing process is one of the easy and cheap process that can be used to realize large volume, low cost and multifunctional metamaterials. In this work, meta-materials were fabricated screen-printing method by using special geometry, which was obtained by CST simulation results. The S-parameters of the designed meta-materials were measured by using cryogenic cooler. We described the use of an additive manufacturing method, screen-printing, as a means of inexpensively integrating artificial electromagnetic properties of meta-materials within a structural composite. In order to fabricate meta-materials, the masks seen Figure 1-2 were designed with special geometry. The quality factors of the meta-materials were calculated from the S parameters (S21). It is observed that the quality factor value was between $10^3$ and $10^4$. We fabricated and characterized two different electromagnetic surfaces to illustrate the concept. It is thought that the results of the work will also benefit companies and organizations operating in this area.**

*Keywords—YBCO, Metamaterial, Screen Printing, Superconducting electronics, High Temperature Superconductors, S parameters*

## I. INTRODUCTION

Meta-materials are not available in nature. They are obtained only engineering techniques [1]. Meta-materials, having thanks to their negative refractive index, they can manipulate the incoming wave. By means of the this extraordinarily special feature, it can be used for energy harvesting, signal absorbing, invisibility. One of the most important applications of meta-materials is excellent signal absorption application. Excellent signal absorption is achieved by damping the electromagnetic wave [2-3].

Electronic devices in today's technologies shrink in size and lower of these devices power consumption is observed. This needs research on obtaining strength with meta-material has caused and increased interest in this field [4-5].

Meta-material produced by Screen Printing method in this study. Screen Printing is a very cheap and easy method for the production of meta-materials. Screen Printing System is seen Figure 3 [6].

## II. MATERIAL AND METHOD

Meta-material was produced by 2 methods. First method was used linseed oil, Xylene and Alpha-terpineol. The linseed oil was boiled for 3 days between 200 °C and 300 °C. In order to make a homogenous mixture, a magnetic mixer was used. When the analog heater was used, the temperature values were controlled by the temperature gauge so that the temperature values were between 200 °C and 300 °C. %85 of the boiled linseed oil, %12.5 Xylene and %2.5 Alpha-terpinol were mixed in a glass cap for 24 hours. %70 of the paste composed of the linseed oil, Xylene and Alpha-terpineol with %30 of the YBCO compound were mixed using magnetic mixer. The printing on the glass was dried at 150 °C for 10 minutes in the circuit. Then it was heated at 300 °C for 3 hours. Alpha-terpineol with Ethyl cellulose were used for the second method. Ethyl cellulose and Alpha-terpineol were mixed at 40 °C for 3 hours (1:12, 1: 9, 1:10 rate). The mixture with YBCO was the same as the other method. The printing on the alumina was dried in the circuit for 10 minutes at 150 °C. Then it was heated at 700 °C for 30 minutes [6].
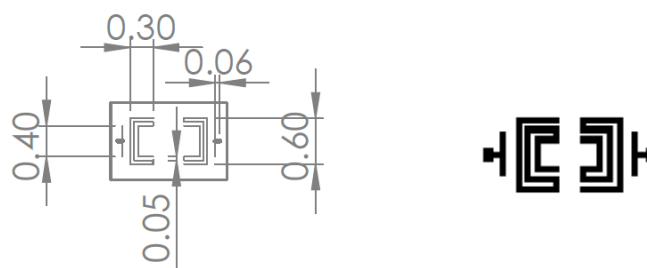


Figure 1. Meta-Material Mask Design and Shape



Figure 2. Print Circuit Board on Glass and Alumina

**Figure 3.** Screen Printing System

Firstly, measurement system of meta-materials seen Figure 4 was vacuum tested. As a result of the test on the system, vacuum holding was observed. Secondly, the system was tested for heat resistance. While the system was holding the vacuum, liquid nitrogen was filled from the end of the metal pipe. It was observed that the temperature decreased to 77 °K. Sufficient temperature to be the superconductor of YBCO is 90 °K. Finally, S parameters of YBCO superconducting meta-material were measured with 2 wired prop.
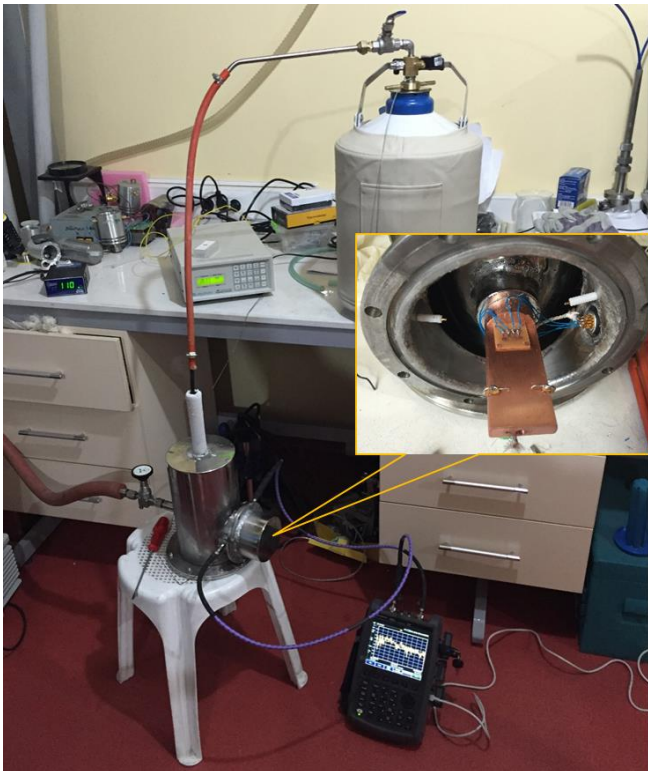


**Figure 4.** Measurement System of Meta-Materials

### III. RESULTS AND DISCUSSION

Both the simulation and the test results show that the meta-materials have resonance frequency around 6 GHz. The resonance frequency is determined by determining the lowest dB value of the S21 measurements and the frequency is calculated by the 3 dB points shown in Figure 5. According

to Formula 1, Quality factors are calculated considering the difference between these points. The quality factor values belonging to the YBCO meta-materials are measured between $10^3$ and $10^4$.
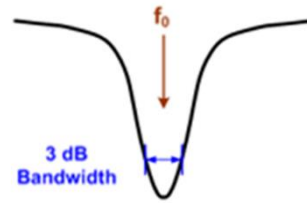


**Figure 5.** Quality Factor Measurement

$$Q=f_o/BW \tag{1}$$
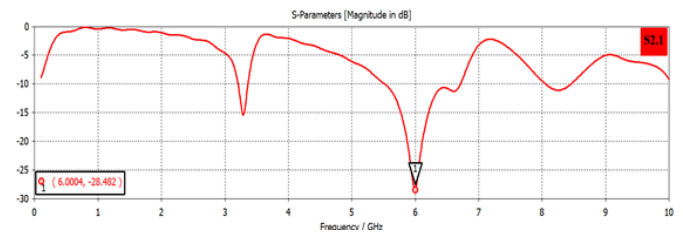


**Figure 6.** S21 Simulation Results with CST Program
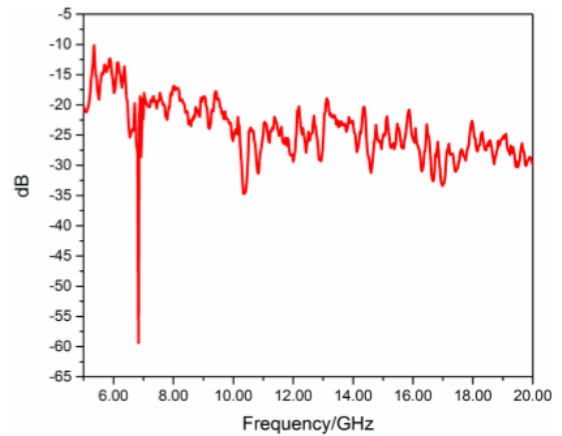


**Figure 7.** Experimental S21 Graph with Network Analyzer

**Table 1.** CST Simulation and Test Result

| Parameter | Resonance Frequency | Quality Factor |
|---|---|---|
| S21-Simulation | 6 GHz | $1,4278 \times 10^3$ |
| S21-Test | 6,837 GHz | $1.6276 \times 10^3$ |

### IV. CONCLUSION

It was observed that quality factors value was between $10^3$ and $10^4$. The results of the simulation (Figure 6) and the test (Figure 7) were quite compatible. High quality factor decreases losses. In the production of metal materials, a relatively inexpensive and easy method was used. We fabricated and characterized two different electromagnetic surfaces to illustrate the concept. It is thought that the results of the work will also benefit companies and organizations operating in this area.

## REFERENCES

[1] Shelby, R.A., Smith, D.R. ve Schultz, S., Experimental verification of a negative index of refraction. Science, 292.5514, 77-79, (2001).K. Elissa, "Title of paper if known," unpublished.

[2] Maci, S.A, Cloaking metamaterial based on an inhomogeneous linear field transformation. antennas and propagation, IEEE Transactions on, 58, 1136-1143, (2010).

[3] Lee, J. ve Lim, S., Bandwidth-enhanced and polarization-insensitive metamaterial absorber using double resonance, Electron. Lett, 47, 8-9, (2012).

[4] Chen, Zhongsheng, et al. "Metamaterials-based enhanced energyharvesting: A review." Physica B: Condensed Matter 438 (2014): 1-8.

[5] Almoneef, Thamer S., and Omar M. Ramahi. "Metamaterial electromagnetic energy harvester with near unity efficiency."Applied Physics Letters 106.15 (2015): 153902.

[6] Abadi M. H. N. S., 2010. Deveopment of Nanocrystalline Thick Film Gas Sensors. PhD Tesis, Faculty of Engineering, Malezya.J. Clerk Maxwell, A Treatise on Electricity and Magnetism, 3rd ed., vol. 2. Oxford: Clarendon, 1892, pp.68–73.

# A Case Study For Structural Model Update By Operational Modal Analysis:

# Erzincan Değirmenliköy Church

Semi Emrah Aslay
Department of Constuction
Erzincan Binali Yıldırım University
Erzincan, Turkey
seaslay@gmail.com

Dilek Okuyucu
Department of Civil Engineering
Erzurum Technical University
Erzurum, Turkey
okuyucu@erzurum.edu.tr

**Abstract-Over ninety percent of Turkey's area lands on Anatolian peninsula. Anatolia is one of the oldest occupation places of the World and hence; hosted numbers of civilisations. These civilisations left their fingerprints on this land by means of historic structures and folkloric applications. To protect and carry these architectural and cultural heritage to the future and commit them to our next generations are of our major responsibilities by civil engineering point of view. On the other hand, Anatolia is one of the most active seismic zones of earth and experienced numbers of highly destructive earthquakes. Erzincan city, located on east Anatolia, is unfortunately well known by its highly destructive seismic history. This study presents details of one part of a research about a strong earthquake survivor; Erzincan Değirmenliköy Church. The church is a stone masonry construction of ~250 years old and still withstand; being good in shape. The only loss of the structure is the abscissa. This historic masonry withstands during 1939 and 1992 Erzincan earthquakes, although numbers of historic masonry buildings of the region were totally collapsed. Hence, a research has been started to understand the seismic behaviour of the church and herein paper provides the details of the first stage of the study. At the first stage, structural modal creation and model update of the church via operational modal analysis were realized and lost abscissa was added to the final model to be used for dynamic analysis. The details of model preparations of Erzincan Değirmenliköy Church are presented.**

*Keywords-Erzincan Değirmenliköy Church, Historic Masonry, Macro Modelling, Operational Modal Analysis, Model Calibration*

## I. INTRODUCTION

Cultural heritage is of primary importance for the occupants of the land. It represents the history and memory of the people and civilisations. Being the great portion of Turkey; Anatolian land hosts numbers of civilisations. Almost everywhere on Anatolia, there exists historic buildings, architectural ruins and folkloric marks. It is a humanitarian responsibility and sign of respect to protect and commit this heritage to the next generations. But; protect from what? Is this question is asked for Anatolia, the answer is generally simple: from earthquakes.

Anatolia is one of the most active seismic zones of earth. Numbers of disastrous earthquakes hit the land and even caused lost of cities. Erzincan city is one of the most effected cities from strong ground motions. The city is located on east Anatolia region. North Anatolian Fault, very well known by seismologists, and some other ones surround the city. [1] Strong ground motions hit Erzincan city for several times and almost no historic masonry building survived. [2]

1939 Erzincan earthquake is one of the most destructive earthquakes of the world for all times. Magnitude of the ground motion is reported to be almost 7.8~8; and total loss of life is stated to be ~33.000. In the 20th century, another major earthquake hit the city again on March 13, 1992. The magnitude of 1992 Erzincan earthquake is reported to be 6.8 and ~700 people died. [3] Hence, the city was seriously affected from the earthquakes by means of life losses and collapse of the buildings. However, two stone masonry buildings are surprisingly standing; although they have experienced both 1939 and 1992 Erzincan earthquakes! The buildings are Erzincan Main Train Station which is constructed on 1938 and Erzican Değirmenliköy Church of 19th century.

This paper is providing information about the first stage of seismic performance evaluation of Erzincan Değirmenliköy Church. This stone masonry building is located just ~20 kilometres away from Erzincan city centre and very close to active faults. It survived both 1939 and 1992 Erzincan earthquakes. The only damage is the loss of the abscissa. The villagers, living in Değirmenliköy Village, mention about the collapse of the abscissa during 1939 Erzincan earthquake. The main purpose of the research is to understand seismic behaviour of the church; such that it withstands during two major, severe ground motions. The first stage is to create a reliable structural model to be used for further analysis. This paper provides information about this stage.

In order to create a reliable structural model, a comprehensive research was realized for information gathering about the church building. Material properties were studied. Structural model was created as to represent existing status and theoretical modal analysis was carried out. Using ambient vibration measurements, operational modal analysis was carried out; experimental mod shapes

and modal frequencies was obtained. Structural model was calibrated as to calculated experimental modal properties and abscissa was added to the model for further dynamic analysis which are planned to be carried out in order to understand dynamic behaviour of the historic masonry.

## II. ERZİNCAN DEĞİRMENLİKÖY CHURCH

Erzincan Değirmenliköy Church is located in Değirmenliköy Village of Erzincan city; which is almost ~20 kilometres away from city centre. Church is officially recognised as a historic building and under protection of Turkish authorities. Construction date is reported to be ~1860's. It has a rectangular plan with the dimensions of 9.80x16.90 meters. Different natural stones like serpentine, andesite and lightweight limestone were utilized for construction. Among the others, lightweight limestone (unit weight is almost 1.3 gr/cm$^3$) is the mostly used material. Whole body of church is generally good in shape only with some cracks over the walls of the building. The abscissa of the church is *absent.* However, the connection points of abscissa with the church body and traces of its foundation are recognizable on the floor. A general view of the church is provided in Figure 1.



Figure 1. General View of Erzincan Değirmenliköy Church

## III. STRUCTURAL MODEL CREATION FOR CURRENT SITUATION

During the information collection, only a very simple plan drawing of the church was obtained which was not enough for structural model creation. Hence, architectural drawings of the church were created to obtain geometric properties reliably. It should be underlined that, there is almost no technical information about the church in the literature or in official records. So, material characterisation and determination of mechanical properties were also done. Schmidt hammer test was mainly used to define compressive strength of stone units. Equations provided in Turkish Seismic Code and Eurocode 6 were used for final calculations of mechanical properties of historic masonry. [4,5] On the other hand, composition of mortar and plaster was evaluated via electron microscope scanning. This study was carried out in High Technology Research Centre (YÜTAM) of Erzurum Technical University. A general view from chemical composition analysis of mortar and plaster is provided in Figure 2.
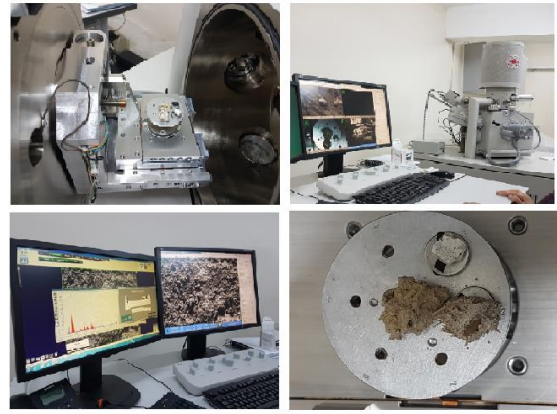


Figure 2. Chemical Composition Analysis of Mortar and Plaster Samples

After determination of geometry and material properties, structural model of the church was created in SAP2000 software. [6] Macro modelling approach was adopted for masonry modelling. [7] The model that represents existing situation of the church consists of total of 2275 solid elements and 5800 joints. A general view of the model is provided in Figure 3.



Figure 3. A General View of The Church Model that Represent the Existing Situation

After the model creation, theoretical modal analysis was carried out in order to calculate mod shapes and related modal frequencies. Results of theoretical modal analysis for initial model are presented in Table 1. Theoretical modal analysis is of primary importance for instrumentation of operational modal analysis. Locations of vibration measuring devices are determined according to theoretical mod shapes.

Table 1. Results of Theoretical Modal Analysis of Initial Model

| Mod Number | Mod Shape | Modal Frequency (Hz) |
|---|---|---|
| 1 | Lateral movement on short direction | 6.38 |
| 2 | Vertical Movement of Vaulted Roof | 7.71 |
| 3 | Torsional Movement | 8.78 |

## IV. OPERATIONAL MODAL ANALYSIS OF THE CHURCH

Since, the material is masonry; a number of assumptions were done. For a more reliable analysis to understand dynamic behaviour of the church; the structural model should be verified. In this stage, operational modal

analysis technique was used to determine in-situ (real) dynamic behaviour parameters like mod shapes and modal frequencies.

Operational Modal Analysis (OMA) is also called output-only modal analysis, ambient response analysis, ambient modal analysis, in-operation modal analysis, and natural input modal analysis. A typical modal test of a structure is performed by measuring the input forces and output responses for a linear, time-invariant mechanical system. The excitation is either transient (impact hammer testing), random, burst-random or sinusoidal (shaker testing). The advanced signal processing tools used in operational modal analysis techniques allow the inherent properties of a mechanical structure (resonance frequencies, damping ratios, mode patterns) to be determined by only measuring the response of the structure without using an artificial excitation. This technique has been successfully used in civil engineering structures (buildings, bridges, platforms, towers) where the natural excitation of the wind is used to extract modal parameters. [8, 9, 10] It is now being applied to mechanical and aerospace engineering applications (rotating machinery, on-road testing, in-flight testing). [11,12, 13] The advantage of this technique is that a modal model can be generated while the structure is under operating conditions. That is, a model within true boundary conditions and actual force and vibration levels. Another advantage of the technique is the ability to perform modal testing in-situ, i.e., without removing parts under test. The test can be performed with other applications or activities in parallel and does not affect or interrupt daily use of the machine or structure.

Considering the advantages of operational modal analysis, ambient vibration measurements were taken from the church. 3D accelerometers of high sensitivity were used for ambient vibration measurements and recordings. Total of 7 wireless devices were used and they were all synchronized via GPS antenna connection. A general view from measurements is provided in Figure 4.



**Figure 4.** General View From Ambient Vibration Measurements

Recorded acceleration data were processed by using Artemis Modal Pro software. [14] Frequency Domain Decomposition (FDD) concept was followed to obtain mod shapes and modal frequencies. Results of operational modal analysis are provided in Table 2.

Table 2. Results of Operational Modal Analysis of Erzincan Değirmenliköy Church

| Mod Number | Mod Shape | Modal Frequency (Hz) |
|---|---|---|
| 1 | Lateral movement on short direction | 3.56 |
| 2 | Vertical Movement of Vaulted Roof | 5.18 |
| 3 | Torsional Movement | 6.89 |

## V. STRUCTURAL MODEL CALIBRATION

Operational modal analysis provided the same mod shapes as that of theoretical modal analysis. However, related modal frequencies differed a lot. So, the model calibration was needed. There exists three major applications for theoretical model update in order to reach experimental mod shapes and modal frequencies. First one is to check the geometry and dimensions. Second one is to update the support conditions and third one is to re-evaluate mechanical properties of the masonry. Since, the mod shapes were obtained as identical for both theoretical and experimental analysis; mechanical properties of the masonry units were updated to reach the experimental modal frequencies. Considering $f_k$ as compressive strength and $E$ as modulus of elasticity of masonry unit and; results of all modal analysis are presented in Table 3. It is clearly seen that, modulus of elasticity values of masonry units were initially overestimated. For updated model, difference of first, second and third modal frequencies from that of experimental ones are %0.2, %2.1 and %23, respectively. Updated model provided first two modal frequencies almost equal to that of experimental ones, assigned mechanical properties of masonry units ($E=27f_k$ - $40f_k$) were accepted and used for the next model creation which represents the initial situation of the church with existence of abscissa.

Table 3. Overall Modal Analysis Results for The Model that Represent the Existing Situation

| Mod Number | Mod Shape | Modal Frequency (Hz) | | |
|---|---|---|---|---|
| | | Initial ($E=200f_k$) | Experimental | Updated ($E=27f_k$ - $40f_k$) |
| 1 | Lateral movement on short direction | 6.38 | 3.56 | 3.57 |
| 2 | Vertical Movement of Vaulted Roof | 7.71 | 5.18 | 5.07 |
| 3 | Torsional Movement | 8.78 | 6.89 | 5.29 |

## VI. STRUCTURAL MODEL CREATION FOR ORIGINAL CONSTRUCTION

As mentioned above, Erzincan Değirmenliköy Church is a strong survivor of 1939 and 1992 Erzincan earthquakes; both of which are two of the most destructive earthquakes of all times. The main aim of the whole research is to understand the dynamic behaviour of Erzincan Değirmenliköy Church. At the meantime, the

abscissa of the church does not exist. However, it was a part of the church when it was constructed. The rumour relies on the issue that; the abscissa was destroyed during 1939 Erzincan earthquake. In order to study and understand, dynamic behaviour of the church original situation of the structure is needed to be analysed. Thus, the reason for the damage of the abscissa can be estimated.

The updated model of the church was accepted with its last material properties. The abscissa was added to the church. It is very important to mention that, there is no information about the geometry and dimensions of abscissa. The traces of the abscissa can be easily detected on the east wall of the church and; traces at the ground level gives idea about the plan geometry. The church architecture of the region of 18th century was studied by art history point of view and the abscissa was added to the model. The addition of abscissa to the model is *a fiction*. A general view of the structural model with the addition of abscissa is presented in Figure 5.
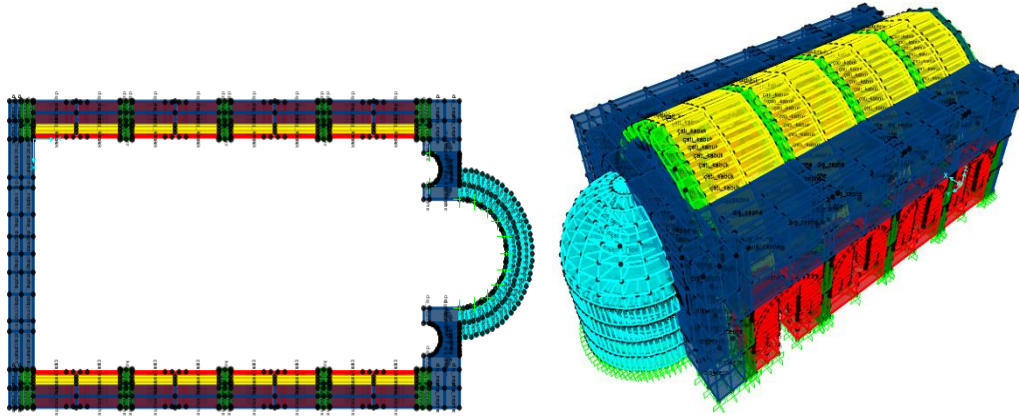


Figure 5. A General View of the Model with the Addition of Abscissa

Final model of the church with the addition of abscissa consist of 3116 solids and 6632 joints. Results of the theoretical modal analysis for updated model with abscissa addition are presented in Table 4. The addition of abscissa did not change the calculated mod shapes. However, slightly different modal frequencies were obtained. First and third modal frequencies were increased compared to that of calibrated model without abscissa. This can be attributed to increase in total mass of the structure. Modal frequency for second mod shape was calculated to be less than that of calibrated model. This is the modal frequency for vertical movement of vaulted roof. The decrease in related modal frequency can be due to increase in vertical stiffness of walls over which the vaulted roof is supported.

This final model is to be used for dynamic analysis in order to understand seismic behaviour of the church.

Table 4. Theoretical Modal Analysis Results for

| Mod Number | Mod Shape | Modal Frequency (Hz) | |
| --- | --- | --- | --- |
| | | Current Situation without Abscissa | Original Situation with Abscissa |
| 1 | Lateral movement on short direction | 3.57 | 3,60 |
| 2 | Vertical Movement of Vaulted Roof | 5.07 | 4,47 |
| 3 | Torsional Movement | 5.29 | 5,48 |

## VII. RESULTS AND CONCLUSIONS

This manuscript presents the details of structural model creation of a historic masonry church. Erzincan Değirmenliköy Church is a survivor of 1939 and 1992 destructive Erzincan earthquakes. The only major damage of the church is the loss of abscissa. In order to understand seismic behaviour of church and reason for the damage of abscissa a reliable structural modal is needed. This model was prepared for further dynamic analysis and the following conclusions can be stated:

- Structural models of historic masonry may need calibration via an appropriate technique. Because, numbers of assumptions are done.
- More studies are needed to obtain mechanical properties of historic masonry by non-destructive experimentation.
- Final finite element model of Erzincan Değirmenliköy Church with addition of abscissa can be used for further dynamic analysis.
- In case of dynamic analysis, there exists a major problem. There is no acceleration record for 1939 Erzincan Earthquake. Hence, it will be a more realistic approach to use synthetic ground motion data, if possible. For 1992 Erzincan earthquake, accelerograms are existing.

## REFERENCES

[1] Gülkan, P. Yücemen, M.S., Başöz, N. Koçyiğit, A. and Doyuran V., "Turkish Seismic Zoning Map Prepared According to Newest Data", Middle East Technical University, Technical Report,

Earthquake Engineering Research centre of Department of Civil Engineering, Report Number: 93-01, 1993. (in Turkish)

[2]   Ambraseys, N., N., and Finkel, C., F., "The Seismicity of Turkey and Adjacent Areas", Translated by Müzeyyen Umur KOÇAK, TÜBİTAK Publications, Ankara, 2006.

[3]   Haçin, İ., "1939 Great Erzincan Earthquake", Cumhuriyet University Journal of Social Sciences, Vol:88, pp.38-69,2014. (in Turkish)

[4]   Turkish Republic the Ministry of Public Works and Settlement (2009). Turkish Earthquake Design Code TEC 2007. Ankara

[5]   "Eurocode 6 : Design of Masonry Structures, Part 1.1: General Rules For Reinforced and Unreinforced  Masonry Structures", European Committee for Standardization, ENV 1996-1-1, 1995.

[6]   SAP2000, Structural Analysis and Design Application Software, Erzurum Technical University, 2017.

[7]   Özkul, M., "Structural Safety Evaluation of a Historic Building via Experimental Modal Analysis", MSc Thesis, Ege University, Institute of Science, Department of Civil Engineering, İzmir, Turkey, 2016. (in Turkish)

[8]   [Brincker, R., Zhang, L., and Andersen, P., "Modal Identification from Ambient Response Using Frequency Domain Decomposition," Proc. of the 18th International Modal Analysis Conference, San Antonio, TX, February 7-10, 2000.

[9]   Schwarz, Brian, and Richardson, M. H., "Modal Parameter Estimation from Ambient Response Data," presented at IMAC 2001, February 5-8, 2001.

[10]  Schwarz, Brian, and Richardson, M. H., "Post-Processing Ambient and Forced Response Bridge Data To Obtain Modal Parameters," Proceedings of the IMAC XIX Conference, Orlando, FL, Feb. 5-8, 2001.

[11]  Herlufsen, H., and Møller, N., "Operational Modal Analysis of a Wind Turbine Wing Using Acoustical Excitation," Brüel & Kjær Application Note, 2002.

[12]  Møller, N., Brincker, R., Herlufsen, H., Andersen, P., "Modal Testing of Mechanical Structures Subject to Operational Forces," IMAC XIX.

[13]  Brincker, R., Andersen, P., and Møller, N., "Output-Only Modal Testing of a Car Body Subject to Engine Excitation," Proc. of the 18th International Modal Analysis Conference, San Antonio, TX, February 7-10, 2000.

[14]  Artemis Modal Pro, Operational Modal Analysis Software, Erzurum Technical University, 2017.

# Determining to Accuracy of Geo-Referencing the Aerial Photographs and High-Resolution Satellite Image: Case Uludag, Bursa

Günay Çakir
Gumuşhane University Gumushane
Vocational School, 29100, Gumushane,
Turkey
cakirgunay@gmail.com

*Abstract*-An ortho image is a geo-referenced image produced from remotely sensed data such as aerial photos and high resolution satellite images. These data has been determined forest and environmental features or values. Remote sensed data can be used in various areas such as forest ecosystem management, pollution, environmental impact and social life. The objective of this study is geo correction to aerial photo / high resolution satellite images by ortho images forest effects. The remote sensed data is aerial photographs in 1970 and high-resolution images in 2004 and 2010. We selected 23 by 23 black and white analog photographs in 1970, which scanned through desktop scanner with a resolution of 400 dpi. Ortho images were created with ERDAS imagine LPS software. Digital Elevation Model used to produce orthophoto images. Results show that orientation and geographic errors of digital ortho image generation for remotely sensed images are 13–15 pixels. In addition to all images total RMS errors was less than 5 meters.

*Keywords: Orthophoto, Accuracy, Digital Image Processing, Environmental Management*

## I. INTRODUCTION

Remote sensing data presents information from previous periods. Aerial photographs and satellite images help decision makers to monitor and analyze environmental changes. Digital remote sensing data saves cost and time when collecting geographic information. The data obtained can be analyzed in Geographical Information System (GIS) in detail.

This study is related to remote sensing and GIS technology for mapping of Uludağ tourism area in Bursa. Remote sensing and GIS are increasingly used worldwide to help collect and analyze images from airplanes, satellites, and even balloons (Aschbacher et al., 1995; Dahdouh-Guebas et al., 2000). Significant advantages of using GIS include the ability to quickly update information, conduct comparative analytical studies, and make it necessary (Silapathong and Blasco, 1992; Long and Skewes, 1994). In addition to providing efficient data storage and retrieval capabilities, GIS offers a cheaper option to monitor forest conditions over time (Long and Skewes, 1996; Ramachandran et al., 1998). The results obtained from this study can provide an additional opportunity for a better understanding of the tourism area and the forests for sustainable management. From a technical standpoint, the results of appropriate tools for the development of management plans for forests in Turkey can be selected in Remote sensing data and GIS applications.

For better planning and management of ecosystems has prepared thematic maps there has been evaluated simultaneous of boundaries and simultaneous different compositions. There is a need for increasing large-scale maps and relevant data to measure, plan and manage socio-economic characteristics at the community level to meet the rapid population demand and demand. The geometrically corrected image orthophoto, environmental resources in a sustainable way for better inventory management and planning are used in environmental studies in Turkey. Environmental information is essential for sustainable planning at landscape levels, from communities to district to regions. Digital photogrammetry paid more attention to producing ortho images to document and measure natural resources and characteristics to synthesize a large number of data sets to understand processes and trends, and to understand future interactions as well as future benchmark studies

## II. MATERIAL AND METHODS

Remote sensing data is a high resolution images and black white aerial photos. The accuracy of remote sensing product was independently checked with traditional and latest land survey methods in ERDAS software. In the study, ground control points, which was GPS data, 1/25000, scale standard topographic map and 2010 QUICBIRD satellite image were used for coordinating the images.

### Study area

The study area fully covers the Uludağ tourism area in Bursa. There is characterized by a rough terrain area and an altitude from 200 to 2220 meter asl. It extends along coordinates to UTM ED 50 datum 35.zone 231000-243000 E and 4516000-4550000 N on the Northwestern Region of Turkey.

The analog aerial photographs flown in 1970 at a scale of 1:20000 black-white focal length 152,79 mm were scanned on a normal desktop scanner with a resolution of 400 dpi (dots per inch). It corresponds to a ground resolution of 0.35-1.50 meters at nominal scale. Finally, land use map sensitivity was affected by orientation errors in images.

### Orthophoto generation

Aerial triangulation measurements had been implemented by using 1:20000 scale aerial photographs. The ERDAS imagine software was used for the development of the Digital Surface Models (DSM) in ±2 meter accuracy. Another model had been produced by standard topographic map collected data in 10-meter interval line there are ±5 meter accuracy (Çakır 2006).

**Digital image mosaic**

The ground control points had been identified and the individual images have been Ortho-rectified. The ortho image accuracy was under 10 meters of the Uludag. This dataset can be used as land cover maps in any GIS application. The field to map the Uludağ watershed and forests was helpful to discuss management issues with the decision makers.

## III. RESULTS AND DISCUSSION

Classification of source areas and action zones were identified on a photo mosaic built for the whole tourism area in Uludağ. Results were evaluated in two ways. In the first, digital orthophoto generation for analog photos with a desktop scanner were realized as 13–15 pixels. It has geometric features of a map and the qualities of photographs. In the second data is high resolution images correction. The geometric error in the ortho images was determined to be less than 5 meters. The amount of error is acceptable in accordance with the purpose of the study.

In addition, the RMS error should be less than 1 in medium-sized satellite images and as close to one as possible in high-resolution images. The main reason for choosing the Nearest Neighborhood Method in the study is that it is easy to use and it is done in a shorter time than other methods on the computer. geographic coordinated satellite image is included in the evaluation with SAM. In 2010 QUICBIRD satellite image was taken positively with a sensitivity of 0.5 meters. Calibration of IKONOS satellite image for the year 2004 was made on the basis of pixels on the satellite image of the year 2010. The operation was carried out from 30 ground control points distributed evenly to the area and the error values given in the table are given. In addition, geographical coordinate values were re-processed using the GPS values together with SAM and the coordinates of the satellite images were analyzed again. The coordinates are recalculated depending on the slope. Sensitivity changes according to the scanning capacity in black and white aerial photographs. Generally, high resolution satellite images were taken as reference data.

Table 1. IKONOS ve QUICBIRD calibration and verification information for satellite images and aerial photographs

| SATELLITE IMAGES | | SUN AZIMUT | | GROUND CONTROL POINTS | | |
|---|---|---|---|---|---|---|
| Name | Time | Azimut | altitude | X error | Y error | Total error |
| IKONOS-2 2004062909135260000011102096 ULUDAG GEOTIFF | 29/06/2004 09:13 GMT Cloud %0 1m x1m piksel | 141.5821 degree | 69.71024 degree | 0,89 pixel | 0,82 pixel | 0,91 pixel |
| QUICBIR PAN IRRGB 10EUSI-1018-01_I001831_FL02-P004647 GEOTIFF | 03/08/2010 08:51 GMT Cloud %0 0.57mx0.57m piksel | 124.65 degree | 40.1166 degree | 1,12 pixel | 1,11 pixel | 1,2 pixel |

Remote sensing has a tool for obtaining information for research purposes as well as to disseminate research results to the community. The final products of orto images can be related to geometric correction, resolution and image acquiring time. The quality of the final images will mainly depend on several major factors such as the accuracy of the clarity of the air photos, scanning resolution and quality, ground control point's accuracy, camera model and mosaicking (Çakır 2006).

## REFERENCES

[1] Aschbacher, J., Ofren, R., Delsol, J.P., Suselo, T.B. and Vibulsresth, S.: 1995, 'An integrated comparative approach to mangrove vegetation mapping using advanced remote sensing and GIS technologies: preliminary results', Hydrobiologia 295, 285–294

[2] Çakır, G., 2006, Hava fotoğrafları ve uydu görüntüleriyle meşcere tiplerinin sayısal üretilmesi ve coğrafi bilgi sistemlerinde kullanılması, KTU Fen Bilimleri Enstitüsü, PhD thesis, Trabzon – Turkey.

[3] Dahdouh-Guebas, Verheyden, F.A., De. Genst, W., Hettiarachchi, S. and Koedam, N.: 2000, 'Four decade vegetation dynamics in SriLankan mangrove sas detected from sequential aerial photography: a case study in Galle', Bulletin of Marine Science 67(2), 741–759.

[4] Long,B.G.andSkewes,T.D.:1994,'GIS and remote sensing improves mangrove mapping', 7th Australasian Remote Sensing Conference, 1–4 March 1994, Melbourne, Australia, Vol. 1, pp. 545–551.

[5] Shrestha, K. B. 2002, Participatory Forest Management in Mynamar, First National Workshop, December 2000 1-4 December 2000. ICIMOD, Department of Forest, Yangon, Myanmar, Institute of Forset. pp 17 –18.

[6] Silapanthog,C.andBlasco,F.:1992,'The application of geographic nformation systems to mangrove forest management: Khlung, Thailand, Asian Pacific', Remote Sensing Journal 5(1), 97–104.

[7] Ramachandran, S., Sundaramoorthy, S., Krishnamoorthy, R., J. Devasenapathy and Thanikachalam: 1998, 'Application of remote sensing and GIS to coastal wetland ecology of Tamil Nadu and Andaman and Nicobar group of islands with special reference to mangroves', Current Science 75(3), 236–244.

# Carbon Dots Photosynthesis Enhancer for High-Tech High-Yield Farming

Suraya Abdul Rashid
Materials Processing and
Technology Laboratory,
Institute of Advanced
Technology, Universiti Putra
Malaysia

Muhammad Nazmin Yaapar
Department of Plant Siences,
Faculty of Agriculture,
Universiti Putra Malaysia.

Tongling Tan,
Materials Processing and
Technology Laboratory,
Institute of Advanced
Technology, Universiti Putra
Malaysia

Mohd Zhafir Abdul Razak
Qarbotech Sdn. Bhd.,
Innohub, Putra Science Park,
Universiti Putra Malaysia.
suraya_ar@upm.edu.my

Carbon Dots (CD) are fragments of carbon, with sizes typically less than 10 nm. They possess unique electrical and optical properties rendering them photoluminescent. The main problems that limit their applications are their exorbitant price due to tedious processing and their method of production which uses harsh chemicals and leaves toxic residue. We have found a solution to address these problems which has significantly reduced price, involves simple processing without toxic chemicals and produces a biocompatible product. This innovation has created an immediate new customer market in the agriculture sector, where CD can be used as a photosynthesis enhancer. By applying the CD to leaves, it increases the photosynthesis rate of the plants which correlates with better yield and shortens the plant growth cycle. Moreover, our studies have shown that the treated plants require less light to achieve maximum photosynthesis and uses less water during the process of photosynthesis. This nanotechnology has a potentially huge impact on the future of food security in Malaysia and around the globe.

# ß 1-3 Glucanase Optimizations for Transfer of 3 Different Melon Varieties by *Agrobacterium tumefaciens*

Büşra Yazıcılar
Erzurum Technical University
Molecular Biology ve Genetic
Departmant

Fatma Böke
Erzurum Technical University
Molecular Biology ve Genetic
Departmant

İsmail Bezirganoğlu
Erzurum Technical University
Molecular Biology ve Genetic
Departmant
ismail.bezirganoglu@erzurum.edu.tr

*Abstract*-In this study, Kırkagac, Pineapple and Winter melon varieties were used because of their high economic value, delicious, efficient and durable. The pKn-glucanase gene was transferred to AGL1, a strain of *Agrobacterium tumefacies*. A culture culture medium (60 µL BA( Benzyl amino purine) , 60 µL NAA (Naphthalene acectic acid, 88 µL IAA ( Indole acetic asid)) was used to transfer AGL1 to the melon plants containing the pKn-glucanase gene. To ensure proper growth conditions of *Agrobacterium tumefacies*, different concentrations of 2 different antibiotics, carbenicillin and cefotaxime, were used and the overgrowth of Agrobacterium tumefacies was prevented. As a result of this study, it was observed that carbenicillin was more effective than cefotaxime against *Agrobacterium tumefacie*s but after 2 days *Agrobacterium tumefacies* grown in carbenicillin. It was also determined that the appropriate concentration of 300 /L at 50 mg / L at different doses used. After this concentration, healthy, green explants with good growth were transferred to the selection medium to obtain transgenic plants.

*Keywords*-Agrobacterium tumefacies, Carbenicillin, Cefotaxime, Melon, glucanase

# Was Leonardo Da Vinci's Golden Horn (Pera) Bridge Possible?

Ahmet Yasir Kanbur
Department of Civil Engineering
Erzurum Technical University
Erzurum, Turkey
ahmetyasir025@gmail.com

Dilek Okuyucu
Department of Civil Engineering
Erzurum Technical University
Erzurum, Turkey
okuyucu@erzurum.edu.tr

*Abstract*-Leonardo da Vinci, is no doubt, one of the great masters of all times. He is a designer, painter, sculptor, architect, engineer and many more. This Renaissance genius has a dream and a special interest to Istanbul. Da Vinci wants to construct the biggest ever arch bridge to Golden Horn of Bosphorous. In 1502, he sends a letter to Ottoman Sultan, Bayezid II and proposes his bridge project. This project has never been constructed; but has always been negotiated. At the beginning of 16th century, Ottoman Government was the super power and proposed project was a *mega* project. The reason lying behind the rejection of the proposal by Ottoman Government is not known. There exists only a number of rumours and non-technical explanations. This study focused on feasibility analysis of the project by all possible point of views and tried to find an answer for the refusal. Design of the bridge was realized, structural model was created and structural analysis was carried out. Financial situation of that time was investigated, social and economic life around Golden Horn was studied and bridge construction politics of Ottoman Government was evaluated. Some basic details of the study is presented in the whole manuscript.

*Keywords-Leonardo da Vinci, Ottoman Empire, Golden Horn, Bridge Project, Structural Analysis*

## I. INTRODUCTION

It is known that Istanbul is the centre of attraction for European merchants and artists with its cultural values. Like many leading artists in the world, we can call the Lord of Renaissance; Leonardo Da Vinci, a sculptor, a painter, an architect and an engineer, wanted to come to Istanbul and leave a work which would be much more pronounced.

It is known that Sultan Bayezid II wanted to build a permanent bridge over the Golden Horn instead of the bridges that were repeatedly destroyed by the fires in the wars. Having learned this request, Leonardo Da Vinci designed his own architectural intelligence to create a bridge, inspired by the Alidossi Bridge in Castel Del Rio. The details of the bridge project are available in Leonardo's personal notebooks. Leonardo Da Vinci wrote a letter to Sultan Bayezid II stating that he was able to build a bridge to the Golden Horn. Today, the translation of the letter into the Ottoman Turkish is present in the archives of Topkapı Palace. Although the real reason is unknown, Sultan Bayezid II did not approve this project. The possible reasons of this project refusal are generally non-technical evaluations.

In terms of engineering, the most mentioned reason why Sultan Bayezid II did not give approval is the fact that the geometry of the building; the height and span of the arch. However, it has not been possible to reach a study which reveals the fact that Leonardo Da Vinci's bridge project cannot be realized with the engineering approach in the literature. According to writers of herein manuscript it is a deficiency to judge the bridge projects over some shortcomings. This project, which can be called the Mega project of the 16th century needs to be investigated by all possible sides like the possible location of the bridge, the construction sector of the time and the materials used and the earthquakes the building could undergo.

In this study, a feasibility study was conducted for Leonardo Da Vinci's Bridge project proposal. As a first; bridge architecture was developed and a structural model was created by using SAP2000 software. For the building, the materials which are possible to supply and use in the 16th century in Istanbul were selected. Structural analysis was carried out for static and dynamic loading conditions. Factors affecting the implementation of the project; such as financing, bridge construction policies, construction technologies and workmanship were studied.

## II. BRIDGE PROJECT PROPOSAL and CREATED DESIGN

Authorized people of the Ottoman Empire, who were aware of the geo-political, commercial, cultural and symbolic value of Istanbul, mobilized all means to enlarge and develop the city. Following in the footsteps of Fatih Sultan Mehmet, the Conqueror, Sultan Bayezid II thought of a bridge over the Golden Horn; but if we believe in Leonardo Da Vinci, he could not find a master to do so. Da Vinci never came to Istanbul. However, he sent a bridge project proposal to be built on the Golden Horn to Sultan Bayezid II. **[1]** The original of the letter today is in the archives of the Topkapı Palace. Within the scope of the study, this letter was provided and evaluations were made over the translation. One of the biggest dreams of the famous architect-engineer Leonardo Da Vinci is to build the biggest and most magnificent bridge until the Golden Horn in Istanbul in the early 16th century. As mostly stated, he was inspired by the largest single-span arch bridge in Europe in the 15th century with a span of 42 meters; Alidossi Bridge in Castel Del Rio. Detailed information on

the bridge project designed by Leonardo for the Golden Horn was accessible from his notebooks. **Figure 1** presents a general view od Da Vinci' s letter to Sultan Bayezid II and one of his sketches.



**Figure 1.** (a)Leonardo Da Vinci's Letter [2]
(b)A Project Skecth from Da Vinci' s Notebooks [3]

*A. Fiction of the Leonardo Da Vinci's Golden Horn (Pera) Bridge*

In his letter to Sultan Bayezid II, Leonardo has provided very limited information about the bridge. At this stage, Leonardo's notebooks were used. The construction of the Da Vinci Golden Horn Bridge; By studying the possible location of the bridge, bridge size and architecture, the seismicity of Istanbul, construction materials and construction techniques of the Ottoman period; Da Vinci's Pera Bridge project was speculated.

*B. The Possible Location of the Leonardo Da Vinci's Golden Horn (Pera) Bridge*

In the project proposal of the bridge in the Golden Horn (Pera) of Da Vinci, the part of the bridge on the water surface is 400 braccia, ie 244 meters. Considering many factors and Ottoman settlement of the 16th century; **Figure 2** presents the proposed location for the bridge over the Golden Horn.



**Figure 2.** Possible Location of Leonardo da Vinci's Golden Horn Bridge

*C. Bridge Dimensions and Design*

When the resources related to the bridge are evaluated together; it is understood that Leonardo designed the bridge high enough for sailing ships. The Golden Horn is a port

and shipyard area at that time. In addition; there is also technical information that the bridge legs are to be designed with the mechanisms to prevent damage from water flows. The information from the letter on the structural system are limited to these. In the bridge design work, information about size and interior design was collected from Leonardo's drawings and notebook. The given length units are given in braccia (1 meter = 1.64 braccia).

The Golden Horn (Pera) bridge in Istanbul; width 40 braccia, height above the water level 70 braccia, total length of 600 braccia; 400 braccia of the length on the sea. The bridge deck is considered to have two storeys. The first one will be 6 braccia high and each of the width of the path is given as 20 braccia. This storey will cover shops and will be used by public. It is stated that public cars and transported loads use the lower level road; the first storey. The upper storey will only be used by the Royal family. [3] Küfeki stone was selected for main arch, marble was selected for columns, pine was as cover material of bridge upstairs, lightweight tuff was selected for spandrel wall and küfeki was again preferred for arch supporting walls for the parts over the land.

It is essential that an arch bridge built on the estuary carries the loads of use safely. However, Istanbul is an earthquake city. The city has experienced many destructive earthquakes in his history. In this context, if the severe earthquakes that occurred after that date in Istanbul are examined, 1509 earthquakes are defined to occur as the nearest date. The 1509 earthquake is known as one of the most devastating earthquakes of the last five centuries. Large damages have occurred due to sea movement in the form of huge waves; Galata walls are also affected by the earthquake. Anatolia and the Rumelihisarı Castle was damaged and after the earthquake Sultan Bayezid II has brought workers, employees and masters from outside the city for repairs. [4] That is why; it is extremely important that the bridge should be earthquake resistant.

### III. PROJECT EVALUATION

The project proposal was evaluated for all possible matters. The first one is structural performance and possibility of the construction. Financial matters and bridge construction policies are some of the other cases that were studied.

*A. Possibility of the Construction*

When examining whether the project can be realized, it is important to reveal the situation of the construction sector of the period. The 16th century is the period when the Ottoman Empire was at its peak. In this period of architecture (*called the classical period*); engineering services and qualified workmanship are provided by controlled trainings. 16th century is the ear of the Great Master Builder Sinan. Therefore; it is believed that there are enough experts for the construction of the bridge.

Considering the size of the bridge, it is clear that a large amount of materials will be required. Therefore; the possibility of obtaining basic construction material and the natural stones such as küfeki and marble and brick and

wooden materials from Istanbul and the surrounding area should be examined.

Küfeki stone was used in Roman and Byzantine period. It is also called Istanbul stone or Bakırköy stone was used by the great Master Builder Sinan can survive for a long time as 2 thousand 500 years. It has been concluded that the küfeki stone used by the great Master Builder Sinan in the production of structural elements can be used in the construction of the Da Vinci Golden Horn Bridge. However, the fact that Istanbul and its environs are rich in küfeki stone beds can be considered as an indication that there will be no problem in terms of material supply.

Marble material is used as decoration material in many historical works in Istanbul. Marble is mostly known from Istanbul and its surrounding marble beds, especially from Marmara Island. It is clear that stone quarries providing marble for Istanbul and the region for thousands of years are active and marble material can be easily provided for Da Vinci's Golden Horn Bridge project.

One of the mostly used materials for the Da Vinci Golden Horn Bridge project will be wood. Because, it is the basic material of the production of wooden scaffolding and it is one of the most important productions of mega bridge construction. In addition, a large amount of wood may be required as covering material. The fact that the Golden Horn is a shipyard area means that wood materials can be supplied for shipbuilding. It is known that necessary amount of wood should to be obtained from forests in Istanbul and its vicinity. In general, it is concluded that the wooden material required for Da Vinci's Golden Horn Bridge project can be easily obtained from Istanbul and its around.

### B. Structural Performance

Leonardo Da Vinci's Haliç (Pera) Bridge was modeled using the SAP2000 program and structural analyzes were performed on the model. [5] Macro modeling technique has been adopted in the study; solid elements were used. A general image of the model is presented in **Figure 3**. The mechanical properties defined for the materials used in modeling are presented in **Table 1**.
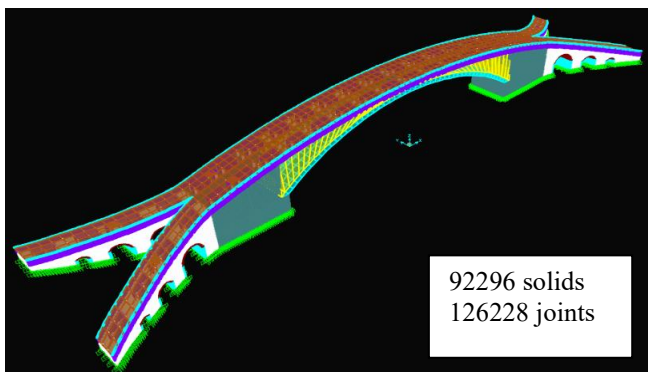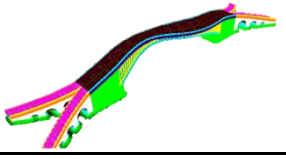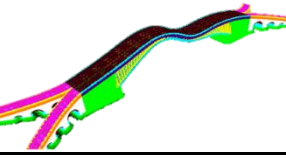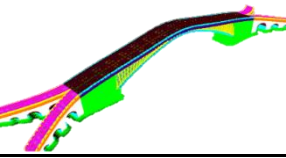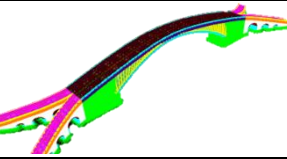


**Figure 3.** Structural Analysis Model for Da Vinci's Pera Bridge

92296 solids
126228 joints

**Table 1.** Selected Materials and Assigned Material Properties [6]

| Element | Material | Compressive Strength (MPa) | Tensile Strength (MPa) | Modulus of Elasticity (MPa) |
|---|---|---|---|---|
| Main Arch | Küfeki | 20 | 2 | 4000 |
| Spandrel Wall | Tuff | 5 | 0.5 | 1000 |
| Arch Supporting Walls (Buttress) | Küfeki | 20 | 2 | 4000 |
| Timber Basement | Pine | 45 | 90 | 10500 |
| Columns | Marble | 100 | 10 | 20000 |

In addition to the modal analysis on the bridge; static and dynamic analysis were carried out. The results of modal analysis are presented in **Table 2**. As a result of the analysis, the first mode was calculated as the horizontal movement of the bridge body in the horizontal direction and the second mode as the movement of the bridge body in the vertical direction. The third and fourth modes are the modes in which torsional behavior is observed. Considering the slender structure of the bridge, it is expected that the bridge body of the first two modes will be calculated as translational movements in the horizontal and vertical directions.

**Table 2.** Results of the Modal Analysis

| Mod | Periot (sec) | Mod Shape | Explanation |
|---|---|---|---|
| 1 | 0.98824 |  | Linear movement in the lateral direction |
| 2 | 0.70907 |  | Linear movement in the vertical direction |
| 3 | 0.66360 |  | Torsional movement in vertical direction |
| 4 | 0.51647 |  | Torsional movement in lateral direction |

The behavior of the bridge structure under the influence of its own weight and usage loads was investigated by static analysis. In addition; The earthquake behavior of the bridge was analyzed by dynamic analysis (time history) considering 1999 Gölcük Earthquake records. The maximum stresses calculated by structural analysis are summarized in **Table 3**. Stresses expressed with green filling are below the strength values whereas the ones by the red fill are the stresses above the strength values.

**Table 3.** Results of Static and Dynamic Analysis

| MAIN MODEL | | | | | | | | | | | | |
|---|---|---|---|---|---|---|---|---|---|---|---|---|
| | COMBO 1: STATIC ANALYSIS | | | | COMBO 2: DYNAMIC ANALYSIS (X) | | | | COMBO 3: DYNAMIC ANALYSIS (Y) | | | |
| | STRESS TYPE | ELEMENT | LOCATION | STRESS (MPa) | STRESS TYPE | ELEMENT | LOCATION | STRESS (MPa) | STRESS TYPE | ELEMENT | LOCATION | STRESS (MPa) |
| S11 | COMPRESSION | Timber Basement | | -15,45 | COMPRESSION | Timber Basement | | -15,00 | COMPRESSION | Timber Basement | | -14,04 |
| | TENSION | Timber Basement | | 5,16 | TENSION | Timber Basement | | 12,49 | TENSION | Timber Basement | | 9,00 |
| S22 | COMPRESSION | Buttress | | -6,93 | COMPRESSION | Buttress | | -5,44 | COMPRESSION | Buttress | | -6,90 |
| | TENSION | Columns | | 5,20 | TENSION | Columns | | 5,40 | TENSION | Columns | | 6,12 |
| S33 | COMPRESSION | Buttress | | -12,63 | COMPRESSION | Buttress | | -9,49 | COMPRESSION | Buttress | | -11,90 |
| | TENSION | Column Base | | 7,00 | TENSION | Column Base | | 9,00 | TENSION | Column Base | | 12,00 |
| | | Columns | | 11,68 | | Columns | | 12,40 | | Columns | | 16,84 |

When the static and dynamic analysis results are evaluated by means of maximum stresses, stress concentrations around key stone of the main arch are observed. Calculated maximum tensile stresses on four columns over the key stone zone and at the basement of them (over küfeki basements) were calculated to be higher than that of the strength values. This can provide a local damage which cannot threaten the overall structural security. Besides, some possible measures can also be taken like increasing the diameter and addition of column bases. **Figure 4** shows a general view of stresses from static analysis.
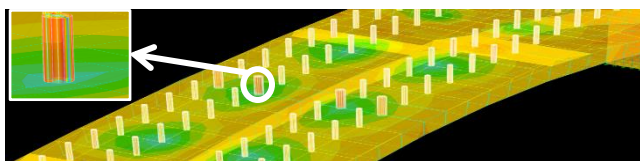


**Figure 4.** A General View from Calculated Stresses of Static Analysis

### C. Financial Evaluation

An examination of the financial situation of the 16th century Ottoman Empire is extremely important for a healthy evaluation of the feasibility of the project. It is known that preliminary exploration works were carried out in the construction works carried out in the Ottoman Empire. So much so; in the classical period, the project is not under construction without preliminary exploration. **[7]** It is possible that the construction work on the Golden Horn Bridge scale was rejected due to the high cost.

When examining the financial situation of the Ottoman Empire in the 16th century, data on the central budget were taken into consideration. According to **[8]** Ottoman central budget provides a budget surplus over the 16th century. The period of 1527 - 1528 is the period when the Ottoman central budget is the highest. When this period is considered and the income from Syria and Egypt is included, the total income of the Ottoman Empire is 537 million *akça*. *Akça* is the Ottoman currency of 16th century. It is stated that 265 million *akça* was spent for the Ottoman regular army. In this case, it is concluded that the money to be spent on construction works should be divided into half of the total income.

As a result of the study conducted by the authors, the cost of the bridge is estimated to be approximately 40,000,000 *akça*. In this calculation, previously the costs of bridges and materials that are expected to be used in Da Vinci bridge are evaluated together.

When we look at the general situation of the central budget of the 16th century Ottoman State, it does not seem to be possible to fund the estimated cost of 40.000.000 *akça* from the budget at one time. However, it is thought that it will be covered within a project which will last for a few years. Besides, it is considered that the shops that will take place in the bridge structure will have rental income and bridge tolls. In the classical period, it is stated that shop rents are between 25 and 40 *akça* per month on average. **[9]** Considering all these points, it is thought that Da Vinci's Golden Horn Bridge Project can be constructed in financial terms within the scope of a project which is spreading in a few years in the 16th century Ottoman Empire.

### D. Trade, Population and Need for a Bridge over Golden Horn

The population of Istanbul of the past is one of the problems that often confronts historians and population scientists. Because the population of the city is often based on speculative data. As a result of the research; it can be said that the experts of 16th century Istanbul provided considerable agreement that the population of the city increased significantly in the 16th century and reached an average of half a million people. Again, the population experts underlines the fact that the population of the the Golden Horn was increasing in 16th century.

Examining the use of soil around the Golden Horn in the 16th century is important for a healthy assessment of the necessity of the bridge. Figure 5 shows the land use around the Golden Horn in the 16th century. As seen in **Figure 5**, Galata, Eyüp and Kasımpaşa were densely settled areas. With the construction of new churches and the opening of the embassies, Galata was also developed in the direction of Pera. The magnificent structures and the mosques on the hills overlooking the Golden Horn caused significant changes in the city's appearance.

When the 16th century Istanbul land use is examined, it is seen that the commercial and residential areas around the Golden Horn are concentrated. The trade element leads to the need for transportation between the two sides of the Golden Horn. One step beyond, it can be thought that easy transportation between the two sides will increase trade. Another striking point here is that there are many harbour structures along the Golden Horn. It is observed that the number of these ports is higher on the historical peninsula over which Topkapı Palace, ie the headquarters of the State administration exist, and ports on the opposite shore have been established near the commercial areas.



**Figure 5.** Land Use of Istanbul in 16th Century **[10]**

The Golden Horn has been the world's trade center since ancient times. The most important reason for this situation is that it is a natural harbour. Deep waters, not affected by southwester and northeaster facilitates the transportation of large commercial vessels to shore and provides great advantages for maritime trade. For this reason, it is clear that the maritime traffic in the Golden Horn is intense. It is also necessary to add boats and raft type vehicles that are used for transportation between both sides. It is thought that freight and passenger transportation between the two sides is a source of livelihood for many people.

In his letter to Sultan Bayezid II, Da Vinci emphasizes that ships can easily pass under the bridge. It can be thought that the easy access between the two sides of the Golden Horn will stimulate the commercial life. However, it is another important issue that tradesmen who ride with the bridge can stay in financially difficult situations.

*E. Bridge Construction Policies*

One of the most important parameters of Leonardo Da Vinci's bridge project feasibility is the bridge building policies of the 16th century Ottoman Empire. The general construction policy of the bridges is to overcome the natural barriers in establishing connections between settlements. When the reasons of construction of the Ottoman bridges in Rumeli and Balkan region were examined; it is seen that there are reasons such as providing connection between the route routes and the trade-caravan routes. Wooden bridges were built to facilitate access and access to the post-conquest and post-conquest zones, and later these bridges were converted into fixed bridges using stone materials. **[11]**

For the 16th century Ottoman Empire, it is the most powerful military and economically strongest country. During this period, 64 bridges were built in the country and only in Rumeli region. **[11]** In this period, the Ottoman Empire built the bridge for military purposes for more conquest movement. During the reign of Suleiman the Magnificent, the conquest of Vienna and the sovereignty of Central Europe was carried out. When examined from this perspective, it would not be wrong to say that the bridges built in Rumeli in the 16th century were built on the road to Vienna. **Figure 6** presents the geographical distribution of the bridges built by the Ottoman Empire in Eastern Europe and the Balkans in the 16th century. The distribution shows that bridges have been built on a line going from Istanbul to the middle of Europe.
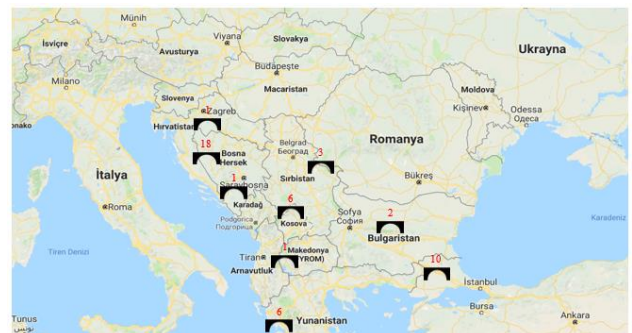


**Figure 6.** Bridges in the Eastern Europe and the Balkans Constructed by the Ottoman Empire in the 16th Century

In 16th century, it is obvious that Ottoman Empire has a bridge construction policy as to reach the central Europe by conquests. In this situation, it might not be meaningful to construct Da Vinci's bridge over Golden Horn to show the

power. This may be the main reason for refusal of the bridge project.

## IV. RESULTS and CONCLUSIONS

Leonardo da Vinci' s bridge Project proposal to Golden Horn of Istanbul was evaluated in this study and the following results can be stated.

- Construction of the project was technically found to be possible.
- Ottoman Government was capable of making the necessary investment to bridge construction during 16th century.
- Construction of the bridge would not negatively affect the port trade and shipyards located around Golden Horn. It might positively affect them all.
- The lack of a strong need for a bridge in between both sides of Golden Horn may be a reason of refusal.
- Bridge construction politics of 16th century's Ottoman Government was not focusing on Anatolian land. Hence, this may be the main reason of the refusal of the project.

It is concluded that the Ottoman Empire, which gave a message to the world with the mega projects of that period, did not realize the mega project coming from the genius of the Renaissance period and that this construction work was not compatible with the bridge construction works developed in accordance with the conquest policies. Because technical infrastructure and economy is sufficient for this mega project.

## ACKNOWLEDGEMENT

## REFERENCES

[1] Kalın, I., "Ben, Ötesi ve Ötesi", 18th Edition, Insan Publications, 2016. (*in Turkish*)

[2] TSMA.E.0754, Leonardo da Vinci's Letter to Ottoman Sultan Bayezid II, Topkapı Palace Archives, 2018. (*in Ottoman Turkish*)

[3] Suh, H., A., "Leonardo's Notebooks", Arkadaş Publications, 2010. (*Translated by Alev SERIN into Turkish*)

[4] Özkılıç, S., K., "1894 Depremi ve İstanbul", Türkiye İş Bankası Publications, 2015. (*in Turkish*)

[5] SAP2000, Structural Software for Analysis and Design, Erzurum Technical University, 2018.

[6] Kanbur, A., Y., "Feasbility of Leonardo Da Vinci's Pera Bridge Project", Bachelor's Degree Thesis, Department of Civil Engineering, Erzurum Technical University, 2018. (in Turkish)

[7] Yılmaz, İ., and Dikmen, S., Ü., "Osmanlı Döneminde Kullanılan Yaklaşık Maliyet Tahmin Yöntemleri", Conference Proceeding, TMMOB Turkish Chamber of Civil Engineers, 6. İnşaat Yönetimi Kongresi, November, 25-26-27 2011, Bursa. (*in Turkish*)

[8] İnalcık, H., "Osmanlı İmparatorluğu'nun Ekonomik ve Sosyal Tarihi", Eren Publications, 2000. (*in Turkish*)

[9] Maydaer, S., "Osmanlı Klâsik Döneminde Kadınların Servet Edinme Yolları (Bursa Örneği)", Uludağ Üniversitesi İlahiyat Fakültesi Dergisi, Vol.15:2, pp. 30-46, 2006. (*in Turkish*)

[10] Ayan, B., "Kent Morfolojisini Etkileyen Nedenler ve Eminönü Tarihi Yarımada Bölgesinin İstanbul Ulaşımına Etkileri", MSc Thesis, Institute of Science, Istanbul Bahçeşehir University, 2010. (in Turkish)

[11] Özkök, M., K., Azsöz, G., and Erşan, Ş., " Erken ve Klasik Döenmde (14.-17. YY) Osmanlı Köprülerinin Tarihsel Gelişlerinin ve Yapım Tekniklerinin İncelenmesi: Edirne / Uzunköprü Örneği" Conference Proceeding, TMMOB Turkish Chamber of Civil Engineers, 3. Köprüler ve Viyadükler Sempozyumu, May 8-9-10, 2015., Bursa. (in Turkish)

# Analysis of the Hunter-Saxton Equation With Caputo-Fabrizio Fractional Derivative

Ercan Çelik
Atatürk Universty
ercelik@atauni.edu.tr

Mustafa Ali Dokuyucu
Ağrı İbrahim Çeçen Universty
madokuyucu@agri.edu.tr

*Abstract*-In this work, we analysed the Hunter-Saxton equation with Caputo-Fabrizio fractional derivative. Using the fixed-point theorem, we present the existence and uniqueness of the coupled solutions for definition of fractional derivatives. We also analysed uniqueness of the solutions. A comparison of the results obtained is given using Mathematica.

*Keywords*-modeling, existence and uniqueness

# A Low Noise Amplifier at 1.5 GHz

Mustafa Samet Çelik
Erzurum Technical University
Electrical and Electronics Engineering
mustafa.celik81@erzurum.edu.tr

Fatih Kaburcuk
Erzurum Technical University
Electrical and Electronics Engineering
fatih.kaburcuk@erzurum.edu.tr

Çağlar Duman
Erzurum Technical University
Electrical and Electronics Engineering
caglarduman@erzurum.edu.tr

*Abstract*-In this paper, a low noise amplifier (LNA) with a bandwidth of 200 MHz operated at 1.5 GHz for wireless communication applications is designed, simulated, built and tested. The circuit is designed and simulated with use of Microwave Office Advance Wave Research (AWR) software. The LNA is fabricated on a FR-4 substrate with dielectric constant of 4.4, thickness of 60-mil and 1 oz. cooper. The Bipolar Junction Transistor (BFG424F) is selected for the LNA. The fabricated LNA provides a noise figure (NF) of 1.5 dB and a gain of 10.58 dB at 1.5 GHz. The LNA is tested and the measurement results are compared with the simulation results. It has been realized that the measurement results are in an acceptable agreement with the simulation results

*Keywords-Low Noise Amplifier (LNA)*

# Cr-Dopant Effect on CdO Thin Films

Demet Iskenderoğlu
Pasinler Vocational School, Departments of Electronics and
Automation, Atatürk University, Erzurum, Turkey,
demettatar@atauni.edu.tr

Harun Güney
Vocational High School, Department of Electric and Energy,
Ağrı İbrahim Çeçen University, Ağrı, Turkey,
hguney@agri.edu.tr
Central Application and Research Laboratory (MERLAB), Ağrı
İbrahim Çeçen University, Ağrı, Turkey

*Abstract*-The undoped and chromium (Cr) doped cadmium oxide (CdO) thin films were synthesized by successive ionic layer adsorption reaction (SILAR) method. CdO thin films have been analyzed for seen Cr effect on with optical, structural and morphological by XRD (X-ray diffraction), absorption and SEM (scanning electron microscope) measurements. XRD measurements of undoped and Cr-doped CdO thin films show the cubic structures and have (111), (200), and (220) peaks. SEM images demonstrate that CdO thin films surfaces varied considerably with the Cr dopant. The calculated bandgap of samples increases with Cr dopant.

# Fabrication of Metal Oxide Carbon Dioxide Detector with Screen Printing Technique for Use on Airplanes

Mehmet Masat
Department of Aviation Management Erzurum Vocational School
Atatürk University
Erzurum, Turkey
mehmet.masat@atauni.edu.tr

Hakan Korul
Department of Aviation Electric and Electronic, Faculty of
Aeronautics and Astronautics
Eskişehir, Turkey
hkorul@anadolu.edu.tr

Ömer Çoban
İspir Hamza Polat Vocational High School,
Atatürk University
Erzurum, Turkey
omercoban@atauni.edu.tr

Mehmet Ertuğrul
Department of Electrical and Electronics Engineering
Atatürk University
Erzurum, Turkey
ertugrul@atauni.edu.tr

*Abstract*— **In this study, metaloxide carbon dioxide and carbon monoxide detector were fabricated by screen printing technique in order to detect carbon dioxide and carbon monoxide gases from the sensors required to be able to monitor the condition and performance of the aircraft and to make the necessary controls.**

*Keywords*— **Screen Printing Technique, Carbon Dioxide, Carbon Monoxide, Gas Sensor**

## I. INTRODUCTION

Measurement is the identification of unknown physical quantities by comparison with known physical quantities. Various measurement and conversion systems have been developed in order to make physical quantities and the changes in these sizes as usable information. Measurement systems are formed according to the method of processing the information received from the systems. While these systems may consist of a single sensor, they may consist of more complex sensor groups and transducer elements[1].

In order to be able to monitor the condition and performance of the aircraft and to perform the necessary checks, it is necessary to know the data about the environment and the current systems of the aircraft. The method of obtaining these data is to place sensor or sensor groups at the points where the relevant data will be obtained[2].

The data obtained is processed through various systems and presented to the flight crew as available information. In addition to the flight crew, it is the system that makes use of these data in systems such as auto throttle and autopilot. Depending on the type of physical size to be measured, the structure and application areas of the systems also change.

The presence of carbon monoxide and other toxic gases is a danger to the flight crew and passengers, but also a possible fire. The pre-inspection of any or both of these gases is important for the prevention of more hazardous situations[3].

Smoke control systems are used for detecting smoke from fire in certain areas of the aircraft. The purpose of smoke control systems is to warn the flight crew with warning lights and lights in the event of a significant amount of smoke before the fire increases in the areas where the fire can occur[4].

In this study, metal oxide carbon dioxide and carbon monoxide detector were fabricated by screen printing technique in order to detect carbon dioxide and carbon monoxide gases from the sensors required to be able to monitor the condition and performance of the aircraft and to make the necessary controls.

## II. EXPERIMENTAL STUDIES

### A. Fabrication of Thick Film Gas Sensor

A thick film gas sensor consists of three main components: heater, electrode and precision layer[5].

The diagram of the gas sensor structure planned to be produced is as given in the Figure 1 .1.
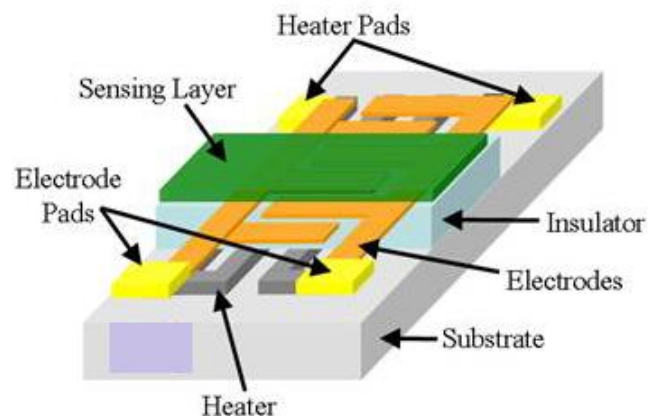


Figure 1.1. Thick film gas sensor structure[5]

### B. Fabrication of Organic Vehicle

Thick film gas sensor pastes usually comprise a semiconducting metal oxide powder, inorganic additives and organic binders[5].

In this research, titanium dioxide ($TiO_2$) was used as the base sensitive metal oxide powders.

For the preparation of the binder, first, linseed stand oil and m–xylene were mixed and they subjected to magnetic stirring at 40 °C on hot plate. The stirring process was continued for about 4 hours.

After that α–terpineol was added then the temperature of was decreased to 30°C. The stirring was continued for about 2 hours to obtain a sticky liquid form binder.

Sensitive powder ($TiO_2$) was mixed with 40 *wt.% and binder* was mixed with 60 *wt.% and* they subjected to magnetic stirring at 40 °C on hot plate for 24 hour.

*C. Film Preparations*

The $TiO_2$ thick films were prepared by screen print technic using $Al_2O_3$ ₓₑsubstrate.

Silver electrodes were printed on an $Al_2O_3$ substrate. After printing the electrodes, it was kept at room temperature for 10 minutes. After this electrodes were kept at 125 °C for 10 minutes for drying. Finally electrodes were kept at 350 °C for 20 minutes for firing. Figure 1.2. shows the structure of electrode elements



Figure 1.2. Silver electrodes printed on alumina substrate.

Sensitive layer was printed with sensitive paste on electrodes. After printing the sensitive layer, films were left at room temperature for 20 min to insure the paste is leveled off and settled and then the films are subjected to a drying and firing process.

The sensitive layer was dried in three steps: first it was subjected to 50°C for 5 minutes and then temperature was increased to 100 °C for another 5 minutes, and finally it was dried at peak temperature of 125 °C for last five minutes.

Finally film was kept at 450 °C for 30 minutes for firing.

## III. RESULTS AND DISCUSSION

The conductivity of the metal oxide film decreases initially with adsorbed oxygen (in case of n type semiconductor) by trapping electrons from surface leading to formation of depleted surface layer. $N_2$ exposed on to film to stabilize the current produced. After some time, test gas is introduced to the chamber where the oxygen can be desorbed by introduction of reducing gas such as (H2, CO, CO2) which relieves the trapped electrons back to conduction band and conductivity of the film increases accordance with concentration of gas[6].
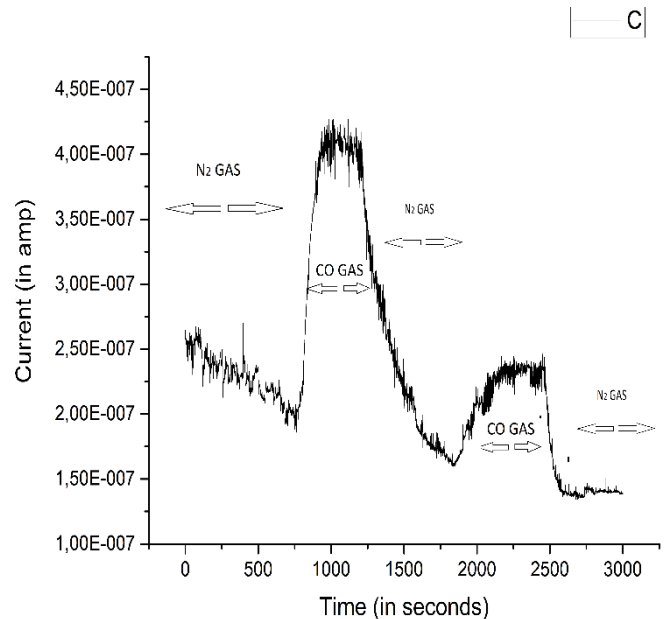


Figure 1.3. Film at 300 °C exposed to 1000 and 500 ppm CO gas.

Fig.1.3. shows the graph of current versus time for the first experiment. In the beginning the $N_2$ for duration about 600s sent into the chamber oxygen ions are adsorbed on the film which resulted in increase in resistance due to formation of depleted surface layer. CO gas is sent into the chamber for about next six hundred seconds and the current increases 210.31 nA to 407,39 nA at 1000 ppm. CO gas is sent into the chamber for about next six hundred seconds and the current is examined at 500 ppm. Current increases 161.31 nA to 239,69 nA The voltage of 5V is maintained throughout experiments..

In this study, thick film metal oxide gas sensors were obtained by using screen printing method. Fabricated metal oxide gas sensors are obtained by screen printing method which is very simple and economical and does not require any technological devices and infrastructure.

The gas sensor properties of the obtained materials were examined and a very high efficiency sensor was obtained from $TiO_2$

## REFERENCES

[1] Kretschmar, M. and Welsby, S. (2005).,"Capacitive and ınductive displacement sensors", (ed: J. Wilson), Sensor Technology Handbook, Newnes: Burlington, MA.

[2] Wang, J., Pan, Y.Y, Lu, S., Guan, Y., Lo, S., Zhang, H.P., (2018). Lag time of fire plume in aircraft cargo compartment fires at reduced pressures, Procedia Engineering 211, p. 719-725.

[3] Wang, J., Pan, Y.Y., Lu, K.Y, Chen, W.S., Zhang, H.J., (2017). Investigation on the CO concentration decay profile and spread velocity of a ceiling jet at reduced pressure in aircraft cargo compartment fires, Applied Thermal Engineering 127, pp. 1246-1251.

[4] https://www.skybrary.aero/index.php/Aircraft_Fire_Detection_System s( Internet acces 01.01.2018 )

[5] Hadı Nezhad Shahrokh Abadı,M.(2010), "Development Of Nanocrystallıne Thıck Fılm Gas Sensors", Universiti Putra Malaysia.

[6] Nataraj J.Ra, Praveen Y Bagalia, M. Krishnaa, M.N.Vijayakumar, (2018) , "Development of Silver Doped Titanium Oxide Thin films for Gas Sensor Applications," Materials Today: Proceedings 5 10670–10680

# Investigation of Structural Changes with the Addition of Graphene to Carbon Aerogel

Meryem Samancı
*Chemical Engineering*
*Atatürk University*
Erzurum, Turkey
meryemsamanci@gmail.com

Ayşe Bayrakçeken Yurtcan
*Chemical Engineering*
*Atatürk University*
Erzurum, Turkey
ayse.bayrakceken@gmail.com

*Abstract*—**Carbon aerogels (CAs) are unique class of high surface area materials derived by sol–gel chemistry. Recently, in addition to resorcinol-formaldehyde (RF) derived amorphous CAs, various carbon allotropes were synthesized in the aerogel form. These carbon allotropes are carbon nanotubes (CNTs), graphene, graphite and diamond. In this study, changes in the structural properties with the addition of a unique material such as graphene to carbon aerogel structure were investigated.**

*Keywords—carbon aerogel, graphene, graphene aerogel, sol-gel chemistry, supercritical carbon dioxide drying*

## I. INTRODUCTION

Aerogels, usually obtained from the supercritical carbon dioxide drying or freeze-drying of the wet gels to replace the solvents with air, are three-dimensional (3D) porous solid materials. They present many intriguing physical properties, including high porosity, lightweight, excellent mass-transfer capability, low bulk density, dielectric permittivity and extraordinary mechanical, thermal, and chemical stability. Carbonaceous aerogels assembled with carbon nanostructures have shown potential in many fields, such as sorption, catalysis, and electrode materials [1].

Since their invention in the early 1990s carbon aerogels have continued to evolve and push the aerogel community forward. This evolution began with the synthesis of the various carbon allotropes (e.g., CNTs, diamond, graphite, and graphene) (fig. 1). Graphene, a two-dimensional carbon nanomaterial, possesses many outstanding properties, such as large specific surface area, excellent chemical stability, and superior optical and electrical properties. The extraordinary and wide-ranging properties of these novel materials continue to be a driver for next generation technologies in energy storage and conversion, filtration and separations, catalysis, and sensors [2].
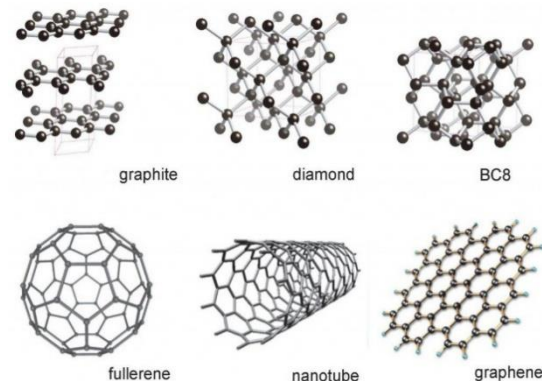

Fig. 1. Graphene and graphene based materials

In this study, carbon aerogel and graphene /carbon aerogel were synthesized. Changes in the structural properties of graphene added to aerogel were examined. These analyzes were performed by Nitrogen adsorption/desorption isotherms (BET), scanning electron microscopy (SEM), Fourier Transform Infrared Spectroscopy (FTIR), Transmission Electron Microscope (TEM) and X-ray diffraction (XRD) analyzes.

## II. METHODS

### A. Synthesis of Carbon Aerogel

Deionized water, 99% resorcinol (R), 37% formaldehyde (F), 99% sodium carbonate ($Na_2CO_3$) were used for the synthesis of resorcinol-formaldehyde aerogels (RFAs). $CO_2$ was used as supercritical fluid in order to dry the samples. The samples were subjected to pyrolysis to obtain carbon aerogels. $N_2$ gas was used as the inert atmosphere during the pyrolysis (fig. 2).


Fig. 2. Carbon Aerogel Synthesis Procedure

The predetermined values of resorcinol, formaldehyde, water and sodium carbonate were mixed together (table 1). This mixture was cured for 1 day at room temperature. This was followed by gelation at 50 $^0$C for 1 day and at 90 $^0$C for 3 days. Then the resulting wet gel was waited for 1 day in acetone solvent exchange of water with acetone. The wet gel was subsequently dried using supercritical $CO_2$ at 2000 psi

and 50 $^0$C to obtain RFA [3]. In order to obtain carbon aerogels (CAs) from RFAs, RFAs were pyrolized at 1000°C under nitrogen atmosphere for 4 h with a heating rate of 15 $^0$C min$^{-1}$.

Table 1. Reactant concentrations in the synthesis of carbon aerogels and graphene/carbon aerogels

| Material | Resorsinol/ Formaldehyde (R/F) molar ratio | Resorsinol/ Water (R/W) molar ratio | Resorsinol/ Catalyst (R/C) molar ratio | Graphene mass % |
|---|---|---|---|---|
| CA | 0.5 | 0.02 | 200 | -------- |
| G/CA | 0.5 | 0.02 | 200 | 0.5 |

### B.Synthesis of Graphene/Carbon Aerogel

In the experiments, pure water, 99% resorcinol (R), 37% formaldehyde (F), 99% sodium carbonate (Na$_2$CO$_3$) and commercial graphite (surface area 800 m$^2$/g) were used for graphene aerogel (G/CA) synthesis. Graphene/carbon aerogel (G/CA) structures were obtained by first standing in acetone for solvent exchange and then by supercritical drying (fig. 3). CO$_2$ was used as a supercritical fluid for supercritical drying. The samples were subjected to pyrolysis to obtain graphene aerogel. N$_2$ gas was used for the inert atmosphere.
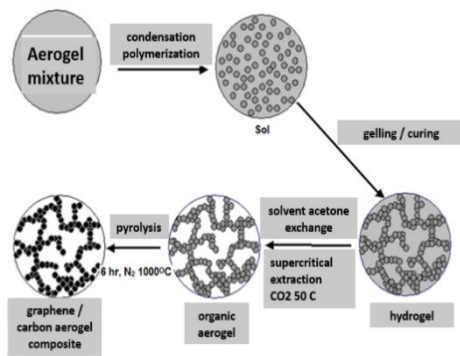


Fig 3. Graphene/Carbon Aerogel Synthesis Procedure

The molar concentration ratios of the reactants in the synthesis stage and the percentage of the mass corresponding to the total solution of the graphene are given in Table 1. Resorcinol, formaldehyde, graphene and water are mixed in desired amounts for the synthesis of graphene/carbon aerogel. Sodium carbonate (Na$_2$CO$_3$) is added as catalyst. The solution is removed from the environment and stirred at room temperature for 2 days in a water bath. After gelation step of the mixture was placed in a sealed tube for 3 days and kept in an oven at 90 ° C. At the end of the third day, the aerogel is removed from the tube and placed in acetone and kept in acetone for 1 day. At this stage, acetone is replaced by water. The sample is dried in order to remove the acetone to obtain graphene /resorcinol formaldehyde aerogel (G/RFA) and then extracted with supercritical carbon dioxide in a reactor at 50 ° C and 2000 psi. Graphene/carbon aerogel was obtained by pyrolysis of G/RF aerogel in a pyrolysis furnace at 1000 °C in nitrogen atmosphere for 3 h.

### III. RESULTS AND FINDINGS

Nitrogen adsorption / desorption isotherms (BET), scanning electron microscopy (SEM), Fourier Transform Infrared Spectroscopy (FTIR), Transmission Electron Microscope (TEM) and X-ray diffraction (XRD) analyzes were made. Structural effects of the addition of graphene to carbon aerogel were investigated.

The BET surface area of the carbon aerogel composite material was calculated as 664.0 m$^2$/g. With the addition of graphene, the BET surface area of the carbon aerogel decreased (table 2). It was also observed that with the addition of graphene, the average pore diameter of the carbon aerogel decreased which led to a decrease in the surface area of the aerogel. The graphene added to the carbon aerogel may be located in the pore walls.

Table 2. Bet results for carbon aerogel and graphene /carbon aerogels

| Materials | BET surface area (m$^3$/g) | Average pore diameter (nm) | BJH pore volume (cm$^3$/g) | DR micropore volume (cm$^3$/g) |
|---|---|---|---|---|
| CA | 664.0 | 9.6 | 1.1005 | 0.2926 |
| G/CA | 519.6 | 3.5 | 0.2893 | 0.2889 |

Fig. 4 shows the SEM images of carbon aerogel (CA) and graphene/carbon aerogel (G/CA). SEM images were taken. It was observed that stratification occurred in the structure of materials with the addition of graphene (fig.4). It is observed that the stratified structure of graphene passes through the aerogel structure.



*a*



*b*



*c*



*d*
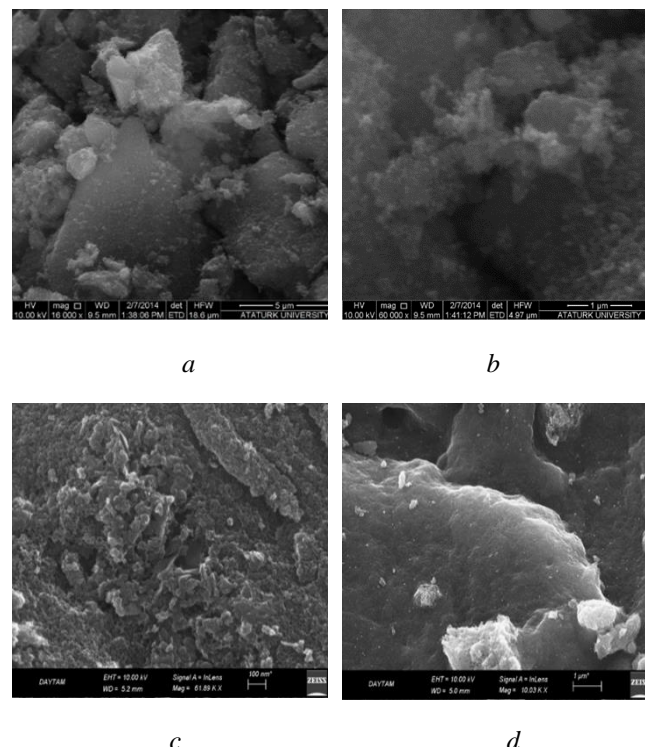
Fig. 4. SEM Images, a,b) carbon aerogel, c,d) graphene/carbon aerogel

XRD analysis of carbon aerogels showed that these materials are amorphous. Moreover, XRD patterns do not give any peaks. When we look at the XRD figure of G/CA, it is seen that there is a peak for C (002) (fig. 5) occurs with the

addition of graphene to carbon aerogel which is also amorphous [4].
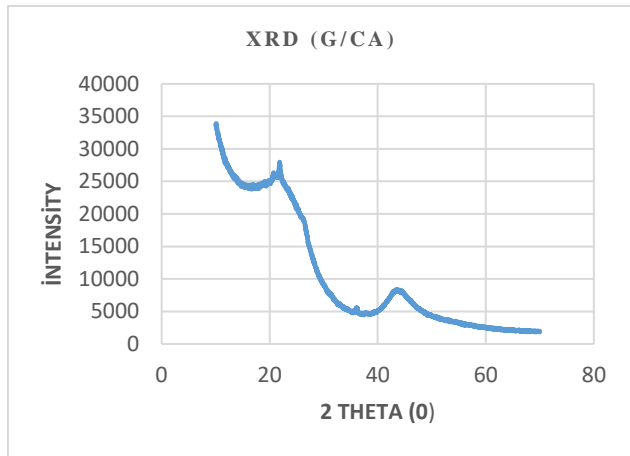


Fig. 5. XRD pattern of graphene/carbon aerogel

FTIR results are given in Figure 6 for carbon aerogel. Eight sharp peaks are seen in the wave numbers of 500, 903, 1067, 1256, 1408, 2902, 2985 and 3673 cm$^{-1}$ for carbon aerogels. The peaks in the 500, 1256 and 1408 cm$^{-1}$ wave numbers indicate C = C stress. Wave numbers of 903 and 1067 cm$^{-1}$ indicate C-O-C stress. 2902 and 2985 cm$^{-1}$ wave numbers indicate C-H stress. The 3673 cm$^{-1}$ wave number indicates the -OH group [5].
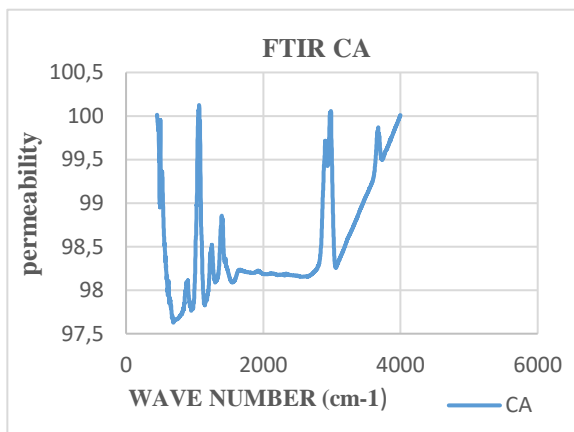


Fig. 6. FTIR graph of carbon aerogel

FTIR results of G/CA are given in Figure 7. There are 6 peaks in 604, 1986, 2003, 2061, 2089, 2191 cm$^{-1}$ wave numbers. The peak at 604 cm$^{-1}$ shows the C = C (C = CH 2) stresses [5]. Among the others in between 1900-2200 cm$^{-1}$, 5 peaks can be attributed to the sequential carbon structure (graphene-like layers) for graphene oxide and graphene-modified materials [6]. Even signal belonging to water molecules encapsulated within structure and stretching vibration of hydroxyl groups, theoretically located around 3500–3000 cm$^{-1}$ was almost completely removed [6]. In the graphene aerogel produced as shown in the FTIR graphs (fig 6., fig 7), the peaks in the 1900 and 2200 cm$^{-1}$ wave numbers were concentrated. This indicates that carbon aerogels were added to graphene or modified graphene.
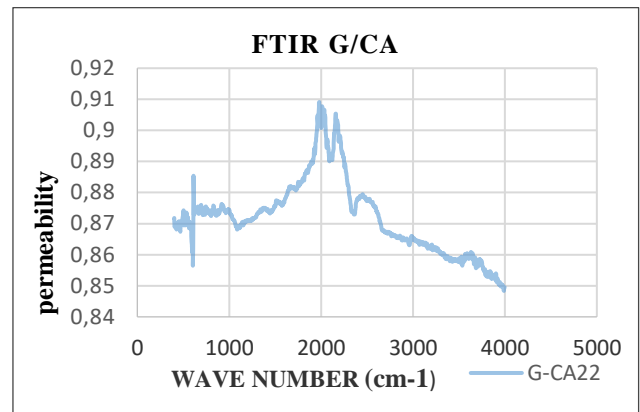


Fig. 7. FTIR graph of graphene/carbon aerogel

## IV. CONCLUSIONS

Due to their outstanding mechanical properties, such as high flexibility and rigidity, graphene aerogels are considered a promising type of aerogel for multiple applications. Recent studies found that by accurately tailoring the three-dimensional alignment of the graphene sheets inside the aerogel, these properties can be further enhanced. In this study, physical characterization of graphene aerogel was performed by adding graphene at the synthesis stage of carbon aerogel. As a result of these characterizations, the structural properties of both carbon aerogel and graphene aerogels were investigated. The effect of graphene on aerogel structure is investigated. Our work will continue by examining the electrochemical changes caused by the addition of graphene to the carbon aerogel.

## REFERENCES

[1] Z. Yin Sui, Y. Na Meng, P. Wen Xiao, Z. Qiang Zhao, Z. Xiang Wei, and B. Hang Han, "Nitrogen-Doped Graphene Aerogels as Efficient Supercapacitor Electrodes and Gas Adsorbents" DOI: 10.1021/am5042065, ACS Appllied Materials Interfaces, 2015, 7, 1431−1438.

[2] Swetha Chandrasekaran, Patrick G. Campbell, Theodore F. Baumann, and Marcus A. Worsleya, "Carbon aerogel evolution: Allotrope, graphene-inspired, and 3D-printed aerogels" J. Mater. Res., 2017- DOI: 10.1557/jmr.2017.411.

[3] Şansım Bengisu Barım, Ayşe Bayrakçeken, Selmi Erim Bozbağ, Lichun Zhang, Rıza Kızılel, Mark Aindow and Can Erkey, "Control of average particle size of carbon aerogel supported platinum nanoparticles by supercritical deposition", Microporous and Mesoporous Materials, 245, 94-103, 2017.

[4] Duan J., Zhang X., Yuan W., Chen H., Jiang S., Liu X., Zhang Y., Chang L., Sun Z. And Du J., "Graphene oxide aerogel-supported Pt electrocatalysts for methanol Oxidation", Journal of Power Sources, 2015, 285-76-79.

[5] Shariff A.M., Beshir D.M., Bustam M.A., and Maitera S., "Some Studies on the Synthesis and characterization of Carbon Aerogel", The Indian Ceramic Society, 2010.

[6] Ciszewski M., Szatkowska E., and Koszorek A., "Magdalena Majka-Carbon aerogels modified with graphene oxide, graphene and CNT as symetric supercapacitor electrodes", 2017, Journal Materials Science: Mater Electron. 28:4897–4903. DOI 10.1007/s10854-016-6137-2.

# Hierarchical CuO@CuS core/shell Nanowires for Supercapacitor Electrode Materials

Yasar Ozkan Yesilbag
*Department of Physics*
*Erzincan Binali Yıldırım University*
Erzincan, Turkey
oyesilbag@erzincan.edu.tr

Fatma Nur Tuzluca
*Department of Physics*
*Erzincan Binali Yıldırım University*
Erzincan, Turkey
ftuzluca@erzincan.edu.tr

Mehmet Ertugrul
*Department of Electrical and Electronics Engineering*
*Ataturk University*
Erzurum, Turkey
ertugrul@atauni.edu.tr

*Abstract*—**Hierarchical CuO@CuS core/shell nanowires (NWs) array is directly synthesized on Cu foam using thermal oxidation and hydrothermal method respectively. The structure, morphology and electrochemical performance of CuO@CuS core/shell NWs arrays are systematically characterized by X-Ray Diffraction Spectroscopy (XRD), Field Emission Scanning Electron Microscopy (FESEM), Energy Dispersion X-Ray Spectroscopy (EDS), Cyclic Voltammetry (CV) and Galvanostatic Charge/Discharge (GCD). This electrode structure demonstrates good electrochemical performance with a maximum areal capacitance of 343 mF cm$^{-2}$ at 2 mA cm$^{-2}$.**

*Keywords*—*CuO@CuS core/shell nanowires, supercapacitor, thermal oxidation.*

## I. INTRODUCTION

In recent years, supercapacitors are of particular interest due to their high power density, fast charge/discharge rate and long cycle life [1]–[3]. Supercapacitors are divided into two types depending on the charge storage mechanisms - electrical double layer capacitors (EDLCs) and pseudocapacitors [3]. EDLCs store charge electrostatically at electrode/electrolyte interface as charge separation. There is no charge transfer between electrode and electrolyte. Pseudocapacitors store by charge transfer between electrode and electrolyte. The charge is transferred at the surface or in the bulk near the surface through adsorption, redox reaction and intercalation of ions [4]. Transition metal oxides and hydroxides are being extensively investigated for use in high performance supercapacitors due to their low cost and low toxicity [5]. Among these metal oxides, CuO has attractive features like low cost, abundant resources, non-toxicity, and easy preparation in diverse shapes of nano-sized dimension, such as nanowires, nanospheres, nanoflowers, nanorods, and nanotubes [6]. It has been extensively studied as a p-type metal-oxide semiconductor [7]. Having direct bandgap of about 1.2 eV and exhibits many excellent physical and chemical properties [8], [9]. CuO have been widely used in many areas such as in anode electrodes for batteries and supercapacitors [10], photovoltaic cells [11], field emission nanodevices [12], and gas sensors [13]. Different approaches have been employed to synthesize 1-D CuO nanostructures such as the hydrothermal method, the thermal decomposition method, and the templating sol-gel method [6].

Recently, different transition metal sulfides such as CoS [14], NiS [15], ZnS [16], and CuS [17], [18] have been investigated as pseudocapacitive electrode materials due to

their high electrochemical performance. Among these transition metal sulfides, CuS is used as electrode material because of low cost, abundance, different morphology in nanoscale and metal-like electronic conductivity (10$^{-3}$ S/cm). In this work, firstly large-scale vertically aligned single crystalline CuO NWs have been synthesized on copper foam at 500°C for 4 h via thermal oxidation method. After then CuS were synthesized on CuO NWs via hydrothermal method to enhance the active sites and the electronic conductivity.

## II. MATERIAL AND METHOD

First of all, large-scale vertically aligned single crystalline CuO NWs were synthesized on Cu foam thermal oxidation method. To remove the oxide layer on the surface the Cu foam, it was cleaned in ultrasonic cleaner for 1 M HCl (50 ml) de-ionized water, absolute ethanol 15 min respectively. The solution of 10 mmol urea ($CH_4N_2O$) and 10 mmol ammonium fluoride ($NH_4F$) with Cu foam was transferred into a teflon-lined stainless steel autoclave and heated at 120°C for 12 h. The Cu foam was then annealed in air at 500°C in the tube furnace and kept for 4 h to obtain CuO NWs. To obtain CuO@CuS core/shell NWs structure, the sample was then placed in an autoclave with 2 mmol of thioacetamide ($C_2H_5NS$) solution dissolved in 35 ml of de-ionized water. The autoclave was heated at 90°C for 1 h. After this process, the autoclave cooled down to room temperature and the sample was dried at 80°C for 2 h.

The crystal structures and morphologies of the CuO@CuS core/shell NWs were determined by using X-Ray Diffraction (PANalytical Empyrean, Cu-K$\alpha$, $\lambda$=1.54060 Å), Field Emission Scanning Electron Microscopy (FEI Quanta 450 FEG) and Energy Dispersion X-Ray Spectroscopy (EDAX, AMETEK Materials Analysis Division). The electrochemical performance were determined by Cyclic Voltammetry and Galvanostatic Charge Discharge analyses using a Gamry Reference 1010E potentiostat instrument.

The electrochemical measurements were performed using 2 M KOH aqueous electrolyte solution. Platinum foil ($1 \times 1$ cm$^2$ in area) and the Ag/AgCl were used as the counter and reference electrodes, respectively. The CuO@CuS electrode ($1 \times 1$ cm$^2$) were immersed in electrolyte and were used directly as a working electrode. The electrochemical measurements were performed in a three-electrode electrochemical cell at room temperature. The areal capacitance (C) was calculated by equation (1):

$$C = \frac{Ixt}{AxV} \qquad (1)$$

where $I$ is the constant discharge current, $t$ is the discharge time, $V$ is the potential window and $A$ is the electrode area.

## III. RESULTS AND DISCUSSION

The XRD diffraction patterns of the sample taken over a 20° to 80° (2θ) range are given in Fig. 1. The XRD peaks can be indexed as monoclinic structured CuO (JCPDS card No. 80-1917), cubic structured cuprous oxide (Cu2O) (JCPDS card No. 78-2076), and fcc Cu metal from the substrate (JCPDS card No. 85-1326). After sulfonation reaction, some diffraction peaks indexed to hexagonal-phase CuS (JCPDS card No. 06-0464). The sharp and intense peaks in the XRD patterns of CuO@CuS core/shell NWs arrays indicate their good crystallinity.
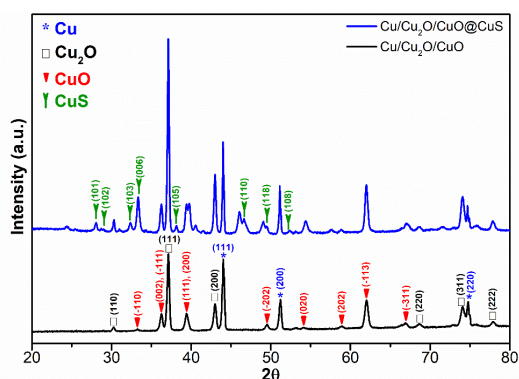


Fig. 1. XRD patterns of CuO and CuO@CuS core/shell NWs.

Fig. 2 shows the FESEM images and EDS analyzes of the morphology of CuO NWs arrays. As seen in figure, CuO NWs have grown onto the Cu foam surface densely and uniformly. The purity and composition of the CuO NWs were further confirmed by EDS analysis. EDS spectrum revealing the existence of Cu and O elements in the sample. According to EDS analysis, the atomic contents of Cu and O are 53.84% and 46.16%, which is nearly in agreement with the 1:1 stoichiometric ratio of CuO NWs, respectively. After sulfur treatment, FESEM images and EDS analyzes of CuO@CuS core/shell NWs arrays are given in Fig. 3. It can been clearly seen that, CuS structure is formed on the surface of CuO NWs. Further analysis with EDAX measurement, only strong peaks for Cu, S and O are found in the spectrum. The atomic ratio of Cu, S and O is 50.57%, 42.50% and 6.92%.
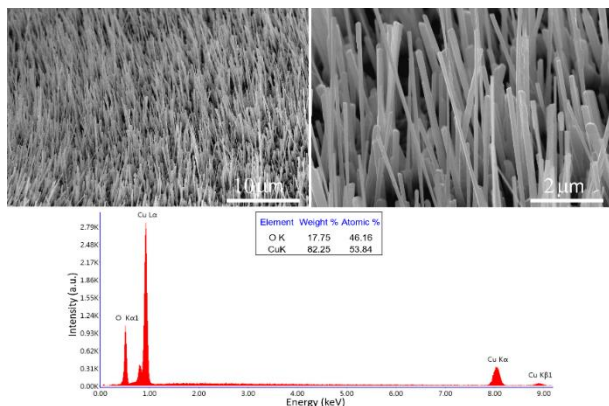


Fig. 2. Low and high magnification FESEM images and EDS analyzes of CuO NWs.
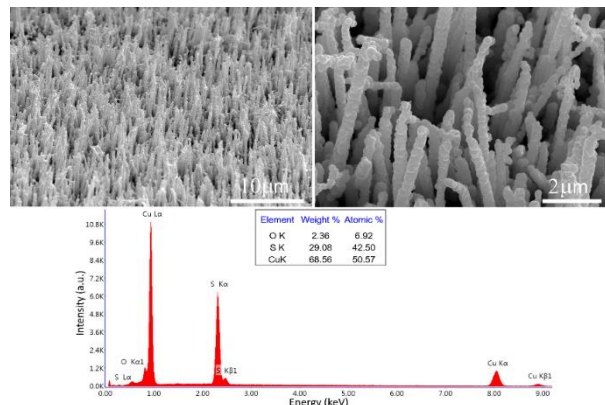


Fig. 3. Low and high magnification FESEM images and EDS analyzes of CuO@CuS core/shell NWs.

Electrochemical properties of CuO@CuS electrode in 2 M KOH aqueous electrolyte are shown in Fig. 4. In Fig. 4a, the typical CV curves of the CuO@CuS electrode measured at various scan rates ranging from 5 to 100 mV s$^{-1}$. It can be seen that the CV curves of the CuO@CuS electrode have two redox peaks, which reveal that pseudocapacitive characteristics of these electrode. In order to evaluate the areal capacitance, GCD measurements were performed. The GCD curves of the CuO@CuS electrode in the voltage range of −0.5 to 0.2 V at various current densities of 2 to 6 mA cm$^{-2}$ are illustrated in Fig. 4b. The nonlinear behavior of the GCD curves confirms that the charge storage in the CuO@CuS electrode mainly originates from pseudocapacitance mechanism. The areal capacitance values of the CuO@CuS core/shell NWs arrays were 343, 257, 171, 107 and 68 mF cm$^{-2}$ at current densities of 2, 3, 4, 5 and 6 mA cm$^{-2}$, respectively in Fig. 4c.
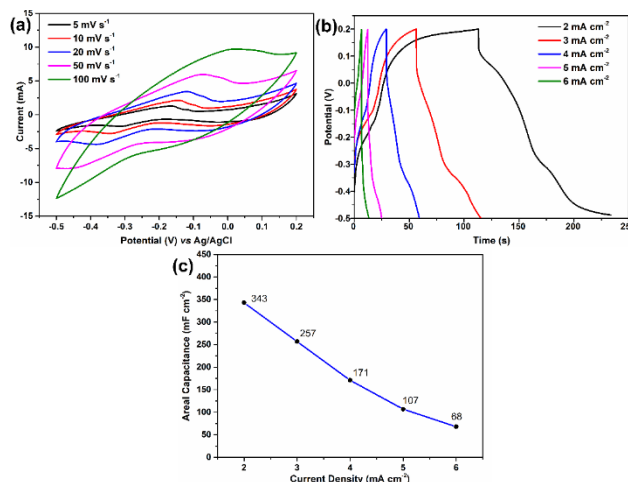


Fig. 4. (a) The CV curves at different scan rates, (b) the GCD curves at different current densities, (c) the areal capacitance vs. different current density.

## IV. CONCLUSION

In conclusion, CuO@CuS core/shell NWs were synthesized on Cu foam by thermal oxidation and hydrothermal method respectively. According to GCD measurements at 2 mA cm$^{-2}$ current density, areal capacitance were obtained 343 mF cm$^{-2}$ for CuO@CuS core/shell NWs. This study also gives different point of view

into the design of metal oxide/sulfide heterostructure electrodes used in a various range of applications.

## ACKNOWLEDGEMENT

## REFERENCES

[1] G. Wang, L. Zhang, and J. Zhang, "A review of electrode materials for electrochemical supercapacitors," *Chem. Soc. Rev.*, vol. 41, pp. 797–828, 2012.

[2] Y. Zhang, L. Li, H. Su, W. Huang, and X. Dong, "Binary metal oxide: advanced energy storage materials in supercapacitors," *J. Mater. Chem. A*, vol. 3, no. 1, pp. 43–59, 2015.

[3] F. Beguin, V. Presser, A. Balducci, and E. Frackowiak, "Carbons and electrolytes for advanced supercapacitors," *Adv. Mater.*, vol. 26, no. 14, pp. 2219–2251, 2014.

[4] V. Augustyn, P. Simon, and B. Dunn, "Pseudocapacitive oxide materials for high-rate electrochemical energy storage," *Energy Environ. Sci.*, vol. 7, no. 5, p. 1597, 2014.

[5] F. Shi, L. Li, X. Wang, C. Gu, and J. Tu, "Metal oxide/hydroxide-based materials for supercapacitors," *RSC Adv.*, vol. 4, no. 79, pp. 41910–41921, 2014.

[6] Q. Zhang *et al.*, "CuO nanostructures: Synthesis, characterization, growth mechanisms, fundamental properties, and applications," *Prog. Mater. Sci.*, 2014.

[7] J. Huang, Y. Zhu, X. Yang, W. Chen, Y. Zhou, and C. Li, "Flexible 3D porous CuO nanowire arrays for enzymeless glucose sensing: In situ engineered versus ex situ piled," *Nanoscale*, 2015.

[8] D. Li, J. Hu, R. Wu, and J. G. Lu, "Conductometric chemical sensor based on individual CuO nanowires," *Nanotechnology*, vol. 21, no. 48, 2010.

[9] M. Vila, C. Díaz-Guerra, and J. Piqueras, "Optical and magnetic properties of CuO nanowires grown by thermal oxidation," *J. Phys. D. Appl. Phys.*, 2010.

[10] Q. Zhang, J. Wang, D. Xu, Z. Wang, X. Li, and K. Zhang, "Facile large-scale synthesis of vertically aligned CuO nanowires on nickel foam: Growth mechanism and remarkable electrochemical performance," *J. Mater. Chem. A*, 2014.

[11] B. G. Ganga, S. M. Seetharaman, P. C. R. Varma, M. A. G. Namboothiry, and P. N. Santhosh, "Photovoltaic properties of low temperature solution processed earth abundant CuO nanocrystal-based hybrid solar cells," *Phys. status solidi*, vol. 214, no. 1, p. 1600671, Jan. 2017.

[12] G. Kaur, K. Saini, A. K. Tripathi, V. Jain, D. Deva, and I. Lahiri, "Room temperature growth and field emission characteristics of CuO nanostructures," *Vacuum*, 2017.

[13] M. Yin, F. Wang, H. Fan, L. Xu, and S. Liu, "Heterojunction CuO@ZnO microcubes for superior p-type gas sensor application," *J. Alloys Compd.*, 2016.

[14] H. Hu, B. Y. Guan, and X. W. (David) Lou, "Construction of Complex CoS Hollow Structures with Enhanced Electrochemical Properties for Hybrid Supercapacitors," *Chem*, 2016.

[15] A. Wang *et al.*, "Controlled synthesis of nickel sulfide/graphene oxide nanocomposite for high-performance supercapacitor," *Appl. Surf. Sci.*, 2013.

[16] N. S. Arul, L. S. Cavalcante, and J. In Han, "Facile synthesis of ZnS/MnS nanocomposites for supercapacitor applications," *J. Solid State Electrochem.*, 2018.

[17] H. Heydari, S. E. Moosavifard, S. Elyasi, and M. Shahraki, "Nanoporous CuS nano-hollow spheres as advanced material for high-performance supercapacitors," *Appl. Surf. Sci.*, 2017.

[18] W. Xu *et al.*, "Synthesis and properties of morphology controllable copper sulphide nanosheets for supercapacitor application," *Electrochim. Acta*, 2016.

# Traffic Sign Recognition Using Deep Convolutional Neural Network

Burcu Tiryaki
Electrical-Electronics Engineering Department
Kafkas University, Kars, TURKEY
Atatürk Univ., Erzurum, TURKEY
burcutiryaki25@hotmail.com

I. Yucel Ozbek
Electrical-Electronics Engineering Department
Atatürk University
Erzurum, TURKEY
iyucelozbek@gmail.com

E. Argun Oral
Electrical-Electronics Engineering Department
Atatürk University
Erzurum, TURKEY
eminoral@atauni.edu.tr

*Abstract*— **It was performed, in this study, the classification of traffic signs to be used in a traffic sign recognition system which plays an important role in driver assistance systems. A Convolution Neural Network (CNN) was utilized for the classification. Both training and test studies of this study were implemented on German Traffic Sign Recognition Benchmark (GTSRB) database which consists of 39209 training and 12630 test images, all taken from real traffic scenes. There are also 43 classes in the database with varying number of samples for each. Training data was first partitioned into five for cross-validation of the training data and data fusion. In each run one of the five partitions was used to validate the model, trained using remaining four partitions, yielding five different trained networks by those test images were classified. Finally, all classification result combined based on separate test probabilities. At the end, was obtained average of 96.23%.**

*Keywords— Deep Learning, Convolution Neural Network (CNN), German Traffic Sign Recognition Benchmark (GTSRB)*

## I. INTRODUCTION

The increase in the number of vehicles and roads along with the developments in the automotive industry has increased the number of traffic signs. Traffic signs provide safe traffic flow by alerting and driving drivers. The shapes and colors are designed to be easily distinguishable from the environment [1]. However, in some severe weather condition such as rain, snow, fog etc. or inadequate lighting as well as partial occlusion, traffic signs may be indistinguishable by drivers. Not properly detected traffic signs are responsible for most of the traffic accidents. In Driver Assistance System (DAS), which provides safety information to drivers, traffic sign recognition plays an important role [2]. Since traffic sign recognition require real-time performance, computers running artificial intelligence algorithms are needed in these systems [3]. In recent years, deep learning which is a branch of machine learning developed from numerical learning and model recognition studies in artificial intelligence of computer science, has been used in many areas such as data analysis, gene analysis and image classification. The reason it is widely used comes from its high accuracy in such problems. In machine learning techniques, some pre-operations must be performed first. In deep learning, however, learning can be performed on raw data without pre-processing.

## II. CONVOLUTIONAL NEURAL NETWORK (CNN)

CNNs are a special form of the neural networks. They are feed-forward neural networks designed to analyze input data and have a multi-layered structure. CNNs are used in many areas such as video analysis, pattern recognition and speech recognition or classification. They are very successful against variable patterns and geometric transformations. It is resistant to distortion on images caused by different lighting conditions and partial occlusion. While feature extractors are designed by hand in conventional models, that are extracted by convolution layers in CNNs. Its ability to replicate layers is the main reason why a CNN structure is more successful than the other methods in terms of classification performance [4]. Convolutional neural networks are used to classify handwritten digits written in 1989 and continued to be using increasingly [5].
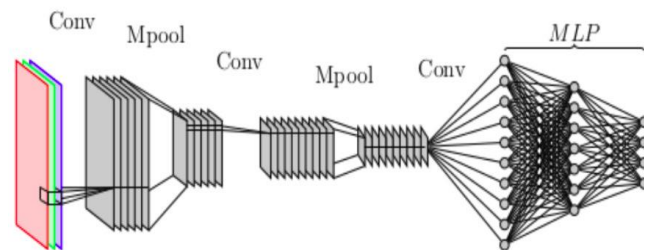


Fig.1. Architecture of CNN [6]

Fig.1 shows the basic structure of CNN. Its input layer can accept a 3-channel color or single-channel monochrome images. Repeating convolution, pooling and ReLU layers are used next. This structure is followed by fully connected layers. A classifier layer is placed at the end of the network. The input data progresses through these layers and creates the final classification output. These layers can be summarized as follows.

*Input Layer:*

It is the layer the raw data is first introduced to the network and resized if necessary. Input data size selection is important. If it is selected large, both the memory need and training time increase. However, the network success may or may not increase accordingly. If the image size is selected small, on the contrary, the memory requirement and training time are reduced at cost of possible decreased network performance. Hence, input layer size must adjusted properly.

*Convolution Layer:*

It is the basic building block of CNNs also called as transformation layer. Most of the calculation is done in this layer [6]. It basically extracts feature and local patterns of input data needed for a particular classification task. Small

size filters of convolutional layer form its trainable parameters.

*Rectified Linear Units (ReLU)*

As a result of mathematical operations obtained in it, the convolution layer is linear. ReLU, also known as activation layer, increases the nonlinear properties of the network for faster learning. Compared to other functions such as hyperbolic tangent and sigmoid, ReLu enables the network progress faster just by replacing negative entries with zero.

*Cross Channel Normalization:*

It comes after the ReLu layer and performs a normalization by replacing each element with a normalized value obtained from its neighboring channel.

*Pooling Layer:*

The pooling layer is used to underline spatial information and obtain deeper features by picking the average or maximum pixel in a sub-region. This layer acts as a down-sampler by reducing its input image size. During this process only the width and height are affected while the channel depth is not changed. Although information loss occurs during down sampling this is beneficial as it reduces the number of calculations and prevents the system from memorizing. Also this layer reinforces the features against noise and deterioration.

*Fully Connected Layer:*

Collects the weight of the previous layer to connect to the next layer and works like neural networks.

*Classification Layer:*

Classification takes place in this layer. The output of this layer is equal to the number of classes. Among various classifiers softmax is usually preferred because of its high performance.

*CNN Paramaters:*

**Strides:** Specifies the number of steps that filters are moved on the image.

**Padding:** Applies a vertical and horizontal fill to the image edges to create a property map of the same size of the input.

## III. PROPOSED WORK

*D. Dataset*

Both training and test studies of this study were implemented on German Traffic Sign Recognition Benchmark (GTSRB) database which consists of 39209 training and 12630 test images. They are all large, lifelike single-images all taken from real traffic scenes. Dataset images suit well to a multi-class classification problem as there are 43 classes in the database with varying number of

samples for each class supplied with their reliable ground-truth data. Although these traffic signs can be grouped into four as mandatory, danger, prohibitory and others, the proposed work is performed as a 43-class classification problem.



Fig.2. Traffic sign examples of the dataset used in study

*E. Experimental Setup*

Training data was first partitioned into five for cross-validation and data fusion. In each run one out of five partitions was used for validation while the others first used for training, yielding five trained networks by these test images were classified. This results in five classification results. As a final step, all classification results are combined to obtain final test probabilities as well as corresponding test results.

*F. Results*

Obtained classification results of traffic signs for five cross-validation tests are given in Table 1. The combined test result also shown in this table. As can be seen from the comparison of these results, 93.04% ratio of average cross-validation test accuracy increases to 96.23% level.

Table 1. Traffic signs test results

|  | Test1 | Test2 | Test3 | Test4 | Test5 |
|---|---|---|---|---|---|
| Cross-validation Results (%) | 93.96 | 92.62 | 94.47 | 92.72 | 91.43 |
| Fused Result (%) | **96.23** | | | | |

The confusion matrix of final fused classification results is shown in Figure 3. As can be seen from this figure, the off-diagonal entries in the confusion matrix have very small values, mostly zero, as expected from that of a good performing classifier.

Class ID

| | 1 | 2 | 3 | 4 | 5 | 6 | 7 | 8 | 9 | 10 | 11 | 12 | 13 | 14 | 15 | 16 | 17 | 18 | 19 | 20 | 21 | 22 | 23 | 24 | 25 | 26 | 27 | 28 | 29 | 30 | 31 | 32 | 33 | 34 | 35 | 36 | 37 | 38 | 39 | 40 | 41 | 42 | 43 |
|---|---|---|---|---|---|---|---|---|---|---|---|---|---|---|---|---|---|---|---|---|---|---|---|---|---|---|---|---|---|---|---|---|---|---|---|---|---|---|---|---|---|---|---|
| 1 | 60 | 0 | 0 | 0 | 0 | 0 | 0 | 0 | 0 | 0 | 0 | 0 | 0 | 0 | 0 | 0 | 0 | 0 | 0 | 0 | 0 | 0 | 0 | 0 | 0 | 0 | 0 | 0 | 0 | 0 | 0 | 0 | 0 | 0 | 0 | 0 | 0 | 0 | 0 | 0 | 0 | 0 | 0 |
| 2 | 0 | 720 | 0 | 0 | 0 | 0 | 0 | 0 | 0 | 0 | 0 | 0 | 0 | 0 | 0 | 0 | 0 | 0 | 0 | 0 | 0 | 0 | 0 | 0 | 0 | 0 | 0 | 0 | 0 | 0 | 0 | 0 | 0 | 0 | 0 | 0 | 0 | 0 | 0 | 0 | 0 | 0 | 0 |
| 3 | 0 | 5 | 743 | 1 | 0 | 1 | 0 | 0 | 0 | 0 | 0 | 0 | 0 | 0 | 0 | 0 | 0 | 0 | 0 | 0 | 0 | 0 | 0 | 0 | 0 | 0 | 0 | 0 | 0 | 0 | 0 | 0 | 0 | 0 | 0 | 0 | 0 | 0 | 0 | 0 | 0 | 0 | 0 |
| 4 | 0 | 0 | 0 | 444 | 1 | 4 | 0 | 0 | 0 | 0 | 0 | 0 | 0 | 0 | 0 | 0 | 0 | 0 | 0 | 0 | 0 | 0 | 0 | 0 | 0 | 0 | 0 | 0 | 0 | 0 | 0 | 0 | 0 | 0 | 0 | 0 | 0 | 0 | 0 | 0 | 0 | 0 | 1 |
| 5 | 0 | 21 | 1 | 0 | 631 | 2 | 0 | 0 | 2 | 0 | 0 | 0 | 0 | 0 | 0 | 0 | 2 | 0 | 0 | 0 | 0 | 0 | 0 | 0 | 0 | 0 | 0 | 0 | 1 | 0 | 0 | 0 | 0 | 0 | 0 | 0 | 0 | 0 | 0 | 0 | 0 | 0 | 0 |
| 6 | 0 | 2 | 10 | 13 | 1 | 602 | 0 | 1 | 1 | 0 | 0 | 0 | 0 | 0 | 0 | 0 | 0 | 0 | 0 | 0 | 0 | 0 | 0 | 0 | 0 | 0 | 0 | 0 | 0 | 0 | 0 | 0 | 0 | 0 | 0 | 0 | 0 | 0 | 0 | 0 | 4 | 0 | 0 |
| 7 | 0 | 0 | 0 | 1 | 0 | 0 | 140 | 0 | 0 | 0 | 0 | 0 | 0 | 0 | 0 | 0 | 0 | 0 | 0 | 0 | 0 | 0 | 0 | 0 | 0 | 0 | 0 | 0 | 0 | 0 | 0 | 0 | 0 | 2 | 3 | 0 | 0 | 0 | 0 | 0 | 4 | 0 | 0 |
| 8 | 0 | 0 | 0 | 4 | 0 | 1 | 0 | 438 | 7 | 0 | 0 | 0 | 0 | 0 | 0 | 0 | 0 | 0 | 0 | 0 | 0 | 0 | 0 | 0 | 0 | 0 | 0 | 0 | 0 | 0 | 0 | 0 | 0 | 0 | 0 | 0 | 0 | 0 | 0 | 0 | 0 | 0 | 0 |
| 9 | 0 | 0 | 0 | 22 | 1 | 0 | 0 | 0 | 425 | 2 | 0 | 0 | 0 | 0 | 0 | 0 | 0 | 0 | 0 | 0 | 0 | 0 | 0 | 0 | 0 | 0 | 0 | 0 | 0 | 0 | 0 | 0 | 0 | 0 | 0 | 0 | 0 | 0 | 0 | 0 | 0 | 0 | 0 |
| 10 | 0 | 0 | 0 | 8 | 0 | 0 | 0 | 0 | 0 | 472 | 0 | 0 | 0 | 0 | 0 | 0 | 0 | 0 | 0 | 0 | 0 | 0 | 0 | 0 | 0 | 0 | 0 | 0 | 0 | 0 | 0 | 0 | 0 | 0 | 0 | 0 | 0 | 0 | 0 | 0 | 0 | 0 | 0 |
| 11 | 0 | 0 | 0 | 0 | 0 | 3 | 0 | 0 | 0 | 2 | 652 | 0 | 0 | 0 | 0 | 0 | 0 | 0 | 0 | 0 | 0 | 0 | 0 | 1 | 0 | 0 | 0 | 0 | 0 | 0 | 0 | 0 | 2 | 0 | 0 | 0 | 0 | 0 | 0 | 0 | 0 | 0 | 0 |
| 12 | 0 | 0 | 0 | 0 | 0 | 0 | 0 | 0 | 0 | 0 | 0 | 395 | 0 | 0 | 0 | 0 | 0 | 0 | 0 | 0 | 1 | 0 | 0 | 0 | 0 | 0 | 0 | 0 | 24 | 0 | 0 | 0 | 0 | 0 | 0 | 0 | 0 | 0 | 0 | 0 | 0 | 0 | 0 |
| 13 | 0 | 0 | 0 | 0 | 0 | 0 | 0 | 0 | 0 | 0 | 0 | 0 | 646 | 1 | 0 | 9 | 0 | 0 | 0 | 0 | 0 | 0 | 0 | 6 | 0 | 0 | 0 | 0 | 0 | 0 | 0 | 0 | 0 | 1 | 0 | 0 | 1 | 0 | 12 | 0 | 14 | 0 | 0 |
| 14 | 0 | 0 | 0 | 0 | 0 | 1 | 0 | 0 | 0 | 0 | 0 | 0 | 0 | 717 | 0 | 0 | 0 | 0 | 0 | 0 | 0 | 0 | 0 | 1 | 0 | 0 | 0 | 0 | 0 | 0 | 0 | 0 | 0 | 1 | 0 | 0 | 0 | 0 | 0 | 0 | 0 | 0 | 0 |
| 15 | 0 | 0 | 0 | 0 | 0 | 0 | 0 | 0 | 0 | 0 | 0 | 0 | 0 | 0 | 270 | 0 | 0 | 0 | 0 | 0 | 0 | 0 | 0 | 0 | 0 | 0 | 0 | 0 | 0 | 0 | 0 | 0 | 0 | 0 | 0 | 0 | 0 | 0 | 0 | 0 | 0 | 0 | 0 |
| 16 | 0 | 0 | 1 | 0 | 0 | 0 | 0 | 0 | 0 | 0 | 0 | 0 | 0 | 0 | 0 | 209 | 0 | 0 | 0 | 0 | 0 | 0 | 0 | 0 | 0 | 0 | 0 | 0 | 0 | 0 | 0 | 0 | 0 | 0 | 0 | 0 | 0 | 0 | 0 | 0 | 0 | 0 | 0 |
| 17 | 0 | 0 | 0 | 0 | 0 | 0 | 0 | 0 | 0 | 0 | 0 | 0 | 0 | 0 | 0 | 0 | 150 | 0 | 0 | 0 | 0 | 0 | 0 | 0 | 0 | 0 | 0 | 0 | 0 | 0 | 0 | 0 | 0 | 0 | 0 | 0 | 0 | 0 | 0 | 0 | 0 | 0 | 0 |
| 18 | 0 | 0 | 0 | 0 | 0 | 0 | 7 | 0 | 2 | 0 | 0 | 0 | 0 | 0 | 0 | 0 | 0 | 351 | 0 | 0 | 0 | 0 | 0 | 0 | 0 | 0 | 0 | 0 | 0 | 0 | 0 | 0 | 0 | 0 | 0 | 0 | 0 | 0 | 0 | 0 | 0 | 0 | 0 |
| 19 | 0 | 0 | 0 | 0 | 0 | 0 | 0 | 0 | 0 | 2 | 0 | 0 | 0 | 0 | 0 | 0 | 0 | 0 | 346 | 0 | 0 | 9 | 1 | 2 | 1 | 1 | 2 | 22 | 2 | 0 | 2 | 0 | 2 | 0 | 0 | 0 | 0 | 0 | 0 | 0 | 0 | 0 | 0 |
| 20 | 0 | 0 | 0 | 0 | 0 | 0 | 0 | 0 | 0 | 0 | 0 | 0 | 0 | 0 | 0 | 0 | 0 | 0 | 0 | 56 | 0 | 0 | 0 | 0 | 0 | 4 | 0 | 0 | 0 | 0 | 0 | 0 | 0 | 0 | 0 | 0 | 0 | 0 | 0 | 0 | 0 | 0 | 0 |
| 21 | 0 | 0 | 0 | 0 | 0 | 0 | 0 | 0 | 0 | 0 | 0 | 0 | 0 | 0 | 0 | 0 | 0 | 0 | 0 | 0 | 90 | 0 | 0 | 0 | 0 | 0 | 0 | 0 | 0 | 0 | 0 | 0 | 0 | 0 | 0 | 0 | 0 | 0 | 0 | 0 | 0 | 0 | 0 |
| 22 | 0 | 0 | 0 | 0 | 0 | 0 | 0 | 0 | 0 | 0 | 0 | 0 | 0 | 0 | 0 | 0 | 0 | 0 | 0 | 0 | 0 | 64 | 26 | 0 | 0 | 0 | 0 | 0 | 0 | 0 | 0 | 0 | 0 | 0 | 0 | 0 | 0 | 0 | 0 | 0 | 0 | 0 | 0 |
| 23 | 0 | 0 | 0 | 0 | 0 | 0 | 0 | 0 | 0 | 0 | 0 | 0 | 0 | 0 | 0 | 0 | 0 | 0 | 0 | 0 | 0 | 0 | 120 | 0 | 0 | 0 | 0 | 0 | 0 | 0 | 0 | 0 | 0 | 0 | 0 | 0 | 0 | 0 | 0 | 0 | 0 | 0 | 0 |
| 24 | 0 | 0 | 0 | 0 | 0 | 0 | 0 | 0 | 0 | 0 | 0 | 0 | 0 | 0 | 0 | 0 | 0 | 0 | 0 | 0 | 5 | 12 | 0 | 133 | 0 | 0 | 0 | 0 | 0 | 0 | 0 | 0 | 0 | 0 | 0 | 0 | 0 | 0 | 0 | 0 | 0 | 0 | 0 |
| 25 | 0 | 0 | 0 | 0 | 0 | 0 | 0 | 0 | 0 | 0 | 0 | 0 | 0 | 0 | 0 | 0 | 0 | 0 | 0 | 0 | 0 | 0 | 0 | 0 | 87 | 0 | 0 | 1 | 2 | 0 | 0 | 0 | 0 | 0 | 0 | 0 | 0 | 0 | 0 | 0 | 0 | 0 | 0 |
| 26 | 0 | 0 | 0 | 0 | 0 | 5 | 0 | 0 | 0 | 0 | 0 | 0 | 0 | 0 | 0 | 0 | 0 | 0 | 0 | 1 | 0 | 0 | 1 | 0 | 0 | 465 | 3 | 1 | 0 | 1 | 0 | 0 | 0 | 0 | 0 | 0 | 0 | 3 | 0 | 0 | 0 | 0 | 0 |
| 27 | 0 | 0 | 0 | 0 | 0 | 0 | 0 | 0 | 0 | 0 | 0 | 0 | 0 | 0 | 0 | 0 | 0 | 0 | 0 | 0 | 0 | 0 | 0 | 0 | 0 | 0 | 180 | 0 | 0 | 0 | 0 | 0 | 0 | 0 | 0 | 0 | 0 | 0 | 0 | 0 | 0 | 0 | 0 |
| 28 | 0 | 0 | 0 | 0 | 0 | 0 | 0 | 0 | 0 | 0 | 0 | 0 | 0 | 0 | 0 | 0 | 0 | 0 | 0 | 0 | 0 | 0 | 0 | 0 | 0 | 0 | 0 | 33 | 27 | 0 | 0 | 0 | 0 | 0 | 0 | 0 | 0 | 0 | 0 | 0 | 0 | 0 | 0 |
| 29 | 0 | 0 | 0 | 0 | 0 | 0 | 0 | 0 | 0 | 0 | 0 | 0 | 0 | 0 | 0 | 0 | 0 | 0 | 0 | 0 | 0 | 0 | 0 | 0 | 0 | 0 | 0 | 147 | 3 | 0 | 0 | 0 | 0 | 0 | 0 | 0 | 0 | 0 | 0 | 0 | 0 | 0 | 0 |
| 30 | 0 | 0 | 0 | 0 | 0 | 0 | 0 | 0 | 0 | 0 | 0 | 0 | 0 | 0 | 0 | 0 | 0 | 0 | 0 | 0 | 0 | 0 | 0 | 0 | 0 | 0 | 0 | 0 | 0 | 90 | 0 | 0 | 0 | 0 | 0 | 0 | 0 | 0 | 0 | 0 | 0 | 0 | 0 |
| 31 | 0 | 0 | 0 | 0 | 0 | 0 | 6 | 0 | 2 | 0 | 0 | 0 | 0 | 0 | 0 | 0 | 0 | 0 | 0 | 16 | 1 | 0 | 6 | 1 | 0 | 0 | 0 | 2 | 22 | 0 | 94 | 0 | 0 | 0 | 0 | 0 | 0 | 0 | 0 | 0 | 0 | 0 | 0 |
| 32 | 0 | 0 | 0 | 0 | 0 | 0 | 0 | 0 | 0 | 0 | 0 | 0 | 0 | 0 | 0 | 0 | 0 | 0 | 0 | 0 | 0 | 0 | 0 | 0 | 0 | 0 | 0 | 0 | 0 | 0 | 0 | 270 | 0 | 0 | 0 | 0 | 0 | 0 | 0 | 0 | 0 | 0 | 0 |
| 33 | 0 | 0 | 0 | 0 | 0 | 0 | 0 | 0 | 0 | 0 | 0 | 0 | 0 | 0 | 0 | 0 | 0 | 0 | 0 | 0 | 0 | 0 | 0 | 0 | 0 | 0 | 0 | 0 | 0 | 0 | 0 | 0 | 60 | 0 | 0 | 0 | 0 | 0 | 0 | 0 | 0 | 0 | 0 |
| 34 | 0 | 0 | 0 | 0 | 0 | 0 | 0 | 0 | 0 | 0 | 0 | 0 | 0 | 0 | 0 | 0 | 0 | 0 | 0 | 0 | 0 | 0 | 0 | 0 | 0 | 0 | 0 | 0 | 0 | 0 | 0 | 0 | 0 | 210 | 0 | 0 | 0 | 0 | 0 | 0 | 0 | 0 | 0 |
| 35 | 0 | 0 | 0 | 0 | 0 | 0 | 0 | 0 | 0 | 0 | 0 | 0 | 0 | 0 | 0 | 0 | 0 | 0 | 0 | 0 | 0 | 0 | 0 | 0 | 0 | 0 | 0 | 0 | 0 | 0 | 0 | 0 | 0 | 0 | 120 | 0 | 0 | 0 | 0 | 0 | 0 | 0 | 0 |
| 36 | 0 | 0 | 0 | 17 | 0 | 0 | 0 | 0 | 0 | 0 | 0 | 0 | 0 | 0 | 0 | 0 | 0 | 0 | 0 | 0 | 0 | 0 | 0 | 0 | 0 | 0 | 0 | 2 | 0 | 0 | 0 | 0 | 0 | 7 | 0 | 361 | 2 | 0 | 0 | 0 | 1 | 0 | 0 |
| 37 | 0 | 0 | 0 | 0 | 0 | 0 | 0 | 0 | 0 | 0 | 0 | 0 | 0 | 0 | 0 | 0 | 0 | 0 | 0 | 0 | 0 | 0 | 0 | 0 | 0 | 0 | 0 | 0 | 0 | 0 | 0 | 0 | 0 | 0 | 0 | 0 | 117 | 0 | 3 | 0 | 0 | 0 | 0 |
| 38 | 0 | 0 | 0 | 0 | 0 | 0 | 0 | 0 | 0 | 0 | 0 | 0 | 0 | 0 | 0 | 0 | 0 | 0 | 0 | 0 | 0 | 0 | 0 | 0 | 0 | 0 | 0 | 0 | 0 | 0 | 0 | 0 | 0 | 0 | 0 | 1 | 0 | 59 | 0 | 0 | 0 | 0 | 0 |
| 39 | 0 | 0 | 0 | 0 | 0 | 0 | 0 | 0 | 0 | 0 | 0 | 0 | 0 | 0 | 0 | 0 | 0 | 0 | 0 | 0 | 0 | 0 | 0 | 0 | 0 | 0 | 0 | 0 | 0 | 0 | 0 | 0 | 0 | 0 | 0 | 0 | 7 | 0 | 680 | 0 | 3 | 0 | 0 |
| 40 | 0 | 0 | 0 | 0 | 0 | 2 | 0 | 0 | 0 | 0 | 0 | 0 | 0 | 0 | 0 | 0 | 0 | 0 | 0 | 0 | 0 | 0 | 0 | 0 | 0 | 0 | 0 | 17 | 0 | 0 | 0 | 0 | 0 | 0 | 0 | 0 | 0 | 0 | 0 | 71 | 0 | 0 | 0 |
| 41 | 0 | 0 | 0 | 0 | 0 | 0 | 0 | 0 | 0 | 0 | 0 | 0 | 0 | 0 | 0 | 0 | 0 | 0 | 0 | 0 | 0 | 0 | 0 | 0 | 0 | 0 | 0 | 0 | 0 | 0 | 0 | 0 | 0 | 0 | 0 | 0 | 0 | 1 | 0 | 0 | 89 | 0 | 0 |
| 42 | 0 | 0 | 0 | 0 | 0 | 0 | 0 | 0 | 3 | 0 | 0 | 0 | 0 | 0 | 0 | 0 | 0 | 0 | 0 | 0 | 0 | 0 | 0 | 0 | 0 | 0 | 0 | 0 | 0 | 0 | 0 | 0 | 0 | 0 | 0 | 0 | 0 | 0 | 0 | 0 | 0 | 57 | 0 |
| 43 | 0 | 0 | 0 | 0 | 0 | 0 | 0 | 0 | 0 | 0 | 0 | 0 | 0 | 0 | 0 | 0 | 0 | 0 | 0 | 0 | 0 | 0 | 0 | 0 | 0 | 0 | 0 | 0 | 0 | 0 | 0 | 0 | 0 | 0 | 0 | 0 | 0 | 0 | 0 | 0 | 0 | 0 | 90 |

Fig.3. Confusion matrix to evaluate the obtained test results

## IV. CONCLUSION AND FUTURE WORK

It was performed the classification of traffic signs using a Convolution Neural Network (CNN). The GTSRB database with 43 classes were used for both training and test studies. In the study the training data was first partitioned into five to obtain five separate trained-networks and test results to be fused to get better results. The performance of the CNN is increased using more layers, but this also results in the increased complexity of the network as well as the time required for training. Increasing the classification accuracy will be investigated as the future work.

## REFERENCES

[1] Hasan Fleyeh, '' Traffic and Road Sign Recognition '', Jully 2008.

[2] Hengliang Luo, Yi Yang, Bei Tong, Fuchao Wu, and Bin Fan,'' Traffic Sign Recognition Using a Multi-Task Convolutional Neural Network '', vol.19,April 2018

[3] Y. MaryReeja, T. Latha and A. MaryAnsalinShalini,'' Traffic Sign Detection and Recognition in Driver Support System for Safety, 2015.

[4] Vedat Tümen, Özal Yıldırım and Burhan Ergen,'' A Convolutional Neural Network Model for Road Flow Direction Detection '', October 2017.

[5] Y. LeCun, B.Boser, J.S. Denker, D.Henderson, R.E. Howard, W. Hubbard and L.D. Jackel,'' Backpropagation Applied to Handwritten Zip Code Recognition'',1989.

[6] Nemanja Veličković, Zeljko Stojković and Goran Dimić, ''Traffic Sign Classification Using Convolutional Neural Network'' Computer Science & Information Technology, pp. 177–186, 2018.

[7] Junqi Jin, Kun Fu, and Changshui Zhang, Member, IEEE,'' Traffic Sign Recognition With Hinge Loss Trained Convolutional Neural Networks '', vol.15, October 2014.

[8] By Samer Hijazi, Rishi Kumar, and Chris Rowen, IP Group, Cadence, '' Using Convolutional Neural Networks for Image Recognition '', 2015.

[9] Özkan İNİK and Erkan ÜLKER,'' Derin Öğrenme ve Görüntü Analizinde Kullanılan Derin Öğrenme Modelleri '', Gaziosmanpasa Journal of Scientific Research, vol.6,pp. 85-104,2017.

[10] https://ujjwalkarn.me/2016/08/11/intuitive-explanation-convnets/

# A Microwave Bandpass Filter Design

Gurkan Kalinay
Department of Electrical and
Electronics Engineering,
Erzurum Technical University,
Erzurum, Turkey
gurkan.kalinay@erzurum.edu.tr

Fatih Kaburcuk
Department of Electrical and
Electronics Engineering,
Erzurum Technical University,
Erzurum, Turkey
fatih.kaburcuk@erzurum.edu.tr

Mehmet Onur Kok
Department of Electrical Engineering
and Computer Science,
Syracuse University,
Syracuse, NY, USA
mokok@syr.edu

*Abstract*— **A microwave bandpass filter from lower cutoff frequency of 5.5 GHz to upper cutoff frequency of 6.5GHz is designed, simulated, fabricated, and measured for wireless communication applications. The electromagnetic (EM) simulation of the filter was performed using ADS software. The substrate used in this design is FR-4 with dielectric constant of 4.4, thickness of 60-mil, and 1 oz. cooper. The measured results are in very good agreement with the simulation results.**

*Keywords— Microwave Bandpass Filter, Electromagnetic Simulation, ADS*

## I. INTRODUCTION

Microwave filters are one of the important components for wireless communication applications. They are mainly used to reject the unwanted frequencies of microwave signals and to permit the wanted frequencies of the signals for good transmission. It means that the filters allow us to control frequencies of the signals at a selected point [1]. The filters are two-port devices and they can be designed by using lumped elements or distributed elements [1-4]. Bandpass filters are essential part of both transmitters and receivers in a system.

In this paper, a coupled line bandpass filter is designed with distributed elements using ADS software on the FR-4 substrate to have a Fractional Bandwidth (FBW) of 170 MHz with 0.2 dB equal-ripple at the center frequency ($\omega_0$) of 5.98 GHz. The measurement results are in very good agreement with the simulation results. The bandpass filter proposed here can be a good candidate for modern communication networks, such as Wi-Fi, Wireless Local Area Network (WLAN), and Long Term Evolution (LTE).

## II. DESIGN PROCEDURE

The specifications of the design parameters are: lower cutoff frequency ($\omega_{c1}$) is 5.5 GHz, upper cutoff frequency ($\omega_{c2}$) is 6.5 GHz, equal-ripple value is 0.2 dB, and attenuation at 8 GHz is better than 25 dB. The FR-4 substrate with dielectric constant of 4.4, and 60-mil thickness, and 1 oz. cooper is chosen for printed circuit board (PCB) material. The center frequency ($\omega_0$) and FBW of the filter are determined by:

$$\omega_0 = \sqrt{\omega_{c1} \times \omega_{c2}} , \qquad (1)$$

$$FBW = \left(\omega_{c1} - \omega_{c2}\right) / \omega_0 . \qquad (2)$$

Design procedure starts with determining the filter order (N), which N=3 in our case, from equal-ripple value using conventional Chebyshev model [2]. There are two circuit models that can be applied to design and fabricate the filter with lumped and distributed elements. In this paper, the filters with both lumped element model and distributed element

model are designed, however, a filter with only distributed element model is fabricated. In the filter design with lumped element model shown in Fig. 1, the inductor (L) and the capacitor (C) values are determined by Table I (standard Chebyshev table) and the formulation in which "g" values plugged in from [2] .

Table I. Chebyshev Values For 0.2 dB Equal-Ripple

| | C1 | L2 | C3 | L4 | C5 | L6 | C7 | L8 | C9 | L10 | C11 |
|---|---|---|---|---|---|---|---|---|---|---|---|
| Value of N | g1 | g2 | g3 | g4 | g5 | g6 | g7 | g8 | g9 | g10 | g11 |
| 1 | 0.4342 | 1 | | | | | | | | | |
| 2 | 1.0378 | 0.6745 | 1.5386 | | | | | | | | |
| 3 | 1.2225 | 1.1525 | 1.2275 | 1 | | | | | | | |
| 4 | 1.3028 | 1.2844 | 1.9761 | 0.8468 | 1.5386 | | | | | | |
| 5 | 1.3394 | 1.337 | 2.166 | 1.337 | 1.3394 | 1 | | | | | |
| 6 | 1.3598 | 1.3632 | 2.2394 | 1.4555 | 2.0974 | 0.8838 | 1.5386 | | | | |
| 7 | 1.3722 | 1.3781 | 2.2756 | 1.5001 | 2.2756 | 1.3781 | 1.3722 | 1 | | | |
| 8 | 1.3804 | 1.3875 | 2.2963 | 1.5217 | 2.3413 | 1.4925 | 2.1349 | 0.8972 | 1.5386 | | |
| 9 | 1.386 | 1.3938 | 2.3093 | 1.534 | 2.3728 | 1.534 | 2.3093 | 1.3938 | 1.386 | 1 | |
| 10 | 1.3904 | 1.3983 | 2.3181 | 1.5417 | 2.3904 | 1.5536 | 2.37 | 1.5066 | 2.1514 | 0.9034 | 1.5386 |

Fig. 2 presents the circuit schematic with distributed element model. For this equivalent circuit, odd mode ($Z_{0o}$) and even mode ($Z_{0e}$) impedances were calculated from the following formulations [2-4].

$$J_{i,i+1} = \frac{1}{Z_0} \left[ \frac{\pi FBW}{2 g_i g_{i+1}} \right]^{0.5} , \qquad (3)$$

$$Z_{0o}\big|_{i,i+1} = Z_0 \left[ 1 - Z_0 J_{i,i+1} + \left[ Z_0 J_{i,i+1} \right]^2 \right]$$

$$Z_{0e}\big|_{i,i+1} = Z_0 \left[ 1 + Z_0 J_{i,i+1} + \left[ Z_0 J_{i,i+1} \right]^2 \right]$$

Then, ADS Line Calc were used to find initial width and length of the coupled line. At the end of each side quarter wavelength, transmission lines were added to complete the circuit.
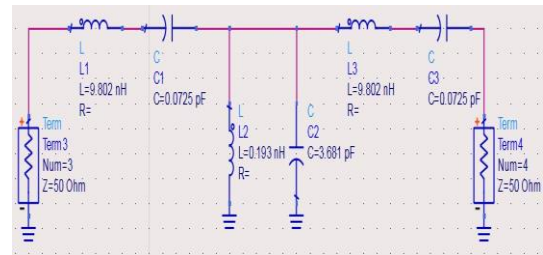


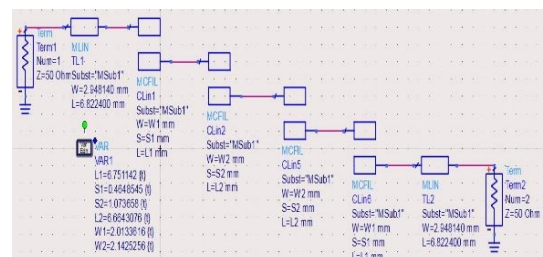Fig. 1. Equivalent circuit models with lumped elements.



Fig. 2. Equivalent circuit models with distributed elements.

## III. SIMULATION AND MEASUREMENT RESULT

Fig. 3 and 4 show the circuit simulation for both models. It can be seen from Fig. 3 and 4 that required specifications are achieved for both circuits and the input reflection ($S_{11}$) and transmission ($S_{21}$) coefficients obtained for lumped element model are better than those obtained for the distributed element model.
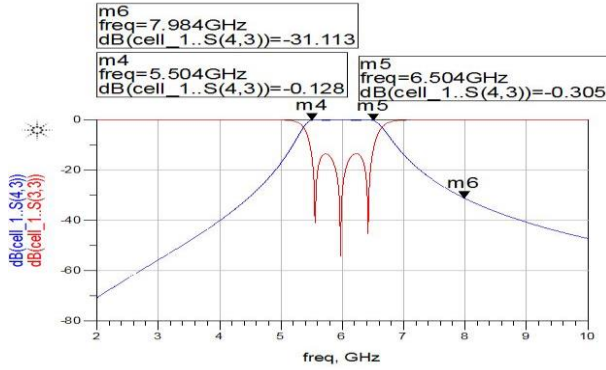


Fig. 3. Circuit simulation results ($S_{11}$ and $S_{21}$) for lumped elements.
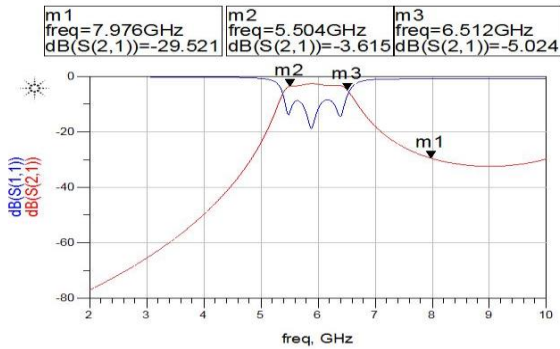


Fig. 4. Circuit simulation results ($S_{11}$ and $S_{21}$) for distributed elements.
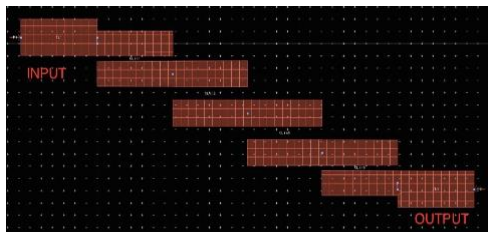


Fig. 5. Layout of the filter with distributed elements.

In order to run the EM simulation, circuit layout, shown in Fig. 5, for distributed circuit model was generated. Fig. 6 represent the EM simulation results. It can be seen from Fig. 6 that attenuation is around -55dB at 8GHz and $S_{11}$ is around -14dB at the center frequency. EM simulation gives better attenuation at 8GHz comparing to circuit simulation. After completing the EM simulation, DXF file of the design is export and import to Circuit Cam program to fabricate the filter on the FR-4 substrate.

The fabricated bandpass filter is shown in Fig. 7. The measurement results are shown in Fig. 8. The $S_{11}$ is around -18dB and attenuation at 8GHz is -41dB. The pass band is slightly shifted. The reason for it could be either fabrication/soldering error or calibration issue with Network Analyzer.
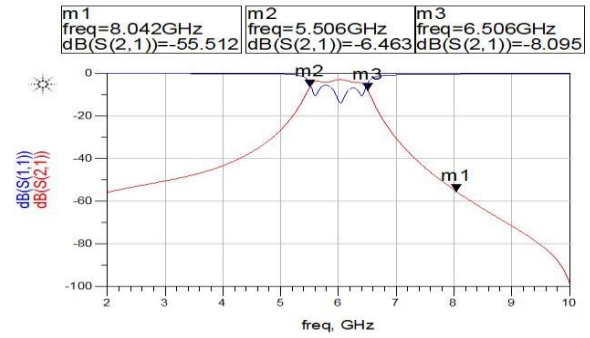


Fig. 6. EM Simulation results ($S_{11}$ and $S_{21}$) for distributed elements.
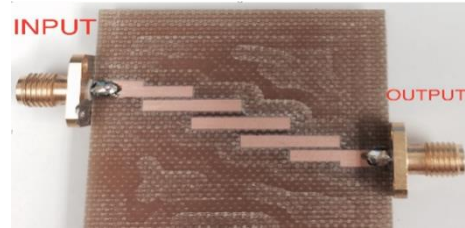


Fig. 7. Picture of fabricated bandpass filter.
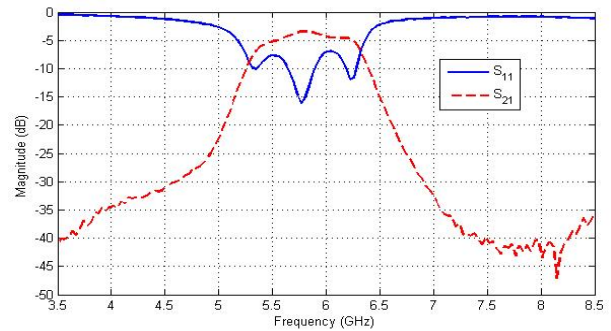


Fig. 8. Measurement results ($S_{11}$ and $S_{21}$) of the fabricated bandpass filter.

## IV. CONCLUSION

A microwave bandpass filter with lower cutoff frequency of 5.5 GHz and upper cutoff frequency of 6.5 GHz is designed, simulated, fabricated and tested. The input reflection coefficient of the fabricated filter is around -18dB at 6 GHz and the attenuation at 8GHz is -41dB. The simulation results are in good agreement with the desired requirements demonstrating the stability of the design procedure at selected frequency range. The fabricated filter can be a good candidate for wireless communication applications, such as Wi-Fi, WLAN, and LTE.

## REFERENCES

[1] E. Arvas, Class notes for ELE 722 MicrowaveFilters, Department of Electrical Engineering and Computer Science, Syracuse University, 2009.

[2] G. Matthaei, L. Young and E. Jones, Microwave Filters, Impedance Matching Networks and Coupling Structures, Artech House, 1980.

[3] D. M. Pozar, Microwave Engineering, Wiley, pp. 408-415, 2012.

[4] J.-S. Hong and M. J. Lancaster, Microstrip Filter for RF/Microwave Applications, Wiley, 2001.

# The Application of Fenton's Reagent as an Efficient System in the Soil Contaminated With Used Lubricating Oils

Ibtihel Zaier

National Institute of Applied Sciences and
Technologies (INSAT), Tunis 1080, Tunisia,
ibtihel@gmail.com

*Abstract* - **Soil pollution is a growing problem that poses a real threat to the environment worldwide and particularly in the developing countries due to the lack of serious environmental regulations. After being neglected until recent times, soil pollution has become a major concern due to the increasing number of polluted sites and their impact on human health, groundwater quality and ecosystems nature and viability.**

**The most common pollutants found in soils are mainly hydrocarbons and heavy metals. Used lubricating oils are a mix of both types of pollutants. Chemical oxidation of contaminants by Fenton's reagent has been applied successfully in the treatment of polluted soils. This technique is one of the advanced oxidation processes (AOP) that rely on the in situ formation of highly reactive chemical species that partially or totally mineralize most organic pollutants.**

**The objective of our work was to evaluate the effectiveness of Fenton's reagent in the degradation of pollution caused by used lubricating oils.**

**The efficiency of the treatment was evaluated by measuring the Total Organic Carbon (TOC) for organic pollutants and by determining the concentration of heavy metals (ICP). Drawdown rates of TOC were in the range of 70% and 80% for Fenton testing, a maximum drawdown of 87.23% was obtained by applying the optimal conditions deduced from the experimental design and which were: pH 2, 3 g of hydrogen peroxide, 13 mg of Mohr's salt, reaction time of 3 hours and a temperature of 70 ° C. Electro-Fenton tests led to more important TOC drawdown rates for a shorter period of time. We got a rate of drawdown of up to 97.53% TOC working with $[Na_2SO_4] = 0.1$ M and $I = 150$ mA. A significant reduction of heavy metals (90.9% for zinc, 69.17 % for nickel and 91.51% for chromium) was achieved by Electro-Fenton tests with increasing slightly the intensity ($I = 250$ mA).**

*Keywords: Fenton's reagent, hydrocarbons, advanced oxidation processes (A.O.P), heavy metals.*

# Water Absorption, Flexural Strength And Calcium Carbonate Content In A Composite Crossarm

Zulkiflle Leman
Department of Mechanical and Manufacturing Engineering,
Faculty of Engineering Laboratory of Biocomposites
Technology, Institute of Tropical Forestry and Forest Product
(INTROP) Universiti Putra Malaysia43400 Serdang,
MALAYSIA
zleman@upm.edu.my

Isma'ila Mukhtar
Department of Mechanical Engineering, Faculty of Engineering
Kano University of Science and Technology Wudil PMB 3244
Kano State, NIGERIA
ismailmuk@gmail.com

Mohd Zuhri Mohamed Yusoff
Department of Mechanical and Manufacturing Engineering,
Faculty of Engineering Universiti Putra Malaysia 43400
Serdang, MALAYSIA
zuhri@upm.edu.my

Mohd Sapuan Salit
Department of Mechanical and Manufacturing Engineering,
Faculty of Engineering Universiti Putra Malaysia 43400
Serdang, MALAYSIA
sapuan@upm.edu.my

*Abstract*—The aim of this research was to study the effect of the calcium carbonate on water absorption, flexural properties and phase changes. Characterizations of the composites such as flexural test, water absorption test and X-ray diffraction (XRD) analysis were conducted. The flexural test was done before and after water absorption test. While the XRD was carried out to show the phase changes due to the incorporation of the calcium carbonate, as well as to determine the various compounds and their percentages in the composites. It appears from the findings that specimen with calcium carbonate had an increase in flexural strength and modulus by 75.5% and 60.7% respectively. However, the flexural properties after water absorption showed a decrease in strength. Similarly, a specimen with calcium carbonate absorbed 2.06% water compared to the specimen without calcium carbonate which absorbed 3.15%. The XRD analysis of the composite with calcium carbonate revealed a high percentage of homogeneous phase of polymer and glass fibre when compared to the composite without calcium carbonate. The analysis confirms there was a presence of 8.7%. calcium carbonate in the composite.

*Keywords—Calcium carbonate, fibre polymer composite, flexural strength, water absorption, XRD*

## [6] Introduction

Water absorption characteristic of fibre reinforced composite is one of the major causes of its degradation due to weathering especially when used in outdoor applications. As time goes by, the absorbed water in the composite will cause failure of the structure. To set the context for discussion, the following sentences describe some of the investigations of the effect of inorganic fillers in fibre reinforced polymer composites. As shown in many investigations, composite properties tend to improve with the addition of fillers, such as metal oxide [1] [2], calcium carbonate ($CaCO_3$) [3] and aluminium oxide ($Al_2O_3$) [4]. Other precursors that are commonly used in composite are nanoclay and talcum [5] [6]. Amongst these fillers, $CaCO_3$ has a potential of enhancing both the mechanical and physical properties of the composite. Some of the fundamental roles played by this filler can be seen in a research investigated by Syafri et. al [7]. The authors reported that optimum value of tensile strength and reduction in water absorption were achieved with the addition of 4% precipitated $CaCO_3$. In another investigation, the effect of the incorporation of nano-$CaCO_3$ through blending and impregnation modification processes was investigated [8]. The investigation reveals that the interfacial property was significantly improved with the addition of the nano $CaCO_3$. Another ceramic particle that found worthy of incorporation in polymer composite is MgO; it can serve as a self-healing agent by healing micro cracks which in turn increases the strength of the composite [9]. Also, the incorporation of the $CaCO_3$ particle within polypropylene reinforced core-shell nanoparticles improves both rheological, thermal and mechanical properties [10]. These research works have demonstrated that the use of $CaCO_3$ and other fillers brought positive effect on both strength and modulus of the composites. Though, the increase will be at the expense of ductility of the base polymer material. As highlighted earlier, the water absorption is one of the critical phenomena that can result in the sudden failure of the fibre reinforced composites.

To minimize the issue of moisture absorption and subsequent reduction in flexural strength a $CaCO_3$ will be incorporated into a glass fibre reinforced polyester composite. Though the effect of adding $CaCO_3$ in terms of mechanical improvement has been investigated [11] [12]. But this research will focus on how calcium carbonate could affect the flexural strength before and after water absorption, as well as

phase changes therein. The base material i.e. the matrix used is unsaturated polyester which is widely used for fibre reinforced composite. The attractive benefits of this thermoset are curable at room temperature, excellent mechanical properties and low cost [13]. Therefore this research is aimed at investigating the phase transformations and flexural strength changes before and after water absorption test due to the incorporation of micro $CaCO_3$ in glass fibre reinforced unsaturated polyester composite. In addition, the effect of coating the sample especially when it's intended to be used in the outdoor application has been investigated. The composites were fabricated using pultrusion process. The fabricated composite plate was characterized based on XRD, water absorption and flexural strength test..

[7] Materials And Methods

*A. Materials*

In this research, glass fibre was used as a reinforcing fibre, while unsaturated polyester served as a matrix. In addition, micro-sized $CaCO_3$ was added as a filler. The specifications of the material is shown in Table I [14]. The glass is in form woven plain mat with an approximate weight and thickness of 400 g/m$^2$ and 0.4 mm respectively.

TABLE I.        REINFORCEMENT AND RESIN PROPERTIES

| Properties | Materials | |
|---|---|---|
| | **Glass** | **Unsaturated polyester** |
| Density (g/cm$^3$) | 2.6 | 1.14 |
| Breaking strength (MPa) | 2400 | 69 |
| Elastic modulus (GPa) | 72 | 3.8 |
| Elongation (%) | 3 | 2.3 |
| Moisture absorption (%) | 0.12 | 0.02 |

*B. Composite Fabrication*

The composite was fabricated in a manufacturing facility using a pultrusion process. The samples were broadly divided into two (2) categories, i.e. with and without $CaCO_3$. Each of the categories was also further divided into two (2) sets, one set was coated with glossy paint and the other set was left uncoated. In total, four (4) samples were considered, and in each sample, there were five (5) replicates for each of the tests conducted. For easy identification, each composite sample was coded and their descriptions are provided, see Table II. The water absorption test specimens are in the form of a rectangular bar with a dimension of 76.2 mm long, 25.4 mm width and a thickness of 6.5 mm, see Figure 1. While the specimen for the flexural test was also in the form of a rectangular bar with a length of 177 mm, 6.5 mm depth and 12.7 mm width, see Figure 2. Two (2) powder samples, with and without calcium carbonate were prepared from the composite plates. The ground powders for the XRD analysis are shown in Figure 3.

TABLE II.        COMPOSITE SAMPLES CODES

| No. | Sample Code | Sample description |
|---|---|---|
| 1 | WCCC | Composite with $CaCO_3$ coated |
| 2 | WCCU | Composite with $CaCO_3$ uncoated |
| 3 | WOCCC | Composite without $CaCO_3$ coated |
| 4 | WOCCU | Composite without $CaCO_3$ uncoated |
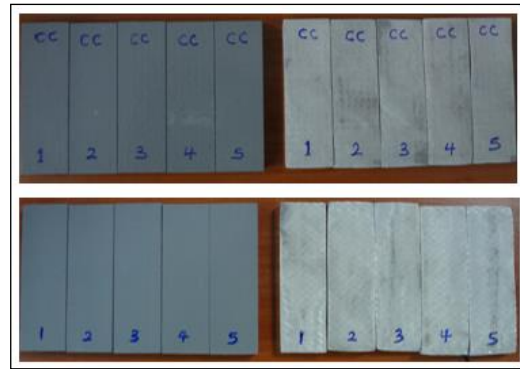


Fig. 5.    Water absorption samples with and without $CaCO_3$
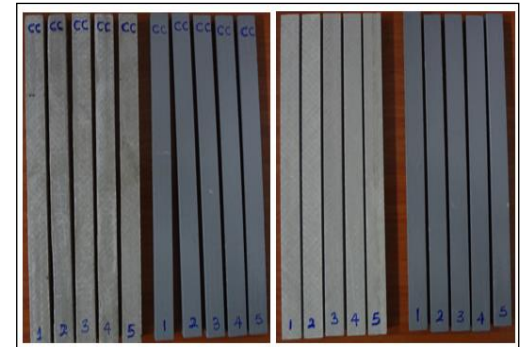


Fig. 6.    Flexural test samples with and without $CaCO_3$
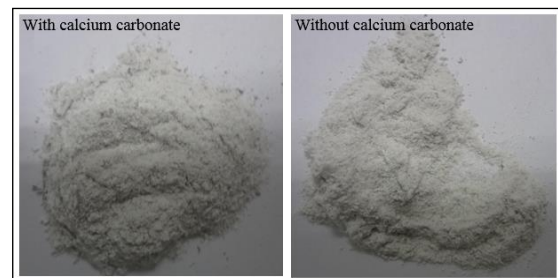


Fig. 7.    XRD samples with and without $CaCO_3$

*C. Characterisations*

The water absorption test was conducted in accordance with ASTM D570-10 (2010) [15]. All the samples were dried in an oven at 50°C for 24 hours. Thereafter, the samples were cooled in a desiccator and weighed using an analytical balance to the nearest 0.0001 g. The conditioned specimens were placed in a water bath containing distilled water at a temperature of 26°C. Long-term immersion was employed. The process began with 24 hours immersion period and subsequently readings were taken after 48 hours until saturation i.e. 45 days. At the end of 24 hours immersion period, the specimens were removed and the surfaces were wiped off to remove excess water. Then, the specimens were immediately measured and recorded. Then the specimens were returned back to the water bath and thereafter measurement was taken at an interval of two days. The percentage increase in weight of the specimen at each interval of time during the immersion period was computed using Equation 1.

$$Water\ Absorption\ W_t = \frac{W_2 - W_1}{W_1} \times 100 \qquad (1)$$

Where ($W_1$) is the weight of the specimen after oven dried and cooled in a desiccator, and ($W_2$) is the weight of the immersed specimen.

The flexural test was conducted using 5kN Instron Model 3365 universal tensile testing machine. The test was conducted based on ASTM D790-15 (2015) [16]. The support span used in this test was 104 mm which was computed based on the span to depth ratio of 1:16. The crosshead speed was computed at 2.8 mm/min according to the standard using Equation 2.

$$R = \frac{Zl^2}{6d} \qquad (2)$$

Where $l$ and $d$ are the support span and depth respectively, while $Z$ is given as 0.01.

The XRD analysis was done using PANalytical (Philips) X'Pert Pro theta-theta PW3050/60 diffractometer. The generator settings were at 40 kV and 40 mA with Cu Kα radiation (1.5418 Å). The measurement was carried out with a detector scanning from 20° to 80° of the 2θ angle range at scanning speed of 15°/min.

[8] Results And Discussion

A. Water Absorption

The water absorption results reveal that the presence of CaCO$_3$ lowered the water absorption of the material drastically. Generally, as shown in Figure 4, the water absorption of the composite increased with the increase in soaking time up to saturation point. Specimens with CaCO$_3$ absorbed 2.06% of water as compared to sample without CaCO$_3$ which absorbed 3.15%. The low water absorption could be attributed to the barrier properties of the filler i.e. calcium carbonate. Moreover, the presence of calcium carbonate served as a filler and at the same time reduced the number of voids in the composite. This will prevent water ingress into the composite. A similar trend was also observed in a composite material with 9% of calcium carbonate added which yields the least amount of absorbed water [6]. The analysis further shows that samples without coating absorbed more water as compared to the coated samples. At the initial stage of the water absorption test, the uncoated composite shows an overshoot behaviour of an absorbed water. It finally stabilized in a zigzag manner due to loss of soluble matter. However, in both cases, the samples without coating had recorded more loss of soluble matter of 1.85% as compared to coated samples with 0.09%.
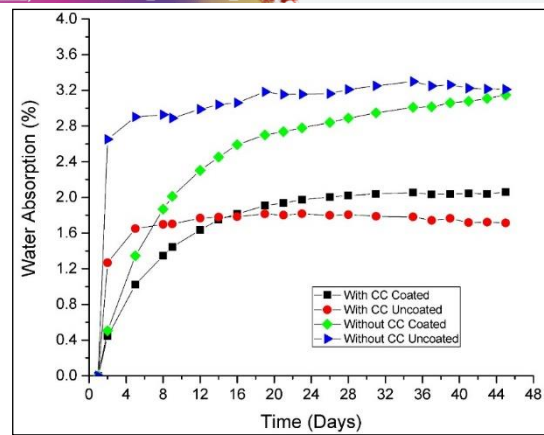


Fig. 8. Water absortion of composite specimens

B. Flexural Strength and Modulus

Flexural stress-strain curves of the glass fibre reinforced unsaturated polyester before and after water absorption is shown in Figure 5(a) and Figure 5(b) respectively. The curves reveal that flexural stress increased with the increase in strain in both cases. However, reduction in flexural stress was noticed after water absorption test with or without incorporation of CaCO$_3$, see Figure 5(b).
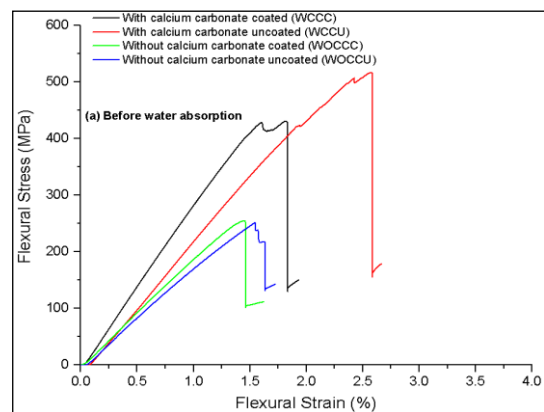


(a)
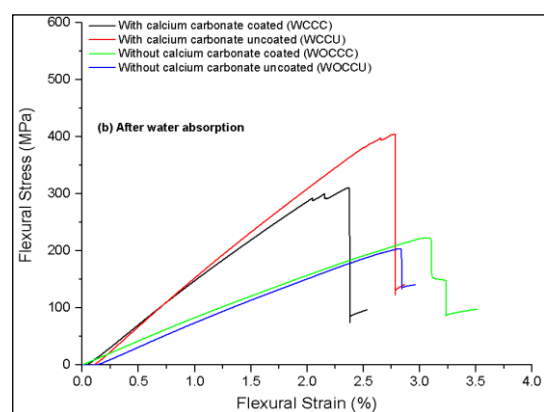


(b)

Fig. 9. Flexural stress-strain curve of the composite (a) before and (b) after water absorption

Figures 6 and 7 represent the flexural strength and modulus properties of the composite samples before and after water absorption respectively. Samples with CaCO$_3$ recorded the highest flexural strength and modulus for both coated and

uncoated samples. Sample with $CaCO_3$ recorded a flexural strength and modulus of 406.28 MPa and 25.25 GPa respectively. Comparatively, this is much higher when compared with a sample without $CaCO_3$ in which the values stood at 228.86 MPa and 15.71 GPa for flexural strength and modulus respectively. The recorded percentage increases for flexural strength and tensile modulus were 75.5% and 60.7% respectively. However, both flexural strength and modulus were reduced after water absorption.
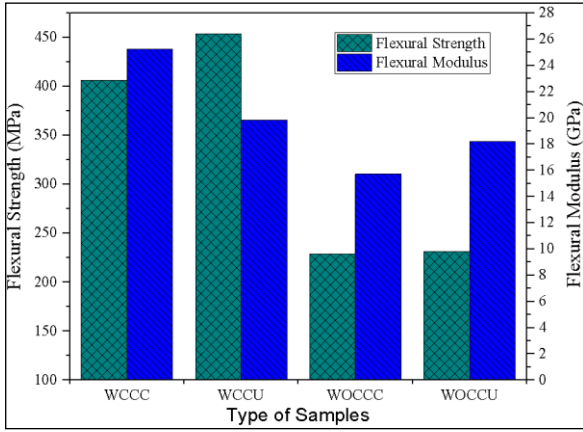


Fig. 10. Flexural strength and modulus before water absorption

Evaluation of the flexural properties after water absorption showed a significant decrease in flexural strength. The reduction of the flexural strength of the composite with $CaCO_3$ is up to 27% from 406.28 MPa to 296.05 MPa. While the sample without $CaCO_3$ has its flexural strength reduced from 228.86 MPa to 205.19 MPa as shown in Figure 7. The reduction is actually due to internal degradation which was caused by water ingress.
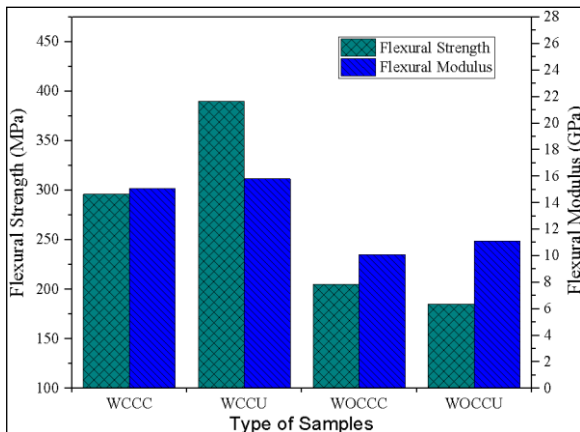


Fig. 11. Flexural strength and modulus before after absorption

## C. Failure Modes

The failure modes of the composite samples are shown in Figure 8. The composite with $CaCO_3$ failed in a progressive manner without delamination of layers, see Figure 8(a). Unlike composite without $CaCO_3$ delamination occurred closed to the point of load application, see Figure 8(b). This clearly depicts the improvement in interfacial adhesion between the glass fibre and the unsaturated polyester with the presence of $CaCO_3$.
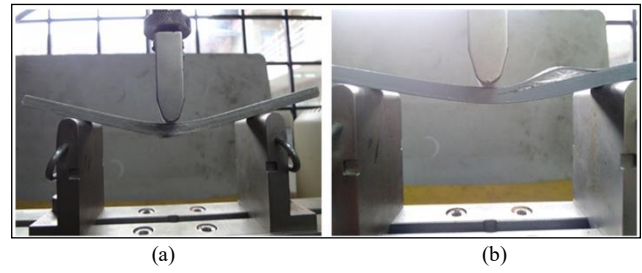


Fig. 12. Failure mode of the flexural test sample (a) with $CaCO_3$ and (b) without $CaCO_3$

## D. XRD Analysis

The result of the XRD analysis after Rietveld refinement of the WCCU composite data shows six (6) different compounds/phases, see Table III. Also shown in Figure 9 is a spectrum of the composite with $CaCO_3$ having a peak at 29.6° 2θ which can be assigned to calcite [17]. The intensity of the peak indicates the relative purity and crystallinity of the $CaCO_3$. Table III shows the identified compounds and their percentages. Through this analysis, the actual percentage of the calcium carbonate was determined to be 8.7% which was added to the polymer.
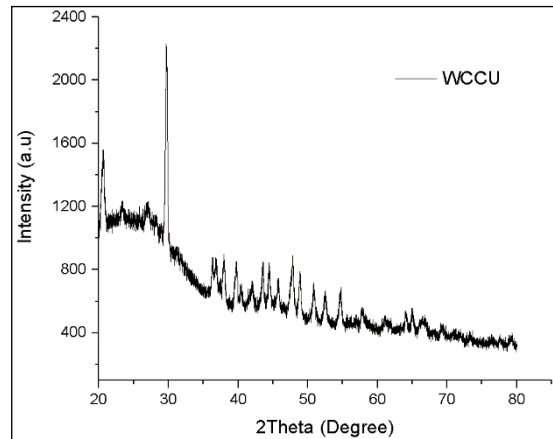


Fig. 13. XRD spectra of the composite with $CaCO_3$ uncoated (WCCU)

TABLE III.   ANALYSIS OF THE IDENTIFIED COMPOUNDS/PHASES FOR THE COMPOSITE WITH $CaCO_3$

| Ref-Code | Compound Name | Chemical Formula | (%) | |
|---|---|---|---|---|
| 96-150-3692 | 1503691 | O16 H136 C84 | 16.5 | Polymer compound |
| 96-150-7751 | 1507750 | Si4 O20 C68 H96 | 57.1 | Polymer + reinforcement phase |
| 96-901-1647 | 9011646 | Si16 | 3.0 | Silica |
| **96-230-0211** | **2300210** | **Ca8 C16 O40 H16** | **8.7** | **Calcium carbonate** |
| 96-900-6569 | 9006568 | Ca4 Si8 O20 | 14.3 | Calcium silicate compound |
| 96-901-2602 | Quartz | Si3 O6 | 0.4 | Silica oxide |

The result of the XRD analysis after Rietveld refinement of the composite without calcium carbonate showed four (4) different compounds/phases. Shown in Figure 10 is the

spectra of the composite with different peaks matched by the compounds/phases. The peak at 29.6° 2θ which was found in Figure 9 disappeared from the spectrum in Figure 10. This shows the absence of the calcium carbonate in the composite system. Table IV shows the identified compound and their percentages. It is clear from the two (2) XRD analyses of the compounds that a high percentage of homogeneous phase of polymer and glass fibre was found in the composite with calcium carbonate.
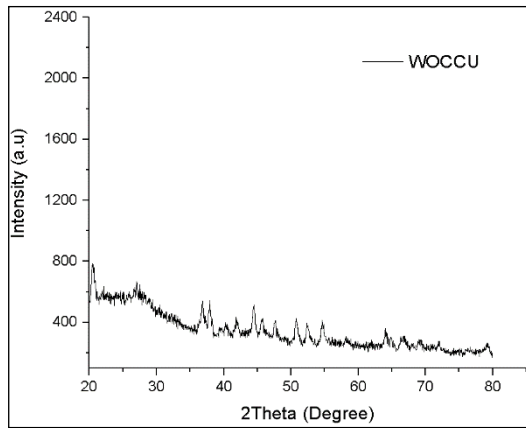


Fig. 14. XRD spectra of the composite without $CaCO_3$ uncoated (WOCCU)

TABLE IV.    ANALYSIS OF THE IDENTIFIED COMPOUNDS/PHASES FOR THE COMPOSITE WITHOUT $CaCO_3$

| Ref-Code | Compound Name | Chemical Formula | (%) | |
|---|---|---|---|---|
| 96-450-5648 | 4505647 | O8 H64 C52 | 52.6 | Polymer compound |
| 96-810-0999 | 8100998 | Si16 O16 C104 H184 | 33.6 | Polymer + reinforcement phase |
| 96-901-1647 | 9011646 | Si16 | 11.1 | Silica |
| 96-900-0781 | Quartz | Si6 O6 | 2.7 | Silica oxide |

## [9] Conclusion

The effect of the incorporation of $CaCO_3$ in glass fibre reinforced polyester composite has been investigated. The outcomes of the study reveal that the use of $CaCO_3$ as filler lowers the water absorption by 34.6%. Furthermore, the addition of the $CaCO_3$ significantly enhanced the flexural strength and modulus of the composite. Though, the flexural strength reduced after the samples were exposed to water absorption prior to the flexural test. Amongst the coated and uncoated samples, the differences in flexural strength and modulus are negligible. The XRD analysis through Rietveld refinement confirms the presence of $CaCO_3$ which enhances the homogeneity of the polymer and fibre phase. In general, the addition of $CaCO_3$ in glass fibre reinforced polyester composite has completely modified and benefited the composite both in terms of mechanical strength and water absorption.

### References

[5] Adhikari, J., Biswas, B., Chabri, S., Bandyapadhyay, N. R., Sawai, P., Mitra, B. C., & Sinha, A. (2017) Effect of functionalized metal oxides addition on the mechanical, thermal and swelling behaviour of polyester/jute composites. Engineering Science and Technology, an International Journal, 20(2), 760-774.

[6] Pender, K., & Yang, L. (2017) Investigation of the potential for catalysed thermal recycling in glass fibre reinforced polymer composites by using metal oxides. Composites Part A: Applied Science and Manufacturing, 100, 285-293.

[7] Yilmaz, M., Unal, H., & Mimaroglu, A. (2008) Study of the strength and erosive behavior of CaCO3/glass fiber reinforced polyester composite. Express Polym Lett, 2, 890-895.

[8] Zhang, X. (2017) Study on the Tribological Properties of Carbon Fabric Reinforced Phenolic Composites Filled with Nano-Al2O3. Journal of Macromolecular Science, Part B, 56(8), 568-577.

[9] Huang, R., Kim, B.-J., Lee, S., Zhang, Y., & Wu, Q. (2013) Co-extruded wood-plastic composites with talc-filled shells: morphology, mechanical, and thermal expansion performance. BioResources, 8(2), 2283-2299.

[10] Srivabut, C., Ratanawilai, T., & Hiziroglu, S. (2018) Effect of nanoclay, talcum, and calcium carbonate as filler on properties of composites manufactured from recycled polypropylene and rubberwood fiber. Construction and Building Materials, 162, 450-458.

[11] Syafri, E., Kasim, A., Abral, H., & Asben, A. (2017) Effect of precipitated calcium carbonate on physical, mechanical and thermal properties of cassava starch bioplastic composites. International Journal on Advanced Science, Engineering and Information Technology, 7(5), 1950-1956.

[12] Wang, C., Yu, X., Smith, L. M., Wang, G., Cheng, H., & Zhang, S. (2017) Interfacial properties of bamboo fiber-reinforced high-density polyethylene composites by different methods for adding nano calcium carbonate. Polymers, 9(11), 587.

[13] Sherir, M. A., Hossain, K. M., & Lachemi, M. (2017) Development and recovery of mechanical properties of self-healing cementitious composites with MgO expansive agent. Construction and Building Materials, 148, 789-810.

[14] Chatterjee, A., & Mishra, S. (2013) Rheological, thermal and mechanical properties of nano-calcium carbonate (CaCO 3)/poly (methyl methacrylate)(PMMA) core-shell nanoparticles reinforced polypropylene (PP) composites. Macromolecular Research, 21(5), 474-483.

[15] Misra, R., Nerikar, P., Bertrand, K., & Murphy, D. (2004) Some aspects of surface deformation and fracture of 5–20% calcium carbonate-reinforced polyethylene composites. Materials Science and Engineering: A, 384(1-2), 284-298.

[16] Tanniru, M., & Misra, R. (2005) On enhanced impact strength of calcium carbonate-reinforced high-density polyethylene composites. Materials Science and Engineering: A, 405(1-2), 178-193.

[17] Mukhtar, I., Leman, Z., Ishak, M. R., & Zainudin, E. S. (2016) Sugar Palm Fibre and its Composites: A Review of Recent Developments. BioResources, 11(4), 10756-10782. doi:10.15376/biores.11.4.10756-10782

[18] Sharba, M. J., Leman, Z., Sultan, M. T., Ishak, M. R., & Hanim, M. A. A. (2015) Effects of kenaf fiber orientation on mechanical properties and fatigue life of glass/kenaf hybrid composites. BioResources, 11(1), 1448-1465.

[19] ASTM D570-10. (2010). Standard test methods for water absorption of plastics ASTM International, West Conshohocken.

[20] ASTM D790-15. (2015). Standard test methods for flexural properties of unreinforced and reinforced plastics and electrical insulating materials ASTM International, West Conshohocken.

[21] Kim, B. J., Yao, F., Han, G., & Wu, Q. (2012) Performance of bamboo plastic composites with hybrid bamboo and precipitated calcium carbonate fillers. Polymer Composites, 33(1), 68-78.

# Step By Step Investigation of Reconfigurable Microstrip Patch Antenna

Hilal Koc
Department of Electrical and
Electronics Engineering
Erzurum Technical University
Erzurum 25700, Turkey
hilal.koc@erzurum.edu.tr

M. Diruba Geyikoglu
Department of Electrical and
Electronics Engineering
Ataturk University
Erzurum 25240, Turkey
dilruba_mdk@hotmail.com

Bulent Cavusoglu
Department of Electrical and
Electronics Engineering
Ataturk University
Erzurum 25240, Turkey
bcavusoglu@atauni.edu.tr

*Abstract*— **In this paper, the effect of PIN diode is investigated in the reconfigurable microstrip patch antenna design. Firstly, a microstrip patch antenna operated at 4.65 GHz has been designed and simulated using CST Microwave Studio software utilizing FR4 dielectric substrate. Impedance matching for this antenna is made through Quarter Wavelength Transformer technique. Then the reconfigurable microstrip patch antenna is designed using PIN diodes. The main design consideration is to provide an antenna geometry where a reconfigurable antenna can be obtained by extending the initial design and combining them by using the switches. Finally, the proposed antennas are fabricated on FR4 substrate. The measurement results of fabricated antennas demonstrate the accuracy of simulation result.**

*Keywords—CST Microwave Studio, PIN diode, Quarter Wavelength Transformer, reconfigurable antenna style.*

## I. INTRODUCTION

The reconfigurable antennas are designed to integrate the function of several antennas into a single emitter antenna. Reconfiguration of an antenna is obtained by redistributing the currents or electromagnetic fields of the antenna as desired and by implementing reconfigurable changes on the impedance or radiation properties of antenna [1]. These changes are activated through various mechanisms such as electrically [2], mechanically [3], optically [4] triggered swiching and by use of liquid metarials [5]. The reconfigurable antennas are divided into four main categories based on the frequency, radiation pattern, polarization and their combination .

The impedance matching is a challenging step to obtaining optimum performance parameters such as return loss, efficiency and gain in antenna design [6].The impedance of an antenna depends on the resonance frequency. The impedance matching at a single frequency (eg. Quarter Wavelength) is relatively simple. However, if impedance matching is desired for a multiple-frequency antenna, impedance matching is difficult. The impedance matching is one of the challenges encountered in the reconfigurable antenna applications.

The current and voltage distribution on the patch determines the impedance value. The electric field value (voltage) is zero in the middle of the patch, it is maximum on the spreading edge and reverses its direction on the opposite edge by taking the maximum value. The magnetic field value (current) is the maximum in the middle of the patch, the edge of the propagation takes zero value. The

behavior of this current and voltage signal on the patch causes a variable impedance value [7]. The control of the input impedance is achieved by positioning the probe at the appropriate location in coaxial probe feed [8]. The feed position of a patch antenna stimulated in basic mode is located in the middle of the patch width and in the direction of the patch resonance length [7].

The impedance value of the rectangular microstrip patch $(Z_a)$ is calculated by "(1)". When the feed length is selected as the quarter wavelength, "Equation (2) is used to match the impedance of the patch $(Z_a)$ to input impedance $(Z_{in})$ in microstrip line feed antennas, for this purpose the characteristic impedance of the feed line $(Z_0)$ is calculated. The relation of the width of the microstrip feed line $(W_0)$ with the characteristic impedance of the feed line $(Z_0)$ is given in "(3)" and "(4)".

$$Z_a = 90 \frac{\varepsilon_r^2}{\varepsilon_r - 1} \left( \frac{L}{W} \right)^2 \qquad (1)$$

$\varepsilon_r$ is the dielectric constant of antenna substrate, $L$ is the length of the patch, W is the width of the patch.

$$Z_0 = \sqrt{Z_{in} Z_a} \qquad (2)$$

For $\dfrac{W_0}{h} \leq 1$ ,

$$Z_0 = \frac{60}{\sqrt{\varepsilon_{reff}}} \ln \left[ \frac{8h}{W_0} + \frac{W_0}{4h} \right] \qquad (3)$$

For $\dfrac{W_0}{h} > 1$ ,

$$Z_0 = \frac{120\pi}{\sqrt{\varepsilon_{reff}} \left[ \dfrac{W_0}{h} + 1.393 + 0.667 \ln \left( \dfrac{W_0}{h} + 1.444 \right) \right]} \qquad (4)$$

## II. ANTENNA DESIGN AND CONFIGURATION

### A. *The Rectangular Microstrip Patch Antenna*

The calculated results for the electrical dimensions of the 4.65 GHz antenna depicted "Fig. 1." designed using FR4 is presented in Table 1. $Z_0$ value for this antenna shown in "Fig. 1" is calculated by accepting $Z_{in} = 50\Omega$ by means of "(2)". $Z_0$ graph for the selected values of $W_0$ at certain range is depicted in "Fig.2". When, the graph is examined, it can be seen that the calculated $Z_0 = 121.56$ value corresponds to $W_0 = 0.24$ value.

TABLE V.   DESIGN PARAMETER OF THE MICROSTRIP PATCH ANTENNA

| | $f_0$ (GHz) | $\varepsilon_r$ | $h$ (mm) | $L$ (mm) | $W$ (mm) | $L_g$ (mm) | $W_g$ (mm) |
|---|---|---|---|---|---|---|---|
| *values* | 4.65 | 4.3 | 1.3 | 15.0 | 19.6 | 22.8 | 27.4 |
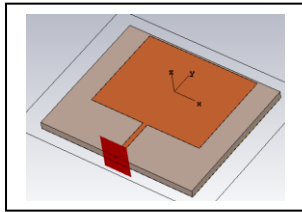


Fig. 1. Geometry of the designed 4.65 GHz antenna
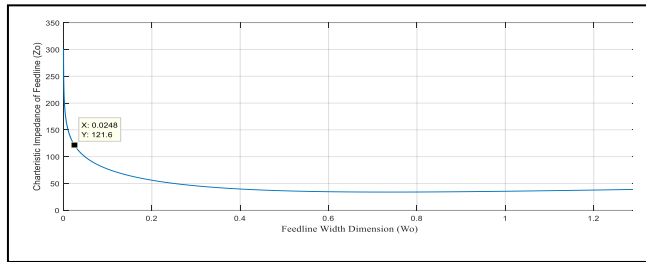


Fig. 2. $Z_0$ graph for the selected values of $W_0$

### B. *The Reconfigurable Antenna*

The calculated electrical dimensions for the designed reconfigurable antenna are presented in Table 2. The main design consideration is to provide an antenna geometry where a reconfigurable antenna can be obtained by extending the initial design and combining them by using the switches. The 4.65GHz antenna can be considered as an inset-feed for the new design. The Quarter Wavelength Transformer is used for the reconfigurable antenna. Four different conditions for reconfigurable antenna design as shown in the "Fig. 3.". The fabricated reconfigurable antenna is shown "Fig. 4.".

TABLE VI.   DESIGN PARAMETER OF THE RECONFIGUABLE MICROSTRIP PATCH ANTENNA

| | $\varepsilon_r$ | $h$ (mm) | $L$ (mm) | $W$ (mm) | $L_g$ (mm) | $W_g$ (mm) |
|---|---|---|---|---|---|---|
| *values* | 4.3 | 1.3 | 45.0 | 39.26 | 56.4 | 43.16 |
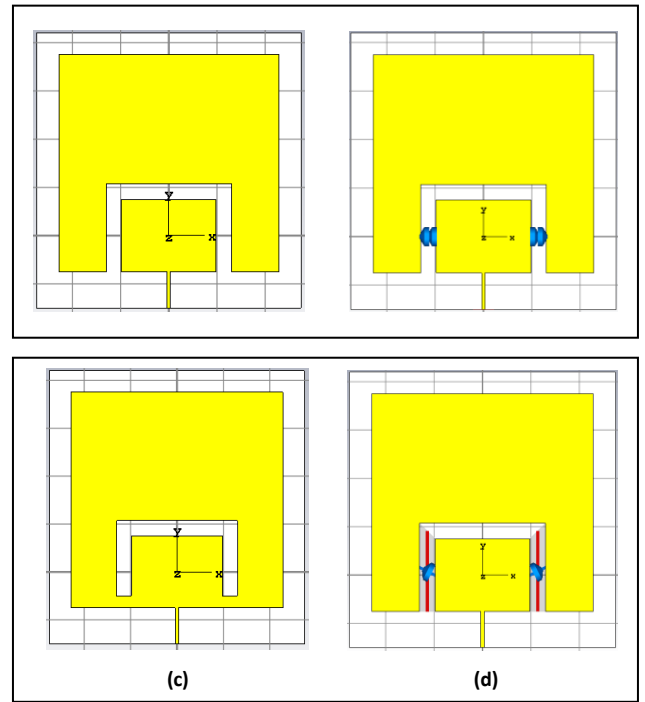


Fig. 3. Geometry of the designed reconfigurable antenna (a) there is no diode between conductive patch (b) off condition diode (c) there is conductive path between conductive patch (d) on condition diode
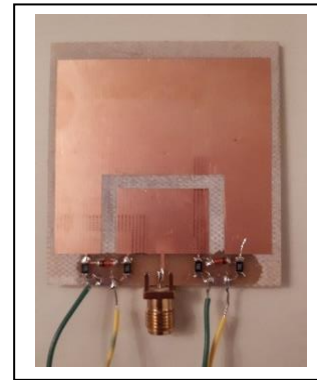


Fig. 4. Picture of the fabricated reconfigurable antenna

## III. COMPARISON OF SIMULATION AND MEASUREMENT RESULTS

The simulation and measurement results of the reflection coefficients (S11) of the proposed 4.65 GHz antenna is depicted in "Fig.5.". The red line shows the simulation and the green line shows the measurement results.
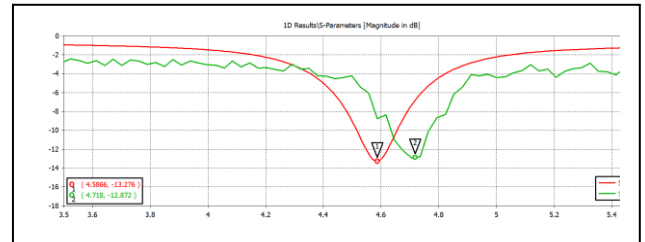


Fig. 5. S11 parameter of the simulated and measured 4.65 GHz antenna

The "Fig. 6." shows S11 values for the cases where there is no diode between conductive patches (solid line), and

where an off condition diode is placed (dashed line). It is seen that both conditions confirm each other from results.
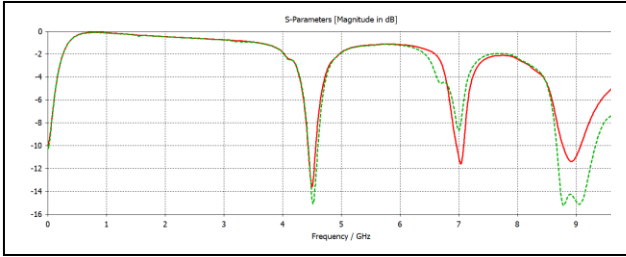


Fig. 6. S11 parameter of the simulated for scenarios in "Fig. 3(a-b)"

The "Fig. 7." shows S11 values for the cases where there is conductive path between conductive patches (solid line), and where an on condition diode is placed (dashed line). It is seen that both conditions confirm each other from results.
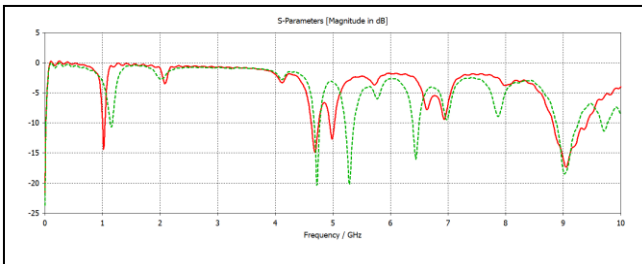


Fig. 7. S11 parameter of the simulated for scenarios in "Fig. 3(c-d)"
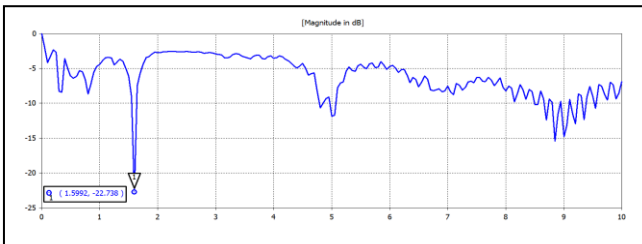


Fig. 8. S11 parameter of the measured reconfigurable antenna

Radiation patterns for the designed antennas are depicted in "Fig. 9.".



(a)

Frequency = 4.5
Main lobe magnitude = 7.34 dBi
Main lobe direction = 21.0 deg.
Angular width (3 dB) = 77.0 deg.
Side lobe level = -10.2 dB

(b)

Frequency = 4.5
Main lobe magnitude = 7.17 dBi
Main lobe direction = 22.0 deg.
Angular width (3 dB) = 79.3 deg.
Side lobe level = -10.0 dB

(c)

Frequency = 1.019
Main lobe magnitude = 3.3 dBi
Main lobe direction = 7.0 deg.
Angular width (3 dB) = 331.8 deg.

(d)

Frequency = 1.16
Main lobe magnitude = 3.16 dBi
Main lobe direction = 168.0 deg.
Angular width (3 dB) = 333.6 deg.

Fig. 9. Radiation pattern diagrams for the reconfigurable antenna; (a) there is no diode between conductive patch (b) off condition diode (c) there is conductive path between conductive patch (d) on condition diode

## IV. CONCLUSION

In this study, first, a patch antenna is fabricated for 4.65GHz. Then, in order to implement reconfigurable features to this antenna an extension is created via the connection of PIN diodes. The effects of PIN diodes are analyzed for a few scenarios and it was concluded that using PIN diodes especially requires additional design and tuning efforts to reach the simulated results. As a solution for this downside optically reconfigurable antennas can be used via optical switches. Moreover, bias circuits and the powering of these circuits can have negative effects on the antenna in terms of both electrical interference and physical space allocation. It should also be noted that using highly efficient

and low power consuming optical switches is important and useful especially for the mobile devices which have small space allocation and low power consumption requirements. Hence the future research direction should follow these type of optically reconfigurable antennas.

## REFERENCES

[1] C. A. Balanis, "Modern Antenna Handbook", John Wiley & Sons, Inc. Hoboken, New Jersey, 2008.

[2] A. Sedghara and Z. Atlasbaf, "A New Dual Band, Dual-Polarized and Single Feed Reconfigurable Antenna", ACES Journal, Vol. 31, No. 1, pp. 26-31, January 2016.

[3] A. Zohur, H. Mopidevi, D. Rodrigo, M. Unlu, L. Jofre and B. A. Cetiner, "RF MEMS Reconfigurable Two-Band Antenna", IEEE Antennas and Wireless Propagation Letters, vol. 12, pp. 72-75, 2013.

[4] S. Pendharker, R. K. Shevgaonkar, "Optically Controlled Frequency-Reconfigurable Microstrip Antenna With Low Photoconductivity," IEEE Antennas and Wireless Propagation Letters, vol. 13, pp. 99-102, 2014.

[5] D. Rodrigo, L. Jofre and B. A. Cetiner, "Circular Beam-Steering Reconfigurable Antenna With Liquid Metal Parasitics", IEEE Transactions On Antennas And Propagation, Vol. 60, No. 4, pp. 1796-1802, April 2012.

[6] S. Sharma, C. C. Tripathi and R. Rishi, "Impedance Matching Techniques for Microstrip Patch Antenna", Indian Journal of Science and Technology, vol 10(28), July 2017.

[7] D. Orban, G. J. K. Moarnaut, "The Basics of Patch Antennas, Updated", Orban Microwave Products.

[8] H. Errifi, A. Baghdad and A. Badri, "Effect of Chance in Feedpoint on the Antenna Performance in the Edge, Probe and Inset-Feed Microstrip Patch Antenna for 10 GHz", International Journal of Emerging Trends in Engineering and Development, vol.1, pp. 80-93, January 2014.

# Lane Detection with Convolutional Neural Network

Hussein Mahmood Abdo Mohammed
Department of Electrical& Electronic
Engineering
*Ataturk University*
Erzurum,Turkey
halameri080@gmail.com

Asli Nur Omeroglu
Department of Electrical & Electronic
Engineering
*Ataturk University*
Erzurum,Turkey
asli.omeroglu@atauni.edu.tr

Nida Kumbasar
Department of Electrical & Electronic
Engineering
*Ataturk University*
Erzurum,Turkey
nida.kumbasar@ogr.atauni.edu.tr

Emin Argun Oral
Department of Electrical & Electronic
Engineering
*Ataturk University*
Erzurum,Turkey
eminoral@atauni.edu.tr

Ibrahim Yucel Ozbek
Department of Electrical & Electronic
Engineering
Ataturk University
Erzurum,Turkey
iozbek@atauni.edu.tr

*Abstract*— **Lane detection plays a vital role in self-driving cars and advanced driver assistance systems as it helps cars to position themselves within the road and avoid collision. A machine learning technique known as Transfer Learning was used in this study. TL is the reuse of a previously developed model for a task as the starting point for a new one with no need for a big dataset. VGG-16, a 16 layers convolutional neural network trained on more than million images for classifying images into 1000 object categories, was used in this study. This model was selected as the starting point to perform semantic segmentation which is evaluating each pixel in the image and categorizing it into a specific class. The Cambridge Driving-Labeled Video Database (CamVid) which provides ground truth labels as each pixel associated to one of the 32 semantic classes was used in the study for both training and test purposes changing the classes from 32 to 2 as Lanes and Others. Based on the experimental results the lane detection accuracy was 97.42% under various illumination conditions and presence of shadows on the road. The experimental results demonstrated the effectiveness of the proposed method in reducing learning time and improving performance, making it suitable for real-time applications.**

**Keywords— Lane Detection, semantic segmentation, self-driving cars, CNN, Transfer Learning, ADAS.**

## I. INTRODUCTION

Autonomous cars, which are vehicles that can travel to a specified destination without the intervention of human beings [1], proved to be quite challenging. This is because of the sophisticated tasks they have to perform like human drivers, a quite challenging task. These complicated tasks include, but are not limited to, their ability to use common sense, become aware of their environment, obey traffic rules forced by traffic signals and signs, speed limits and etc. [2]. This paper aims to implement semantic segmentation method for road lane detection using transfer learning. In this sense, lane detection plays a vital role in self-driving cars and advanced driver assistance systems as it helps cars to position themselves within the road and avoid collision.

There are many traditional techniques used to detect lane in the road [3-4]. More recent methods have utilized deep convolutional neural networks (CNNs) for this purpose [5-6].



Fig.1 Illustrate semantic segmentation [7].
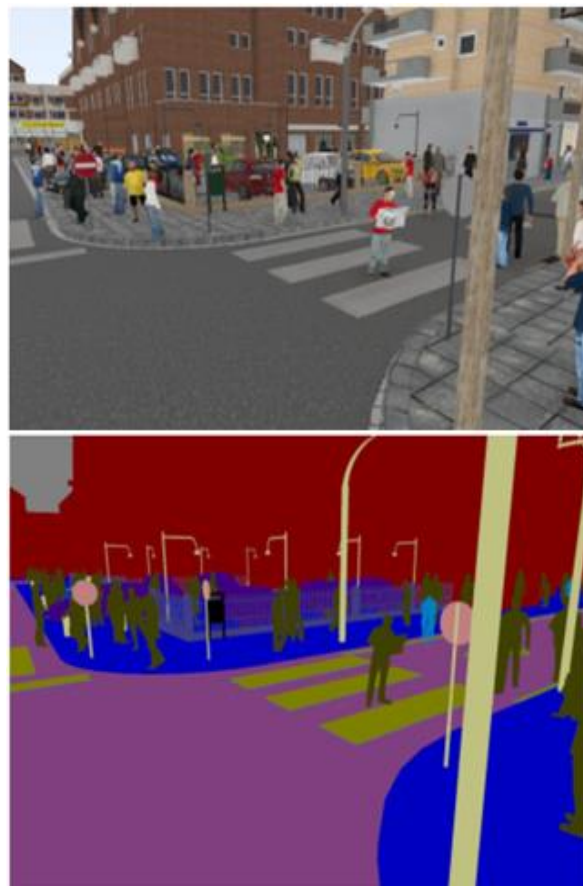
## II. SEMANTIC SEGMENTATION

Image segmentation is a technique that involves grouping pixels of a digital image into multiple regions as shown in Fig.1. Representing a digital image in segments which are meaningful and easy to analyze is the main goal of image segmentation process. Semantic segmentation, on the other hand, is the process of associating each pixel in a digital

image to a specified class it belongs [8]. Medical Image segmentation [9-11], and traffic signal, sign recognition and segmentation [12] are some of the common applications of image segmentation.

An encoder network followed by a decoder network is a typical architecture of a general semantic segmentation approach. Fig. 2 shows the SegNet architecture for semantic segmentation. Feature extraction, transforming an input image into a multidimensional feature representation as the initial step of segmentation, is carried out by the encoder network. Decoder network, on the other hand, maps encoder features to produce the final segmentation on the original image.

A CNN architecture is composed of multiple layers to
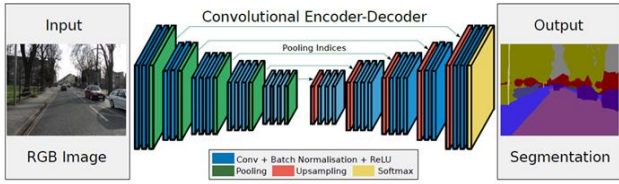


Fig. 2. Illustrate of the SegNet architecture containing Encoder and Decoder , [13].

perform different tasks as briefly described below.

**The Convolutional Layer:** This layer extracts features from the input image by sliding learnable kernels over the image. These learnable kernels must have the same depth of the input image.

**Batch Normalization layer:** It normalizes output of previous layers for faster training network. This layer is generally located between the Convolutional and ReLU layers. Batch Normalizing Transform Algorithm presented in [14] is as follows.

$Input$: $Values\ of\ x\ over\ a\ mini\ batch$: $B\{x_{1\ldots\ldots m}\}$;
$Parameters\ to\ be\ learned$: $\gamma, \beta$
$Output$: $\{y_i = BN_{\gamma,\beta}(x_i)\}$

$$\mu_B \leftarrow \frac{1}{m}\sum_{i=1}^{m} x_i \qquad // \ mini - batch\ mean$$

$$\sigma_B^2 \leftarrow \frac{1}{m}\sum_{i=1}^{m}(x_i - \mu_B)^2 \quad // \ mini - batch\ variance$$

$$\widehat{x_i} \leftarrow \frac{x_i - \mu_B}{\sqrt{\sigma_B^2 + \epsilon}} \qquad // \ normalize$$

$$y_i \leftarrow \gamma\widehat{x_i} + \beta \equiv BN_{\gamma,\beta}(x_i) \quad // \ scale\ and\ shift$$

**Rectified Linear Unit (ReLU) Layer:** This layer introduces nonlinearity to the system by removing all negative pixel values in the feature map and placing zero instead.

**Max Pooling Layer (downsampling):** It is used to reduce the dimensionality of each feature map without losing the important information.

## Transfer Learning

Application of a CNN requires long training time based on the large data set required by deep networks. One approach to overcome this obstacle is application of transfer learning. It is the reuse of a previously developed model as the starting point for a new task without the need for the use of a big dataset. Hence, transfer learning enables to take advantage of the previously obtained knowledge of another task when a new one has small amount of data [15].
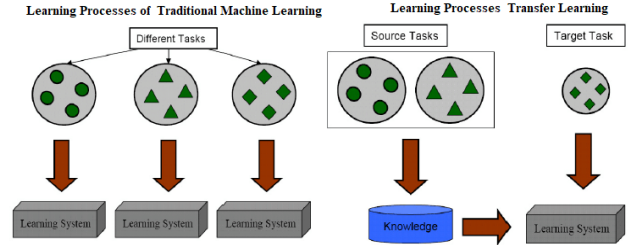


Fig. 3. Illustrate the Learning Processes for Traditional Machine Learning and Transfer Learning. [15]

## VGG Model Architecture

VGG-16 net [16] is a deep convolutional neural network trained on more than million images for classifying images into 1000 object categories. The VGG-16 model involves 144 million parameters to learn and has 16 convolutional layers as 5 max-pooling layers, 3 fully-connected layers followed by a ReLU activation layer applied before a final soft-max layer.
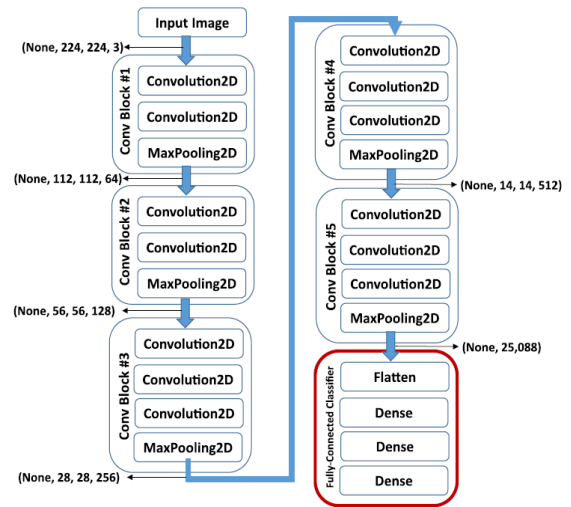


Fig.4. Illustrate A schematic of the VGG-16 Deep Convolutional Neural [17]

## III. DATABASE

The Cambridge Driving-Labeled Video Database (CamVid) [18], used both for training and test, contains 701 images and provides ground truth labels as each pixel associated to one of the 32 available semantic classes. We decreased number of classes into two for the binary classification as "Lanes" and "Others" just by combining all

classes of the original database other than "Lanes" into one class.

## IV.   PROPOSED ARCHITECTURE

The architecture of our segmentation network is similar to the architecture of SegNet [13]. The architecture of encoder network   contains 13 convolution layers of the pretrained VGG-16 [16].  To reconstruct the original size of the input image an inverse convolution (upsampling) is carried out by the decoder network. It achieves this task using a trainable multi-channel upsampling kernel.

The proposed architecture, as illustrated in the Fig.7, starts with an augmentation step to increase the accuracy of the system to detect road-lanes under different circumstances such as various illumination conditions or presence of shadows. This increases the number of images from 701 to 1402 of which 1122 used as training data and the remaining 280 used as test data. Images are then resized in the input layer to decrease the training time. For transfer learning, which initializes the model weights, the fully connected layers of VGG-16 model are removed to reduce the number of parameters in the encoder [8] and the decoder network.
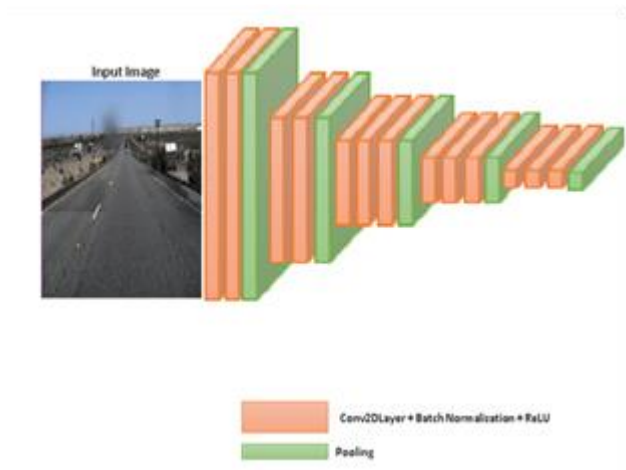


Fig.5. Illustrate The architecture of our encoder.
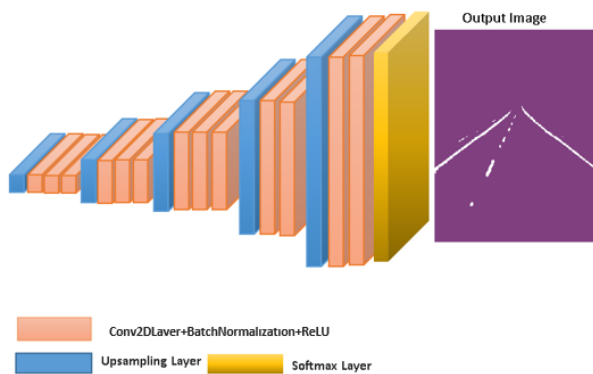


Fig.6. Illustrate The architecture of our Dececoder.

Stochastic Gradient Descent with Momentum (SGDM) optimization algorithm used with a learning rate 0.001 and momentum 0.9. It is carried out on a GPU (Quadro M5000)

with compute capability of 5.2, and it took about 12 hours to train the model.
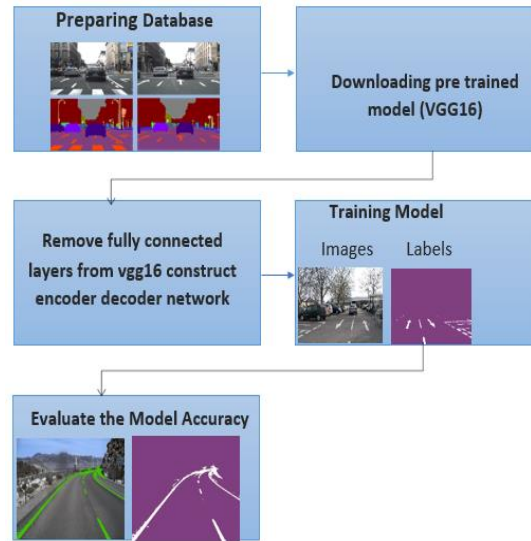


Fig.7. Methodology

## V.   EXPERIMENTAL RESULTS

Accuracy and the Jaccard similarity coefficient are used to evaluate our algorithm's efficiency. **Accuracy is** defined as the percentage of the number of times the evaluation measure correctly matches evaluation result divided by the total number of comparisons in the experiment. Intersection over Union (IoU), also known as a Jaccard index, is also used to measure the accuracy of object detection. The IoU metric measures the ratio of intersection of a particular class pixels in label and prediction data to union of that class pixels in two sets. Table 1 shows the experimental results. Hence, our proposed method correctly identifies lane segments with an accuracy of 97.42%. The corresponding confusion matrix is also given in Fig. 8.

Table 1. Experimental results

| Classes | Accuracy | IoU |
|---------|----------|------|
| Lanes | 97.42 | 97.34 |
| Others | 95.42 | 39.64 |
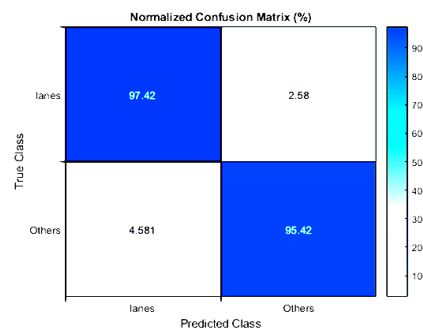


Fig. 8.Confusion matrix
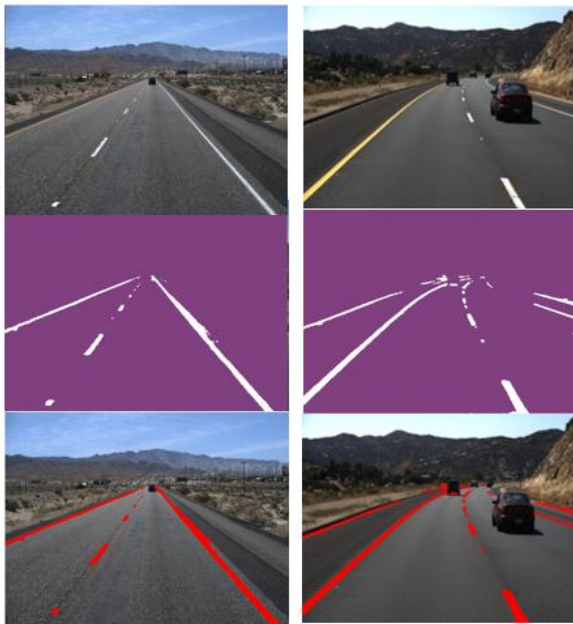
Fig. 9. Illustrate of the testing the model on images
from Simple Dataset [19].

## VI. Conclusion

In this paper, we have presented a method to identify the lane segments in a road image using semantic segmentation and transfer learning. We used The Cambridge Driving-Labeled Video (Camvid) Database for both training and test purposes changing the classes from 32 to 2 as lanes and others. The number of images are doubled through data augmentation to represent different illumination conditions. The experimental results proved the eligibility of this method for future lane detection studies.

## REFERENCES

[1] K. Bimbraw, "Autonomous cars: Past, present and future a review of the developments in the last century, the present scenario and the expected future of autonomous vehicle technology," IEEE., vol.01, pp. 191 - 198, December 2015.

[2] M.Campbell, M.Egerstedt,J.P.How,R.M. Murray, "Autonomous driving in urban environments: approaches, lessons and challenges," Phil. Trans. Roy. Soc., vol.368, pp. 4649–4672 September 2010.

[3] J. Hur, . Kang, and S. Seo," Multi-Lane Detection in Urban Driving Environments Using Conditional Random Fields,"IEEE, October 2013.

[4] H.Jung, J.Min and J.Kim," An Efficient Lane Detection Algorithm For Lane Departure Detection,"IEEE, June 2013.

[5] D.Neven, B.De Brabandere, S.Georgoulis, M.Proesmans,and L.V.Gool," Towards End-to-End Lane Detection: an Instance Segmentation Approach," arXiv:1802.05591v1, Feb 2018

[6] T.Yan,J.Gelernter,X.Wang,W.Chen,J.Gao, Z.Yujie,and L. Xiaolan ," Lane marking detection via deep convolutional neural network," Elsevier Ltd,vol.280,pp.46-55 March 2018.

[7] http://synthia-dataset.net/download-2/8

[8] M.Thoma," A Survey of Semantic Segmentation," arXiv:1602.06541v1,Feb 2016.

[9] N.Sharma, L.M Aggarwal, "Automated medical image segmentation techniques," journal of Medical Physics., vol. 35, pp. 3-14 Jan 2010.

[10] A.Hazra,A.Dey, S.K.Gupta, Md. A.Ansari , "Brain tumor detection based on segmentation using MATLAB," IEEE., June 2018.

[11] A.K.Singh, and B.Gupta, "A Novel Approach for Breast Cancer Detection and Segmentation in a Mammogram, " Elsevier Ltd, vol.54,pp. 676-682 2015.

[12] L.Bruno,G.Parla,C.Celauro, "Improved Traffic Signal Detection and Classification via Image Processing, " Elsevier Ltd., vol.53, pp. 810-820 October 2012.

[13] V.Badrinarayanan,A.Kendall,R.Cipolla,"SegNet: A Deep Convolutional Encoder-Decoder Architecture for Image Segmentation, " IEEE., vol.39, pp. 2481 – 2495 January 2017.

[14] S.Ioffe,C.Szegedy, "Batch Normalization: Accelerating Deep Network Training by Reducing Internal Covariate Shift, " Elsevier Ltd., vol.37, pp. 448-456 July 2015.

[15] S. J. Pan ,and Q.Yang," A Survey on Transfer Learning," IEEE,vol.22,pp.1345-1359 October 2010 .

[16] K.Simonyan,and A.Zisserman," VERY DEEP CONVOLUTIONAL NETWORKS FOR LARGE-SCALE IMAGE RECOGNITION," arXiv:1409.1556v6, Apr 2015.

[17] K.Gopalakrishnan,S. K. Khaitan , A.Choudhary, A. Agrawal," Deep Convolutional Neural Networks with transfer learning for computer vision-based data-driven pavement distress detection," Elsevier Ltd,vol.157,pp.322-330 December 2017

[18] http://mi.eng.cam.ac.uk/research/projects/VideoRec/CamVid/.

[19] https://github.com/TuSimple/tusimple-benchmark/wiki#download-link.

# Determination of Negative Constitutive Parameters Based on a Square Split Ring Resonator Left Handed Metamaterial Using Waveguide

Yunus Kaya
Department of Electricity and Energy
Bayburt University
69000, Bayburt, Turkey
ykaya@bayburt.edu.tr

Gokhan Ozturk
Department of Electrical and Electronics Engineering
Ataturk University
25240, Erzurum, Turkey
gokhan.ozturk@atauni.edu.tr

Ugur Cem Hasar
Department of Electrical and Electronics Engineering
Gaziantep University
27310, Gaziantep, Turkey
uchasar@gantep.edu.tr

Mehmet Ertugrul
Department of Electrical and Electronics Engineering
Ataturk University
25240, Erzurum, Turkey
ertugrul@atauni.edu.tr

*Abstract*—This study presents the negative refractive index, permittivity, and permeability of a square split ring resonator (S-SRR) left handed material (LHM) as a simulation and how it can be obtained experimentally. The LHM structure consists of a three square slit ring resonator on one side of the dielectric substrate and a series of wire pairs on the other side. The CST Microwave Studio is used to model the LHM structure to calculate scattering parameters ($S_{11}$ and $S_{21}$) where complex refractive index, permittivity, and permeability can be found. The MATLAB program is also used to verify the negative values of the parameters of the structure. The simulations were performed using two-port rectangular waveguide setup at the X-band (8.2-12.4 GHz) frequencies.

*Keywords*—*metamaterial (MM), split ring resonator (SRR), left handed material (LHM), negative permittivity, negative permeability, negative refractive index*

## I. INTRODUCTION

It is very important to properly characterize the electromagnetic (EM) parameters of materials for the design and optimization of practical structures used in industry. Researchers have sought alternative ways over the past century due to the limitations of conventional (traditional) materials in nature. Metamaterials (MMs) is now known as artificial material with increasing interest and having many potential applications in science, technology, and medicine. All materials can be electrically defined by complex permittivity ($\varepsilon$) and permeability ($\mu$) in frequency domain. These parameters can determine the response of the material to EM radiation. Because of the unpredictability of production processes, the only way to find the parameters of the materials is to measure them. These materials are also called to as left handed materials (LHMs). LHMs is an artificial material with EM properties not found in nature. The MMs were first examined by Veselago [1]. Many papers have demonstrated the benefit of MMs that lead to negative permittivity, permeability, and refractive index [2-8]. Following the studies of reference [3], [4], and [9], Smith et al. produced the first left handed material in 2000 [10-11]. These left handed metamaterials (LHMMs) are made from a series of conductive continuous wires to obtain negative permittivity and the SRR arrays to obtain negative permeability. In order to ensure negative permittivity and permeability, a double wire is used at the back of the FR4

dielectric substrate while a square split ring resonator is used at the front. The wires at the back of this structure give negative permittivity while SRR gives negative permitability and the negative refraction index is made up of the structure itself. The LHM structure has been simulated in CST Microwave Studio. Afterwards, scattering parameters ($S_{11}$ and $S_{21}$) were extracted to calculate the negative values of permittivity, permeability, and refractive index using the direct rectrieval method [2, 12].

LHM has many applications in microwave engineering. The most important application of LHM is to use it as substrate or superstrade to increase the antenna's direction and gain [12]. Other applications of LHMs are cloak of invisibility. The most interesting concept of the LHM is excellent lenses and near field imaging. [2, 13-14].

## II. METHODOLOGY

The LHM structure was printed on a square FR4 substrate material with partial permittivity $\varepsilon_{sub}$ = 4.3, thickness $d_{sub}$ = 1 mm, and a side length p = 10.18 mm. The design of the LHM structure combines the three square split ring resonator of copper with different lengths ($a_1$ = 4 mm, $a_2$ = 7 mm, and $a_3$ = 10 mm). Copper (conductivity $\sigma_{cu}$ = 58 × $10^6$ S/m) is used for metallization. The gap width of each SRR unit cell is g = 0.75 mm, the metal strip width is w = 0.75 mm, the separation width is s = 0.75 mm, and the metal thickness is $t_m$ = 0.035 mm. On the other side of the substrate, three rectangular wires are printed with the same length and the same metal strip width as substrate. The h distance between these rectangular wires is 4.25 mm. The structure of the LHM front view (S-SRR) and the back view (wires) are shown in Fig. 1a and 1b, respectively.
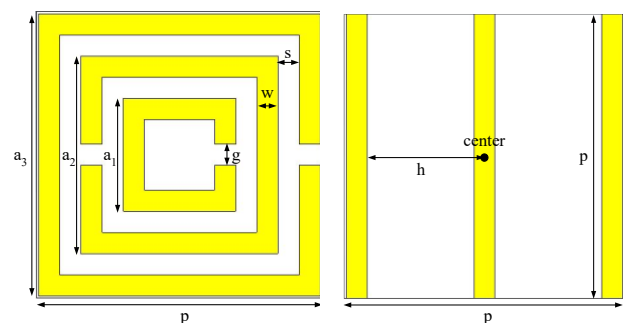
(a)                              (b)
Fig. 1. (a) S-SRR front view, (b) wires back view.

Several methods have been used to obtain negative refractive index, permittivity, and permeability from simulated complex values of S-parameters. The Nicolson-Ross-Weir (NRW) method is one of the over-developed methods to find the negative values of permittivity and permeability [2]. The Lorentz model and other methods using the Drude model have made some hypotheses about negative permittivity and permeability [2]. In this study, direct retrieval method having a more appropriate and understandable among all other ways will be used [12].

In the proposed method, LHM is placed between two rectangular WR-90 waveguide inputs to the left and right of the z axis. The wave is stimulated from positive x-axis (port 1) to negative x-axis (port 2) to calculate complex $S_{11}$ (reflection of port 1 at 1) and complex $S_{21}$ (transmission at port 2 due to 1) parameters. The y and x planes are defined as a perfect electric conductor (PEC) [13-14]. The simulations are taken on the X-band (8.2-12.4 GHz). The simulated LHMM structure between two waveguide ports is shown in Fig. 2.



(a)                              (b)



(c)                              (d)
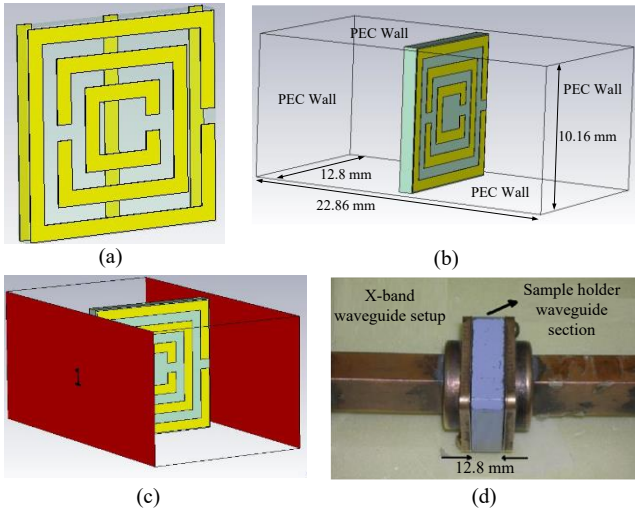
Fig. 2. X-band waveguide setup used in simulation and experiments (a) transparent image of LHM structure, (b) setup display of X-band waveguide and LHM structure, (c) representation of ports, (d) photo of sample holder waveguide section with installation of X-band waveguide [15].

S-parameters can be obtained from the relevant structure using the transmission/reflection (T/R) method by CST Microwave Studio. To find the negative values of refractive index, permittivity, and permeability, scatter parameters ($S_{11}$ and $S_{21}$) must be transferred to MATLAB using the following equations [12]:

$$\varepsilon = n/z \qquad (1)$$

and

$$\mu = nz \qquad (2)$$

where

$$n = \frac{1}{kd}\cos^{-1}\left[\frac{1}{2S_{21}}\left(1 - S_{11}^2 + S_{21}^2\right)\right] \qquad (3)$$

and

$$z = \sqrt{\frac{(1+S_{11})^2 - S_{21}^2}{(1-S_{11})^2 - S_{21}^2}} \qquad (4)$$

Here are ε permittivity, μ permeability, n refractive index, and z wave impedance representations. When the reference [12] is examined, it is understood that the "kd" is approximately 1 (kd~1).
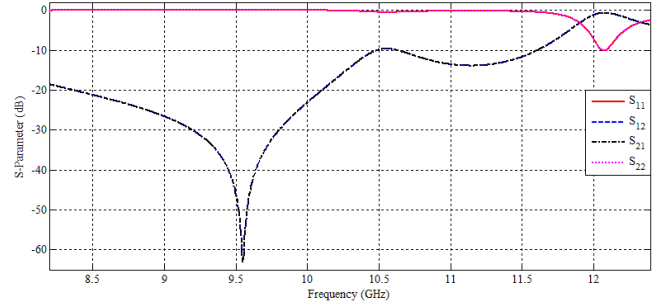


Fig. 3. The simulated parameters $S_{11}$, $S_{12}$, $S_{21}$, and $S_{22}$ ($S_{11} = S_{22}$ and $S_{12} = S_{21}$, i.e. reflection and transmission symmetric).
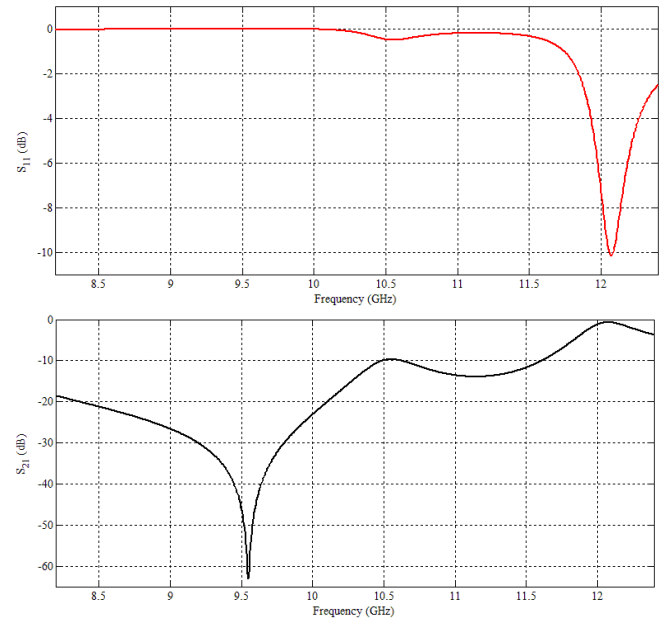


Fig. 4. Simulated $S_{11}$ and $S_{21}$ parameters.
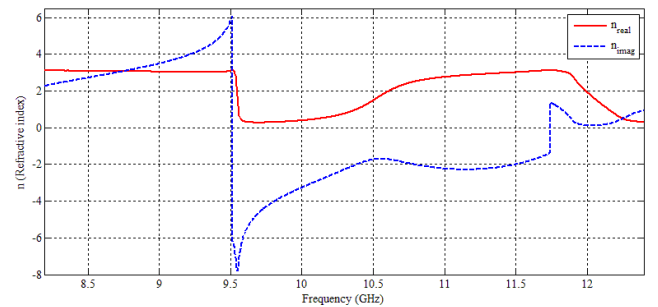


Fig. 5. Simulated refractive index (n) and frequency.

155
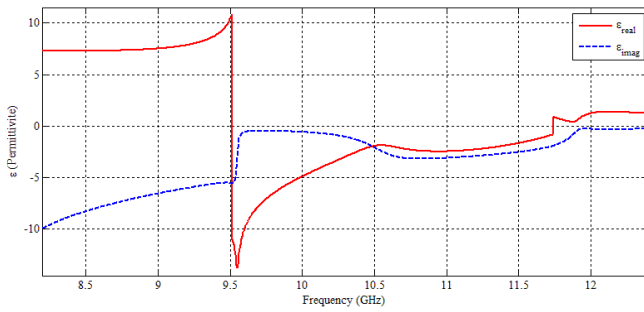
Fig. 6. Simulated permittivity ($\varepsilon$) and frequency.
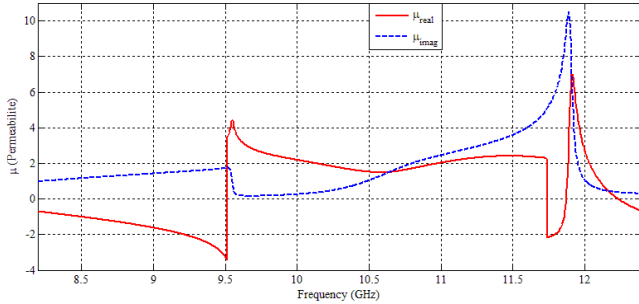


Fig. 7. Simulated permeability ($\mu$) and frequency.

S-parameter measurements can be carried out experimentally using the apparatus of Fig. 2d, with the help of a vector network analyzer (VNA) after the LHM structure is produced.

## III. SIMULATED RESULTS DISCUSSION

Fig. 1 shows the front and back view of the S-SRR. Fig. 2a shows the LHM transparent image, Fig. 2b and 2c CST Microwave Studio X-band waveguide installation, and the experimental sample connection photo in Fig. 2d. S-parameters are key terms for obtaining negative refractive index, permittivity and permeability. Complex scattering parameters $S_{11}$ and $S_{21}$ are extracted from CST Microwave Studio. The simulated scattering parameters are shown in Fig. 3 and 4. The LHM structure resonates in the X-band frequency range.

Simulated S-parameters are transferred to MATLAB. By using the equations (1)-(4) of the direct rectrieval method, negative refractive index, permittivity and permeability are obtained in the X-band frequency range as shown in Fig. 5, 6, and 7 respectively. These figures give the confirmation results of the negative behavior of the periodic structure.

## IV. CONCLUSION

The design has been successfully analyzed. The negative values of the refractive index, permittivity, and permeability were generated through MATLAB software from T/R method using direct retrieval method from the simulated $S_{11}$ and $S_{21}$. Negative parameters are obtained at different operating frequencies. The LHM constructs in this study may be of interest in areas where the negative refraction index needs to be improved the gain and radiation characteristics of the antennas in the specific frequency range. The structure can also be widely used for the development of different antenna parameters.

## REFERENCES

[1] V. G. Veselago, "The electrodynamics of substances with simultaneously negative values of $\varepsilon$ and $\mu$," Soviet Physics Uspekhi, vol. 10, no. 4, pp. 509-514, 1968.

[2] M. A. Hindy, R. M. ElSagheer, and M.S. Yasseen, "Experimental retrieval of the negative parameters "permittivity and permeability" based on a circular split ring resonator (CSRR) lefthanded metamaterial," Journal of Electrical Systems and Information Technology, vol. 5, no. 2, pp. 208-215, 2018.

[3] J. B. Pendry, "Negative refraction makes a perfect lens", Physical Review Letter, vol. 85, no. 18, pp. 3966-3969, 2000.

[4] J. B. Pendry, A .J. Holden, D. J. Robbins, and W. J. Stewart, "Magnetism from conductors and enhanced nonlinear phenomena," IEEE Transactions on Microwave Theory and Techniques, vol. 47, no. 11, pp. 2075-2084, 1999.

[5] D. R. Smith and N. Kroll, "Negative refractive index in left-handed materials," Physical Review Letters, vol. 85, no. 14, pp. 2933-2936, 2000.

[6] R. A. Shelby and D. R. Smith, S. C. Nemat-Nasser, and S. Schultz, "Microwave transmission through a two-dimensional, isotropic, left-handed metamaterial," Applied Physics Letters, vol. 78, no. 4, pp. 489-491, 2001.

[7] A. Grbic and G. V. Eleftheriades, "Experimental verification of backward-wave radiation from a negative refractive index metamaterial," Journal Applied Physics vol. 92, no. 10, pp. 5930-5935, 2002.

[8] R. W. Ziolkowski, "Superluminal transmission of information through an electromagnetic metamaterial," Physics Review E, vol. 63, no. 4, pp. 46604, 2001.

[9] J. B. Pendry, A. J. Holden, W. J. Stewart, and I. Youngs, "Extremely low frequency plasmons in metallic mesostructures," Physical Review Letters, vol. 76, no. 25, pp. 4773–4776, 1996

[10] D. R. Smith, W. J. Padilla, D. C. Vier, S. C. Nemat-Nasser, and S. Schultz, "Composite medium with simultaneously negative permeability and permittivity," Physical Review Letters, vol. 84, no. 18, pp. 4184-4187, 2000.

[11] R. A. Shelby, D. R. Smith, and S. Schultz,"Experimental verification of a negative index of refraction," Science, vol. 292, no. 5514) pp. 77-79, 2001.

[12] D. R. Smith, D. C. Vier, T. Koschny, and C. M. Soukoulis, "Electromagnetic parameter retrieval from inhomogeneous metamaterials," Physics Review E, vol. 71, no. 3, pp. 36617, 2005.

[13] U. C. Hasar, A. Muratoglu, M. Bute, J. J. Barroso, and M. Ertugrul, "Effective constitutive parameters retrieval method for bianisotropic metamaterials using waveguide measurements," IEEE Transactions on Microwave Theory and Techniques, vol. 65, no. 5, pp. 1488-1497, 2017.

[14] U. C. Hasar, G. Buldu, Y. Kaya, and G. Ozturk, "Determination of effective constitutive parameters of inhomogeneous metamaterials with bianisotropy," IEEE Transactions on Microwave Theory and Techniques, vol. 66, no. 8, pp. 3734-3744, 2018.

[15] E. Ekmekci and G. Turhan-Sayan, "Multi-functional metamaterial sensor based on a broad-side coupled SRR topology with a multi-layer substrate," Applied Physics A, vol. 110, pp. 189-197, 2013.

# Using Convolutional Neural Network for Android Malware Detection

Isil Karabey Aksakalli
Department of Computer Engineering,
Erzurum Technical University,
Erzurum, Turkey
{isil.karabey}@erzurum.edu.tr

*Abstract*—With the increasing usage of smart mobile devices, the number of applications developed for these devices is already increasing day by day. Nearly all functionalities (sending emails, searching the internet, messaging via internet, making bank account transactions etc.) performed by using computer are carried out on mobile devices anymore. However, misuse of personal information emerges through malicious applications in the devices and these applications render the devices unusable. In the literature and industry, new methodologies have been proposed for mobile malware detection; however, there is still a research challenge to identify malwares on mobile applications and take precautions. In this paper, a permission-based model is implemented to detection of malware applications in mobile devices which have Android operating system. Permission-based features have been extracted from the apk files in the AndroTracker data set which is previously created in the literature. The results of classification techniques have been evaluated by applying four types of machine learning techniques (Support Vector Machine, k-Nearest Neighbor, Back Propagation) and these techniques have been compared with Convolutional Neural Network. The experimental results show that the permission-based model is highly successful using both machine learning technique and deep learning in the AndroTracker data set. Back Propagation gives the best result among the other machine learning techniques by 96.1% acurracy rate. Also Convolutional Neural Network has achieved success rate of 96.71%. This demonstrates that the accuracy rates of CNN and classical machine learning techniques close to each other and they have high accuracy rate because of small number of targets which are benign and malware.

*Keywords*—Android, permission-based malware detection, convolutional neural network, machine learning.

# Improvement Water Management in PEM fuel cell by Using Microporous Layer With PDMS Polymer and Polystyrene-Silica Nanoparticles

Ayşenur Öztürk
Chemical Engineering Department
Atatürk University
Erzurum, Turkey
aysenur.ozturk@atauni.edu.tr

Ayşe Bayrakçeken Yurtcan
Chemical Engineering Department
Atatürk University
Erzurum, Turkey
ayse.bayrakceken@gmail.com

*Abstract—* **Water management is still at issue of polymer electrolyte membrane (PEM) fuel cells because it is directly related with cell performance thus it must be solved effectively as much as possible. In this context, microporous layer (MPL) was formed on the gas diffusion layer (GDL) using two different polydimethylsiloxane (PDMS) polymers and polystyrene (PS)-silica (SiO₂) particles for providing respectively hydrophobicity and roughness to MPL structure. It was expected that the increased hydrophobicity and roughness of the MPL surface will facilitate the removal of excess water inside the PEM fuel cell.**

*Keywords— Polydimethylsiloxane, polystyrene-silica nanoparticles, hydrophobicity, water management, microporous layer, PEM fuel cell*

## I. INTRODUCTION

In PEM fuel cells, flooding occurs commonly due to the produced water at the cathode side or condensation of humidified reactant gases. It is undesirable phenomena because excess water plugs the active sites for reaction and leads reactant starvation at these regions. Effective water management must prevail inside the cell in order to ensure high performance.

The general way of providing water management in PEM fuel cell is treating the gas diffusion layer or microporous layer with hydrophobic materials with the aim of water removal facilitation. PDMS polymer has been especially highlighted as hydrophobic material in recent years because of its advantageous properties [1],[2]. Additionally surface roughness is also indicated as an important parameter for obtaining superhydrophobicity because of trapped air between the asperities. Silica nanoparticles were generally chosen for this purpose in some studies [3],[4]. Thus in this study, two different molecular weights of PDMS polymer (as hydrophobic material) and PS-SiO₂ nanoparticles (as roughness agent) were used in order to make MPL surfaces for improving water management ability of PEM fuel cell.

## II. EXPERIMENTAL METHOD

### A. Synthesis PS-SiO₂ Particles

The experimental method of [1] was conducted in the same manner for the synthesis of polystyrene/silica core-shell nanoparticles.

### B. Preparation of Microporous Layer

The microporous layer was constructed on the plain GDL by using various amounts of PDMS polymer with two different molecular weights and fixed amount of carbon black (Vulcan) and PS-SiO₂ nanoparticles. The solution consisted of these materials was applied on GDL via spraying. Each of the prepared MPLs was calcined at the 180ºC. Table I shows the properties of all MPLs prepared in the scope of this study.

TABLE I. MPL PROPERTIES

| MPL | PDMS | Carbon | PS-SiO₂ |
|---|---|---|---|
| 1 | 1 % wt. (PDMS-1) | 1 mg/cm² | 1 % wt. |
| 2 | 3 % wt. (PDMS-1) | 1 mg/cm² | 1 % wt. |
| 3 | 5 % wt. (PDMS-1) | 1 mg/cm² | 1 % wt. |
| 4 | 1 % wt. (PDMS-2) | 1 mg/cm² | 1 % wt. |
| 5 | 3 % wt. (PDMS-2) | 1 mg/cm² | 1 % wt. |
| 6 | 5 % wt. (PDMS-2) | 1 mg/cm² | 1 % wt. |

### C. Preparation of Membrane Electrode Assembly (MEA)

Subsequently the preparation of MPLs on the GDL, the catalyst ink was prepared and applied on MPL surfaces via spraying. Anode and cathode electrodes were completed after the loading appropriate amount of Pt catalyst. Two electrodes were hot-pressed (400 psi, 130ºC) as the polymer electrolyte membrane (Nafion) was placed between them.

### D. Physical and Electrochemical Characterization

The surface and cross-section images of MPL surfaces were obtained with SEM. FTIR analysis was made in order to characterize special chemical bonds. TGA analysis was conducted for the determination of degradation temperature and weight loss of samples due to high temperature. Contact angle measurements were taken with Attension Theta tensiometer for the information of MPL surface hydrophobicity. Finally, PEM fuel cell performance tests were applied on the purpose of electrochemical characterization.

## III. RESULTS AND DISCUSSION

FTIR anaysis of the prepared MPL surfaces were shown through Fig. 1.(a) and (b). Fig. 1.(a) and Fig. 1.(b) respectively belong to the MPL surfaces prepared with low molecular weight PDMS (PDMS-1@236,53 g/mole) and high molecular weight PDMS (PDMS-2@117000 g/mole). The peaks appeared at 3463, 2960 ve 1108 cm⁻¹ represent the Si–OH, –CH₃ ve Si–O–Si chemical bonds of PDMS polymer [5].
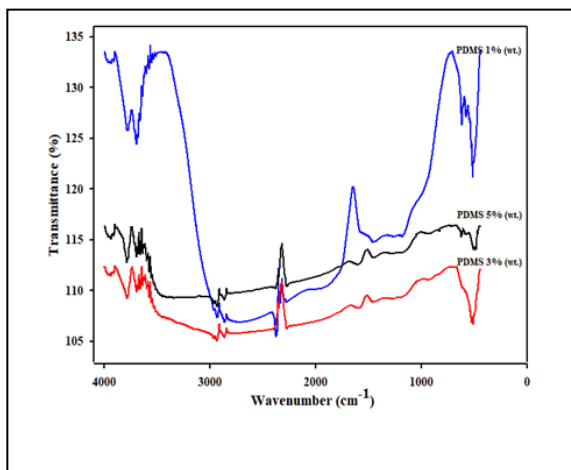
**(a)**
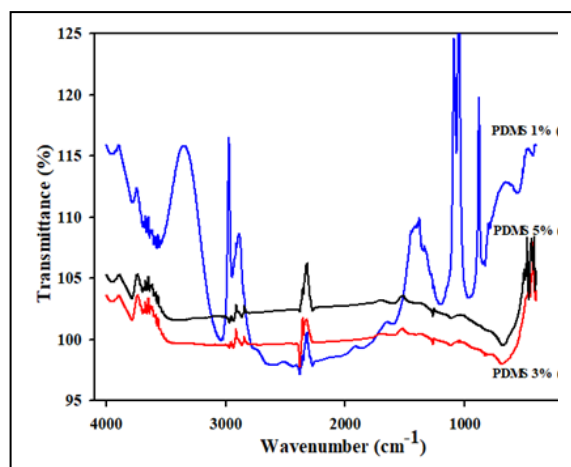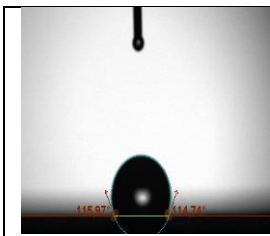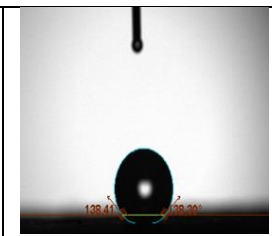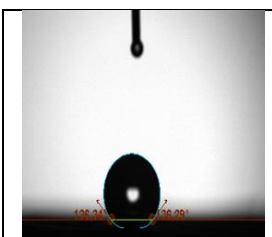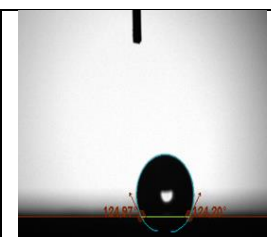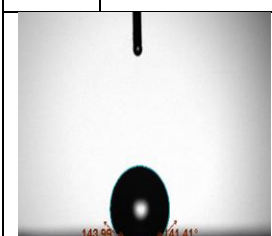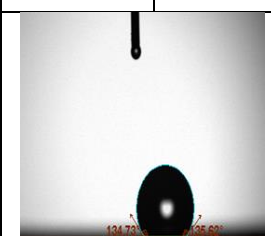


**(b)**

Figure 1. FTIR results of cells with MPLs contain 1%, 3%, 5% (wt.) (a) PDMS-1 (b) PDMS-2.

Hydrophobic properties of the prepared MPL surfaces are substantial for the better water removal from the PEM fuel cell. Therefore, contact angle measurements of MPL surfaces were illustrated in Table II. According to the results, all of samples have hydrophobic property due to their contact angles greater than 90º.

Table II. Contact angle measurements of mpls



| 1 | 120.8º | 2 | 122.2º |



| 3 | 116.7º | 4 | 125.1º |
| 5 | 142.1º | 6 | 133.4º |

REFERENCES

[1] C-H. Xue, Z-D. Zhang, J. Zhang, S-T. Jia, "Lasting and self-healing superhydrophobic surfaces by coating of polystyrene/SiO2 nanoparticles and polydimethylsiloxane," J. Mater. Chem. A, vol. 2, pp. 15001-15007, 2014.
[2] R. P. S. Chakradhar, V. Dinesh Kumar, J. L. Rao, B. J. Basu, "Fabrication of superhydrophobic surfaces based on ZnO–PDMS nanocomposite coatings and study of its wetting behavior," App. Surf. Sci., vol. 257, pp. 8569-8575, 2011.
[3] L. Mammen, X. Deng, M. Untch, D. Vijayshankar, P. Papadopoulos, R. Berger, E. Riccardi, F. Leroy, D. Vollmer, "Effect of Nanoroughness on Highly Hydrophobic and Superhydrophobic Coatings," Langmuir, vol. 28, pp. 15005-15014, 2012.
[4] S. Cheng, L-Q. Ge, Z-Z. Gu, "Fabrication of super-hydrophobic film with dual-size roughness by silica sphere assembly," Thin Solid Films, vol. 515, pp. 4686-4690, 2007.
[5] K. Li, X. Zeng, H. Li, X. Lai, H. Xie, "Effects of calcination temperature on the microstructure and wetting behavior of superhydrophobic polydimethylsiloxane/silica coating," Colloids Surf., A., vol. 445, pp. 111-118, 2014.

# Production and Characterization of TiO₂ and ZnS Doped TiO₂ Nanotube Photocatalysts

Hakan Kızıltaş
Department of Chemical Engineering
Atatürk University
Erzurum/TURKEY
h.kiziltas@atauni.edu.tr

Taner Tekin
Department of Chemical Engineering
Atatürk University
Erzurum/TURKEY
ttekin@atauni.edu.tr

Derya Tekin
Department of Metallurgical and
Materials Engineering
Atatürk University
Erzurum/TURKEY
deryatekin@atauni.edu.tr

*Abstract*— In this study, the TiO2 nanotube photocatalysts were synthesized using the anodization method. The anodization process was performed under 20V potential for 3 hours. After the anodization, successive ionic layer adsorption and reaction (SILAR) method was used ZnS doping. The crystal structures of the nanotube photocatalysts were characterized using the X-Ray diffraction (XRD), and its morphology and elemental composition were characterized using the scanning electron microscopy (SEM-EDS). Orange G dye was used for photocatalytic activity experiments. The results showed that ZnS doping increased the photocatalytic activity of TiO2.

*Keywords*— *TiO2 nanotube, photocatalyst, Orange G, dye removal.*

## I. INTRODUCTION

Titanium is a very important material for applications in industry, medicine and scientific research [1-3]. TiO2 nanotube arrays synthesized by electrochemical methods are commonly used in dye sensitive solar cells [4], photo-decomposition of pollutant organisms [5], humidity sensors [6] and hydrogen generation [7].

TiO2 has long been recognized as the most promising photocatalyst due to its high photocatalytic activity, long-term chemical stability, non-toxicity, and relatively low prices, and finds broader applications in the breakdown of many organic pollutants, such as persistent toxic substances, paints.

However, the photocatalytic oxidation technology, using TiO2 as a photocatalyst, aims to overcome the difficulties of separating suspended TiO2 particles from aqueous solutions and the low yield resulting from the rapid incorporation of photogenic electrons and voids [8]. To solve the separation problem, many researchers have developed thin-film technology to immobilize TiO2 on a solid carrier, but there are some defects. The surface area of the thin-film TiO2 photocatalyst exposed to the solution is from the TiO2 nanoparticles released into the solution. On the other hand, poor adhesion of the TiO2 film to the supporting carriers can block the electron mass transfer [9]. Accordingly, TiO2 nanotubes formed by anodizing on the titanium substrate show more photocatalytic activity than the immobilized TiO2 film [10].

In this study, TiO2 and ZnS doped TiO2 nanotube photocatalysts were synthesized and XRD and SEM-EDS results were used for characterization. In order to determine the photocatalytic activities, the decomposition of Orange G dyestuff was investigated.

## II. EXPERIMENTAL

### E. Materials

Titanium sheets with 99.7% purity were used in the production of nanotube TiO2 photocatalysts. Sodium fluoride (BDH Lab.), Phosphoric acid (Merck, 85%) and distilled water were used for the anodization process. Zinc chloride (Merck, pure), sodium sulfide (Sigma Aldrich,> 98%) and distilled water (H2O) was used for ZnS doping.

### F. Anodic oxidation process

The two electrode system was used for the anodization process. The titanium plate and the platinum were connected as anode (+) and cathode (-), respectively. The distance between the electrodes was kept 3 cm during the anodization. 0.5 M Phosphoric Acid (H3PO4) and 0.14M Sodium Fluoride (NaF) aqueous solution were used the electrolyte solution. During the anodization process, 20V voltage was used. The anodization time was chosen for 1 hour under the continuous stirring. After the anodization, TiO2 nanotubes were calcined at 500 ° C for 3 hours.

### G. Production of NiS / TiO2 nanotube photocatalyst by SILAR method

The SILAR method is based on the slow formation of solution ions on the sub-base of the substance to be dosed. In order to avoid a homogeneous precipitation that may occur in the solution, the reaction and adsorption of the ions in the solution and the solution after each dipping with deionized water are the basis of the SILAR method.

The four basic steps in the SILAR method are:

1. Metal adsorption
2. Rinse with deionized water
3. Surface reaction
4. Rinsing with deionized water

In this study, ZnS nanoparticles were doped on TiO2 by SILAR method. Four different beakers were used in the doping process and the contents of these beakers were as follows:

1. Beaker: 0,025 M ZnCI2 aqueous solution
2. Beaker: Deionized water
3. Beaker: 0,025 M Na2S
4. Beaker: Deionized water

In this way, ZnS was doped on the nanotube TiO2, then calcined at 500°C for 3 hours.

## H. Photocatalytic Activity Tests

The photocatalytic experiments were carried out in a batch reactor with light. A 44 W / m2 lamp was used as a source of UV light. O2 was provided by pumping air at a constant flow rate to provide a saturated concentration of reaction medium.

## III. RESULT AND DISCUSSION

SEM and EDS analysis of TiO2 nanotube photocatalyst was shown in Figure 1.



**Figure 1.** SEM and EDS analysis of TiO2 nanotube photocatalyst

As can be seen in Figure 1, TiO2 nanotubes are formed and distributed homogeneously on the surface. The average diameter of the nanotubes ranges from 99-116 nm. Any contamination is not observed on the nanotubes. The EDS analysis of TiO2 nanotube photocatalyst proved the presence of titanium and oxygen in the sample. The presence of carbon in the sample indicates the presence of trace amounts of pollution.

The results of SEM and EDS analysis of ZnS/TiO2 nanotube photocatalyst are given in Figure 2.



Figure 2. SEM and EDS analysis of ZnS/TiO2 nanotube photocatalyst

As can be seen from the SEM image of the ZnS doped nanotube photocatalyst given in Figure 2, ZnS was doped around the nanotubes. The EDS analysis of the same photocatalyst revealed the presence of titanium, oxygen and zinc in the sample.

Figure 3 shows the XRD diagram of the nanotube TiO2 and ZnS doped TiO2 photocatalysts.
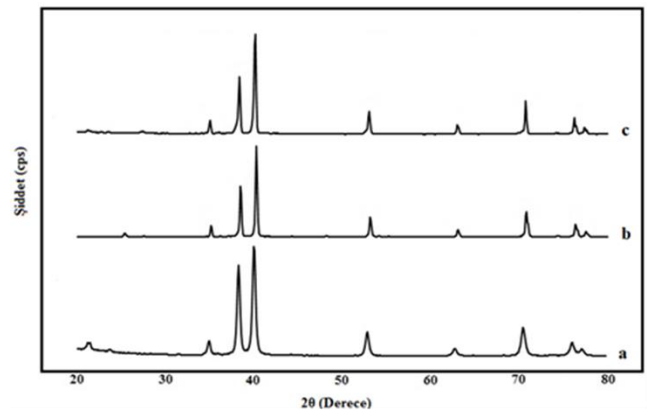


Figure 3. XRD patterns of the titanium plate (a), the nanotube TiO2 (b) and the ZnS doped nanotube TiO2 (c) photocatalysts

As shown in Figure 3a-b, it was found that the nanotube TiO2 peak is more sharply in the anatase phase than the titanium plate. Compared to Fig. 3b-c, it is observed that the anatase peaks of the ZnS-doped photocatalyst are more pronounced and become sharper.

The photocatalytic degradation values of Orange G dye on the TiO2 and ZnS/TiO2 nanotube photocatalysts in the batch reactor are shown in Figure 4.
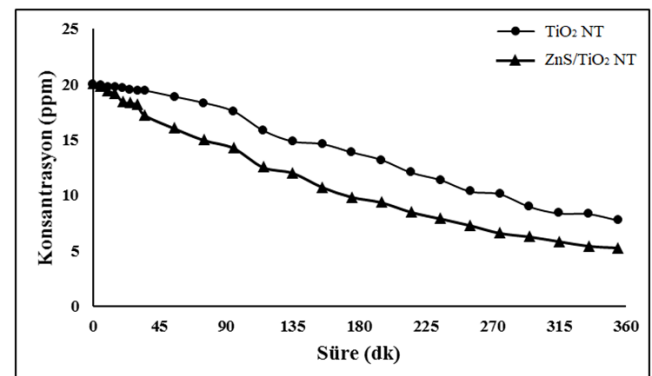


Figure 4. Decomposition of Orange G dyes on TiO2 and ZnS / TiO2 nanotube photocatalysts

When the graph is examined, the difference between the removal of the two photocatalysts is noticeable. For the TiO2 photocatalyst, 61,08% of the dye was removed in 6 hours, whereas the ZnS doped nanotube TiO2 photocatalyst removed 73,69% of the dye after 6 hours.

## IV. CONCLUTION

TiO2 nanotube photocatalysts were synthesized by electrochemical method of anodization. After anodization, successive ionic layer adsorption and reaction (SILAR) method was used to dope ZnS nanoparticles. The crystal structure of the nanotube photocatalysts produced was characterized using X-Ray diffraction (XRD), and its morphology and elemental composition were determined by using scanning electron microscopy (SEM-EDS). Orange G dyestuff was used for photocatalytic activity experiments. The results showed that ZnS doping increased the photocatalytic activity of TiO2.

# REFERENCES

[1] Roy, P., S. Berger, and P. Schmuki, TiO2 Nanotubes: Synthesis and Applications. Angewandte Chemie International Edition, 2011. 50(13): p. 2904-2939.

[2] Wang, Q., et al., Recent progress in all-solid-state quantum dot-sensitized TiO2 nanotube array solar cells. Journal of Nanoparticle Research, 2016. 18(1): p. 7.

[3] Wang, H., et al., One-dimensional titania nanostructures: Synthesis and applications in dye-sensitized solar cells. Thin Solid Films, 2014. 558: p. 1-19.

[4] Bozkurt Çırak, B., et al., Synthesis, surface properties, crystal structure and dye sensitized solar cell performance of TiO2 nanotube arrays anodized under different voltages. Vacuum, 2017. 144: p. 183-189.

[5] Srimuangmak, K. and S. Niyomwas, Effects of Voltage and Addition of Water on Photocatalytic Activity of TiO2 Nanotubes Prepared by Anodization Method. Energy Procedia, 2011. 9: p. 435-439.

[6] Yang, L., et al., A review on TiO2 nanotube arrays: Fabrication, properties, and sensing applications. Chinese Science Bulletin, 2010. 55(4): p. 331-338.

[7] Sun, Y. and K.-P. Yan, Effect of anodization voltage on performance of TiO2 nanotube arrays for hydrogen generation in a two-compartment photoelectrochemical cell. International Journal of Hydrogen Energy, 2014. 39(22): p. 11368-11375.

[8] Choi, W., A. Termin, and M.R. Hoffmann, The Role of Metal Ion Dopants in Quantum-Sized TiO2: Correlation between Photoreactivity and Charge Carrier Recombination Dynamics. The Journal of Physical Chemistry, 1994. 98(51): p. 13669-13679.

[9] Candal, R.J., W.A. Zeltner, and M.A. Anderson, Effects of pH and Applied Potential on Photocurrent and Oxidation Rate of Saline Solutions of Formic Acid in a Photoelectrocatalytic Reactor. Environmental Science & Technology, 2000. 34(16): p. 3443-3451.

[10] Li, X.Z., et al., Photoelectrocatalytic Oxidation of Rose Bengal in Aqueous Solution Using a Ti/TiO2 Mesh Electrode. Environmental Science & Technology, 2000. 34(20): p. 4401-4406.

# Thermal decomposition kinetics of copper hydroxide sulfate (Cu₄(SO₄)(OH)₆) prepared by chemical precipitation method

Jale Naktiyok
Department of Chemical Engineering
Ataturk University
Erzurum, Turkey
jalenaktiyok@atauni.edu.tr

Abdulkadir Özer
Department of Chemical Engineering
Ataturk University
Erzurum, Turkey
kadirozer@atauni.edu.tr

*Abstract*— **Copper hydroxide sulfate was synthesized by chemical precipitation method from a mixed solution of CuSO₄ and NaOH. The reaction pathway and kinetics of the thermal decomposition of the Cu₄(OH)₆SO₄ were investigated by means of thermoanalytical techniques. TG-DTG data taken in air atmosphere from 298 to 1273 K at different heating rates (2.5, 5, 7.5 and 10 Kmin⁻¹) were plotted under non-isothermal heating conditions. TG and DTG measurements indicated that thermal behavior of copper hydroxide sulfate has two-region degradation. Kinetic parameters were determined from the TG and DTG curves for the regions I and II by using Ortega method. The activation energy (Ea) and g(α) mechanism of the material was determined. The average activation energies (Eₐ) are 53.5 kJmol⁻¹ and 188.5 kJmol⁻¹ for regions I and II, respectively. The decomposition process of copper hydroxide sulfate proceeds by one-way diffusion (D₁) for region I, followed by two-dimensional random nucleation and nuclei growth (A₂) mechanism for region II.**

*Keywords—copper hydroxide sulfate, thermal analysis, kinetics analysis, Ortega method*

## I. INTRODUCTION

Because various basic copper (II) salts are suitable precursors for CuO with various desired properties and appear as a co-precipitate in the precursors for many Cu-containing ceramics, it is expected that detailed investigations on the kinetics and mechanisms of the thermal decomposition of basic copper (II) salts provide valuable information to improve the ceramic processing through thermal decomposition route [1].

Copper oxide is an important catalyst, and it is widely used because of its high activity and selectivity in oxidation/reduction reactions. It is also used in gas sensors, thermoelectric materials, etc [2,3]. Various methods such as sol-gel, precipitation-stripping, solid state reaction, alkoxide-based synthesis, sonochemical preparation, microwave irradiation and precipitation–pyrolysis are used to prepare copper oxide nanoparticles [4]. However, most of the reported methods suffer from such limitations as the use of organic solvents, long times and complicated equipment requirements [5].

In this study, a rapid synthesis of Cu₄(SO₄)(OH)₆ was examined by chemical precipitation method for a mixed solution of CuSO₄ and NaOH. The reaction pathway and physico-chemical events taking place during the course of the thermal decomposition processes were investigated in order to find some kinetic-related phenomena required to interpret the kinetic results. Kinetic analyses for the respective reaction steps were carried out for the kinetic rate data under linearly increasing temperature.

## II. KINETICS ANALYSIS

It can be determined the mechanism of the physical and chemical processes occurring during decomposition at TG-DTG analysis.

Kinetic parameters can be calculated by both model-fitting and isoconversional methods. For non-isothermal experiments, model-fitting includes fitting different models to α–T curves and simultaneously determining Ea and A. There are numerous non-isothermal model-fitting methods; the Coats–Redfern method, and the method suggested by Ortega are popular. Thus, the model that gives the best linear-fit is usually selected as the model [6].

In the present study, it was applied the model-fitting technique for the kinetics analysis at non-isothermal conditions.

In the kinetic analysis, it is very important the knowledge of the dependence of the temperature with the conversion value of the decomposition (α). It provides to explain multistep processes and gives information about their reaction mechanisms. When the rate of a solid-state decomposition reaction under non-isothermal condition is determined, α is firstly calculated as follows:

$$\alpha = \frac{W_0 - W_t}{W_0 - W_\infty} \qquad (1)$$

$W_0$, $W_t$, and $W_\infty$ are the initial, actual, and final mass of the sample, respectively.

The reaction-rate of a material is usually explained as;

$$\frac{d\alpha}{dt} = kf(\alpha) \qquad (2)$$

$f(\alpha)$ is a function related to the reaction mechanism and k is the specific rate constant at the Arrhenius equation:

$$k = A \exp(-\frac{Ea}{RT}) \qquad (3)$$

A is the pre-exponential factor (min⁻¹), Ea is the activation energy (kJmol⁻¹), R is the universal gas constant (Jmol⁻¹K⁻¹), and T is the absolute temperature (K). $\beta$ is the constant heating rate for the non-isothermal system.

| Two dimensions | $(-\ln(1-\alpha))^{1/2}$ | A$_2$ |
| Three dimensions | $(-\ln(1-\alpha))^{1/3}$ | A$_3$ |

$$\frac{dT}{dt} = \beta \tag{4}$$

From Eq. 2, it is obtained

$$\frac{d\alpha}{dt} = \left(\frac{d\alpha}{dT}\right).\left(\frac{dT}{dt}\right) = kf(\alpha) \tag{5}$$

$$\frac{d\alpha}{f(\alpha)} = \frac{A}{\beta}.\exp\left(-\frac{E_a}{RT}\right).dT \tag{6}$$

When above equations are rearranged, it is found Eq. (7)

$$\ln(g(\alpha)) = \ln\left(\frac{AE}{\beta R}\right) - 5.331 - 1.052\left(\frac{E}{RT}\right) \tag{7}$$

The mechanism of the reactions can be predicted from the method suggested by Ortega [6]. It is used Eq. (7) to determine the kinetics parameters (activation energy and pre-exponential constant) of the reactions. $g(\alpha)$ is the reaction mechanism under linear heating and in other words, $g(\alpha)$ is the integral function of conversion. A plot of $\ln[g(\alpha)]$ against $1/T$ should give a straight line with a slope equal to $-1.052$ $E_a/R$. The $g(\alpha)$ affects from the mechanism controlling the reaction, the size and the shape of the particles. When the $g(\alpha)$ is predicted correctly, the graph of $\ln[g(\alpha)]$ against $1/T$ will a straight line with high correlation coefficient ($R^2$) at linear regression analysis, that $E_a$ and $A$ can be attainable.

Eq. (7) is rearranged, it is found Eq. (8)

$$g(\alpha) = \int_0^\alpha \frac{d\alpha}{f(\alpha)} = \frac{AE_a}{\beta R}\ p(u) \tag{8}$$

This equation is dependent on evaluating the function $p(u)$. Doyle [7] has evaluated $p(u)$ and suggested.

$$p(u) = 0.00484\exp(-1.0516) \tag{9}$$

The Master-plot method provides the solution of Eq. (8) by using a reference at point $\alpha=0.5$, and then the following Eq. (10) is found.

$$g(\alpha) = \left(\frac{AE}{\beta R}\right)p(u_{0.5}) \tag{10}$$

$$u_{0.5} = E/RT_{0.5} \tag{11}$$

Eq. (12) is obtained by dividing Eq. (8) to Eq. (9)

$$\frac{g(\alpha)}{g(0.5)} = \frac{p(u)}{p(u_{0.5})} \tag{12}$$

The curves of $\frac{g(\alpha)}{g(0.5)}$ versus $\alpha$ are the theoretical master plots values, and the curves of $p(u)/p(u_{0.5})$ versus $\alpha$ are experimental ones at different heating rates. Doyle equation can be used to draw the curves of $p(u)/p(u_{0.5})$. Eq (12) shows that the theoretical values are equivalent the experimental values, when it is found the suitable kinetics model for a given $\alpha$ value.

It was used to the six solid state mechanisms '$g(\alpha)$' which for the prediction of reaction mechanisms from TG data at Table 1.

Table 1. $g(\alpha)$ for solid state mechanisms

| Mechanism | $g(\alpha)$ | Symbol |
|---|---|---|
| **Chemical reaction** | | |
| First order | $-\ln(1-\alpha)$ | F$_1$ |
| Second order | $1/(1-\alpha)$ | F$_2$ |
| **Diffusion mechanism** | | |
| One-dimensional diffusion | $\alpha^2$ | D$_1$ |
| Two-dimensional diffusion | $\alpha+(1+\alpha)\ln(1-\alpha)$ | D$_2$ |
| **Random nucleation and nuclei growth** | | |

## III. EXPERIMENTAL

### A. Synthesis

Copper hydroxide sulphate was prepared by the chemical precipitation method. A solution of 50 ml 0.1 M NaOH was added drop by drop to a vigorously stirred salt solution of 50 ml 0.5 M CuSO$_4$·5H$_2$O. The resulting suspension was aged at 60 °C for 8 h. The mixture was filtered and then washed with double distilled water and ethanol for several times. Finally, the solid phase was dried at 80°C.

Thermogravimetric and differential thermal analyses (TG–DTG) curves were obtained on a NETZSCH STA 409 PC Luxx at different heating rates of 2.5, 5, 7.5 and 10 Kmin$^{-1}$ under air flow in the temperature range from 298 to 1273 K.

### IV. RESULTS AND DISCUSSION

In the present study, a simple chemical precipitation method for the synthesis of the precursor copper hydroxide sulfate [Cu$_4$(SO$_4$)(OH)$_6$] from CuSO$_4$ and NaOH solution at 60°C is presented. The reaction pathway of the thermal decomposition of copper hydroxide sulfate to copper (II) oxide included the thermal dehydroxylation and desulfation processes.

$$Cu_4(OH)_6SO_4 \rightarrow Cu_2OSO_4 + 2CuO + 3H_2O \tag{13}$$
$$Cu_2OSO_4 \rightarrow 2CuO + SO_3 \tag{14}$$
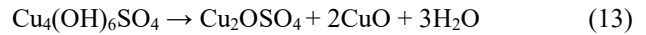
Pure CuO nanoparticles were obtained by calcining the precursor powder at 1173 K in air.

### A. TG-DTG Analysis

In this study, the thermal decomposition of synthetic copper hydroxide sulfate (Cu$_4$(OH)$_6$SO$_4$) was investigated to determine its thermal behavior and decomposition temperature by means of TG-DTG. The experimental TG-DTG curves of Cu$_4$(OH)$_6$SO$_4$ at different heating rates of 2.5, 5, 7.5, and 10 Kmin$^{-1}$ from 298 K to 1273 K are given at Fig. 1 and 2. TG and DTG curves display that thermal behavior of Cu$_4$(OH)$_6$SO$_4$ has two-region degradation. At the first region that corresponds to dehydoxylation reaction, the thermal decomposition occurs at temperatures ranging from 298 to ~700 K according to the heating rates. The mass loss of dehydoxylation process is approximately 14-15%. In the literature, it is explained that the sample (Cu$_4$(OH)$_6$SO$_4$) turns into Cu$_2$OSO$_4$ in the region [1]. It wasn't observed any mass change between 700 and 850 K. The second region proceeds from 850 to 1100 K, in which the desulfation decomposition process takes place. It observed that the dehydrated compound decomposed to CuO about 20% in the region. It has been reported that the decomposition of Cu$_2$OSO$_4$ corresponds to the crystallization of CuO in the region [1]. It is also represented that the volume shrinkage of the sample assemblage during release of the gas caused the thermal decomposition of structure, too.
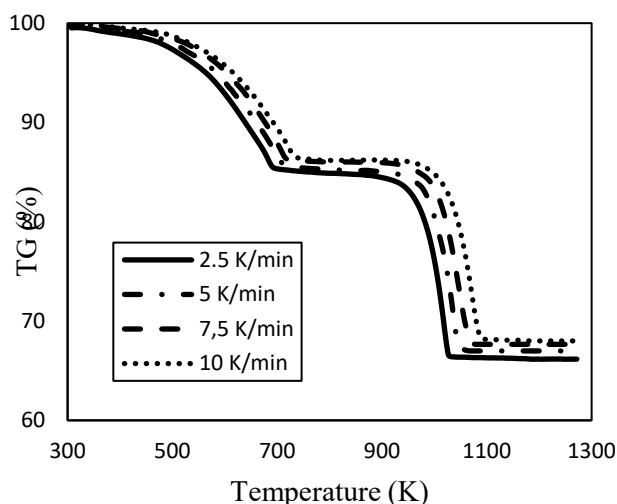
**Figure 1**. TG curves of copper hydroxide sulfate at different heating rates
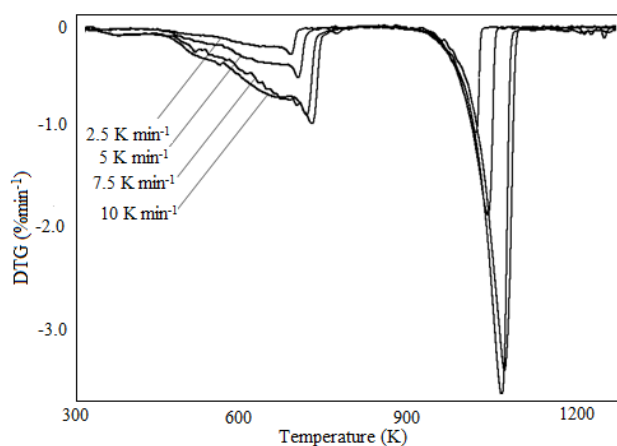


**Figure 2.** DTG curves of copper hydroxide sulfate at different heating rates

## B. Kinetics Analysis

The model-fitting method (Ortega equation) with results obtained from TG data was used to determine the kinetics expressions for region I and II. The conversion values ($\alpha$) were calculated from the TG data.

In Table 2 and 3, it is tabulated the activation energies corresponding to the $g(\alpha)$ values that are six general reaction mechanisms and calculated by the method suggested by Ortega for region I and II, respectively.

Table 2. Activation Energies Corresponding Various Solid-State Mechanisms For Region I

| Mechanism | Sym | Ea (kJmol$^{-1}$) | | | |
|---|---|---|---|---|---|
| Heating rate (Kmin$^{-1}$) | | $\beta$=2.5 | $\beta$=5 | $\beta$=7.5 | $\beta$=10 |
| *Chemical reaction* | | | | | |
| First order | F$_1$ | 31.1 | 34.9 | 38.6 | 39.8 |
| Second order | F$_2$ | 41.9 | 47.4 | 52.4 | 54.1 |
| *Diffusion mechanism* | | | | | |
| One-dimensional | **D$_1$** | **46.2** | **51.9** | **57.1** | **58.8** |
| Two-dimensional | D$_2$ | 50.6 | 56.9 | 62.6 | 64.5 |
| *Random nucleation and nuclei growth* | | | | | |
| Two dimensions | A$_2$ | 15.5 | 17.5 | 19.3 | 19.9 |
| Three dimensions | A$_3$ | 10.4 | 11.7 | 12.9 | 13.3 |

**Table 3.** ACTIVATION ENERGIES CORRESPONDING VARIOUS SOLID-STATE MECHANISMS FOR REGION II

| Mechanism | Sym | Ea (kJmol$^{-1}$) | | | |
|---|---|---|---|---|---|
| Heating rate (Kmin$^{-1}$) | | $\beta$=2.5 | $\beta$=5 | $\beta$=7.5 | $\beta$=10 |
| *Chemical reaction* | | | | | |
| First order | F$_1$ | 368.4 | 391.8 | 377.4 | 386.4 |
| Second order | F$_2$ | 506.9 | 538.3 | 517.8 | 531.6 |
| *Diffusion mechanism* | | | | | |
| One-dimensional | D$_1$ | 498.9 | 572.5 | 552.2 | 565.8 |
| Two-dimensional | D$_2$ | 537.9 | 630.7 | 608.1 | 623.3 |
| *Random nucleation and nuclei growth* | | | | | |
| Two dimensions | **A$_2$** | **175.9** | **195.9** | **188.7** | **193.6** |
| Three dimensions | A$_3$ | 112.9 | 122.7 | 125.8 | 129.0 |

It is selected the mechanism with the highest correlation coefficient ($R^2$) from these values in the analysis. In the region I, $D_1$ mechanism has yielded the highest correlation.

In the region II, it is seen that some mechanisms have high $R^2$ values. Therefore, the Master-Plot method was applied to better decision the desulfation process mechanism of sample at region II. It was obtained that it is best described A$_2$ (two-dimensional) mechanism. According to the results, the average activation energies for region I and II are 53.5 and 188.5, respectively.

## V. CONCLUSION

The decomposition process of copper hydroxide sulfate was investigated by TG-DTG analyzes and obtained that the thermal decomposition process consists of two-region degradation (dehydoxylation and desulfation region). The average activation energies (E$_a$) calculated by using Ortega method are 53.5 and 188.5 kJmol$^{-1}$ for regions I and II, respectively. The decomposition process of copper hydroxide sulfate proceeds by one-way diffusion (D$_1$) for region I, followed by two-dimensional random nucleation and nuclei growth (A$_2$) mechanism for region II.

## REFERENCES

[1] N. Koga, A. Mako, T. Kimizu, and Y. Tanaka, "Thermal decomposition of synthetic antlerite prepared by microwave-assisted hydrothermal method", Thermochimica Acta vol. 467, 2008, pp. 11–19.

[2] J.Pike, S.W.Chan, F. Zhang, X. Wang, and J. Hanson, "Formation of stable Cu$_2$O from reduction of CuO nanoparticles", J Appl Catal A General, vol. 303, 2006, pp. 273-277.

[3] K. Zhou, R. Wang, B. Xu, and Y. Li, "Synthesis, characterization and catalytic properties of CuO nanocrystals with various shapes", Nanotechnology, vol.17, 2006, pp. 3939-3943.

[4] Q.H. Wu, X.W. Wei, M.W. Shao, J.S. Gu, M.Z. Qu, "Synthesis of copper oxide nanoparticles using carbon nanotubes as templates", Chem Phys Lett. vol. 364, 2002, pp. 152-156.

[5] L. Sun, Z. Zhang, Z.Wang, Z.Wu, H. Dang, "Synthesis and characterization of CuO nanoparticles from liquid ammonia", Mater. Res. Bull, vol.40, 2005, pp. 1024-1031.

[6] A. Ortega, Some successes and failures of the methods based on several experiments,Thermochimica Acta 284 (1996) 379–387.

[7] C.D. Doyle, Estimating isothermal life from thermogravimetric data, Journal of Applied Polymer Science 6 (1962) 639–642.

# Investigation of Sulfonation Time on Ion Exchange Capacity of Cationic Membrane

Mehmet Semih Bingöl
DAYTAM
Ataturk Universitesi
Erzurum, Türkiye
semih.bingol@atauni.edu.tr

Osman Nuri Ata
Kimya Mühendisliği
Atatürk Üniversitesi
Erzurum, Türkiye
oatar@atauni.edu.tr

Neslihan Alemdar Yayla
Kimya Mühendisliği
Marmara Üniversitesi
İstanbul, Türkiye
neslihanalemdar@marmara.edu.tr

*Abstract*— **Advances in membrane technology, which is used often in separation processes, especially in new materials, can make this technology more competitive with traditional, high-energy intensive, environmentally undesirable and costly processes. Ion exchange membranes are used particularly in waste water treatment and preparation of process and drinking water together with other separation techniques. Cation exchange membranes have been used in various industries such as production of drinking water from sea water, recovery of useful metal salt from waste water in metal plating, production of fuel cells, chlor-alkali processes. Because of its wide application area, the development and improvement of membrane technology has become a very important position. For this reason, the cation exchanger membrane was prepared separately from the styrenated oil and polystyrene in the study and a certain amount of graphene oxide was used as an additive. It is aimed to have better membrane properties in this study which is different from the literature. Parameters and ranges used in the study were: Stirred oil / polystyrene based, graphene oxide additive (0.5-1-3-5%) and sulphonation time (1-6-12-24 hours). Membranes prepared in this study were characterized by ion exchange capacity,. As a result of the studies performed on the character set, optimum parameters were styrene oil, 3% graphene oxide contribution and 24 hours sulphonation time.**

**Keywords: Cation exchange membranes, ion exchanger, grafene oxide, polystyreneIntroduction Introduction**

## I.INTRODUCTİON

Nowadays, membrane technology has a wide range of applications in the industry. Nowadays, various membranes are used in large scale for producing drinking water from sea and bitter water, cleaning industrial wastes and recovering valuable chemical components, fractional molecular mixtures in food and pharmaceutical companies and recycling of separate gases and vapors in petrochemical process [1, 2]. Electrically Loaded Membranes; The electrically charged membranes can be dense or microporous, but are usually very thin micro-porous, porous walls carry fixed positive or negatively charged ions. A membrane with fixed positive charged ions is called the anion exchange membrane because it binds the anions in the surrounding fluid. Similarly, a membrane containing fixed, negatively charged ions is called a cation exchange membrane. [1].

In this study, cation exchange membrane was prepared. This membrane was prepared with styrene oil and graphene oxide. This study, which is different from the literature, is intended to have better membrane properties.

## II. EXPERIMENTAL DETAILS

The cation exchanger membrane prepared was carried out in 3 steps. The prepared polymer was then placed in the second stage as graphene oxide. In the last step, the prepared resin was sulfonated.

### Step 1: Preparation of classical styrenated oil sample

Styrenated oil production will be obtained according to conventional methods in the literature. Accordingly, 55 mL of sunflower oil, 45 mL of styrene, 1.9 mL of divinylbenzene, 43 mL of xylene and 0.6 grams of benzoyl peroxide were heated in inert medium at 150 0C for 24 hours. At the end of this process, the reaction mixture was washed several times in methanol and the precipitated portion was dried in vacuo.



Fig.2.1. Experimental Setup

### Step 2. Insertion of graphene oxide into styrened oil

As a result of interaction between carboxyl groups and vinyl groups on Graphene oxide (Figure 2.2), styrene oil structure or graphene oxide into polystyrene is thought to be added successfully..
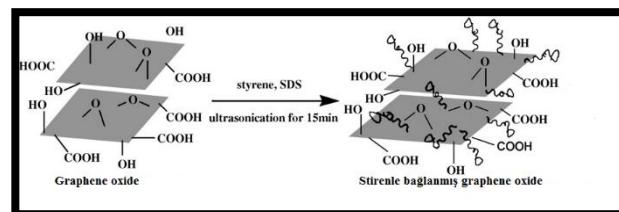


Fig. 2.2: Graphene oxide and styrene interaction

As it can be seen from Figure 2.2, graphene oxide is very hydrophilic due to its groups. The fact that the polymeric and additive materials used in the membrane production are hydrophilic have a positive effect on the performance of membrane. Because the more hydrophilic the structure will be, the stronger the interaction between the membrane and

water molecules, and this will allow the water to dissociate more easily.

It was first dried under vacuum at 100 ° C to remove moisture from the graphene oxide. 250 mg of dried graphene oxide powders are then mixed in inert medium with 25 mL of dehydrated DMF. After the medium was inert, 2 mL of phenyl isocyanate was added to the system. It was then mixed in a 3 hour ultrasonic mixer followed by 24 hours in a magnetic stirrer. The resulting solution was precipitated by centrifugation and washed again with DMF. The washed GO was stirred in DMF for 30 minutes. In this way, graphene oxide plates were prepared in DMF. The polystyrene pellets are then dissolved by stirring in DMF. The polystyrene solution is then mixed with graphene oxide in DMF for 15 minutes. The precipitate is filtered off and washed several more times with ethanol. Poured onto a glass surface and dried under vacuum at 100 ° C [3].

• **Step 3. Sulfonation of graphene oxide modified styrene oil or polystyrene**

The obtained product was kept in the 98% H2SO4 solution at 25 C for a period of time and the sulfonation was achieved and the cation exchange membrane was obtained.

### 2.2 Membrane characterization

**Measurement of ion exchange capacity**

The ion exchange capacity in the membrane is a measure of proton conductivity. Additives are used to increase ion exchange capacity. The membranes are allowed to stand at a certain temperature in 50 ml of 0.1 N NaOH solution. During this time H + ions are replaced by Na + ions. The membranes are then removed from the NaOH solution and titrated with 0.1 N HCl. The ion exchange capacity is calculated as follows.

$$IEC = \frac{(M_{NaOH} \times V_{NaOH} \times Ts_{NaOH}) - (M_{HCl} \times V_{HCl} \times Ts_{HCl})}{m_{membran}}$$

**M: Molarity, V: Volume spent, Ts: Effect valence.**
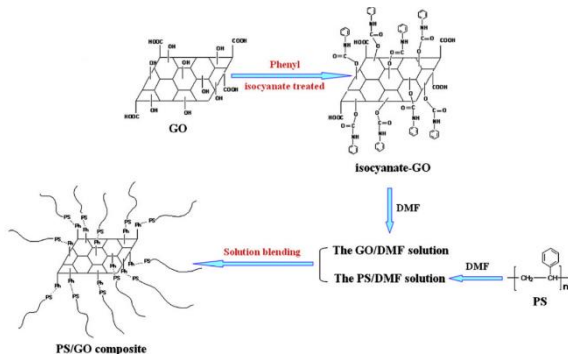


Fig 2.3. Polystyrene graphene oxide formation method
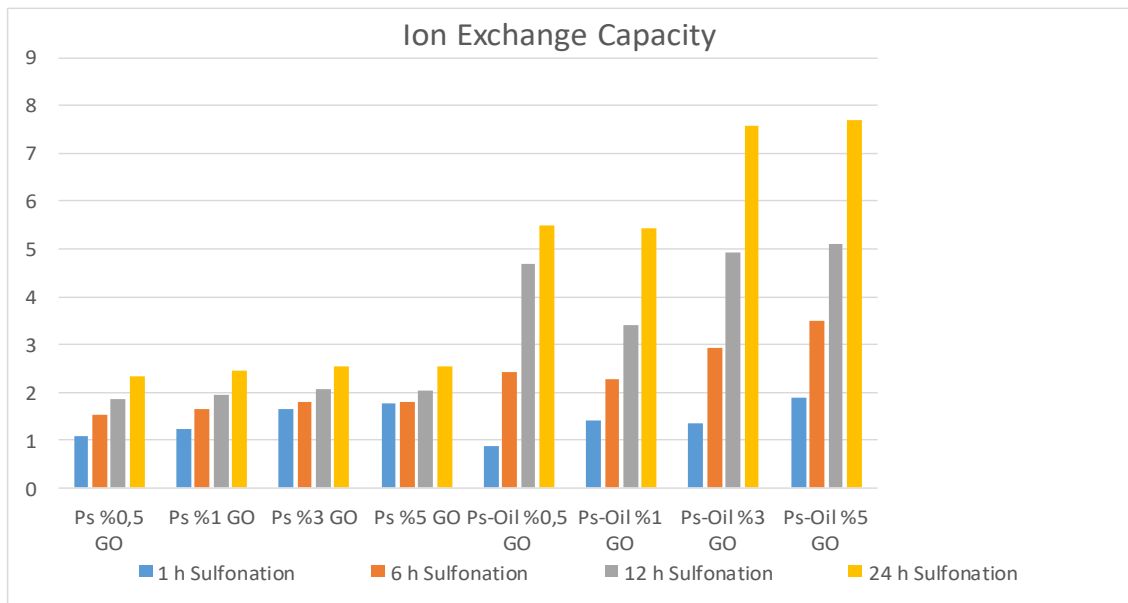


Fig.3.1 Ion Exchange capacity results

## III. FINDINGS

### 3.1 Ion Exchange capacity

As can be seen from Figure 3.1, ion exchange capacity increased as sulphonation time increased according to the literature. The ion exchange capacity of the styrene oil was found to be higher than that of polystyrene. The reason for this is that the graphene oxide is better absorbed in the oil molecules and the styrene oil has a high ion exchange capacity due to the electrical properties of the graphene oxide.[4].

### 4.Result

- As a result of experiments and characterization studies, styrened oil based samples were better than polystyrene based samples.

- The best results were styrene oil, 5% graphene oxide and 24 hours sulfonation.

- As a result of the optimum experiments, the ion exchange capacity was 7.58%.

- According to the results of this cation exchange membrane produced by this study, styrened oil and graphene oxide were found to have a positive effect according to the literature(Ali, McCoy et al. 2017).

- It is seen that styrened oil is much better than polystyrene based membranes prepared for electrical properties that can be used in membrane production.

**REFERENCES**

1. Baker, R.W., *Membrane technology and applications.* Membrane Technology, 2004.
2. Lau, W., et al., *A recent progress in thin film composite membrane: a review.* Desalination, 2012. **287**: p. 190-199.
3. Yang, J., et al., *Preparation, characterization, and supercritical carbon dioxide foaming of polystyrene/graphene oxide composites.* The Journal of Supercritical Fluids, 2011. **56**(2): p. 201-207.
4. Ali, M., et al., *Synthesis and Characterization of Graphene Oxide–Polystyrene Composite Capsules with Aqueous Cargo via a Water–Oil–Water Multiple Emulsion Templating Route.* ACS Applied Materials & Interfaces, 2017. **9**(21): p. 18187-18198.

# Investigation of Effect of Initial Salt Concentration on Acid and Base Production From KCl Solution By Bipolar Membrane Electrodialysis

Said Rajab Abdullahi
Chemical Engineering
Atatürk University
Erzurum, Turkey
saidchemist2@gmail.com

Osman Nuri Ata
Chemical Engineering
Atatürk University
Erzurum, Turkey
oatar@atauni.edu.tr

*Abstract*— **In this study, A bipolar membrane electrodialysis process (BMED) was used to produce potassium hydroxide and hydrochloric acid from an aqueous salt solution consisted of potassium chloride. the effects of the initial potassium chloride concentration on the produced amount of hydrochloric and potasium hydroxide were investigated, The experiments were performed at different initial concentrations : 60g/l, 90g/l, 120g/l . The results shows that highest conversion obtained from initial salt concentrations was a 120 g/l with 82% conversion. The study shows that the initial salt concentration has a significant effect on the process.**

*Keywords—Electrodialysis, Bipolar Membrane, KOH, HCl, KCl*

## I. INTRODUCTION

Electrodialysis (ED) is an electro-membrane separation process in which cations and anions could be separated, concentrated and purified from the aqueous solution using the driving force of an electrical potential gradient [1].

Electrodiaiysis (ED) was invented in the early 1900s as a modification of the dialysis process. Since the 1940s, electrodiaiysis has evolved into a membrane based separation process for separating electrolyte feed solution into a product and a residual feed solution using an electric field and ion exchange membranes[2].

Potassium hydroxide - known as caustic potash, is a widely used industrial chemical. About 700,000 to 800,000 tons is produced annually which is used as a strong base and can be purchased in both liquid and dry forms. . It has universal applications in soaps and detergents, fertilizers, and industrial operations. KOH is commonly used in the food industry due to its excellent detergent and strong antimicrobial properties. KOH is classified as an alkaline cleaning agent. It is produced by the electrolysis of potassium chloride, using membrane or mercury cell technology where in aqueous KCI solution is electrolyzed between metal anodes and flowing mercury cathode. $Cl_2$ is liberated at the anode. Potassium is discharged at the cathode forming potassium amalgam, which flows over to the decomposer where it reacts with water forming KOH solution and $H_2$ gas. However, this process involves the hazardous pollutant, mercury. About 60-90 grams of mercury is lost per tonnc of caustic potash. As stringent pollution control regulations are stipulated, caustic potash industry world over is switching over to the modern membrane cell process.

A bipolar membrane (BM) is a laminar functional composition of membrane that at least consists of a layer ion-exchange structure composed of a cation selective membrane (with negative fixed charges) and an anion selective membrane (with positive fixed charges)[3]. The water splitting behavior of the bipolar membrane was studied first by Frilette 1956[4]. Particularly, electrodialysis with bipolar membrane (EDBM) technology, has acted as a new growth point in electrodialysis industries due to its superiority to conventional water electrolysis in the points [5].

The EDBM consists of a repeated unit BM-CEM-AEM-BM. An electrolyte concentrate solution (MX) is introduced into the "feed compartment", which is limited by the CEM and the AEM, and through direct current applied by the electrodes, water splitting is produced inside the BM. Protons ($H^+$) formed are moved towards the cathode and hydroxyl ions ($OH^-$) towards the anode. At the same time, due to the electric current, cations ($M^+$) are moved towards the cathode (negative), crossing the cationic membranes, but not towards the anionic ones. Then, they are retained in the "basic compartment", which is delimitated between the anionic permeable side of the BM and the CEM. Similarly, anions ($X^-$) are moved towards the anode (positive), crossing the anionic membranes but not towards the cationic ones. They are then retained in the "acid compartment", which is delimitated by an AEM and the cationic permeable side of a BM. Finally, the products are formed: MOH (in the basic compartment) and HX (in the acid compartment). Also, there is a diluted salt solution stream in the feed compartment[6].

In this study, environmentally friendly BMED system was used to synthesize potassium hydroxide. The effects of initial salt concentration on acid-base conversion by the cell were also investigated.

## II. EXPERIMENTAL

The chemicals used in the experiments were obtained from MERCK, including; HCl (hydrochloric acid 37%), KCl (Potassium chloride 99%), KOH (Potassium hydroxide 85%), NaOH (Sodium Hydroxide 99%) phenolphthalein and methyl orange indicator. membranes and spacers used in the Bipolar membrane electrodialysis system were carried out with PCCELL which was manufactured by PCCELL GMbH

Heusweiler, Germany. Used cell and spacer properties are shown in Tables 1 and 2.

Table 1. Anion exchange and cation exchange membrane properties

| Membrane Type | Transfer Number KCl (0.1 / 0.5 N) (a) Acid (0.7/3N) (b) | Resistance ($\Omega cm^2$) | Thickness ($\mu m$) | Ion Form As shipped | Burst strength kg/cm$^2$ |
|---|---|---|---|---|---|
| AEM | >0.95 | ~ 2 | 160-200 | Cl$^-$ | 4 – 5 |
| CEM | >0.95 | ~ 2,5 | 160-200 | NH$^{4+}$ | 4 – 5 |

Table 2. Elektrodialysis cell characteristics

| | |
|---|---|
| Cell type | ED 64 |
| Characteristics | ED/EDBM |
| Effective membrane Area cm$^2$ | 64 |
| Membrane size | 11x11 |
| Over cells mm | 0,5 |
| Proses Length cm | 8 |
| Nominal flow through/Cell L/h | 8 |
| Membrane per unit max pcs | 60 |
| Effective membrane Area/Unit max m$^2$ | 0,38 |
| Anode | Titanium, coating MMO |
| Cathode | Titanium, Coating MMO |

Experiments were carried out according to the following experimental scheme to examine the effect of the initial concentration of the KCl salt on acid and base Production.

Table 3.Expreimental Plane

| Test | İnitial Salt Conc (KCl g/L) | Temperature (°C) | Current density (A/cm$^2$) | Flow rate (L/h) | İnitial Acid and Base Conc (M) |
|---|---|---|---|---|---|
| 1 | 60 | 25 | 0.078125 | 15 | 0,25M |
| 2 | 90 | 25 | 0.078125 | 15 | 0,25M |
| 3 | 120 | 25 | 0.078125 | 15 | 0.25M |

The performance criteria for the bipolar membrane electrodialysis process was calculated as follows:

1. Amount of acid and base produced / concentration:

$$C = \frac{n_t}{V_t}(mol/l)$$

$n_t$: Concentration of acid or base at time t, $V_t$: volume amount of acid or base at time t.

2. Conversion

$$\% \text{ Conversion} = \frac{C_t - C_0}{C_{Top}} x100$$

$C_t$(mol/l): is the concentration of acid or base in sample compartment at time , $C_0$(mol/l): is the initial concentration of acid or base in sample compartment , $C_{Top}$ (mol/l): is the acid and base concentration to be obtained when the salt in the feed solution is completely converted into product .

### III. RESULTS AND DISCUSSION

In this study, production of potassium hydroxide and hydrochloric acid using KCl salt solution in a three-compartment cell with anion exchange, cation exchange and special bipolar membrane type was examined.

Figure 1 shows the graph of salt concentration versus time. In this Figure , it is seen that the salt conductivity in the salt tank for the salt concentration drops to approximately 1 mS / cm, that is, the majority of the ions are transferred from the membranes.

In the experiments, the ions in the salt solution are all transferred, but the transferred ions did not completely converted to acids and bases.

Because when a co-ion transition occured, the base returned to salt and reduced the concentration and the conversion percentage. The same result was also observed at the acid tank.

Table 4. Test Data

| Test No | Acid concentration (mol/l) | Base Concentration (mol/l) | %Salt Conversion (Acid based) | %Salt conversion /Base Based) |
|---|---|---|---|---|
| 1 | 0.84 | 0.85 | 75 | 77 |
| 2 | 1.22 | 1.16 | 77 | 77 |
| 3 | 1.62 | 1.52 | 82 | 82 |
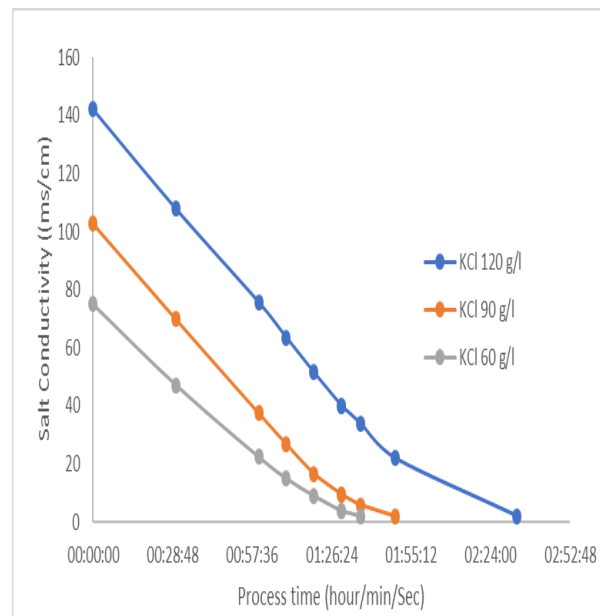


Figure 1. Experiments in different initial salt (KCL) concentrations.
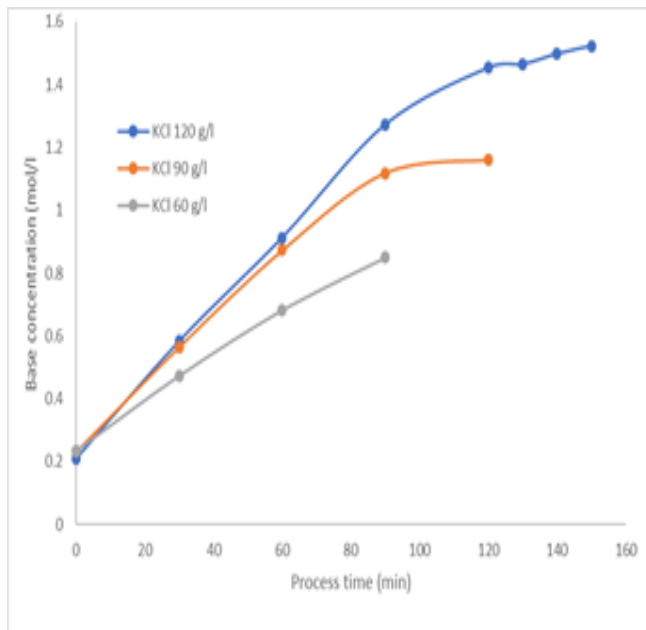
Figure 2. Experiments in different initial salt (KOH)concentrations
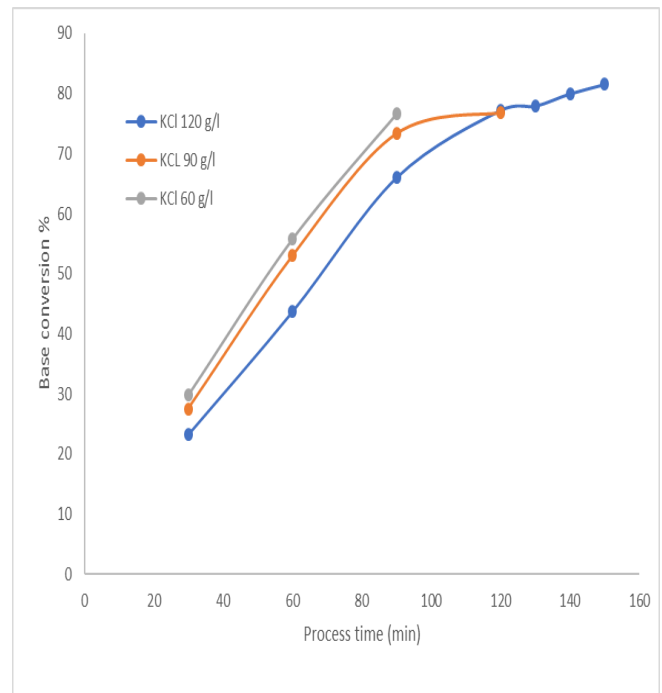


Figure 4. Variation of base-based salt conversion against time at different initial salt concentrations.
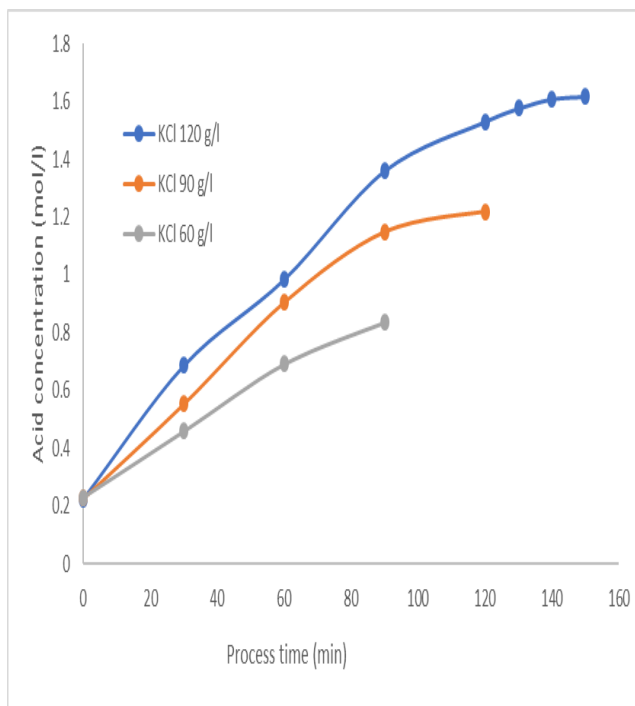


Figure 3. Variation of acid (HCI) concentration at different initial salt concentrations against time.

It has been observed that the concentrations of acid and base from Figures 2 and 3 have increased throughout the process. At the same time, increased initial salt concentration appears to have a positive effect on the products formed (Figure 4 and 5).
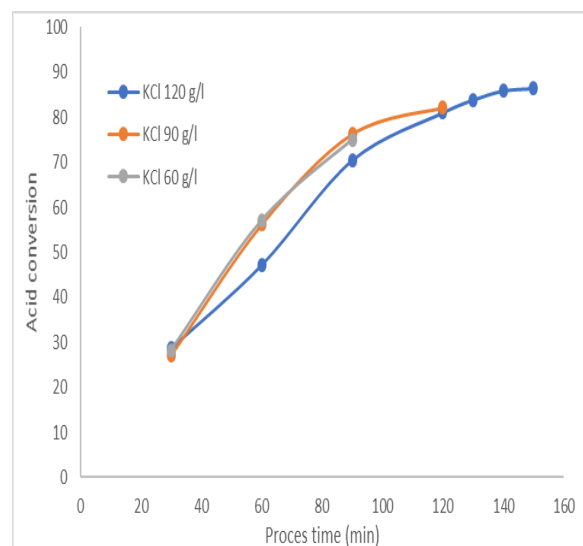


Figure 5. Variation of base-based salt conversion against time at different initial salt concentrations.

## CONCLUSION

In this study three-compartment electrodialysis cell with bipolar membranes consisting of anion-exchange, cation-exchange and a special type of membrane with combination of them were used to develop an environmentally friendly process in which potassium hydroxide, hydrochloric acid and usable water will be produced from the potassium chloride solution and the factors affecting the performance of the production process was examined. It was planned and carried out as an alternative to mercury cell and membrane cell technologies.

It was determined that both the amount of acid and base and the percentage of acid and base conversion increased as the initial salt concentration increased. This study shows that

the initial salt concentration has a significant effect on the process.

## REFERENCESS

[1] S. Bunani, K. Yoshizuka, S. Nishihama, M. Arda, and N. Kabay, "Application of bipolar membrane electrodialysis (BMED) for simultaneous separation and recovery of boron and lithium from aqueous solutions," *Desalination,* vol. 424, pp. 37-44, 2017.

[2] H. Strathmann, "Electrodialysis, a mature technology with a multitude of new applications," *Desalination,* vol. 264, no. 3, pp. 268-288, 2010.

[3] T. Xu, "Development of bipolar membrane-based processes," *Desalination,* vol. 140, no. 3, pp. 247-258, 2001.

[4] V. J. Frilette, "Preparation and characterization of bipolar ion exchange membranes," *The Journal of Physical Chemistry,* vol. 60, no. 4, pp. 435-439, 1956.

[5] Y. Yang, X. Gao, A. Fan, L. Fu, and C. Gao, "An innovative beneficial reuse of seawater concentrate using bipolar membrane electrodialysis," *journal of membrane science,* vol. 449, pp. 119-126, 2014.

[6] A. K. Pabby, S. S. Rizvi, and A. M. S. Requena, *Handbook of membrane separations: chemical, pharmaceutical, food, and biotechnological applications*. CRC press, 2008.

# Smart Parking System: A Case Study of Istanbul

Emre Kuşkapan
Erzurum Technical University, Faculty of Engineering and Architecture, Department of Transportation
Erzurum Technical University, 25050, Erzurum, Turkey
+90 444 5 388 e-mail: emre.kuskapan @erzurum.edu.tr

K.Diler Alemdar
Erzurum Technical University, Faculty of Engineering and Architecture, Department of Transportation
Erzurum Technical University, 25050, Erzurum, Turkey
+90 444 5 388 e-mail: kadir.alemdar @erzurum.edu.tr

Ömer Kaya
Erzurum Technical University, Faculty of Engineering and Architecture, Department of Transportation
Erzurum Technical University, 25050, Erzurum, Turkey
+90 444 5 388 e-mail: omer.kaya @erzurum.edu.tr

M. Yasin Çodur
Erzurum Technical University, Faculty of Engineering and Architecture, Department of Transportation
Erzurum Technical University, 25050, Erzurum, Turkey
+90 444 5 388 e-mail: mycodur @erzurum.edu.tr

*Abstract*— In recent years, together with the growing population in developed and developing countries, the number of vehicles has also increased. This situation causes a serious problem for finding parking spaces especially in metropolitan cities such as Istanbul. Parking lots and garages have been built in various parts of the city to overcome this problem by local municipalities. These areas do not work at full capacity due to the poor management of parking areas. Smart parking management that is an application of intelligent transportation systems can solve this problem. Thanks to information and communication technology evolution, drivers can more efficiently use parking spaces with smart parking services. In this study, the application of smart parking systems in İstanbul city are examined and evaluated for the current situation. The main goal of the study with alternative solutions is to reduce the energy consumption and air pollution caused by the searching parking space in heavy traffic.

*Keywords—Intelligent transportation system, parking policies, traffic congestion*

## I. INTRODUCTION

The world population is increasing day by day. According to the United Nations World Population Forecasts Report; the world population is 7.6 billion [1]. With increasing population, very crowded cities are consist. There are more than 12 million people in the 20 metropolitian cities in the world. An example of these 20 cities are located in Istanbul, Turkey [2]. Istanbul has nearly 15 million people and the population density of Istanbul is 2,892 people / km². In cities where population density is high, the number of vehicles per unit area is much higher. Istanbul has 4 million 91 thousand vehicles registered to traffic [3]. The fact that the number of vehicles is very high and this number increases day by day, this situation has made the studies about parking spaces compulsory. For this purpose, the company called "Ispark" which works in Istanbul Metropolitan Municipality has made parking spaces in various areas of the city. In recent years intelligent transport systems have also been integrated into parking lots. In this way, parking spaces use more efficiently; so time loss and material losses are prevented.

Barhani and Ergün examined of the dimensions and types of car parking problem, it is recommended that various parking management policies be implemented. In general, for Istanbul parking lot sharing, parking-apartment sales departure, strategies such as parking arrangements, financial incentives, application of parking fees, increasing parking fees based on taxation of parking fees and / or parking areas, and various combinations of these strategies have been proposed [4]. Yardım and Demir thought that intelligent transportation systems (ITS) are a collection of systems consisting of transport coordination centers, passengers, transport and transport network arrangements. In order to obtain the benefit and utility expected from ITS in the park management, is an important requirement. Nowadays, it is planned to use those system solutions that are best adapted to Istanbul. With these systems in connection with; mobile phones, credit cards, pre-paid and post-paid cards are on the agenda. About these systems; some solutions or studies are being carried out [5]. Şahin studies analyses the investor behaviors over past development activities of parking garages. It also examines the cost of high technology car parking systems and the profitability of these types of projects. He studies also covers the high technology parking garage costs and the discussion of how this costs can be reduced or what can be the alternative methods. He mentioned the early parking garages and the development theories. Actual development land is taken as a debate subject and development activities is tried to be explained over this land. Alternative parking garage models is also mentioned on this land according to the various feasibility studies. This study includes and discuss parking garage costs, car parking problems and the responsibilities of the government [6]. Another study mentioned on the importance of technological and automation applications in car park management and supervision in parallel with technological developments. This scope of work; to provide inadequate capacity by parking the necessary and appropriate places, to encourage off-road parking, to implement strategies to reduce parking demand, to minimize the negative effects of public transportation technological applications have been explored rather than focusing on known solutions such as making public transport attractive, promoting parks that support transfer centers, disseminating parking areas, and designing and arranging effective parks [7]. According to

Şimsek that transportation affects every human being in the course of his daily activities and it is difficult to conceive a situation where transportation does not play significant role in the life of any individual. Transportation helps to achieve the basic objectives of living in the city which is the functional efficiency of land uses, infrastructure, services and improvement in the quality of life. The urban transportation problems are as a result of the fast growth of the urban areas both in terms of population and area size. This study aims to determine the Park & Ride user profile in Turkey, identify the behavior patterns of the target audience, show the feasibility and benefits of Park& Ride system which is well known and practiced in the world. For this aim, questionnaires were realized in certain localities and Park & Ride areas in Istanbul [8]. In another study; the increase in the number of vehicles in the world is mentioned in terms of parking problems. As urbanization continues, the number of vehicles increases and parking problems increase. Well-managed car parks make it difficult to accommodate an increasing number of vehicles properly, so it is necessary to have an efficient and intelligent parking system. Smart parking systems provide great convenience to vehicle owners. In the work done, a website called "Park Easy" is available for use in the smartphone application; was created with a camera used as a sensor to take photos to show the occupancy rate of the car parks. The driver who requests to park the vehicle allocates the parking area, calculates the parking fee when the car parks. Smart Park Practice, "Park Easy" also provides access to all possible routes to park in any area of the city. Thanks to this work, it real-time predicts the correctness of the vehicle fullness and helps to recognize it correctly [9]. Doğru et al. examined parking problem in historic area of Istanbul, Turkey. The concept of park planning is important for urban planners to design park facilities. In the article, statistical analysis was performed to analyze the park behavior characteristics of each sub-area. Also, a selection model has been developed to achieve the important factors that influence the choice of park policies. In addition, different park management policies have been selected with sub-areas [10]. The purpose of another work in this area is to pay for parking lots, one of the major problems that big cities have experienced. It examines the alternative payment systems used in Istanbul to effectively provide value and parking services produced by using the Istanbul Card. In terms of Istanbul, more reliable methods of intelligent transport systems are mentioned. The results of the "Urban Park Alternative Payment Systems and the Use of Istanbul Card" questionnaire conducted within the scope of the study were also shared in the last part of the research. Within the scope of the questionnaire, comments of 100 drivers in Istanbul province were taken into consideration [11]. According to Kuşkapan et al. the car parks and existing car parks cannot be used at full capacity and the fact that the parking lots are not managed well has not solved this problem and caused the problem to grow. Intelligent Transportation Systems applications are becoming compulsory in order to solve the problems in transportation in the direction of science and technology developments. There are many studies on this subject in various regions of the world. Increasing and improving the work done is possible thanks to ITS. The areas of use of the system used for parking management in

the study are discussed. These systems are mentioned in terms of their working methods and the benefits they provide in urban transportation [12].

When the studies are examined, it is understood that smart parking systems are in the daily life very important. It has been mentioned that smart parking systems, in particular, have indispensable in metropolitan cities. In this study, the methods applied by Ispark in the Istanbul Metropolitan Municipality are tackled. It is mentioned that the applied methods should be developed and applied to all parking lots. In addition, the convenience and benefits provided by smart parking systems are mentioned.

## II. MATERIALS AND METHODS

There is a lot of work to be done in advance to make parking in a district. For example, parking demands are collected from people in that area and vehicle counts are made in that area. The most important factor is to determine the parking claim. While the parking lot request is observed, the areas where the shopping center, hospitals and work places are preferred. Along with all these, it is determined that the intended area for parking is suitable for zoning. If all conditions are met, build parking lot is possible. In the Fig. 1. a map of the parking lot for Istanbul is given and it is seen that the intensity is increasing in the near side of the Istanbul Bosporus.
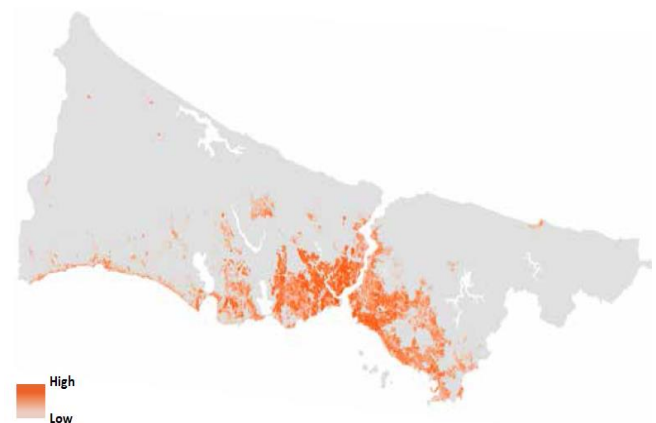


Fig. 1. Car parking demand map in Istanbul [13].

Due to the need for parking, Ispark was established by the Istanbul Metropolitan Municipality in 2005. In this study, the parking lots that made throughout the city were examined. The methods applied in these parking lots have been examined in detail. There are a total of 693 parking lots within the scope of Ispark in Istanbul Metropolitan Municipality as of year 2017. These car parking have 308 outdoor parking, 318 indoor parking, 62 multi-storey car parks and 13 semiautomatic and mechanical lift car park systems. The parking areas are usually located near the coast, which is the area where the population and day-to-day mobility are intense (Fig. 2.). As mentioned before, demand for parking is already concentrated in these regions. In other words, parking lots were built so that demand and supply could be adjusted. One of the reasons for the large number of car parks in these areas is the

presence of ferry piers, which are transfer points for maritime transport.
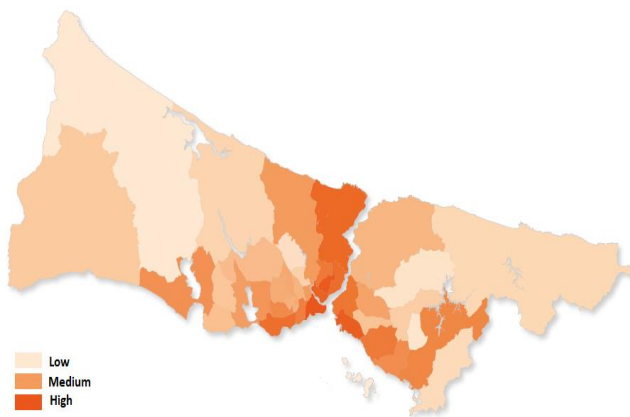


Fig. 2. Istanbul current car parking area density map [14].

The fact that the number of parking lots is so high constitutes a necessity to work within a certain system. Ispark applies various methods for this purpose. Various methods have been applied especially thanks to the enlargement of intelligent transport systems and the developing technology. Another purpose of the construction of parking areas should be a transfer point of the parking area. These transfer points can be a transition point for a different transport. In addition, it may be a transit transportation area belonging to the highway. Many parking lots were built by Ispark for this purpose. In addition, there are many studies conducted in accordance with Park & Ride and Park & Bike (in other words Isbike) models which are applied in many regions around the world.
Park & Bike and Park & Ride systems;

• Decrease traffic congestion
• Maintain air quality by reducing emission intensity
• Alternative to expensive city center car parks
• Reduces transportation costs and avoids economic losses
• Protect the city center from negative effects of transport
• In the city center passenger finds car parking for passenger cars
• Provides protection of the urban environment
• Reduces vehicle entry into the city center and supports pedestrian mobility in this area
• Shorten the travel time
• Reduce traffic intensity at peak hours

These park policies have many positive aspects, but they are not enough to solve all the problems. One of the things that needs to be implemented as a solution is the effective use of intelligent transport systems. Thanks to the developing technology, ITS produce different solutions. As days go by, new ideas emerge and over time these ideas are passed on. In many countries of the world new methods of smart parking systems are being implemented. For this reason, Ispark applies a great deal of studies related to

intelligent transportation systems and contributes to the addition of innovations to these ideas. So, Ispark is a leader in intelligent parking systems in Turkey.

### III. RESULTS AND DISCUSSION

Smart parking systems is an application of intelligent transportation systems. This system gives to people convenience in many matters concerning parking lots in daily life. Smart parking systems, which are used to use parking spaces more efficiently, to prevent waste of time and to save fuel, are actively used in many parts of the world. The methods of intelligent parking systems vary according to the location and can only be appropriate there. The methods of this system may not be able to provide the same benefits wherever they are applied. Therefore, Ispark determines the methods of smart parking systems that are most suitable for its own structure and develops some of them. Some applications are not yet implemented and are in the development stage. Thanks to the efficient use of smart parking systems, parking management is done well. Parking management has various benefits. For instance;

• Cost savings
• Improved service quality
• More flexible plant location and design
• Revenue generation
• Efficient land use

• Demand management and rational growth
• Reduced infrastructure management costs
• Reduced water pollution and global warming impact
• The creation of settlement centers.

In order to better understand the studies and deficiencies; it is necessary to examine and evaluate the methods of intelligent transportation systems in Istanbul.

#### A. Mobile Application, Website and Navigasyon

The smartphone application, which is prepared and uploaded in application markets, determines the parking lots nearest to the point where citizens are located and can easily reach the parking lot with navigation application. In addition, the capacity and price information of the parking lots and the occupancy rates are easily learned through the application. In addition, the Parking Information and Routing Signs located near the parking areas in the central points of the city allow drivers to easily access parking services and track occupancy information.

#### B. Automatic Payment Systems

Automatic payment points located in the parking lots and parking fees can be done with cash, credit card and Istanbul Card. Citizens can make parking payments quickly and easily. In addition, the easiness of payment with Istanbul Card The latest innovation that Ispark has brought into operation is the fast transit system which continues to work on infrastructure and pilot applications will be tried in the near future.

175

## C. Fast and Safe Parking with Hand-Held Terminal

Providing faster and safer service with multifunctional hand terminals, Ispark immediately monitors the entrance and exit rates of parking lots and instantly transfers data to the center.

## D. Easy Parking with Smart Tables

Parking information and routing tables allow drivers to easily access parking services and track occupancy information.

## E. Inspection and Security Services

All of the parking lots are connected to the center via Virtual Private Network (VPN) and Access Point Name (APN) infrastructure to provide safe and uninterrupted communication. In this respect, Ispark which serves 600 locations throughout the city, can be easily managed from a single center. With various remote sensing devices, automatic / mobile inspection of the roadside parks and the personnel there can be done. In addition, indoor and outdoor parking, entrance and it is also possible to make real-time inspections with the cameras and sensors installed in the outputs. Especially in indoor, underground and above ground parking lots, electronic center fire alarm system is a system that should be apply.

## F. Applications for Increasing Capacity

Particularly suitable road edges and to increase the capacity in outdoor parking; semi-automatic car parks and technological parking solutions that do not require lifts and valets that require valet can be used. Another solution used to increase capacity is automatic parking systems. These systems use vehicles computer controlled, electromechanical limited by the transport of systems to the parking lots and the return enabling parking spaces in areas, increasing capacity and productivity software, mechanical, electronic and control systems integrated with parking facilities and parking management systems.

## G. Both the Park and Charge System

In recent years the number of electric vehicles has increased considerably. Thanks to this system, vehicles are both parked and charged.

## H. Solar Powered Lighting

In this system, environmentally friendly signposts that allow drivers to park their vehicles more conveniently and easily are stored with a special energy system that they receive from the sun during the day. After the dark weather, the illuminated signboards provide great convenience for drivers to find parking spaces and contribute to a cleaner environment. In addition, lighting of some parking lots is also provided by this method as a starting point.

Apart from the systems that are applied on smart parking systems, there are also studies that have not yet been implemented. These studies are in the preliminary investigation stage and the applicability is tested. For example, work is being done on the appointment system for parking lots. The purpose of the appointment system is to locate the vehicle before taking it to the parking lot. So the search for a parking lot will be terminated. Another study is the vehicle parking meter system. This work is private

portable parking meter and card. The portable parking meter is housed in the vehicle and provides the activation of a pre-paid smart parking card in the driver. This device is positioned in the vehicle in such a way that the parking control element can be seen from the outside. For example, it's like hanging in a mirror console. After each parking, the charge is stored in the memory of the smart card. Apart from these, thanks to technological developments, many new studies can be taken into consideration when they are taken into consideration by Ispark and deemed appropriate.

## CONCLUSION

The smart parking systems that are being implemented and continue to work by Ispark, which talked about in this study, provide important contributions to the solution process of Istanbul's many urban traffic problems. Parking management and supervision, supported by advanced technology, for sustainable urban transportation in Istanbul has become an inevitable necessity today. For this purpose, it is necessary to work with both private and public car parks. The performance of the system can be measured on a real-time, minute, hourly, daily, weekly, monthly and yearly basis; the quality index for parking lots should be identifiable. It should use controlled system by centralized real-time. It is completely open to information technology, it's an extensible system beside, if necessary manual, it should also allow operations. With all these improvements, efficient use of parking lots and working with smart parking systems will provide positive results in many directions. Because the technology focused parking lots; are facilitating mobility, supports the economy, increase customer satisfaction, contributes to ecology, simplifying management.

## REFERENCES

[1] United Nations World Population Forecasts Report. Available at: https://www.un.org/development/desa/publications/world-population-prospects-the-2017-revision.html, 2017.

[2] World City Populations. Available at: http://worldpopulationreview.com/world-cities/, 2018.

[3] Turkish Statistical Institute. Available at: http://www.tuik.gov.tr/PreIstatistikTablo.do?istab_id=159, 2017.

[4] Barhani, E., and E. Gökmen, Sustainable transportation convenient parking management strategies: Istanbul application, 7th Transportation Congress, Istanbul, 2007.

[5] Yardım, M.S., and D. Abdullah. Istanbul car park management use of intelligent transportation Systems, 8th Transportation Congress, 2009.

[6] Şahin, A. Car park development analysis: Istanbul Merter underground parking host, Master's Thesis, 2009.

[7] Yardım M.S., and D. Abdullah. 2011. Integrated technology in car park management applications: Istanbul sample, Transist 4th Transportation Symposium, 2011.

[8] Şimsek, A.V. Method for continuing parking for special vehicles for transportation by transportable transportation policies from sustainable transportation policies; Istanbul sample, Master's Thesis, 2014.

[9] Abdul Ahad, A., Khan, Z.R., and Ahmad, S.A. Intelligent Parking System, World Journal of Engineering and Technology, 2016. 4:160-167.

[10] Doğru, A., S. Malaitham, M. Okamura, A. Fukuda, and T. Fukuda, Parking management policies based on behavior analysis at Fatih district in Istanbul, Turkey, Transportation Research Procedia, 2017. 25: 5205–5219.

[11] Güngör, A., and Ö. Erdinç. Istanbul card application in the car park systems Ispark examples, Istanbul Commerce University, Journal of Science, 2017. 16(31): 73-84.

[12] Kuşkapan, E., A. Ahmet, A.K. Diler, and C.M.Yasin. Applications of intelligent transportation systems in urban parking management: A case study of Erzurum, 1. International Conference on Intelligent Transportation Systems, Bandırma University, 2018. 279-282.

[13] Istanbul Car Park Main Plan. Available at: http://ispark.istanbul/wpcontent/uploads/2016/10/istanbul-otopark-ana-plani.pdf, 2016.

[14] Istanbul Metropolitan Municipality Activity Report. 2017. Available at: https://www.ibb.istanbul/SitePage/Index/176, 2017.

177

# Measurement of Efficiency of Branches for A Firm with Data Envelopment Analysis

Özlem Çomaklı Sökmen
Continuing Education Application and Research Center
Erzurum Technical University
Erzurum, Turkey
ozlem.sokmen@erzurum.edu.tr

Şeyma Emeç
Industrial Engineering
Ataturk University
Erzurum, Turkey
seyma.yayla@atauni.edu.tr

Mustafa Yılmaz
Industrial Engineering
Ataturk University
Erzurum, Turkey
mustafay@atauni.edu.tr

Gökay Akkaya
Industrial Engineering
Ataturk University
Erzurum, Turkey
gakkaya@atauni.edu.tr

*Abstract*— **Data Envelopment Analysis (DEA) is a linear programming-based technique that aims to measure the relative performance of decision-making units where inputs and outputs measured by multiple and different scales or having different measurement units make comparison difficult. This technique is widely used in areas such as banking, public, health, education, hotel, textile, agriculture. In this study, data envelope analysis technique was used to measure the efficiency of branches in a province by using data belonging to a company with 7 branches operating in the service sector. Afterwards, solution suggestions were made in order to enable ineffective branches to become effective.**

*Keywords— data envelopment analysıs, linear programming, mathematical modeling*

## I. INTRODUCTION

The determination of the performance of the companies is very important for the company management and investors. However, it is not possible to measure with a single criterion the performance of firms. Companies have different functions and objectives that have different input-output combinations.

Performance is a broad concept that includes dimensions such as efficiency, effectiveness and productivity. Effectiveness is a performance dimension that determines the extent to which companies achieve the objectives as a result of their activities. Efficiency shows the extent to which actual performance is closer to standard performance compared to actual performance and standard performance (predetermined). In technical terms, efficiency is defined as "the ratio between the amount of goods and services produced and the inputs used in the production of this quantity of goods and services". The concepts of productivity and efficiency are often used synonymously. Productivity emphasizes a more technical situation. It can also be expressed as obtaining the most output (gain) with minimum resource (cost).

Data Envelopment Analysis (DEA), which is an efficiency measurement technique, is a mathematical programming based technique used to measure the relative efficiency of organizational units with multiple inputs / outputs, doing similar jobs.

In this study, the relative efficiency of the branches of a firm was measured by using Data Envelopment Analysis (DEA). General solution suggestions are presented according to the results of the analysis. In addition, the target values and the potential improvement rates were calculated to enable ineffective branches of firm to become effective.

## II. DATA ENVELOPMENT ANALYSIS

Data Envelopment Analysis (DEA) is a relatively new "data oriented" approach for evaluating the performance of a set of peer entities called Decision Making Units (DMUs) which convert multiple inputs into multiple outputs [13].

> Data envelopment analysis, as a nonparametric method was first proposed by Charnes et al. (1978). It can be used to evaluate the relative efficiency of a set of homogeneous decision-making units.

> In addition, it does not require a specific form of the production function and is especially suitable for multi-input and multi-output scenarios.

> For the effectiveness in identifying the best-practice frontier and ranking the DMUs of DEA method, it has been popularly used in benchmarking and efficiency evaluation of schools, hospitals, bank branches and so on [8].

Table I shows the literatür survey about DEA.

Table I. The literature survey

| Type of Problem | Author/s | Year of Publication |
|---|---|---|
| Tennis Courts | Lewin | 1982 |
| Banking | Gold et. al. | 1982,1983,1985 |
| Hospitals | Bedard et.al. | 1985, 1983, 1984 |
| Sydney Olympic Games | Villa, Lozano | 2002 |
| Water and Sewerage Services | Marques, Monteiro | 2004 |
| Electrical Productivity Benchmarking | Lavado | 2004 |
| Productivity in Graduate Programs | Mello et.al. | 2006 |
| Insurance Companies | Yang | 2005 |
| Thermoelectric Power Plants | Barros, Peypoch | 2008 |
| Hotels in Africa | Barros, Dieke | 2008 |

| Environmental Efficiency in China | Bian, Yang | 2009 |
|---|---|---|
| Railway Station | Mahojeri, Amin | 2010 |
| Supply Chain | Chen, Yan | 2011 |
| Public Transport | Caulfield et.al. | 2013 |
| Human Resource Controlling | Monika et.al. | 2015 |
| Energy Efficiency in Turkey | Çayır Ervural et.al. | 2016 |
| Intermodal Freight Transport Terminals | Cavone et.al. | 2017 |
| Banking | Henriques et.al. | 2018 |

Figure 1 presents the steps of DEA.
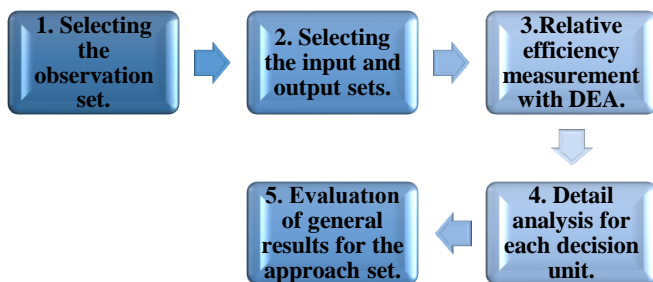


Fig 1. The Steps of DEA

Figure 2 presents the mathematical models of DEA;
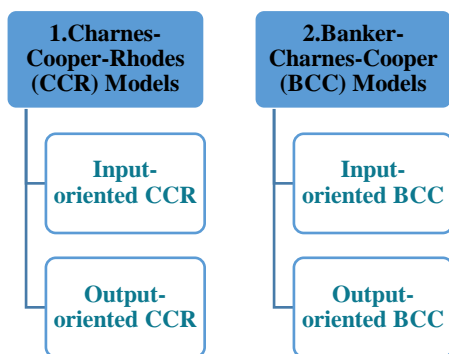


Fig 2. The Mathematical Models of DEA

The CCR Model is based on constant returns to scale while BCC Model is based on variable returns to scale. The CCR and BCC Models were used to calculated technical efficiency (TE) and poor technical efficiency (PTE).

Scale efficiency computes the variation of efficiency scores between CCR and BCC Model and calculated as the ratio of TE to PTE. Generally, the TE always lower than PTE, the value of TE and PTE varies between zero and one; where a value of one indicates the DMU is highly efficient. The values lower than one implies that the DMU is inefficient [20].

Model selection;

- *Why we are using CCR Model?*
  In the literature, CCR Model is used predominantly to measure the efficiency of firms in DEA applications.

- *Why we are using Input- oriented?*
  Since there is little control over the outputs, an input-oriented model has been used in DEA.

*Input-oriented CCR:* Input orientation is defined as the examination of changes in input quantities by keeping output amounts constant. The general of CCR is presented as follows:

$$\text{Min} h_0 = \theta_0 - \varepsilon \left( \sum_{i=1}^{m} s_i^- + \sum_{r=1}^{s} s_i^+ \right)$$

$$\theta_0 X_{i0} - \sum_{j=1}^{n} x_{ij}\lambda_j - s_i^- = 0 \qquad i = 1,\ldots,m$$

$$\sum_{j=1}^{n} y_{rj}\lambda_j - s_r^+ = y r_0 \qquad r = 1,\ldots,s$$

$$\lambda_j, s_i^-, s_r^+ \geq 0 \qquad j = 1,\ldots,n$$

Where;

$y_{rj}$: the $r^{th}$ output of DMU$_j$
$x_{ij}$: the $i^{th}$ input of DMU$_j$
$\lambda_j$: the model variables.
$s_i^-$: the value of slack for the $i^{th}$ input
$s_r^+$: the value of slack for the $r^{th}$ outinputs
$\theta_0^*$: the efficiency in input orient. ($0 \leq \theta_0 \leq 1$)
$\varepsilon$ : a very small number.
If both of the following conditions are met, DMU is efficieny.
1. $\theta_0^* = 1.0$
2. All slack variables ($s_i^-$, $s_r^+$). are zero.

III. APPLICATION

The selected company has seven branches in the pilot region. Figure 3 presents the products sold:
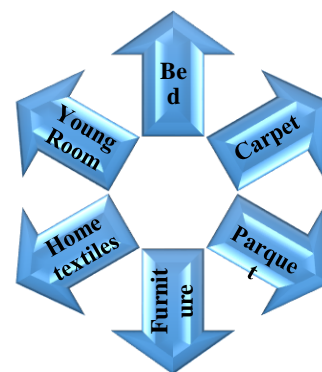


Fig 3. The Mathematical Models of DEA

In order to measure the effectiveness of company branches, input-oriented CCR Model is used. The inputs and outputs for the application are as follows:

**Inputs:** Rent, electricity, water, telephone-ADSL, salary-insurance, the number of personnel, transportation and labor cost.

**Outputs:** Endorsement, the number of incoming customers. Table II shows the information of company. That

information is obtained from the company representative. For example rent of A branch is 1200.

Table II. The Information Of Company

| Branches/ Constrained | A | B | C | D | E | F | G |
|---|---|---|---|---|---|---|---|
| Rent | 1200 | 6000 | 5000 | 4000 | 2000 | 5000 | 2000 |
| Electricity, Water, Telephone-ADSL | 400 | 1200 | 1000 | 800 | 650 | 1000 | 350 |
| Salary-insurance | 2860 | 12390 | 9530 | 953 | 2859 | 2224 | 1906 |
| The number of personnel | 3 | 13 | 10 | 1 | 3 | 8 | 2 |
| Transportation and labor cost. | 4800 | 14400 | 14000 | 12000 | 4800 | 12000 | 10000 |
| The number of incoming customers | 100 | 250 | 100 | 200 | 100 | 100 | 100 |
| Endorsement | 30000 | 90000 | 80000 | 75000 | 30000 | 75000 | 70000 |

A model has been established for each branch to measure their efficiency. The model of A is presented as follows:

### MODELS

### For A Branch;

**Min $h_0 = \theta_0 - \varepsilon(s_1^- + s_2^- + s_3^- + s_4^- + s_5^- + s_6^+ + s_7^+)$**

**Rent:** $1200\theta_0 - 1200\lambda_1 - 6000\lambda_2 - 5000\lambda_3 - 4000\lambda_4 - 2000\lambda_5 - 5000\lambda_6 - 2000\lambda_7 - s_1^- = 0$

**Electricity, water, telephone-adsl:** $400\theta_0 - 400\lambda_1 - 1200\lambda_2 - 1000\lambda_3 - 800\lambda_4 - 650\lambda_5 - 1000\lambda_6 - 350\lambda_7 - s_2^- = 0$

**Salary-insurance :** $2860\theta_0 - 2860\lambda_1 - 12390\lambda_2 - 9530\lambda_3 - 953\lambda_4 - 2859\lambda_5 - 2224\lambda_6 - 1906\lambda_7 - s_3^- = 0$

**The number of personnel:** $3\theta_0 - 3\lambda_1 - 13\lambda_2 - 10\lambda_3 - 1\lambda_4 - 3\lambda_5 - 8\lambda_6 - 2\lambda_7 - s_4^- = 0$

**Transportation and labor cost:** $4800\theta_0 - 4800\lambda_1 - 14400\lambda_2 - 14000\lambda_3 - 12000\lambda_4 - 4800\lambda_5 - 12000\lambda_6 - 10000\lambda_7 - s_5^- = 0$

**The number of incoming customers :** $100\lambda_1 + 250\lambda_2 + 100\lambda_3 + 200\lambda_4 + 100\lambda_5 + 100\lambda_6 + 100\lambda_7 - s_6^+ = 100$

**Endorsement:** $30000\lambda_1 + 90000\lambda_2 + 80000\lambda_3 + 75000\lambda_4 + 30000\lambda_5 + 75000\lambda_6 + 70000\lambda_7 - s_7^+ = 30000$

$s_1^-, s_2^-, s_3^-, s_4^-, s_5^-, s_6^+, s_7^+, \lambda_j \geq 0, \qquad j = 1,2,\ldots,7$

Lingo 17.0 package program is used in model solution. Table III present the results of. If $\theta=1$, brances are efficiency. Table IV shows the dual results of models. These values are used to enable ineffective branches of firm to become effective.

Table III. The Results Of Lingo

| BRANCHES /Constrained | Variables İn Optimal Solution | $\theta$ | Efficient? |
|---|---|---|---|
| A | $\lambda_1 = 1$ | 1.00 | yes |
| B | $\lambda_1 = 1.4$ $\lambda_5 = 0.73$ $\lambda_7 = 0.37$ $s_1' = 1932.5$ $s_3' = 5211.288$ $s_4' = 5.47$ | 0.96 | **no** |
| C | $\lambda_7 = 1.14$ $s_1' = 1795.92$ $s_2' = 416.33$ $s_3' = 5601.31$ $s_4' = 5.78$ $s_6' = 14.29$ | 0.82 | no |
| D | $\lambda_4 = 1$ | 1.00 | yes |
| E | $\lambda_5 = 1$ | 1.00 | yes |
| F | $\lambda_4 = 0.42509$ $\lambda_7 = 1.02$ $s_1' = 22.65$ $s_2' = 504.34$ $s_4' = 5.085$ $s_6' = 11.09$ | 0.89 | no |
| G | $\lambda_7 = 1$ | 1.00 | yes |

Table IV. The Dual Results Of Lingo

| BRANCHES/ Constrained | B | C | F |
|---|---|---|---|
| Rent | 0.00 | 1795.92 | 2265.25 |
| Electricity, Water, Telephone-ADSL | 0.00 | 416.33 | 504.35 |
| Salary-insurance | 5211.29 | 5601.31 | 0.00 |
| The number of personnel | 0.00 | 0.00 | 0.00 |
| Transportation and labor cost. | 5.47 | 5,88 | 5,09 |
| The number of incoming customers | 0.00 | 0.00 | 0.00 |
| Endorsement | 0.00 | 14.29 | 11.09 |

Table V shows the dual results of lingo and the general solution suggestion. For example an improvement of %35 is required fort he rent of branch.

Table V. The Dual Results Of Lingo And The General Solution Suggestion

| Branches | İnputs/outputs | Variables | Actual | CCR Skor | Planned | Improvement |
|---|---|---|---|---|---|---|
| B | Input | Rent | 6000 | 0.96 | 6000 | 0,00% |
| | | Electricity, Water, Telephone | 1200 | | 1200 | 0,00% |
| | | salary-insurance | 12390 | | 7178.71 | 42,10% |
| | | transportation and labor cost. | 14400 | | 14394,53 | 0,04% |
| | | The number of personnel | 13 | | 13 | 0,00% |
| | Output | Endorsement | 90000 | | 90000 | 0,00% |
| | | The number of incoming customers | 250 | | 250 | 0,00% |
| C | Input | Rent | 5000 | 0.82 | 3204,08 | 35,92% |
| | | Electricity, Water, Telephone | 1000 | | 583,67 | 41,63% |
| | | salary-insurance | 9530 | | 3928,69 | 58,78% |
| | | transportation and labor cost. | 14000 | | 13994,12 | 0,04% |
| | | The number of personnel | 10 | | 10 | 0,00% |
| | Output | Endorsement | 80000 | | 79985,71 | 0,02% |
| | | The number of incoming customers | 100 | | 100 | 0,00% |
| F | Input | Rent | 5000 | 0.89 | 2734,75 | 45% |
| | | Electricity, Water, Telephone | 1000 | | 495,65 | 50,44% |
| | | salary-insurance | 2224 | | 2224 | 0,00% |
| | | transportation and labor cost. | 12000 | | 11994,91 | 0,04% |
| | | The number of personnel | 8 | | 8 | 0,00% |
| | Output | Endorsement | 75000 | | 75000 | 0,00% |
| | | The number of incoming customers | 200 | | 188,91 | 5,54% |

The general solutions offered are as follows:

- Training of staff
- Advertising
- Change of price policy
- Promotion and campaign
- Moving to a new place
- Purchase of the store

## IV. CONCLUSION

In this study, input and output variables of the firm are determined, and then the steps of DEA were carried out as described in Section 2. According to analysis; B, C and F branches were found to be ineffective. The solutions are suggested for ineffective branches to become effective.

In this study, CCR model was applied to determine effecieny of braches of company.

The future studies can be applied both CCR and BCC models to compare in order to be tested validity of results. In additionally, DEA can be applied companies which are in the different sectors.

REFERENCES

[1] Barros, C. P., & Dieke, P. U. (2008). Technical efficiency of African hotels. *International Journal of Hospitality Management*, *27*(3), 438-447.

[2] Barros, C. P., & Peypoch, N. (2008). Technical efficiency of thermoelectric power plants. *Energy Economics*, *30*(6), 3118-3127.

[3] Bin, Y. A. N. G. (2009). RESEARCH ON REGIONAL ECO-EFFICIENCY OF CHINA FROM 2000 TO 2006——AN

EMPIRICAL ANALYSIS BASED ON DEA [J]. *Economic Geography*, *7*, 029.

[4] Brockett, P. L., Cooper, W. W., Golden, L. L., Rousseau, J. J., & Wang, Y. (2005). Financial intermediary versus production approach to efficiency of marketing distribution systems and organizational structure of insurance companies. *Journal of Risk and Insurance*, *72*(3), 393-412.

[5] Caulfield, B., Bailey, D., & Mullarkey, S. (2013). Using data envelopment analysis as a public transport project appraisal tool. *Transport Policy*, *29*, 74-85.

[6] Cavone, G., Dotoli, M., Epicoco, N., & Seatzu, C. (2017). Intermodal terminal planning by Petri Nets and Data Envelopment Analysis. *Control Engineering Practice*, *69*, 9-22.

[7] Chen, C., & Yan, H. (2011). Network DEA model for supply chain performance evaluation. *European journal of operational research*, *213*(1), 147-155.

[8] Chen, L., & Jia, G. (2017). Environmental efficiency analysis of China's regional industry: a data envelopment analysis (DEA) based approach. *Journal of Cleaner Production*, *142*, 846-853.

[9] Chen, Y., Wang, J., Zhu, J., Sherman, H. D., & Chou, S. Y. (2017). How the great recession affects performance: a case of Pennsylvania hospitals using DEA. *Annals of Operations Research*, 1-23.

[10] de Mello, J. C. C. S., Gomes, E. G., Meza, L. A., de Mello, M. H. C. S., & de Mello, A. J. R. S. (2006). Engineering post-graduate programmes: A quality and productivity analysis. *Studies in Educational Evaluation*, *32*(2), 136-152.

[11] Ervural, B. C., Ervural, B., & Zaim, S. (2016). Energy efficiency evaluation of provinces in Turkey using data envelopment analysis. *Procedia-Social and Behavioral Sciences*, *235*, 139-148.

[12] Henriques, I. C., Sobreiro, V. A., Kimura, H., & Mariano, E. B. (2018). Efficiency in the brazilian banking system using data envelopment analysis. *Future Business Journal*, *4*(2), 157-178.

[13] Kim, C., Kim, S. W., & Kang, H. J. (2016). Driving Sustainable Competitive Advantage in the Mobile Industry: Evidence from US Wireless Carriers. *Sustainability*, *8*(7), 659.

[14] Kirigia, J. M., Emrouznejad, A., & Sambo, L. G. (2002). Measurement of technical efficiency of public hospitals in Kenya: using data envelopment analysis. *Journal of medical systems*, *26*(1), 39-45.

[15] Lavado, R. F. (2004). Benchmarking the efficiency of Philippines electric cooperatives using stochastic frontier analysis and data envelopment analysis.

[16] Lozano, S., Villa, G., Guerrero, F., & Cortés, P. (2002). Measuring the performance of nations at the Summer Olympics using data envelopment analysis. *Journal of the Operational Research Society*, *53*(5), 501-511.

[17] Marques, R. C., & Monteiro, A. J. (2004). Benchmarking the economic performance of Portuguese water and sewerage services. *Data Envelopment Analysis and Performance Management*, 63.

[18] Mohajeri, N., & Amin, G. R. (2010). Railway station site selection using analytical hierarchy process and data envelopment analysis. *Computers & Industrial Engineering*, *59*(1), 107-114.

[19] O'Neill, L., Rauner, M., Heidenberger, K., & Kraus, M. (2008). A cross-national comparison and taxonomy of DEA-based hospital efficiency studies. *Socio-Economic Planning Sciences*, *42*(3), 158-189.

[20] Paramesh, V., Arunachalam, V., Nikkhah, A., Das, B., & Ghnimi, S. (2018). Optimization of energy consumption and environmental impacts of arecanut production through coupled data envelopment analysis and life cycle assessment. *Journal of Cleaner Production*, *203*, 674-684.

[21] Seiford, L. M. (1997). A bibliography for data envelopment analysis (1978-1996). *Annals of Operations Research*, *73*, 393-438.

# Arc Routing Problem and Solution Approaches in Directed Networks

Ferhat Yuna
Industrial Engineering
Ataturk University
Erzurum, Turkey
ferhat.yuna@atauni.edu.tr

Burak Erkayman
Industrial Engineering
Ataturk University
Erzurum, Turkey
erkayman@atauni.edu.tr

Mustafa Yılmaz
Industrial Engineering
Ataturk University
Erzurum, Turkey
mustafay@atauni.edu.tr

*Routing problems are divided into two classes as node and arc routing problems. The node is involved in the routing of the node of a network under a variety of constraints, while in the differential routing problems network distances are taken into account. In the literature, there are many publications related to node routing problems but there are a limited number of publications related to the arc routing. The aim of the arc routing problem is to have the shortest tour / tours at least once in all the ways in a given network. Problem of arc routing; It can be used in many areas such as distribution of letters, collection of garbage, combating snow and ice on streets and highways, street cleaning activities, scheduling of school services and police patrol vehicles, water and newspaper distribution and determination of effective website usability. Arc routing problems are examined in three parts based on the non-directed, directed and mixed aspects of the network. In this study, a network with all aspects is considered and a heuristic solution approach to this problem is presented. The mathematical model of the problem was firstly created and the optimal results were obtained for the test problems. However, in addition to optimal results in routing problems, it is of great importance to obtain the solution quickly. For this reason, a solution was sought with the nearest neighbor search heuristic, which does not guarantee the optimal solution to the problem addressed, but offers faster solutions and is frequently used in the literature, especially in routing problems. The mathematical model is run in GAMS version 24.2.3 using the Cplex 12.6.0.0 solver and the heuristic is coded in Matlab 2016a. Both solution approaches were tested with different size test problems and the best results and CPU times were reported. According to the results, the heuristic approach achieved optimal results in small sized problems and in the case of large-scale problems, it was found that the results were near-optimal.*

*Keywords— Arc routing, directed network mathematical model, heuristic approach*

# Investigating the Relationship Between Summer Rainfall Variability in Niger and El Niño3 Index

Zakari Seybou Abdourahamane
Department of Civil Engineering
Graduate School of Natural and Applied Sciences, Atatürk
University Erzurum, Turkey
abdourahamane.zakari.seybou14@ogr.atauni.edu.tr

*Abstract*—**An adequate grasp of the teleconnection between the oceanic basins and rainfall fluctuations over a specific region is essential for water related-disasters mitigation and an efficient water resources management. In this study, the influence of El Niño3 sea surface temperature (SST) index on the rainfall variability over Niger is modelled at an interannual to multidecadal timescales by applying a combined wavelet transform and mutual information. The accumulated rainfall amounts of July to September (JAS) at Niamey-Aero and Zinder climate stations, which have the longest rainfall records in the country (from 1905 to 2016), were used as the response variables, whereas El Niño3 SST index was used as the explanatory variable. A cross-wavelet analysis and mutual information-based correlation analyses were first performed using the original series of the JAS rainfall and the Niño3 Index. The analyses were then repeated using the approximation and detail coefficients of the variables obtained through a discrete wavelet transform (DWT). Results revealed that El Niño3 had significantly contributed to the JAS rainfall's decrease during the Sahelian prolonged drought from the early 1960s to the late 1980s. The negative impact of El Niño3 on the JAS rainfall occurred at a timescale varying between 4 years and 7 years at Zinder station and 11 to 15 years at Niamey-Aero station. After the year 2000, the analyses revealed that the link between El Niño3 and the JAS rainfall patterns has become insignificant. Therefore, after the year 2000, the use of El Niño3 as rainfall predictor in forecast models over Niger may appear inappropriate.**

*Keywords—Mutual Information, Niño3, Sahel, Teleconnection, Wavelet Transform*

## I. INTRODUCTION

The rainfall patterns over the West African Sahel are characterized by a strong spatiotemporal variability. On an inter-seasonal timescale, rainfalls over this region are controlled by three principal processes: A South-North flow of moist air associated with the onset of the West African Monsoon (WAM), the seasonal movement of the Inter-Tropical Convergence Zone (ITCZ), and a dry wind (known as Harmattan) from the Sahara Desert. Precipitations in this region are also known to be highly sensitive to climate change and global warming [1].

From the early 1960s to the late 1980s, the Sahel countries have experienced a devastating and unprecedented drought that corresponded to an abrupt change in the rainfall series. In this period, the rainfall deficit was about 180-200 mm per year in comparison to the preceding decade [2]. This is significant for a region where annual precipitations amounts are about 600-800 mm. The decrease in the rainfall amount and the consequent drought are among the most undeniable and major climate changes witnessed by climate experts [3]. The magnitude of the resulting socio-economic consequences has

prompted researchers [4-7] to investigate the teleconnection between Sahelian rainfall variabilities and the remote oceanic-atmospheric activities.

Folland, Palmer [6] have shown for the first time that rainfall pattern in the Sahel region is linked to the global SST anomalies from an inter-annual to decadal time scale with the emphasis of a possible role of the El Niño events on the Sahelian wet and dry conditions. Ward [8] found a significant correlation between the Atlantic SST and Sahelian rainfall series during the wet years of the 1950s and the dry periods of the 1970s and 1980s. Moreover, after investigating the seasonality between African rainfall and the El Niño Southern Oscillation (ENSO), Camberlin, Janicot [9] found a strong correlation between the two phenomena during July-September. They further defined the impact of El Niño Southern Oscillation (ENSO) as a phenomenon that tend to increase North Easterlies by reducing monsoon flow and consequently enhance dry conditions over West Africa near the surface position of the ITCZ in July-September. Giannini, Saravanan [1] attributed the Sahelian persisting drying to warmer-than-normal low-latitude waters around the African continent, concluding that positive trend in the Equatorial Indian Ocean SSTs between East Africa and Indonesia is the probable cause of the Sahelian drought. Mohino, Janicot [10] found that rainfalls over West Africa were statistically interconnected to the long-term warming of SSTs. They further conclude that the global warming and the inter-decadal Pacific Oscillation are responsible of rainfall shortage over the Sahel while a positive Atlantic Multi-Decadal Oscillation (AMO) increases rainfall.

Most of the previous studies used conventional statistical methods such as linear correlation analysis or numerical weather models such as the GCMs. However, the inevitable presence of noise and serial correlation in hydroclimatic data make difficult the use of conventional statistical methods for parameters modelling. On the other hand, numerical models require the use of advanced technologies (weather satellite, radar networks and super computers) that are not always accessible to researchers of developing countries.

Nowadays, one of the most efficient tools in time series analysis and signal processing is wavelet transform (WT). WT was theoretically proposed by Grossmann and Morlet [11], and can perform discontinuity detection, long-term evolution detection and identification of pure frequencies in time series. The main purpose behind the use of WT is the achievement of a comprehensive representation of the localized and temporary phenomena happening in a signal at different time scale [12-14]. It has been successfully used in hydro-climatic time series modelling [15, 16].

Additionally, mutual information is a method that can model the interdependence between two variables regardless to the nature of their relationship [17]. It has a wide application in the field of hydroclimatology [18, 19].

Currently, the link between El Niño effect and Sahelian rainfall pattern has not been investigated in terms of El Niño regions, temporal variability and its evolution over different periods at a station scale. In a climate change context, a clear picture of the teleconnection between rainfall variability over Niger and the El Niño3 phenomenon, which is one of the ENSO regions, can help decision-makers and water users to take sustainable actions for drought and flood preparedness and mitigation.

The objective of this paper is to investigate the relationship between seasonal rainfall variability over Niger and the El Niño3 SST index using a conjunction of DWT, cross-wavelet analysis and Mutual information. A cross-wavelet and a mutual information based-correlation analyses were first performed using the original series of the JAS rainfall series and the El Niño3 index. The analyses were then repeated using the approximation and detail coefficients of the variables obtained through a DWT decomposition.

## II. MATERIALS AND METHODS

### A. Study Area and Data

Niger is a landlocked country in the West Africa located between the longitudes 00° 10' 00'' East and 16° 00' 00'' East, and the latitudes 11° 41' 00'' North and 23° 31' 00'' North. It covers an area of 1 266 000 km$^2$ of which 500 000 km$^2$ are deserts. The population is estimated to 18.5 millions of inhabitants, having one of the highest population growth rate of the world with 3.9% per year [20]. About the 75% of the population lives in rural area and their income is based on rain-fed agriculture and livestock raising. The low pace of growth, inflation and the external and internal imbalances that characterize the economy and recurrent droughts severely affect people's standard of living.

From a climate perspective, the country is divided into four principal zones (Fig. 1). The Northern part is characterized by the hyper dry Sahara climate. The central-south is semi-arid with a Sahara-Sahelian climate, the South is typically Sahelian and a small portion of the Southern-West is dominated by the humid Soudanian climate. Rainfall are season-dependent and are linked to the movement of the ITCZ. Therefore, the rainfall amount increases from North to South about 150 to 850 mm, whereas the annual average temperature increases from South to North between 9 °C and 45 °C depending on the season. The rainy season is short (4 months) and 80% of the rain is recorded in July-September. The river Niger is the only permanent watercourse of the country. The hydrographic network is characterized by an important network of watersheds and several seasonal watercourses.

Rainfall in the country are recorded with a network of climate stations and rain gauges monitored by the national meteorological office [21]. Also, institutions such as the Permanent Interstates Committee for Drought Control in the Sahel (Comité Inter-Etats de Lutte contre la Sécheresse au Sahel, CILSS) possesses their own rain gauges over the country.
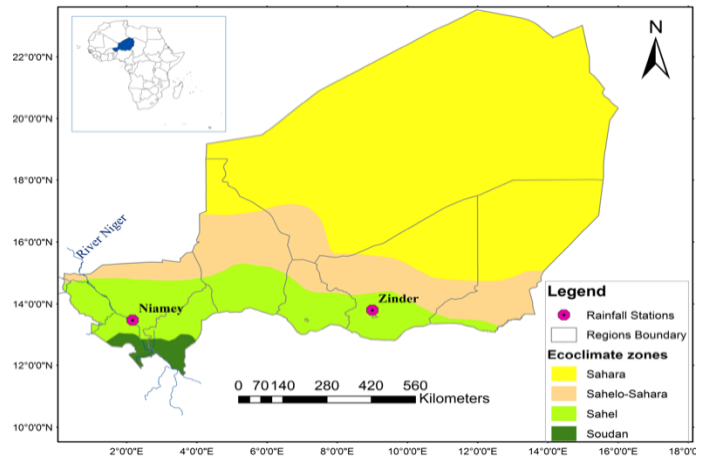


Figure 1. Niger country map and location of the climate stations

The climate stations of Niamey-Aero and Zinder (Fig. 1) are chosen in this study as they possess the longest rainfall record over the country, since 1905.

The Pacific Ocean basin is the world largest and deepest oceanic basin. Variations in the physical parameters of this basin has significant influence on global and regional climate of many areas of the world. The El Niño phenomenon is defined as an increase in the sea surface temperature (SST) of the tropical Pacific Ocean, from the International Dateline to the west coast of South America, generating changes in the local and regional ecology. To simplify data sampling of SSTs, the El Niño phenomenon has been divided into five regions which are the El Niño1, Niño2, Niño3, Niño4, and Niño3.4 (Fig. 2). Niño1 is the area defined by 80º-90ºW and 5º-10ºS, Niño2 is delineated by the longitudes 80º-90ºW and latitudes 0º-5ºS, Niño3 is between 90º-150ºW and 5ºN-5ºS, Niño4 is the area between 150ºW-160ºE and 5ºN-5ºS and Niño3.4 happens between 120Wº-170ºW and 5ºN-5ºS [22].

The Niño3 series used in this study were download from the National Oceanic and Atmospheric Administration [23].
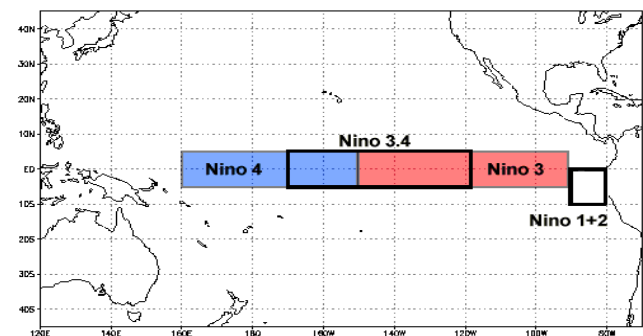


Figure 2. El Niño regions - source National Centre for Environmental Information
(https://www.ncdc.noaa.gov/teleconnections/enso/indicators/sst.php)

### B. Discrete Wavelet Transform

Discrete wavelet transform (DWT) is a tool that can decompose and reconstruct signal (or time series) in wavelet coefficients at different time scale. DWT eliminates redundant

information in the wavelet coefficients for detecting the true processes contained in the signal [24]. The decomposition is carried out throughout an iterative process using a series of low-pass and high-pass filters at different levels (Fig. 3). The form of the wavelet coefficients $W_\psi(a,b)$ with dilation step of 2 and location variable of 1 is given as follows:

$$W_\psi(a,b) = \frac{1}{(2)^{\frac{a}{2}}} \sum_{t=0}^{N-1} X_t\, \Psi\left(\frac{t}{2^a} - b\right) \qquad (1)$$

In this equation, $\Psi$ stands for the mother wavelet; $a$ and $b$ are integers representing the amount of dilation (scale factor) and translation of the wavelet, respectively; $Xt$ is the time series; and, $t$ is the discrete time.

The rainfall amount of July-September at Niamey-Aero and Zinder stations as well as the El Niño3 series were decomposed into approximation and detail coefficients at different levels using different types of wavelet families (Daubechies, Haar, Morlet, Symlets and others).

A first step of the decomposition process produces two sets of coefficients from the original series (S): approximation coefficients (A1) and detail coefficients (D1) having the same length with the original series. These coefficients are obtained by convolving S with the low-pass filter for A1, and with the high-pass filter for D1, followed by dyadic downsampling. In the next step, the A1 are split in two part following the same scheme in step 1 by replacing S by A1 and producing A2 and D2. The same process is repeated until the desired decomposition level is reached (Fig. 3). The decomposition was carried out in MATLAB_R2016b.

of the cross-wavelet power with background power $P_k^X$ and $P_k^Y$ is defined as [25]:

$$D\left(\frac{\left|W_n^X(s)W_n^{Y^*}(s)\right|}{\sigma_X\sigma_Y} < p\right) = \frac{Z_\nu(p)}{\nu}\sqrt{P_k^X P_k^Y} \qquad (3)$$

In equation 3, $Z_\nu(p)$ is the confidence level associated with a probability $p$; $\sigma_X$ and $\sigma_Y$ are the standard deviation of the series $X$ and $Y$; and $\nu$ is the degree of freedom. For $\nu = 1$ (real wavelets) $Z1$ (95%) = 2.182, while for $\nu = 2$ (complex wavelets) $Z2$ (95%) = 3.999.

*D. Mutual information*

Mutual information (MI) estimates the relationship between two random variables $X$ and $Y$. It measures the information shared by $X$ and $Y$ through the similarity between their joint probability $p(x, y)$ and the product of their marginal probabilities $p(x)$ and $p(y)$. MI is mathematically expressed as [18]:

$$I(X;Y) = \iint p(x_i,y_i) ln\left[\frac{p(x_i,y_i)}{p(x_i)p(y_i)}\right] dxdy \qquad (4)$$

In this equation, $(x_i, y_i)$ is the i-th bivariate sample data pair; $N$ is the sample size, $p(x_i, y_i)$ is the joint probability mass function of $X$ and $Y$; and $f_X(x_i)$ and $f_Y(y_i)$ are their marginal probability mass functions, respectively. The *ln* represents the natural logarithm.

The MI can only have a value greater or equal to zero, since $p(x_i, y_i)$ is greater than $p(x_i)p(y_i)$. An $I(X;Y)$ equal to zero occurs when $p_{XY}(x,y) = p_X(x)p_Y(y)$; in such a case,



Figure 2. Iterative decomposition process of DWT for the rainfall series

*C. Cross-wavelet analysis*

In general, the wavelet cross spectrum of two time series $X$ and $Y$ having their wavelet transform $W_n^X(s)$ and $W_n^Y(s)$, respectively, is defined as [25]:

$$W_n^{XY}(s) = W_n^X(s)W_n^{Y^*}(s) \qquad (2)$$

In this Equation, $W_n^{Y^*}(s)$ is the complex conjugate of $W_n^Y(s)$.

The cross-wavelet power is the absolute value of the wavelet cross spectrum $|W_n^{XY}(s)|$. The theoretical distribution

$X$ and $Y$ are two independent variables. The MI of two dependent variables is greater than zero.

The MI of two discrete variables can be approximated using the probability density functions (PDFs) as follows:

$$I(X;Y) \approx \frac{1}{N}\sum_{i=1}^{N} ln\left[\frac{f_{X,Y}(x_i,y_i)}{f_X(x_i)f_Y(y_i)}\right] \qquad (5)$$

The MI analysis was carried out using the Kernel density estimator for the density approximation. The analysis was performed by considering the period 1905-2016 and the three different episodes of the Sahelian climatology, mainly the pre-drought (1905-1960), the drought (1961-1989) and the post-drought (1990-2016) periods.

186

## III. RESULTS

### A. Discrete Wavelet Transform

The DWT analysis was performed using different wavelet families at different decomposition levels. The approximation and details coefficients that have the highest correlation with the original series were retained for the cross-wavelet and MI analyses. Hence, the Morlet wavelet at one level decomposition resulted the most suitable wavelet family and decomposition level, respectively. The DWT coefficients of the rainfall series are shown in Fig. 3 and Fig. 4 at each station.
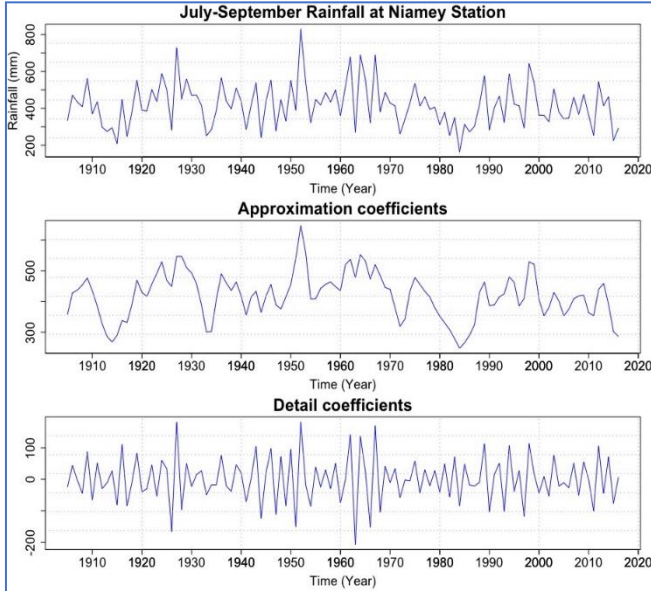


Figure 4. DWT coefficients of the JAS Rainfall at Niamey-Aero Station
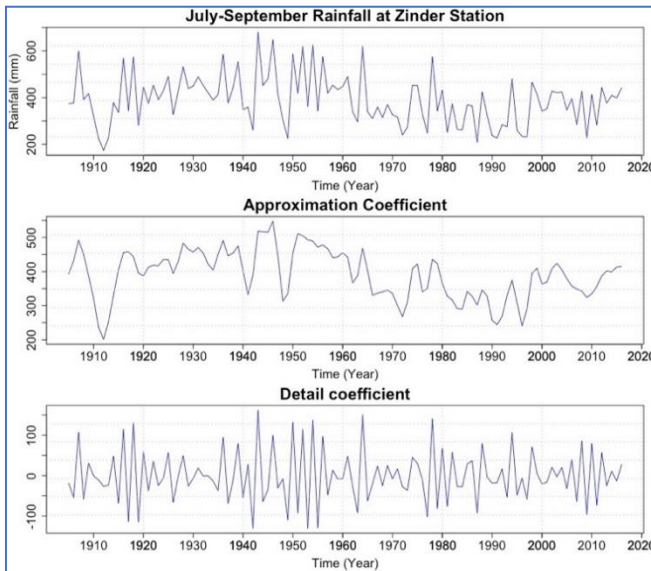


Figure 5. DWT coefficients of the JAS Rainfall at Zinder Station

### B. Cross-Wavelet and mutual information analyses

The cross-wavelet spectrums of the JAS rainfall amount at Niamey-Aero station and the El Niño3 SST index lagged from 1 to lag 6-month respect to the JAS rainfall are presented in Fig. 6(a) to Fig. 6(f). The results of the same analysis are shown in the Fig. 7(a) to Fig. 7(f) at Zinder station. The cross-wavelet analysis using the approximation

and details coefficients are presented in Fig. 8 and Fig. 9 at each station.

In these figures, the thick contour represents the 1% significance level against red noise and the arrows inside this thick contour indicate the phase oscillation. The cone of influence is delineated with white colour.
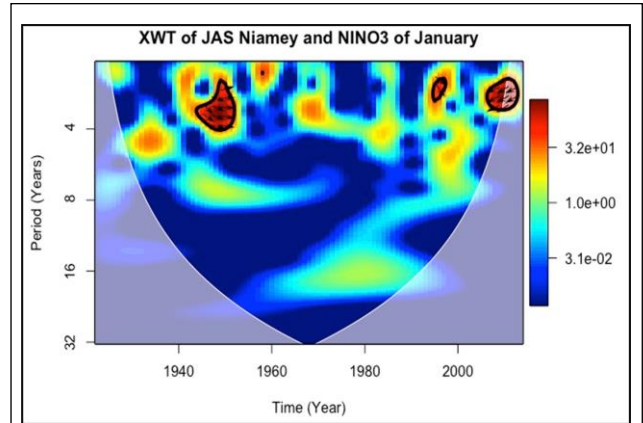


Fig. 6 (a)
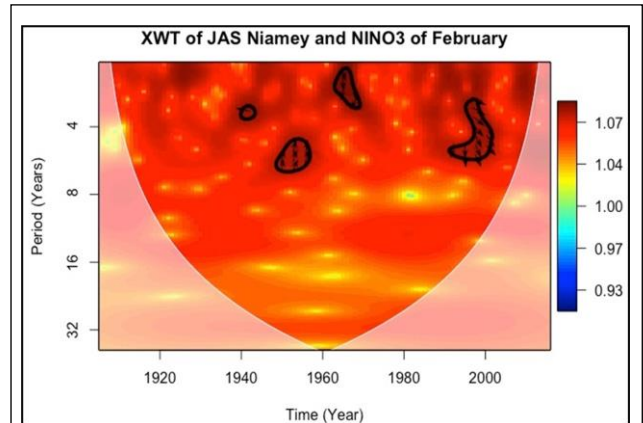


Fig. 6 (b)

The computed MI between the original rainfall series and the Niño3 index are exhibited in Table 3, whereas the MI calculated from the approximation coefficients are shown in Table 4 for the period 1905-2016, and in Table 5, Table 6 and Table 7 for the periods 1905-1960, 1961-1989, 1990-2016, respectively.
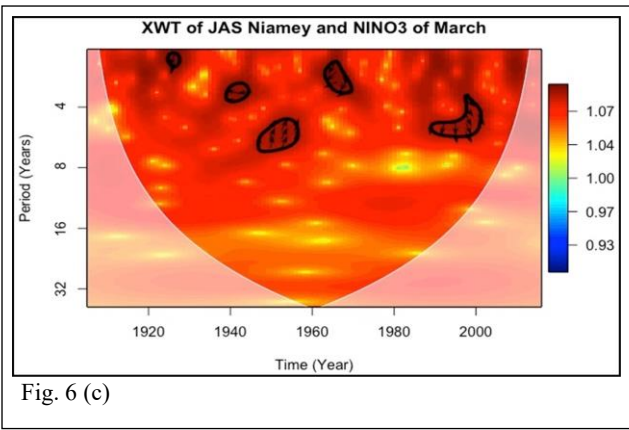
Fig. 6 (c)
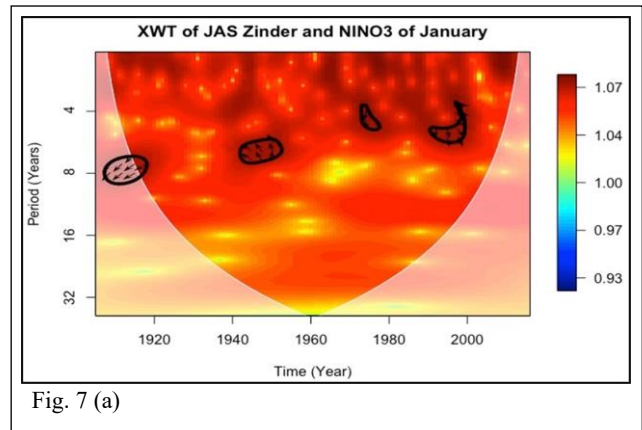


Fig. 6 (e)
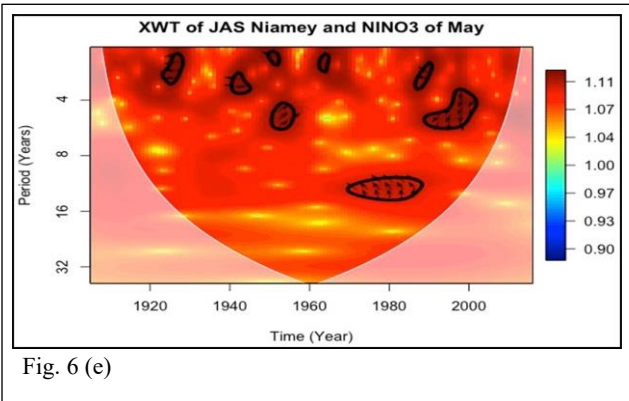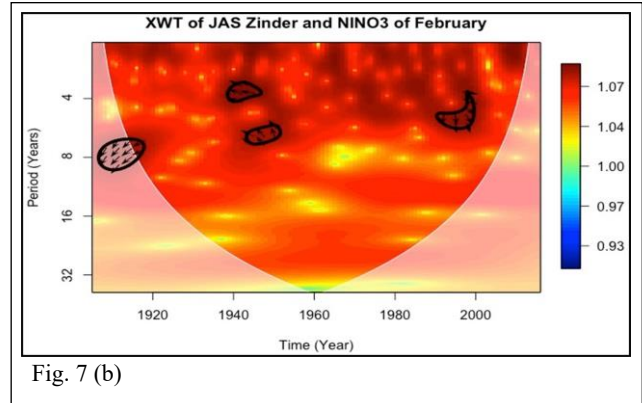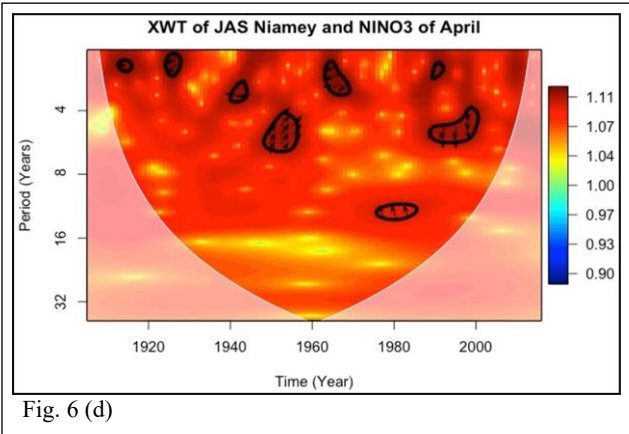


Fig. 6 (d)
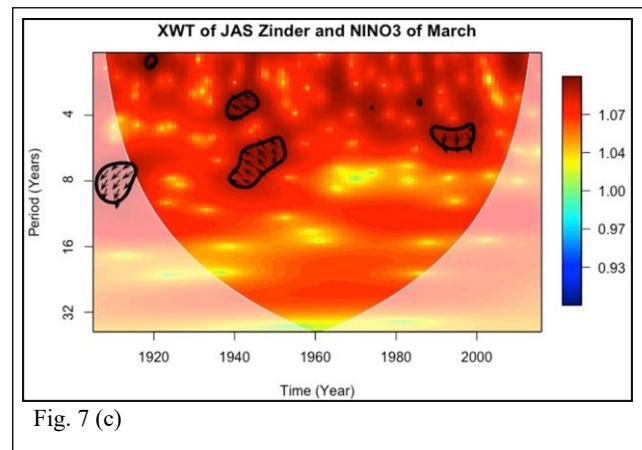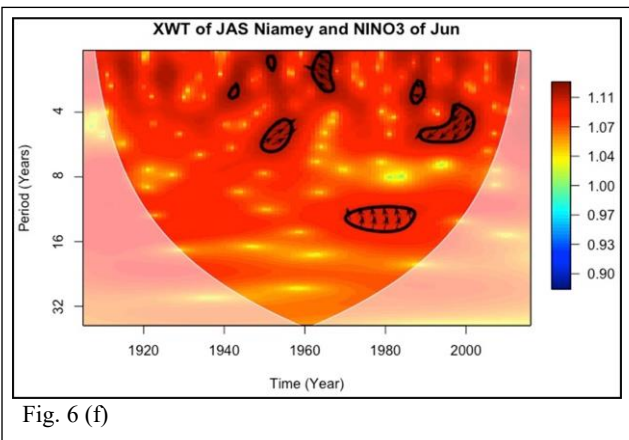


Fig. 6 (f)
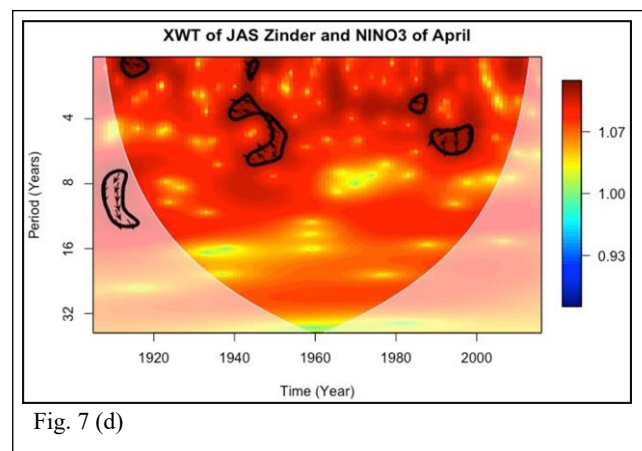
Figure 3. Cross-wavelet spectrum Between Seasonal rainfall of Niamey and El Niño3



Fig. 7 (a)



Fig. 7 (b)



Fig. 7 (c)



Fig. 7 (d)
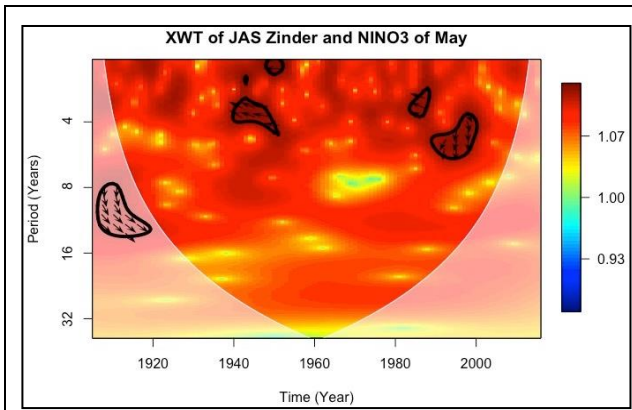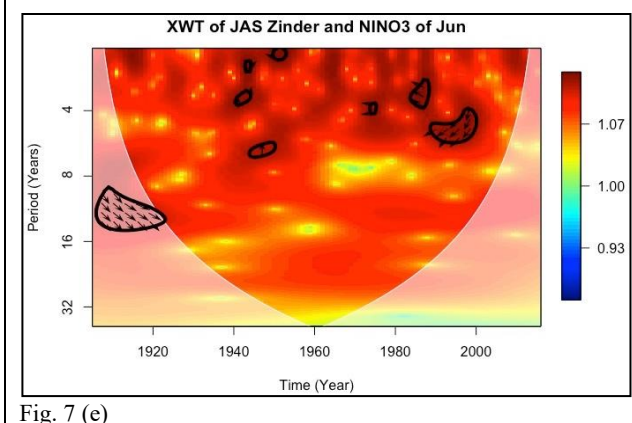
Fig. 7 (e)



Fig. 7 (e)

Figure 7. Cross-wavelet spectrum Between Seasonal rainfall of
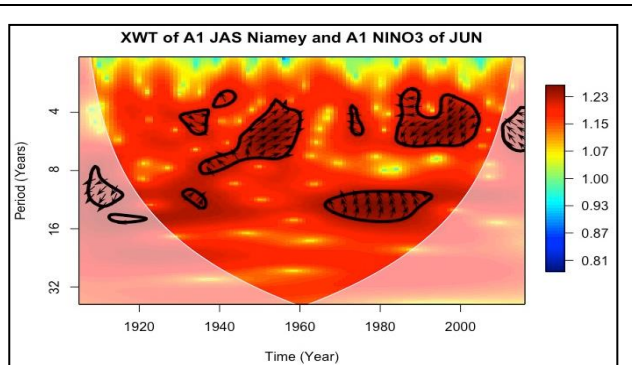


Fig. 8 (a) Cross wavelet power spectrum of the approximation coefficients at Niamey-Aero station
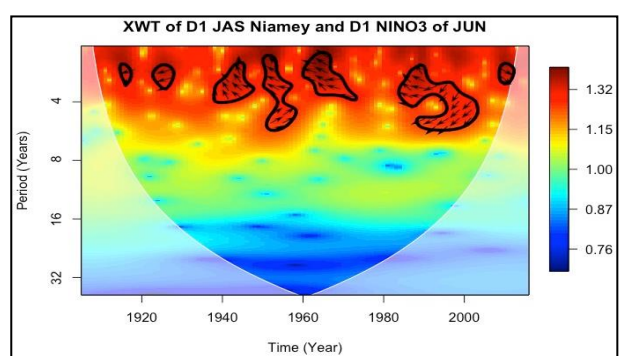


Fig. 8 (b) Cross wavelet power spectrum of the detail coefficients at Niamey-Aero station
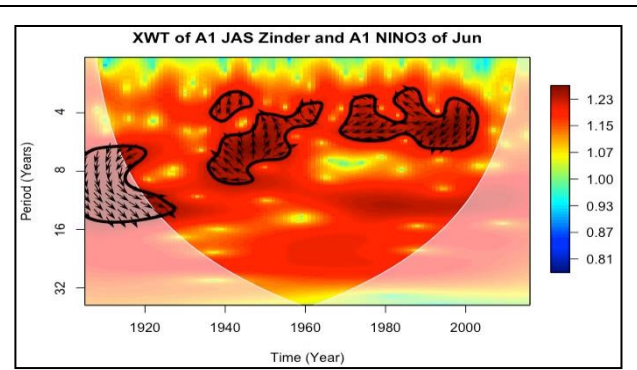


Fig. 9 (a) Cross wavelet power spectrum of the approximation coefficients at Zinder station
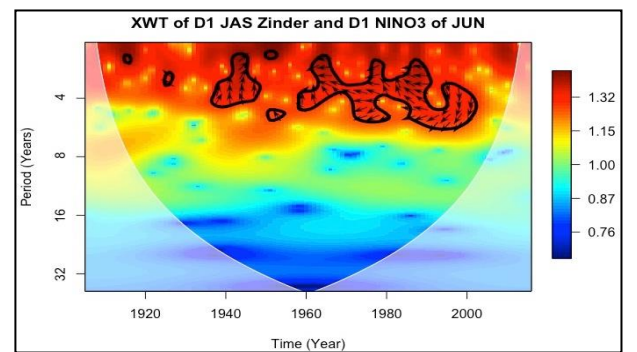


Fig. 9 (b) Cross wavelet power spectrum of the detail coefficients at Zinder station

Table 1. MI of the original series

| Climate Station | Mutual Information: $I(Niño3; JAS)$ | |
|---|---|---|
| | (nats) | (bits) |
| Niamey-Aero | 0.043 | 0.062 |
| Zinder | 0.034 | 0.049 |

Table 2. MI during 1905-2016 of the approximation coefficients

| Climate Station | Mutual Information: $I(Niño3; JAS)$ | |
|---|---|---|
| | (nats) | (bits) |
| Niamey-Aero | 0.269 | 0.387 |
| Zinder | 0.110 | 0.158 |

Table 3. MI during the pre-drought (1905-1960) period of the approximation coefficients

| Climate Station | Mutual Information: I(Niño3; JAS) | |
|---|---|---|
| | (nats) | (bits) |
| Niamey-Aero | 0.031 | 0.045 |
| Zinder | 0.018 | 0.026 |

Table 4. MI during drought period (1961-1989) of the approximation coefficients

| Climate Station | Mutual Information: I(Niño3; JAS) | |
|---|---|---|
| | (nats) | (bits) |
| Niamey-Aero | 0.37 | 0.533 |
| Zinder | 0.206 | 0.297 |

Table 5. MI during drought post-period (1990-2016) of the approximation coefficients

| Climate Station | Mutual Information: I(Niño3; JAS) | |
|---|---|---|
| | (nats) | (bits) |
| Niamey-Aero | 0.003 | 0.004 |
| Zinder | 0.002 | 0.003 |

## IV. DISCUSSIONS

In this study, the influence of El Niño3 SST index on the seasonal rainfall variability at two climate stations of Niger was investigated. From the cross-wavelet analysis using the original series, the El Niño3 index of Jun has the most significant influence on the JAS rainfall series at the two station. As it can be seen in Fig. 6(f), between approximately 1950 and 1960, a significant common power existed between the JAS rainfall of Niamey and El Niño3 in a quasi-phase oscillation at a time scale of 4 to 6 years. During the period 1970-1990, the significant common power had a time scale of 11 to 15 years with a clear leading of the seasonal rainfall on the El Niño3 and an anti-phase oscillation. From 1990 to 2000, a 4 to 6 years timescale significant common power can be observed between the two variables. In this period, a tendency to an anti-phase oscillation has occurred.

As for Zinder station, the cross-wavelet power spectrums of the original series presented in Fig. 7(a) to Fig. 7(f) reveals the presence of two periods during which the JAS rainfall and the El Niño3 of Jun (Fig. 7(f)) displayed significant common power. From 1940 to 1950 the two variables oscillated at a scale of 4 to 8 years and during the period 1990-2000 at a scale of 4 to 6 years. However, due to the low contrast of the 1% significance level contour, it is difficult to make inferences about the importance of this link. Therefore, the approximation and detail coefficients were used to repeat the cross-wavelet analysis at both stations.

The computed mutual information using the original series, presented in Table 3, does not show a significant connection between the JAS rainfall at both stations and the El Niño3 indices.

The cross-wavelet analysis using the DWT coefficients displays a clear picture of the wavelet spectrum between the JAS rainfall and the El Niño3.

The power spectrum obtained from the cross-wavelet analysis between the approximation coefficients of the seasonal rainfall and the El Niño3 of Jun appeared as an amplification of the cross-wavelet performed on the original series. New significant levels against red noise were displayed and the ones from the original data analysis appeared with more details. As we can appreciate in Fig. 8(a), the same three periods of significant common power appeared at Niamey station by maintaining the same phase relationship. In Fig. 8(a), these periods can be better described as follows: from 1940 to 1960 the phase of the common power varied from anti-phase to phase oscillation with a slight leading of the JAS over the El Niño3 of Jun at a scale ranging from 4 to 6 years. Between the late 1960s to the late 1980s the oscillation had shifted from phase to anti-phase with a leading of the JAS at a scale of 11 to 15 years. Finally, from 1985 to 2005 an anti-phase oscillation occurred between the variables at a timescale of 4 to 6 years.

At Zinder station, the same remark can be done for the cross-wavelet analysis using the approximation coefficients. The spectrum in Fig. 9(a) displays two main periods of common oscillations between the seasonal rainfall of Zinder and the El Niño3 of Jun. Between 1935 and 1965, both variables displayed a common power with a phase oscillation varying from anti-phase to a leading of the seasonal rainfall at a time scale of 4 to 12 years. During the period 1970-2000, the timescale of the common power was 4

to 7 years with an anti-phase oscillation, from 1970 to 1985 and a leading of the El Niño3 between 1985 and 2000.

As for the cross-wavelet using the detail coefficients, the wavelet power spectrum is presented in Fig. 8(b) for Niamey station and in Fig. 9(b) for Zinder station. Here, only the significant common power at 4 year-timescale and less were detected. The cross-wavelet power spectrum is completely different from the one obtained from the original series at the low frequency level. The cross-wavelet analysis using the detail coefficients are likely to detect only significant common power at high frequency level.

Furthermore, the MI analysis using the approximation coefficients clearly shows the intensity of the El Niño3 effect on the JAS rainfall at the considered stations. As can be seen in from Table 5 to Table 7, the influence of the El Niño3 was particularly significant over the period 1961-1989, confirming hence the results from the cross-wavelet analysis. The El Niño3 phenomenon was undoubtedly one the of the driving forces of the Sahelian prolonged drought.

The connection between the ENSO and the mean rainfall over the Sahel has been reported in many literature [1, 6, 9, 26].

Nowadays, Niño3 is still being used as predictor in many rainfall forecast model over the Sahel. It is one of the main predictor used by the National Meteorological Service of Niger to forecast seasonal rainfall over the country ([21]). After the 2000s, the use of El Niño3 index in rainfall forecast models over Niger as input may appear inappropriate.

## V. CONCLUSIONS

The link between seasonal rainfall over Niger and El Niño3 SST index was investigated using wavelet transform and Mutual information analyses. The investigation showed that the El Niño3 index had contributed to the rainfall decrease over the country during the Sahelian prolonged drought. After the year 2000, the influence of El Niño3 on the study area has become insignificant; therefore, the use of EL Niño3 as a rainfall predictor in forecast models over Niger may result inappropriate.

Additionally, the use of the level-1 approximation coefficients for the cross-wavelet and the mutual information analyses provide a better picture mapping of the link between the rainfall variability and the El Niño3 index. The cross-wavelet analysis using the level-1 details coefficients detects only the common power between the variables at the low periods (high frequency levels).

The method used in the present work can be applied to assess the influence of different oceanic-atmospheric dynamics on the rainfall variability over other regions with different climate conditions. The use of and appropriate wavelet family for the wavelet analysis and a suitable probability distribution for the mutual information computation determine the accuracy the proposed method.

REFERENCES

1. Giannini, A., R. Saravanan, and P. Chang, *Oceanic forcing of Sahel rainfall on interannual to interdecadal time scales.* Science, 2003. **302**: p. 1027-1030.

2. Le Barbe, L., T. Lebel, and D. Tapsoba, *Rainfall variability in West Africa during the years 1950-90.* Journal of Climate, 2002. **15**: p. 187-202.

3. Dai, A., Lamb P. J., Trenberth, K. E., Hulme M., Jones, P. D., Xiee, P., *THE RECENT SAHEL DROUGHT IS REAL.* INTERNATIONAL JOURNAL OF CLIMATOLOGY, 2004. **24**: p. 1323–1331.

4. Folland, C., et al., *Prediction of seasonal rainfall in the Sahel region using empirical and dynamical methods.* Journal of Forecasting, 1991. **10**: p. 21-56.

5. Dieppois, B., et al., *Low-frequency variability and zonal contrast in Sahel rainfall and Atlantic sea surface temperature teleconnections during the last century.* Theoretical and Applied Climatology, 2015. **121**: p. 139-155.

6. Folland, C.K., T.N. Palmer, and D.E. Parker, *Sahel rainfall and worldwide sea temperatures, 1901-85.* Nature, 1986. **320**: p. 602-607.

7. Giannini, B.A., Verstraete M., Michel M., *A climate model-based review of drought in the Sahel: Desertification, the re-greening and climate change.* Global and Planetary Change, 2008. **64**(3–4): p. 119-128.

8. Ward, M.N., *PROVISIONALLY CORRECTED SURFACE WIND DATA, WORLDWIDE OCEAN ATMOSPHERE SURFACE FIELDS, AND SAHELIAN RAINFALL VARIABILITY.* Journal of Climate, 1992. **5**: p. 454-475.

9. Camberlin, P., S. Janicot, and I. Poccard, *Seasonality and atmospheric dynamics of the teleconnection between African rainfall and tropical sea-surface temperature: Atlantic vs. ENSO.* International Journal of Climatology, 2001. **21**: p. 973-1005.

10. Mohino, E., S. Janicot, and J. Bader, *Sahel rainfall and decadal to multi-decadal sea surface temperature variability.* Climate Dynamics, 2011. **37**: p. 419-440.

11. Grossmann, A. and J. Morlet, *Decomposition of Hardy function into square integrable wavelets of constant shape.* J. Math. Anal., 1984. **5**: p. 723-736.

12. Sang, Y.F., *A review on the applications of wavelet transform in hydrology time series analysis.* Atmospheric Research, 2013. **122**: p. 8-15.

13. Labat, D., *Wavelet analysis of the annual discharge records of the world's largest rivers.* Advances in Water Resources, 2008. **31**(1): p. 109-117.

14. Wang, H.R., et al., *Problems in wavelet analysis of hydrologic series and some suggestions on improvement.* Progress in Natural Science, 2007. **17**(1): p. 80-86.

15. Ozger, M., A.K. Mishra, and V.P. Singh, *Low frequency drought variability associated with climate indices.* Journal of Hydrology, 2009. **364**(1-2): p. 152-162.

16. Dash, M.K., et al., *Variability in the ENSO-induced southern hemispheric circulation and Antarctic sea ice extent.* INTERNATIONAL JOURNAL OF CLIMATOLOGY, 2013. **33**: p. 778-783.

17. Babel, M.S., G.B. Badgujar, and V.R. Shinde, *Using the mutual information technique to select explanatory variables in artificial neural networks for rainfall forecasting.* Meteorological Applications, 2015. **22**(3): p. 610-616.

18. Sharma, A., *Seasonal to interannual rainfall probabilistic forecasts for improved water supply management: Part 1 - A strategy for system predictor identification.* Journal of Hydrology, 2000. **239**(1-4): p. 232-239.

19. Asghari, K. and M. Nasseri, *Spatial rainfall prediction using optimal features selection approaches.* Hydrology Research, 2015. **46**(3): p. 343-355.

20. INS-Niger, *Tablo de Bord Social.* 2016, Institut Nationale de la Statistique du Niger: Niamey, Niger.

21. DMN. *Direction de la Météorologie Nationale.* 2015 05-11-2017]; Available from: http://www.meteo-niger.org.

22. NOAA. *National Oceanic and Atmospheric Administration.* 2012 [cited 2017 5-11-2017]; Available from: http://www.noaa.gov.

23. Rayner, N.A., et al., *Global analyses of sea surface temperature, sea ice, and night marine air temperature since the late nineteenth century.* Journal of Geophysical Research-Atmospheres, 2003. **108**(D14).

24. Daubechies, I., *Ten Lectures on wavelets.* Philapdelphia: Society for Industrial and Applied Mathematics, 1992.

25. Torrence, C. and G.P. Compo, *A practical guide to wavelet analysis.* Bulletin of the American Meteorological Society, 1998. **79**: p. 61-78.

26. Janicot, S., S. Trzaska, and I. Poccard, *Summer Sahel-ENSO teleconnection and decadal time scale SST variations.* Climate Dynamics, 2001. **18**: p. 303-320.

# The Effect of *Hypericum Perforatum* and *Plantago Major* Plant Extracts On Human Sh-Sy5y Cell Line

Özge Çağlar
Erzurum Technical University
ozge.caglar@erzurum.edu.tr

Mehmet Enes Arslan
Erzurum Technical University
enes.aslan@erzurum.edu.tr

Hasan Türkez
Erzurum Technical University
hasan.turkez@erzurum.edu.tr

*Abstract*-Studies on medicinal plants have been rapidly increasing due to the improvement in the production of plants or molecules for the research of active new substances and the herbal medicine industries. The World Health Organization reported that medicinal plants are the best source of medicine. However, these plants need to be investigated for their outstanding properties, safety and effectiveness. *Hypericum perforatum* also known as John's wort, it is a well-known plant that has been used over the years and It is a representative of the *Hypericaceae* family with verified therapeutic effects on burns, bruises, swelling, anxiety, mild-moderate depression, antidepressant, antiviral, wound healing, analgesic, hepatoprotective, antioxidant and antimicrobial activity. *Plantago major* has been reported to be used as a pain reliever and antipyretic drug in tumors in almost all regions of the world in skin diseases, infectious diseases, digestive and respiratory problems related circulatory organs. In this study anti-proliferative effect of *Hypericum perforatum* and *Plantago major* extracts was investigated on human Sh-Sy5y neuroblastoma cell line. For this purpose, cytotoxicity of plant extracts was assessed by MTT and LDH analysis. In addition, oxidative stress in the cell culture were explored via total oxidative stress (TOS) and total antioxidant capacity (TAC) levels analysis.

# Vehicle Detection Based on Semantic Segmentation

Asli Nur Omeroglu
Department of Electrical & Electronic
Engineering
Ataturk University
Erzurum,Turkey
asli.omeroglu@atauni.edu.tr

Nida Kumbasar
Department of Electrical & Electronic
Engineering
Ataturk University
Erzurum,Turkey
nida.kumbasar@ogr.atauni.edu.tr

Hussein Mahmood Abdo Mohammed
Department of Electrical & Electronic
Engineering
Ataturk University
Erzurum,Turkey
halameri080@gmail.com

Emin Argun Oral
Department of Electrical &
Electronic  Engineering
*Ataturk University*
Erzurum,Turkey
eminoral@atauni.edu.tr

Ibrahim Yucel Ozbek
Department of Electrical &
Electronic Engineering
Ataturk University
Erzurum,Turkey
iozbek@atauni.edu.tr

*Abstract—* **Semantic segmentation is a computer vision problem that aims to divide an image into multiple regions and assigns an object label to each pixel. It unifies the image segmentation and object recognition problems. Vehicle recognition is important problem in self-driving technologies to drive car safely. It also performs vital role in civilian applications. In this paper, we investigate deep learning application to vehicle segmentation for images taken over a large range of modalities and conditions. The approach we used was a SegNet architecture in which feature map, produced in the encoding phase, is also used during the decoding phase allows for the better localization by the network. In this study, the pre-trained VGG-19 network was used for transfer learning during segmentation.**

*Keywords—Vehicle Detection, Transfer Learning, VGG-19*

## I. INTRODUCTION

During the history of computer vision, one of the grand challenges has been semantic segmentation which is the ability to segment an unknown image into different parts and objects (e.g., car, people and road). Image segmentation is different from image classification or object recognition in that it is not necessary to know what the visual concepts or objects are beforehand. To be specific, an object classification will only classify objects that it has specific labels such as car, road, pedestrian. An ideal image segmentation algorithm will also segment unknown objects, that is, objects which are new or unknown. Semantic segmentation is widely used in various applications i.e., autonomous driving, scene understanding and etc.  The scene understanding as a core problem has been addressed in the past using various traditional computer vision and machine learning techniques. Early methods benefit from using the hand-engineered features, such as Scale Invariant Feature Transform (SIFT) and Histograms of Oriented Gradient (HOG) [1-5]. The convolutional neural network (CNN), the most important part of deep learning, has been the preferred method in many computer vision and remote sensing problems. Generally, CNN approaches are surpassing others with a large margin in terms of accuracy and sometimes efficiency [6-7]. Ammour et al. divided an input image into homogeneous superpixels, utilizing a pre-designed deep CNN to extract features and trains a SVM to classify these candidate zones [8]. In recent years, highly comprehensive learning-based detection frameworks have been proposed. Deep learning based methods such as SPP net [9], Fast R-CNN [10], Faster R-CNN [11], R-FCN [12] contain two-step approaches. However, because of the two-stage process, it takes a long time and is difficult to learn. Several approaches have also used semantic labeling to increase the detection performance in image data. A mask R-CNN [13] is proposed expanding the original Faster R-CNN by adding a semantic labeling branch for each candidate region. Recent researches have shown that the method based on semantic knowledge can improve the detection outcome [14]. In this paper, we investigate sematic segmentation using deep learning technique for vehicle detection. The purpose of this study is to detect vehicles using the SegNet network based on pre-trained VGG-19.

This paper is organized in the following way: Section-II mentions related work, Section-III provides a detailed description of the semantic segmentation, Section-IV details the training process and shows the experimental results of the system, and Section-V concludes the paper.

## II. RELATED WORK

Vehicle detection by semantic segmentation labels each pixel in an image into vehicle class or other categories (e.g., building, tree and pedestrian). Compared to vehicle detection, it can give more accurate pixel extraction results. For example, Audebert et al. [15] proposes a deep learning-based "segment-before-detect" method for classifying various types of vehicles in high-resolution remote sensing images. In the remote sensing images, Kampffmeyer et al. [16] less prioritized semantic segmentation to obtain a good overall

accuracy for small objects (e.g. Tools). To solve this problem, they train FCNs with the median frequency balancing-weighted cross entropy loss function proposed by Eigen and Fergus [17]. Using SegNet in this method may produce additional pixel-based features for semantic mapping of vehicles [18].

## III. MODEL

### *Semantic Segmentation*

The purpose of semantic image segmentation is to label each pixel of an image with a corresponding class of the representation. Semantic segmentation provides very detailed image information from image classification or object detection. This detailed information is critical to a wide range of areas such as autonomous driving, robotics and image search engines [19]. There are multiple methods to perform semantic segmentation. One of the most used approach for pixel-wise segmentation is the deep encoder-decoder architecture. Encoder-decoder models consist of two parts. The first one, the encoder network, takes the input and maps it to an encoded representation with a lower dimension. That is, encoder extracts image features using deep convolutional network. The decoder network takes the encoded representation and maps the feature representation back into the input data space. That is, decoder up-samples feature map back to image resolution with final output having the same size with the pixel classes.

### *SegNet*

In this paper we implemented SegNet [20], a deep fully convolutional neural network architecture for semantic pixel-wise segmentation. SegNet is a complete convolutional network of 13 encoders and 13 decoder layers. It is one of the first deep encoder-decoder architectures developed (see Fig. 1). Our model creates the SegNet network with weights initialized from the VGG-19 network.
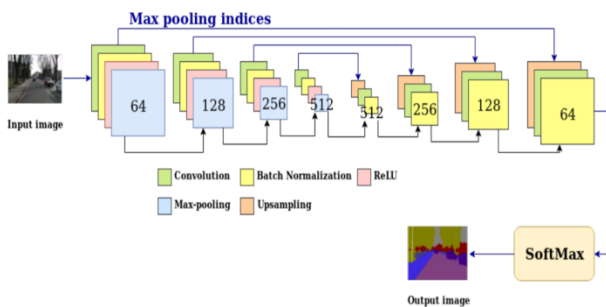


Fig. 1. Architecture of SegNet [20]

The main processes are sequentially applied in the encoder network. These are convolution with the filter bank, batch normalization, ReLU, maxpooling in $2 \times 2$ non-overlapping windows and sample-reduction in 2 multipliers. After each max pooling operation, the index of the largest attribute values in the pooling windows is stored to be used in the decoder network.

On the other hand, each decoder performs an up-sample of its input feature map using the max-pooling indexes of the corresponding encoder. Therefore, the decoding does not involve any parameter learning, but it is only a direct application of max-pooling indexes generated in the encoder.

Then, these features are used to produce dense batch normalized maps.

### *VGG-19*

The VGG network architecture initially proposed by Simonyan and Zisserman, [21] have 16 layers (VGG-16) or 19 layers (VGG-19). With these network architectures, Visual Geometry Group (VGG) team was the first and second in the localization and classification areas in the Imagenet 2014 competition.

The VGG-19 architecture is structured starting with five blocks of convolutional layers followed by three fully-connected layers (see Fig. 2). Convolutional layers use 3x3 kernels with a stride of 1 and padding of 1. A rectified Linear Unit (ReLU) activation is performed immediately after each convolution. To reduce spatial dimension, max pooling is occasionally applied. Max pooling layers use 2x2 kernels with a stride of 2 and no padding. Two fully-connected layers are then used before the final 1000 fully-connected softmax layer.
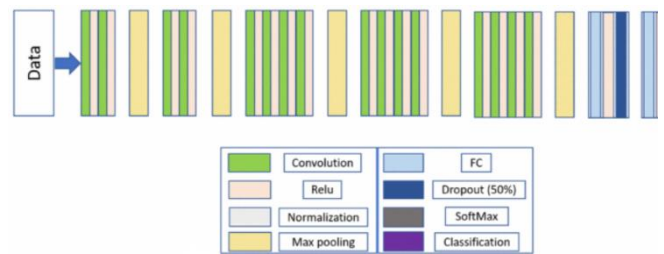


Fig. 2. VGG19 architecture [21]

### *Model*

The objective of the used method is to detect vehicles on a highway. The common highway environment includes a variety of buildings, trees, advertisement boards, sky, road or traffic signs as background. Such scenes have more pixels than vehicle pixels. If not handled correctly, this imbalance can be detrimental to the learning process because the learning is biased in favor of the dominant classes. To improve training, we used class weighting to balance the classes. It is often difficult to train a deep neural network from scratch. Besides, a dataset of sufficient size is required, and the training on the data sets in these experiments can take a very long time. Even if a large enough dataset is available, it is often helpful to start with pre-trained weights instead of random initialized ones. The major principle of transfer learning is to fine-tune the weights of a pre-trained network with available training data. For this purpose, in this study, we have used the pre-trained VGG-19 network to decrease the training time. stochastic gradient descent with momentum (SGDM) is used in the optimization process during the training. We also used data augmentation to provide more examples to the network as it helps to increase the accuracy of the network. Fig. 3 shows the scheme of the study.
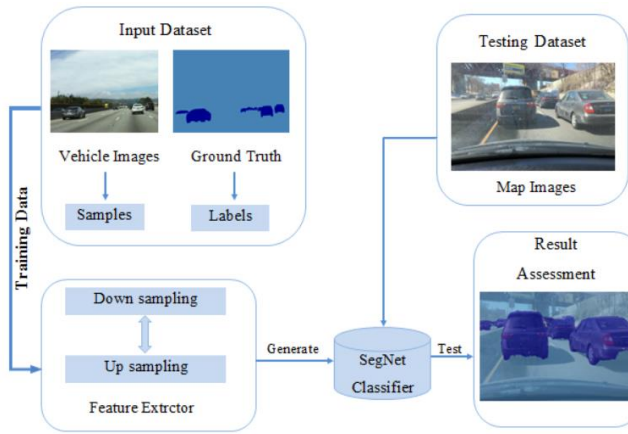
Fig. 3. Block-diagram of semantic segmentation

## IV. EXPERIMENT RESULTS AND DISCUSSION

### Dataset

The training and test sets were provided by the BDD100K dataset sponsored by Berkeley Deep Drive Industry Consortium. The BDD100K dataset is the largest and the most diverse open driving dataset for computer vision research, consisting of 100,000 videos. These videos were collected from diverse locations in the United States and covers different weather conditions including sunny, overcast, and rainy as well as different times of day including daytime and nighttime. The BDD100K dataset also provides a 10K images subset with full-frame instance segmentation. An example training set image and corresponding labels are shown in Fig.4.
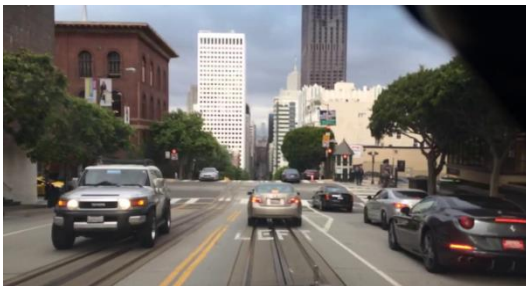


1.  Training image



2.  Label of training image

Fig. 4. An example training set image (a) and labels (b)

Only 3300 of these images were used in this study of which 2300 for training and 1000 for test. To reduce the training time and memory usage, the original 720x1280 BDD100K images as well as corresponding labels were resized to 360x480. Also, all classes other than "vehicle" in the original dataset are grouped together to reduce classes into two as "vehicle" and "non-vehicle".

### Performance Assessment

We have achieved the performance of the SegNet architecture with the following measures.

1.  Global Accuracy (GA): The GA corresponds to the percentage of pixels correctly classified to all pixels in the dataset.

$$GA = \frac{correct\ pixels}{total\ pixels} \qquad (1)$$

2.  Class Average Accuracy (CA): The CA is the mean of the predictive accuracy over all classes.

3.  Mean Intersection Over Union (mIoU): The IoU is defined as the ratio of Intersection of "prediction" and "ground truth" to their Union. For a given class, IoU is given by Equation 2, in terms of true positives (TP), false positives (FP), and false negatives (FN). Averaging all classes considered in segmentation study gives mIoU score.

$$IoU = \frac{TP}{TP+FP+FN} \qquad (2)$$

### Result and Discussion

The training process carried out on GPU (Quadro M5000) took about 5 hours for training the model. Our initial test results trained for 20 epochs are presented in Table 1. Also, the obtained confusion matrix and a test result are shown Table 2 and Fig.5, respectively.

Table. 1 Test Result

| Model | Global Accuracy | Mean IoU |
|---|---|---|
| SegNet | %98 | %88 |

Table. 2 Confusion Matrix

| True Class | Predicted Class | | |
|---|---|---|---|
| | | Vehicle | Non-vehicle |
| | Vehicle | %88.6 | %11.4 |
| | Non-vehicle | %0.12 | %98.75 |
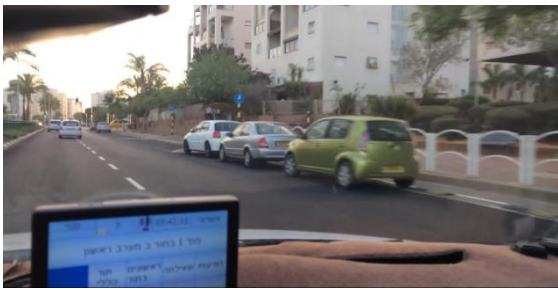
a) SegNet with VGG-19 prediction



b) Test image

Fig. 5. Effect of training on test set

## V. CONCLUSION AND FUTURE WORK

Performing segmentation without knowing the exact identity of all objects in the scene is an important part of visual understanding process. Given an image, we performed semantic segmentation based on VGG-19 and transfer learning approach tuned for vehicle detection. The initial experimental results based on real scenes demonstrate the effectiveness of our investigated method. As future research, we intend to explore semantic segmentation extracted from different deep network models.

## REFERENCES

1. N. Silberman, R. Fergus, "Indoor scene segmentation using a structured light sensor", Proceedings of the IEEE International Conference on Computer Vision Workshops (2011), pp. 601-608

2. S. Gupta, P. Arbelaez, J. Malik, "Perceptual organization and recognition of indoor scenes from RGB-D images",Proceedings of the IEEE Conference on Computer Vision and Pattern Recognition (2013), pp. 564-57

3. S.H. Khan, M. Bennamoun, F. Sohel, R. Togneri, "Geometry driven semantic labeling of indoor scenes", Proceedings of the European Conference on Computer Vision (2014), pp. 679-694

4. D.G. Lowe, "Object recognition from local scale-invariant features ", Proceedings of the IEEE International Conference on Computer Vision (1999), pp. 1150-1157

5. N. Dalal, B. Triggs, "Histograms of oriented gradients for human detection", Proceedings of the IEEE Conference on Computer Vision and Pattern Recognition (2005), pp. 886-893

6. F. Ning, D. Delhomme, Y. LeCun, F. Piano, L. Bottou, and P. E. Barbano, "Toward automatic phenotyping of developing embryos from videos," IEEE Transactions on Image Processing, vol. 14, no. 9, pp. 1360–1371, 2005

7. C. Farabet, C. Couprie, L. Najman, and Y. LeCun, "Learning hierarchical features for scene labeling," IEEE transactions on pattern analysis and machine intelligence, vol. 35, no. 8, pp. 1915–1929, 2013.

8. N. Ammour, H. Alhichri, Y. Bazi, B. Benjdira, N. Alajlan, M. Zuair, "Deep learning approach for car detection in UAV imagery", Remote Sens., vol. 9, no. 4, pp. 312, 2017.

9. K. He, X. Zhang, S. Ren, J. Sun, "Spatial pyramid pooling in deep convolutional networks for visual recognition" in ECCV, Springer, pp. 346-361, 2014.

10. R. Girshick, "Fast r-cnn" in ICCV, pp. 1440-1448, 2015.

11. S. Ren, K. He, R. Girshick, J. Sun, "Faster r-cnn: Towards real-time object detection with region proposal networks" in Advances in neural information processing systems, pp. 91-99, 2015.

12. J. Dai, Y. Li, K. He, J. Sun, "R-fcn: Object detection via region-based fully convolutional networks" in Advances in neural information processing systems, pp. 379-387, 2016.

13. K. He, G. Gkioxari, P. Dollár, R. Girshick, Mask r-cnn, 2017.

14. Geiger, M. Lauer, C. Wojek et al., "3D traffic scence understanding from movable platform", IEEE Trans. Pattern Anal. Mach. Intell., vol. 36, no. 5, pp. 1012-1025, May 2014.

15. N. Audebert, B. Le Saux, S. Lefèvre, "Segment-before-detect: Vehicle detection and classification through semantic segmentation of aerial images", Remote Sens., vol. 9, no. 4, pp. 368, 2017.

16. M. Kampffmeyer, A.-B. Salberg, R. Jenssen, "Semantic segmentation of small objects and modeling of uncertainty in urban remote sensing images using deep convolutional neural networks", Proc. IEEE Int. Conf. Comput. Vis. Pattern Recognit. (CVPR) Workshop, Jun. 2016.

17. Eigen, R. Fergus, "Predicting depth surface normals and semantic labels with a common multi-scale convolutional architecture", Proc. IEEE Int. Conf. Comput. Vis. Pattern Recognit. (CVPR), pp. 2650-2658, Dec. 2015.

18. V. Badrinarayanan, A. Kendall, R. Cipolla, SegNet: A deep convolutional encoder-decoder architecture for image segmentation, 2015, [online] Available: https://arxiv.org/abs/1511.00561.

19. Garcia-Garcia, S. Orts-Escolano, S. Oprea, V. Villena-Martinez, and J. Garcia-Rodriguez, "A review on deep learning techniques applied to semantic segmentation," arXiv preprint arXiv:1704.06857, 2017.

20. V. Badrinarayanan, A. Kendall, and R. Cipolla, "Segnet: A deep convolutional encoder-decoder architecture for image segmentation," arXiv preprint arXiv:1511.00561, 2015.

21. K. Simonyan, A. Zisserman, Very deep convolutional networks for large-scale image recognition, 2014.

# Detection of Diabetic Retinopathy with Integration of Deep Learning

Hilal Kübra Sağlam
Faculty of Engineering,
Deparment of Electrical
and Electronics
Engineering
Atatürk University
Erzurum, Turkey
hks.erz@gmail.com

Rabiye Kılıç
Faculty of Engineering,
Deparment of Electrical
and Electronics
Engineering
Atatürk University
Erzurum, Turkey
rabiyaklc0@gmail.com

Emin Argun Oral
Faculty of Engineering,
Department of Electrical
and Electronics
Engineering
Atatürk University
Erzurum, Turkey
eminoral@atauni.edu.tr

İbrahim Yücel Özbek
Faculty of Engineering,
Department of Electrical
and Electronics
Engineering
Atatürk University
Erzurum, Turkey
iozbek@atauni.edu.tr

*Abstract*—**Diabetic Retinopathy (DR) is a disease of retina. If not diagnosed at an early stage, it causes blindness. To detect this disease some manual classification methods are used. However, these methods are highly time consuming. Also inter observer variability is another problem to deal with. Hence, computer automated diagnostic systems are preferred for retina images classification. In this study, it is aimed to classify DR existence and its level using transfer learning for Convolutional Neural Network (CNN) using the data of Kaggle and Messidor-2 datasets which contain five-classes and four-classes, respectively. The classification accuracy was obtained as 74.72% in Kaggle dataset for normal, mild, moderate, severe and end-stage classes.**

*Keywords—Deep Learning (DL), Convolutional Neural Network (CNN), Transfer Learning, Image Classification, Machine Learning, Diabetic Retinopathy (DR)*

## I. INTRODUCTION

Deep learning (DL) includes calculation methods that allow an algorithm to work in a desired manner and to program with a wide variety of examples. DL is a machine learning technique that directly learns the most predictive features from images given a large set of labeled samples [1]. Machine learning is used for various classification tasks, including automatic classification of diabetic retinopathy (DR). In this paper, a deep learning-based CNN (Convolutional Neural Network) method is introduced for the problem of DR classification in fundus images. Intensive research is required to determine the applicability of the application of this algorithm in the clinical setting to determine whether it will lead to a better care or not, and the results are compared to the current ophthalmological evaluation.

### A. Objectives

DR is retinal disease that can be transformed into irreversible vision loss [2]. If DR is detected at an early stage, it is possible to treat it, which makes early detection vital [3]. Manual detection of DR is extremely time consuming using grading of subtle pathological features by trained experts [2]. The ability to detect a non-functional retina in fundus images is an important component of a device to automatically detect diabetic retinopathy in the real world applications [3]. In the determination of the specific features of retinal scans, high variance and low bias classification techniques were used. There are new approaches that examine other pathological features such as SVM (support vector machine), K-nearest neighbor and ensemble-based methods [2]. Convolutional Neural Networks (CNNs) is a sub-branch of deep learning. It is widely used in image analysis and interpretation applications. A network, developed with CNN architecture using augmentation, can define complex features in the classification task, such as micro-aneurysms, exudates and hemorrhages in the retina. Hence, it provides a diagnosis without the need for a human evaluation. Currently, large CNNs are used to effectively handle very complex image recognition tasks in a remarkable standard with many object classes [3]. The Alexnet architecture is a deep learning structure that can distinguish up to 1000 objects trained on more than a million images on ImageNet. In general, when a previously trained network is used for a different problem, transfer leafrning is an alternative approach by which last layers of pre-trained network is changed while the parameters, representing previously learned abstract information such as colors, layers, etc., are kept. CNNs are also used in many current image classification tasks such as ImageNet, GoogleNet and AlexNet [2]. This study aims to detect retinopathy at an early stage using retinal images that are publicly available. CNNs are specific to all types of lesions and the parameters differ slightly between them. Alexnet was inspired by network architectures [4].

### B. Classification of DR

Computer automated diagnostics for screening retinal scans considerably reduce costs, decrease observer dependency and probably allows for more common screening programs as well as earlier detection of diabetic retinopathies. Automatic classification of diabetic retinopathy is a popular research area in computer vision [2]. The advantages of automated grading are increased efficiency, reproducibility and benefits in application of screening programs. Thus, it provides the opportunity to improve the patient with early diagnosis and treatment. In order to maximize the clinical benefit of automatic grading, an algorithm is needed to determine countable diabetic retinopathy [1].

## II. MATERIAL AND METHODS

### C. Data Sets

We used two different datasets in this study. Messidor-2, the first dataset, was collected in four French hospitals, containing 1200 fundoscopic images with 4-class labels. Namely,

- R0: Normal (546 image)
- R1: Mild Retinopathy (153 image)
- R2: Moderate Retinopathy (247 image)
- R3: Severe Retinopathy (254 image)

This available data was partitioned into three as training, validation and test datasets to be used in the study. Of the available data of Messidor-2 dataset, 70% was used for training while 10% and 20% used for validation and test, respectively. This dataset consists of color images ranging in height and width from hundreds to thousands of pixels from different patient population with a significant proportion of early diabetic retinopathy. Black edges are cropped in all dataset images, with normalized pixel intensities. Representative Messidor-2 retinal images in different stages are shown in Fig. 1.

Although Messidor-2 data set consists of high-quality retinal images, it is not sufficient for good presentation of the disease to be used in learning algorithms in the sense that it does not contains both left and right retina images per subject. This is an obstacle with scanning algorithms designed for two images per eye which gives more satisfactory results.
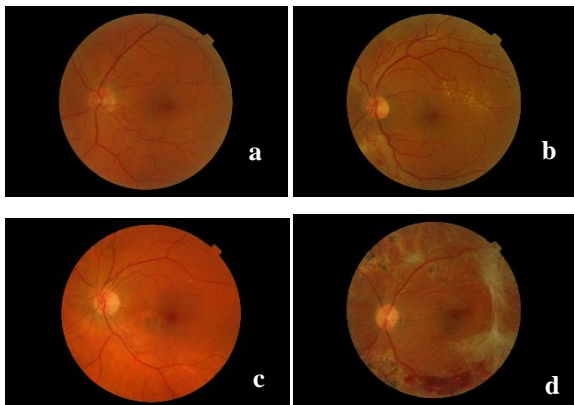


Figure 1. Messidor-2 Data Set: (a) normal, (b) mild retinopathy, (c) moderate retinopathy, (d) severe retinopathy

On the contrary, the second dataset, Kaggle, has two retina images for each subject. This data set contains 35000 fundoscopic images with 5-class labels.

These are;

- R0: Normal (25.808 image)
- R1: Mild Retinopathy (2442 image)
- R2: Moderate Retinopathy (5291 image)
- R3: Severe Retinopathy (873 image)
- R4: End-stage Retinopathy (708 image)

Kaggle retinal image example in different stages of disease are given in Fig. 2-6. We trained the network for both datasets using a graphics processor unit (GPU).
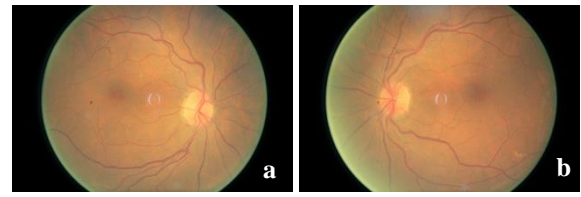


Figure 2. Kaggle dataset R0-class (a) left (b) right
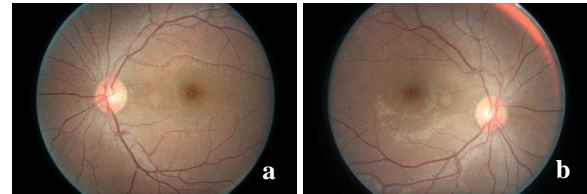


Figure 3. Kaggle dataset R1-class (a) left (b) right
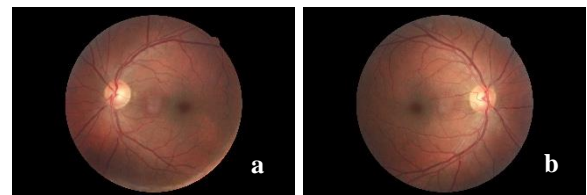


Figure 4. Kaggle dataset R2-class (a) left (b) right
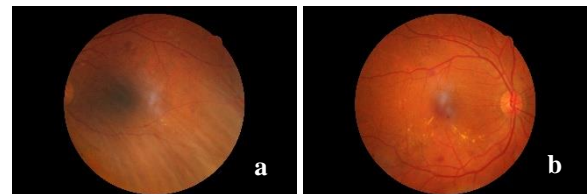


Figure 5. Kaggle dataset R3-class (a) left (b) right
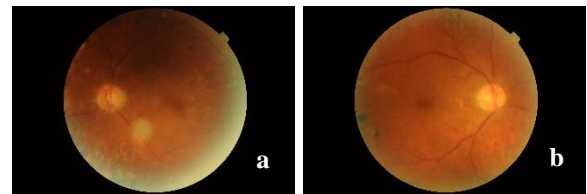


Figure 6. Kaggle dataset R4-class (a) left (b) right

### D. Proposed Work

Training a neural network, a classification function with many parameters to be optimized, that performs a specific learning task. It requires a large set of images with already known severity of diabetic retinopathy, the training set. Through the training operation, the parameters of the function are initially set to random values. During the training, the disease class is defined by the function and compared to that of the training set label to obtain the classification error which is performed for each image. Later, the degree of severity of the function is compared with the degree of training set and the parameters are changed slightly to reduce the error for each image. Based on this error rate the parameters are modified to reduce the average error. This procedure is repeated until the type of diabetic retinopathy is correctly classified. With large enough training data, the result is a general function that can calculate the class of diabetic retinopathy in new images [1].

The network used in this study is a convolutional neural network, which first connects nearby pixels to local characteristics, and then uses a function that passes them to global features. Although the algorithm is not explicitly identified (hemorrhages, micro-aneurysms), it learns to recognize them using local characteristics.

In our study, we replaced the last three layers of Alexnet with layers suited to the problem in hand as a transfer lerarning step. Thanks to this change, the algorithm was able to distinguish the classes of DR.

### III. RESULTS

Extensive research has been conducted on methods for a double classification of DR for Messidor-2 data set, with encouraging results. In the literature, the detection accuracy across all four classes of the severity spectrum towards no-DR (R0), mild DR (R1), moderate DR (R2), and severe DR (R3) varies significantly.

When we used four classes (normal, mild retinopathy, moderate retinopathy, severe retinopathy), the accuracy was founded %52.92. If two classes (healthy and patient) was used, accuracy was %69.17. Also class R0 and class R1 were selected as database, result was %78.57. Finally specific two classes were selected (normal and severe retinopathy) accuracy was %80 (Table 1).

Similarly, the accuracy rate of our initial study is as follows when we use Kaggle database. When we used five classes (normal, mild retinopathy, moderate retinopathy, severe retinopathy, end-stage retinopathy), the accuracy was founded %74.72. If two classes (healthy and patient) were used, accuracy was %74.49. Finally specific two classes were selected (normal and end-stage retinopathy) accuracy was %97.81 (Table 2).

R0 : Normal
R1 : Mild retinopathy
R2 : Moderate retinopathy
R3 : Severe retinopathy
R4 : End-stage retinopathy

Table 1. Accuracy of Messidor-2 results

| Class Number | Accuracy |
|---|---|
| 4 classes : R0-R1-R2-R3 | % 52.92 |
| 2 classes : R0-(R1+R2+R3) | % 69.17 |
| 2 classes : R0-R1 | % 78.57 |
| 2 classes : R0-R3 | % 80 |

Table 2. Accuracy of Kaggle results

| Class Number | Accuracy |
|---|---|
| 5 classes : R0-R1-R2-R3-R4 | % 74.72 |
| 2 classes : R0-(R1+R2+R3+R4) | % 74.49 |
| 2 classes : R0-R4 | % 97.81 |

To explore the strengths and weaknesses of CNNs, we trained a AlexNet model on a combined dataset from Messidor-2, containing over 1000 fundoscopic images and Kaggle, containing over 35000 fundoscopic images. To conclude, we have shown that CNNs have the potential to be trained to identify the features of Diabetic Retinopathy in fundus images. CNNs have the potential to be incredibly useful to DR clinicians in the future as the networks and the datasets continue improving and they will offer real-time classifications.

We studied on detection of diabetic retinopathy with CNN. Messidor-2 and Kaggle datasets were used which consisted of 1200 and 35122 images respectively.

### REFERENCES

1. Gulshan, V., Peng, L., et al. . Development and Validation of a Deep Learning Algorithm for Detection of Diabetic Retinopathy in Retinal Fundus Photographs.
2. Lam, C., Seneviratne, M., et al. . Learning Of Subtle Features In Retinal Images.
3. Pratt, H., Coenen, F., et al. 2016. Convolutional Neural Networks for Diabetic Retinopathy. International Conference On Medical Imaging Understanding and Analysis 2016, MIUA 2016, 6-8 July 2016, Loughborough, UK, Procedia Computer Science 90 (2016) 200 – 205.
4. Abramoff, M.D., et al. 2016. Improved Automated Detection of Diabetic Retinopathy on a Publicly Available Dataset Through Integration of Deep Learning. DOI:10.1167/iovs.16-19964

# Ship Detection In Satellite Images

Merve Polat
Department of Electrical & Electronic
Engineering
Ataturk University
Erzurum,Turkey
merve.polat12@ogr.atauni.edu.tr

Hussein Mahmood Abdo Mohammed
Department of Electrical & Electronic
Engineering
Ataturk University
Erzurum,Turkey
halameri080@gmail.com

Emin Argun Oral
Department of Electrical & Electronic
Engineering
Ataturk University
Erzurum,Turkey
eminoral@atauni.edu.tr

İbrahim Yucel Ozbek
Department of Electrical &
Electronic Engineering
Ataturk University
Erzurum,Turkey
iozbek@atauni.edu.tr

*Abstract*—Detection of small vessels and ships plays a crucial role in preventing illegal activities such as drug and human trafficking and illegal fishing .The main objective of this work is semantic segmentation using transfer learning to detect ships from satellite images. The airbus ship detection challenge database is used for this purpose.

*Keywords*—Vessel Detection, Ship Detection, Object Detection, CNN, Semantic Segmentation, Transfer Learning, VGG-16

## I. INTRODUCTION

Images constructed by assigning different visible colors for detected different component of invisible light by satellites sensors are called satellite images. These satellite images are useful in remote detection of different surfaces and objects as they react differently to each radiation wavelength. When it is difficult to manually process these images machine learning and computer vision algorithms are utilized to make the process easier and automatic.

It is important to identify small vessels, boats and ships to prevent some illegal activities, such as drug and human trafficking and illegal fishing etc. The most common technique for satellite imaging is the use of Synthetic Aperture Radar (SAR), achieved by reflected signal and therefore, robust to various weather conditions but sometimes insufficient to detect small vessels, boats and ships [1],[2]. Optical or visual-based detection considered as an important alternative is less developed [3], [4]. This detection method should be non-invasive and should not require special equipment. UAV is used for non-invasive detection of small vessels [5].

In the literature, cascade approach is used for ship detection by which a rapid localization of the similar regions are extracted first. Image segmentation [6] and saliency detection based methods are then applied. In the following step, the regions are classified accordingly using different approaches such as Histogram of Oriented Gradients (HOG) [7], Local Binary Patterns (LBP) [8], Scale Invariant Feature Transform (SIFT) [9] and SVM [10].

## II. PROPOSED WORK

### A. Convolutional Neural Network (CNN)

Convolutional Neural Network (CNN or Conv Net), one of the most popular algorithms of deep learning. It is a type of machine learning algorithm where a model is trained to perform classification from images, video, texts or voice. CNNs, used in different applications, are most commonly used to recognize scenes, faces and objects. The difference of CNNs from other neural networks is that they are consist of multiple layers. They are composed of two main parts such as extraction and classification.

*Feature extraction part (hidden layers)*: This part of the network performs a series of convolutions and pooling operations during which the features are detected. If a car is introduced to CNN, this is the part where the network would recognize windows, tires etc., namely features, by means of passing the input data through many layers.

*Classification part*: Fully connected layers serve as a classifier on top of extracted features obtained from previous layers and assign a probability for the input object being a member of any particular class.

### B. Semantic Segmentation

In semantic segmentation each pixel in the image is assigned to an object class (class ID) results in bringing together parts of the image as shown in Fig. 1. It is also necessary to specify the boundaries of each segments such as person who is riding the bike and the bike itself. Semantic segmentation is used in various applications.



*Fig. 1. Input image (left) and its semantic segmented image (right) [11].*

Semantic segmentation is quite different from other image-based tasks such as Image Classification, defines what is in the picture, or Object Recognition (and Detection), determines what is in the image as well as it is location defined with a Bounding Box.
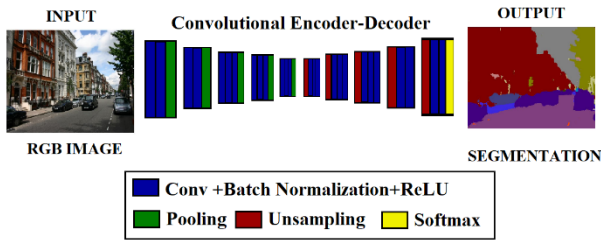


Fig.2.Typical encoder-decoder architecture of CNN based semantic segmentation network (image source [12]).

### C. Transfer Learning

Transfer learning is a machine learning technique in which a model trained for a task is redesigned for another application. The purpose of this technique is to improve learning in the target task by leveraging the knowledge obtained from another task. It supplies additional source of information, coming from one or more related tasks, apart from the standard training data. Hence, it is an optimization method that provides rapid progress or improved performance. It enables three common measures such as increased initial performance, decreased training time and higher achievable performance.VGG-16 is used for transfer learning. For this purpose, the initial layers of VGG-16 are kept and its final layers are replaced for the problem in hand.

### III. EXPERIMENTAL RESULT

#### A. DataSet

The purpose of this study is to locate all ships in a given satellite image and place a bounding box around them. The dataset is provided from Kaggle [13]. This dataset contains 192.556 train and 15,606 test entries, all are 768x768 RGB images. While some images in the dataset contain more than one ship, some others do not contain any ship. Also, ships in images may differ in size, location and their surrounding environment such as open sea, docks, marinas, etc.
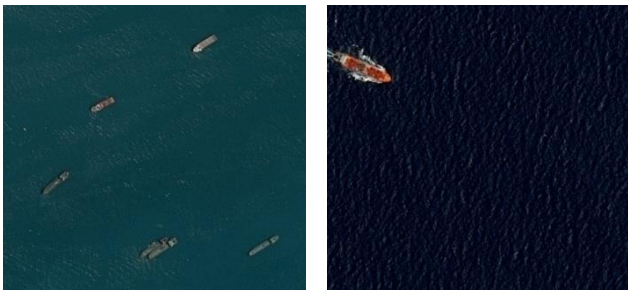




Fig.3. Examples of ships extracted from the dataset [13].



Fig. 4. Left-original image Right- image label

750 monochromatic images were used in this study as a preliminary work. In the proposed model, the last three layers of VGG-16 was adapted to the binary-classification problem for "ship" and "non-ship" classes.

As a result of the training, the test was performed with 225 images and accuracy was found as 91.35%.

Tablo.1 Test Results

| Classes | Accuracy (%) | IoU |
|---------|-------------|------|
| ship | 91.35 | 0.1172 |
| Non-ship | 96.49 | 0.9645 |

Our initial test results are presented in Table 1. Also, the obtained confusion matrix and a test result images are shown Fig.5 and Fig.6, respectively.
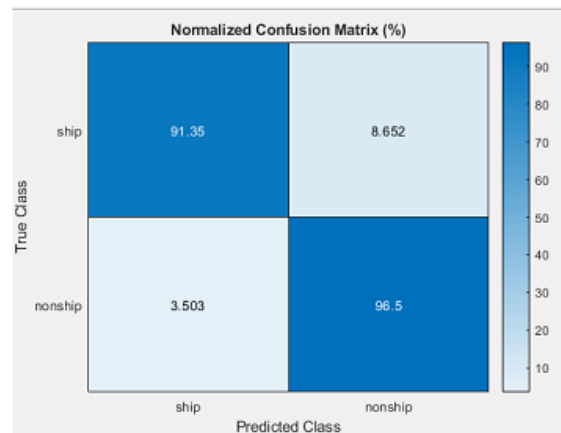


Fig. 5. Confusion Matrix
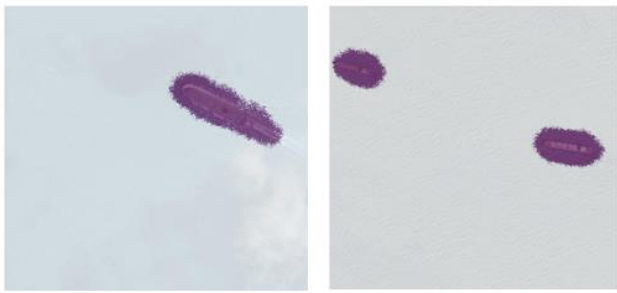
*Fig.6. Testing of model on some images*.

## IV. CONCLUSION

Satellite images are obtained from publicly available from Kaggle. In this study, by applying semantic segmentation and transfer learning algorithms to satellite images, the ships in the images were detected.

## REFERENCES

[1] Armando Marino , Maria J. Sanjuan-Ferrer , Irena Hajnsek and Kazuo Ouchi ,"Ship Detection with Spectral Analysis of Synthetic Aperture Radar: A Comparison of New and Well-Known Algorithms",Remote Sens.2015,7,5416-5439 doi:10.3390/rs70505416

[2] Shengli Song, Bin Xu, Zenghui Li, and Jian Yang, Senior Member, IEEE,"Ship Detection in SAR Imagery via Variational Bayesian Inference",IEEE GEOSCIENCE AND REMOTE SENSING LETTERS, VOL. 13, NO. 3, MARCH 2016

[3] ] C. Corbane, L. Najman, E. Pecoul, L. Demagistri, and M. Petit, "A complete processing chain for ship detection using optical satellite imagery," International Journal of Remote Sensing, vol. 31, no. 22, pp. 5837–5854, 2010.

[4] C. Zhu, H. Zhou, R. Wang, and J. Guo, "A novel hierarchical method of ship detection from spaceborne optical image based on shape and texture features," Geoscience and Remote Sensing, IEEE Transactions on, vol. 48, no. 9, pp. 3446–3456, 2010.

[5] T. Arnesen and R. Olsen, "Literature review on vessel detection," FFI/Rapport-2004/02619, Forsvarets Forskningsinstitutt, Kjeller, Norway, 1-168, 2004.

[6] Xu C, Zhang D, Zhang Z, Feng Z. BgCut: Automatic ship detection from UAV images. Hindawi Publishing Corporation. The Scientific World Journal. 2014; (2014):1– 11. DOI:10.1155/2014/171978.

[7] Qi S, Ma J, Lin J, Li Y, Tian J. Unsupervised ship detection based on saliency and S-HOG descriptor from optical satellite images. IEEE Geoscience and Remote Sensing Letters. 2015, 12(7):1451–5. DOI: 10.1109/LGRS.2015.2408355.

[8] Haigang S, Zhina S. A novel ship detection method for large-scale optical satellite images based on visual LBP feature and visual attention model. The International Archives of the Photogrammetry, Remote Sensing and Spatial Information Sciences, XXIII ISPRS Congress 2016, XLI-B3; 2016. p. 917–21. DOI:10.5194/isprs-archives-XLIB3-917-2016.

[9] Feineigle PA, Morris DD, Snyder FD. Ship recognition using optical imagery for harbor surveillance. Proceedings of Association for Unmanned Vehicle Systems International (AUVSI); 2007 Jun. p. 1–17.

[10] Yifan Li,Huadong Zhang,Qianfeng Guo,Xiaoshi Li,"Machine Learning Methods for Ship Detection in Satellite Images"

[11] Available from:
http://host.robots.ox.ac.uk/pascal/VOC/voc2012/segexamples/index.html

[12] Available from:
http://mi.eng.cam.ac.uk/projects/segnet/

[13] Available from:
https://www.kaggle.com/c/airbus-ship-detection

# Classification of Images Obtained by SAR (Synthetic Aperture Radar) Data

Nida Kumbasar
Department of Electrical & Electronic
Engineering
*Ataturk University*
Erzurum,Turkey
nida.kumbasar@ogr.atauni.edu.tr

Asli Nur Omeroglu
Department of Electrical & Electronic
Engineering
*Ataturk University*
Erzurum,Turkey
asli.omeroglu@atauni.edu.tr

Hussein Mahmood Abdo Mohammed
Department of Electrical & Electronic
Engineering
*Ataturk University*
Erzurum,Turkey
halameri080@gmail.com

Emin Argun Oral
Department of Electrical &
Electronic Engineering
*Ataturk University*
Erzurum,Turkey
eminoral@atauni.edu.tr

Ibrahim Yucel Ozbek
Department of Electrical &
Electronic Engineering
Ataturk University
Erzurum,Turkey
iozbek@atauni.edu.tr

*Abstract*— **Parallel to the rapid increase in the visual surveillance in military and security applications, studies in this area have gained importance. One application area of Synthetic Aperture Radar (SAR) in the military field is the classification of SAR images. A military SAR image frame may contain formations other than the military objects. The aim of this study is to accelerate the correct classification ratio of images contained in a high-resolution SAR dataset, namely publicly available MSTAR SAR data. These dataset images contain military objects such as vehicles or structures. They are classified by Convolutional Neural Network (CNN) method to define eight classes they belong to. We obtained 99.8% classification accuracy is with the proposed work.**

*Keywords*—**Synthetic Radar (SAR), Convolutional Neural Network (CNN)**

## I. INTRODUCTION

Synthetic Aperture Radar (SAR) is one of the most important sensors in the field of remote sensing. Due to the increase in the resolution and increasing amount of SAR images taken from air and satellite, the need to process these images automatically increases rapidly. High-resolution SAR images have a very important role in fields such as military target recognition, classification, space surveillance, source research and etc. SAR images are high resolution data captured from long distance during day and night under different environmental conditions. Effective feature extraction and high speed processing algorithms are key points for SAR image processing.

In general learning algorithms are divided into two as supervised and unsupervised. Xiang et al. [1] used the K-means classifier with cross scattering for urban area SAR image classification as an unsupervised approach. However, the unsupervised classification method is often indeterminate as the result of the SAR image classification as it requires more information of the object. Hence, most SAR image classification uses the supervised method in which labels for data are also part of the learning process [2]. Some of the supervised learning algorithms are Linear, Logistic Regression, SVM, and Neural Networks of which

Neural Network (NN) is one of the most common classification approach. [3][4][5]

Deep learning, as a new machine learning method, are recently used in many areas such as speech recognition, object detection and image classification etc. Convolutional Neural Network (CNN), on the other hand, plays an important role in the areas of image and speech processing, as one of the most popular deep learning methods. In 2012, the convolutional neural network model developed by Alex Krizhevsky et al. created a break point in the classification problems by increasing the accuracy rate in the ImageNet competition [6], and then showed superior performance than human [7-8]. Deep learning method has then been used in many areas including SAR image classification. Since then CNN has moved the technology in the field of computer vision to a different level [9]. It is basically a neural network with a special structure in which traditional neural networks are modified [10]. Chen et al. [11] used the sparse connection method for each layer to improve CNN, which makes the network trained well with a small amount of training data and reduces the risk of over-fitting. Wang et al. [12] molten sea ice double polarization CNN applied to classify SAR images. Geng et al. [13] proposed the Convolutional Auto Encoder (CAE) method, combined with the scale transform, for high resolution SAR image classification.

## II. PROPOSED WORK

In this work SAR images are classified for the purpose of military vehicle detection using CNN. A general CNN structure is composed of repeating layers as shown in Fig. 1. Main block diagram of the proposed method on the other hand is shown in Fig. 2. The corresponding CNN layers' details and their parameters are explained as follows.

Fig. 1 A General CNN Structure



imageInputLayer (54,54,1)

Convolution2dLayer
Modifing parameters
'filterSize'
'numfilters'
'Padding'

N

batchNormalizationLayer

reluLayer

maxPooling2dLayer
Modifing parameters
'poolSize'
'Stride'

fullyConnectedLayer(8)

softmaxLayer

classificationLayer
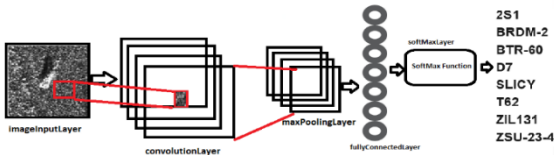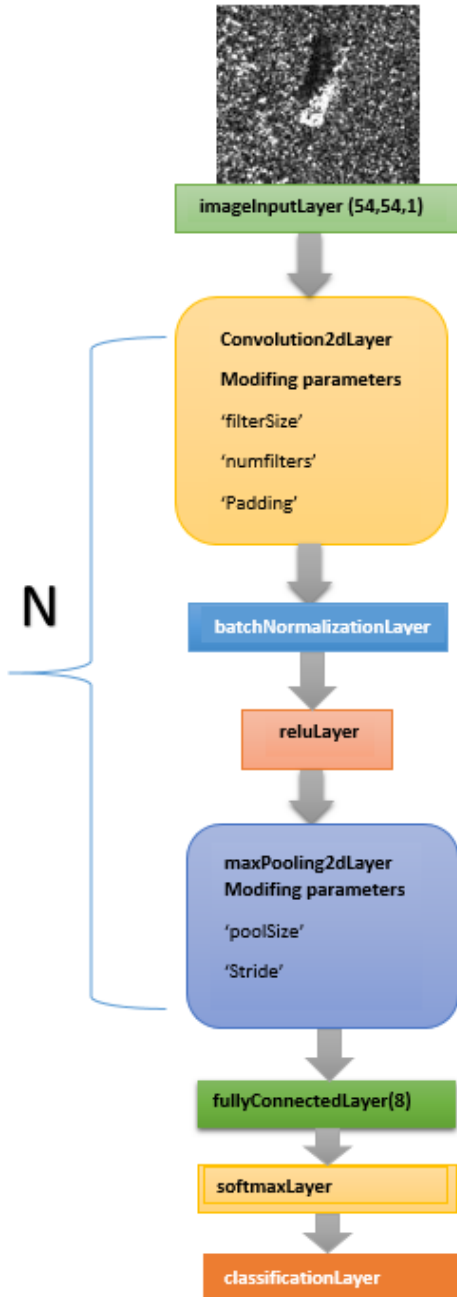
N: number of repeat

Fig. 2 Main block diagram of the proposed method

## 1. Input Layer

It is the first layer of the CNN structure [14]. The data is first adjusted by resizing and then transmitted to the network for processing through this layer. Selecting a low image size reduces the depth of the training while reducing training time. High image size increases the process load and duration, but can increase the success of the network [14]. In this study, the smallest image size of 54x54x1 available in the dataset is selected as the input layer size.

## 2. Convolution Layer

This layer basically filters the input images through the use of convolution kernels composed of parameters to be optimized during the training. Input data features are obtained during this step. The filter size, number of filters (channel size) and padding size are the parameters of this layer. Filters size defines the kernel size, channel size defines the number of different filtering options while padding enables the use of border pixels in the image.

## 3. Batch Normalization Layer

The incoming data is normalized in this layer [15]. It enables non-efficient nonlinear points operable as well as reducing the sensitivity to initial weights.

## 4. ReLU (Rectified Linear Units) Layer

The operations performed in convolution layer are linear. To introduce a non-linear structure ReLU activation function as shown in Fig. 3 is used. This allows the network to take precautions against vanishing gradient problem [16].

$$f(u) = \max(0, u)$$
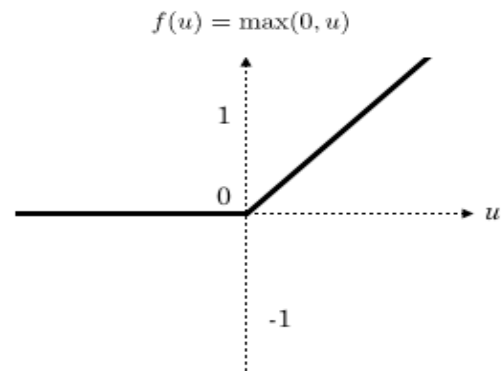


Fig. 3 ReLU Activation Function [17]

## 5. Pooling Layer

It is the layer in which a specific element is picked while all others are eliminated in the sub-matrix of the incoming image. Frequently used pooling methods are *Max pooling, Min Pooling and Mean Pooling to* select the biggest, smallest and mean value in the sub-matrix, respectively. Max pooling technique is used in this study as suggested by [18]. The design parameters of pooling layer are *Pool Size to d*etermine the width and height of the sub-matrix and Stride to define the shift amount to define the sub-matrices.

## 6. Fully Connected Layer

All the previous layers' output represents the high-level properties of the input image, and the purpose of the fully connected layer is to connect each class with each of these properties. Since each of them is used as a connection technique, it is called a fully connected layer [14].

## 7. Softmax Layer

It is the layer that calculates the probability that the input data belongs to any class [17]. The sum of probabilities for

each class must be equal to one. In this study, the softmax function used for an 8-class problem as shown in Fig.4
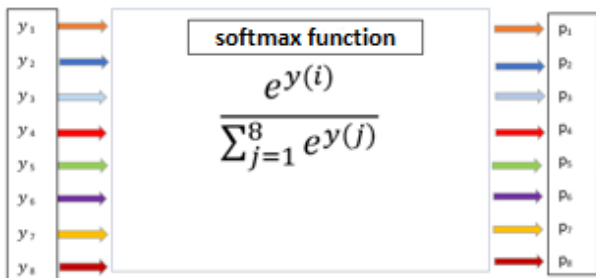


Fig. 4 Softmax Layer

## 8. Classification Layer

It is the layer in which the input data is analyzed according to the probability values from the softmax layer.

In this publication, a 15-layer CNN structure is used.

Details are given in Table 1.

Table 1. CNN structure

|  | Layers | Filter Size | numFilters | Pool Size | Padding | Stride |
|---|---|---|---|---|---|---|
| 1 | Image Input 54x54x1 | | | | | |
| 2 | Convolution | 3x3 | 8 | | same | [1 1] |
| 3 | Batch Normalization | | | | | |
| 4 | ReLU | | | | | |
| 5 | Max Pooling | | | 2x2 | [0 0 0 0] | [2 2] |
| 6 | Convolution | 3x3 | 16 | | same | [1 1] |
| 7 | Batch Normalization | | | | | |
| 8 | ReLU | | | | | |
| 9 | Max Pooling | | | 2x2 | [0 0 0 0] | [2 2] |
| 10 | Convolution | 3x3 | 32 | | same | [1 1] |
| 11 | Batch Normalization | | | | | |
| 12 | ReLU | | | | | |
| 13 | Fully Connected (8) | | | | | |
| 14 | Softmax | | | | | |
| 15 | Classification Output | | | | | |

## III. EXPERIMENTAL WORK

### 1. Dataset

In this study, publicly available MSTAR SAR images are used for classification. These data, owned by U.S Air Force - Sensor Data Management System (SDMS) [19] and published by Sandia National Laboratory, composed of JPEG images with 15, 17, 30 and 45-degree depression angles captured by using 1-foot resolution X-band STARLOS sensor in Spotlight mode. These JPEG files contain the information of 2S1, BDRM-2, BTR-60, D7, SLICY, T62, ZIL-131, ZSU-23-4.

In this study, only 15 and 17-degree depression angles images of targets are blended. The target images come in different numbers and sizes. Some of the images are shown in Fig. 5, and the corresponding details are given Table 2.
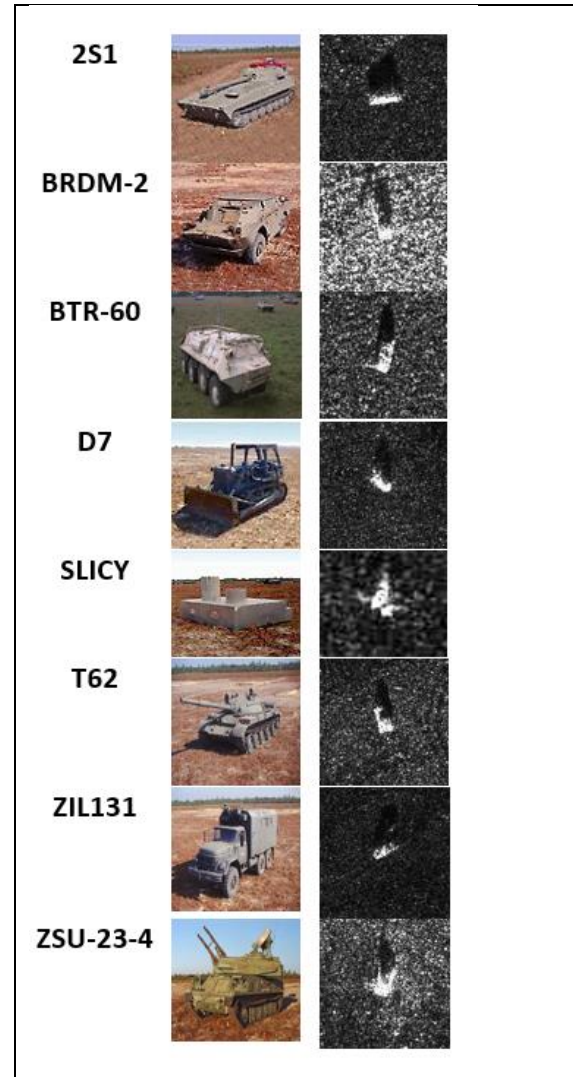


Fig. 5 Visual samples from data [19]

Table 2 Dataset

| Vehicle type | 15 and 17 depression angle | |
|---|---|---|
| | #images | size |
| 2S1 | 573 | 158x158x1 |
| BRDM-2 | 572 | 128x129x1 |
| BTR-60 | 451 | 128x128x1 |
| D7 | 573 | 177x178x1 |
| SLICY | 572 | 54x54x1 |
| T62 | 573 | 172x173x1 |
| ZIL131 | 573 | 192x193x1 |
| ZSU-23-4 | 573 | 158x158x1 |
| **Total** | **4460** | |

### 2. Experimental Results

The experimental results are shown in Table 3.

Table 3. Result Table

| #Epoch | 10 |
|---|---|
| #Epoch Iteration | 5 |
| Random Data Distribution | %70 Train, %10 Validation, %20 Test |
| Optimization Algorithm | Root Mean Square Propagation |
| **Accuracy** | **99.8%** |

For better examination confusion matrix of the proposed method is also given in Table 4.

Table 4. Confusion Matrix



**Confusion Matrix**

| Output Class | 2S1 | $BRDM_2$ | $BTR_60$ | D7 | SLICY | T62 | ZIL131 | $ZSU_23_4$ | |
|---|---|---|---|---|---|---|---|---|---|
| 2S1 | 57 | 0 | 0 | 0 | 0 | 0 | 0 | 0 | 100% |
| $BRDM_2$ | 0 | 57 | 0 | 1 | 0 | 0 | 0 | 0 | 98.3% |
| $BTR_60$ | 0 | 0 | 45 | 0 | 0 | 0 | 0 | 0 | 100% |
| D7 | 0 | 0 | 0 | 56 | 0 | 0 | 0 | 0 | 100% |
| SLICY | 0 | 0 | 0 | 0 | 57 | 0 | 0 | 0 | 100% |
| T62 | 0 | 0 | 0 | 0 | 0 | 57 | 0 | 0 | 100% |
| ZIL131 | 0 | 0 | 0 | 0 | 0 | 0 | 57 | 0 | 100% |
| $ZSU_23_4$ | 0 | 0 | 0 | 0 | 0 | 0 | 0 | 57 | 100% |
| | 100% | 100% | 100% | 98.2% | 100% | 100% | 100% | 100% | 99.8% |

Target Class

## IV. CONCLUSION

In this study, we have presented a method to classify images obtained by SAR using CNN method. Publicly available MSTAR SAR image dataset used for this work, and 99.8% classification accuracy result obtained experimentally for a an eight class problem.

## V. FUTURE WORK

It is aimed to get the most rapid and accurate result by applying different deep learning algorithms on dataset and other databases. In later studies, performance measurements will be performed by applying the Transfer learning methods.

## REFERENCES

[1] D Xiang, T Tang, Y Ban et al., "Unsupervised polarimetric SAR urban area classification based on model-based decomposition with cross scattering", Isprs Journal of Photogrammetry & Remote Sensing, vol. 116, pp. 86-100, 2016.

[2] S. B. Kotsiantis. "Supervised machine learning: A review of classification techniques", Informatica (Slovenia), 31(3):249--268, 2007.

[3] S.J. Russell and P Norvig, "Artificial Intelligence: A Modern Approach " (Prentice Hall, Englewood Cliffs, NJ, 1995).

[4] Christopher M. Bishop,"Pattern Recognition and Machine Learning "(Information Science and Statistics), Springer-Verlag, Berlin, Heidelberg, 2006

[5] Gerstner W. "Supervised learning for neural networks: A tutorial with Java Exercises",Technical Report. Laboratory of Computational Neuroscience at the Swiss Federal Institute of Technology Lausanne. (1998).

[6] A Krizhevsky, I Sutskever, G E. Hinton, "Imagenet classification with deep convolutional neural networks", Advances in neural information processing systems, pp. 1097-1105, 2012.

[7] Sun Yi, Wang Xiaogang, Tang Xiaoou, "Hybrid Deep Learning for Face Verification", IEEE International Conference on Computer Vision, pp. 1489-1496, 2013.

[8] Y Sun, X Wang, X. Tang, "Deep Learning Face Representation by Joint Identification-Verification", Advances in Neural Information Processing Systems, vol. 27, pp. 1988-1996, 2014.

[9] LeCun, Y., Bengio, Y. & Hinton, G. "Deep learning", Nature 521, 436–444 (2015)

[10] O. Abdel-Hamid, L. Deng, D. Yu, "Exploring convolutional neural network structures and optimization techniques for speech recognition", Proceedings of IIVTERSPEECH, pp. 3366-3370, 2013.

[11] S Chen, H Wang, F Xu et al., "Target Classification Using the Deep Convolutional Networks for SAR Images", IEEE Transactions on Geoscience and Remote Sensing, vol. 54, no. 8, pp. 4806-4817, 2016.

[12] L Wang, K A Scott, L Xu et al., "Sea Ice Concentration Estimation During Melt From Dual-Pol SAR Scenes Using Deep Convolutional Neural Networks: A Case Study", IEEE Transactions on Geoscience and Remote Sensing, vol. 54, no. 8, pp. 4524-4533, 2016.

[13] J Geng, J Fan, H Wang et al., "High-Resolution SAR Image Classification via Deep Convolutional Autoencoders", IEEE Geoscience and Remote Sensing Letters, vol. 12, no. 11, pp. 2351-2355, 2015.

[14] İnik, Ö., Ülker, E., "Derin Öğrenme ve Görüntü Analizinde Kullanılan Derin Öğrenme Modelleri", Gaziosmanpasa Journal of Scientific Research, cilt 6, pp. 85-104, 2017.

[15] S. Ioffe and C. Szegedy. "Batch normalization: Accelerating deep network training by reducing internal covariate shift", In ICML, 2015.

[16] Hochreiter, Sepp. "The vanishing gradient problem during learning recurrent neural nets and problem solutions." International Journal of Uncertainty, Fuzziness and Knowledge-Based Systems 6.02 pp. 107-116, 1998

[17] Pauly, L.; Peel, H.; Hogg, D.; Fuentes, R. "Deeper Networks for Pavement Crack Detection", In Proceedings ofthe 34th International Symposium on Automation and Robotics in Construction (ISARC 2017), Taipei, Taiwan,28 June–1 July 2017; pp. 1–7.

[18] Scherer, Dominik, Andreas Müller, and Sven Behnke. "Evaluation of pooling operations in convolutional architectures for object recognition." International Conference on Artificial Neural Networks. Springer Berlin Heidelberg, 2010.

[19] https://www.sdms.afrl.af.mil/index.php?collection=public-data&page=public-data-list

# Detection of Plant Disease From Plant Image

Rabiye Kılıç
Faculty of Engineering,
Department of Electrical and
Electronics Engineering
Atatürk University
Erzurum, Turkey
rabiyaklc0@gmail.com

Hilal Kübra Sağlam
Faculty of Engineering,
Department of Electrical and
Electronics Engineering
Atatürk University
Erzurum, Turkey
hks.erz@gmail.com

Emin Argun Oral
Faculty of Engineering,
Department of Electrical and
Electronics Engineering
Atatürk University
Erzurum, Turkey
eminoral@gmail.com

İbrahim Yücel Özbek
Faculty of Engineering,
Department of Electrical and
Electronics Engineering
Atatürk University
Erzurum, Turkey
iozbek@gmail.com

*Abstract*—**Plants are of great importance in providing ecological balance. They are not only a source of nutrients but also a source of oxygen. Therefore, plants need to be protected. By looking at the appearance of a leaf one can decide what disease it has. With early detection of the disease in plants, excessive damage can be prevented. For this purpose we implemented a method to detect plant diseases from picture of its leaves. This method is based on deep learning classification which is carried out by convolutional neural networks. Various experiments were performed using the PlantVillage database. This database includes 54,305 images for 12 different plants for which there exists one healthy and different number of disease classes each.**

**There is total of 38 classes with 26 different diseases. We obtained 98.47% success rate for the classification of diseases.**

*Keywords*—*Deep Learning, Convolutional Neural Networks, Plant Disease Classification, Deep Learning Algorithms*

## I. INTRODUCTION

Plants are the most important sources of life. Moving these resources to the future in a healthy way is an essential issue in terms of the importance of vital activities. Some plants should be taken under protection and should be included in the life. Therefore, early and accurate detection of the disease in the plant is very important. Diseases in plants can be diagnosed form their leaves. Classification of plant diseases with multiple classes is not an easy task to perform manually or visually in terms of its time cost. For this reason, an automated plant disease classification based on machine learning algorithms is preferred. The computerized vision process gives very good results in the classification and identification problems [1]. Various deep learning algorithms were used to classify plant diseases. The basic deep learning tool used in this work is Convolutional Neural Networks (CNNs) [2-4]. CNNs constitute one of the most powerful techniques for modeling complex processes and performing pattern recognition in applications with large amount of data. A CNN system for the automated recognition of plants based on leaves' images developed a relatively simple and powerful neural network for the successful identification of three different species based on the morphological patterns of leaves' veins [5].

## II. PROPOSED METHOD

CNN is one of the basic structures used in image classification problems. They perform classification by means of passing the input image through various layers. Each layer carries out its task and pass it to the next layer.

In this work, we have implemented a CNN structure using transfer learning based on AlexNet. The Main Block Diagram of our approach is shown in Fig. 1. It is a multi-layered learning structure performing processes on separate layers. These layers and their operations are as follows:

### Convolutional Layer

The given picture is expressed in pixels and converted to matrix form. The filter matrix is step-by-step on the image and the element-by-element multiplication is performed to create a new-filtered matrix.
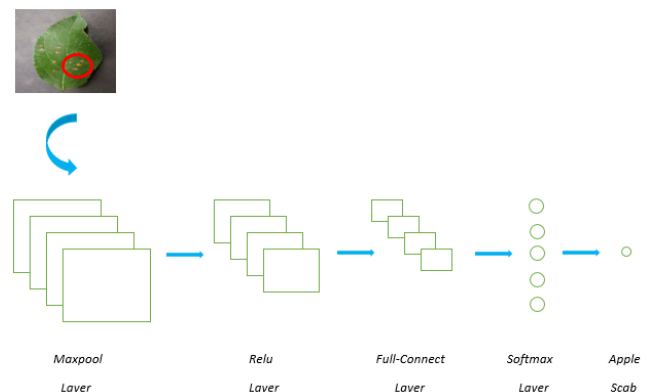


Figure 1. Block Diagram of proposed method

### Maxpool Layer

In this layer after the convolution process, a new matrix is created by moving a blank square matrix over the filtered matrix and taking the largest values.

### Relu (Rectified Linear Unit) Layer

It occurs as the layer in which the activation function takes place. There are many activation functions to be used in this layer. Some of these functions include sine, step, threshold functions.

### Full-Connected Layer

The data in the layer before it is set as a one-dimensional matrix in this layer. Neurons are completely attached to this layer. Each neuron binds to the neuron after it. It is therefore known as a fully bound layer [6].

### Softmax Layer

It takes the values from the previous layer and performs the probability value production in the classification process. Produces a value closer to the class when making the classification. The probability value generated in the layer within the deep learning network makes a probalistic calculation of the probability value for each class. [7].

### Transfer Learning

Alex Krizhevsky is a deep learning algorithm proposed by Ilya Sutskever and Geoffrey Hinton [8].

In this deep convolutional neural network consisting of 25 layers, 5 convolution layers, 3 maxpool layers, 2 dropout layers, 3 full bound layers, 7 relu layers, 2 normalization layers, softmax layer, input and classification (output) layer are formed. . The image to be placed in the input layer measures 227x227x3. In the last layer, the classification number value in the input image is given by classification.

### III. EXPERIMENTAL WORK

#### A. Dataset Description

There are 54,305 images in the PlantVillage database with 38 classes for 12 different plants. 12 classes out of 38 represent the healthy leaves' images while the remaining 26 classes represent various disease images of these 12 plant classes. Some example images are shown in Fig. 2 and Fig. 3 for healthy and non-healthy images, respectively. Database partitioned into three as training, validation and test sets, with ratio of 70%, 10% and 20% of the whole dataset, respectively.
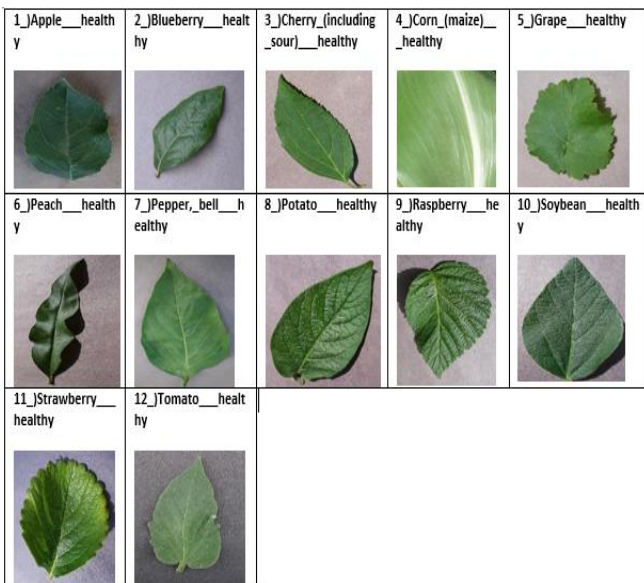


Figure 2. Image of Plant Healthy from dataset
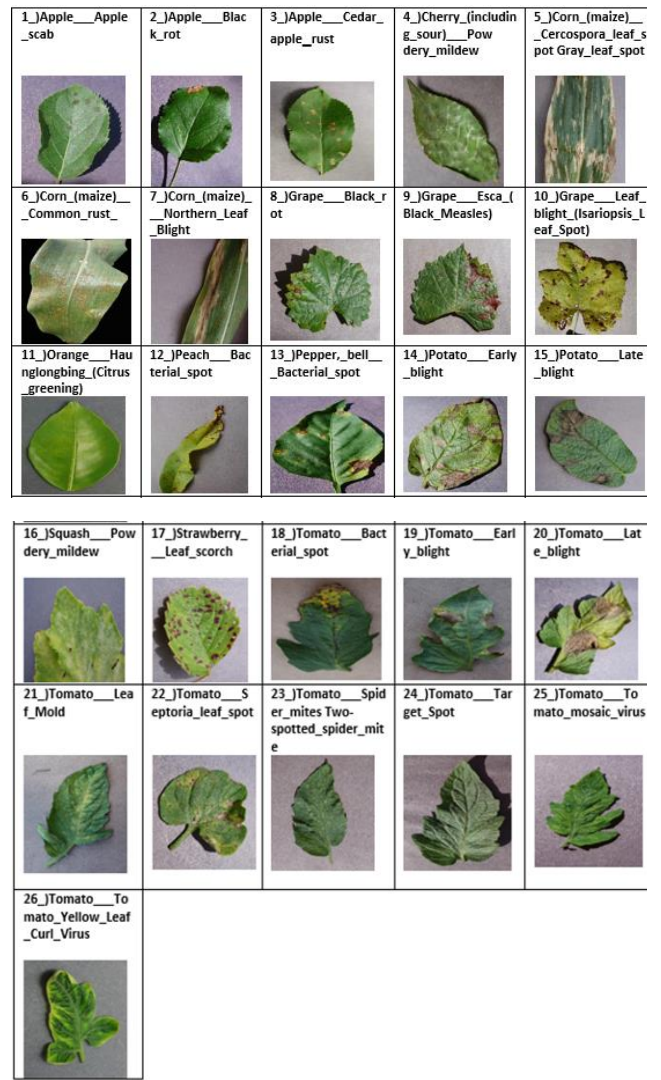


Figure 3. Image of Plant Disease from dataset

#### B. Experimental Result

We have obtained two different experimental results in the study with and without transfer learning. The accuracy of our method without transfer learning is 85.05% while it increased to 98% with the application of transfer learning.

Also, corresponding confusion matrix with transfer learning is given in Fig. 4.

**Figure 4.** Proposed method result is shown by a 38x38 confusion matrix: 12 entries represent the health classes while the remaining 26 represent the plant-diseases classes.

## IV. CONCLUSION

We have proposed a method to detect plant diseases from their images of leaves. This work is based on deep learning classification using convolutional neural networks. Experiments, performed using the PlantVillage database, includes 54,305 images with 26 different diseases classes and 12 healthy plant classes. Based on the experimental results we have obtained classification accuracy of 98.47% for this study.

REFERENCES

[1] Szegedy, C., Ioffe, S., Vanhoucke, V., & Alemi, A. A. (2017, February). Inception-v4, inceptionresnet and the impact of residual connections on learning. In AAAI (Vol. 4, p. 12).

[2] LeCun, Y., Bottou, L., Bengio, Y., Haffner, P., 1998. Gradient-based learning applied to document recognition. Proc. IEEE 86 (11), 2278–2324.

[3] Lee, S.H., Chan, C.S., Wilkin, P., Remagnino, P. 2015. Deep-plant: Plant identification with convolutional neural networks. 2015 IEEE Intl Conf. on Image Processing, pp. 452–456.

[4] Grinblat, G.L., Uzal, L.C., Larese, M.G., Granitto, P.M., 2016. Deep learning for plant identification using vein morphological patterns. Comput. Electron. Agric. 127, 418–424.

[5] Mohanty, S.P., Hughes, D.P., Salathé, M., 2016. Using deep learning for image-based plant disease detection. Front. Plant Sci. 7http://dx.doi.org/10.3389/fpls.2016. 01419. Article: 1419.

[6] Adler, A., Elad, M., & Zibulevsky, M. (2016). Compressed Learning: A Deep Neural Network Approach. arXiv preprint arXiv:1610.09615.

[7] Tang, Y. (2013). Deep learning using linear support vector machines. arXiv preprint arXiv:1306.0239.

[8] Krizhevsky, A., Sutskever, I., & Hinton, G. E. (2012). Imagenet classification with deep convolutional neural networks. In Advances in neural information processing systems (pp. 1097-1105).

[9] Using Deep Learning for Image-Based Plant Disease Detection (Front. Plant Sci., 22 September 2016 )

# The Comparison of Anticandidal Activity derived from Protein and Non-protein Compounds of Two *Penicillium* species

Ayşenur Yazıcı
Department of Molecular Biology and Genetics
Erzurum Technical University
Erzurum / Turkey
aysenur.ozdemir@erzurum.edu.tr

Alpgiray Turgut
Department of Molecular Biology and Genetics
Erzurum Technical University
Erzurum / Turkey
agiraytrgt@gmail.com

Abdul Saltuk Buğra DAŞ
Department of Molecular Biology and Genetics
Erzurum Technical University
Erzurum / Turkey
bugra.das@gmail.com

Serkan Örtücü
Department of Molecular Biology and Genetics
Erzurum Technical University
Erzurum / Turkey
serkan.ortucu@erzurum.edu.tr

Mesut Taşkın
Department of Molecular Biology and Genetics
Atatürk Üniversity
Erzurum / Turkey
mesut.taskin@atauni.edu.tr

*Abstract*— Candidiasis is a fungal infection caused by yeasts that belong to the genus *Candida*. Approximately 20 different *Candida* species are infected in humans. On the other hand, *Penicillium* species are a source of natural antibiotics such as protein and non-protein (secondary metabolite). In this study, it was aimed to compare extracellular, protein and non-protein antimicrobial compounds from *P. brevicompactum* A02 and *P. chrysogenum* A03 isolated from soil against *Candida* species. For this purpose, these species were incubated with yeast peptone glucose medium for 7 days at 25 °C, 150 rpm. Then, the culture filtrates were treated with trypsin / proteinase K enzymes and it was compared with non-treated culture filtrate. As a test organism, *Candida albicans* (ATCC 10231) and non-albicans species (*C. dubliniensis* CBS 7987, *C. glabrata* ATCC 2001, *C. parapsilosis* ATCC22019 and *C. tropicalis* KUEN 1025) were used. As a result, the source of anticandidal activity for *P. chrysogenum* was proteins however, for *P. brevicompactum* was derived from secondary metabolite. This work was supported by the Erzurum Technical University Research Foundation (ETU-BAP: 2017-15).

Keywords— *Penicillium* spp, Candidiasis, Antimicrobial, Protein

## I. INTRODUCTION

Candidiasis is a fungal infection caused by yeasts that belong to the genus *Candida*. Approximately 20 different *Candida* species are infected in humans (1). Effects of candidiasis vary depending on the area of the body that is infected such as thrush in the mouth, frequent vaginal discharge in women and weakening of the immune system (2).

Destruction of bacteria in the body due to the use of the wrong antibiotic leads to the development of the C*andida* species. *C. albicans* is the most important cause of the candidosis. However, in recent years there has also been an increase in candidiasis caused by non-albicans species. Mechanisms of resistance to antibiotics developing in microorganisms require the screening of new generation antibiotics (2).

Anticandidal activity may be caused by protein or non-protein metabolites (secondary metabolites). In recent years, studies on proteins with antimicrobial properties have increased especially in bacterial infections (3). In this study, two types of *Penicillium* spp. with anticandidal activity were used. We investigated the molecules contains anticandidal activity of these two isolates.

## II. MATERIALS and METHODS

### A. Materials

Chemicals were purchased from Sigma Aldrich (St Louis, MO, USA). This study was conducted in Molecular Microbiology Laboratory in Erzurum Technical University (Erzurum, Turkey).

### B. Methods

1. Culture and Growth Condition of *Penicillium* spp: *P. brevicompactum* A02 and *P. chrysogenum* A03 were isolated from soil. These filamentous fungi were cultured in yeast peptone glucose agar medium (10 g/L yeast extract, 20 g/L peptone, 20 g/L D-glucose, 15 g/L agar with pH: 6,2) for 7 days at 25°C.

2. Molecular Identification of Fungi: DNA isolation was performed with Mobio DNA extraction kit. For amplification of ITS1, 5S and ITS2 regions, universal primers ITS1 (5′TCC GTA GGT GAA CCT TGC GG 3′) and ITS4 (5′TCC TCC GCT TAT TGA TAT GC 3′) were used. Polymerase chain reaction (PCR) reaction was carried out according to the condition in the previous articles (4). Briefly, PCR mix was prepared with 0,5 µM of each primer, 10 µM deoxynucleotides, 2 mM MgCl2 and 10x buffer (Sigma). PCR conditions were; initial denaturation at 95 °C, 35 cycles of denaturing at 94°C for 1 min;

annealing at 55,2°C for 2 min and extension at 72°C for 3 min; and final extension at 72°for 10 min for termal cycler (qiagen).

3. Candida Spp.: To determine anticandidal activity *Candida albicans* (ATCC 10231) and non-albicans species (*Candida dubliniensis* CBS 7987, *C. glabrata* ATCC 2001, *C. parapsilosis* ATCC22019 and *C. tropicalis* KUEN 1025) were used. Candida spp. were grown on potato dextrose agar (PDA) medium at 30°C.

4. Screening Anticandidal Activity: Two *Penicillium* spp. were cultured in yeast peptone glucose broth medium for 7 days at 25 °C, 150 rpm. Then, the culture filtrates were treated with trypsin / proteinase K (10 mg/ml) enzymes for 6 hours at 37 °C [5].

5. Agar Diffusion Assay: Anticandidal activity was determined with well diffusion assay. Briefly, 6 mm hole opened on PDA plate and 100 µL trypsin / proteinase K treated culture filtrate and 100 µL non-treated culture filtrate were added in the hole. After incubation 30 °C at 24 hours, clear zone was observed.

## III. RESULTS

In the screening of filamentous fungi isolated from soil, two filamentous fungi were determined to be the anticandidal molecule producer. In classical analysis, it was found that these two species belonged to the genus of *Penicillium*. To determine anticandidal activity, we used extracellular culture medium of these species and both species show anticandidal activity shown in Table1 and 2.

PCR is done for molecular characterization and sequence chromatograms were assembled into one complete sequence and the sequence was compared to all known sequences in the Genbank by use of BLASTN 2.2.26+ program and the isolates were identified as *P. brevicompactum* A02 and *P. chrysogenum* A03.

Table I: Agar Diffusion Assay Results for *C. albicans*

| Anticandidal Activity for *C. albicans* (mm: millimeter) | | |
|---|---|---|
| *P. brevicompactum* | 22 | |
| *P. chrysogenum* | 15 | |

Table II: Agar Diffusion Assay Results for non- *albicans spp.*

| Anticandidal Activity for *Non -albicans* (mm: millimeter) | | |
|---|---|---|
| | *P. brevicompactum* | *P. chrysogenum* |
| *C. dubliniensis* | 25 | 12 |
| *C. parapsilosis* | 24 | 15 |
| *C. glabrata* | 24 | 14 |
| *C. tropicalis* | 24 | 14 |

Culture filtrates of *P. brevicompactum* and *P. chrysogenum* were treated with proteolytic enzymes to determine whether the anticandidal activity was protein-induced or not. Protein-induced anticandidal activity should be reduced or terminated after proteolytic cleavage.

Comparison of the results with agar diffusion test revealed that *P. brevicompactum* has anticandidal activity derived from a non-protein (secondary metabolite). However, *P. chrysogenum* has protein induced anticandidal activity. These results shown in figure 1.
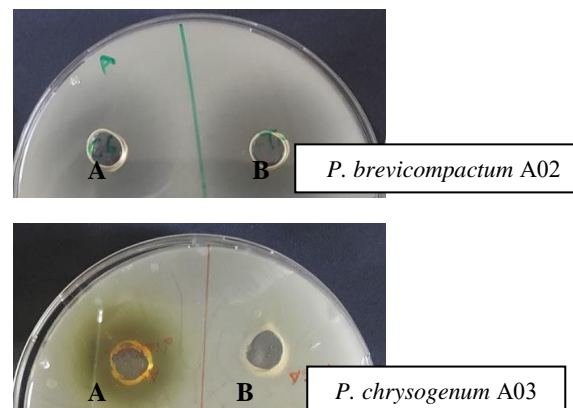


Figure 1: Agar diffusion assay for *C. albicans*. A. Culture filtrate B. Culture filtrates were treated with trypsin / proteinase K.

## IV. DISCUSSION

Filamentous fungi, especially *Penicillium* species, are the best sources of antimicrobial molecules. *P. chrysogenum* is known penicillin producer (6). In this study our isolate, *P. chrysogenum* A03, only produce antimicrobial protein. This situation may be due to the conditions which this isolate is grown and media composition.

*P. brevicompactum* is compactin producer. Compactin is antifungal metabolite. At the same time, *P. brevicompactum* is also the source of metabolites in many different pathways (7).

Today, the efficacy of anticandidal molecules used in various infections caused by *Candida* spp. is discussed (2). In our study, anticandidal activity from metabolite appears more effective shown in Table 1 and 2. However, anticandidal activity and toxicity studies of the two isolated species should be completed.

### Acknowledgement

### REFERENCES

[1] Abi-Said, D., Anaissie, E., Uzun, O., Raad, I., Pinzcowski, H., & Vartivarian, S "The epidemiology of hematogenous candidiasis caused by different Candida species." Clinical Infectious Diseases, 1997, 24(6), 1122-1128.

[2] Seyedmousavi, S., İlkit, M., Durdu, M., Ergin, Ç., Hilmioğlu-Polat, S., Melchers, "Candida ve Kandidoz: Epidemiyoloji, Tanı, Tedavi, Antifungal İlaç Direnci ve Konağın Genetik Yatkınlığında Güncel Durum". 2015, 45(1):1-11, 2015.

[3] Pollock, J. J., Denepitiya, L., MacKay, B. J., & Iacono, V. J. (1984). Fungistatic and fungicidal activity of human parotid salivary histidine-rich polypeptides on Candida albicans. Infection and immunity, 44(3), 702-707.

[4] Schilling, A. G., Moller, E. M., & Geiger, H. H. Polymerase chain reaction-based assays for species-specific detection of Fusarium culmorum, F. graminearum, and F. avenaceum. 1997 Phytopathology, 86(5), 515-522.

[5] Dusane, D. H., Damare, S. R., Nancharaiah, Y. V., Ramaiah, N., Venugopalan, V. P., Kumar, A. R., & Zinjarde, S. S. Disruption of

microbial biofilms by an extracellular protein isolated from epibiotic tropical marine strain of Bacillus licheniformis. 2013, PLoS One, 8(5), e64501.

[6] Huber, A., Hajdu, D., Bratschun-Khan, D., Gȧspȧri, Z., Varbanov, M., Philippot, S., ... & Galgóczy, L. New antimicrobial potential and structural properties of PAFB: a cationic, cysteine-rich protein from Penicillium chrysogenum Q176. 2018, Scientific reports, 8(1), 1751.

[7] Allan G. Brown, Terry C. Smale, Trevor J. King, Rainer Hasenkamp and Ronald H. Thompson, Crystal and molecular structure of compactin, a new antifungal metabolite from Penicillium brevicompactum, J. Chem. Soc., Perkin Trans. 1, 1976,0, 1165-1170.

# Synthesis and Characterization of Rgo/Tio2/Peg Nanocomposite

Derya Tekin
Metallurgical and Materials
Engineering
Ataturk University
Erzurum,TURKEY
deryatekin@atauni.edu.tr

Derya Birhan
Metallurgical and Materials
Engineering
Ataturk University
Erzurum,TURKEY
deryacirhan38@gmail.com

Taner Tekin
Chemical Engineering
Ataturk University
Erzurum,TURKEY
ttekin@atauni.edu.tr

*Abstract*-**Polyethylene glycol (PEG) is a covalent modification of biological macromolecules and a highly suitable polymer for surfaces in many biotechnical applications. The graphene oxide (GO) layer is designed to stabilize the shape of the phase change material studied for thermal storage of polyethylene glycol (PEG) during the solid-liquid phase change. Graphene oxide, which is the most remarkable support material of recent times, is widely used in polymer matrix because it supports thermal and structural properties. The $TiO_2$ semiconductor photocatalyst has been used in many applications to improve the photocatalytic process. However, its wide band-gap range is the biggest disadvantage of $TiO_2$. It is intended to improve the properties of both polymer matrix and semiconductor photocatalyst using graphene oxide as support material.**

**For this purpose; RGO-$TiO_2$-PEG nanocomposite structure was synthesized by using the solution casting technique and thermal, antibacterial and photocatalytic activities were investigated.**

*Keywords*- Polyethylene glycol(PEG), $TiO_2$, reduce graphene oxide(rGO), nanocomposite

## I. INTRODUCTION

For the last few years, the synthesis of thin film hybrid materials consisting of both organic layer and oxide layer has been developed with the aim of producing surfaces with special by-products. Such developed hybrid materials are known to have good thermal properties and high chemical stability for sensor applications for the detection of contaminants in thermoelectric applications or at very low concentrations of water samples(Drevet, Dragoé et al. 2016). Polymer nanoparticles have been found to have superior properties in terms of electrical, mechanical and thermal properties compared to conventional polymer types(Feng, Yin et al. 2013). In general, polymer composites consist of two or more components and two or more phases. The filling materials added in the polymer matrix allow the composite structure to have the desired properties by filling a certain volume within the structure(Szeluga, Kumanek et al. 2015). In general, composite materials consist of metal-nonmetal or organic-inorganic materials. Polymers are used as organic materials, and inorganic materials are used as semiconductor photocatalysts such as $TiO_2$, $WO_3$, CdS, ZnS, GaN, ZnO, $In_2O_3$ and $BiVO_4$. As the $TiO_2$ from the semiconductor photocatalysts exhibits excellent biocompatibility, high chemistry and unique photocatalytic properties, $TiO_2$ has become an indispensable structure for many applications. $TiO_2$, which is used in the photo-catalytic process, is widely used for the purpose of eliminating the toxic and undesirable organic components, the removal of waste water, the removal

of dyes, the destruction of harmful bacteria and cancerous cells(Naghibi, Hosseini et al. 2014). $TiO_2$ is a transition metal oxide chemically inert and stable. anatase, rutile and broxite have three different crystal structure. The anatase phase of $TiO_2$ is much more photoactive than the rutile phase, because the surface area of the anatase is larger than the rutile. The preparation of a semiconductor thin film is the easiest way to facilitate semiconductor applications as a solar cell and photocatalyst in the degradation of harmful chemical compounds(Ritonga, Faiqoh et al. 2015). Recently, $TiO_2$ nanoparticles with excellent photocatalytic properties have been prepared and the biological applications of titanium dioxide nanoparticles prepared due to the excellent properties of these TNPs (titanium nanoparticles) are modified with biocompatible polymers. Polyethylene glycol (PEG) is a type of polymer that functionalizes the $TiO_2$ surface. Ethylene glycol (EG) is known as repeating units in polyethylene glycol. PEG has superior safety record and is widely used in biotechnology, medicine(Rahim, Ghamsari et al. 2012). Polyethyleneglycol (PEG) is promising in the production of shape-memory materials with molecular weight due to their desirable properties such as high phase change enthalpy, chemical and thermal stability, biodegradable, toxic and non-corrosive low vapor pressure and adjustable suitable melting temperature. However, the leakage of the liquid phase above the melting temperature Tm is the feedback of the PEG required to encapsulate containers, in particular marine-controlled(Qi, Liang et al. 2014). In recent years, graphene-based polymer nanocomposites have been combined to produce high value-added materials that combine the advantageous properties of the two components(Roussou and Karatasos 2016). Graphene has emerged as a 2D dimensional material with superior physical properties. Graphene is actively being researched for potential applications to affect quantum physics, nanoelectronic devices, transparent conductors and nanocomposites(Liu, Robinson et al. 2008). The graphene history is a highly conjugated, two-dimensional and monatomic nanocarbon material dating back to 1859. High Young's Modulus (~ 1100 GPa), high fracture strength (~ 12GPa), excellent electrical properties (~ 106S / cm), thermal conductivity (~ 5000W / mK), rapid mobility of load carriers (~ 200.000cm2 / Vs) and excellent features such as the original surface area(Ji, Xu et al. 2016). However, due to its oxygen functionality, it provides weak electronic conductivity. It is therefore intended to reduce the graphene oxide to increase the electrical conductivity by using reducing agents such as $N_2H_4$ and $NaBH_4$, which are not very

environmentally friendly, or by refluxing GO in DMF and to repair the hybrid network of GO(Xiao, Guo et al. 2016).

In this study, rGO-TiO$_2$-PEG structure was synthesized by supporting polymer matrix and semiconductor photocatalyst rGO. Investigation of the thermal, antibacterial, photocatalytic activity of the composite structure and the improvement of the rGO on the structure is aimed.

## III. MATERIAL AND METHOD

### a. Materials

Graphite Powders(powder<45μm≥99.99%), Sulfuric acid (H$_2$SO$_4$,95-97%), Sodium Nitrate(NaNO$_3$), Potassium Permanganate(KMNO$_4$), TiO$_2$ nanoparticles, **:** Polyethylene glycol (PEG, wt 8.000 powder) , Hydrogen peroxide (H$_2$O$_2$, %30).

### b. Synthesis of Graphene Oxide

Graphene oxide graphite powder is synthesized according to the Hummer method. First 69 ml of sulfuric acid, 3 *g* of graphite powder, 1.5 *g* of NaNO3 were mixed in a 250 ml erlene. The solution was then placed in an ice bath to cool the temperature to 0 ° C. After the temperature dropped to 0 ° C, 9 *g* of potassium permanganate (3/3/3) was added to the solution. After the addition of potassium permanganate, the solution was removed from the ice bath and put on hold to allow the temperature to rise to room temperature. Then, 138 ml of ionized water was added and the mixture was stirred at 98 ° C for 15 minutes, then 480 ml of water was added and 30% H$_2$O$_2$ was added dropwise to oxidize the brown color to yellow. The resulting graphene oxide was washed several times with ethanol and ionized water to provide pH balance. The final stage is filtered and kept in a 60 ° C oven until it is completely dry.

### c. rGO Synthesis

0.8 *g* of GO powders were dissolved in 400 ml of DMF under ultrasonication for 6 h. After 6 hours of treatment, the rGO powders were filtered, washed with ethanol and water and dried in an oven at 60 ° C.

### d. rGO-TiO$_2$ Synthesis of Nanocomposite Structure

0.1 *g* of rGO powder was mixed with 10 ml of ethanol and 20 ml of water and subjected to sonication for 1 hour. At the end of 1 hour of treatment, TiO$_2$ nanoposicles in the form of 0.2 *g* of anatase were added to the rGO solution and the solution was poured into petri dishes and dried in an oven at 60 °C. Finally, rGO-TiO$_2$ nano-powders were obtained.

### e. Synthesis of rGO-TiO$_2$-PEG Nanocomposite Structure

1*g* Polyethylene glycol (PEG) is dissolved in 10 ml of ionized water at room temperature for 1 h by stirring magnetically in PEG water. In the second stage, 0.1 *g* of rGO-TiO$_2$ structure was sonicated for 20 minutes in 20 ml of ionized water. At the end of the mixing, rGO-TiO$_2$ structure was added dropwise to the PEG solution and after stirring for 1h at room temperature, poured into a petri dish and dried at 60°C. to give rGO-TiO$_2$-PEG nano-powders.

### f. Characterization Techniques

Wide-angle X-ray diffraction(XRD) pattern of the samples was obtained under Cu-Kα radiation (Λ=0.154 nm) under a voltage of 40kV and a current of 40 mA. Samples were scanned in the range of diffraction angle 2Θ=2°-45° with a scan speed of 3°/min at room temperature. A SEM device was used to examine the structural properties of rGO/TiO$_2$/PEG nanopowders

## IV. RESULTS

### a. . XRD Analysis

It was observed that rGO / TiO$_2$ / PEG nanocomposites yielded the diffraction peak of rGO at 2 Θ = 10.281 in XRD graphs. However, after dispersing in the rGO PEG matrix, XRD peaks of rGO / TiO$_2$ / PEG nanocomposites showed PEG diffraction peaks. The break peaks of rGO disappeared, suggesting that the crystallization of nanocomposites is well protected, sufficiently flaking, and that the GO layers are homogeneously distributed(Qi, Liang et al. 2014).

### b. SEM Analysis

The morphologies of the PEG/rGO/TiO$_2$ composites are characterized by TEM and SEM.

The physicochemical properties of the nanocomposite obtained by the presence of TiO$_2$ rGO which was used as PEG matrix and photocatalyst was determined. Accordingly, a dense and tightened layer was formed by the addition of rGO into the matrix(Mansourpanah, Shahebrahimi et al. 2015). It was observed that there was no phase separation in PEG matrix and PEG chain was mixed well with rGO plates(Xiong, Chen et al. 2015).

## V. CONCLUSION

TiO$_2$ nanoparticles in the anatase form were synthesized using PEG storage material and supplemented with rGO using rGO / TiO$_2$ / PEG nanocomposite solution casting technique. PEG has been shown to affect the sol-gel reaction and crystallization process of TiO$_2$ nanoparticles. To ensure a good size distribution of the polyethylene glycol, it must first be dissolved in ionized water, as it is due to the fact that the PEG is a surface-active substance, thus preventing the formation of TiO$_2$ nanoparticles on the surface.

In this study, the wide band-gap range of TiO$_2$, which is a semiconductor photocatalyst using rGO support material, has been reduced, used as rGO support material for energy absorption and photo-thermal energy conversion.

## REFERENCES

[1] Drevet, R., D. Dragoé, M. Barthés-Labrousse, A. Chaussé and M. Andrieux (2016). "XPS-nanocharacterization of organic layers electrochemically grafted on the surface of SnO$_2$ thin films to produce a new hybrid material coating." Applied Surface Science **384**: 442-448.

[2] Feng, Y., J. Yin, M. Chen, M. Song, B. Su and Q. Lei (2013). "Effect of nano-TiO$_2$ on the polarization process of polyimide/TiO$_2$ composites." Materials Letters **96**: 113-116.

[3] Ji, X., Y. Xu, W. Zhang, L. Cui and J. Liu (2016). "Review of functionalization, structure and properties

of graphene/polymer composite fibers." <u>Composites Part A: Applied Science and Manufacturing</u> **87**: 29-45.

[4] Liu, Z., J. T. Robinson, X. Sun and H. Dai (2008). "PEGylated nanographene oxide for delivery of water-insoluble cancer drugs." <u>Journal of the American Chemical Society</u> **130**(33): 10876-10877.

[5] Mansourpanah, Y., H. Shahebrahimi and E. Kolvari (2015). "PEG-modified GO nanosheets, a desired additive to increase the rejection and antifouling characteristics of polyamide thin layer membranes." <u>Chemical Engineering Research and Design</u> **104**: 530-540.

[6] Naghibi, S., H. R. M. Hosseini, M. A. F. Sani, M. A. Shokrgozar and M. Mehrjoo (2014). "Mortality response of folate receptor-activated, PEG–functionalized $TiO_2$ nanoparticles for doxorubicin loading with and without ultraviolet irradiation." <u>Ceramics International</u> **40**(4): 5481-5488.

[7] Qi, G.-Q., C.-L. Liang, R.-Y. Bao, Z.-Y. Liu, W. Yang, B.-H. Xie and M.-B. Yang (2014). "Polyethylene glycol based shape-stabilized phase change material for thermal energy storage with ultra-low content of graphene oxide." <u>Solar Energy Materials and Solar Cells</u> **123**: 171-177.

[8] Rahim, S., M. S. Ghamsari and S. Radiman (2012). "Surface modification of titanium oxide nanocrystals with PEG." <u>Scientia Iranica</u> **19**(3): 948-953.

[9] Ritonga, H., C. E. Faiqoh, D. Wibowo and M. Nurdin (2015). "Preparation of $TiO_2$-PEG Thin Film on Hydrophility Performance and Photocurrent Response." <u>Biosciences Biotechnology Research Asia</u> **12**(3): 1985-1189.

[10] Roussou, R.-E. and K. Karatasos (2016). "Graphene/poly (ethylene glycol) nanocomposites as studied by molecular dynamics simulations." <u>Materials & Design</u> **97**: 163-174.

[11] Szeluga, U., B. Kumanek and B. Trzebicka (2015). "Synergy in hybrid polymer/nanocarbon composites. A review." <u>Composites Part A: Applied Science and Manufacturing</u> **73**: 204-231.

[12] Xiao, H., W. Guo, B. Sun, M. Pei and G. Zhou (2016). "Mesoporous $TiO_2$ and Co-doped $TiO_2$ nanotubes/reduced graphene oxide composites as electrodes for supercapacitors." <u>Electrochimica Acta</u> **190**: 104-117.

[13] Xiong, W., Y. Chen, M. Hao, L. Zhang, T. Mei, J. Wang, J. Li and X. Wang (2015). "Facile synthesis of PEG based shape-stabilized phase change materials and their photo-thermal energy conversion." <u>Applied Thermal Engineering</u> **91**: 630-637.

# Energy Analysis of Asphalt Plants

Kenan Yakut
Ataturk University
Engineering Faculty
Mechanical Engineering
Erzurum, TURKEY
kyakut@atauni.edu.tr

Özer Kaya
Ataturk University
Engineering Faculty
Mechanical Engineering
Erzurum, TURKEY
ozerkaya_81@hotmail.com

Muhammet Harun Osta
Ataturk University
Engineering Faculty
Mechanical Engineering
Erzurum, TURKEY
harun.osta@atauni.edu.tr

Ahmet Numan Özakin
Ataturk University
Engineering Faculty
Mechanical Engineering
Erzurum, TURKEY
ahmet.ozakin@atauni.edu.tr

*Abstract*: **Although there are many components of the road construction the asphalt which is the showcase part of the work is always more privileged. Asphalt, the top layer of the road, is manufactured in asphalt plants as an industrial product with its recyclability. Asphalt plants are being modernized every day with technology indexed. In addition to this modernization, renewable energy use, recycling and energy saving issues are now frequently mentioned. In these matters, the social state has a duty to set an example and guide to society. In this context, a detailed energy study was carried out as the first step for energy saving in the Asphalt Plant of the 18th Regional Directorate of Highways (Kars).**

**In the scope of the study, flue gas analyzes were performed for hot oil boiler and dryer unit. In addition, energy losses were calculated via thermal imaging for hot oil boiler and dryer unit. The operating characteristics of the electric motors in the plant have been determined by energy analyzers. As a result, according to the average energy consumption and cost data of the years 2015-2016, the total energy input of the asphalt plant, including heat and electricity energy, was calculated as 8.167.967.585,79 kcal and the energy loss was calculated as 1.111.395.999,56 kcal. This amount of energy loss corresponds to approximately 15%.**

*Keywords: Asphalt plant, flue gas, energy consumption, energy*

## I. INTRODUCTION

Energy analysis; It is the first and most important step of an effective energy management in order to minimize energy costs and achieve energy efficiency. In our country, the legal infrastructure has been prepared by the Energy Efficiency Law No. 5627 published in the Official Gazette dated 02/05/2007 and numbered 26510 and by the Regulation on Increasing the Efficiency in the Use of Energy Resources and Energy published in the Official Gazette dated 27/10/2011 and numbered 28097. Related to the subject; Özsoy (1997) examined an asphalt storage facility with a thermal oil boiler of 750.000 kcal/h having heat capacity. The time required for the heating of the AC150-200 bitumen stored in tanks to 150 ºC was calculated as 31 hours[1]. Yonar (2007) compared the production stages, performance and capacities of asphalt plants used in road superstructure studies. As a result of this comparison, the weighted asphalt plants are more advantageous in terms of feeding, mixing and storing the mixture compared to continuous type asphalt plants[2]. Rodriguez-Alloza et al. (2015) stated that warm mix asphalt has recently been instead of hot mix asphalt, and the warm mixture is carried out by adding organic or chemical additives to the bitumen asphalt or by water based emission applications. In this study, the benefits of bitumen in terms of fuel savings, emissions and environmental impacts are stated due to be heated at 30-40ºC lower temperatures instead of 160-170ºC, which is the regime temperature value[3]. Huchet et al. (2016) investigated the effects of the thermophysical parameters of the asphalt plant on the asphalt components in the drier unit of a drum-mix asphalt plant. In the drying unit, both the drying of the aggregate and the bitumen spraying are carried out. In this study, the effects of the thermophysical events in the drier were investigated with the temperature sensors placed on the drier unit, the hot mix asphalt, the warm mixture asphalt and the hot mix asphalt products with 20% recycled asphalt[4]. Sivilevičius et al. (2017), using mathematical programming techniques to determine the optimum content of the components of the asphalt mixture has revealed various algorithms. These principles are based on three basic principles of these principles; minimum bitumen content, low cost of aggregate, technological requirements for the production of asphalt mixture[5].

Within the scope of this study, the related Asphalt Plant and its units were briefly given and the energy consumption and costs of 2015 and 2016 were presented as data. In addition, consumption and cost information is supported by graphs. It has been determined that the energy consumption in the asphalt plant is realized under the headings of electricity and heat energy. The heat energy was obtained by burning liquefied natural gas (LNG) in the burner. In the light of this information, the energy consumption of each unit in the asphalt plant was examined and energy losses were calculated by making detailed measurements in the units where energy was consumed extensively.

## II. MATERIAL AND METHOD

### A. *Investigation of Industrial Plants Energy Consumption*

Energy consumption of the facility was evaluated as electricity and LNG. In 2015, 794,14 TEP energy was consumed and a cost of TL 1,577,371,67 was generated. In 2016, 653.63 TEP energy was consumed and a cost of 1.226.257.56 TL was realized.
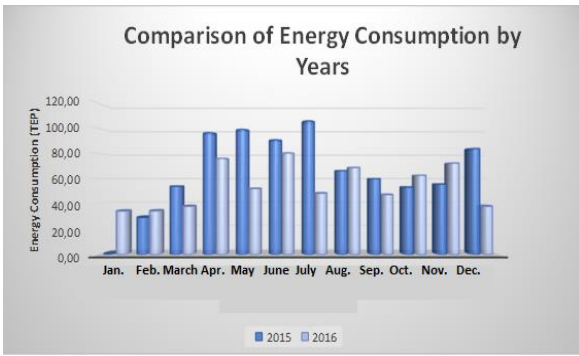
Figure 1. Comparative graph of energy consumption in 2015 and 2016

When energy consumption is analyzed, there is an increase and decrease in 2016 compared to 2015. Here, it is clear that the change in production amounts has an effect. The units with intensive energy consumption are as follows.

• Hot Oil Boiler: The facility has 3 pieces of 50 tons capacity Bitumen tank, 2 units of 50 Sm³ capacity LNG tank and a 500,000 kcal/h thermal oil boiler with the capacity to increase the bitumen to the desired temperature during the production. The superheated oil boiler is used to increase the bitumen to 150-170 $^0$C set values before the production starts.



Figure 2. Hot oil boiler.

• Dryer Unit: It is the unit in which the aggregates are taken from the cold aggregate silos in desired size and weight. The drier unit is a cylindrical industrial oven with a diameter of 2000 mm and a length of 8000 mm. The outer surface of the dryer unit is covered with a 100 mm thick insulation material (stone wool) and the vanes are placed to mix the aggregates. The dryer unit is mounted with an angle of 5% (slope) to transport the aggregates to the hot aggregate elevator.

The dryer unit is rotated around its axis by rotating drums with an electric motor drive of four points 11 kW. By the flame obtained from the burner in the outlet of the dryer unit, the aggregates are dried and brought to the desired temperature value. When the dryer unit is poured into the inlet port, the gases formed by the combustion of the dust and burner are vacuumed by the filter fan and sent to the filter by the dirty gas channel located at the top of the inlet.120 tons per hour plant, 5% according to humidity rate max. It has an industrial type burner with a heat capacity of 9,974,208,00 kcal/h. The capacity of the dryer burner fan electric motor is 18.5 kW.



Figure 3. Dryer unit.

Table 1. Technical characteristics of the dryer unit and burner

| Technical Spesifications | |
|---|---|
| Length of the dryer (mm) | 8.000 |
| Diameter of dryer (mm) | 2.000 |
| Dryer burner brand and model | Baltur TS 36N-D ME/L |
| Constructor burner capacity Min-Max (kW) | 4800-11600 |
| Desiccant burner fan motor (kW) | 18,50 |

• Electric Motors: Electricity consumption at the asphalt plant was carried out; superheated oil pump in the hot oil boiler room, flat belt and inclined belt electric motors, dryer burner fan and dryers rotating motors, mixer reducer motors, chimney fan and drive motor of asphalt pump. Images of electric motors in the asphalt plant are presented in Figure 4.



Figure 4. Electric motors in asphalt plant

One of the important points to be taken into consideration in the energy consumption of electric motors is the analysis of the speed control to the motors operating at long and variable load. Table 2 shows the power and efficiency information of the electric motors in the asphalt plant.

Table 2. Power and efficiency data of electric motors in asphalt plant

| Portion | Quantitiy | Power (kW) | Speed Cont. | Eff. Class |
|---|---|---|---|---|
| Cold Silo Six Flat Tape Elect. Engine | 4 | 3 | Available | EFF2 |
| Inclined Belt Electric Motor | 1 | 4 | Unavailable | EFF2 |
| Filter Flue Outlet Fan Motor | 1 | 75 | Unavailable | EFF2 |
| Burner Fan Motor | 1 | 18,5 | Unavailable | EFF2 |
| Asphalt Pump | 1 | 7,5 | Unavailable | EFF2 |
| Dryer Rotary Motor | 4 | 11 | Unavailable | EFF1 |
| Mixer Motor | 2 | 30 | Unavailable | EFF2 |
| Elavator Electric Motor | 1 | 18,5 | Unavailable | EFF2 |

*B. Research Findings and Discussion*

It has been determined that the heat losses in the asphalt plant are intensely realized in the hot oil boiler and dryer unit. Measurements were made to obtain the heat losses from the unit surfaces in order to calculate the combustion efficiency of the hot oil boiler and dryer unit. In Fig. 2, the hot oil boiler and in Fig. 3, thermal camera images of the dryer unit are included.
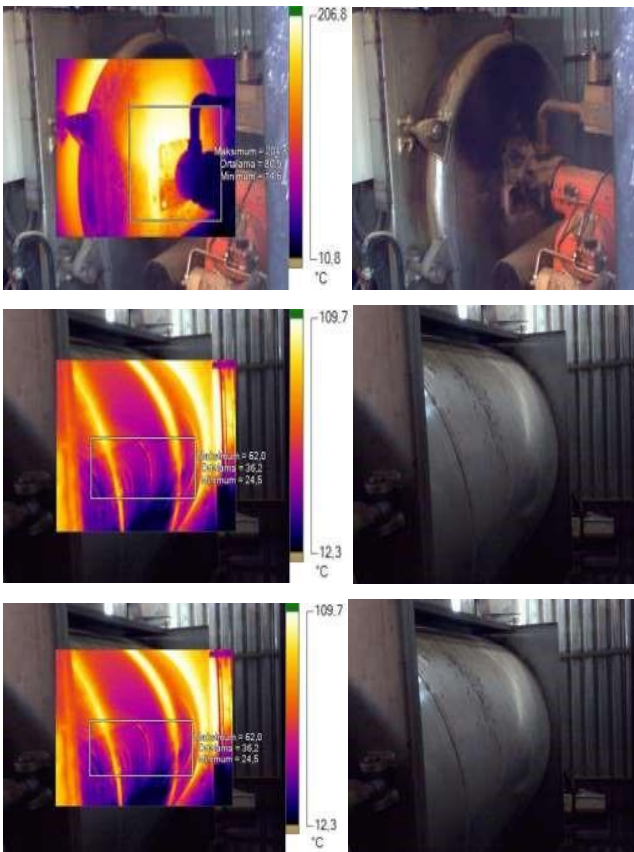


Figure 5. Surface thermal imaging of hot oil boiler.



Figure 6. Surface thermal imaging of drying unit.

The exhaust gas emission values resulting from combustion in the hot oil boiler and dryer unit are important parameters used to calculate the combustion efficiency of the unit. At this point, the combustion efficiency can be obtained with the calculations to be made depending on the values taken from the chimneys. In Table 3, the hot oil boiler and in Table 4, the dryer unit flue gas measurement values are presented.

Table 3. Flue gas measurement results of hot oil boiler

| Hot Oil Boiler | Flue Gas Temp. (°C) | CO (ppm) | $O_2$ (%) | Ambient temp. (°C) |
|---|---|---|---|---|
| Measurement-1 | 321 | 5 | 9,7 | 12 |
| Measurement-2 | 314 | 4 | 9,7 | 8 |
| Measurement-3 | 315,5 | 4 | 9,7 | 9 |
| Average | **316,8** | **4,3** | **9,7** | **9,7** |

Table 4. Flue gas measurement results of the dryer unit

| Dryer Unit | Flue Gas Temp. (°C) | CO (ppm) | $O_2$ (%) | Ambient Temp. (°C) |
|---|---|---|---|---|
| Measurement-1 | 186,1 | 4,7 | 9,6 | 12 |
| Measurement-2 | 185,7 | 4,1 | 9,6 | 8,5 |
| Measurement-3 | 184,3 | 4,0 | 9,6 | 10 |
| Average | **185,3** | **4,26** | **9,6** | **10,16** |

The ideal emission values for flue gas in a natural gas boiler are shown below;
$O_2$ (%)   : 1 - 4,5
CO (%) : 9,5 - 11,5
Flue gas temperature: 160 °C

When the data above is examined, for the hot oil boiler and dryer unit; The $O_2$ value is higher than the limit value. It also appears that the flue gas temperatures are far above the required temperatures.
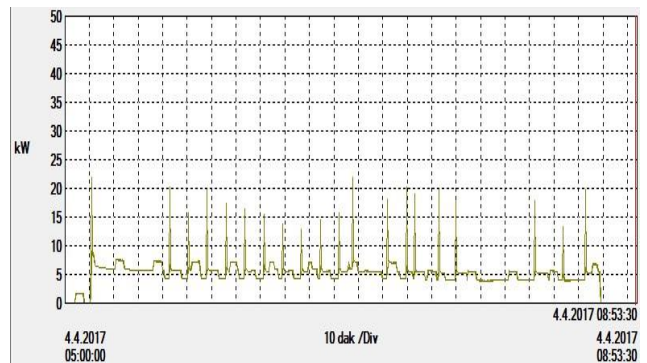


218

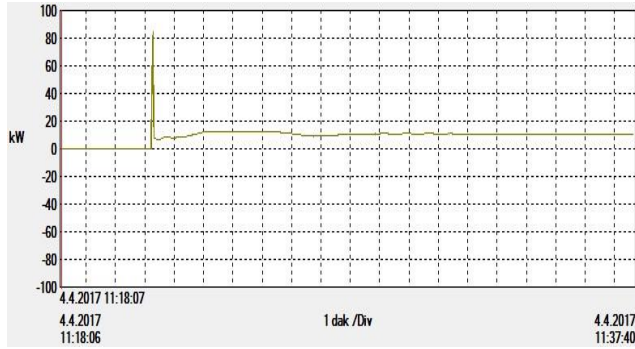Figure 7. Hot oil boilers burner fans power consumption.



Figure 8. Dryer units burner fans power consumption.

Electricity consumption among the electric motors in the asphalt plant is the most important part of the filter outlet. The related electric motor is connected in a star-delta shape. In addition, electric motor fan connection is in belt pulley system. The flap system is used for flow control.

Table 5. The technical characteristics of the fan electric motor.

| Brand and model | Gamak GM 280-94 |
|---|---|
| Yield Type | EFF2 |
| Cos φ | 0,87 |
| Voltage | Δ 380- Y 440 Volt |
| Frequency | 50-60 Hz |
| Transfer | 1475-1770 re /min |
| Current | 140 -140 A |
| Power | 75 kW |

In the fan motor at the outlet of the filter shaft, measurements were taken with the energy analyzer to see the operating characteristics. The power consumption of the burner fan motor is shown in Figure 9.
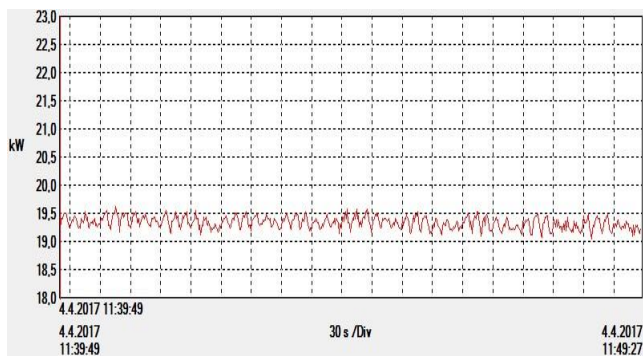


Figure 9. Filter flue output fan motor power consumption.

As a result of these measurements, it was found that the average power consumption was 19.3 kW. This fan motor with a power consumption of 75 kW operates at a load of 25%.

## III. RESULTS AND SUGGESTIONS

### A. Heat Loses In Hot Oil Boiler

• The average fuel consumption of the hot oil burner is 101.5 Sm³/hour and the energy obtained of the hot oil boiler is 912.549,96 kcal per hour.

• The hot oil burner operates an average of 605.67 hours per year.

• An average of 61.475.37 Sm³ LNG is used annually in the hot oil burner to produce 552.702.920.54 kcal energy in the hot oil boiler.

• The average loss of energy obtained in the hot oil boiler is 163.255.19 kcal per hour and 98.878.552.48 kcal per year by dry flue gas.

• Due to the humidity in the flue gas some of the energy generated in the hot oil boiler is lost. The energy loss is 33,855,60 kcal per hour and 20,505,278,35 kcal per year.

• A significant amount of the energy obtained in the hot oil boiler is lost by the heat loss of the boiler surface at an average of 7.839.20 kcal per hour and 4.747.957.84 kcal of energy per annum.

• The total energy loss in the hot oil boiler is 204.949.99 kcal per hour and the average annual amount is 121.131.788.68 kcal. This rate is around 23%.

### B. Heat Loses In Hot Oil Lines

• The heat transferring from the hot oil boiler to the hot oil, the bitumen in the bitumen tanks, the valves on the bitumen lines and the bitumen pump in the mixing unit are heated.

• The amount of heat transferring from hot oil boiler to hot oil is 707.599.97 kcal per hour and it is 428.571.131,86 kcal per year.

• Some of the energy transferred to the hot oil is lost through the serpentine pipes. This amount is approximately 7.839.20 kcal per hour and an average of 4.747.957.84 kcal per year.

• About 1% of the heat from the hot oil to the bitumen storage tanks is lost.

### C. Heat Loses In Bitumen Storage Tanks.

• The present mixture in the bitumen tanks used in the production of asphalt is heated through the heat transferred from the hot oil.

• The amount of heat transferring through the bitumen storage tanks is 660,727.22 kcal per hour and the average amount of heat per year is 400.181.775.71 kcal.

• The energy transferred from the hot oil to the bitumen storage tanks is lost an amount of 27.917,04 kcal per hour and the average annually 16,908,476,49 kcal.

• The amount of energy passing into the bitumen is 632,810,18 kcal / h per hour and an average of 383,273,299,23 kcal per year. Also the amount of lost energy is around 4%.

552.702.920,54 kcal heat energy generated as a result of burning LNG in hot oil boiler is subjected to 169.429.621.31 kcal loss due to the reasons mentioned above and is given to bitumen as 383.273.299.23 kcal energy. During this process, approximately 31% of the energy is lost. The energy flow diagram in the hot oil boiler is shown in Figure 10.
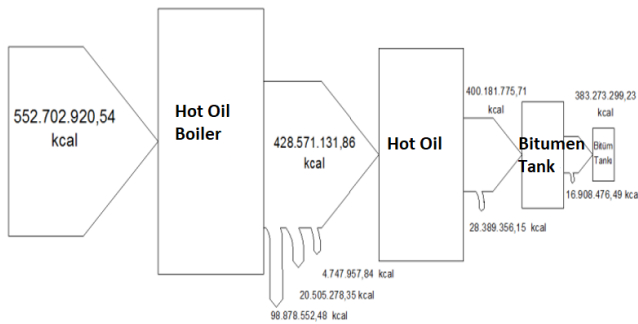
Figure 10. Energy flow diagram for energy amounts and energy losses obtained by LNG in hot oil boiler

*D. Heat Loses In Dryer Unit*

• The average fuel consumption of the dryer unit burner is 778 Sm³/hour and the generated energy in the dryer unit is 6.994.717.92 kcal/h per hour.

• The dryer unit burner operates an average of 1060.33 hours per year.

• The dryer unit burner uses an average of 721.650,32 Sm³ LNG per year and a desiccant unit of 7.416.704.511.25 kcal is obtained.

• A significant portion of the energy obtained in the drying unit is lost through the dry flue gas. This loss is 700.171.26 kcal per hour and an average of 742.412.121.58 kcal energy loss per year.

• Due to the humidity in the flue gas some of the energy generated in the dryer unit is lost. The energy loses 171.370.59 kcal/h per hour and average energy loss of 181.709.260.53 kcal per year.

• A significant amount of the the energy obtained from the drying unit is lost through heat loss of the dryer surface. The lost amount is 4.229.72 kcal/h per hour and the average energy loss is 4.484.896.14 kcal per year.

• Total energy loss in the dryer unit is 885,771,57 kcal/h per hour and an average of 658,606,278,25 kcal per annum. This rate is around 9%.

• The heat energy is transferred to the aggregate to be used in the production from the drying unit. This amount is 6.118.946.35 kcal / h per hour and the annual average is 6.488.098.233,00 kcal. The energy flow diagram in the dryer unit is shown in Figure 11.
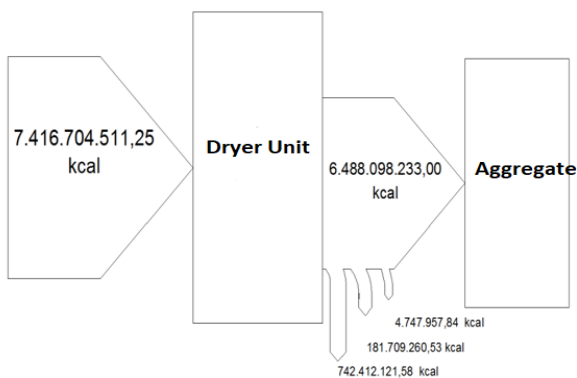


Figure 11. Energy flow diagram for energy quantities and energy losses obtained by LNG in dryer unit

*E. Electrical Loses*

• Electrical energy losses mostly occur in the compressor and filter fan electric motors. Other electrical motors in the plant have not detected any significant energy loss due to the application of inverters.

• The average amount of electricity used in the plant is 230.883,90 kWh.

• The energy loss due to the compressor operation is 8,943,00 kWh.

• Depending on the operation of the filter fan electric motor, the consumption energy is 6.592,00 kWh.

• Total electrical energy loss of the plant is 13.360.100.00 kcal. This amount is approximately 7% of the total average electrical energy used.

• Total energy input, including heat and electrical energy in the plant, is 8.167.967.585.79 kcal and energy loss is 1.111.395.999.56 kcal. This corresponds to a ratio of approximately 13%.

REFERENCES

[1] Özsoy, A., 1997. Thermo-economic analysis of asphalt plants. Thesis, Süleyman Demirel University, Institute of Science and Technology, Isparta

[2] Yonar, F., 2007. Evaluation of asphalt plants in terms of production stages and performances. Thesis, Istanbul Technical University, Institute of Science and Technology, Istanbul

[3] Rodriguez-Alloza, A. M., Malik, A., Lenzen, M., and Gallego, J., 2015. Hybrid input-output life cycle assessment of warm mix asphalt mixtures. Journal of Cleaner Production, (90), 171-182

[4] Huchet, F., Le Guen, L., Richard, P., Piton, M., Cazacliu, B., Semelle, P., Matheus, J., Riche, H., and Tamagny, P., Influence of 2018 asphalt Road Materials and Pavement Design, (19), 104-119.

[5] Sivilevičius, H., Vislavičius, K., and Braži ,nas, J., 2017. Technological and economic design. Technological and Economic Development of Economy, (23), 627-648.

# Assessment of the Vocational Qualifications Gained Through The Curriculum of the Forestry and Forestry Products Department

Osman Komut
Gümüşhane Üniversitesi, Gümüşhane Meslek
Yüksekokulu, Ormancılık Bölümü, 29000,
Gümüşhane, TÜRKİYE
osmankomut@gumushane.edu.tr

Murat Han Ertuğrul
Gümüşhane Üniversitesi, Fen Bilimleri
Enstitüsü, Ormancılık ve Çevre Bilimleri
Anabilim Dalı, 29000, Gümüşhane, TÜRKİYE

*Abstract*-Public ownership of 99% of Turkey's forests is the reason for state agency–based employment in the forestry field. In recent years, the schools offering short-term training, which were important for meeting the needs of forestry staff, were abandoned, and policies were developed for graduates of vocational schools located within the forestry and forestry products department for employment by forestry organizations. Besides the qualifications and training strategies of the forestry departments in many different regions, a limited number of employment opportunities have led to problems in the field of vocational education.

This study contains qualitative research that determined the education that students in the forestry department receive, the professional expectations, and the adequacy of the training received by the graduates from this sector who are employed in state forest enterprises in meeting professional expectations. In this context, students in relevant departments and employees who graduated from these departments surveyed about lecturers, lectures, legislation, safety regulations, and the efficiency of field training.

In this study, some potential points of discussion received from the students and employees were solicited, such as whether there are too many theoretical courses in the forestry department and too little practice in the field, and whether there is enough technical information provided about legislation and safety issues.

*Keywords*-Forestry, Vocational Schools, Vocational Training, Employment.

## I. INTRODUCTION

The public owns 99% of the forests in Turkey, which are governed by the central and provincial organizations of the General Directorate of Ministry of Forestry and Water Affairs (General Directorate) [1]. The vocational training for a forest guard officer began in 1952 with the opening of the Forest Guard Officer School, and it continues in the forestry department within the university's vocational school [2]. This field carries enormous potential because it corresponds to approximately one-third of the staff of the General Directorate [3], and the number of schools providing corresponding training have significantly increased.

It is clear that modern forestry activities under the General Directorate can be governed with high efficiency and suitable methods only as long as staff has sufficient knowledge and experience [3;4]; however, it is also apparent that without providing enough technical and academic infrastructure, students who began their education in forestry and forest products will never have the necessary knowledge and experience to govern.

There are many studies that report on how crucial it is for institutions to provide vocational training by considering the requirements in specific employment areas and cooperating with the corresponding sector [5;6]. The aim of our study was to solicit the opinions of forestry organization staff who graduated from the Forestry and Forest Products Department on the vocational training they received.

## II. MATERIALS AND METHODS

The sampling universe of this study was sophomore-year students and graduates of the Forestry and Forest Products Department of the Gümüşhane Vocational School of Higher Education, Gümüşhane University, Turkey. The graduates are employed within the forestry organization. The study method was used to describe the current educational situation, and qualitative data were obtained [7]. The data were collected through semi-structured interviews conducted with 12 current students and 8 graduates of the corresponding department who work in Amasya, Kastamonu, Denizli, Ankara, and Bolu Regional Directorates of Forestry under Turkey's General Directorate of Forestry. Data were collected using 10 survey questions divided into 3 main parts that related to training sufficiency, training needs, and suggestions for improvement.

## III. RESULTS AND DISCUSSION

Through direct interviews, opinions of the students and graduates of the Forestry and Forest Products Department were provided on the training curriculum, the knowledge needed in the working office, and the expectations of the forestry organization. The data collected are provided in Table 1.

Table 1. Opinions of the students and graduates of the Forestry and Forest Products Department on training received.

| Surveyed Group | Answers | In general, was the training you received in vocational school sufficient for the work? | Was your theoretical training sufficient? | Was your practical training sufficient? | Is the process of internship sufficient? | Was the training you received sufficient for the entrance examination for the job? | Was the training you received, and the knowledge required for your job compatible? | Was your training related to occupational safety sufficient? | Had you previously experienced personal protective equipment in your workplace? | Should the opinion of the staff of the forestry organization be taken into consideration when preparing the curriculum? |
|---|---|---|---|---|---|---|---|---|---|---|
| Students | Yes | 10 | 5 | 2 | 7 | 5 | 6 | 6 | 3 | 12 |
| | No | 2 | 7 | 10 | 5 | 7 | 6 | 6 | 9 | 0 |
| Guard Officers | Yes | 8 | 8 | 0 | 3 | 5 | 6 | 0 | 0 | 8 |
| | No | 0 | 0 | 8 | 5 | 3 | 2 | 8 | 8 | 0 |

The participants who currently work as forest guard officers reported that courses in the following subjects should be included in the theoretical curriculum: forestry-related laws and application-oriented legislation, the tasks and responsibilities of the forest guard officers, forest fires, production, tree marking/stamping, job knowledge, and occupational safety.

According to the study results, the students and graduates of the vocational school generally considered their training to be sufficient. These results are similar to those of the study done on students of the Forestry Department of the Vocational School of Süleyman Demirel University [2] and the students of the Forestry Department of the Forestry Faculty of the same university [8].

On the other hand, the employed graduates pointed out insufficiencies in the training received through the vocational school. The same participants stated that the internship program, in which theoretical knowledge is applied in a practical context, was also not satisfactory.

IV. CONCLUSION AND SUGGESTIONS

The conclusions reached in this study stem from the fact that the student internship period coincides with the very busy period within the forestry organization, when production and field practices are intense. Even though this provides the students with an opportunity to closely monitor these practices, the number of staff who can allocate time to the students is very low and restrictions on participating in fieldwork results in negativity regarding the efficiency of the internship program.

The results indicate that the graduates find the training insufficient in terms of occupational safety and personal protective equipment. On the other hand, according to ~50% of the students, the training regarding these two subjects was sufficient. These results can be interpreted to mean that the curriculum does not adequately include the corresponding subjects, the students are unable to clearly evaluate the

requirements of the workplace, and/or the field practices on these subjects are not sufficient.

Both the students and graduates believed that the opinions of the staff of the forestry organization should be considered when preparing the curriculum. Both groups of participants believed that education and work life should be compatible.

From our findings, the following suggestions can be made to reduce the problems the graduates of the vocational school confront work life on the job and to train forestry technicians in the qualifications expected by the forestry organizations of Turkey:

- The theoretical courses should be oriented to the application and should be managed with the cooperation of State Forest Enterprises during weekly, monthly, and semester periods.
- The internships should be evaluated with previously determined scales and controlled activity should be increased.
- The curriculum should contain courses on the laws pertaining to forestry and the legislation relevant to the situations that can arise in the workplace.
- The curriculum should include courses on the increasingly important subject of occupational safety, and field practices should support this course.

REFERENCES

[1] Aktan Ü (2013) Serbest Ormancılık Büroları ve Orman Mühendisi İstihdamına Etkisi, AÇÜ FBE Orman Müh. ABD Yüksek Lisans Tezi (Yayımlanmamış), 76 s., Artvin.

[2] Alkan, H., 2013. Ormancılık ve Orman Ürünleri Programı Öğrencilerine Yönelik Bir Araştırma. SDÜ Orman Fakültesi Dergisi 2013, 14: 88-94 Isparta.

[3] Öztürk, A., 2013. Orman Muhafaza Memurlarının Sorunları Üzerine Bir Araştırma. Artvin Çoruh Üniversitesi Orman Fakültesi Dergisi ISSN:2146-1880, e-ISSN: 2146-698X Cilt: 14, Sayı:2, Sayfa: 253-271, Ekim 2013.

[4] Yavuz, Ö., 2007. Orman Genel Müdürlüğü'nün Personel Yapısı ve Sorunları. İÜ Fen Bilimleri Enstitüsü Yüksek Lisans Tezi (Yayımlanmamış), 105 s., İstanbul.

[5] Adıgüzel, O. C., 2009. Meslek Yüksekokulu Öğrencilerinin İşyeri Eğitimi Öğrenme Ürünlerinin Değerlendirilmesi.

Ondokuz Mayıs Üniversitesi Eğitim Fakültesi Dergisi. Sayı(27), 115-128.

[6] Türker, M. F., 2009. Ülkemiz Yüksek Öğreniminin Çağdaşlaştırılması Sürecinde Ormancılık Anlayışları, 5531 Sayılı Kanun ve AÇÜ ile KTÜ Orman Fakültelerinin Konumu. 5531 Sayılı Orman Mühendisliği, Orman Endüstri Mühendisliği ve Ağaç İşleri Endüstri Mühendisliği Hakkında Kanun'un Yüksek Öğretim-Eğitim ve Uygulamaya Yansımaları, Alınması Gereken Önlemler konulu panel, TMMOB Orman Mühendisleri Odası, 16-19 Kasım 2009, Antalya.

[7] Büyüköztürk, Ş., Çakmak, E. K., Akgün, Ö. E., Karadeniz, Ş. ve Demirel, F., 2012. Bilimsel Araştırma Yöntemleri. Geliştirilmiş 13. Baskı. Pegem Akademi Yayıncılık. ISBN 978-9944-919-28-9, Ankara 341 s.

[8] Korkmaz, M. Alkan, H. Akyol, A. Tolunay, A. 2008. Süleyman Demirel Üniversitesi Orman Fakültesi öğrencilerinin fakülte kültürünü algılamaları. III. Ulusal Ormancılık Kongresi, Türkiye Ormancılar Derneği, 20- 22 Mart 2008, Ankara, s.85-94.

# The Effect of Mistletoe on the Growth of Scots Pine

Murat Han Ertuğrul
[1]Gümüşhane Üniversitesi, Fen Bilimleri Enstitüsü, Ormancılık ve Çevre Bilimleri Anabilim Dalı, 29000, Gümüşhane, TÜRKİYE

Osman Komut
Gümüşhane Üniversitesi, Gümüşhane Meslek Yüksekokulu, Ormancılık Bölümü, 29000, Gümüşhane, TÜRKİYE
osmankomut@gumushane.edu.tr

*Abstract*-Scots pine (*Pinus sylvestris*) is the third most common pine found within the pine forests of Turkey. Because of their status, the biotic and abiotic factors that have a negative impact on this species are significant. Mistletoe (order: Santalales) is a semi-parasite plant that affects the growth and increment of Scots pine, fir (*Abies*), and all deciduous tree species under many conditions.

Our study was conducted in the natural regeneration and afforestation area of the Gümüşhane region, Turkey. While selecting the areas to study, our priority was that there would be no significant differences in growth conditions for Scots pine. From each area, two healthy and two mistletoe-infected; eight young Scots pine were selected for study. The trunk of the trees was analyzed and the vertical growth rates were investigated. In addition, whether there was any correlation between the Erinç index and vertical growth rate was determined.

At the end of the study, we determined that the regional climate has a more negative impact on young Scots pine growth than mistletoe.

*Keywords*-Mistletoe, tree trunk analysis, regeneration

## I. INTRODUCTION

The total acreage in Turkey comprises 28.6% forest. These forests are composed of 33% deciduous trees, 48% coniferous trees, and a 19% mix of both types. [1]. There are many abiotic and biotic factors that affect Turkey's forest trees, and semiparasites are one of the most significant of these factors.

Mistletoe is an evergreen semi-parasitic plant that grows on the trunk and branches of trees and contains chlorophyll for photosynthesis [2]. The plant creates dryness within the host, making it more vulnerable to insects, fungi, and similar secondary pests and causing the host to lose its vital biological functions. [3] Although mistletoe is considered to be a pest in Scots pine stands, it has important medicinal properties, which is why the fight to eradicate this plant is an unclear phenomenon in forestry management [4].

The aim of this study was to uncover whether mistletoe impacts the vertical growth rate of Scots pine trees in natural regeneration and afforestation areas by analyzing the characteristics of tree trunks.

## II. METHODS

Studies were conducted within the borders of the Gümüşhane Forest Directorate natural regeneration and afforestation regions in Turkey. The area lies between 40º32' and 40º14' north latitudes and 39º56' and 40º20' east longitudes in Gümüşhane Province. To amplify the differences in natural regeneration and afforestation, the selected areas were under the same growth conditions for Scots pine.

The Erinç index was used to determine the climatic properties of the study area. The index depends on the ratio between annual precipitation and annual average maximum temperature within a region (1). For calculating the Erinç index, the precipitation values within the study area over the last 20 years was obtained from the Turkish State Meteorological Service.

$$I_m = \frac{P}{T_{om}} , \qquad (1)$$

where $I_m$ is the precipitation index, P is the annual precipitation (mm), and $T_{om}$ is the annual average maximum temperature (°C). After calculating the precipitation index, the following table based on the Erinç index was used to determine the types of climate within the study area (Table 1).

Table 1. Types of the climates according to the Erinç index*.

| Climate Class | Precipitation Index | Vegetation |
|---|---|---|
| Completely Dry | $I_m < 8$ | Desert |
| Dry | $8 < I_m$ | Desert-Steppe |
| Semi-Dry | $15 < I_m < 23$ | Steppe |
| Semi-Wet | $23 < I_m < 40$ | Park-Like Forest |
| Wet | $40 < I_m < 55$ | Wet Forest |
| Extremely Wet | $55 < I_m$ | Very Wet Forest |

*[5]

From the study areas, trunk analyses were conducted on two healthy and two mistletoe-infected trees from each region, for a total of eight trees, to determine the differences in growth and increment (per-year growth at a specified age). The distribution of the trees for trunk analyses is provided in Table 2.

Table 2. Distribution of the analyzed trees (D stands for "doğal" means natural in Turkish, and A "ağaçlandırma" means afforestation in Turkish).

| Regeneration Type | Mistletoe Infection | |
|---|---|---|
| | Present | Absent |
| Natural | D1, D2 | D3, D4 |
| Afforestation | A1, A2 | A3, A4 |

The sample trees were cut down in the field and separated into different sections. Cross sections were taken from lowermost 0.30 m high sections. For each tree, the number of rings on the 0.30-m-high cross sections were counted, and the age of a corresponding tree at a height of 0.30 m was added to calculate its age. Using MS Excel, the height–age curve for each tree was created. Using this curve, the height a tree reaches in 5-year-intervals was calculated, and using these values, the average increment for each tree was determined.

## III. RESULTS AND DISCUSSION

The determined average increment rates for Scots pine individuals from the tree trunk analyses are provided in Fig. 1 for the afforestation area and in Fig. 2 for the natural regeneration area.
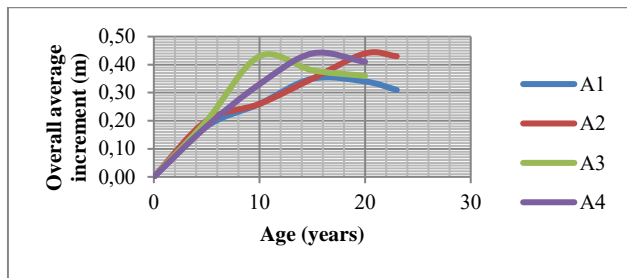


Figure 1. General average increment values for trees in the afforestation area calculated by tree trunk analyses.
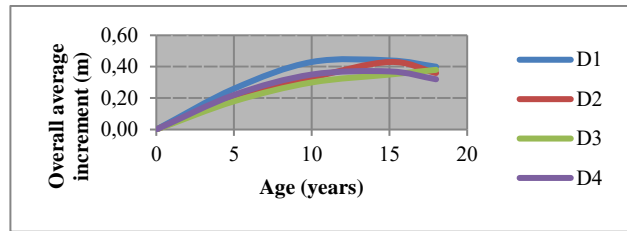


Figure 2. General average increment values for trees in the natural regeneration area calculated by tree trunk analyses.

From the graphs, it is apparent that vertical growth rate decreases in both healthy and mistletoe-infected trees, and that mistletoe has no significant effect on this rate. In addition, according to the Erinç index, the climate type within the region is semiarid. According to the literature, the vertical growth rate decreases from dry to wet regions and, when field stress is considered, the growth rate in trees facing north is lower than in those facing south [6]; however, even in south-facing stands, if the climate is not humid enough, growth rates decrease. The fact that these areas are not humid enough and the fields faced south explains why the growth rate was decreasing.

## IV. CONCLUSIONS AND FUTURE SUGGESTIONS

The effects of mistletoe, the growth conditions in the region, and the regional climate on the development of the Scots pine stand were examined using an analysis of tree trunk characteristics. The mistletoe had no negative effect on the trees, based on the data obtained from healthy and infected individuals; however, but both the regional climate and growth conditions are factors that affect growth rate. Although the mistletoe had no negative effect on growth rate, the plant is still considered to be semiparasitic because it degrades the trunk quality of individual trees. In addition, because mistletoe is important in medicine and is a significant forage for livestock, it can be classified under nonwood forest products; therefore, not only can the villagers in the area find employment opportunities in the industry, but also the positive results can enhance the management of mistletoe stress on trees

## V. ACKNOWLEDGEMENTS

## REFERENCES

[1] OGM, 2015. Türkiye Orman Varlığı, Orman İdaresi ve Planlama Dairesi Bşk., s.26

[2] Yüksel, B., Akbulut, S. ve Keten, A., 2005. Çam Ökseotu (Viscum Album ssp. Austriacum (Wiesb.) Vollman)'nun Zararı, Biyolojisi ve Mücadelesi, Süleyman Demirel Üniversitesi Orman Fakültesi Dergisi, Sayfa: 111-124

[3] Dobbertin, M. ve Rigling, A., 2006. Pine Mistletoe (Viscum Album ssp. Austriacum) Contributes to Scots Pine (Pinus sylvestris) Mortality in the Rhone Valley of Switzerland, Forest Pathol., 36, 349-322.

[4] Bilgili, E., 2014. Ökseotu (Viscum album L.)'nun Doğu Karadeniz Bölgesi Sarıçam (PinusSylvestris L.) Meşcerelerinde Yayılışının Belirlenmesi ve Çap Artımı Üzerine Olan Etkisinin Modellenmesi, TÜBİTAK Projesi, Proje No: 112O258.

[5] Erinç, S., 1965. Yağış Müessiriyeti Üzerine Bir Deneme ve Yeni Bir İndis, İ.Ü.Coğrafya Enstitüsü Yayın No:41, İstanbul, 1965.

[6] OGM, 2015. Sündiken Dağlarında (Eskişehir) Sarıçam (Pinus sylvestris L.) Ağaçlarının Yetişme Ortamı Özelliklerine Göre Beslenme ve Büyüme İlişkilerinin Belirlenmesi, Ormancılık Araştırma Bülteni, Sayı:2, s.4.

# Energy Efficiency and Energy Management in Asphalt Plants

Özer Kaya
Ataturk University
Engineering Faculty
Mechanical Engineering
Erzurum, TURKEY
ozerkaya_81@hotmail.com

Kenan Yakut
Ataturk University
Engineering Faculty
Mechanical Engineering
Erzurum, TURKEY
kyakut@atauni.edu.tr

Ahmet Numan Özakin
Ataturk University
Engineering Faculty
Mechanical Engineering
Erzurum, TURKEY
ahmet.ozakin@atauni.edu.tr

Muhammet Harun Osta
Ataturk University
Engineering Faculty
Mechanical Engineering
Erzurum, TURKEY
harun.osta@atauni.edu.tr

*Abstract*: **Road transport is one of the most important parameters of industrialization. The argument of a comfortable transportation is asphalt, which is the upper layer of the road. With the development of technology and the decrease in production costs, the number of asphalt plants used in asphalt production is increasing day by day. Energy saving has an important place in scientific research. A significant portion of the energy used in industrial facilities belonging to public and private sector, such as asphalt plant facilities, is lost and increases the costs of asphalt production. Increasing energy cost per unit product due to lost energy causes serious damage to country economy. In this study, a detailed energy management and efficiency investigation was carried out in the asphalt plant of the 18th Regional Directorate of Highways (Kars). In the scope of the study, flue gas analyzes were performed for hot oil boiler and dryer unit. In addition, thermal imaging is done for the hot oil boiler and dryer unit. The operating characteristics of the electric motors in the plant have been determined by energy analyzers. As a result of these measurements, calculations have been made according to measurement points and energy losses have been determined. As a result, it is calculated that 29,25 TEP energy will be gained by the implementation of the mentioned projects. 4.58% of the savings is caused by electricity and 95.42% by LNG consumption. Furthermore, there will be 91,90 tons less CO2 emissions to the environment.**

*Keywords: Asphalt plant, flue gas, energy consumption*

## I. INTRODUCTION

Energy is one of the main concepts of engineering as a value that can be transformed into the work. Energy efficiency and energy management are the main issues that should be examined due to decreasing energy sources and increasing energy costs in our world where technology is developing rapidly. In our country, the most important stage regarding energy efficiency and energy management was recorded with the Energy Efficiency Law No. 5627 published in the official newspaper dated 02/05/2007 and numbered 26510. This law was followed by the Regulation on Increasing the Efficiency of Energy Resources and Energy Usage published in the official newspaper dated 27/10/2011 and numbered 28097. Republic of Turkey in relation to the subject depending on the Ministry of Energy and Natural Resources 02/11/2011 date and 28103 (bis) numbered Official Gazette published in Renewable Energy by Decree Law No. 662 established General Directorate. Thus, studies have been started in order to raise awareness about the efficient use of energy in industry and houses. Energy efficiency should not be perceived as energy saving by reducing production and living comfort. Explains the standard of living and service quality in buildings

and energy savings per unit of service or product quantity without leading to a decrease in the quality and quantity of production in industrial enterprises.

Mumlu (2008) has designed various energy saving projects by making measurements in these factories to save energy costs to the lowest levels. As a result of these applications, a total of 7.926.305,00 kWh/year energy saving will be made from 6.875.789,00 kWh/year natural gas and 1.050.516,00 kWh/part of electricity, 51.084.968,00 kWh/year of which is the annual energy consumption of the factory of 15%[1]. Özkök (2010) has listed the applications required to reduce energy consumption at the Ankara Sheraton Hotel and Conference Center. The first investment costs, annual energy gains and repayment periods of these applications are calculated and an annual energy gain of 870.733,00 TL will be calculated for the first investment cost of 2.582.701,00 TL. The repayment period of these investments is estimated as 3,026 years[2]. Acar (2012) stated the practices related to energy efficiency at the Ankara Turkish Tractor Factory; When the initial investment costs, annual energy gains and repayment periods of these applications are compared, it is calculated that there is an annual energy gain of 2.205.076,00 TL for the first investment cost of a total of 617.360,00 TL in the system. The repayment period of these investments is foreseen as 3.81 years[3]. The energy losses were determined by Arkat (2013) at an airport and the total cost of the applications required to prevent energy losses was calculated as TL 970.796,00 and the annual energy saving amount was 579.099,00 TL[4]. Kemaloğlu (2014) made an energy analysis of the Erzurum Sugar Factory's power plant, determined the points where energy losses were high and offered solutions in the framework of his calculations and stated that because of these practices, he could make a profit of TL 959,758,094 in the factory[5]. In an industrial enterprise in Kayseri, which employs more than a thousand employees, Bulanıkoğlu (2014) determined the air surplus coefficient and distribution of the gases formed because of the flue gas analysis in order to increase the energy efficiency. As a result of different applications, it was stated that the savings made in the quarter were 19,17% fuel saving and the repayment period was expressed as 17 months[6].

In this study, the energy expenditures of the related Asphalt Plant in 2015 and 2016 were analyzed and annual energy consumption was calculated. Studies on energy management for the facility will be examined. A detailed energy study was conducted based on this research and investigations. During the energy study, detailed

measurements were made at all energy consumption points in the facility. In terms of energy efficiency; To minimize energy losses and to increase efficiency, the proposed solutions and the approximate costs of these solutions are presented. An energy management is discussed in the light of energy losses, solution proposals and necessary measures.

## II. MATERIAL AND METHOD

### A. Investigation of Industrial Plants Energy Consumption

Energy consumption of the facility will be evaluated as electricity and LNG. In 2015, 794,14 TEP energy was consumed and a cost of TL 1.577.371,67 was generated. In 2016, 653,63 TEP energy was consumed and a cost of 1.226.257,56 TL was realized.
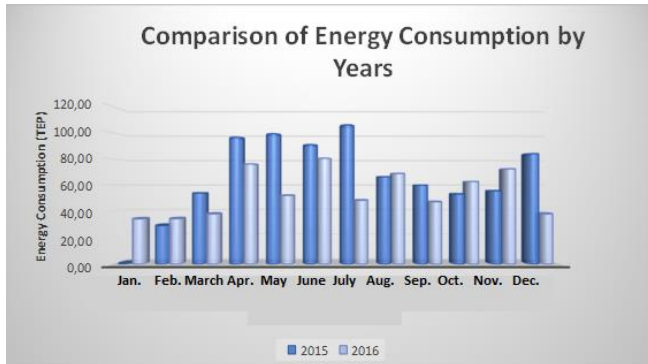


Figure 1. Comparative graph of energy consumption in 2015 and 2016

In 2016, energy consumption is seen as an increase and decrease compared to 2015. Here, it is clear that the change in production amounts has an effect. The intensive units of energy consumption are as follows;

• Hot Oil Boiler: The facility has 3 pieces of 50 tons capacity Bitumen tank, 2 units of 50 Sm³ capacity LNG tank and a 500,000 kcal / h thermal oil boiler with the capacity to bring the bitumen to the desired temperature during the production. The superheated oil boiler is used to bring the bitumen to 150-170 0C set values before the production starts.

• Dryer Unit: It is the unit in which the aggregates are taken from the cold aggregate silos in desired size and weight. The drier unit is a cylindrical industrial oven with a diameter of 2000 mm and a length of 8000 mm. The outer surface of the dryer unit is covered with a 100 mm thick insulation material (stone wool) and the vanes are placed to mix the aggregates. The dryer unit is mounted with an angle of 5% (slope) to transport the aggregates to the hot aggregate elevator.

The dryer unit is rotated around its axis by rotating drums with an electric motor drive of four points 11 kW. By the flame obtained from the burner in the outlet of the dryer unit, the aggregates are dried and brought to the desired temperature value. The gases formed as a result of the burning of the aggregates from the inlet of the dryer unit and the gases formed as a result of the combustion in the burner are vacuumed by the filter fan and sent to the filter by the dirty gas channel located at the top of the inlet. 120 tons per hour plant, 5% according to humidity rate max. It has an industrial type burner with a heat capacity of 9.974.208,00 kcal/h. The capacity of the dryer burner fan electric motor is 18.5 kW.

Table 1. Technical characteristics of the dryer unit and burner

| Technical Spesifications | |
|---|---|
| Length of the dryer (mm) | 8.000 |
| Diameter of dryer (mm) | 2.000 |
| Dryer burner brand and model | Baltur TS 36N-D ME/L |
| Constructor burner capacity Min-Max (kW) | 4800-11600 |
| Desiccant burner fan motor (kW) | 18,50 |

• Electric Motors: Electricity consumption at the asphalt plant; superheated oil pump in the hot oil boiler room, flat belt and inclined belt electric motors, dryer burner fan and dryers rotating motors, mixer reducer motors, chimney fan, asphalt pump drive is carried out on the motor. Images of electric motors in the asphalt plant are presented in Figure 2.



Figure 2. Electric motors in asphalt plant

One of the important points to be taken into consideration in the energy consumption of electric motors is the analysis of the speed control to the motors operating at long and variable load. Table 2 shows the power and efficiency information of the electric motors in the asphalt plant.

Table 2. Power and efficiency data of electric motors in asphalt plant

| Portion | Quantitiy | Power (kW) | Speed Cont. | Eff. Class |
|---|---|---|---|---|
| Cold Silo Six Flat Tape Elect. Engine | 4 | 3 | Available | EFF2 |
| Inclined Belt Electric Motor | 1 | 4 | Unavailable | EFF2 |
| Filter Flue Outlet Fan Motor | 1 | 75 | Unavailable | EFF2 |
| Burner Fan Motor | 1 | 18,5 | Unavailable | EFF2 |
| Asphalt Pump | 1 | 7,5 | Unavailable | EFF2 |
| Dryer Rotary Motor | 4 | 11 | Unavailable | EFF1 |
| Mixer Motor | 2 | 30 | Unavailable | EFF2 |
| Elavator Electric Motor | 1 | 18,5 | Unavailable | EFF2 |

### B. Research Findings and Discussion

It has been determined that the heat losses in the asphalt plant are intensely realized in the hot oil boiler and dryer unit. Measurements were made to obtain the heat losses from the unit surfaces in order to calculate the combustion efficiency of the hot oil boiler and dryer unit. In Fig. 3, the hot oil boiler and in Fig. 4, thermal camera images of the dryer unit are included.
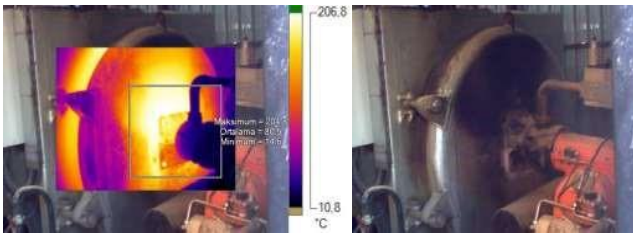
Figure 3. Surface thermal imaging of hot oil boiler.



Figure 4. Surface thermal imaging of drying unit.

The exhaust gas emission values resulting from combustion in the hot oil boiler and dryer unit are important parameters used to calculate the combustion efficiency of the unit. At this point, the combustion efficiency can be obtained with the calculations to be made depending on the values taken from the chimneys. In Table 3, the hot oil boiler and in Table 4, the dryer unit flue gas measurement values are presented.

Table 3. Flue gas measurement results of hot oil boiler

| Hot Oil Boiler | Flue Gas Temp. (°C) | CO (ppm) | O₂ (%) | Ambient temp. (°C) |
|---|---|---|---|---|
| Measurement-1 | 321 | 5 | 9,7 | 12 |
| Measurement-2 | 314 | 4 | 9,7 | 8 |
| Measurement-3 | 315,5 | 4 | 9,7 | 9 |
| Average | **316,8** | **4,3** | **9,7** | **9,7** |

Table 4. Flue gas measurement results of the dryer unit

| Dryer Unit | Flue Gas Temp. (°C) | CO (ppm) | O₂ (%) | Ambient Temp. (°C) |
|---|---|---|---|---|
| Measurement-1 | 186,1 | 4,7 | 9,6 | 12 |
| Measurement-2 | 185,7 | 4,1 | 9,6 | 8,5 |
| Measurement-3 | 184,3 | 4,0 | 9,6 | 10 |
| Average | **185,3** | **4,26** | **9,6** | **10,16** |

The ideal emission values for flue gas in a natural gas boiler are shown below;
$O_2$ (%)   : 1 - 4,5
CO (%) : 9,5 - 11,5
Flue gas temperature: 160 °C

When the data above is examined, for the hot oil boiler and dryer unit; The $O_2$ value is higher than the limit value. It also appears that the flue gas temperatures are far above the required temperatures.

Electricity consumption among the electric motors in the asphalt plant is the most important part of the filter outlet. The related electric motor is connected in a star-delta shape. In addition, electric motor fan connection is in belt pulley system. The flap system is used for flow control.

Table 5. The technical characteristics of the fan electric motor.

| Brand and model | Gamak GM 280-94 |
|---|---|
| Yield Type | EFF2 |
| Cos φ | 0,87 |
| Voltage | Δ 380- Y 440 Volt |
| Frequency | 50-60 Hz |
| Transfer | 1475-1770 re /min |
| Current | 140 -140 A |
| Power | 75 kW |

In the fan motor at the outlet of the filter shaft, measurements were taken with the energy analyzer to see the operating characteristics. The power consumption of the burner fan motor is shown in Figure 5.
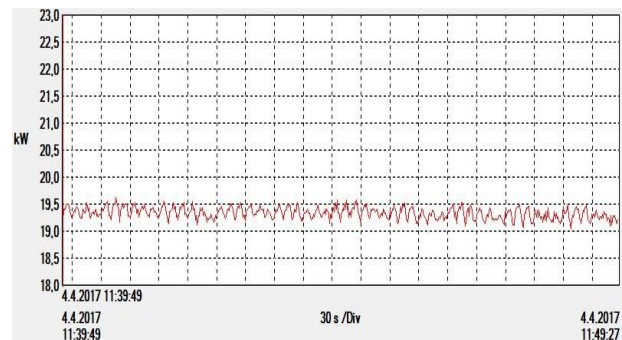


Figure 5. Filter flue output fan motor power consumption (kW)

As a result of the measurement, it was found that the average power consumption was 19,3 kW. This fan motor with a power consumption of 75 kW operates at a load of 25%.

### III. RESULTS AND SUGGESTIONS

• With the burner setting of the hot oil boiler, a profit of TL 8.965.22 will be achieved by saving 4.813,52 S³ per year. This amount is equal to 4,33 TEP per year. In addition, 12.82 tons of $CO_2$ emission is expected to decrease with this application. The cost of the investment is 6.000,00 TL and the repayment period is 0,73 years. It is an effective solution in the short term.

• The economizer application to the hot oil boiler will save 4.604,51 S³ per year and will generate a profit of 7.806,75 TL. This amount is equal to 4,12 TEP per year. With this application, a reduction of 12,23 tons of $CO_2$ per year is expected. The cost of the investment is 30.000,00 TL and the repayment period of this application is 3,84 years. It is an effective solution in the long term.

• With the addition of automatic combustion control to the drying unit, a profit of TL 36.703,67 will be achieved by

saving 21.649,51 SM³ per year. This amount is equal to 19,46 TEP per year. With this application, a reduction of 57,64 tons of $CO_2$ per year is expected. The cost of the investment is 60.000,00 TL and the repayment period is 1,63 years. It is an effective solution in the medium term.

• Adding an inverter application to the compressor will save 8.943,00 kWh in a year and will make a profit of 2.869,07 TL. This amount is equal to 0,77 TEP per year. In addition, with this application, a reduction of 5.21 tons of $CO_2$ per year is expected. The cost of the investment is 18.000,00 TL and the repayment period is 6,27 years. It is an effective solution in the long term.

• Adding a speed control application to the filter fan electric motor will save 6.592,00 kWh a year and a profit of 2.116,67 TL will be achieved. This amount is equal to 0,57 TEP per year. In addition, with this application, a reduction of 4 tons of $CO_2$ per year is expected. The cost of the investment is 12.000,00 TL and the repayment period of this application is 5,67 years. It is an effective solution in the long term.

• With the implementation of the projects, 29,25 TEP energy savings will be ensured. 4,58% of this savings will be from electricity and 95,42% from LNG consumption.

• The total amount of LNG to be saved in 2015-2016 average LNG consumption is 0,03967. The average annual LNG consumption will save 3.97%. The amount of money paid for the average LNG consumption in 2015-2016 is 52.675,64 TL.

• The total value of the electricity saved in total electricity consumption in the years 2015-2016 is 6,73% per year. Monetary average of 2015-2016 for electricity consumption is 4.985,74 TL.

• As a result of LNG and electricity savings, an annual gain of TL 57.661,38 will be provided. The cost of this investment is 126.000 TL.

• As a result of these studies, 91,90 tons of CO2 will not be emitted to the environment.

• In order to monitor the results of the improvements to be made and at the same time to observe the efficiency of the plant, energy analyzers must be placed in the appropriate parts. It is important to monitor energy consumption in terms of energy efficiency.

*İ.  Current situation assessments and recommendations on energy management*

The energy consumption of the asphalt plant is 723,89 TEP per year and it varies according to the amount of asphalt production. There is an obligation to employ an energy manager in this publicly owned facility with an annual energy consumption of over 250 TEP. In addition, an energy management unit should be established. After carrying out the applications mentioned in this study, it is necessary to conduct an energy study for energy efficiency.

In the world where there is no endless energy source, the most important measure that can be taken despite the increasing energy costs and energy consumption; to educate the individuals who use the energy from the manager to the employees and to give the necessary training in energy saving. Recommendations on energy management are as follows;

• The infrastructure should be established with the support of an expert in the sense of energy management.

• Energy management unit should be established and regular meetings should be held.

• The energy management unit should monitor the current status of the facility and identify and follow up the improvement issues.

• The energy consumption values of the facility shall be monitored continuously and compared with the production values.

• Periodic maintenance and adjustment of units that increase energy consumption values should be monitored.

• Follow-up forms of electricity and liquefied natural gas meters should be established and followed up regularly.

• Energy consumption and production performance should be monitored by calculating specific energy consumption.

• Energy consumption and production targets on the basis of units should be established and monitored in the facility.

• Production and energy monitoring automation systems should be monitored for efficiency.

## REFERENCES

[1] Mumlu, G., 2008. Enerji yönetim sistemi ve bir sanayi tesisinde enerji yönetim uygulaması. Y.Lisans Tezi, Sakarya Üniversitesi Fen Bilimleri Enstitüsü, Sakarya.

[2] Özkök, M., 2010. Enerji yoğun bir tesiste enerji verimliliği proje tasarımı ve uygulama çalışması. Y.Lisans Tezi, Gazi Üniversitesi Fen Bilimleri Enstitüsü, Ankara.

[3] Acar, E., 2012. Enerji yoğunluklu bir fabrikanın enerji verimliliği özelinde incelemesi. Y.Lisans Tezi, Gazi Üniversitesi Fen Bilimleri Enstitüsü, Ankara.

[4] Arkat, A., 2013. Bir havalimanında enerji verimliliği ve enerji yönetim sisteminin kurulumunun uygulanması. Y.Lisans Tezi, Yıldız Teknik Üniversitesi Fen Bilimleri Enstitüsü, İstanbul.

[5] Kemaloğlu, A., 2014. Erzurum Şeker Fabrikası enerji analizi. Y.Lisans Tezi, Atatürk Üniversitesi Fen Bilimleri Enstitüsü, Erzurum.

[6] Bulanıkoğlu, H., 2014. Bir enerji sisteminde yanma verimi ve ısı iletim hatlarının iyileştirilmesi ile enerji verimliliğinin arttırılması. Y.Lisans Tezi, Erciyes Üniversitesi Fen Bilimleri Enstitüsü, Kayseri

# Molecular Genetic and Biochemical Responses in Primary Human Airway Epithelial, Liver Hepatocytes and Peripheral Blood Cell  Cultures Exposed to Zinc Oxide Based Nanoparticles in Vitro

Elanur Aydın Karataş
Department of Molecular Biology and Genetics, Faculty of Science, Erzurum Technical University , Erzurum, Turkey
elanuraydinn@gmail.com

Kübra Nur Bayındırlı
Department of Molecular Biology and Genetics, Faculty of Science, Erzurum Technical University , Erzurum, Turkey
kubranur.byndrl@gmail.com

Hasan Türkez
Department of Molecular Biology and Genetics, Faculty of Science, Erzurum Technical University , Erzurum, Turkey
hasanturkez@hotmail.com

Erdal Sönmez
Department of Mathematics and Science Education, Kazım Karabekir Faculty of Education, Atatürk University, Erzurum, Turkey
esonmez@atauni.edu.tr

Elif Öztetik
Department of Biology, Faculty of Science, Anadolu University, Eskişehir, Turkey
eoztetik@anadolu.edu.tr

Özlem Özdemir Tozlu
Department of Molecular Biology and Genetics, Faculty of Science, Erzurum Technical University , Erzurum, Turkey
ozdemirozlem1@gmail.com

*Abstract*— **Zinc oxide (ZnO) nanoparticles, which are widely used in textile, medical diagnosis, paint, nanoelectronics, sun creams, cosmetics, pharmaceuticals and biomedical applications, are the richest member of the nano-structured family of materials. In order to develop nanoparticles with wide application areas, which can be used in many sectors, multidimensional evaluation of the possible effects of these particles on human health and environment is important for their biosecurity. For this reason, in this study we investigated the use of doped and dopless ZnO nanoparticles in the cell in the human blood, alveolar epithelium and primary human liver hepatocyte cell lines in vitro. The aim of this study was to investigate changes in expression profiles of genes involved in different biological processes.  In our study, firstly 3- (4,5-dimethyl-thiazol-2-yl) 2,5-diphenyltetrazolium bromide (MTT), neutral red (NR) and lactate dehydrogenase (LDH) release tests were performed to determine the toxic dose. The effect of doped and non-doped ZnO nanoparticles on peripheral human blood, alveolar epithelium and primary human liver hepatocyte cell cultures were investigated by using the RT$^2$ Profiler PCR Arrays method to determine gene expression profile in pathways involved in molecular processes.  Doped and unpaired ZnO nanoparticles resulted in a change in the expression of different genes involved in basic metabolic processes such as apoptosis, necrosis, DNA damage or repair, mitochondrial energy metabolism, fatty acid metabolism (oxidation), oxidative stress or antioxidant response, heat shock response, ER stress or unfolded protein response, cytochrome P450s or phase I drug metabolism, steatosis, cholestasis, phospholipidosis and immunotoxicity in all three cell lines.**

*Keywords*— *Airway epithelial cell, Primary liver hepatocyte cell, Peripheric blood cultures, In vitro gene expression, Nanotoxicity, Zinc oxide*

# Reactive Red 45 of Textile Dyestuff Electrochemical Treatment

Serkan Bayar
Ataturk University, Faculty of
Engineering, Department of
Environmental Engineering
Erzurum, Turkey
sbayar@atauni.edu.tr

*Abstract—* **The objective of the present study was to assess the electrocoagulation treatment of Reactive Red 45 (RR45) azo dye material using an iron plate electrode. Treatment was carried out in a batch system. The influences of current density (from 1 to 5 A), initial pH of wastewater (from 3 to 9), and colorant concentrate (from 25 to 100 mg $L^{-1}$) on removal yield were investigated to determine the optimal experimental conditions. Color removal efficiency 98.0% was obtained under optimum experimental conditions where initial solution pH is 7, the concentration of RR45 colorant is 50 mg $L^{-1}$, current density is 0.5 A, stirring speed is 150 rpm, reaction temperature is 293 K and experiment time is 20 min.**

*Keywords—Electrocoagulation, RR45, pH, current density*

## I. INTRODUCTION

The color absorbs sunlight and prevents the process of photosynthesis in the receiving environment and causes a decrease in dissolved oxygen in the environment. It causes the extinction of living creatures in the receiving environment, changing species. For the treatment of wastewater, physical, chemical and biological methods can be used alone or used together. Chemical oxidation, adsorption, chemical coagulation, membrane, ion exchange and electrochemical processes can be used for color removal. Biological processes can achieve lower color removal compared to other methods. Due to the high water consumption of the textile industry, wastewater generation is more in comparison with other industries. In addition to the existing classical treatment systems, it is of great importance to try new technologies and share the results to be able to demonstrate feasible and economic solutions. In recent years, electrochemical methods have been started to be used in the treatment of textile wastewaters containing dyestuffs, providing ease of application and providing economic solutions and studies on this subject have been of great importance.

Electrochemical methods such as electrocoagulation-electroflocculation and electroflotation, electro-reduction, direct electro-oxidation, indirect electro-oxidation by using redox mediators such as active chlorine and, hydrogen peroxide in the process known as electro-Fenton, and photo-assisted electrochemical methods such as photo-electro-Fenton, photo-electrocatalysis have been applying for the treatment of wastewaters.

In electrocoagulation process, anode soluble Fe and Al ions are oxidized to $Fe^{+2}$ and $Al^{+3}$ forms while in cathode, as the result of the electrolysis of water, $H^+$ and $OH^-$ ions are formed. $OH^-$ ions are diffused in the solution and reacted to form $Fe(OH)_2$ or $Al(OH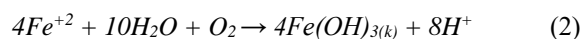)_3$. During that time, organic and colloidal pollutants are subsidized simultaneously by combing with $Fe(OH)_2$ or $Al(OH)_3$ complex [1-2].

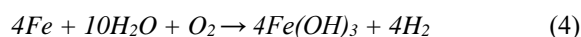Electrode reactions when iron is used to be electrode material are as follows [3-4]:

Anode:

$$4Fe_{(k)} \rightarrow 4Fe_{(s)}^{+2} + 8e^- \qquad (1)$$

And with solved oxygen in solution;

$$4Fe^{+2} + 10H_2O + O_2 \rightarrow 4Fe(OH)_{3(k)} + 8H^+ \qquad (2)$$

Cathode:

$$8H^+ + 8e^- \rightarrow 4H_{2(g)} \qquad (3)$$

Eventually total reaction can be summarized as follows

$$4Fe + 10H_2O + O_2 \rightarrow 4Fe(OH)_3 + 4H_2 \qquad (4)$$

In this study, it is aimed to reveal the color removal by electrocoagulation process (EP) which is one of the most used electrochemical processes of reactive red 45 (RR45) textile dyestuff wastewater of azo dye group which is prepared synthetically. The effect of initial pH, current density and initial dye concentration on treatment efficiency was investigated. Iron plate electrode was used in the studies. In addition, energy consumption costs were also determined.

## II. MATERIALS AND METHODS

Reactive red 45 (RR45) colorant was obtained from a commercial company, Duraner Boya A.Ş. Molecular weight of azo colorant, molecular formula of which is $C_{27}H_{19}ClN_7Na_3O_{10}S_3$, is 802.1 g $mol^{-1}$. RR45 exhibits a complex structure together with azo aromatic groups and used commonly in textile industry. As the result of spectrum scanning of colorant, maximum absorbance was found to be 243 nm, 283 nm and 541 nm. Molecular structure of RR45 colorant is given in Fig.1. The electrocoagulation cell was constructed from plexiglass having a dimension of 15 cm× cm×10 cm× 10 cm.The total volume of wastewater used in each experiment was approximately 600 mL. İron (Fe) plates 45 mm height ×75 mm width × 3 mm thickness in dimension was used for the sacrificial electrodes, arranged in monopolar configurations. The eight plates were constructed in the electrochemical reactor and the distance between plates was fixed at approximately 5 mm. These plates were used as four anodes and four cathodes. Electrocoagulation experiments were conducted using experimental design given in Fig. 2.The removal efficiency and energy consumption in RR45 treated by electrocoagulation is calculated as follows;

$$\eta\ (\%) = \left( \frac{C_0 - C_e}{C_0} \right) x100 \qquad (5)$$

$$W(kW - h\,m^{-3}) = \frac{VxIxt}{v} \qquad (6)$$

where, η; removal yield, $C_e$: final concentration of (RR45) (mg $L^{-1}$), $C_0$: initial concentration of (RR45) (mg $L^{-1}$), V: cell voltage (V), I: current density (A), t: the operating time (minute) and ν : the volume of wastewater (L)
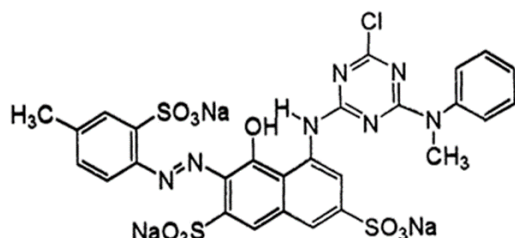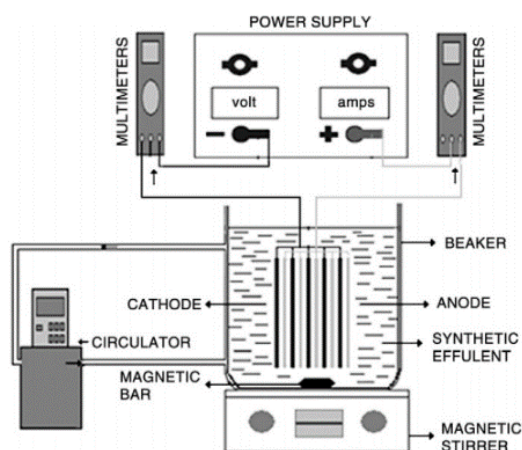


Fig. 1. Structure of RR45 dye



Fig. 2. Experimental set-up

## III. RESULT AND DISCUSSIONS

### A. Effect of initial pH on the performance of the system

Among the most important parameters in electrocoagulation is pHi of solution [5-6]. Since pH of unprocessed solution can affect the stability of hydroxide types, it may also have effect on pollutant removal yield. As the result of anode and cathode reactions, pH of solution can change. Therefore, based on pH of solution, electrolytic soluble metal ions ($Al^{+3}$, $Fe^{+2}$ etc.) can form different metal hydroxide types at different pH values.

Effect of pHi was investigated in the range of pH 3-9. Results obtained are given graphically in Fig. 3. Throughout the experiment period, constant current density was 0.5 A, stirring speed was 150 rpm, $C_o$= 50 mg $L^{-1}$, and temperature was 293 K. Color removal efficiency values (η) obtained after 20 minute reaction period are 73.6%; 83%; 98.1%; and 96.9% for initial pH values ranging from 3 to 9. The highest color removal yield is 98% at pH 7.
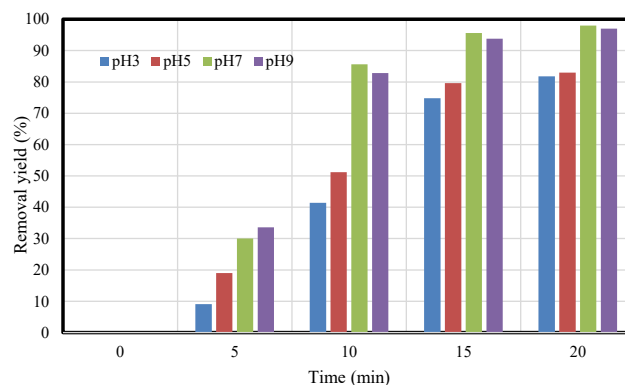


Fig. 3. The effect of initial pH on color removal yield

### B. Effect of current density on the performance of the system

Current density is defined to be the rate of current per unit of electrode area and it is a parameter determining process rate. Current density determines the amount of aluminum and iron removed from electrode, formation rate and size of gaseous bulbs and development of flocks [2-7]. Therefore, current density is an important parameter affecting the removal efficiency of pollutants. The effect of current density on the color removal efficiency was examined at current densities ranging from 1 to 5 A. Throughout the experiment period, constant initial pH was 7, $C_o$=50 mg $L^{-1}$, stirring speed was 150 rpm and temperature was 293 K. Color removal efficiency values (η) obtained after 20 minute reaction period are 92.2%; 98.0%; and 99.9% for current density values ranging from 1 to 5 A. The highest color removal yield is 99.9% at 5 A. As shown Fig. 4, color removal increased with increasing current density because the electrochemical solubility rate of iron increases and therefore more $Fe(OH)_2$ and $Fe(OH)_{3)}$ reacts with constant pollutant amount, and more pollutant amount is removed from the medium.
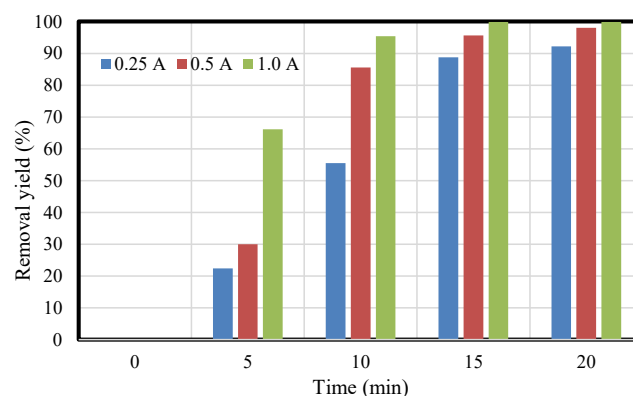


Fig. 4. The effect of current density on color removal yield

Energy consumption was calculated (by Eq. 6) with the help of findings from the experiments where the effect of current density on the treatment of waste water. Data obtained is presented in Fig. 5. As the current density increases, potential difference applied to the system also increases increasing energy consumption. This situation is supported by the findings in literature [8-9].
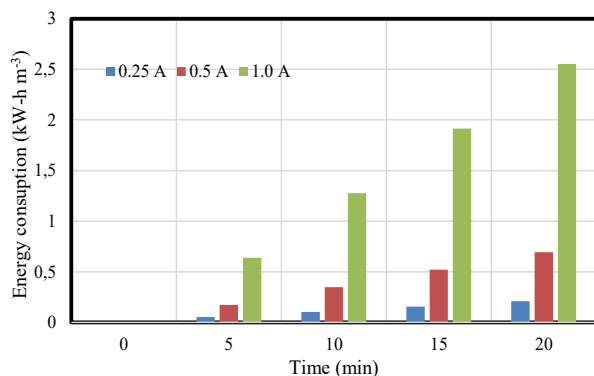
Fig. 5.The effect of current density on energy consumption

## C. The effect of initial colorant concentration

The effect of initial RR45 concentration on the removal yield in electrocoagulation process was studied with dye concentrations of 25, 50 and 100 mg L$^{-1}$. Experiments were conducted under the conditions, where pH is 7, stirring speed is 150 rpm, T is 20 min and current density is 0.5 A. Experimental results is shown graphically in Fig.6. As can be seen from Fig.6. as the initial colorant concentration increases color removal yields decreased. With the increase in initial colorant concentration from 25 mg L$^{-1}$ to 100 mg L$^{-1}$, color removal yield decreased from 99.9% to 79.3%
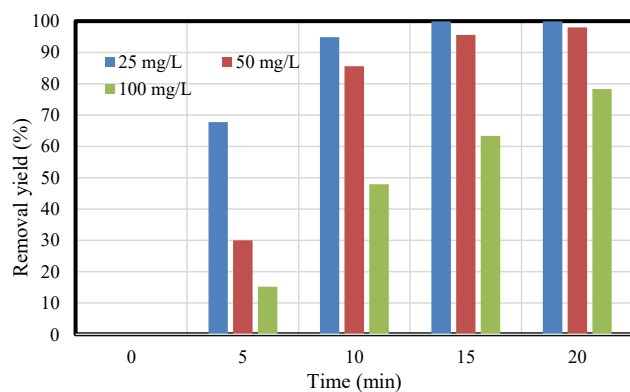


## IV. CONCLUSIONS

This study showed that the electrocoagulation process for color removal from reactive red 45 dyestuff is an effective method. The obtained experimental results showed that efficiency of color removal increased with increasing current density. Increasing current density, applied potential increased and thus energy consumption increased. As the initial colorant concentration increased, the color removal rate slowed down. Decreasing the pH decreased the color removal efficiency.

## REFERENCES

[1] G. Eason, B. Noble, and I. N. Sneddon, "On certain integrals of Lipschitz-Hankel type involving products of Bessel functions," Phil. Trans. Roy. Soc. London, vol. A247, pp. 529–551, April 1955. *(references)*

[2] G. Chen, "Electrochemical technologies in wastewater treatment. Sep.Purif.Technol, vol.38, pp.11-41. 2004.

[3] S. Bayar, R. Boncukcuoğlu, AE Yilmaz, et al, "Pre-Treatment of Pistachio Processing Industry Wastewaters (PPIW) by Electrocoagulation using Al Plate Electrode", Sep. Sci. Tec vol.49, pp.1008-1018. 2014.

[4] B. Khemila, B. Merzouk, A. Chouder et al, "Removal of a textile dye using photovoltaic electrocoagulation", Sustain. Chem.Pharmacy vol. 7, pp. 27-35. 2018.

[5] N. Adhoum and, L. Monser, "Decolourization and removal of phenolic compounds from olive mill wastewater by electrocoagulation", Chem. Eng. Process, vol.43, pp.1281-1287. 2004.

[6] P. Ratna Kumar, S. Chaudhari, Khilar. KC et al, "Removal of arsenic from water by electrocoagulation", Chemosphere vol. 55, pp.1245-1252. 2004.

[7] M. Uğurlu, A. Gürses, Ç. Doğar et al, "The removal of lignin and phenol from paper mill effluents by electrocoagulation", J. Environ. Manage, vol.87, pp. 420-428. 2008.

[8] H. Cheng Cu(II) Removal from lithium bromide refrigerant by chemical precipitation and electrocoagulation. Sep. Purif. Technol, vol. 52, pp.191-195. 2006

[9] P. Gao, X. Chen, F. Shen, G. Chen, "Removal of chromium(VI) from wastewater by combined electrocoagulation–electroflotation without a filter", Sep Purif Technol, vol.43,pp. 117-123. 2005.

# Enhancement of Energy and Power Density of Batteries and Supercapacitors: Electrode Hybridization

Fatma Nur Tuzluca
Department of Physics
Erzincan Binali Yıldırım University
Erzincan, Turkey
ftuzluca@erzincan.edu.tr

Yasar Ozkan Yesilbag
Department of Physics
Erzincan Binali Yıldırım University
Erzincan, Turkey
oyesilbag@erzincan.edu.tr

Mehmet Ertugrul
Department of Electrical and
Electronics Engineering
Ataturk University
Erzurum, Turkey
ertugrul@atauni.edu.tr

*Abstract*— **Design and synthesis of electrochemical energy storage devices, which have a long cycle life as well as a high energy and power density, are very important. One of the newest and most promising of energy storage devices that are currently being studied to improve energy storage technologies is the hybrid SC-LIBs with hybrid electrodes. Hybrid SC-LIBs are asymmetric electrodes formed by internal serial hybridization by replacing one of the electrodes of a symmetrical supercapacitor (SC) with a lithium-ion battery (LIB) electrode. It is very important that the charges on both electrodes of the hybrid SC-LIBs are balanced during high-rate charge/discharge operations and that the battery-type electrode contributes to the total capacitance of the device and further increases its working potential. For this reason, the studies focused on hybrid SC-LIBs with hybrid electrodes. These new devices consist of a hybrid SC-LIB electrode and a SC electrode with high power density or a LIB electrode with high energy density. In these devices, which have a wider cell working voltage and a larger capacity, the key factors that reveal the full working potential of the hybrid electrodes are the correct composition and morphological structure of the electrode materials.**

*Keywords*— *Supercapacitor, Battery, Hybrid structure, Energy density, Power density.*

## I. INTRODUCTION

The fact that storage of energy has become a global problem for modern societies increases the demand for high-performance energy storage devices every day. In addition, energy storage devices with high efficiency and low cost are required for continuous use of energy from renewable energy sources such as solar and wind energy [1]. The diversity of energy types and applications indicates the need for different perspectives in the development of energy storage devices. Thanks to strategies for developing new materials and designs in particular, energy storage devices that are aimed at overcoming the challenges of meeting energy needs stand out as the promising systems in global scale. Among the most important energy storage devices of the 21st century are batteries, supercapacitors, and fuel cells. The common feature of all three systems is that they are based on storing the produced energy by the reactions that occur at the electrode and electrolyte interface. In R & D activities, the performance of energy storage devices can be improved by better understanding and improving the electrochemical processes in this interface. In many areas, particularly in smart and portable electronic devices and electric vehicles, it is important to store a lot of energy at low costs. As a result, the energy and power densities of energy storage devices should be increased to a considerable level with the developing technology. The performance of energy storage devices depends on the electrode material, electrolyte, and device design. In this respect, studies on designing battery-type electrodes with new materials are available in the literature. In these studies, it is stated that the material design is made in two ways. The first is balancing the size and morphology of the electroactive particles in the materials with the sizes of the electrolyte ions. The second is the addition of materials with high conductivity to these electroactive particles. Furthermore, the use of aqueous electrolytes as well as organic electrolytes has resulted in a wider working potential range. These advances in electrode material and electrolyte lead researchers to design new hybrid electrode hybrid devices by electrode hybridization.

Current energy storage devices include lead-acid batteries, nickel-metal hybrid batteries, lithium-ion batteries and supercapacitors [2]. These energy storage devices in question differ from one another in cost, cycle life, safety, specific power, and energy density since the energy storage mechanisms of these devices are quite different from each other. Among these devices, the most intriguing are LIBs with high energy density and SCs with high power density [1], [3], [4]. LIBs that have high energy density due to the intercalation and de-intercalation reactions of lithium ions in the active electrode material are widely used in laptops, mobile phones and electric vehicles [5], [6]. However, the $Li^+$ storage mechanism in the LIB causes a lower power density due to the slowing of solid-state ion diffusion and the faradaic reactions in the bulk electrodes. Moreover, degradation of the electrode structures and volume expansion after cyclic charge/discharge processes reduces the cycle life of LIBs [2], [7]. At this point, electrical double-layer capacitor (EDLC) are of particular interest as materials with high power density and long cycle life due to the high rate of ion transfer (adsorption-desorption) in the active electrode material. However, the fact that the energy densities of the SCs are rather low compared to the LIBs is a significant disadvantage (Table 1) [8], [9].

Table 1. Characteristics of LIB and SC Energy Storage Devices

| Parameters | LIB | SC |
|---|---|---|
| Energy density (Wh $kg^{-1}$) | 20-150 | 1-10 |
| Power density (W $kg^{-1}$) | <1000 | 500-10000 |
| Cycle life | ~1500 | >500000 |
| Efficiency | 0.7-0.85 | 0.85-0.99 |
| Calendar Life (year) | 0.5-5 | 5-20 |
| Charge time | 1-5 h | 30 $sn^{-1}$ min |
| Discharge time | 0.3-3 h | 30 $sn^{-1}$ min |

Because the electric charge in the LIB electrodes is stored via redox (faradaic) reactions, the charge storage mechanism on them is a non-capacitive faradaic process. On the contrary, the charge storage mechanism in SCs is capacitive. While the EDLCs show capacitive characteristics, pseudocapacitors exhibit both capacitive and faradaic characteristics (Fig. 1). In SC electrodes, the electric charge can be stored EDL, pseudocapacitive or both [10].
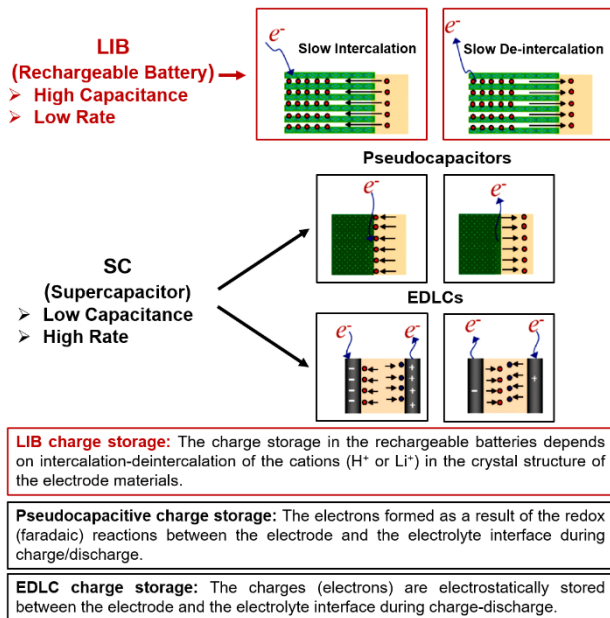


Fig. 1. Demonstration of charge storage mechanisms in LIB and SC [10].

For this reason, new hybrid energy storage devices called "Supercapattery (=**Supercapa**citor + ba**ttery**)" have recently been developed [11], [12] (Fig. 2); they combine the advantages of both capacitive and faradaic charge storage mechanisms and represent a wide range of devices. Researchers plan to produce eco-friendly, low cost and high-performance systems for these new devices by combining SC and LIB, which are complementary of each other thanks to different charge storing mechanisms [13].
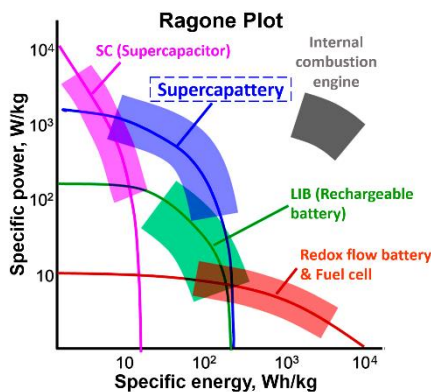


Fig. 2. Ragone plot of energy storage devices [14].

## II. ELECTRODE HYBRIDIZATION

As shown in Fig. 3, the charge-potential curve of the single-electrode SC during charge/discharge is linear. However, as the phase change occurs due to the redox reactions during charge/discharge of single-electrode LIB, the potential value is constant as in Fig. 4 according to the

phase rule. Therefore, SCs have high power and low energy density, while LIBs have high energy and low power density. That is, the energy stored in the SC is half the energy stored in a LIB [15].
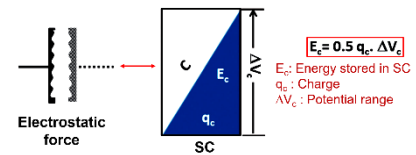


Fig. 3. Charge-potential curve of single-electrode SC in aqueous electrolyte and the corresponding energy storage.
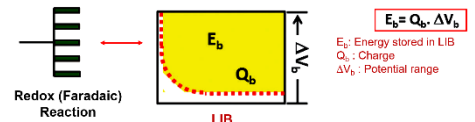


Fig. 4. Charge-potential curve of single-electrode LIB in aqueous electrolyte and the corresponding energy storage.

The performance of the energy storage device is determined by the electrolyte, electrode material and design (hybridization) [1], [16]. This results from the fact that the specific energy and power density values expressing device performance depend on the working potential range and capacity/capacitance of the device [6]. For this reason, some methods schematized in Fig. 5 are being studied to obtain devices with high energy and power density. These methods are the construction of asymmetric electrodes, the use of organic electrolytes and the design of hybrid devices with new hybrid electrodes in a single device [17]. Methods for both constructing asymmetric electrodes and the design of hybrid devices with new hybrid electrodes are investigated within the scope of internal hybridization (Fig. 6) [18].
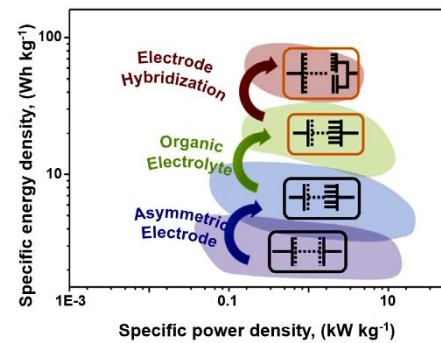


Fig. 5. Development process of specific energy and power density values from symmetrical electrode → asymmetric electrode → organic electrolyte → electrode hybridization [17].
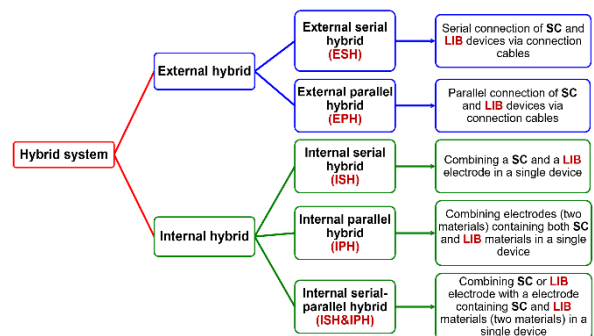


Fig. 6. Different combinations of SC-LIB hybrid structures [18].

CHARGE STORAGE MECHANISM OF HYBRID SC-LIBs

The asymmetric electrodes consist of a SC and a LIB type electrode. Combining these electrodes in a single device is internal serial hybridization (ISH). As shown in Fig. 7 this device, compose of combining the high power density of SC with the high energy density of LIB, is called the hybrid SC-LIB. It is important to use a high working potential ($\Delta V$) to achieve the redox potential ($\Delta V_b$) of the LIB electrode at the initial stage of charging in the hybrid SC-LIB. In this way, the amount of energy stored can be increased according to single-electrode structures. In contrast to the SC electrode, however, the contribution of the LIB electrode to the total capacitance value in the hybrid SC-LIB should be increased. This is due to the fixed electrochemical potential value of the LIB electrode. Furthermore, another disadvantage in hybrid SC-LIBs is that the LIB electrode cannot perform as fast as the SC electrode during charge/discharge. The main reason for this difference between the electrodes is that the charge storage process in the LIB electrode (faradaic) is slower than that of the SC electrode (electrostatic). Thermodynamically, the hybrid SC-LIBs can take full advantage of the different working potential ranges of both electrodes to ensure maximum working potential. In this way, both the specific capacitance and the energy density increase significantly. However, in order to achieve the maximum working potential, it is important to balance the charges stored in both electrodes at high rates in charge/discharge operations [17].
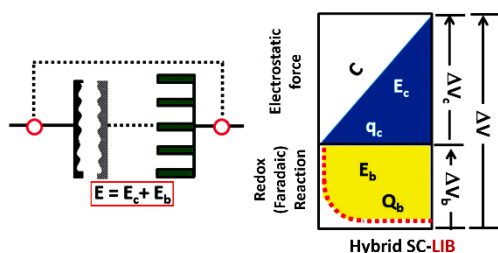


Fig. 7. Charge-potential curve of hybrid SC-LIB in aqueous electrolyte and the corresponding energy storage [15].

Recent research shows that the design of new electrode materials can help balance the low charge transfer kinetics in redox reactions in LIB electrodes [19]–[21]. Electrode material design can be done in two ways. The first is to control the size and morphology of the electroactive particles in the electrode material. The second is the addition of high conductivity materials to this electrode material [22]. The first approach is to shorten the diffusion paths of the charge-balancing ions by the electroactive particles synthesized in the nanosize. Thus, as the charge storage mechanism in the LIB electrodes will improve, solid-state ion diffusion will increase. At the same time, the size and morphology of these electroactive nanoparticles and the size of the electrolyte ions will be balanced. The second approach, which aims to increase the conductivity of the LIB electrode, is discussed in different ways. It is most preferred that these nanoparticles be doped with metals or coated with carbon [6], [23]. Furthermore, the working potential range ($\Delta V_o$) of organic electrolytes in hybrid SC-LIBs is higher than that of aqueous electrolytes ($\Delta V$) (Fig. 8).
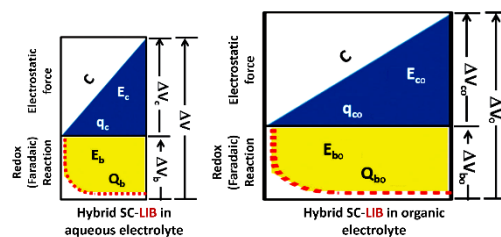


Fig. 8. Charge-potential curve of hybrid SC-LIB in aqueous and organic electrolyte and the corresponding energy storage.

CHARGE STORAGE MECHANISM OF HYBRID ELECTRODE WITH HYBRID SC-LIBs

The new hybrid electrode hybrid device consists of a SC or LIB electrode and a hybrid SC-LIB electrode. The combination of a single-material electrode and a double-material electrode in a single device is called internal serial-parallel hybridization (ISH&IPH). For example, Fig. 9 shows a hybrid electrode hybrid device comprising a SC electrode and a hybrid SC-LIB electrode. In the hybrid SC-LIB electrode, the energy is stored both as faradaic and capacitive. In the initial stage of charging of the hybrid SC-LIB electrode, the SC component stores up to $q_1$ charge through electrostatic forces until the LIB component reaches the redox potential ($\Delta V_b$). The LIB component is charged with $Q_b$ through the redox reaction until it reaches full charge state. After the full charge ($Q_b$) of the LIB component, the SC component is again charged up to $q_2$ through electrostatic forces until the hybrid SC-LIB electrode reaches the maximum potential ($\Delta V_{bc}$). Thus, the amount of charge in the hybrid SC-LIB electrode is equal to the sum of the amounts of charge caused by both the SC ($q_c = q_1 + q_2$) and the LIB ($Q_b$) component [15].
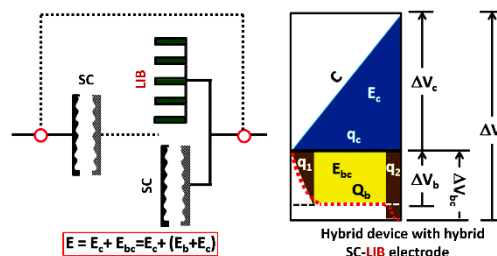


Fig. 9. The charge-potential curve of the hybrid device with hybrid electrode and the corresponding energy storage [15].

On the other hand, the maximum working potential ($\Delta V$) of the hybrid device is equal to the sum of the potentials of the SC electrode ($\Delta V_c$) and the hybrid SC-LIB electrode ($\Delta V_{bc}$). Thus, the total amount of energy stored (E) in this hybrid device is equal to the sum of the energies stored on the SC electrode ($E_c$) and the hybrid SC-LIB electrode ($E_{bc} = E_b + E_c$). The structural nature of the hybrid SC-LIB electrode allows it to have a higher power density than the LIB electrode since the SC component of the hybrid SC-LIB electrode increases the electron transfer rate of the LIB component even at high-rate charge/discharge operations. The electrochemical performance of the hybrid SC-LIB electrode material depends on the hybridization of SC and LIB components. For this reason, the key factors that reveal the complete working potential compared to conventional electrode materials are the correct composition and morphological structure of the material in hybrid SC-LIB electrode material [15]. Hybrid SC-LIB

electrodes produced for hybrid devices by internal serial hybridization of both LIB and SC components;

- Should work like a single electrode although it consists of double material. Otherwise, this electrode will arrive at the full charge state directly without charging the LIB component due to the faster charge transfer kinetics of the SC component.

- Should have a porous structure and a high surface area for high energy density and good ionic conductivity since the three-dimensional porous network structure increases charge transfer kinetics while maintaining the ionic conductivity of these electrode materials [16].

To improve the electrochemical performance of energy storage devices, these new hybrid-electrode hybrid SC-LIBs will act as milestones in the future [15].

Hybrid SC-LIBs produced from different electrode materials with the same or different charge storage mechanisms are shown in Table 2. Thus, these hybrid SC-LIBs are considered as promising devices in terms of eliminating gaps in their weakness due to the good aspects of both energy storage systems. In addition, the general strategy for the design of electrodes and hybrid SC-LIBs is summarized in Table 2. There are many different options available in the literature regarding electrode materials to be used in the production of hybrid SC-LIBs [24] (Fig. 10).

Table 2. Specific energy density, specific power density and cycling life values of energy storage devices with the same or different charge storage mechanisms [25].

| Device | Supercapacitor-battery(Supercapattery) | | | | | |
|---|---|---|---|---|---|---|
| | Supercapacitor | | | Hybrid SC-LIB | | Battery |
| | EDLC | Pseudocapacitor | | | | |
| | NFCS | NFCS | CFS | NFCS | CFS | NCFS |
| Electrode Materials | 1+1 1+2 | 1+3 | 1+1 1+2 | 1+3 | 1+2 | 1+1 1+2 |
| | NFCS | CFS | CFS | NCFS | NCFS | NCFS |
| Specific Energy (Wh kg⁻¹) | 6.7 [25], 10.2 [26] | 3.6 [27], 14.3 [28] | 26.6 [29] | 204 [30], 230 [31] | 103 [32], 114 [33] | 250 [34] |
| Specific Power (kW kg⁻¹) | 111.6 [25] | 24.7 [27], 0.68 [28] | 13 [29] | 55 [30] | 56 [32] | 1.5 [34] |
| Cycling life | >10000 [26] | >5000 [27] | >5000 [29,35] | >1000 [30] | >1000 [32] | >1200 [34] |

**NFCS:** Non-Faradaic Capacitive Storage = EDLC Storage
**CFS:** Capacitive Faradaic Storage = Pseudocapacitive Storage
**NCFS:** Non-Capacitive Faradaic Storage = Battery-Type Storage
**1+1:** Symmetrical device of the same electrode material;
**1+2:** Asymmetrical device of different materials with the same storage mechanism;
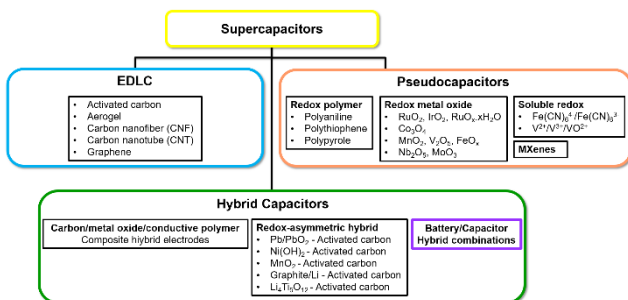**1+3:** Asymmetrical device of different materials with different storage mechanism.



Fig. 10. Classification of supercapacitors [24].

The mass and charge of the electroactive nanoparticles in the positive and negative electrode materials in the hybrid SC-LIBs should be in equilibrium as indicated in the Equation (1). That is, the amount of charge stored on both electrodes must be equal [14].

$$Q_- = m_- Q_{sp-} = m_+ C_{sp+} \Delta E_+ = Q_+ \rightarrow \frac{m_+}{m_-} = \frac{Q_{sp-}}{C_{sp+} \Delta E_+}$$

(1)

where, $Q_+$:charge at positive electrode, $Q_-$:charge at negative electrode, $m_+$:mass of electroactive nanoparticles in the positive electrode, $m_-$:mass of electroactive nanoparticles in the negative electrode, $Q_{sp}$:specific charge, $C_{sp}$:specific capacitance and $\Delta E$:potential range. The CV curves of the battery, EDLC and hybrid SC-LIB are given in Fig. 11. The reason for the observation of peaks in CV curves is that the charges on both electrodes in the batteries (or pseudocapacitors) are stored by faradaic redox reactions. For both electrodes in EDLCs, CV curves are rectangular since the charges are stored electrostatically. However, the charges in the hybrid SC-LIBs are stored by faradaic redox reactions in one of the electrodes while the other is electrostatically stored. Therefore, two different CV curves are observed in hybrid SC-LIBs. Peaks are observed in one of these curves while the other is rectangular.
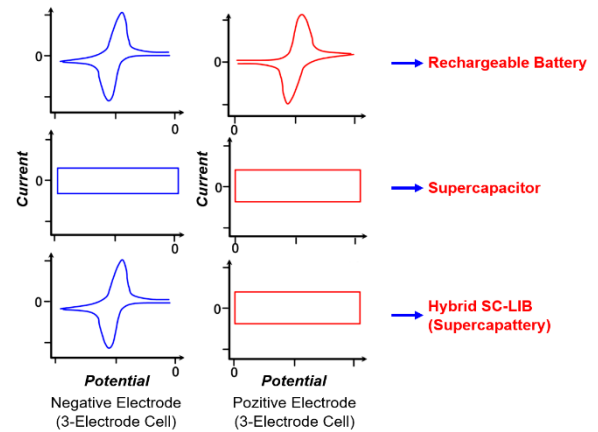


Fig. 11. Cyclic voltammetry (CV) curves of rechargeable battery, supercapacitor and hybrid SC-LIBs [14].

As seen in Fig. 12, the minimum voltage value during discharge in the supercapacitor ($U_{min}$=0) and hybrid SC-LIBs ($U_{min} \geq 0$) is decreased to zero, while the minimum voltage value ($U_{min} >> 0$) during the discharge in the batteries cannot be decreased to zero due to the possibility of irreversible reactions. Because the minimum discharge potential in the hybrid SC-LIBs is greater than or equal to zero ($U_{min} \geq 0$), the energy stored in these devices is calculated by the Equation (2) [14].

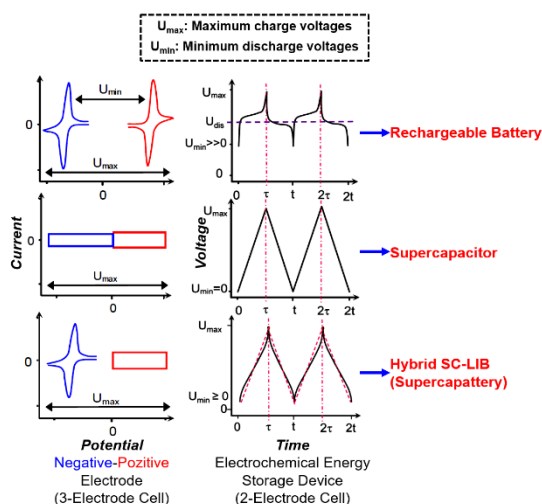$$E = \frac{C_{sp,device}}{2}(U_{max}^2 - U_{min}^2)$$

(2)

Fig. 12. Cyclic voltammetry (CV) and galvanostatic charge-discharge (GCD) curves of rechargeable battery, supercapacitor and hybrid SC-LIBs [14].

The GCD curves and electrode-device potential ranges of some hybrid SC-LIBs composed of different electrode materials are given in Fig. 13(a-c). As shown in Fig. 13(a), the negative electrode in the hybrid SC-LIBs with different charge storage mechanism is lithium metal or $LiC_6$, while the positive electrode is activated carbon. The negative electrode in the hybrid SC-LIBs with the same charge storage mechanism in Fig. 13 (b) is lithium metal or $LiC_6$, while the positive electrode is pseudocapacitive. In the hybrid SC-LIBs with the same charge storage mechanism, the negative electrode is the battery-type, while the positive electrode is pseudocapacitive (Fig. 13(c)). Thus, hybrid SC-LIBs with hybrid electrodes can be constructed by combining different combinations of capacitive (EDL, Pseudo, EDL: Pseudo) and battery-type electrode materials (Fig. 14).
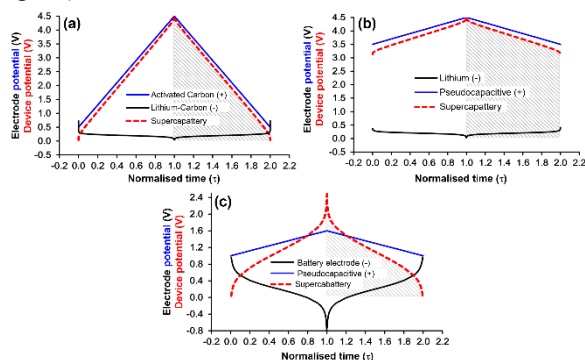


Fig. 13. Galvanostatic charge-discharge curves and electrode-device potential ranges of hybrid SC-LIBs consisting of different electrode materials [25], [37], [38].
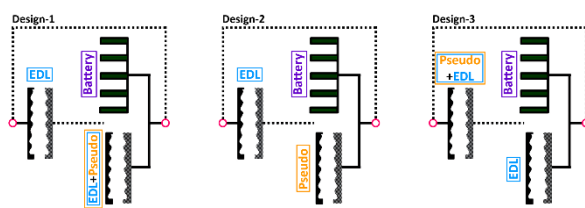


Fig. 14. Different designs of hybrid SC-LIBs with hybrid electrodes.

## CONCLUSION

Carrying out many experimental studies has become inevitable to design and manufacture hybrid SC-LIBs with hybrid electrodes. The reason for this is that a better understanding of the surface chemistry between the SC and LIB components will ensure overcoming the challenges in the combination of high energy and power density in a single device. In particular, it is important that the current collector-electrode and electrolyte interfaces with the electroactive nanoparticles have a highly homogeneous distribution to increase charge transfer. Nanoparticles present in porous structures and in redox active materials can, capacitively or not, be used in the production of these devices since the charge can be stored both in capacitive and faradaic ways. This helps derive excellent electrochemical results from the right hybridization of highly polarized (positive and negative charge) SC and LIB components in the device.

## REFERENCES

[1] M. R. Lukatskaya, B. Dunn, and Y. Gogotsi, "Multidimensional materials and device architectures for future hybrid energy storage," *Nat. Commun.*, vol. 7, pp. 1–13, 2016.

[2] P. Simon and Y. Gogotsi, "Materials for electrochemical capacitors," *Nat. Mater.*, vol. 7, no. 11, pp. 845–854, 2008.

[3] V. Aravindan, Y. S. Lee, and S. Madhavi, "Research Progress on Negative Electrodes for Practical Li-ion Batteries: Beyond Carbonaceous Anodes," *Adv. Energy Mater.*, vol. 5, no. 13, 2015.

[4] V. Aravindan, J. Gnanaraj, Y. S. Lee, and S. Madhavi, "Insertion-type electrodes for nonaqueous Li-ion capacitors," *Chem. Rev.*, vol. 114, no. 23, pp. 11619–11635, 2014.

[5] S. Goriparti, E. Miele, F. De Angelis, E. Di Fabrizio, R. Proietti Zaccaria, and C. Capiglia, "Review on recent progress of nanostructured anode materials for Li-ion batteries," *J. Power Sources*, vol. 257, pp. 421–443, 2014.

[6] N. Nitta, F. Wu, J. T. Lee, and G. Yushin, "Li-ion battery materials: Present and future," *Mater. Today*, vol. 18, no. 5, pp. 252–264, 2015.

[7] R. Yi, S. Chen, J. Song, M. L. Gordin, A. Manivannan, and D. Wang, "High-performance hybrid supercapacitor enabled by a high-rate Si-based anode," *Adv. Funct. Mater.*, vol. 24, no. 47, pp. 7433–7439, 2014.

[8] A. G. Pandolfo and A. F. Hollenkamp, "Carbon properties and their role in supercapacitors," *J. Power Sources*, vol. 157, no. 1, pp. 11–27, 2006.

[9] P. Simon, Y. Gogotsi, and B. Dunn, "Where Do Batteries End and Supercapacitors Begin?," *Science (80).*, vol. 343, no. 6176, pp. 1210–1211, 2014.

[10] Y. Wang, Y. Song, and Y. Xia, "Electrochemical capacitors: mechanism, materials, systems, characterization and applications," *Chem. Soc. Rev.*, vol. 45, no. 21, pp. 5925–5950, 2016.

[11] C. Klumpner, G. Asher, and G. Z. Chen, "Selecting the power electronic interface for a supercapattery based energy storage system," *2009 IEEE Bucharest PowerTech Innov. Ideas Towar. Electr. Grid Futur.*, pp. 1–7, 2009.

[12] A. J. Stevenson *et al.*, "Supercapatteries with Hybrids of Redox Active Polymers and Nanostructured Carbons," *Nanocarbons Adv. Energy Storage*, vol. 1, pp. 179–210, 2015.

[13] B. Li *et al.*, "Activated Carbon from Biomass Transfer for High-Energy Density Lithium-Ion Supercapacitors," *Adv. Energy Mater.*, pp. 1–6, 2016.

[14] G. Z. Chen, "Supercapacitor and supercapattery as emerging electrochemical energy stores," *Int. Mater. Rev.*, vol. 62, no. 4, pp. 173–202, 2017.

[15] D. P. Dubal, O. Ayyad, V. Ruiz, and P. Gómez-Romero, "Hybrid energy storage: the merging of battery and supercapacitor chemistries," *Chem. Soc. Rev.*, vol. 44, no. 7, pp. 1777–1790, 2015.

[16] W. Zuo, R. Li, C. Zhou, Y. Li, J. Xia, and J. Liu, "Battery-Supercapacitor Hybrid Devices: Recent Progress and Future Prospects," *Adv. Sci.*, vol. 4, no. 7, pp. 1–21, 2017.

[17] H. S. Choi and C. R. Park, "Theoretical guidelines to designing high performance energy storage device based on hybridization of lithium-ion battery and supercapacitor," *J. Power Sources*, vol. 259, pp. 1–

14, 2014.

[18] D. Cericola and R. Kötz, "Hybridization of rechargeable batteries and electrochemical capacitors: Principles and limits," *Electrochim. Acta*, vol. 72, pp. 1–17, 2012.

[19] H. S. Choi, J. H. Im, T. Kim, J. H. Park, and C. R. Park, "Advanced energy storage device: a hybrid BatCap system consisting of battery–supercapacitor hybrid electrodes based on $Li_4Ti_5O_{12}$–activated-carbon hybrid nanotubes," *J. Mater. Chem.*, vol. 22, no. 33, p. 16986, 2012.

[20] H. K. Kim *et al.*, "Exploring High-Energy Li-I(r)on Batteries and Capacitors with Conversion-Type $Fe_3O_4$-rGO as the Negative Electrode," *ChemElectroChem*, vol. 4, no. 10, pp. 2626–2633, 2017.

[21] H. K. Kim *et al.*, "$TiO_2$-reduced graphene oxide nanocomposites by microwave-assisted forced hydrolysis as excellent insertion anode for Li-ion battery and capacitor," *J. Power Sources*, vol. 327, pp. 171–177, 2016.

[22] L.-L. Xing, K.-J. Huang, S.-X. Cao, and H. Pang, "Chestnut shell-like $Li_4Ti_5O_{12}$ hollow spheres for high-performance aqueous asymmetric supercapacitors," *Chem. Eng. J.*, vol. 332, no. July 2017, pp. 253–259, 2018.

[23] F. Yao, D. T. and Pham, and Y. H. Lee, "Carbon-Based Materials for Lithium-Ion Batteries, Electrochemical Capacitors, and Their Hybrid Devices," *ChemSusChem*, vol. 8, no. 14, pp. 2284–2311, 2015.

[24] F. Beguin and E. Frackowiak, *Supercapacitors Materials, Systems, and Applications*. Wiley, 2012.

[25] L. Yu and G. Z. Chen, "Redox electrode materials for supercapatteries," *J. Power Sources*, vol. 326, pp. 604–612, 2016.

[26] J. H. Chae and G. Z. Chen, "1.9 V Aqueous Carbon-Carbon Supercapacitors With Unequal Electrode Capacitances," *Electrochim. Acta*, vol. 86, pp. 248–254, 2012.

[27] A. Lewandowski, A. Olejniczak, M. Galinski, and I. Stepniak, "Performance of carbon-carbon supercapacitors based on organic, aqueous and ionic liquid electrolytes," *J. Power Sources*, vol. 195, no. 17, pp. 5814–5819, 2010.

[28] X. Zhou, C. Peng, and G. Z. Chen, "20 V Stack of Aqueous Supercapacitors with Carbon (-), Titanium Bipolar Plates and CNT-Polypyrrole Composite (+)," *AIChE J.*, vol. 58, no. 3, pp. 974–983, 2012.

[29] C. Peng, S. Zhang, X. Zhou, and G. Z. Chen, "Unequalisation of electrode capacitances for enhanced energy capacity in asymmetrical supercapacitors," *Energy Environ. Sci.*, vol. 3, no. 10, p. 1499, 2010.

[30] Z. H. Huang, Y. Song, X. X. Xu, and X. X. Liu, "Ordered Polypyrrole Nanowire Arrays Grown on a Carbon Cloth Substrate for a High-Performance Pseudocapacitor Electrode," *ACS Appl. Mater. Interfaces*, vol. 7, no. 45, pp. 25506–25513, 2015.

[31] F. Zhang *et al.*, "A high-performance supercapacitor-battery hybrid energy storage device based on graphene-enhanced electrode materials with ultrahigh energy density," *Energy Environ. Sci.*, vol. 6, no. 5, p. 1623, 2013.

[32] L. Yu and G. Z. Chen, "High energy supercapattery with an ionic liquid solution of $LiClO_4$," *Faraday Discuss.*, vol. 190, pp. 231–240, 2016.

[33] S. A. Klankowski, G. P. Pandey, G. A. Malek, J. Wu, R. A. Rojeski, and J. Li, "A Novel High-Power Battery-Pseudocapacitor Hybrid Based on Fast Lithium Reactions in Silicon Anode and Titanium Dioxide Cathode Coated on Vertically Aligned Carbon Nanofibers," *Electrochim. Acta*, vol. 178, pp. 797–805, 2015.

[34] S. Makino *et al.*, "4 V class aqueous hybrid electrochemical capacitor with battery-like capacity," *RSC Adv.*, vol. 2, no. 32, p. 12144, 2012.

[35] Web-link, "https://en.wikipedia.org/wiki/Lithium-ion_battery#cite_note-7." .

[36] S. Zhang, C. Peng, K. C. Ng, and G. Z. Chen, "Nanocomposites of manganese oxides and carbon nanotubes for aqueous supercapacitor stacks," *Electrochim. Acta*, vol. 55, no. 25, pp. 7447–7453, 2010.

[37] G. Z. Chen, "Understanding supercapacitors based on nano-hybrid materials with interfacial conjugation," *Prog. Nat. Sci. Mater. Int.*, vol. 23, no. 3, pp. 245–255, 2013.

[38] B. Akinwolemiwa, C. Wei, and G. Z. Chen, "Mechanisms and Designs of Asymmetrical Electrochemical Capacitors," *Electrochim. Acta*, vol. 247, pp. 344–357, 2017.

# Modeling of Dsawr Sensor for Different Resistance Values of Active Layer

Hilal Kübra Sağlam
*Faculty of Engineering, Deparment of Electrical and Electronics Engineering*
*Atatürk University*
Erzurum, Turkey
hks.erz@gmail.com

Ömer Çoban
*Vocational school of Ispir*
*Atatürk University*
Erzurum, Turkey
omercoban@atauni.edu.tr

Mehmet Ertuğrul
*Faculty of Engineering, Department of Electrical and Electronics Engineering*
*Atatürk University*
Erzurum, Turkey
ertugrul@atauni.edu.tr

*Abstract*—**DSAWR has become popular in recent years for its gas detection due to its superior features such as durability, selectivity and sensitivity. In this study, it was revealed that the resonance frequencies of the resonators and the resistance of the active layer should be done before the experimental studies. Although the resistance of the active layer is in a wide range, the DSAWR has a good performance with two resonator resonators with 433.92 MHz and 433.42 MHz. In addition, it has been shown that the resistance value of the active layer also has an effect on Q quality factors.**

*Keywords—SAW Resonator, Gas Sensor, SAW Sensor, DSAWR*

## I. INTRODUCTION

Acoustic wave technology has been used for gas detection applications for several decades [Yunusa, Z., Hamidon, M.N., 2016, Binhack et al 2003, Yunusa, Z., 2015, Ebeoğlu at al 2014]. The Surface Acoustic Wave (SAW) sensor allows the development of a small, light, battery-free, maintenance-free and multi-sensor wireless inquiry process. Main advantages of SAW sensors are high precision, low power consumption, wireless capacity and placement in moving or rotating parts and hazardous environments. The detection mechanism of the acoustic wave sensors is based on changes in the physical properties of the sheet when it comes into contact with the surface of the device. These properties used for gas detection include mass (m), elastic modulus (E), viscosity ($\rho$), electrical conductivity ($\sigma$), permeability and temperature (T). Any change in these parameters changes the electrical or mechanical boundary conditions that change the propagation of the acoustic wave velocity. SAW sensors are mass-sensitive chemical sensors. SAW technologies can also be called a kind of scale in which molecular changes of mass can be measured accurately. As molecules pass through the crystal surface, they attach to the sensor surface covered with sensor molecules, causing changes in the oscillation frequency of the sensor. These frequency changes caused by molecular interactions are used in real time characterization. Two types are available. SSAWR and DSAWR.

Single SAW resonators have been used for gas detection and have proven to be reliable and successful. However, the effects of noise on the double SAW resonator are less than a single SAW resonator. The dual SAW resonator (DSAWR) is a configuration containing two SAW resonators and has proven to be reliable in sensor applications. The advantage of DSAWR is that it can be used for wireless applications. It can also compensate for the smallest temperature losses. In Figure 1, DSAWR equivalent circuit is shown and frequency is found 434 MHz (Fig 2).
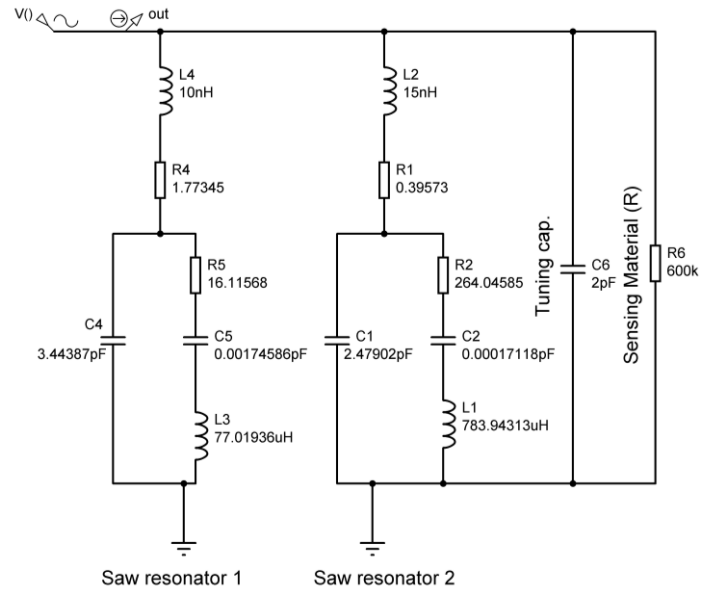


Figure 1. DSAW Resonator Equivalent circuit

## II. MATERIAL AND METHODS

Generally, the resistance of the active layers produced from different materials and different conditions shows significant differences from each other. For a known resonator with resonance frequency, impedance matching difficulties can be observed for the value of the resistance of the active layer (sensing material). For this reason, it is necessary to determine the resonator in the range of resistance value of the active layer by means of simulation to determine the appropriate resonator. In this study, a simulation of a DSAWR sensor is performed to obtain working range of active layer in term of resistivity for a given sensor with a resonant frequency. SAW resonators with resonance frequencies of 433.92 MHz and 433.42 MHz were used in the DSAWR system configuration.
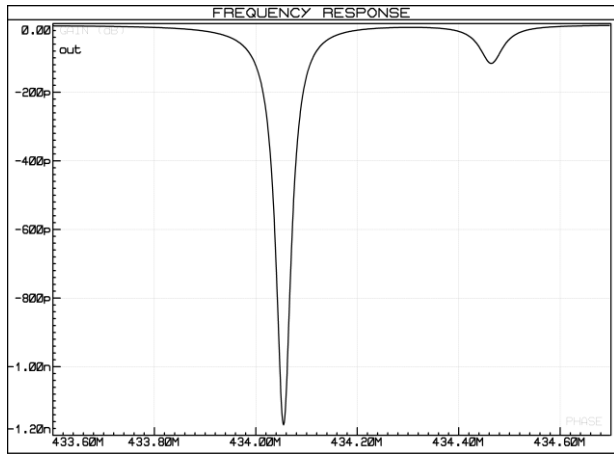
Figure 2. DSAW Resonator Frequency Response

Firstly, an equivalent circuit (Fig 1) for each resonator was obtained from the literature [Yunusa, Z., Hamidon, M.N., 2016, Binhack et al 2003, Yunusa, Z., 2015]. Using these circuits and DSAWR sensor structure, a suitable circuit was obtained and simulation studies for frequency response of the circuit were performed (Fig 2).
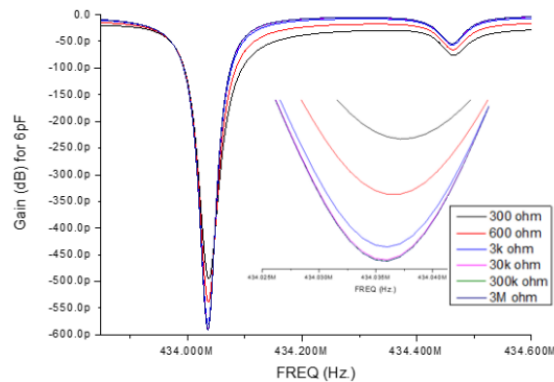


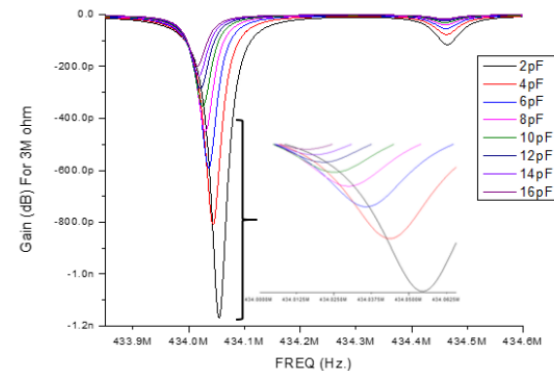Figure 3. Frequency response for different resistance values



Figure 4. Frequency response for different capacitance values

The resistance of the active layer was changed from 300 ohms to 6 MOhm and the change in resonance frequency was determined (Fig 3 and Fig 4). During this calculation, the set capacitor value is set to 2pF.

## III. RESULTS AND DISCUSSION

The DSAWR sensor for the given resonator circuit indicates that it can be a suitable sensor for the active layer with a resistance value between 300 Ohm and 6 MOhm. While the resonance frequency changes slightly in this resistance range, it can be a more suitable sensor for high resistance values. Therefore, it is recommended to use higher resistant active layers in this sensor structure. On the other hand, the resonance frequency shift occurs when the capacitance value changes. This shows that the tuning capacitance is important for the current design.

It is understood that the active sheet material may have an effect on the sensitivity and sensitivity of the sensor as well as the selectivity and sensitivity of the sensor. To increase sensitivity, different resonators with different series resonance frequencies, Q-factors and resonator impedances should be used.

## REFERENCES

[1] [1] Yunusa, Z., Hamidon, M.N., 2016. Hydrogen Gas Sensor Using Double SAW Resonator System. 2016 International Conference on Advances in Electrical, Electronic and System Engineering
[2] [2] Binhack, M., Klett, S., Guliyev, E., Buff, W., Hamsch, M., Hoffmann R., 2003. Modelling Of Double Saw Resonator Remote Sensor. 2003 IEEE Ultrasonics Symposium-1416
[3] [3] Ebeoğlu, M.A., Taşaltın, C., Gökçimen, F., 2014. The classification and determination the quantity of chemical gases considering the effect of moisture with SAW sensor arrays. 2014 IEEE 22nd Signal Processing and Communications Applications Conference (SIU 2014)
[4] [4] Yunusa, Z., 2015. Development Of Double Surface Acoustıc Wave Resonator System For Gas Sensing Application. Master Thesis, Institute of advanced technology, Universiti Putra Malaysia, 43400 UPM Serdang, Selangor, Malaysia

# Fabrication and characterization of CdS/CdTe solar cells by electrochemical deposition

**Serdar AYDIN [1]**

[1] *Computer Research and Application Center*

*Atatürk University, Erzurum – TURKEY*

serdar@atauni.edu.tr

**Abstract:** In this study CdS/CdTe solar cells are deposited on Indium Tin Oxide (ITO) substratesby electrochemical deposition. The electrical morphological and optics properties ofCdS/CdTe solar cells prepared by electrochemical deposition were investigated. Crystalstructure and grain size of solar cell layers were investigated by X-ray diffraction(XRD) analysis according to XRD analysis CdS crystalized in hexagonal, whereas CdTe was cubic. The grains shapes, sizes and distributions of the surface formed on thelayers of the films were investigated by Scanning electron microscopy (SEM) and Atomic force microscope (AFM).The cell parameters like open circuit potential, short circuit current, fill factor, cellefficency, series resistant and shunt resistant were investigated by I-V characterization.As a result of this analysis, our CdS/CdTe solar cells had an efficiency of %9,95. Finally, the experimental findings obtained by comparing the similarities anddifferences with other experimental and theoretical data in the literature were discussed.

## INTRODUCTION

Renewable energy (sources) is the energy obtained from the existing energy flow in continuous natural processes. Solar energy is one of the most important and renewable energy sources. Solar energy; It is a renewable energy source that comes from the sun and has a constant intensity of 1370 W/m2 outside the earth's atmosphere and varies between 0-1100 W/m2 on the earth's surface. It can be used in a controlled manner from heating to cooling and in electricity generation. Electricity generation from solar energy; It is carried out with two different methods as direct transformation and indirect transformation [1] Today, solar energy is used in residences and workplaces, agricultural technology, industry, transportation vehicles, communication tools, signaling and automation, and electricity generation.

## MATERIALS AND METHODS

Electrochemical deposition method, which is an effective method for obtaining thin films, was used as an experimental method. Electrochemical storage; is the reduction of metal ions in an electrolytic solution onto the cathode [2]. Electrochemical storage is based on the electrolysis phenomenon. Michael Faraday's recognition of the basics of electrolysis in the early 19th century led to new applications. The basic parts of the electrochemical storage cell are an anode and a cathode, which can come into contact with an electrolyte. At the cathode, reduction of the reacting substance takes place with electron gain. In other words, electrons are transferred from the cathode to the substance in the electrolyte. At the anode, there is oxidation of the reacting substance with the loss of electrons. Electrons are transferred in the electrolyte towards the anode. Parameters such as the potential to enlarge the properties of the films obtained in electrochemical storage, the type and amount of substances added to the electrolyte, solution pH, current density, growth time, electrolyte temperature, chemical additives added into the solution affect [3].
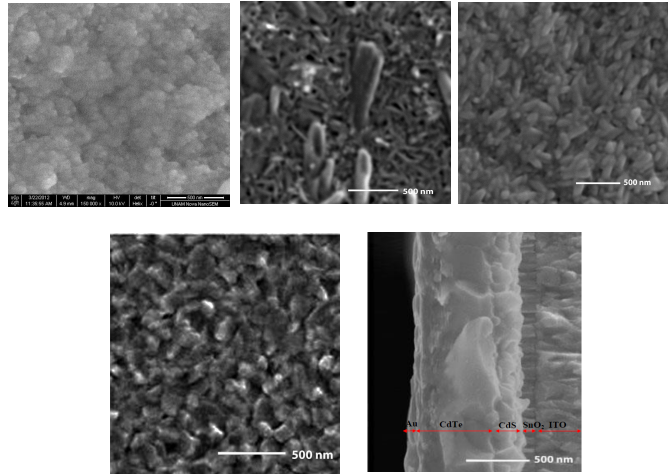


**Figure 1.** The SEM images of $SnO_2$, CdS, CdTe, Au layers and Au/CdTe/CdS/ITO solar cell

We performed SnO2 growth on ITls by electrochemical storage method. drowth was done at room temperature using a solution containing 20mM $SnO_2.2H_2O$, 0.1 M $NaNO_3$ and 75 mM $HNO_3$ içeren. Electrostorage was performed using a three-electrode cell. ITl substrates with a surface resistance of 100 ohm/cm2, platinum wire, and Ag/Ag l in saturated potassium chloride solution were used as working, counter and reference electrodes, respectively, and the storage area on the working electrode is 1 cm².

CdS films were prepared potentiostatically from 0.3 M $CdSO_4$ and 0.02 M $Na_2S_2O_3$ solutions by electrodeposition. A few drops of sulfuric acid were added to adjust the pH of the solution to 2. The solution was continuously heated at about 85°C during deposition.

CdTe layer growth was obtained from solutions containing 0.75 M CdSO4 and 115 mM TeO2 on CdS films prepared by electrochemical storage at growth times of 100, 300, 500, 700 and 900 minutes. The pH of the solution prepared to grow the CdTe layer was adjusted to 1.8 by adding sulfuric acid to this solution.

## RESULTS AND DISCUSSION

In this study, the production of thinfilm p-CdTe/n-CdS solar cells was aimed. In our study, the electrochemical storage method was preferred for the production of CdTe solar cells because it is simple, convenient and economical. While producing the solar cell, transparent conductive oxide (ITO) was chosen as the front contact. Thus, it is aimed to pass the sun's rays directly to the p-n junction without being absorbed in the front contact.

The remaining CdS layers of the most efficient solar cells produced are 200 nm, and the thickness of the CdTe layers is around 750 nm. The electrical data of these solar cells under A.M 1.5 are as follows, theoretical power Pt=18.17W, maximum power

Pmax=9.95W, open circuit potential Voc = 0.69 V, short circuit current Jsc= 26.34 mA/cm2, cell efficiency η = 9.95%, while the filling factor was calculated as FF= 54.76%, the series resistance of the cell was calculated as 5.2 Ω.cm2 and the shunt resistance as 226,757 Ω.cm2. As a result, solar cells with 9.95% efficiency at room temperature were produced. The structural properties of these solar cells were investigated.

When the structural properties of the films obtained are examined, In2Sn2O7-x (222) and (511) peaks belonging to Indium Tin Oxide and In2O3 (521) structures according to JCPDS:06-0416, (110), (101), (211) and (301) peaks belong to tetragonal SnO2 peaks (JPDS card no: 41-1445). CdS (002) (101) (103) (112) (004) (202) (203) (114) (213) peaks belonging to the hexagonal structure obtained are compatible with JCPDS card no 80-006, CdTe film grown according to this spectrum is JCPDS It belongs to CdTe cubic structure, which is compatible with card no 15-0770. This film grew in the preferential orientation of (111), and CdTe (220) (311) and (331) peaks were also observed, albeit at low intensity.

Au/CdTe/CdS/SnO2/ITO films were structurally examined by SEM. According to the SEM data, the thickness of the SnO2 layer is around 100 nm, the thickness of the CdS film is around 200 nm, and the thickness of the CdTe film is around 750 nm. The thickness of the Au coating is around 100 nm.

According to the electrical and structural properties of the films obtained, it was observed that the growth of the CdS layer at different growth times significantly affected the cell performance.

## CONCLUSIONS

In this study, ITO/SnO2/CdS/CdTe/Au solar cell structure with a high efficiency of 9.95% was successfully obtained by electrochemical storage method. In line with the results obtained, the following suggestions can be given to increase the efficiency of solar cells.

-Pre-contact with higher conductivity than ITO can be used instead of ITO, or these layers can be enlarged with different magnification systems to further increase conductivity and permeability.

- Efficiency can be increased by making the CdS layer thinner. Thickness

- Efficiency improvement can be made by growing high resistive conductive oxides between ITO and CdS in different thicknesses.

- As the back contact, other metals such as molybdenum can be evaporated instead of gold, preventing the loss of efficiency that may occur due to the resistance of the rear contact.

-Diffusion between CdS and CdTe layers can be minimized by changing the duration of the CdCl2 treatment and the temperature at which the process is performed.

## REFERENCES

[1] Alaçakır, F. B., 2001. "Ülkemizde elektrik üretimini destekleyen bir çözüm: Güneş pilleri", Yenilenebilir Enerji Kaynakları Sempozyumu, 182-185. İzmir, Türkiye.

[2] Bütün, H., 2007. FexZn1-X İnce Filmlerinde kβ/Kα Şiddet Oranının Ölçülmesi, Yüksek Llisans Tezi, Kahraman Maraş Sütcü İmam Üniversitesi Fen Bilimleri Enstitüsü

[3] Özdemir, R., 2010. Elektrodepolama Yöntemi ile Elde Edilen ZnFe İnce Filmlerinin Elektriksel Özdirenç Özelliklerinin Sezgisel Yöntemler Yardımıyla İncelenmesi, Yüksek Lisans Tezi, Kilis 7 Aralık Üniversitesi Fen Bilimleri Enstitüsü, Kilis.

# POSTER PRESENTATIONS

# Indices and Computer Models Used to Calculate and Estimate Outdoor Human Thermal Comfort

Süleyman Toy

*City and Regional Planning Dept.*
*Architecture and Design Faculty of Atatürk*
*University*
Erzurum, Turkey
suleyman.toy@atauni.edu.tr

*Abstract*-**Indices and Computer Models Used to Calculate and Estimate Outdoor Human Thermal Comfort Humans feel the features of atmosphere all together at one time i.e. combined effect of ambient air conditions. This effect is felt as temperature. Effect of atmospheric features on humans is called thermal effect. People are satisfied or dissatisfied with the conditions of the atmosphere. When they are satisfied with them so they are in comfort and vice versa. Although the definition of thermal comfort is very diverse and changeable depending on the fields, it can often be defined as the condition of ambient air where 80% of the people present there feels no discomfort with it. Thermal comfort is effective on human health, workforce performance, emergence and dissemination of critical illnesses, energy consumption, ecological destruction, water consumption etc. Therefore, due to its various aspects this concept is worth studying scientifically.**

**Since the beginning of 20th century (Haldane 1905) scientists have been interested in under what air conditions people are comfortable. To date more than 200 indices and models have been developed to calculate, estimate, determine, categorise, compare and even distribute thermal comfort values and also use this information to design spaces and buildings. This study is related to the indices and models used to calculate / estimate human thermal comfort and even design spaces considering the bioclimatic information they produce. In the scope of the study, brief information is given about the concept of human thermal comfort and the simple and complex indices (e.g. RayMan) calculating it and some detailed information is also given about the computer models (e.g. ENVIMET) used to design spaces considering several human thermal comfort factors.**

*Keywords*-**Human thermal comfort, simple indices, complex indices, ENVIMET, Rayman, bioclimatic comfort**

# Characterization and synthesis of high quality binary metal oxide electrode materials by electrochemical methods on conductive substrates

Fatma Bayrakçeken Nişancı
Program of Food Technology Narman
Vocational Training High School,
Ataturk University, 25530, Erzurum, Turkey
fbayrakceken@atauni.edu.tr

*Abstract*— **Co₃O₄-NiO double transition metal oxides (TMO) that can provide high capacitance due to recycled oxidation and reduction in a wide potential range, can be used at low cost without any binder, due to well-defined electrochemical behaviors and high theoretical capacity with flexible synthesis method, in lithium ion batteries (LIB) and high-performance alternative electrode materials was successfully prepared for lithium-ion battery applications which are defined as future technology The electrode materials were characterized by atomic force microscopy (AFM), scanning electron microscopy (STM), X-ray diffraction (XRD), Raman and UV-visible spectroscopy techniques.**

**Keywords— electrode material, electrodeposition, energy storage, metal oxides, thin film, nanostructures**

## I. INTRODUCTION

The nanostructures of the electrode materials are widely studied because of their new properties associated with their size, specificity, shape and imperfect nature, as they exhibit superior qualities to their traditional mass counterparts. It is one of the main electrode materials that can produce high capacitance through a transition metal oxide, its reversibility in oxidation and a reduction in a wide potential range [1]. Electrochemical production methods are of great interest because of the unique principles and flexibility of electrode materials that control the structure and morphology [2-3]. In order to create more high-performance Li-ion batteries, new methods need to be developed that can easily control both particle size and reduce interface defects [4].

## II. EXPERIMENTAL

A BAS 100B/W electrochemical workstation connected to a three-electrode cell (C3 Cell Stand, BAS) was used for the electro-chemical experiments. In all cases, a Ag/AgCl (3 M NaCl) electrodeserved as the reference electrode, and a platinum wire was used as the counter electrode. ITO-coated quartz (10 $\Omega$ cm$^{-2}$) and Au was used as the working electrode for the electrochemical measurements, All of the electrolyte solu-tions used in this study were prepared using deionized water (i.e.,>18 M ) from a Milli- system.

## III. RESULTS AND DISCUSSION

### A. NiO Morphological Analysis on Electrodeposition on Co₃O₄ Films

Co₃O₄ nanostructures were deposited with potential controlled by electrolysis method in 2 mM Co(NO₃)₂, 0.5 M

KHCO₃ suspension dissolved O₂ gas nanostructures at 900 mV, on ITO substrate. Then obtained by electrodepositing NiO nanocrystals for 5 minutes at a constant potential of -650 mV in solution of 2 mM NiSO₄ and 0.1 M Na₂SO₄ (pH: 4.66) on Co₃O₄ films. The resulting Co₃O₄-NiO films are shown in Fig 1 for the films obtained from different deposition times of the same concentrations.
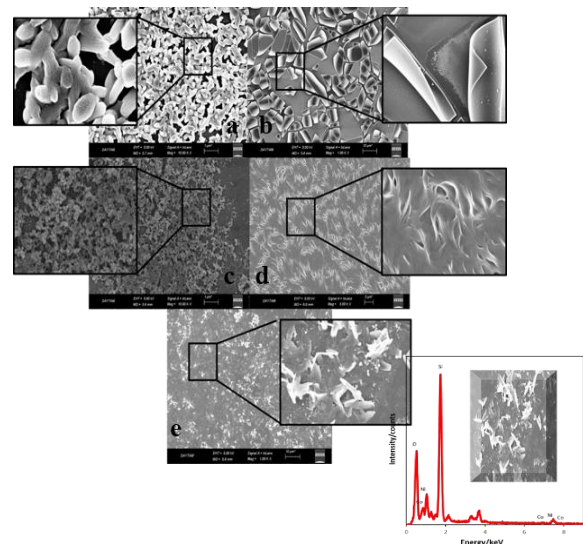


Fig. 1. SEM micrographs of the electrodeposited nanostructures on ITO electrodes (a) (900 mV) 5 minutes Co₃O₄ - (-650 mV) 5 min NiO (b) (900 mV) 60 min Co₃O₄ - (-650 mV) 10 min NiO (c) (900 mV) 5 min Co₃O₄ - ( -650 mV) 10 min NiO (d) (900 mV) 5 min Co₃O₄ - (-650 mV) 3 min NiO and (e) (900 mV) 10 min Co₃O₄ - (-650 mV) 5 min NiO, EDS spectrum of Co₃O₄ / NiO film synthesized electrochemically.

As can be seen from the SEM images, the deposition times of Co₃O₄ and NiO metal oxides can be changed and the desired properties of materials can be easily produced without using any organic binders. EDS analysis of Co₃O₄ / NiO films deposited on ITO substrates is given in Figure 1. The qualitative analysis of the EDS spectra of cobalt, oxygen and nickel containing films shows the structure of Co, O and Ni (0.5 /2/1) for the films on which Co₃O₄ films are modified by NiO and also from the substrate. By adjusting the composition ratio by changing the deposition time, the desired stoichiometries can be provided in the films.

### B. Structural Analysis with XRD of Co₃O₄-NiO

There Figure 2 are XRD diffractograms of the two compounds metal oxide (Co₃O₄-NiO) semiconductor films

prepared in aqueous medium. Au substrate and semiconductor XRD data of $Co_3O_4$ and NiO were observed in practice. These XRD diffractograms, a predominant $Co_3O_4$ (311), $2\theta = 35.28$ diffraction peaks were observed on a $2\theta = 37.28$ and $2\theta$ bir scale $Co_3O_4$ coating. As the NiO ratio on $Co_3O_4$ increases the diffraction peak in $Co_3O_4$ (311) shifts to more positive values $2\theta$. In our study, $2\theta = 37{,}9$ 77.3, which belongs to Au plane which we use as substrate, has diffraction peaks at 81.7.

Fig. 2. XRD diffractograms of NiO (10 min deposition at -650 mV), $Co_3O_4$
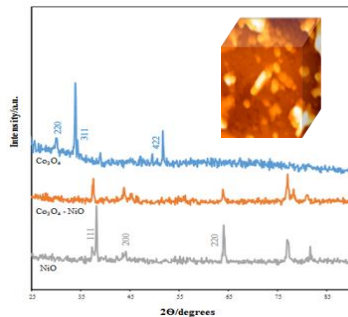


/ NiO (NiO for 5 min at 900 mV for 10 min on $Co_3O_4$ for 5 min), $Co_3O_4$ (10 min deposition at 900 mV) at room temperature on Au electrode.

### C. Analysis of $Co_3O_4$-NiO Raman Spectroscopy

Figure 3 NiO on ITO glass electrode electrode (10 min deposition at -650 mV), $Co_3O_4$/ NiO (NiO deposition for 5 min at -650 mV over 10 min $Co_3O_4$ at 900 mV), $Co_3O_4$ (10 min deposition at 900 mV) Raman spectra measured by planar oriented laser polarization of the films are shown.
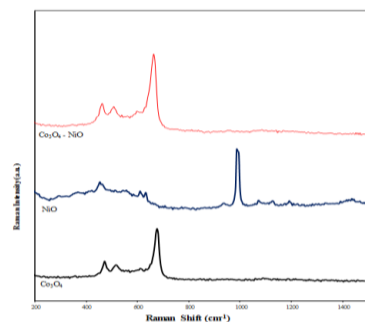


Fig. 3. (10 min deposition at -650 mV), $Co_3O_4$ / NiO (NiO for 5 min at 900 mV for 10 min on $Co_3O_4$ for 5 min), Co3O4 (10 min at 900 mV at room temperature on ITO coated glass electrode micro-Raman spectra measured by planar oriented laser polarization of deposition films

These notable Raman spectra 476 $cm^{-1}$, 520$cm^{-1}$ and 676 $cm^{-1}$ bands correspond to the modes of the $Co_3O_4$ particle phase. The single phonon (1P) in the Raman spectra of the NiO nanocrystals with a particle size of 300 nm and 100 nm yields peaks due to two phonons (2P) scattering; The vibration source of the first four bands is indicated by a phonon (1P) TO / LO, two phonon (2P) 2TO, TO + LO and 2LO modes Micro-raman at room temperature NiO spectra at 532 nm excitation wavelength using the band transverse optics (TO) observed at 457 $cm^{-1}$ and 614 $cm^{-1}$ longitudinal optics (LO) phonon, modes of NiO single crystals and 632 $cm^{-1}$ 2TO, 935 $cm^{-1}$ TO + LO, 991 $cm^{-1}$ and 2LO NiO modes correspond to combination phonon modes. Figure 3 shows the $Co_3O_4$/NiO films formed by NiO deposition for 5 minutes at -650 mV for 10 minutes on $Co_3O_4$, in the raman spectra of 480 $cm^{-1}$ and

520 $cm^{-1}$. Includes 457 $cm^{-1}$ TO and 614 $cm^{-1}$ LO modes for NiO crystals.

### D. Optical Analysis of $Co_3O_4$-NiO

The wavelength values of the absorption peaks of NiO, Co3O4 / NiO, $Co_3O_4$ particles, and thus the change of energy values are shown (Fig. 4). In addition, the absorption spectra of $Co_3O_4$-NiO can be explained by the fact that the NiO and $Co_3O_4$ spectra exhibit a severity in the middle of the spectra and the blue slip quantum limiting effect in the absorption spectra.
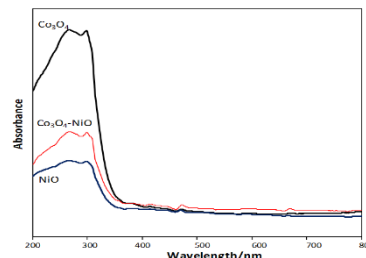


Fig. 4. NiO 10 min deposition at -650 mV, $Co_3O_4$ / NiO (900 mV) 10 min -$Co_3O_4$ (-650 mV) 5 min NiO deposition, $Co_3O_4$ 10 min deposition at 900 mV on ITO coated glass electrode, absorption spectra of films.

### [10] CONCLUSIONS

This study aims to efficiently utilize the three-dimensional (3D) electrodes obtained by forming a non-binding $Co_3O_4$-NiO binary transition metal oxides by a new electrochemical method, as a lithium ion battery (LIB) electrode with high capacity ratio and fast recycling life. Various effective strategies have been developed to improve the recycling and speed capacity and cycle life of materials based nanostructures of NiO on $Co_3O_4$. $Co_3O_4$-NiO with high conversion efficiency are synthesized by electrochemical methods which have more practical, environmentally friendly, inexpensive and inherent parameters that allow the deposition of interface and size controlled material. $Co_3O_4$-NiO having the desired composition, structure and size with this electrochemical method within the scope of this project are easily deposited by controlling the electrochemical parameters such as potential and time.

### ACKNOWLEDGMENT

### REFERENCES

[1] T. Zhang, D. Li, Z. Tao, J. Chen, "Understanding electrode of rechargeable lithium batteries via DFT calculations," Materials International, vol. 23, pp. 256–272, March 2013.

[2] F. Bayrakçeken Nisancı and U. Demir, "Size controlled electrochemical growth of PbS nanostructures into electrochemically patterned self assembled monolayers," Langmuir, vol. 28, pp. 8571–8578, May 2012.

[3] P. Jiang, Q. Wang, J. Dai, W. Li, "Fabrication of NiO-$Co_3O_4$ core shell nanofibres for hibh performance supercapacitors," Materials Letters, vol. 188, pp. 69–72, October 2013.

[4] F. Bayrakçeken Nisancı, T.Oznülüer,U.Demir, "Photoelectrochemical properties of nanostructured ZnO prepared by controlled electrochemical under potential deposition" Langmuir, vol. 108, pp. 281–287,2013

# Synthesis and Characterization of Graphene Aerogel and Graphene Aerogel/Polypyrrole Support Materials for PEM Fuel Cells

Emine Öner
*Chemical Engineering*
*Atatürk University*
Erzurum, Turkey
eemineteke@gmail.com

Ayşe Bayrakçeken Yurtcan
*Chemical Engineering*
*Atatürk University*
Erzurum, Turkey
ayse.bayrakceken@gmail.com

*Abstract—* **In this study, three-dimensional (3D) structured graphene aerogel (GA) and polypyrrole (PPy)/GA supported Pt electrocatalysts were synthesized through a self- assembly hydrothermal process. Graphene oxide was prepared from graphite powder by using modified Hummer's method. 3D GA was synthesized by hydrothermal assembly of GO and subsequently freeze-drying. Then 3D GA hybrid with polypyrrole was synthesized. Crystal structure of the synthesized support materials was determined by X-Ray diffraction (XRD), the morphology and pore structure were characterized using scanning electron microscopy (SEM), Transmission Electron Microscope (TEM) and Brunauer, Emmet and Teller (BET) analysis.**

*Keywords— Graphene aerogel, Pt-based catalyst, PEM fuel cell*

## I. INTRODUCTION

Developing technology, increasing population and welfare level enhance energy consumptions. Greenhouse gas emissions are increasing with the extensive use of hydrocarbon-based energy production. Every day, environmentally friendly alternative energy production systems are increasing slightly. One of them is PEM fuel cell technology.

The fuel cells are the systems based on the principle of generating energy as a result of electrochemical reactions of the reactants used. Pure water and heat are released as a result of the reaction. A fuel cell basically formed from anode, cathode, and electrolyte in contact with them. The electrodes have got a porous structure with high gas permeability. Reduction / oxidation reactions among fuel and oxygen occurs while electric current and heat are generated.

As the air/oxygen passes over the cathode surface, hydrogen or hydrogen-rich gas passes through the anode surface. Electrons are transported through an external circuit towards the cathode, while hydrogen ions migrate through the electrolyte in the anode. Water is released by reacting oxygen and hydrogen ions with electrons in the cathode. The flow of electrons through the external circuit generates electricity. Due to the high efficiency in fuel use, the by-product from this electrochemical process is only water and heat[1]. Polymer electrolyte membrane fuel cells are fuel cell types especially developed for transportation applications. In the last 5 years, there has been a large increase in the cost and

performance of PEM fuel cells. These studies focused on the production of large quantities of catalyst, membrane and bipolar plates.

In PEM fuel cell Pt and Pt-based alloys are commonly used catalysts. Because Pt has very good working conditions with high catalytic activity, chemical stability, high current density. The use of carbon black for the electrode material is supported by metal catalysts (usually platinum or platinum based catalysts)[2, 3]. However, the fact that Pt resources are limited and the costs are high have led to the search for different catalysts. Traditionally Vulcan (XC-72R), Cabot Corp (250 $m^2$/g), Shawinigan (Chevron, 80 $m^2$/g), Black Pearl (BP2000), Cabot Corp. (1500 $m^2$/g), Ketjen Black (KB EC600JD & KB Carbon blacks with high conductivity and surface area such as EC600J), Ketjen International (1270 $m^2$/g and 800 $m^2$/g) and Denka Black (DB, Denka, 65 $m^2$/g) are used as support materials for fuel cell electrocatalysts. But other than carbon black many different types of materials as catalyst supports were also investigated. The interest in nanostructured materials has increased since it has been conducting faster electron transfer over the last 10 years and has seen higher electrocatalytic activity. Graphene is one of the highest conductivity materials and has fast electron transfer. So, graphene in fuel cell research is a subject of interest as the catalyst support material. Graphene is seen as a potential support material due to its high electron transfer rate, high surface area and high conductivity. Researches on the use of 3-Dimensional structures based on graphene and graphene as fuel cell catalyst support materials are ongoing[4].

In this study, the catalyst support materials for PEM fuel cell was synthesized from graphene aerogel and graphene aerogel/polypyrrole hybrid materials. Synthesized materials were physically characterized. It is aimed to improve the fuel cell performance with these support materials.

## II. EXPERIMENTAL

### A. Synthesis of Graphene Oxide by Modified Hummer's Method

Graphite is exposed to a preliminary oxidation process to prevent the formation of graphite-core/graphite oxide-shell structures in the final product. In this study, graphite pre-oxidation was achieved by using mixing graphite with definite amounts of $H_2SO_4$, $K_2S_2O_8$ and $P_2O_5$ in a beaker and

kept at 80°C for 6 h.[5]. The resulting mixture was washed with distilled water and dried at room temperature. The resulting product was used in the Hummer method. Pre-oxidized graphite oxide was mixed with $H_2SO_4$ and $NaNO_3$ in a beaker. The mixture was added to ice bath and added $KMnO_4$ slowly to a temperature not to exceed 5 °C. The mixture was stirred in the ice bath for 30 minutes and taken and then at 35°C stirred for further 3 hours. Then distilled water was added very slowly to the mixture. Here, care is taken to keep the temperature around 50°C. After stirring for half an hour, water were added. 30% $H_2O_2$ was added dropwise to the mixture and then washed with 10% HCl solution. After this process, it was washed twice with pure water and dried at 60°C in the oven.

### B. Synthesis of Graphene Aerogel (GA)

Graphene oxide dissolved in distilled water. This mixture was kept in a Teflon coated autoclave at 180 °C for 12 hours. The obtained hydrogel is freeze-dried and turned into graphene aerogels (GAs)[6].

### C. Synthesis of GA supported Pt nanoparticles via microwave irradiation technique

Both energy and time saving catalyst preparation technique, microwave irradiation, is used for the decoration of Pt nanoparticles over GA with a 20% nominal Pt loading. Briefly, definite amount of supports and aqueous solution of $H_2PtCl_6$ (Aldrich) were added in 50 mL ethylene glycol and then stirred for 30 min [7, 8]. Then the resulting solution was put in a microwave oven and heated for 1 min at 800 W. After microwave treatment, the mixture was cooled down with ice water, then filtered, washed with acetone and deionized water. Finally dried at 100°C in a vacuum oven for 12 h.

### D. Synthesis of GA/PPy composites

Conducting polymer/GA composites based on polypyrrole (PPy) were synthesized by in-situ chemical oxidative polymerization of corresponding pyrrole (Py, Merck) monomers on GA at 25 °C. Ammonium persulfate (APS, Sigma Aldrich) was used as the oxidant and p-toluene sulfonic acid (p-TSA, Sigma Aldrich) was used as the dopant in order to increase the electrical conductivity of the composites. In this study, graphene aerogel was dissolved in ethanol and stirred for 30 minutes. Pyrrole was dissolved in pure water and added to this mixture with stirring for 30 minutes. APS (Amonyumpersulfate) and p-TSA were added to the pure water in different beakers and added to the first mixture. The prepared solution was allowed to stir for 24 hours. The mixture was then filtered and the resulting material was washed with ethanol, distilled water and acetone. Dried at room temperature[9].

### E. Synthesis of Pt/ GA/PPy

Pt reduction was performed on the PPy / GA composites prepared with the same procedure as given in Section C.

### III. RESULTS AND FINDINGS

XRD results for GO, GA, GA/PPy catalysts are given in fig. 1. XRD pattern of GO exhibited diffraction peak at $2\Theta=10.1705°$.[10]. The diffraction peaks at $2\Theta=26.4°$ and $2\Theta=24.6°$ correspond to amorphous PPy and C.
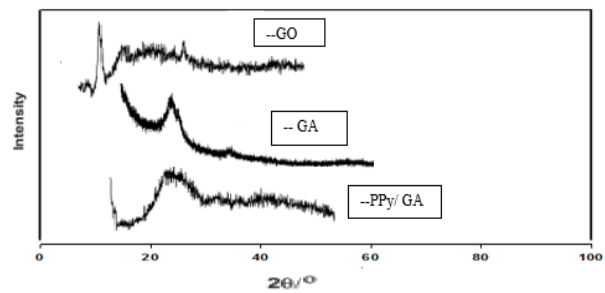


Fig. 1. XRD patterns for synthesized GO, GA, PPy/GA

Specific surface areas of the synthesized GA and PPy/GA were found to be 265 m²/g (GA) and 24 m²/g (GA / PPy) by Brunauer-Emmett-Teller (BET) surface analysis. Pore volumes of the composites decreased with an increase in PPy amount in the composite.

Table 1. Structural properties of synthesized materials

|  | BET surface area (m²/g) | Average pore diameter (nm) | t-plot micropore volume (cm³/g) | BJH pore volume (cm³/g) |
|---|---|---|---|---|
| GA | 265 | 4.8 | 0,013259 | 0.237018 |
| GA/PPy | 24 | 9.5 | NA | 0.053832 |

Figure 2 (a) shows the SEM images of graphene aerogels. The images show a three-dimensional network consisting of random orientations of thin plate-shaped folded layers [5]. In fig. 2. (b), PPy formations on the GA structure are observed. This shows that PPy/GA composite was successfully synthesized.
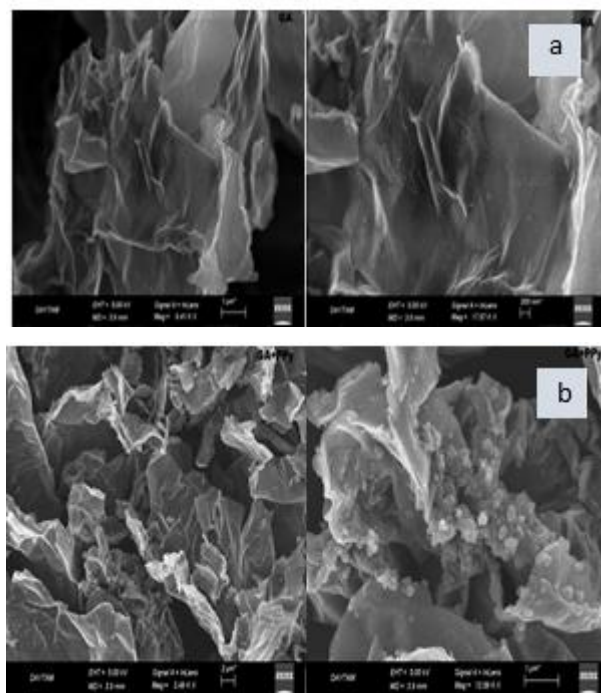


Fig. 2. SEM images of (a) GA (b) GA/PPy

Fig. 3 (a)-(b) show the TEM images of GA and Pt/GA materials. It is seen that Pt is distributed on the surface of GA. In fig. 3 (c)-(d) TEM images of GA/PPy and Pt/GA/PPy are given. Polypyrrole formation on the GA is observed. Figure 2 (d) shows the homogeneous distribution of the Pt nanoparticles on support material. In TEM images, GA / PPy is distributed homogeneously and it was seen that almost spherical Pt nanoparticles were successfully prepared by microwave irradiation technique.
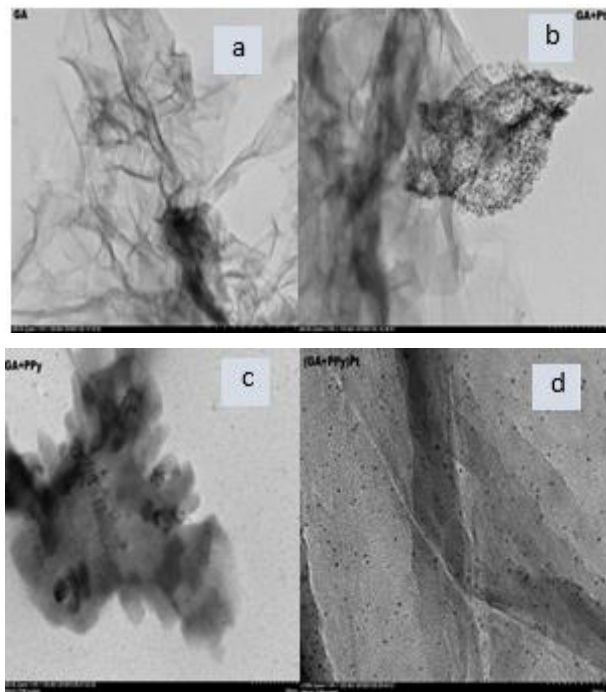


Fig. 3. TEM images of (a) GA (b) Pt/GA (c) PPy/GA (d) Pt/PPy/GA

## V. CONCLUSIONS

Fuel cell technology is more efficient and sustainable than other energy conversion systems. But the high cost of platinum, which is the precious metal used in the cathode and anode, is one of the biggest obstacles to its widespread utilization. Various carbon support materials have been used to reduce the amount of platinum. In this study, the use of graphene aerogel and GA/PPy as support materials for Pt nanoparticles was investigated. Platinum nanoparticles were decorated onto the carbon support material by microwave irradiation technique.

Analysis of the prepared support materials was carried out. XRD, SEM, BET and TEM analyzes were performed to investigate the properties of the support materials and electrocatalysts. As a result of the analyzes, it was seen that the support materials were successfully synthesized. The synthesized materials will be tested in PEM fuel cell environment. The impact on fuel cell performance will then be evaluated.

## REFERENCES

[1] F. San, S. Özdemir, N. Örs, E. Kalafatoğlu, and T. Bahar, "Hidrojen Yakıt Pilleri: Otomotiv Endüstrisindeki Uygulamalar ve Geleceği," ed: TÜBİTAK, 2001.

[2] E. Antolini, "Graphene as a new carbon support for low-temperature fuel cell catalysts," *Applied Catalysis B: Environmental,* vol. 123, pp. 52-68, 2012.

[3] A. Witkowska, G. Greco, S. Dsoke, R. Marassi, and A. Di Cicco, "Structural change of carbon supported Pt nanocatalyst subjected to a step-like potential cycling in PEM FC," *Journal of Non-Crystalline Solids,* vol. 401, pp. 169-174, 2014.

[4] R. Yıldırım, "PEM yakıt pilleri için anot ve katot malzemelerinin geliştirilmesi," YTÜ Fen Bilimleri Enstitüsü, 2014.

[5] N. I. Kovtyukhova *et al.*, "Layer-by-layer assembly of ultrathin composite films from micron-sized graphite oxide sheets and polycations," *Chemistry of materials,* vol. 11, no. 3, pp. 771-778, 1999.

[6] L. Zhao, Z.-B. Wang, J.-L. Li, J.-J. Zhang, X.-L. Sui, and L.-M. Zhang, "Hybrid of carbon-supported Pt nanoparticles and three dimensional graphene aerogel as high stable electrocatalyst for methanol electrooxidation," *Electrochimica Acta,* vol. 189, pp. 175-183, 2016.

[7] H.-W. Wang, R.-X. Dong, H.-Y. Chang, C.-L. Liu, and Y.-W. Chen-Yang, "Preparation and catalytic activity of Pt/C materials via microwave irradiation," *Materials Letters,* vol. 61, no. 3, pp. 830-833, 2007.

[8] A. Bayrakçeken, L. Türker, and İ. Eroğlu, "Improvement of carbon dioxide tolerance of PEMFC electrocatalyst by using microwave irradiation technique," *international journal of hydrogen energy,* vol. 33, no. 24, pp. 7527-7537, 2008.

[9] F. Memioğlu, A. Bayrakçeken, T. Öznülüer, and M. Ak, "Synthesis and characterization of polypyrrole/carbon composite as a catalyst support for fuel cell applications," *International Journal of Hydrogen Energy,* vol. 37, no. 21, pp. 16673-16679, 2012.

[10] İ. Tiyek, U. Dönmez, B. Yıldırım, M. H. Alma, M. S. Ersoy, and Ş. Karataş, "Kimyasal yöntem ile indirgenmiş grafen oksit sentezi ve karakterizasyonu," *Sakarya University Journal of Science,* vol. 20, no. 2, pp. 349-357, 2016.

# Production and Characterization of TiO2 and NiS Doped TiO2 Nanotube Photocatalysts

Hakan Kızıltaş
Department of Chemical Engineering
Atatürk University
Erzurum/TURKEY
h.kiziltas@atauni.edu.tr

Taner Tekin
Department of Chemical Engineering
Atatürk University
Erzurum/TURKEY
ttekin@atauni.edu.tr

Derya Tekin
Department of Metallurgical and
Materials Engineering
Atatürk University
Erzurum/TURKEY
deryatekin@atauni.edu.tr

*Abstract—* **Nanotube TiO2 photocatalysts were synthesized using the anodization method. NiS nanoparticles were doped on the surface of the anodized TiO2 nanotubes by sequential ionic layer adsorption and reaction. The crystal structure of the produced TiO2 and NiS/TiO2 nanotube photocatalysts was characterized using X-Ray diffraction (XRD) and its morphology and elemental composition was characterized using scanning electron microscopy (SEM-EDS). Acid Black I was used for photocatalytic activity experiments. The results showed that NiS doping increased the photocatalytic activity of TiO2.**

*Keywords— TiO2 nanotube, photocatalyst, Acid Black I, NiS/TiO2 nanotube*

## I. INTRODUCTION

TiO2 nanotubes (NTs) obtained by electrochemical anodization on the surface of a metallic titanium plate have been extensively studied in photocatalytic applications due to their unique geometry and functionality combinations [1]. The wide surface area of nanotubes is frequently used for many photoelectrochemical and photocatalytic applications including unique electronic and ionic properties, contaminant degradation, water treatment [2, 3].

In the photocatalytic applications, unlike photoelectrochemical reactions, TiO2 photo-induced charge carriers react with the environment without an externally applied voltage. Under the aeration conditions, the conduction band electrons react with O2 to form O2 radicals or superoxides, while the valence band cavities can react with water to form OH radicals or to oxidize organic species directly to CO2 and H2O. This effect is used for photocatalytic degradation of unwanted contaminants in air or waste water. In general, reactive oxygen species produced in the valence band and in the conduction band can contribute to the efficient destruction of organic pollutants. Additive catalysts are often used to increase the efficiency by accelerating the charge transfer rate of the electron transfer to the environment [4, 5]. The most doped metals on TiO2 are noble metals such as Au, Pt or Pd [6, 7]. General co-catalyst activity has been shown to be not only dependent on the size and distribution of the noble metal particles but also on their relative location on the nanotubes [8].

In this study, TiO2 and NiS doped TiO2 nanotube photocatalysts were synthesized and its results of XRD and SEM-EDS were used for characterization. In order to determine their photocatalytic activity, the decomposition of Acid Black 1 dye was investigated.

## II. EXPERIMENTAL

### A. Materials

In the production of nanotube TiO2 photocatalysts, Aldrich titanium plates of $3 \times 1$cm with 99.7% purity were used. Sodium fluoride (Sigma-Aldrich, 99%), phosphoric acid (Merck, 85%) and distilled water were used for the anodization process.

NiS was added to the produced nanotubes. To obtain the solutions, nickel chloride (Merck, pure), sodium sulfide (Sigma Aldrich,> 98%) and distilled water were used.

### B. Anodic oxidation process

The two electrode system was used for the anodization process. The titanium plate and the platinum were connected as anode (+) and cathode (-), respectively. The distance between the electrodes was kept 3 cm during the anodization. 0.5 M Phosphoric Acid ($H_3PO_4$) and 0.14M Sodium Fluoride (NaF) aqueous solution were used the electrolyte solution. During the anodization process, 20V voltage was used. The anodization time was chosen for 1 hour under the continuous stirring. After the anodization, TiO2 nanotubes were calcined at 500 ° C for 3 hours.

### C. Production of NiS / TiO2 nanotube photocatalyst by SILAR method

The SILAR method is based on the slow formation of ions of the substance to be doped on the surface of the substance to be added. After each immersion, washing with water is based on the adsorption and surface reaction of ions to avoid the formation of agglomeration on the surface.

Four different beakers were used in the doping process;

1. Beaker: 0,025 M NiCl2 aqueous solution
2. Beaker: Deionized water
3. Beaker: 0,025 M Na2S
4. Beaker: Deionized water

In this way, the nanotube was doped onto TiO2, then calcined at 500 °C for 3 hours.

### D. Photocatalytic Activity Tests

The photocatalytic experiments were carried out in a batch reactor with light. A 44 W / m2 lamp was used as a source of UV light. O2 was provided by pumping air at a constant flow rate to provide a saturated concentration of reaction medium.

## III. RESULT AND DISCUSSION

SEM and EDS analysis of TiO2 nanotube photocatalyst was shown in Figure 1.
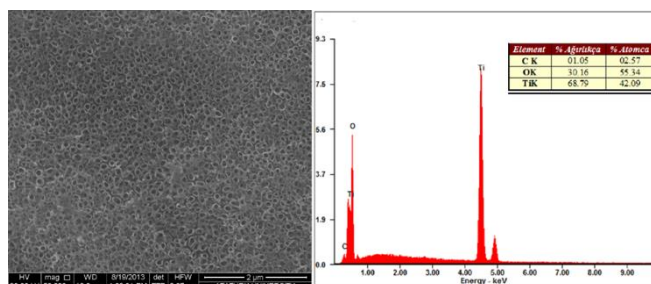


Figure 1. SEM and EDS analysis of TiO2 nanotube photocatalyst

As can be seen in Figure 1, TiO2 nanotubes are formed and distributed homogeneously on the surface. The average diameter of the nanotubes ranges from 99-116 nm. Any contamination is not observed on the nanotubes. The EDS analysis of TiO2 nanotube photocatalyst proved the presence of titanium and oxygen in the sample. The presence of carbon in the sample indicates the presence of trace amounts of pollution.

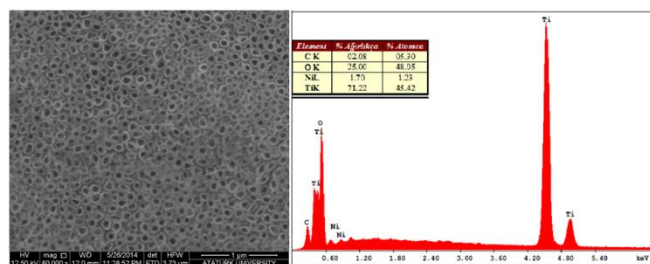The results of SEM and EDS analysis of NiS/TiO2 nanotube photocatalyst are given in Figure 2.



Figure 2. SEM and EDS analysis of NiS/TiO2 nanotube photocatalyst

As can be seen from the SEM image of the NiS doped nanotube photocatalyst given in Figure 2, NiS has been doped around the nanotubes. The presence of titanium, oxygen and nickel in our sample has been proven by the EDS analysis of photocatalyst.

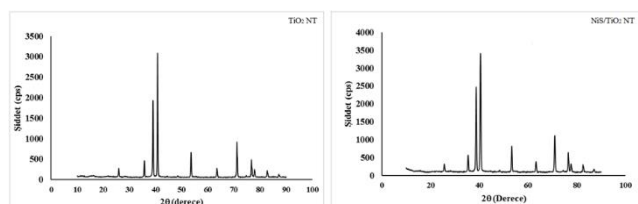Figure 3 shows the XRD patterns of the nanotube TiO2 and NiS doped TiO2 photocatalysts.



Figure 3. XRD patterns of nanotube TiO2 and NiS doped nanotube TiO2 photocatalysts

It is seen that the length of the anatase peaks of the photocatalyst doped NiS is prolonged and sharpened.

The photocatalytic degradation values of Acid Black I dye nn the TiO2 and NiS / TiO2 nanotube photocatalysts in the batch reactor, are shown in Figure 4.
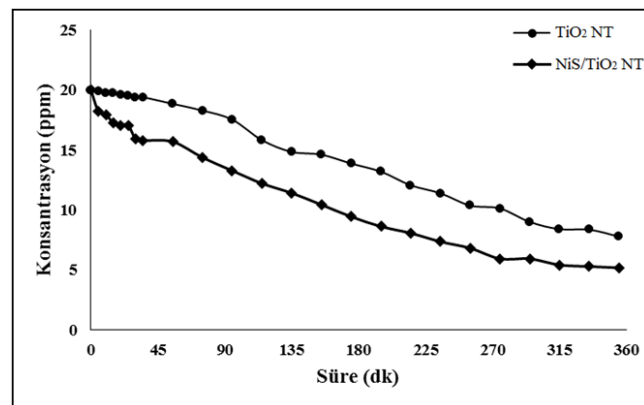


Figure 4. Decomposition of Acid Black I dye on TiO2 and NiS / TiO2 nanotube photocatalysts

When the graph is examined, the difference between the removal of the two photocatalysts is noticeable. For the TiO2 photocatalyst, 59.2% of the dye was removed in 6 hours, whereas the NiS doped nanotube TiO2 photocatalyst removed 74.8% of the dye after 6 hours.

## IV. CONCLUTION

Nanotube TiO2 photocatalysts were synthesized using the anodization method. NiS nanoparticles were coated by sequential ionic layer adsorption and reaction on the surface of the anodized TiO2 nanotubes. The crystal structure of the TiO2 and NiS / TiO2 nanotube photocatalysts produced was characterized using X-Ray diffraction (XRD), and its morphology and elemental composition was characterized using scanning electron microscopy (SEM-EDS). Acid Black I was used for photocatalytic activity experiments. The results showed that NiS doping increased the photocatalytic activity of TiO2.

## REFERENCES

[1] Roy, P., S. Berger, and P. Schmuki, TiO2 nanotubes: Synthesis and applications. Angewandte Chemie - International Edition, 2011. 50(13): p. 2904-2939.

[2] Roy, P., et al., TiO2 nanotubes and their application in dye-sensitized solar cells. Nanoscale, 2010. 2(1): p. 45-59.

[3] Park, S., et al., Effects of functionalization of TiO2 nanotube array sensors with Pd nanoparticles on their selectivity. Sensors (Switzerland), 2014. 14(9): p. 15849-15860.

[4] Fujishima, A., T.N. Rao, and D.A. Tryk, Titanium dioxide photocatalysis. Journal of Photochemistry and Photobiology C: Photochemistry Reviews, 2000. 1(1): p. 1-21.

[5] Kontos, A.I., et al., Self-organized anodic TiO2 nanotube arrays functionalized by iron oxide nanoparticles. Chemistry of Materials, 2009. 21(4): p. 662-672.

[6] Mohapatra, S.K., et al., Functionalization of self-organized TiO2 nanotubes with Pd nanoparticles for photocatalytic decomposition of dyes under solar light illumination. Langmuir, 2008. 24(19): p. 11276-11281.

[7] Yu, H., et al., Photocatalytic degradation of malathion in aqueous solution using an Au-Pd-TiO2 nanotube film. Journal of Hazardous Materials, 2010. 184(1-3): p. 753-758.

[8] Zhou, X., N. Liu, and P. Schmuki, Photocatalysis with TiO2 Nanotubes: "Colorful" Reactivity and Designing Site-Specific Photocatalytic Centers into TiO2 Nanotubes. ACS Catalysis, 2017. 7(5): p. 3210-3235.

# Electrochemical fabrication of PEDOT/ERGO/Au Nanocomposite Electrodes for Dopamine Sensor

Mesut Eryiğit
Department of Nanoscience and
Nanoengineering
Nanomaterials Sciences
Atatürk University
Erzurum, Turkey
mesut.eryigit54@gmail.com

Bingül Kurt Urhan
Department of Nanoscience and
Nanoengineering
Nanomaterials Sciences
Atatürk University
Erzurum, Turkey
bingul.kurt@hotmail.com

Eftade Pınar Gür
Department of Chemistry
Faculty of Sciences
Atatürk University
Erzurum, Turkey
eftadepinargur@gmail.com

Emir Çepni
Department of Nanoscience and
Nanoengineering
Nanomaterials Sciences
Atatürk University
Erzurum, Turkey
emircepni@windowslive.com

Mohammad Hosseinpour
Department of Chemistry
Faculty of Sciences
Atatürk University
Erzurum, Turkey
mehmetazaktoprak@gmail.com

Hülya Öztürk Doğan
Department of Chemistry and Chemical
Processing Technologies
Erzurum Vocational College
Atatürk University
Erzurum, Turkey
hdogan@atauni.edu.tr

Tuba Öznülüer Özer
Department of Chemistry
Faculty of Sciences
Atatürk University
Erzurum, Turkey
tozkim@atauni.edu.tr

Ümit Demir
Department of Chemistry
Faculty of Sciences
Atatürk University
Erzurum, Turkey
udemir@atauni.edu.tr

*Abstract*—**Ascorbic acid (AA) and dopamine (DA) play a significant role in the function of the central nervous, renal and hormonal systems. The deficiency or incompatibility of their levels may lead to the symptoms of many diseases such as cancer, Parkinson's disease and cardiovascular disease. Because of their electrochemical activity, AA and DA detection is always attracting the intense interest in electroanalysis.Unfortunately, AA is always coexisting with DA in organisms, sharing a similar oxidation potential in electrochemical detection. To overcome this problem, various carbon based materials including carbon nanotubes, carbon nanofibers and graphene have been combined with conducting polymers, metals or metal oxides. In this study, we reported that fabrication of poly(3,4-ethylenedioxythiophene) /electrochemically reduced graphene oxide (PEDOT/ERGO) nanocomposites on Au electrode. The characterization of PEDOT/ERGO/Au electrode was performed by XPS, EDS, and SEM techniques. Synthesized PEDOT/ERGO/Au nanocomposite electrode was used as an electrocatalysts for dopamine biosensor application. PEDOT/ERGO/Au electrode was exhibited to the higher catalytic effect compared to naked Au, PEDOT-modified Au, and ERGO-modified Au electrodes.**

*Keywords*— *PEDOT, graphene nanocomposite, reduced graphene oxide, dopamine*

# Photoelectrochemical Properties of Electrochemical Fabricated TiO₂ Nanostructures

Emir Çepni
Department of Nanoscience and
Nanoengineering
Nanomaterials Sciences
Atatürk University
Erzurum, Turkey
emircepni@windowslive.com

Eftade Pınar Gür
Department of Chemistry
Faculty of Sciences
Atatürk University
Erzurum, Turkey
eftadepinargur@gmail.com

Mohammad Hosseinpour
Department of Chemistry
Faculty of Sciences
Atatürk University
Erzurum, Turkey
mehmetazaktoprak@gmail.com

Hülya Öztürk Doğan
Department of Chemistry and Chemical
Processing Technologies
Erzurum Vocational College
Atatürk University
Erzurum, Turkey
hdogan@atauni.edu.tr

Tuba Öznülüer Özer
Department of Chemistry
Faculty of Sciences
Atatürk University
Erzurum, Turkey
tozkim@atauni.edu.tr

Ümit Demir
Department of Chemistry
Faculty of Sciences
Atatürk University
Erzurum, Turkey
udemir@atauni.edu.tr

*Abstract*—Thin films of titanium dioxide (TiO₂) are extensively studied because of their interesting chemical, electrical and optical properties. These kind of materials can be used as an anti-reflective and protective coating on optical elements, and as a protective layer for very large scale integrated circuits due to their high refractive index, excellent optical transmittance and good insulating properties. Optical properties of TiO₂ include a wide electron energy band gap, transparency throughout the visible spectrum and a high refractive index over a wide spectral range from the ultraviolet to the far infrared. In the past decade, the fabrication of TiO₂ nanostructures by electrochemical anodization of titanium, which titanium foil was used as a substrate, was investigated by many researchers and the cathodic deposition of TiO₂ was available only at a limited studies. In this study, cathodic constant potential electrodeposition of TiO₂ from aqueous solutions was successfully provided in 0,04 M TiOSO₄, 0,1 M H₂O₂, and 0,5 M KNO₃ solution. The characterization of TiO₂ thin films was performed by XRD, XPS, EDS, and SEM techniques.

*Keywords*—*Titanium dioxide, photoelectrode, electrodeposition*

# Lead Oxide-Electroreduced Graphene Oxide (PbO-ERGO) Nanocomposite for Non-enzymatic Glucose Sensor

Bingül Kurt Urhan
Department of Nanoscience and Nanoengineering
Nanomaterials Sciences
Atatürk University
Erzurum, Turkey
bingul.kurt@hotmail.com

Mesut Eryiğit
Department of Nanoscience and Nanoengineering
Nanomaterials Sciences
Atatürk University
Erzurum, Turkey
mesut.eryigit54@gmail.com

Hülya Öztürk Doğan
Department of Chemistry and Chemical Processing Technologies
Erzurum Vocational College
Atatürk University
Erzurum, Turkey
hdogan@atauni.edu.tr

Tuba Öznülüer Özer
Department of Chemistry
Faculty of Sciences
Atatürk University
Erzurum, Turkey
tozkim@atauni.edu.tr

Ümit Demir
Department of Chemistry
Faculty of Sciences
Atatürk University
Erzurum, Turkey
udemir@atauni.edu.tr

*Abstract*—The development of fast and reliable methods for glucose detection is of considerable importance in a variety of fields including clinical diagnosis, food analysis, and bioreactor monitoring. Numerous nanostructured materials have been explored to develop innovative nonenzymatic glucose sensors with a great catalytic effect on the oxidation of glucose. The nonenzymatic glucose sensors based on metal oxides (Cu$_2$O, NiO, MnO$_2$, Co$_3$O$_4$, etc.) and metal hydroxide (Ni(OH)$_2$, Cu(OH)$_2$,etc.) are of great interest in recent years and display a lot of advantages of fast response, high sensitivity, low detection limit, good stability and low cost. In this study, PbO-ERGO thin films have been prepared with a facile electrochemical process, based on co-deposition from the same solution. Synthesized PbO-ERGO nanocomposite electrodes were used as an electrocatalysts for non-enzymatic glucose biosensor application.

*Keywords— Reduced graphene oxide, lead oxide, nonenzymatic glucose sensor, electrocatalyst*

# The Effect of Temperature on Acid and Base Production From NH₄Cl-NaCl Salt Solution By Bipolar Membrane Electrodialysis

Muhammed Raşit Öner
Chemical Engineering
Atatürk University
Erzurum, Turkey
m.rasitoner@gmail.com

Osman Nuri Ata
Chemical Engineering
Atatürk University
Erzurum, Turkey
oatar@atauni.edu.tr

*Abstract*— **In this study, the effect of temperature on the production of acid (HCl) and base (NH₄OH-NaOH) with bipolar membrane electrodialysis system from NH₄Cl-NaCl solution which is semi-finished Solvay process was investigated. The experiments were performed at four different values: 25, 30, 35, 40 ºC. The effect of temperature, on salt conversion, formed acid-base and their flux was followed. Although the flux values have improved especially with the increase of temperature, the temperature did not have a significant effect on the improvement of the process parameters since the vaporization enthalpy of the ammonium hydroxide in the system and the co-ion transition increased.**

*Keywords— Electrodialysis, Bipolar Membrane, Solvay, Desalination, NH4Cl, NaCl*

## I. INTRODUCTION

Soda ash (soda), which is mainly used in glass industry, detergent, chemical production, paper, pigment, textile, food and animal feed sectors, is produced in two ways as natural and synthetic. Naturally, soda is produced from various ores and synthetically produced by Solvay process. Synthetic soda accounts for about 2/3 of soda production. In the production of synthetic soda, one of the dense energy industry branches; As a result of the rapid increase in energy prices after the middle of the seventies, synthetic soda costs increased. In addition, meticulous implementation of measures in environmental protection is a second factor that increases costs in the synthetic soda industry producing large quantities of waste. On the other hand, the production of synthetic soda has a more harmful effect on the environment than natural soda production, and it provides advantages to natural soda producers due to both cost and environmental impacts [1].

Several researches have been done to reduce the energy costs and environmental impacts associated with synthetic soda production, and hundreds of articles have been written for the modification of the Solvay process. Kazikowski and his colleagues obtained calcium sulfate in the form of gypsum from the calcium ions in the distillation waste. They made this with sulphate ions in the remaining solid waste after salt purification[2].

$$CaCl_2 + NaSO_4 + 2H_2O \rightarrow CaSO_4.2H_2O + 2NaCl$$
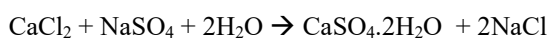
In another study by Kazikowski et al.[3], to reduce the effects of soda ash plants on the natural environment, treatment of purified salt with orthophosphoric acid ($H_3PO_4$), production of calcium and magnesium phosphate, limestone production from soda waste, gypsum and semi-finished

products salt production, flue gas desulphurisation in power plants and distillation waste for the use of various experiments and have achieved successful results. In another study, Forster conducted a study to reduce the carbon dioxide emission in the solvent process and to benefit more from renewable energy sources. In this study, the production of net carbon dioxide in the traditional ammonia soda process and the by-products that are ecologically harmful are examined. The feasibility of modifying the production of sodium carbonate and hydrochloric acid to ammonium soda process using carbon dioxide, sodium chloride and water has been examined technically and experimentally[4]. In this study, we aimed to prevent the occurrence of $CaCl_2$, which is the main waste by means of produce acid and base from $NH_4Cl$-NaCl mixture which is semi-finished in Solvay process.

Bipolar membranes can be used in the production of acids and bases from salt solutions[5], in the control of impurities, in chemical processes with high efficiency and low waste capacity. There are some studies in the literature about the production of organic and inorganic acids and bases using bipolar membrane. In addition, there are some researches on the effect of electrical field, electrical resistance, potential reduction, applied current density, high current density, concentration-electrical properties, selectivity, current efficiency and pollution on membrane processes. Erkmen examined boric acid and sodium hydroxide formation from borax solutions in a three-chamber electrodialysis cell with bipolar membrane[6]. Shee et al. used bipolar membrane electroacidification (BMEA) technology to remove residual oils from whey protein concentrates[7]. Xu in a study in the production of acid and acid salt solution, conventional ion exchange method with bipolar membrane electrodialysis method compared with the study of the energy consumption of 10-12 mA / cm² current density has decreased to 1 kWh / kg has determined that[8].

In this study, acid (HCl) and base ($NH_3$ and NaOH) were produced from ammonium chloride and sodium chloride solutions without secondary salt pollution by using bipolar membrane electrodialysis unit. The effect of temperature, on salt conversion, formed acid-base and their flux was investigated.

## II. EXPERIMENTAL

Chemicals used in the experiments were obtained from MERCK HCl (37%), $NH_4Cl_2$ (99,8), $Na_2SO_4$ (%99), NaOH (%99)phenolphthalein and methyl orange indicator. Bipolar

membrane electrodialysis system, electrodialysis membranes and spacers were obtained from PCCELL. The cell and spacer properties used are shown in Tables 1and 2.

Table 1. Anion and cation exchange membranes properties

| Membrane species | Transference number KCl (0.1 / 0.5 N) Acid(0.7/3N) | Resistance (Ωcm$^2$) | Thickness (μm) | Ionic form as shipped |
|---|---|---|---|---|
| ADM | >0.95 | ~ 2 | 160-200 | Cl- |
| KDM | >0.95 | ~ 2,5 | 160-200 | NH$^{4+}$ |

Table 2. Bipolar membrane properties

| | Thickness(mm) | Water splitting efficiency | Water splitting voltage (V) |
|---|---|---|---|
| Bipolar Membrane | 0,2-0,35 | >0,95 | 0,8-1,0 |

Performance criteria for electrodialysis process with bipolar membranes are as follows:

1. Amount/Concentration of acid and base produced.

$$C = \frac{n_t}{V_t} \ (mol/l) \qquad (1)$$

n$_t$: The molar amount of acid or base at any given moment, V$_t$: the acid or base volume at any time

2. Product based salt conversion:

$$\% \ Conversation = \frac{C_t - C_0}{C_{Top}} x100 \qquad (2)$$

$C_t$ : acid or base concentration at any given moment (mol/l), $C_0$: acid in the acid or base tank, or base concentration (mol/ l), $C_{Top}$: The acid and base concentration to be obtained when the salt in the feed solution is completely converted to product(mol / l).

3. Product-based flux

$$N_{iyon} = \frac{n_t - n_o}{A.t} \qquad (3)$$

n$_t$: amount of acid in a given moment (mol), n$_o$: initially the acid content in the acid tank (mol), $A$: active area of 5 ion exchange membranes used in the cell (64x5 cm$^2$), $t$: time (h)

III. RESULTS AND FINDINGS

Experiments were conducted for 4 different temperatures to examine the effect of temperature on process performance. From the data obtained in the experiments, the conductivity of the feed solution, the ion fluxes transferred from the membrane, the change in the percentage of the conversion of the salt in the products change over time are given in Figure 1-3.
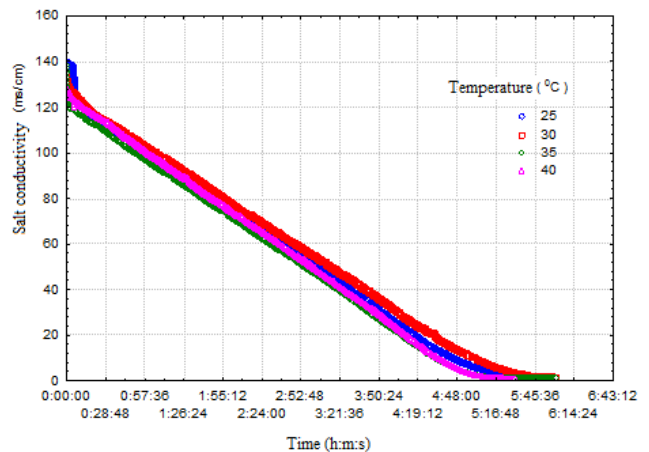


Fig.1. Change in conductivity of a solution in a salt tank against time.

In experiments conducted at different temperatures, it can be seen that the temperature does not have a significant effect on the process performance (salt conversion, acid and base and flux formed) Figure 1-3. It has been observed that the amount of acid and base produced by increasing temperature has a small increase in conversion and flux.



Fig. 2.Change in Flux against time.



Fig. 3. % Conversation cahnge against time.

In fact, the increased temperature was expected to contribute positively to process performance. However, increasing temperature increased the evaporation rate of ammonia and increased ammonia loss. In addition, some of

the ammonia was transferred to the acid compartment and some to the salt compartment. Therefore, the resulting acid and base amounts were less than expected and resulted in low product based salt conversion.

## III. CONCLUSIONS

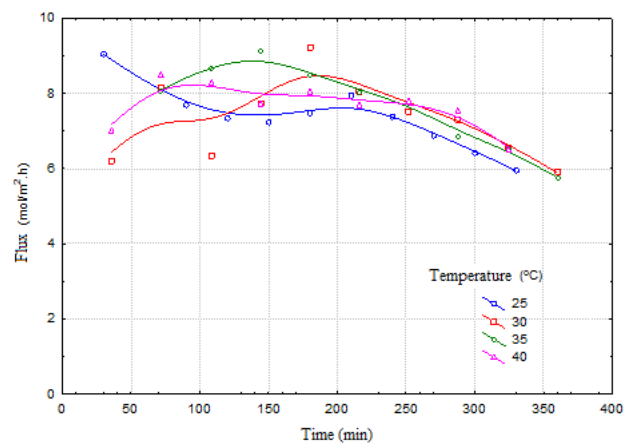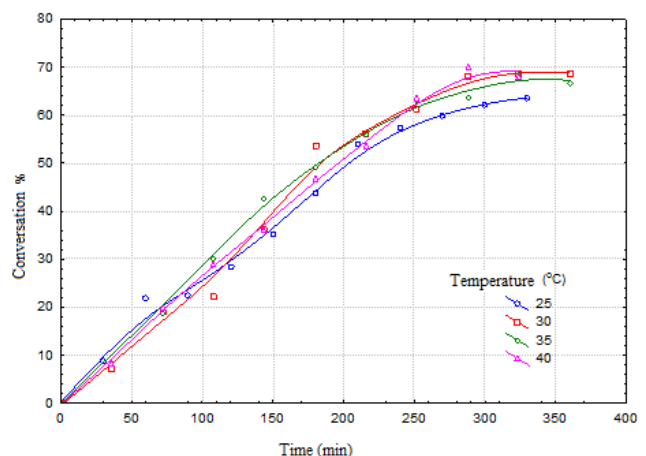In the study, an ion-exchange, cation exchange and a combination of these and a special membrane type, bipolar membranes are used in a three-compartment electrodialysis cell, from NaCl-NH4Cl solution, sodium hydroxide, ammonia, hydrochloric acid and usable water production will be realized and an environmentally friendly process will be developed. and to investigate the factors affecting the performance of the production process, to eliminate the waste problem of soda industry and to recover the NaCl discharged into the sea and to create a sustainable soda production process. As a result of the experiments conducted for these purposes, it was determined that the temperature change did not have positive effect on the process.

## ACKNOWLEDGMENT

## REFERENCES

[1] G. Sayın, E. Aygören, and İ. Olcasoy, "Soda Külü ve Krom Kimyasalları Çalışma Grubu Raporu," Ankara2006.

[2] T. Kasikowski, R. Buczkowski, B. Dejewska, K. Peszyńska-Białczyk, E. Lemanowska, and B. Igliński, "Utilization of distiller waste from ammonia-soda processing," *Journal of Cleaner Production,* vol. 12, no. 7, pp. 759-769, 2004.

[3] T. Kasikowski, R. Buczkowski, and E. Lemanowska, "Cleaner production in the ammonia–soda industry: an ecological and economic study," *Journal of environmental management,* vol. 73, no. 4, pp. 339-356, 2004.

[4] M. Forster, "Investigations for the environmentally friendly production of Na 2 CO 3 and HCl from exhaust CO 2, NaCl and H 2 O," *Journal of Cleaner Production,* vol. 23, no. 1, pp. 195-208, 2012.

[5] Y. Wang, X. Zhang, and T. Xu, "Integration of conventional electrodialysis and electrodialysis with bipolar membranes for production of organic acids," *Journal of Membrane Science,* vol. 365, no. 1, pp. 294-301, 2010.

[6] J. Erkmen and S. Yapici, "A environmentally friendly process for boric acid and sodium hydroxide production from borax; bipolar membrane electrodialysis," *Desalination and Water Treatment,* vol. 57, no. 43, pp. 20261-20269, 2016.

[7] F. Lin Teng Shee, P. Angers, and L. Bazinet, "Delipidation of a whey protein concentrate by electroacidification with bipolar membranes," *Journal of agricultural and food chemistry,* vol. 55, no. 10, pp. 3985-3989, 2007.

[8] X. Tongwen, "Electrodialysis processes with bipolar membranes (EDBM) in environmental protection—a review," *Resources, conservation and recycling,* vol. 37, no. 1, pp. 1-22, 2002.

# Preparation of ZnO Nanoparticles Using Polyol and Hydrothermal Methods

Elif Erçarıkcı
Department of Chemistry
Faculty of Sciences
Atatürk University
Erzurum, Turkey
elif.ercarikci@atauni.edu.tr

Murat Alanyalıoğlu
Department of Chemistry
Faculty of Sciences
Atatürk University
Erzurum, Turkey
malanya@atauni.edu.tr

*Abstract*— **Nanostructured materials have attracted extensive attention due to their valuable physical and chemical properties which fluctuate strongly from their bulk material and prospective applications in numerous nano-optical or nano-electric devices. The ZnO nanoparticles (ZnO-NPs) are one of the most promising nanostructured materials for optoelectronic and biosensors applications due to its wide band gap of 3.37 eV and large exciton binding energy of 60 meV [1] and its electrochemical catalytic activity, superior surface properties, biocompatibility, and nontoxicity [2]. ZnO-NPs has been prepared successfully by various methods, such as hydrothermal method [3], sol-gel method [4], direct precipitation method [5], and polyol method [6]. Among them, hydrothermal method is popular for researchers owing to the advantages of convenience, low cost, and environmental friendly approach.**

**In this study, we reported the preparation of ZnO-NPs using both hydrothermal and polyol methods. Comparison of these synthesized ZnO-NPs has been carried out using numerous techniques, such as scanning electron microscopy, X-ray diffraction, and UV-Vis. absorption spectroscopy.**

*Keywords— Zinc oxide; Nanoparticles; Semiconductor*

## REFERENCES

[1] V. Pandiyarasana, J. Archanaa, Y. Hayakawaa, H. Ikeda, "Hydrothermal growth of reduced graphene oxide on cotton fabric for enhanced ultraviolet protection applications," Materials Letters. 188, 123-126, 2017.

[2] P. Nayak, B. Anbarasan, S. Ramaprabhu, "Fabrication of Organophosphorus Biosensor Using ZnO Nanoparticle-Decorated Carbon Nanotube–Graphene Hybrid Composite Prepared by a Novel Green Technique," J. Phys. Chem. C. 117, 13202-13209, 2013.

[3] S. M. Saleh, B. Gadgil, "Influence of solvent in the synthesis of nano-structured ZnO by hydrothermal method and their application in solar-still," Journal of Environmental Chemical Engineering. 5, 1219-1226, 2017.

[4] A. K. Zak, M.E. Abrishami, R. Yousefi, S.M. Hosseini, "Solvothermal synthesis of microsphere ZnO nanostructures in DEA media," Ceram. Int. 37, 393-398, 2011.

[5] M. Kahouli, A. Barhoumi, S. Guermazi, "Structural and optical properties of ZnO nanoparticles prepared by direct precipitation method," Superlattices and Microstructures. 85, 7-23, 2015.

[6] S. Leea, S. Jeonga, M. Jeonb, J. Moon, "ZnO nanoparticles with controlled shapes and sizes prepared using a simple polyol synthesis," Superlattices and Microstructures. 43, 330-339, 2008.

# Response of Five Triticale Genotypes to Salt Stress in in Vitro Culture

Serap Karaman
Department of Molecular
Biology and Genetics,
Erzurum Technical University,
Erzurum, Turkey

Beyza Reisoğlu
Department of Molecular
Biology and Genetics,
Erzurum Technical University,
Erzurum, Turkey

Fatma Böke
Department of Molecular
Biology and Genetics,
Erzurum Technical University,
Erzurum, Turkey

Murat Kizilkaya
Department of Molecular
Biology and Genetics,
Erzurum Technical University,
Erzurum, Turkey

İsmail Bezirganoğlu
Department of Molecular Biology
and Genetics, Erzurum Technical
University, Erzurum, Turkey
İsmail.bezirganoglu@erzurum.edu.tr

*Abstract-* **Salinity is one of the important abiotic stresses that restrict plant development. Triticale is a highly adaptable crop, known for its high-quality grain, yield potential, and resistance to disease. Responses of five cultivated genotypes (Ümran Hanım, Mikham 2002, Melez 2001, Tatlıcak, and Alper Bey) of triticale to salt stress were tested in callus and embryogenic callus formation in this study. Cotyledon explants were selected as explants for callus induction and embryogenic callus formation. The five tested triticale genotypes varied in their callus growth and embryogenic callus formation. Ümran Hanım, Tatlıcak, and Alper Bey were observed for better callus induction; similarly, the same genotypes responded with better embryogenic callus formation in the salt in vitro media. A significant decrease in embryogenic callus growth was observed under salt stress. Based on the responses to NaCl in terms of embryogenic callus, the five triticale genotypes were ranked in the order of Tatlıcak > Ümran Hanım > Alper Bey > Mikham 2002 > Melez 2001. More proline and sugar were accumulated in these five triticale genotypes than in control plants when all were subjected to salt stress. Proline level peaked at 200 mM while the lowest and highest content was obtained at 0–200 mM salt concentrations. The accumulation of soluble sugars was strongly linked to 0–200 mM salt concentrations. Antioxidant enzyme activities exhibited an increasing trend in response to the increasing concentration of NaCl.**

*Key words-Triticale, embryogenic callus, salt stress, proline, sugar*

# Synthesis and Characterization of Rgo/Tio₂/Pva Nanocomposite

Derya Tekin
Metallurgical and Materials
Engineering
Ataturk University
Erzurum,TURKEY
deryatekin@atauni.edu.tr

Derya Birhan
Metallurgical and Materials
Engineering
Ataturk University
Erzurum,TURKEY
deryacirhan38@gmail.com

Taner Tekin
Chemical Engineering
Ataturk University
Erzurum,TURKEY
ttekin@atauni.edu.tr

*Abstract*— **Nanofibers are used in many application areas such as unique structures, low weights, controllable porosity structures and filtration applications with large surface areas, engineering subjects, sensors electron and photon materials. Polyvinyl alcohol is water soluble, mechanical, thermal (melting point> 200 ° C), besides its antibacterial properties, disadvantages. Both the disadvantages and the semiconductor photocatalyst TiO₂ nanoparticles have been focused on how the doped rGO affects the properties of the polymer matrix and the TiO₂ to reduce the wide band-gap range and to absorb the visible region.**
**At this point, rGO-TiO₂-PVA nanocomposite structure was synthesized by using the solution casting technique and it was aimed to find out which improvements rGO contributed to the structure.**

**Keywords— Polyvinyl alcohol(PVA), TiO₂, reduce graphene oxide, nanocomposite**

## I. INTRODUCTION (*Heading 1*)

In recent years, nanocomposite materials have great importance both academically and industrially. Nanomaterials significantly increase the properties of polymeric materials due to their small size, wide specific surface areas, quantum limitation and strong interfacial interactions(Shehap and Akil 2016). Polyvinyl Alcohol (PVA) is a non-adherent property, excellent film structure, dissolves in water and forms a transparent solution. Due to its favorable mechanical , thermal resistance (melting point>200°C), biodegradable properties and flexibility PVA has been widely applied in manufacturing fibers , coatings, food packages and medical devices. In addition to, its nontoxic, odorless and biocompatibility features make PVA films promising candidates in biotechnological applications, such as tissue engineering, drug delivery, articular cartilage and biosensors(Zhu, Wang et al. 2015). Polyvinylalcohol (PVA) has some disadvantages such as poor thermal and mechanical stability when used in some practical applications, as well as being difficult to dissolve in some applications (Wang, Chen et al. 2014). The moisture present in the structure reduces the stability and stability of the polymer. Several approaches are made to prepare PVA-based nanocomposite polymers to help reduce such problems (Hdidar, Chouikhi et al. 2018). Titanium dioxide (TiO₂) is an excellent semiconductor used for removal of wastewater and paints, dye sensitive solar cells, high photocatalytic activities (Wang, Chen et al. 2014). TiO₂ nanoparticles have excellent stability, high refractive index, hydrophilicity, UV resistance, excellent transparency for visible light. Besides, TiO₂ is a low cost

material that removes organic pollutants, shows high photocatalytic activity, has low cost, strong redox effect, is used in water and air purification, killing bacteria(Maruthamani, Divakar et al. 2015). Graphene is a carbon layer with a honeycomb structure with a 2D lattice sp² hybridization and a distance of 0.142 nm between carbon atoms. Excellent electronic, mechanical and chemical properties since its discovery(Li, Li et al. 2017). One of the ideal ways to improve the photocatalytic activity of TiO₂ is to modify the semiconductor photocatalyst with graphene. The purpose of synthesizing the graphene-TiO₂ structure is to reduce the TiO₂ recombination rate. The small amount of oxygen, which contains the functional groups on the reduced graphene oxide (rGO) edge and basal planes, which are the two-dimensional reduced structure of graphene, is of great importance in the structure. rGO reduces the recombination of electron-holl pairs of supported TiO₂ nanoparticles and adsorbs the surface, adsorbs organic dyes and helps photocatalytic activity by improving charge transfer rate(Sohail, Xue et al. 2017).

In this study, rGO-TiO₂-PVA structures are synthesized by using the solution casting technique and the thermal and antibacterial properties of the polymer are improved.

## 2. MATERIAL AND METHOD

### a. Materials

Graphite Powders(powder<45μm≥99.99%), Sulfuric acid (H₂SO₄,95-97%), Sodium Nitrate(NaNO₃), Potassium Permanganate(KMNO₄), TiO₂ nanoparticles, Polyvinyl alcohol (Mw 9,000-10,000,80% hydrolyzed,PVA), Hydrogen peroxide (H₂O₂, %30)

### b. Synthesis of Graphene Oxide

Graphene oxide graphite powder is synthesized according to the Hummer method. First 69 ml of sulfuric acid, 3 *g* of graphite powder, 1.5 *g* of NaNO3 were mixed in 250 ml erlene.

The solution was then placed in an ice bath to cool the temperature to 0 ° C. After the temperature dropped to 0 ° C, 9 *g* of potassium permanganate (3/3/3) was added to the solution. After the addition of potassium permanganate, the solution was removed from the ice bath and put on hold to allow the temperature to rise to room temperature. Then, 138 ml of ionized water was added and the mixture was stirred at 98 ° C for 15 minutes, then 480 ml of water was

262

added and 30% $H_2O_2$ was added dropwise to oxidize the brown color to yellow. The resulting graphene oxide was washed several times with ethanol and ionized water to provide pH balance. The final stage is filtered and kept in a 60 ° C oven until it is completely dry.

### c. rGO Synthesis

0.8 *g* of GO powders were dissolved in 400 ml of DMF under ultrasonication for 6 h.  After 6 hours of treatment, the rGO powders were filtered, washed with ethanol and water and dried in an oven at 60 ° C.

### d. rGO-TiO2 Synthesis of Nanocomposite Structure

0.1 *g* of rGO powder was mixed with 10 ml of ethanol and 20 ml of water and subjected to sonication for 1 hour. At the end of 1 hour of treatment, $TiO_2$ nanoposicles in the form of 0.2 *g* of anatase were added to the rGO solution and the solution was poured into petri dishes and dried in an oven at 60 °C. Finally,  rGO-TiO2 nano-powders were obtained.

### e. Synthesis of rGO-TiO2-PVA Nanocomposite Structure

2 g of PVA was dissolved in 30 ml DI water at 95 °C under reflux to form an aqueous solution. Subsequently, GO powder (at 0.3 wt% of PVA) was sonicated in 20 ml DI water to form a black colloidal solution. The as obtained solutions were mixed together under vigorous stirring for about 2 h at 60 °C to form a colloid. The resulting solution was stirred at 60 ° C for 1 hour. At the end of the mixture rGO-TiO2-PVA structure was dried at 40 ° C for 48 hours

### f. Characterization Techniques

XRD analysis was performed to determine the presence of rGO / $TiO_2$ nanotabals in the polyvinyl alcohol (PVA) matrix and the existing crystals of nanocomposite films. XRD analyzes were performed at 45 kV and 40 mA with CuKα (1.5406 Å). Nanocomposite films were screened with a scan speed of 0.5 min$^{-1}$ in the range of 10 ° to 45 ° for 2 hours. The scanning electron microscope (SEM) was used to determine the degree and quality of the filling of PVA in the PVA matrix.

## III. RESULTS

### a. XRD Analysis

According to the XRD results, the density of the main peaks in rGO / $TiO_2$-doped PVA matrices decreases and peaks are observed to be frequent. While there was a decrease in crystallinity, some interactions were observed between polymer chains and filler(Salavagione, Martínez et al. 2009).

### b. SEM Analysis

The images obtained represent the phase morphology of the PVA film rGO / $TiO_2$ doped. It is seen that the surfaces of PVA samples with rGO / $TiO_2$ added in the images are smooth and regular. It has been observed that rGO / $TiO_2$ nano-layers are peeled and dispersed well in the PVA matrix(Aslam, Kalyar et al. 2017).

## IV. CONCLUSION

rGO / $TiO_2$ / PVA nanocomposites were successfully synthesized by solution casting technique by doppling with semiconductor photocatalyst and polymer matrix rGO support. The structural properties of the PVA matrix in rGO / $TiO_2$ / PVA nanocomposite were significantly improved by the addition of filler and the $TiO_2$ nanoparticles were distributed homogeneously over the rGO support material. Due to the high conductivity of carbon-based support materials, $TiO_2$ was effective in inhibiting the recombination of electron-holl pairs produced from $TiO_2$ due to the homogeneous distribution of nanoparticles on the support material.

## REFERENCES

[1] Aslam, M., M. A. Kalyar and Z. A. Raza (2017). "Fabrication of reduced graphene oxide nanosheets doped PVA composite films for tailoring their opto-mechanical properties." Applied Physics A **123**(6): 424.

[2] Hdidar, M., S. Chouikhi, A. Fattoum, M. Arous and A. Kallel (2018). "Influence of $TiO_2$ rutile doping on the thermal and dielectric properties of nanocomposite films based PVA." Journal of Alloys and Compounds **750**: 375-383.

[3] Li, J., Y. Li, S. Niu and N. Li (2017). "Ultrasonic-assisted synthesis of phosphorus graphene oxide/poly (vinyl alcohol) polymer and surface resistivity research of phosphorus graphene oxide/poly (vinyl alcohol) film." Ultrasonics sonochemistry **36**: 277-285.

[4] Maruthamani, D., D. Divakar and M. Kumaravel (2015). "Enhanced photocatalytic activity of $TiO_2$ by reduced graphene oxide in mineralization of Rhodamine B dye." Journal of Industrial and Engineering Chemistry **30**: 33-43.

[5] Salavagione, H. J., G. Martínez and M. A. Gómez (2009). "Synthesis of poly (vinyl alcohol)/reduced graphite oxide nanocomposites with improved thermal and electrical properties." Journal of Materials Chemistry **19**(28): 5027-5032.

[6] Shehap, A. and D. S. Akil (2016). "Structural and optical properties of $TiO_2$ nanoparticles/PVA for different composites thin films." International Journal of Nanoelectronics & Materials **9**(1).

[7] Sohail, M., H. Xue, Q. Jiao, H. Li, K. Khan, S. Wang and Y. Zhao (2017). "Synthesis of well-dispersed TiO2@ reduced graphene oxide (rGO) nanocomposites and their photocatalytic properties." Materials Research Bulletin **90**: 125-130.

[8] Wang, B., Z. Chen, J. Zhang, J. Cao, S. Wang, Q. Tian, M. Gao and Q. Xu (2014). "Fabrication of PVA/graphene oxide/TiO2 composite nanofibers through electrospinning and interface sol–gel reaction: Effect of graphene oxide on PVA nanofibers and growth of $TiO_2$." Colloids and Surfaces A: Physicochemical and Engineering Aspects **457**: 318-325.

[9] Zhu, Y., H. Wang, J. Zhu, L. Chang and L. Ye (2015). "Nanoindentation and thermal study of polyvinylalcohol/graphene oxide nanocomposite film through organic/inorganic assembly." Applied Surface Science **349**: 27-34.

# Nanobiosynthesis of CdTe Quantum Dots by *Viridibacillus arenosi* K64

Özlem Baris
Department of Nanoscience and
Nanoengineering, Institute of Naturel and
Applied Sciences, Atatürk University,
Erzurum – TURKEY
Department of Biology, Faculty of Science,
Atatürk University, Erzurum – TURKEY
ozlembaris@gmail.com

Atefeh Varmazyari
Department of Nanoscience and
Nanoengineering, Institute of Naturel and
Applied Sciences, Atatürk University,
Erzurum – TURKEY

*Abstract*— **In present study the production of CdTe quantum dot particles was investigated by using biosynthesis method which provides environmentally friendly, economical, reliable and controlled production with using *Viridibacillus arenosi* K64 isolate. With this bacterium selected it is possible that this bacterium can survive for up to 3 days even in high doses in experiments with special buffer solutions, can last up to 3 days. Preliminary experiments with a large number of isolates from stock cultures have continued to work with active isolates as a result of experiments conducted with consideration for the viability of biosynthesis processes. In this way, an ideal environment in which the bacterium can optimally operate has been prepared and the ideal bacteria and environment for particle formation have been determined. Several preliminary experiments have been carried out to determine the correct bacteria and environment and partial optimization studies have been completed. Inspection with fluorescent microscope for the formation of fluorescent particles was done for control purposes. UV-VIS-NIR spectrophotometer analysis for the optical properties of synthesized nanoparticles, DLS-zetasizer for structural analysis; scanning electron microscopy (SEM) measurement techniques were used for their morphological characteristics.**

*Keywords (Nanoparticles, CdTe, Biosynthesis, Bacteria)*

## I. INTRODUCTION

Developing technology and ever-increasing needs of human beings promotes interest in new and innovative technologies. Especially accessibility in technology, suitable in size and dimensions and production low cost have been preferred [9]. Semiconductor nanoparticles (NPs) or quantum dots (QDs) are bimetallic structures of elements like Cd, S, Se or Te that given their particular physicochemical and optoelectronic properties exhibit great technological potential [5].

An important challenge of research in nanoparticle synthesis are growing need to develop reliable, nontoxic, clean, ecofriendly, and green experimental protocols [3- 4]. One of the important options is use of natural processes such as use of enzymes, microbial enzymes, vitamins, polysaccharides, biodegradable polymers, microorganisms, and biological systems for synthesis of NPs. The goal of recent studies, provide a controlled and up-scalable process for biosynthesis of monodispersed and highly stable NPs. Thus, a wide range of bacterial species have been used in green nanotechnology for the synthesis of NPs like gold, silver, platinum, palladium, titanium, titanium dioxide, magnetite, cadmium sulphide, and so forth [2]. There is currently little to no evidence about green synthesize of CdTe using bacteria. Hence, it is essential to widen the range of biosynthesized CdTe NPs toxicity investigations. Development of new, simpler, less toxic and environmentally friendly synthesis procedures is then a subject of growing interest. Among various QDs, cadmium telluride (CdTe) nanocrystals have attracted significant attention for energy, electronics and biomedical applications [7]. because of their tunable size-dependent emission within the whole visible range.

## II. METHODS

### A. Chemicals and reagents

Bacterial isolates obtained in our previous studies and included in our culture collection (Atatürk University Eastern Anatolia High Technology Application and Research Center Laboratory) (DAYTAM) have been used.

It is commercially available as a chemically soluble chemistry which is a component of the nanoparticles whose synthesis is intended.

### B. Bacteria used for biosynthesis of CdTe NPs

The biosynthesis process is preferred to obtain highly biocompatible material that can be used for living organisms. *Viridibacillus arenosi* K64 (GenBank Accession Number: KR873397), isolated from caves and is involved in the precipitation of calcium compounds has been previously described and found at Atatürk University DAYTAM culture collection, were used for biosynthesis of CdTe.

### C. Biosynthesis of CdTe NPs

The isolates were first incubated in a special buffer (MSB = Mineral Salt Basal) (0.75 g / L K2HPO4, 0.2 g / L KH2PO4 and 0.09 g / L MgSO4 pH 7.0 sterilized with filter 0.22 µ) (Zinc chloride, Cadmium acetate, Titanium nitrate etc.) at different doses (0.1, 1, 5 mM). Secondly, at the end of 3 days, biosynthesis was carried out with the highest dose determined in the isolates (M9 medium, Luari Bertani Medium and Thrypticase Soybean Broth) that preserved their viability [10].

In our biosynthesis *V. arenosi* K64 was grown with aeration at 34 °C in Luria Bertani (LB) medium. When the absorbance of bacteria cultures rose to 0.6 at 600 nm (A$_{600}$) 1

ml of *V. arenosi* K64 solution was diluted to 45 ml with LB medium in a single necked flask and then 4 ml of 0.04 mol l$^{-1}$ cadmium chloride, 100 mg of trisodium citrate dihydrate, 1 ml of 0.04 mol l$^{-1}$ Na2TeO3, 60 mg of mercaptosuccinic acid and 50 mg sodium boronhydride were added in under stirring, followed by incubation at 37 °C on a rotary shaker (200 rpm). Using this approach CdTe nanocrystals could be reproducibly biosynthesized [1].

Bacteria free LB medium containing bacteria secreted proteins was prepared as follows. After 1 day in culture the bacteria were removed from the medium by centrifugation at 6000 g for 10 min. Before biosynthesis the prepared LB medium was filtered using a polycarbonate membrane (Millipore) with a pore size of 200 nm. Subsequently, 4 ml of 0.04 mol l$^{-1}$ CdCl2, 100 mg of trisodium citrate dihydrate, 1 ml of 0.04 mol l$^{-1}$ Na$_2$TeO$_3$, 60 mg of MSA and 50 mg of NaBH$_4$ were added to the medium for the biosynthesis of CdTe nanocrystals.

### D. Characterizations of biosynthesized CdTe QDs

The biosynthesized CdTe nanoparticles were characterized by UV-VIS-NIR spectrophotometric (Agilent Cary Eclipse, Shimadzu UV-3600 Plus), SEM (Zeiss Sigma 300, Germany), EDS (Zeiss Sigma 500) and Zetasizer (Malvern Zetasizer Nano ZSP). All analyses were made through the purchase of services from Atatürk University DAYTAM.

### E. Isolation and purification of CdTe nanoparticles

After 24 h at room temperature, the synthesis solution was transferred to a 50 mL tube and centrifuged at 10,000 rpm at 20 °C for 10 m. The precipitate containing CdTe was washed with n-hexane, methanol and ddH$_2$O, respectively. After each wash, the wash solutions were removed by repeating the centrifugation step of 10,000 rpm at 20 °C for 10 m [6-7]. The resulting precipitate was dried for 24 h at 60 °C prior to the characterization process.

## III. RESULTS

### A. UV-VIS-NIR spectrophotometric analysis

It has been found that the spectrum has a very clear absorption, the absorption in the spectrum of CdTe nanoparticles begins at a wavelength of 220 nm and the absorption density is at a wavelength of 396 nm.

### B. Zetasizer analysis

Particle size and distribution of CdTe quantum dots, particle size and distribution were determined. (Figure 2) CdTe nanoparticles size 100-350, 700-1010 and 1600-1900 nm was seen.

### C. SEM and EDX analysis

From the SEM images (Figure 3) taken from the prepared material, it was observed that NPs existed in different sizes (8 to 25 nm, with the average size around 18 nm) and formed in clusters. However, it was observed that the clusters which were formed were comprised of NPs of a variety of sizes that did not exhibit a homogeneous distribution. When evaluated in terms of shape and structure, NPs obtained through

biosynthesis are thought to be in spherical and hexagonal structures.

Corresponding peaks were determined by considering the materials targeted specifically (Cd and Te) in the EDX spectrum. However, different elements are also observed that do not match the Cd or Te peak. Such a contamination may result from the organic structure, which cannot be removed by coating or washing processes for sample analysis (Figure 4).

## IV. DISCUSSION

In this work, there are 64 bacteria isolates in our culture collection that can be used for nanobiosynthesis. It has been determined that isolates may exhibit resistance even at the lowest dose (0.1 mM) against most of the precursor substances applied. Dose and viability rates were taken into account when choosing the isolate to be used for biosynthesis. Seven isolates resistant to all tested chemicals were selected and identified. As a result, resistant isolates which can be used in nanobiosynthesis processes have been selected.

Through SEM imagery and in particular spectrophotometric analysis, the resulting data is very effective in explaining the individual dimensions of the particles. Our data showed NPs as large clusters (~180 nm) in size in SEM images. SEM images still provide results that can be evaluated in terms of particle size and shape.

### A. Figures and Tables
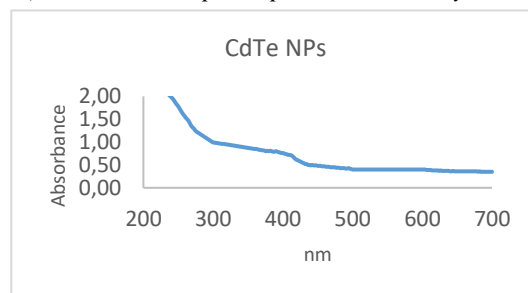
#### a) UV-VIS-NIR spectrophotometric analysis:



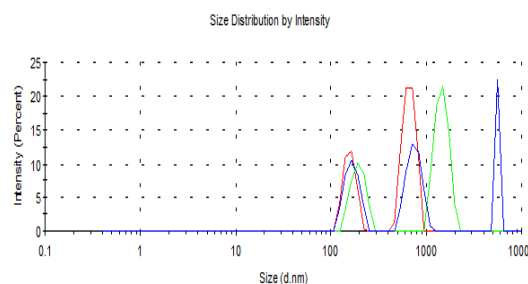Fig. 1. UV-VIS-NIR spectrophotometric.

#### b) Zetasizer analysis:



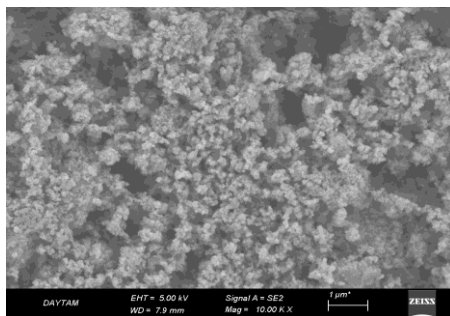Fig. 2. Zetasizer of CdTe nanoparticles

#### c) SEM and EDX analysis:

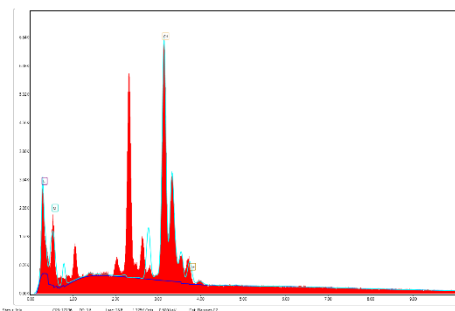Fig. 3. Scanning electron microscopy (SEM) images of CdTe NPs shapes and size. (EHT=4.00 kV)



Fig 4. EDX and elemental mapping of CdTe nanoparticles. The estimated band gap value for CdTe is 2.02 eV

## ACKNOWLEDGMENT

In conclusion, although CdTe NPs may be used in biological system but there need future studies to evaluation for chronic exposure of CdTe toxicity condition in laboratory animal. In conclusion CdTe is proper to be used in biological system but there need future studies to evaluation for acute and chronic exposure of CdTe toxicity condition in laboratory animal.

## REFERENCES

[1] H. Bao, Z. Lu, X. Cui, Y. Qiao, J. Guo, J. M. Anderson and C.M. Li, "Extracellular microbial synthesis of biocompatible CdTe quantum dots," Acta Biomaterialia, 2010, 6, 3534–3541.

[2] Si. Iravani, "Bacteria in Nanoparticle Synthesis: Current Status and Future Prospects," International Scholarly Research Notices Volume 2014, Article ID 359316, pp,18.

[3] M. Marosfoi, N. Korin, M.J. Gounis, O. Uzun, S. Vedantham, E.T. Langan, A.L. Papa, O.W. Brooks, C. Johnson, A.S. Puri, D. Bhatta, M. Kanapathipillai, B.R. Bronstein, J.Y. Chueh, D.E. Ingber and A.K. Wakhloo, "Marosfoi, M.G., et al., Shear-Activated Nanoparticle Aggregates Combined with Temporary Endovascular Bypass to Treat Large Vessel Occlusion," Stroke, 2015. 46(12), pp. 3507-3513.

[4] P. Modlitbova, K. Novotny, P. Porizka, J. Klus, P. Lubal, H. Zlamalova-Gargosova, J. Kaiser, "Comparative investigation of toxicity and bioaccumulation of Cd-based quantum dots and Cd salt in freshwater plant Lemna minor L. Ecotoxicology and Environmental Safety," 2018, 147, pp. 334-341.

[5] J.P. Monra, V. Diaz, D. Bravo, R. A. Montes, T. G. Chasteen, I.O. Osorio-Roman, C.C. Vasquez and J.M. Perez-Donoso, "Enhanced Glutathione Content Allows the in Vivo Synthesis of Fluorescent CdTe nanoparticles by Escherichia coli." 2012, Vol. 7, Issue 11, e48657.

[6] T. Okamura, N. Akai, and M. Nakata, "Reversible Photoisomerization among Triplet Amino Naphthylnitrene, Triplet Diimine Biradical, and Indazole: Matrix Isolation IR Spectra of 8-Amino-1-naphthylnitrene, 1,8-Naphthalenediimine, and 1,2-Dihydrobenz[cd]indazol," Journal of Physical Chemistry A, 2017, 121(8), pp, 1634-1638.

[7] H.M. Saleh, Y.S. El-Sayed, S.M. Naser, A.S. Eltahawy , A. Onoda, M. Umezawa, "Efficacy of alpha-lipoic acid against cadmium toxicity on metal ion and oxidative imbalance, and expression of metallothionein and antioxidant genes in rabbit brain," Environmental Science and Pollution Research, 2017. 24(31): p. 24593-24601.

[8] J.F. Shao, M.F. Kashino, N. Yamaji, S. Fukuoka, R.F. Shen and J. F. Ma, "Isolation and characterization of a rice line with high Cd accumulation for potential use in phytoremediation," Plant and Soil, 2017. 410 (1-2): pp, 357-368.

[9] A. Varmazyari, O. Baris, "Selection of Bacterial Isolates for Use in nanobiosynthesis Processes," International Conference On Advances in Natural And Applied Sciences ICANAS 2017,18 – 21 April 2017, Kundu Antalya / TURKEY.

[10] X. Zhu, D. Kumari, M. Huang, V. Achal, "Biosynthesis of CdS nanoparticles through microbial induced calcite precipitation. Materials and Design," 2016, 98, 209–214.

# Comparison of 1300nm Hybrid Diode Lasers with InGaAsP/InP Mqw Lasers

Hilal Kübra Sağlam
Faculty of Engineering, Deparment of
Electrical and Electronics Engineering
Atatürk University
Erzurum, Turkey
hks.erz@gmail.com

Çağlar Duman
Faculty of Engineering and
Architecture, Department of Electrical
and Electronics Engineering
Erzurum Technical University
Erzurum, Turkey
caglarduman@erzurum.edu.tr

Bülent Çakmak
Faculty of Engineering and
Architecture, Department of Electrical
and Electronics Engineering
Erzurum Technical University
Erzurum, Turkey
bulent.cakmak@erzurum.edu.tr

*Abstract*—The modeling of hybrid semiconductor lasers, which have been popular in recent years, has been carried out comparatively. Semiconductor lasers are often preferred in optical communication systems due to their superior performance and compactness. In this study, it is aimed to investigate the output characteristics of photonic structures that are grown on silicon material. For this purpose, modeling has been carried out by using LaserMOD (RSoft) commercial software program. Hybrid InGaAsP/InP laser and InGaAsP/InP MQW laser simulation were realized. Optical spectra are also widely used to investigate the spectral properties, lasing frequency and frequency components of light at the laser output. Improving the output characteristics of hybrid lasers increases the potential for their use in photonic integrated circuits.

*Keywords—Semiconductor Lasers, Silicon Photonics, SOI, Hybrid Integration*

## I. INTRODUCTION

One of the essential elements for efficient and multifunctional systems is that the laser source is compact. In this search for miniaturization, SOI technology are very important[2]. The SOI platform provides the advantage in terms of the medium and large scale integration. It can also operate at 1300nm and 1550nm wavelengths[3]. The use of silicon substrate is advantageous because silicon is the basic material for semiconductor electronics. III-V materials are important for optoelectronic devices such as lasers and LEDs. Low-cost and multi-functional optoelectronic integrated circuits are required to achieve high-speed communication connections. A silicon-based technology platform will be the key for this demand[1]. The hybrid lasers can be produced by the integration of the III-V epitaxial active layer on a SOI chip to transmit light to other parts of the devices. Subsequently, standard photolithography and etching processes can be performed to obtain the hybrid laser[4].

## II. MATERIAL AND METHODS

In this study, a 1300 nm hybrid semiconductor lasers which are popular in recent years were modeled and simulated by using LaserMOD (RSoft) commercial software. Also, same 1300 nm InGaAsP / InP laser structure without SOI layer was modeled and simulated with same software. This structure is a multi quantum well (MQW) laser. Electrical and optical properties of the lasers were investigated. In Figure 1 and 2, hybrid and MQW laser structures are shown, respectively.
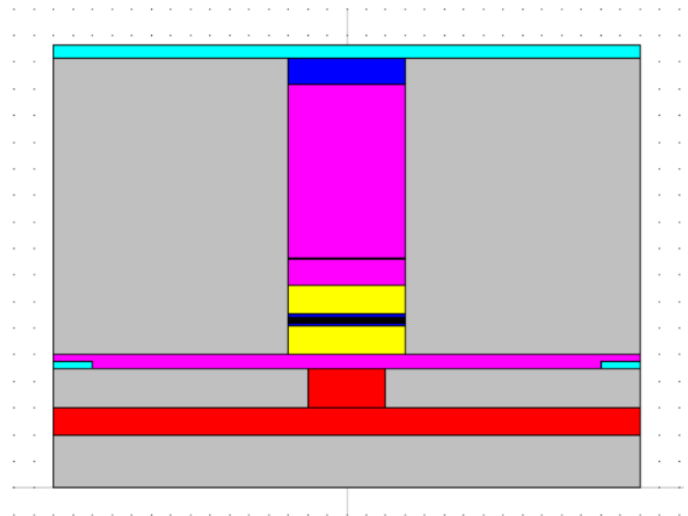


Figure 1. Hybrid InGaAsP/InP laser structure

Types, thicknesses, carrier densities and molar ratios of the layers of MQW laser is as given in Table 1. Unlike the MQW laser structure, the hybrid laser structure has an additional SOI layer at the bottom.
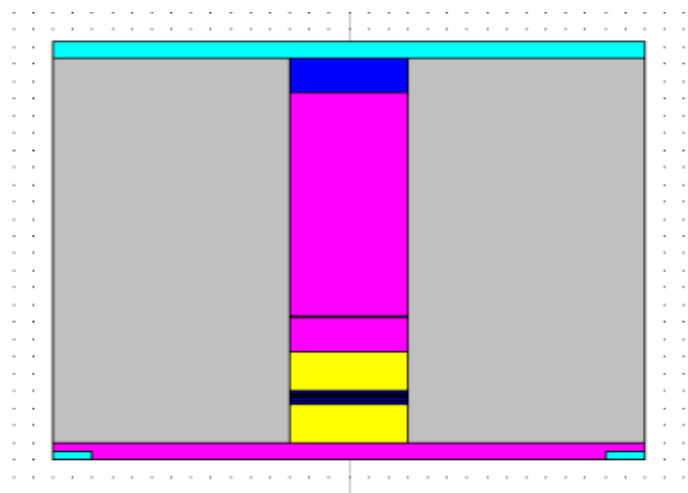


Figure 2. InGaAsP/InP laser without SOI structure

Table 1. Structure of the InGaAsP/InP MQW laser

| Layer number | Layer name | Material | Mole (x,y) | Thickness (μm) | ND, NA | Type |
|---|---|---|---|---|---|---|
| 12 | Contact | $In_xGa_{1-x}As$ | 0.53 | 0.2 | 2e19 | p+ |
| 11 | Cladding | InP | - | 1.3 | 5e17 | p |
| 10 | Etch stop | $In_xGa_{1-x}As_yP_{1-y}$ | x=0.85 y=0.32 | 0.008 | 2.5e17 | p |
| 9 | Upper Cladding | InP | - | 0.2 | 2.5e17 | p |
| 8 | SCH | $In_xGa_{1-x}As_yP_{1-y}$ | x=0.88 y=0.24 | 0.22 | - | - |
| 7 | Barrier | $In_xGa_{1-x}As_yP_{1-y}$ | x=0.85 y=0.32 | 0.2 | - | - |
| 6 | QW | $In_xGa_{1-x}As_yP_{1-y}$ | x=0.67 y=0.69 | 0.008 | - | - |
| 5 | Barrier | $In_xGa_{1-x}As_yP_{1-y}$ | x=0.85 y=0.32 | 0.01 | - | - |
| 4 | QW | $In_xGa_{1-x}As_yP_{1-y}$ | x=0.67 y=0.69 | 0.008 | - | - |
| 3 | Barrier | $In_xGa_{1-x}As_yP_{1-y}$ | x=0.85 y=0.32 | 0.02 | - | - |
| 2 | SCH | $In_xGa_{1-x}As_yP_{1-y}$ | x=0.88 y=0.24 | 0.22 | - | - |
| 1 | Lower Cladding | InP | - | 0.1 | 8e17 | n |





Figure 3. Optical output power changes of the lasers; (a) Hybrid InGaAsP/InP laser (b) InGaAsP/InP laser without SOI structure

## III. RESULTS

In the simulations, variations of the optical power output with driving currents of the hybrid laser and the MQW laser were observed. The threshold current value of the hybrid laser (InGaAsP/InP) with SOI structure used in the modelling was approximately 5 mA and the optical output power was obtained as 26.99 mW (Figure 3a) while bias current was 53.38 mA.

The threshold current value for the laser without SOI structure was approximately 5 mA and the optical output power was obtained as 24.37 mW (Figure 3b) while bias current was 53.25 mA. This demonstrates that, the hybrid laser that contains a SOI structure was found to have a higher optical power than that of the laser without SOI structure.
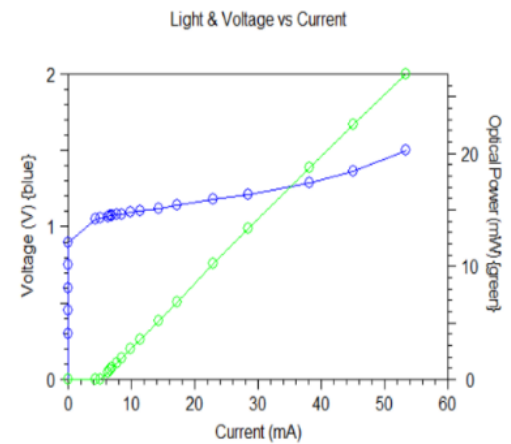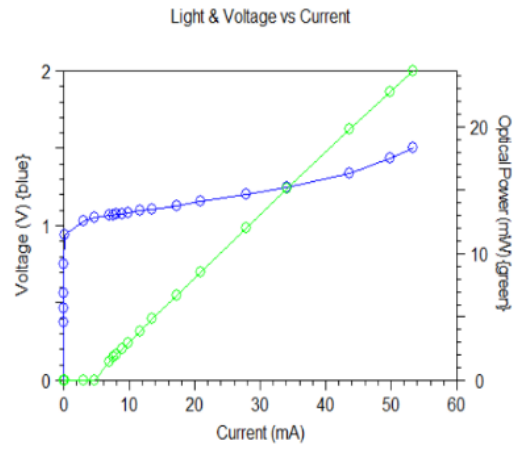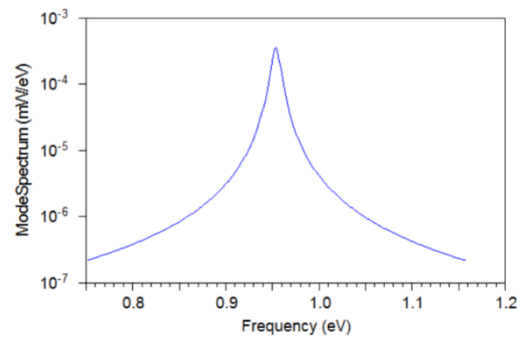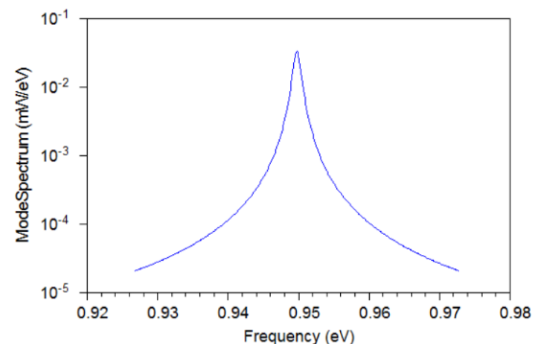




Figure 4. Optical Spectra Distribution; (a) Hybrid InGaAsP/InP laser (b) InGaAsP/InP laser without SOI structure.

267

In the simulation, optical spectrums of the hybrid laser and the laser without SOI layer were also compared (Figure 4).

While central frequency of the optical spectrum for the hybrid InGaAsP/InP laser was found to be 0.949 eV, which corresponds to 1307.76 nm; central frequency of the optical spectrum for the InGaAsP/InP laser without SOI layer was found to be 0.951 eV, which corresponds to 1304.33 nm.

## IV. CONCLUSION

In the graphs, a higher optical power output is available in the hybrid laser that contains the SOI structure. In similar studies, 25mW output power was obtained [5]. When we look at the literature, we have found comparable results with the modeled hybrid laser in this study.

## REFERENCES

[1] Benyoucef, M., Alzoubi1, T., Reithmaier, J.P., Wu, M., Trampert, A., 2014. Nanostructured Hybrid Material Based On Highly Mismatched III-V Nanocrystals Fully Embedded in Silicon. Physica Status Solidi Applications and Materials Science, 211 (No. 4, 817-822).

[2] Bondarenko, O., Fang, C., Vallini, F., Smalley, J.S.T., Fainman, Y., 2015. Extremely Compact Hybrid III-V/SOI Lasers: Design and Fabrication Approaches. Optics Express, Vol. 23 (No. 3, 2696-2712). DOI: 10.1364/OE.23.002696.

[3] Heck, M.J.R., Bauters, J.F., Davenport, M.L., Doylend, J.K., Jain, S., Kurczveil, G., Srinivasan, S., Tang, Y., Bowers, J.E., 2013. Hybrid Silicon Photonic Integrated Circuit Technology. IEEE Journal of Selected Topics in Quantum Electronics, Vol. 19 (No. 4, 6100117). DOI: 10.1109/JSTQE.2012.2235413.

[4] Lee, A., Liu, H., Seeds, A., 2012. Semiconductor III–V Lasers Monolithically Grown on Si Substrates. Semiconductor Science And Technology, 28 (2013) 015027

# Design and Production of an Amperometry Device For Measuring Neurotransmitter Concentration

M. Dilruba Geyikoğlu
Elektrik ve Elektronik Mühendisliği
Bölümü, Atatürk Üniversitesi
Erzurum 25240, Türkiye
dilruba_mdk@hotmail.com

Hilal Koç
Elektrik-Elektronik Mühendisliği
Bölümü, Erzurum Teknik Üniversitesi
Erzurum 25700, Türkiye
hilal.koc@erzurum.edu.tr

Bülent Çavuşoğlu
Elektrik ve Elektronik Mühendisliği
Bölümü, Atatürk Üniversitesi
Erzurum 25240, Türkiye
bcavusoglu@atauni.edu.tr

*Abstract*— In this study, it is aimed to design a device to be used in the diagnosis and treatment of brain diseases by taking the concentrations of the neurotransmitters in the brain and the time-based measurements of these concentration amounts in time. When designing this device, amperometry technique was used in which the change of current over time due to activated neurotransmitter concentration was measured. The transempedance amplifier was used to increase the currents of 10-9 A obtained from the neurotransmitter measurements. In the device, all the noise-generating elements are taken into account during wiring and circuit design and noise levels are minimized. The Bluetooth module was used to provide wireless communication. Also, the circuit providing the constant reference voltage required for neurotransmitter activation was added to this device. Thus, a mobile neurotransmitter concentration measuring device was obtained which could work independently without the need for other systems.

*Keywords* — Amperometry, Transempedance.

# Magnetite (Fe₃O₄) nanoparticles as adsorbents for Cu removal from aqueous solutions

Raba′ah Syahidah Azis
Department of Physics, Faculty of
Science, 43400 Universiti Putra
Malaysia, Serdang, Selangor.
Materials Synthesis and
Characterization Laboratory (MSCL),
Institute of Advanced Technology
(ITMA), 43400 Universiti Putra
Malaysia, Serdang, Selangor, Malaysia.
rabaah@upm.edu.my

Syazana Sulaiman
Materials Synthesis and
Characterization Laboratory (MSCL),
Institute of Advanced Technology
(ITMA), 43400 Universiti Putra
Malaysia, Serdang, Selangor, Malaysia.
syazana2104@gmail.com

Nur Asyikin Ahmad Nazri
Materials Synthesis and
Characterization Laboratory (MSCL),
Institute of Advanced Technology
(ITMA), 43400 Universiti Putra
Malaysia, Serdang, Selangor, Malaysia.
adeqikin@gmail.com

Ismayadi Ismail
Materials Synthesis and
Characterization Laboratory
(MSCL), Institute of Advanced
Technology (ITMA), 43400
Universiti Putra Malaysia,
Serdang, Selangor, Malaysia.
ismayadi@upm.edu.my

Abdul Halim Shaari
Department of Physics, Faculty
of Science, 43400 Universiti
Putra Malaysia, Serdang,
Selangor.
ahalim@upm.edu.my

Nurul Ayuni Mohd Azuan
Department of Physics, Faculty
of Science, 43400 Universiti
Putra Malaysia, Serdang,
Selangor.
ayuniazuan@yahoo.com

Nurshahiera Rosdi
Materials Synthesis and
Characterization Laboratory
(MSCL), Institute of Advanced
Technology (ITMA), 43400
Universiti Putra Malaysia,
Serdang, Selangor, Malaysia.
nurshahierarosdi5243@gmail.com

*Abstract —In this study, magnetite nanoparticles, Fe₃O₄ (MNp) were used as low-cost metal adsorbents metal removal in wastewater treatment process. MNp were synthesized from the waste mill scales used as Cu (II) ions adsorbents. The parameters such as contact time, temperature and different copper metal concentration of the solution were studied. The magnetite was milled mechanical alloying for 3, 6 and 9 hours, respectively, using High-energy ball milling (HEBM). The nanomaterials were characterized using X-rays Diffraction (XRD), Vibrating Sample Magnetometer (VSM), Atomic Adsorption Spectrophotometer (AAS) and Transmission Electron Microscopy (TEM). An equilibrium time of 30 minutes was required for the adsorption of Cu (II) ions. The results showed that nano-sized Fe₃O₄ has a potential to remove cationic heavy metal species from industrial wastewater.*

*Keywords—Magnetic nanoparticles (MNp), Waste mill scales, Adsorption, Cu (II) metals removal, wastewat*

# Green Synthesis of Zinc Oxide and Application in Microbially Active Biopolymer Packaging Films

Rosnita A. Talib
Department of Process and Food
Engineering
Universiti Putra Malaysia
Serdang, Malaysia
rosnita@upm.edu.my

Siti Hajar Othman
Department of Process and Food
Engineering
Universiti Putra Malaysia
Serdang, Malaysia
s.hajar@upm.edu.my

Hasbullah Hassan Basri
Department of Process and Food
Engineering
Universiti Putra Malaysia
Serdang, Malaysia
hasbullah.hassanbasri08@gmail.com

Rashidah Sukor
Department of Process and Food Engineering
Universiti Putra Malaysia
Serdang, Malaysia
rashidah@upm.edu.my

Hidayah Ariffin
Institute of TropicalForestry and Forest Products
Universiti Putra Malaysia
Serdang, Malaysia
hidayah@upm.edu.my

*Abstract*— **Green synthesis of zinc oxide nanoparticles (ZnO NPs) can be an alternative to conventional methods due to its simplicity and eco-friendly. Zinc oxide nanoparticles have antibacterial and antifungal properties, thus can be applied in the application of active packaging. In the present study, ZnO NPs were synthesised using pineapple peel extract and zinc nitrate hexahydrate (as a precursor). The synthesis methods involve heating at 60 °C and without heating to study the influence of synthesis temperature against the shape and size of ZnO NPs. The produced ZnO NPs were characterised using XRD, EDX, FTIR spectroscopy and FESEM. The surface morphological analyses demonstrated different shape and size of ZnO NPs produced. When the synthesis was heated, it produced flower-shaped NPs with a smaller average size of 13-17 nm as compared to the synthesis without heating where rod-shaped NPs with a size of 15-60 nm were produced. Next, the ZnO-starch nanocomposite films were developed by incorporating various concentration of ZnO NPs (1%, 3% and 5%) into dissolved starch by film casting method. These nanocomposite films were tested for their antibacterial activity against Gram positive and Gram-negative bacteria, while for their potential antifungal yeast was used. The disc diffusion method results revealed that maximum zones of inhibition were observed Gram positive bacteria *Bacillus subtilis* and followed by fungi *Aspergillus brasiliensis* when increased the concentration of ZnO NPs in the films.**

*Keywords*— *zinc oxide nanoparticle, green synthesis, antibacterial, antifungal, pineapple waste*

# Fabrication of WS₂ Field Effect Device

Merve Acar

Atatürk Universty

Engineering Faculty, 25240 Erzurum

merve.acar@atauni.edu.tr

*Abstract-*The transition metal dichalcogenides (TMDCs) are attractive for use in next-generation nanoelectronics compared to one -dimensional meterials. (TMDCs) have been used for various applications such as logic, optical devices, and sensors. The TMDCs including MoS2, MoSe₂, WS₂, WSe₂ have demonstrated graphene like properties. Metal-Oxide-Semiconductor-Field-Effect transistors (MOSFETs) composed of 2D materials (TMDCs), have demonstrated high potential. Lately, researchers have been concerned with WS₂ MOSFETs due to for its electrical, optical and mechanical properties. This work shows fabrication steps high performance field-effect transistors with sputter-grown single layer WS2.

*Keywords-*MOSFET, WS₂, Fabrication

# Sleep Stage Classification Using EEG Signals Based on Duration Depended Hidden Markova Model

Hamed Shamsi

Shahid Beheshti Technical and Vocational University, Urmia, Iran

hamed.shamsi@yahoo.com

*Abstract*-Sleep disorders among the people can endanger the ability to work and mental health of individuals. In the past, trained technicians manually analyzed the vital signals by identifying the sleep stages every 30 seconds. Among these courtesy signals, EEG signals contain useful and rich information in the brain that can be used to extract the different stages of sleep. Today, researchers have been able to achieve a high percentage of sleep segregation by using different techniques of data mining and pattern recognition. Identifying the sleep cycle and the steps that a person walks during sleep has various therapeutic and research applications, such as examining types of insomnia and examining the behavior of children. So that the normal level of mental activity is characterized by sleep cycles.

Detection of sleep stages requires a suitable method to determine every stage of sleep, as well as manual methods and using existing knowledge in this field. In this research, by extraction of appropriate statistical and frequency characteristics, Electroencephalography (EEG) and Electrooculography (EOG) data during sleep, as well as the previous stage of sleep as a feature, are used to determine the sleep stages using a time-dependent secret-based Markov model. The results show that using a surveyed modeling model has far better results than similar ones.

*Keywords-Sleep Stage, Classification, EEG Signals, Duration Depended Hidden Markova Model*

# Nanostructured Organic Semiconductor Thin Films as Surface Enhanced Raman Spectroscopy (SERS) Platforms

Mehmet Yilmaz
Ataturk University
ylmzmehmet@yahoo.com

*Abstract*-Surface-Enhanced Raman Spectroscopy (SERS) has attracted remarkable interest as a powerful analytical tool for the detection of chemical and biological molecules for the last four decades. In SERS studies, basically, the enhancement of Raman signals fundamentally stems from the electromagnetic field in close vicinity of nanostructures with plasmonic features on a surface. Although utilization of plasmonic nanostructures for SERS applications seems to be a simple and inexpensive procedure, the high cost of coinage metals (gold, silver or copper) and the limitation in their production procedures lead to discrepancy in the resulting SERS signals and hamper their usage in practical SERS application. Despite the significant progress, SERS systems are still facing challenges for practical applications related to their sensitivity, reliability, and selectivity. To overcome these limitations, recently, we have proposed a simple yet facile concept by depositing nanostructured organic semiconductor thin films via physical vapor deposition technique.1-2 In our first attempt, we employed thin layer films of p-type organic semiconductor, 2,7-dioctyl[1]benzothieno[3,2-b][1]benzothiophene (C8-BTBT), as SERS platforms.1 After deposition of gold layer, we observed that both chemical and electromagnetic enhancement could be created with this novel system. In our second attempt, we tested the n-type organic semiconductor molecule namely, α,ω-diperfluorohexylquaterthiophene, DFH-4T.2 Interestingly, remarkable enhancement in Raman signal was detected without the presence of plasmonic nanostructure due to the chemical enhancement mechanism. After deposition of a thin layer of gold, sub-femtomolar concentrations of analyte molecule could be observed via this low-cost, facile and effective SERS platform. In the context of this study, I will discuss the emergence of organic semiconductors as SERS systems in detail.

1- Yilmaz, Mehmet, et al. "Micro-/Nanostructured Highly Crystalline Organic Semiconductor Films for Surface-Enhanced Raman Spectroscopy Applications." Advanced Functional Materials 25.35 (2015): 5669-5676.

2- Yilmaz, Mehmet, et al. "Nanostructured organic semiconductor films for molecular detection with surface-enhanced Raman spectroscopy." Nature materials 16.9 (2017): 918.

*Keywords-organic semiconductors, nanostructured thin films, surface enhanced Raman spectroscopy*

# Synthesis of Carbon Nanotube from Waste Cooking Oil Catalysed by Mill Scale Waste for Development of Microstrip Patch Antenna

Ismayadi Ismail
Institute of Advanced Technology
Universiti Putra Malaysia
Serdang, Selangor, Malaysia
ismayadi@upm.edu.my

Mohd Nizar Hamidon
Institute of Advanced Technology
Universiti Putra Malaysia
Serdang, Selangor, Malaysia
mnh@upm.edu.my

Muhammad Syazwan Mustaffa
Institute of Advanced Technology
Universiti Putra Malaysia
Serdang, Selangor, Malaysia
one_9494@yahoo.com

Intan Helina Hasan
Institute of Advanced Technology
Universiti Putra Malaysia
Serdang, Selangor, Malaysia
i_helina@upm.edu.my

Zulkifly Abbas
Dept. of Physics, Fac. of Science
Universiti Putra Malaysia
Serdang, Selangor, Malaysia
za@science.upm.edu.my

Rosiah Osman
Institute of Advanced Technology
Universiti Putra Malaysia
Serdang, Selangor, Malaysia
rosiah@upm.edu.my

*Abstract*— The synthesis of carbon nanotube (CNT) using waste cooking oil (WCO) as green starting material was carried out in a floating catalyst thermal vapor deposition reactor by using mill scale waste which is iron oxide nanoparticles (IONP) as a catalyst. Their morphology, composition, mass of substance changes, Raman characteristics and electromagnetic (EM) wave absorption performance were measured by Field Emission Scanning Electron Microscope (FESEM), Energy Dispersive X-ray (EDX), Thermal Gravimetric Analysis (TGA), RAMAN spectroscopy and Vector Network Analyzer (VNA). Results indicated that iron nanoparticles were distributed on MWCNT surface with agglomeration, and MWCNT crucially affected the magnetic properties of iron nanoparticle. Samples with higher degree of carbon graphitization as confirmed by Raman characteristic possess higher absorption value. The enhanced EM-wave absorption performance was mainly ascribed to the increased of interfacial polarization and dielectric loss that resulting from the introduction of MWCNT. The result illustrated that the introduction of MWCNT into magnetic materials can enable the efficient design of excellent patch antenna for wireless communication application.

*Keywords: Carbon nanotubes, waste cooking oil, microstrip patch antenna*

## INTRODUCTION

The dumping of cooking palm oil waste has triggered a major concern over its effect towards the environment. We are looking at the beneficial use of waste cooking oil as the starting material for the synthesis of carbon nanotube (CNT) powder. It will be synthesized via modified chemical vapour deposition (CVD) method by using the injection of waste cooking oil as the carbon source and mill scale waste ($Fe_3O_4$) as the catalyst. CNT exhibit a great range of remarkable properties, including unique mechanical and electrical characteristics have led to the use of CNT as microstrip patch antenna (MPA) in the past few years (1-3). Previous studies have embarked on the usage of carbon fibre composites such as CNT that has caught the interest of many researchers in the attempt to replace metals in antenna. This research intends to explore the application of CNT made from waste cooking oil as a patch antenna and discuss the design and fabrication of these structures and the properties of the acquired antenna

## MATERIALS AND METHODS

The methodology of the research work is divided into three stages: (a) Synthesis of carbon nanotube (CNT), (b) preparation of CNT thick film paste and (c) Microstrip patch antenna (MPA) fabrication. During the synthesis, the catalyst used was mill scale waste crushed to nanosize powders and waste cooking cooking oil used as the carbon source and argon as carrier gas. The CNT obtained was then characterized. The as-synthesized CNT was further used as an active element in the thick film paste to be fabricated into microstrip patch antenna via screen printing. The microstrip patch antenna was printed onto kapton tape substrate and its return loss and resonant frequency were measured in the frequency range of 1-8 GHz.

## RESULTS AND DISCUSSION

The web-like structure consists of nanotube bundles were observed. The bundling results from the attractive Van-der Waals forces between nanotubes.

Fig. 1, the min reflection loss (*RL*) of sample synthesized at 650°C was 12.42 dB at 5.46 GHz. Moreover, sample synthesized at 750°C, the minimum *RL* was 15.97 dB at 3.75 GHz. As for the sample prepared at 850°C, it shows the highest *RL* that is around 27.82 dB at 3.03 GHz. These results revealed that the existence of MWCNT enhanced its EM-wave absorption performance. MWCNT can form conductivity net, and enhance the dielectric loss capability. In addition, the interfacial between magnetite nanoparticles (mill scale waste) and CNT enhanced the interfacial polarization capability.

## CONCLUSIONS

MWCNT were achieved by using waste cooking oil as a carbon source via modified CVD. Different characterization techniques were used to investigate the formation of MWCNT. FESEM measurements showed that the amount of carbon content can be adjusted by changing the experimental condition. By changing the sintering temperature can result in better properties of CNT that

would affect the properties in the electron transport in CNT hence giving better absorption in microwave patch antenna.
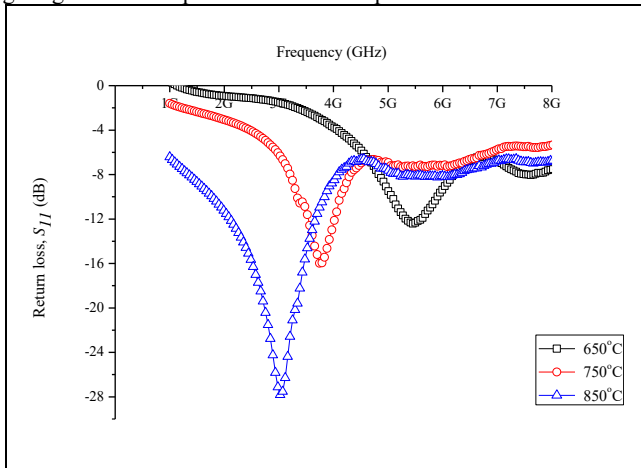


**Fig. 1: Reflection loss, $S_{11}$ of MPA at different sintering temperature.**

This study demonstrates that waste cooking oil, a low-cost and readily available resource, can be used as an inexpensive carbon source for the production of CNT and as an active element for microstrip patch antenna.

REFERENCES

[1] Baddour CE, Fadlallah F, Nasuhoglu D, Mitra R, Vandsburger L, Meunier JL, *Carbon*, 2008, **47**, 313.

[2] Bhatia R., Prasad V, *Solid State Communications*, 2010, **150**,311.

[3] Kumar M, Ando Y, *Journal of Nanoscience and Nanotechnology*, 2010, **10**, 3739.

# Properties of Silica Ceramics Derived from Rice Husk Ash

Rosiah Osman
Institute of Advanced Technology
Universiti Putra Malaysia
Serdang, Selangor, Malaysia
rosiah@upm.edu.my

Ismayadi Ismail
Institute of Advanced Technology
Universiti Putra Malaysia
Serdang, Selangor, Malaysia
ismayadi@upm.edu.my

Mohd Nizar Hamidon
Institute of Advanced Technology
Universiti Putra Malaysia
Serdang, Selangor, Malaysia
mnh@upm.edu.my

Intan Helina Hasan
Institute of Advanced Technology
Universiti Putra Malaysia
Serdang, Selangor, Malaysia
i_helina@upm.edu.my

Khamirul Amin Matori
Dept. of Physics, Fac. of Science
Universiti Putra Malaysia
Serdang, Selangor, Malaysia
khamirul@upm.edu.my

Nor Hapishah Abdullah
Institute of Advanced Technology
Universiti Putra Malaysia
Serdang, Selangor, Malaysia
hapishah@upm.edu.my

*Abstract*— **Rice Husk (RH) is the most outer layer of paddy grain. It is considered as agriculture waste material. It is usually being openly burnt in the wasteland, causing air pollution. Although it has been used in cement, alloy and ceramic industry but still millions of tons were wasted worldwide. This project will look into how this agriculture abundant waste (RH) will be regenerated and turned into economic potentials. Previous studies show that Rice Husk (RH) contains about 20wt% silica. With proper thermal treatment, this silica will be converted into cristobalite which is a crystalline form of silica ($SiO_2$). It should have piezoelectric properties and behave just like quartz crystal. Piezoelectric materials can be used as sensors and actuators in electronic applications. In this research, physical and electrical characteristics of silica derived from Rice Husk (RH) were analyzed. The result shows that RH silica slightly possesses piezoelectric properties.**

*Keywords: Rice Husk, silica, cristobalite, piezoelectric materials*

# Ferrites Based Thick Film for Enhanced Microstrip Patch Antenna

Intan Helina Hasan
Institute of Advanced Technology
Universiti Putra Malaysia
Serdang, Malaysia
i_helina@upm.edu.my

Mohd Nizar Hamidon
Institute of Advanced Technology
Universiti Putra Malaysia
Serdang, Malaysia
mnh@upm.edu.my

Alyani Ismail
Faculty of Engineering
Universiti Putra Malaysia
Serdang, Malaysia
alyani@upm.edu.my

Ismayadi Ismail
Institute of Advanced Technology
Universiti Putra Malaysia
Serdang, Malaysia
ismayadi@upm.edu.my

Saman Azhari
Institute of Advanced Technology
Universiti Putra Malaysia
Serdang, Malaysia
samanar@gmail.com

Rosiah Osman
Institute of Advanced Technology
Universiti Putra Malaysia
Serdang, Malaysia
rosiah@upm.edu.my

*Abstract*— **The present work investigated the fabrication of nickel zinc ferrite (NZF) and yttrium iron garnet (YIG) thick film layer as substrate inclusion to enhance the performance of microstrip patch antenna (MPA). In this paper, Ferrite nanopowder was mixed with organic vehicle which consists of linseed oil, m-xylene and α-terpineol. Then the mix was stirred at 150rpm for 3 hours at 40°C in order to obtain homogenous paste, followed by printing it onto FR4 substrate using the screen printing technique to form the ferrite thick film layer before dried and later fired at 200°C. A patch antenna using silver paste was printed onto the ferrite thick film layer and was compared with another patch antenna which was been printed without the ferrite thick film layer. The results shown that the antenna with ferrite thick film layer has improved the performance of MPA compared to the antenna without the layer.**

*Keywords—thick film, ferrites, microstrip patch antenna*

## I. Introduction

Thick film technology is widely used in producing electronics components. The thick film paste used in the fabrication process mainly consists of active element which determines the properties of the thick film; and organic vehicle which gives rheology properties of the paste [1], [2]. Meanwhile, microstrip patch antenna (MPA) has been gaining popularity especially in telecommunication devices due to its planar profile and ease of fabrication [3], [4]. It still, however, has some advantages such as narrow bandwidth and low gain [5]. Ferrites have been studied as substrates for MPA to enhance the performance since it has high resistivity and low losses at high frequency [6]–[8]. This work aims to study and compare the effect of inclusion of ferrites, specifically nickel zinc ferrite (NZF) and yttrium iron garnet (YIG), to the bandwidth of MPA.

## II. Methodology

NZf and YIG nanopowder was each mixed with organic vehicle, stirred at 150rpm for 3 hours at 40°C in order to obtain homogenous paste, followed by printing it onto FR4 substrate with dimension of 20 x 20 mm using the screen printing technique and dried at 100°C. A basic 10 x 10 mm square shape patch antenna using silver (Ag) paste was printed onto the ferrite layer and was compared with another patch antenna which was been printed without the ferrite layer.

## III. Results and Discussion

Fig. 1 shows the design of the MPA fabrication with ferrite thick film layer, and the actual fabricated MPA. The ferrite thick film was printed to cover the whole FR4 substrate, therefore it is visible from the top.
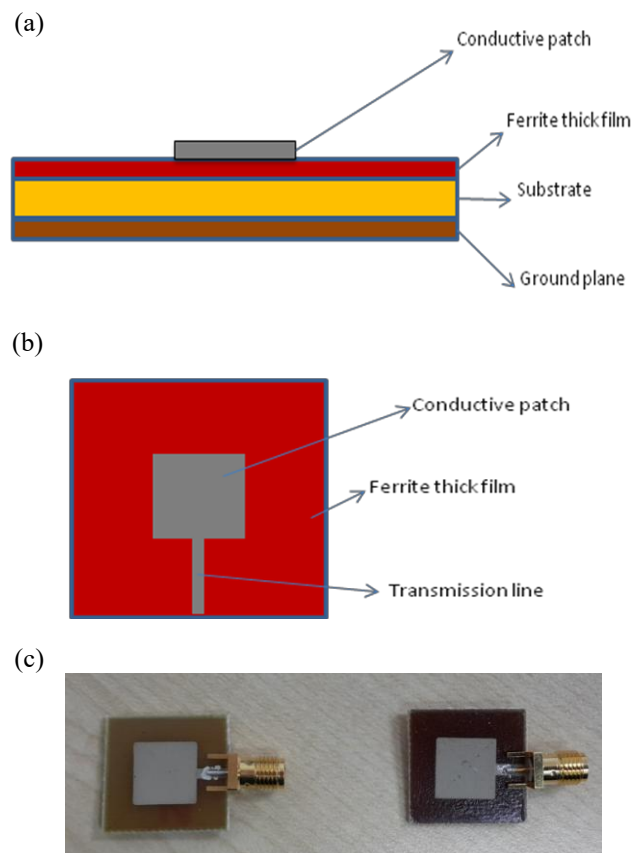
(a)



(b)



(c)



Fig. 1. Fabrication of MPA: (a) side view, (b) top view, (c) actual fabricated MPA (top view only).

Fig. 2(a) shows the measurement of MPA with NZF thick film inclusion using vector network analyzer, while Fig. 2(b) shows the measurement of MPA with YIG thick film inclusion. Both measurements were compared with MPA without any ferrite thick film inclusion. Table 1 summarized the results of the measurements. From the table, it is clearly observed that the inclusion of ferrite thick film significantly enhanced the bandwidth of MPA, while better return loss can also be observed. The resonant frequency shifted a little due to increased permittivity of the substrate coupled with ferrite thick film layer.
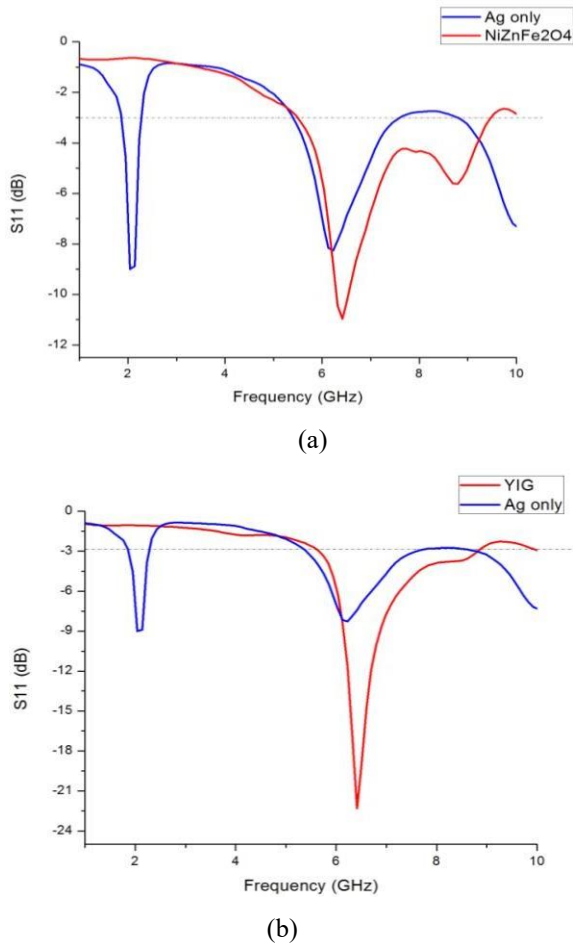


(a)



(b)

Fig. 2. The return loss and resonant frequency of silver patch antenna with and without ferrite thick film loading.

TABLE I.      MEASUREMENT RESULTS OF MPA WITH AND WITHOUT FERRITE THICK FILM LOADING

| Antenna material | Antenna parameters | | |
|---|---|---|---|
| | Resonant frequency (GHz) | Return Loss (dB) | Bandwidth (GHz) |
| Ag only | 6.22 | -8.25 | 2.09 |

| Antenna material | Antenna parameters | | |
|---|---|---|---|
| | Resonant frequency (GHz) | Return Loss (dB) | Bandwidth (GHz) |
| Ag - NZF | 6.42 | -10.97 | 3.90 |
| Ag - YIG | 6.42 | -19.67 | 3.13 |

IV. CONCLUSION

The results proved that ferrite thick film can be used to enhance MPA performance, specifically the bandwidth and return loss of MPA, which have always been disadvantages of using MPA in devices. Future works will include the study of MPA with ferrite thick film on selected frequency, and fabrication using flexible substrates.

REFERENCES

[1]    B. Morten, M. Prudenziati, and A. Taroni, "Thick-film technology and sensors," *Sensors and Actuators*, vol. 4, no. C, pp. 237–245, 1983.

[2]    M. Prudenziati and B. Morten, "Thick-film sensors: an overview," *Sensors and Actuators*, vol. 10, no. 1–2, pp. 65–82, 1986.

[3]    M. Elhefnawy and W. Ismail, "A Microstrip Antenna Array for Indoor Wireless Dynamic Environments," *IEEE Trans. Antennas Propag.*, vol. 57, no. 12, pp. 3998–4002, 2009.

[4]    D. Guha and Y. M. M. Antar, *Microstrip and Printed Antennas: New Trends, Techniques and Applications*. 2010.

[5]    C. A. Balanis, *Antenna Theory: Analysis and Design*, Third edit. John Wiley & Sons, Inc., 2012.

[6]    S. S. Pattnaik, R. K. Mishra, and N. Das, "Elliptical microstrip antenna on ferrite substrate," *Electron. Lett.*, vol. 26, no. 22, 1990.

[7]    A. Rahman, N. M. Yi, A. U. Ahmed, T. Alam, M. J. Singh, and M. T. Islam, "A compact 5G antenna printed on manganese zinc ferrite substrate material," *IEICE Electronics Express*, vol. 13, no. 11. 2016.

[8]    S. N. Das and S. K. Chowdhury, "Rectangular Microstrip Antenna on a Ferrite Substrate," *IEEE Trans. Antennas Propag.*, vol. 30, no. 3, pp. 499–502, 1982.

| ISASE 2018 TIME TABLE | | |
|---|---|---|
| **ORHAN YAVUZ AMPHI, SCIENCE FACULTY** | | |
| | **NOV 27TH TUESDAY** | **NOV 28TH WEDNESDAY** |
| | | **Session-OY4 (Chair: Prof. Dr. Sebahattin Tüzemen)** |
| 08.30-09.00 | Registration | - |
| 09.00-09.20 | Opening Ceremony | **Assist. Prof. Burcu Savaşkan** Trapped magnetic field properties of multi-seeded bulk YBCO superconductors fabricated by using top-seeded melt growth process |
| 09.20-09.40 | | **Assist. Prof. Ferhunde Aysin** Evaluation of the Protective Effect of Boric Acid against Renal Ischemia-Reperfusion Injury |
| 09.40-10.00 | | **Kübra Solak** Catechin for Cancer Immunotherapy |
| 10.00-10.20 | **Prof. Dr. Taşkın Öztaş** Introduction of Ataturk University | **Assist. Prof. Dilek Okuyucu** A Case Study For Structural Model Update By Operational Modal Analysis : Erzincan Değirmenliköy Church |
| **Break** | **Session-OY1 (Chair: Assoc. Prof. Ayşe Bayrakçeken Yurtcan)** | **Session-OY5 (Chair: Prof. Dr. Emre Gür)** |
| 10.40-11.00 | **Prof. Dr. Hamdullah Kılıç** Mechanistic Studies on the Epoxidation and Aziridination Reactions **(Invited Paper)** | **Prof. Dr. Hasan Efeoğlu** Growth Rate Enhancement of TiO2 by R-HiPIMS and Application to Memristor Fabrication **(Invited Paper)** |
| 11.00-11.20 | **Assoc. Prof. Dr. Abdul Halim Abdullah** Degradation of methyl orange dye by visible light driven photocatalyst | **Assoc. Prof. Dr B.T. Hang Tuah Baharudin** Stent Manufacturing using Medical Grade ASTM F75 Cobalt Chromium (CoCrMo) by Selective Laser Melting (SLM) Technology **(Invited Paper)** |
| 11.20-11.40 | **Prof. Dr. Sebahattin Tüzemen** LED, Solar-Cell and Gas Sensor Applications of Micro and Nano-Structures in Oxide and Perovskite Materials **(Invited Paper)** | **Assoc. Prof. Ayşe Bayrakçeken Yurtcan** Fuel Cell Materials **(Invited Paper)** |
| 11.40-12.00 | **Assoc. Prof. Dr. Mohd Nizar Hamidon** Fabrication of Piezoresistive Nanocomposite using Functionalized Carbon Nanotubes (fCNT) and Polydimethylsiloxane (PDMS) towards pressure Sensing Applications **(Invited Paper)** | **Assit. Prof. Canan Aksoy** Comparison of Superconducting Joints Fabricating by Using Different Techniques |
| **LUNCH** | **Session-OY2 (Chair: Assoc. Prof. Dr. Mohd Nizar Hamidon)** | **Session-OY6 (Chair: Prof. Dr. Bülent Çakmak)** |
| 13.40-14.00 | **Prof. Dr. İhsan Efeoğlu** Functional Depositions and Applications for Defense Industry **(Invited Paper)** | **Prof. Dr. Emre Gür** Growth of 2D WS2 by RF Sputtering and Applications **(Invited Paper)** |
| 14.00-14.20 | **Assoc. Prof. Dr. Khamirul Amin Matori** Current Trend and Status of Bioceramics for Dental Applications in UPM, Malaysia **(Invited Paper)** | **Assist. Prof. Şahin Coşkun** Silver Nanowire Based Transparent Electrodes and Heaters |
| 14.20.14.40 | **Prof. Dr. Dia Abualnadi** Model Order Reduction of LTI Systems Using Particle Swarm Optimization **(Invited Paper)** | **Dr Haslina Jaafar** Graphene-Latex Conductive Film |
| 14.40-15.00 | **Prof. Dr. Süleyman Toy** Indices and Computer Models Used to Calculate and Estimate Outdoor Human Thermal Comfort | **Assist. Prof. Mehmet Yılmaz** Novel Approaches in Synthesis of Chiral Nanostructures |

| Break | Session-OY3 (Chair: Prof. Dr. Dia Abualnadi) | Session-OY7 (Chair: Assoc. Prof. Dr. Khamirul A. Matori) |
|---|---|---|
| 15.20-15.40 | **Assoc. Prof. Dr. Suraya Abdul Rashid** Biochar-derived Carbon Quantum Dots: Preparation, Characterization and Potential Applications | **Assoc. Prof. Dr. Jasronita Jasni** Transformer Health Index Assessment Model |
| 15.40-16.00 | **Prof. Dr. Bülent Çakmak** Fabrication and Characterization of Semiconductor Lasers **(Invited Paper)** | **Prof. Dr. German F. de la Fuente** Laser Surface Modification of Materials **(Invited Paper)** |
| 16.00-16.20 | **Assoc. Prof. Dr. Zulkiflle Leman** Water Absorption, Flexural Strength And Calcium Carbonate Content In A Composite Crossarm | **Assist. Prof. Mustafa Tolga Yurtcan** Pulsed Laser Deposited $CeO_2/LaAlO_3$ Thin Film Orientations at Different Temperatures |
| 16.20-16.40 | **Assist. Prof. Nihal Simsek Ozek** Treatment Potential of Boric Acid Supplementation on Liver Injury Induced by Renal Ischemia-Reperfusion | **Ibtihel Zaier** The Application of Fenton's Reagent as an Efficient System in The Treatment of Soil Contaminated with Used Lubricating Oils |
| 16.40-17.00 | **Assist. Prof. İsmail Bezirganoğlu** An evaluation of antibiotics for the elimination of Agrobacterium tumefaciens from Melon (Cucumis melo L.) cotyledon explants | **Assist. Prof. Dr. Ömer Faruk Karataş** Tumor Suppressive Role of ING5 in Prostate Cancer **(Invited Paper)** |
| 17.00-17.20 | **Hilal Kübra Sağlam** Modeling of DSAWR Sensor for Different Resistance Values of Active Layer | **Fatma Nur Tuzluca** Enhancement of Energy and Power Density of Batteries and Supercapacitors Electrode Hybridization |
| **POSTER SESSION** | | |
| 17.00 | RETURN to HOTEL | **CLOSING CEREMONY** |

| K9 LECTURE HALL, SCIENCE FACULTY | | |
|---|---|---|
| | **NOV 27TH TUESDAY** | **NOV 28TH WEDNESDAY** |
| | | **Session-LH5 (Chair: Assit. Prof. Canan Aksoy)** |
| 09.00-09.15 | - | **Yasar Ozkan Yesilbag** Hierarchical CuO@CuS coreshell nanowires for supercapacitor electrode materials |
| 09.15-09.30 | | **Aykut Coşkun** YBCO Metamaterials Fabricated by Screen Printing Method |
| 09.30-09.45 | | **Derya Tekin** Synthesis And Characterization Of Rgo/Tio2/Peg Nanocomposite |
| 09.45-10.00 | - | **Mehmet Masat** Fabrication of Metal Oxide Carbon Dioxide Detector with Screen Printing Technique for Use on Airplanes |
| 10.00-10.15 | - | **Meryem Samancı** Investigation of Structural Changes with the Addition of Graphene to Carbon Aerogel |
| **Break** | **Session-LH1 (Chair: Assist. Prof. Ferhunde Aysin)** | **Session-LH6 (Chair: Assoc. Prof. Dr. Suraya Abdul Rashid)** |
| 10.35-10.50 | **Ahmet Dumlu** PID Type Sliding Mode Controller Design for an Autonomous Electric Wheelchair | **Gürkan Kalınay** A Microwave Bandpass Filter Design |
| 10.50-11.05 | **Hacı Mehmet Güzey** Sub-Optimal Consensus-Based Formation Control of Fixed-Wing MUAV's | **Işıl Karabey Aksakallı** Using Convolutional Neural Network for Android Malware Detection |
| 11.05-11.20 | **Kağan Koray Ayten** Sliding Mode Controller Design for PMDC Motor | **Yunus Kaya** Determination of Negative Constitutive Parameters Based on a Square Split Ring |

| | | Resonator Left Handed Metamaterial Using Waveguide |
|---|---|---|
| 11.20-11.35 | **Ahmet Numan Özakın**<br>Energy Efficiency and Energy Management in Asphalt Plants | **Hilal Koç**<br>Step By Step Investigation of Reconfigurable Microstrip Patch Antenna |
| 11.35-11.50 | **Faruk Yeşildal**<br>The Effect of Spray Characteristics Drop Diameters And SMD Correlations | **Burcu Tiryaki**<br>Traffic Sign Recognition Using Deep Convolutional Neural Network |
| 11.50-12.05 | **Taner Tekin**<br>Synthesis of core-shell SiO2/ZnO Nanoparticles and Determination of their Photocatalytic Activity | **Hussein Mahmood Abdo Mohammed**<br>Road Lane Detection with CNN |
| **LUNCH** | **Session-LH2 (Chair: Prof. Dr. Emre Gür )** | **Session-LH7 (Chair: Prof. Dr. Cavit Kazaz)** |
| 13.40-13.55 | **Alpgiray Turgut**<br>The Comparison of Anticandidal Activity derived from Protein and Non-protein Compounds of Two Penicillium species | **Mehmet Semih Bingöl**<br>Polar Membrane Preparation and Characterization |
| 13.55-14.10 | **Sumeyra Gurkok**<br>Antifungal potential of Serratia plymuthica chitinase against phytopathogens | **Hakan Kızıltaş**<br>Production and Characterization of TiO2 and NiS Doped TiO2 Nanotube Photocatalysts |
| 14.10.14.25 | **Ayşe Üstün**<br>Antibiofilm Effect of Levofloxacin-Loaded Polymeric Nanoparticles against Staphylococcus aureus | **Said Rajab ABDULLAHI**<br>Investigation of Effect of Initial Salt Concentration on Acid and Base Production From KCl Solution By Bipolar Membrane Electrodialysis |
| 14.25-14.40 | **Özge Çağlar**<br>The Effect of Hypericum Perforatum and Plantago Major Plant Extracts on Human Sh-Sy5y Cell Line | **Jale Naktiyok**<br>Copper hydroxide sulfate was synthesized by chemical precipitation method from a mixed solution of CuSO4 and NaOH |
| 14.40-14.55 | **Taner Tekin**<br>Synthesis of core-shell SiO2 / TiO2 Nanoparticles and Determination of their Photocatalytic Activity | **Ayşenur Öztürk**<br>Improvement water management in PEM fuel cell by using microporous layer with PDMS polymer and polystyrene-silica nanoparticles |
| **Break** | **Session-LH3 (Chair: Prof. Dr. Hasan Efeoğlu)** | **Session-LH8 (Chair: Assist. Prof. Dilek Okuyucu)** |
| 15.20-15.35 | **Günay Çakir**<br>Determining To Accuracy Of Geo-Referencing The Aerial Photographs And High-Resolution Satellite Image: Case Uludag, Bursa | **Ahmet Yasir Kanbur**<br>Was Leonardo Da Vinci's Golden Horn Bridge Possible? |
| 15.35-15.50 | **Meryem Samancı**<br>Graphene Aerogel Synthesis Methods for Energy Conversion and Storage Applications | **Emre Kuşkapan**<br>Smart Parking System: A Case Study of Istanbul |
| 15.50-16.05 | **Meltem Gör Bölen**<br>A Comparison of Proton transfer properties of PS and Nafion | **Mustafa Ali Dokuyucu**<br>Analysis of the Hunter-Saxton equation with Caputo-Fabrizio fractional derivative |
| 16.05-16.20 | **Sinan Kul**<br>Investigation of the Effect of Particulate Size and Mixing Speed on Copper Removal from Aqueous Solutions Used as Adsorbent Activated Sludge | **Abdourahamane Zakari Seybou**<br>Investigating the Relationship Between Summer Rainfall Variability in Niger and El Niño3 Index |
| 16.25-16.40 | **Elanur Aydın Karataş**<br>Molecular genetic and biochemical responses in primary human airway epithelial, liver hepatocytes and peripheral blood cell cultures exposed to zinc oxide based nanoparticles in vitro | **Özlem Çomaklı Sökmen**<br>Measurement Of Efficiency Of Branches For An Firm With Data Envelopment Analysis |
| 16.40-16.55 | **Mojtaba Farhangmehr**<br>The formation of transparent Glass-Ceramic thin film with changeable optical absorption | **Ferhat Yuna**<br>Arc Routing Problem and Solution Approaches in Directed Networks |
| **Break** | **Session-LH4 (Chair: Assoc. Prof. İ. Yücel Özbek)** | **Session-LH9 (Chair: Assist. Prof. Emin A. Oral )** |
| 17.15-17.30 | **Damla Rüzgar** | **Nida Kumbasar** |

| | Investigation Of Multiple Enzyme Activity of Thermophilic Bacillus Species | Classification of Images Obtained by SAR (Synthetic Aperture Radar) Data |
|---|---|---|
| 17.30-17.45 | **Merve Şimşek**<br>Isolation and Identification of Pigment Producing Bacteria and Evaluation of Their Usage Potentials as Biocolorants in Biotechnology | **Aslınur Ömeroğlu**<br>Object Detection with Faster R-CNN algorithm |
| 17.45-18.00 | **Mustafa Samet Çelik**<br>A Low Noise Amplifier at 1.5 GHz | **Rabiya Kılıç**<br>Detection Of Plant Disease From Plant İmage |
| 18.00-18.15 | **Muhammet Harun Osta**<br>Energy Analysis of Asphalt Plants | **Merve Polat**<br>Ship Detection |
| 18.15-18.30 | **Ayşe Bayrakçeken Yurtcan**<br>Drawbacks in Carbon Supported Electrocatalysts of PEM Fuel Cells | **Hilal Kübra Sağlam**<br>Detection of Diabetic Retinopathy with Integration of Deep Learning |
| 18.30-18.45 | **Serkan Bayar**<br>Reactive Red 45 of Textile Dyestuff Electrochemical Treatment | **Serdar AYDIN**<br>Fabrication and characterization of CdS/CdTe solar cells by electrochemical deposition |
| 18.45-19.00 | **Murat Han Ertuğrul**<br>The Effect of Mistletoe on The Growth of Scots Pine | **Osman Komut**<br>Assessment of The Vocational Qualifications Gained Through The Curriculum of The Forestry and Forestry Products Department |

| **POSTER SESSION (SCIENCE FACULTY ENTRANCE HALL)**<br>**NOVEMBER 27th-TUESDAY, 14:00-17:00** |
|---|
| **Süleyman Toy**<br>Evaluation of the effects of meteorological events on flights, example of Erzurum International Airport |
| **Ismayadi Ismail**<br>Synthesis of Carbon Nanotube from Waste Cooking Oil Catalysed by Mill Scale Waste for Development of Microstrip Patch Antenna |
| **Intan Helina Hasan**<br>Ferrites based thick film for enhanced microstrip patch antenna |
| **Fatma Bayrakçeken Nişancı**<br>Characterization and synthesis of high quality binary metal oxide electrode materials by electrochemical methods on conductive substrates |
| **Rosiah Osman**<br>Properties of Silica Ceramics derived from Rice Husk Ash |
| **Hilal Kübra Sağlam**<br>COMPARISON of 1300nm HYBRID DIODE LASERS with InGaAsP/InP MQW LASERS |
| **Raba'ah Syahidah Azis**<br>Magnetite (Fe3O4) nanoparticles as adsorbents for Cu removal from aqueous solutions |
| **Emine Öner**<br>Syntehesis and characterization of GA and GA/Ppy Support Materials for PEM Fuel Cell |
| **Rosnita A Talib**<br>Green Synthesis of Zinc Oxide and Application in Microbially Active Biopolymer Packaging Films |
| **Merve Acar**<br>Fabrication of WS2 Field Effect Device |
| **Mesut Eryiğit**<br>Electrochemical Fabrication Of Pedot/Ergo/Au Nanocomposite Electrodes For Dopamine Sensor |
| **POSTER SESSION (SCIENCE FACULTY ENTRANCE HALL)**<br>**NOVEMBER 27th-TUESDAY, 14:00-17:00** |
| **Emir Çepni**<br>Photoelectrochemical Properties of Electrochemical Fabricated TiO2 Nanostructures |
| **Bingül Kurt Urhan**<br>Lead Oxide-Electroreduced Graphene Oxide (PbO-ERGO) Nanocomposite for Non-enzymatic Glucose Sensor |
| **Muhammed Raşit Öner**<br>The Effect of Temperature on Acid and Base Production From NH4Cl-NaCl Salt Solution By Bipolar Membrane Electrodialysis |
| **Derya Tekin**<br>Synthesis And Characterization of RGO/TİO2/PVA Nanocomposite |
| **Elif Erçarikci**<br>Preparation OF ZnO Nanoparticles Using Polyol And Hydrothermal Methods |

| |
|---|
| **M.Dilruba Geyikoğlu** |
| Design And Production Of An Amperometry Device For Measuring Neurotransmitter Concentration |
| **İsmail Bezirganoğlu** |
| Response of five triticale genotypes to salt stress in in vitro culture |
| **Hamed Shamsi** |
| Sleep Stage Classification Using EEG Signals Based on Duration Depended Hidden Markova Model |
| **Özlem Barış** |
| Nanobiosynthesis of CdTe Quantum Dots by Viridibacillus arenosi K64 |
| **Mehmet Yılmaz** |
| Nanostructured Organic Semiconductor Thin Films as Surface Enhanced Raman Spectroscopy (SERS) Platforms |
| **Hakan Kızıltaş** |
| Production and Characterization of TiO2 and ZnS Doped TiO2 Nanotube Photocatalysts |

# ISASE2018

## SECRETARIAT

Prof. Dr. Mehmet Ertugrul : +90-533 6670124

Department of Electrical-Electronics Engineering,

Faculty of Engineering, Ataturk University,

25240 Erzurum, TURKEY

Orhan Yavuz Anfisi, Science Faculty (Fen Fakültesi), Erzurum

**Email** : isase2018@atauni.edu.tr

**Website** : https://isase2018.atauni.edu.tr